DNA-Modified Surfaces and Frameworks for Sensing and Imaging Applications

Jack Dismorr

A thesis submitted to the University of Birmingham for the degree of Doctor of Philosophy

School of Chemistry
College of Engineering and Physical Sciences
University of Birmingham
March 2024

Abstract

Nucleic acids act as biomarkers for a host of diseases and conditions. Various technologies, almost all employing some form of modified DNA, have been developed to sense extracellular nucleic acids. An important component of many nucleic acid biomarkers are single nucleotide variants (SNVs). SNVs are positions in DNA in which a single nucleotide or base pair is altered, and include single nucleotide polymorphisms, point deletions, and epigenetic mutations. Some SNVs are directly or indirectly linked to certain diseases, and therefore their detection can offer valuable diagnostic and prognostic information. Currently, fluorescence-based methods are the dominant approaches used to sense or map SNVs. Whilst effective, their drawbacks include the need for careful experimental design to avoid false-positives, the inability to interrogate the nature of a mutation (*i.e.*, to determine which other base is present), and their often complex and time-consuming nature.

Electrochemical sensing of SNVs offers an alternative to fluorescence, with the potential for greater synchronisation with our increasingly digital, device-led world. The bulk of this thesis reports on the development of a surface-immobilised heterobimetallic DNA probe capable of electrochemically distinguishing between nucleobases at a single site (*i.e.*, SNVs) in target DNA strands. Two redox-active complexes, a copper cyclidene macrocycle and a ferrocene unit, are incorporated into DNA using automated solid-phase synthesis. The copper cyclidene is incorporated internally and the ferrocene is appended to the 5′ end of the probe, with each producing a distinct electrochemical signal allowing for a ratiometric sensing approach. Key properties of the probe, including sensitivity, stability, and regeneration capability are determined. Clinically relevant SNV mutations associated with cancer and COVID-19 are detected using the bimetallic probe. Additionally, investigations into the SNV sensing

mechanism of the copper cyclidene, efforts to improve the sensitivity of the probe, and the expansion of targets to include RNA biomarkers are described.

Also included in this thesis is the functionalisation of metal-organic frameworks (MOFs) with fluorescently-modified DNA. MOFs are crystalline materials composed of metal ions or clusters connected through organic linkers, the different combinations of which allow for the tuning of a MOF's properties. The functionalisation of two different MOFs with complementary fluorescently-modified DNA, and efforts to bind them together *via* DNA hybridisation to create a single material that combines the properties of each individual MOF, are described herein.

Chapter 1 – Introduction

This chapter describes the structure and function of nucleic acids, their ability to act as biomarkers for certain diseases and conditions, and the artificial modification of oligonucleotides in the laboratory. Additionally, a review of fluorescence-based and electrochemical techniques used to sense nucleic acids is provided.

Chapter 2 – Techniques

This chapter provides an overview of the techniques used throughout this thesis.

Chapter 3 – Synthesis and Characterisation of Redox Labels and Modified DNA

This chapter describes the synthesis of the redox-active copper cyclidene and ferrocene phosphoramidites, and the design, synthesis, and characterisation of a library of modified DNA oligonucleotides used in this thesis.

Chapter 4 – Electrochemical Sensing of Single Nucleotide Variants Using Redox-Modified DNA Probes

This chapter describes the sensing of SNVs using the heterobimetallic probe synthesised in Chapter 3. The probe is immobilised onto the surface of an electrode to form a self-assembled monolayer, and key sensor properties are determined. SNVs in a well-studied test sequence are sensed, before the probe is used to detect clinically relevant SNVs associated with cancer, COVID-19, and epigenetic mutations.

Chapter 5 – Efforts to Understand, Enhance, and Expand the Sensing of Nucleic Acids Using Redox-Modified DNA Probes

This chapter firstly investigates the SNV sensing mechanism of the copper cyclidene, with a proposed mechanism incorporating: 1) the precise position of the copper cyclidene within the probe–target duplex; and 2) the thermodynamic stabilities of different probe–target duplexes. Efforts to improve the sensitivity of the probe using different probe designs and alternative electrochemical techniques are also described. Finally, the sensing of RNA targets as well as sensing in complex biological media are investigated.

Chapter 6 – Functionalisation of Metal-Organic Frameworks with Fluorescently-Modified DNA

This chapter describes the functionalisation of MOFs with complementary fluorescently-modified DNA and efforts to bind different MOFs together *via* DNA hybridisation. Cy3- and Cy5-modified oligonucleotides are attached to Hf- and Zr-based MOFs using copper-catalysed click chemistry. Efforts to bind these DNA-functionalised MOFs together *via* DNA hybridisation are described, as well as the detection of DNA hybridisation at the MOF surfaces using Cy3 → Cy5 Förster Resonance Energy Transfer emission.

Chapter 7 – Experimental

This chapter describes in detail the experimental procedures used to produce this thesis.

Chapter 8 – Appendix

This chapter includes additional data that supplements the main text of the thesis.

Acknowledgements

As with any meaningful work, this thesis would not be possible without the collaboration and help from a great many people. First and foremost, I would like to thank my primary supervisor, Professor James Tucker. Jim is the embodiment of a calm and encouraging PI; no matter what confusing result, equipment failure, or other setback, Jim will take the news in his stride and help to point you in the right direction. I am extremely grateful for his guidance and patience over the last four years. Additionally, I would like to thank my secondary supervisors Professor Tony Belli and Dr John Wilkie for their infrequent yet insightful input. Special thanks must also go to Dr Sarah Horswell, who, despite me not officially being her student, has dedicated many hours to helping and improving my research. Without a doubt, this thesis would be immeasurably poorer were it not for Sarah's efforts. A huge thank you also goes to the analytical team in the chemistry department, particularly Chris, who has patiently answered many more mass spec questions than I'd like to admit.

I would like to thank the extended Tucker group, both past and present: Francia, Edd, Georgina, Charlotte, Jake, Marium, Aldrich, Yifeng, La, Lydia, Liyao, Ruba, and an assortment of masters students. In particular, I'm thankful for Edd for showing me the dark arts of electrochemistry in the early days, and for Francia, the best post-doc any PhD student could hope to have. Additionally, I would like to thank my Sci-Phy cohort for sharing the trials and tribulations of the last five years together. A special shoutout goes to Patricia and Hugo, my fellow chemists, whose friendship and encouragement have made this journey that much more bearable. Thank you also to the brilliant people I've been lucky to live over the last few years: Matt, Kat, Aubrey, Dara, George, Meg and Sam – it's been a blast living in the wonderful city that is Birmingham with you.

Finally, thank you to my dearest and nearest. To Natalie, words cannot adequately describe my appreciation of your love and support over the last two years. Your calming presence has made the hardest part of any doctorate studies – the final third – infinitely more enjoyable. And to Mum, Dad and Will, I am eternally grateful for your unconditional love and support, no matter my endeavours and missteps. This thesis is dedicated to you.

Contents

1. Introduction 1
1.1. Nucleic Acids: Structure, Stability, and Function 1
1.1.1. Nucleotide Structure 1
1.1.2. Double-Helix Structure 2
1.1.3. Duplex Stability 4
1.1.4. Biological Function of Nucleic Acids 5
1.2. Nucleic Acids as Biomarkers 6
1.2.1. Cell-Free Nucleic Acids 6
1.2.2. Single Nucleotide Variants 7
1.3. Modified Nucleic Acids 9
1.3.1. Base Modification 9
1.3.2. Sugar Ring Modification 12
1.3.3. Phosphate Backbone Modification 15
1.3.4. Common Fluorescent and Electrochemical Modifications 16
1.4. Sensing Nucleic Acids 18
1.4.1. Fluorescence-Based Nucleic Acid Sensing 18
1.4.2. Electrochemical Nucleic Acid Sensing 22
1.5. Summary 26
1.6. References 28
2. Techniques 34
2.1. Automated Solid-Phase DNA Synthesis 34
2.1.1. Nucleobase Phosphoramidites 34
2.1.2. DNA Synthesis Cycle 35
2.1.3. Ultramild Conditions 38
2.2. High Performance Liquid Chromatography 38
2.2.1. Reversed-Phase High Performance Liquid Chromatography 39
2.3. Mass Spectrometry 40
2.3.1. Ionisation Methods 40
2.3.2. Data Analysis 41
2.4. Thermal Melting 41
2.4.1. Ultraviolet Thermal Melting 41
2.4.2. Fluorescent Thermal Melting 42
2.5. Ultraviolet Visible Spectroscopy 43
2.5.1. Oligonucleotide Concentration Determination 44

2.6. Fluorescence Spectroscopy 44
2.7. Electrochemical Techniques....46
2.7.1. Electrochemical Setup....46
2.7.2. Cyclic Voltammetry 49
2.7.3. Square Wave Voltammetry 53
2.8. Self-Assembled Monolayer Formation 55
2.9. Confocal Fluorescence Microscopy 57
2.10. References 59
3. Synthesis and Characterisation of Redox Labels and Modified DNA....61
3.1. Introduction 61
3.1.1. Electrochemical Modifications....61
3.1.2. Linking Modifications....62
3.1.3. Fluorescent Modifications....63
3.1.4. Spacer Modifications....64
3.2. Redox Label Synthesis 65
3.2.1. Copper Cyclidene Macrocycle Phosphoramidite Synthesis....65
3.2.2. Ferrocene Phosphoramidite Synthesis....71
3.3. Oligonucleotide Probe Synthesis....72
3.3.1. General Design Considerations....72
3.3.2. Oligonucleotide Synthesis....76
3.3.3. Oligonucleotide Purification 77
3.3.4. Oligonucleotide Characterisation and Quantification 81
3.4. References 83
4. Electrochemical Sensing of Single Nucleotide Variants using Redox-Modified DNA Probes...85
4.1. Introduction 85
4.1.1. Fluorescent Intercalators and Reporter/Quencher Probes 85
4.1.2. Fluorescent Microarrays and Sequencing Technologies....87
4.1.3. Electrochemical Mismatch Detection....88
4.1.4. Electrochemical Enzymatic Single Nucleotide Variant Sensing....89
4.1.5. Electrochemical Ratiometric Single Nucleotide Variant Sensing....91
4.1.6. Electrochemical Copper Macrocycle Single Nucleotide Variant Sensing 92
4.2. Chapter Aims....93
4.3. Probe Design and Self-Assembled Monolayer Formation 94
4.3.1. Probe Design and Function 94
4.3.2. Confirming Self-Assembled Monolayer Formation....96
4.3.3. Evaluating Probe Electrochemical Characteristics....97

4.3.4. Probe Surface Coverage 99
4.3.5. Electrochemical Electrode Roughening 100
4.4. Thermal Melting Studies 102
4.5. Key Properties and Sensing 104
4.5.1. Ratiometric Sensing 104
4.5.2. Detection of Binding Events and Selectivity 106
4.5.3. Electrochemical Stability Studies 106
4.5.4. Limit of Detection 109
4.5.5. Probe Regeneration 113
4.6. Electrochemical Single Nucleotide Variant Sensing 115
4.6.1. Test Probe 115
4.6.2. Cancer-Based Probes 117
4.6.3. COVID-19-Based Probes 120
4.6.4. Methylated Cytosine 122
4.7. Conclusions and Future Work 124
4.8. References 126
5. Efforts to Understand, Enhance, and Expand the Sensing of Nucleic Acids Using Redox-Modified DNA Probes 130
5.1. Overview and Chapter Aims 130
5.2. Investigations into the Single Nucleotide Sensing Mechanism 131
5.2.1. Sensing with (*S*)-T1 131
5.2.2. Duplex Stability and Electrochemical Current Signal Correlation 132
5.2.3. Target Saturation and SAMs Assembled from Preformed Duplexes 133
5.2.4. Proposed SNV Sensing Mechanism and Solution Versus Surface Differences 138
5.2.5. Through-DNA Charge Transport Studies 140
5.3. Efforts to Enhance the Sensing of CuCy-/Fc-Modified Probes 148
5.3.1. Increasing Probe Sensitivity 148
5.3.2. Modification Sequence Position and Effect on Electrochemical Signal 151
5.3.3. Square Wave Voltammetry: Initial Studies 155
5.3.4. Square Wave Voltammetry: Buffer/Electrolyte Studies 157
5.3.5. Square Wave Voltammetry: Frequency and Amplitude Studies 160
5.3.6. Differential Pulse Voltammetry Studies 168
5.4. Expanding Sensing to RNA Targets and Complex Media 170
5.4.1. Sensing RNA Targets 170
5.4.2. Sensing in Complex Media 172
5.4.3. miR135-1 Probe Studies 174

5.5. Conclusions and Future Work 178
5.6. References 181
6. Functionalisation of Metal-Organic Frameworks with Fluorescently-Modified DNA 184
6.1. Introduction 184
6.1.1. Structure of MOFs 184
6.1.2. Applications of MOFs 185
6.1.3. Post-Synthetic DNA Functionalisation of MOFs 187
6.1.4. Förster Resonance Energy Transfer 191
6.2. Chapter Aims 192
6.3. Design and Pre-Functionalisation Studies of DNA 193
6.3.1. DNA Design 193
6.3.2. Thermal Melting Studies 194
6.3.3. Solution Fluorescence Spectroscopy 196
6.4. MOF Synthesis and Characterisation 199
6.5. DNA Functionalisation and Confocal Imaging 201
6.5.1. DNA Functionalisation of MOFs 201
6.5.2. DNA-Functionalised MOF Binding Efforts 204
6.6. Conclusions and Future Work 208
6.7. References 210
7. Experimental 213
7.1. Chemical Syntheses 213
7.1.1. Copper Cyclidene Phosphoramidite Synthesis 214
7.1.2. Ferrocene Phosphoramidite Synthesis 220
7.2. Oligonucleotide Synthesis 226
7.2.1. Standard Synthesis 226
7.2.2. Ultramild Synthesis 227
7.3. Oligonucleotide Purification 228
7.3.1. Purification of CuCy- and Fc-Modified Oligonucleotides 228
7.3.2. Purification of Cy3- and Cy5-Modified Oligonucleotides 228
7.3.3. Purification of C3 Spacer-Modified and Unmodified Oligonucleotides 229
7.4. Oligonucleotide Characterisation 229
7.5. Thermal Melting Studies 231
7.6. Electrochemistry 231
7.6.1. Equipment and Preparation 231
7.6.2. Self-Assembled Monolayer Preparation 232
7.6.3. Electrochemical Sensing Procedure 233

7.7. Fluorescence Spectroscopy 233
7.8. MOF Synthesis and Characterisation 234
7.8.1. MOF Synthesis 234
7.8.2. MOF Characterisation 235
7.8.3. DNA Functionalisation of MOFs 235
7.9. Confocal Fluorescence Microscopy 236
7.9.1. Sample Preparation 236
7.9.2. Confocal Microscope Setup 236
7.9.3. Imaging and Analysis 237
7.10. References 238
8. Appendix 239
8.1. Modified Oligonucleotide Characterisation 239
8.2. Electrochemical Sensing of Single Point Variants Using Redox-Modified DNA Probes 264
8.2.1. Self-Assembled Monolayer Formation 264
8.2.2. Single Point Variant Probe Thermal Melting Data 267
8.2.3. Electrochemical Stability Cyclic Voltammograms 272
8.2.4. Limit of Detection Cyclic Voltammograms 272
8.2.5. Destructive Probe Regeneration Using Sonication 273
8.2.6. Electrochemical Single Point Variant Sensing 273
8.3. Efforts to Understand, Enhance, and Expand 282
8.3.1. Representative (*S*)-T1 Sensing Cyclic Voltammograms 282
8.3.2. Mismatched and Abasic Duplexes Thermal Melting Data 283
8.3.3. Mismatched and Abasic Duplexes Cyclic Voltammograms and Processed Anodic Traces 284
8.3.4. High Target Concentration and Preformed Duplex SAM Cyclic Voltammograms 285
8.3.5. T1-21mer and B1-30mer Thermal Melting Data and Cyclic Voltammograms 288
8.3.6. 1 nM Target Sensing with (*S*)-T1 and Mg^{2+}-Containing Solution 289
8.3.7. Shifted Modification Location Cyclic Voltammograms and Thermal Melting Data 289
8.3.8. Square Wave Voltammetry Studies 291
8.3.9. T1 Sensing RNA Targets and Thermal Melting Data 292
8.3.10. T1 Cyclic Voltammograms in Buffer/Serum Solutions 294
8.3.11. miR135-1 Thermal Melting Data and 1 nM Target Sensing 295
8.4. Functionalisation of Metal-Organic Frameworks with Fluorescently-Modified DNA 296
8.4.1. Fluorescently-Modified Oligonucleotide Thermal Melting Data 296
8.4.2. Solution Fluorescence Spectroscopy 298
8.4.3. MOF Characterisation 299

Abbreviations

5mC – 5-methylcytosine

A – Adenine

C – Cytosine

cf – cell-free

CPG – Controlled Pore Glass

CuAAC – Copper-catalysed Azide-Alkyne Cycloaddition

CuCy – Copper Cyclidene

CV – Cyclic Voltammogram

Cy3 – Cyanine 3

Cy5 – Cyanine 5

DBCO – Dibenzylcyclooctyne

DCM – Dichloromethane

ddNTP – dideoxynucleotide

DPV – Differential Pulse Voltammogram

DIPEA – N,N-diisopropylethylamine

DMF – Dimethylformamide

DMT – Dimethoxytrityl

DNA – Deoxyribonucleic Acid

EDTA – Ethylenediaminetetraacetic Acid

λ_{em} – Emission Wavelength

ΔE_p – Peak Separation

E_p^a – Anodic Peak Potential

E_p^c – Cathodic Peak Potential

ESI – Electrospray Ionisation

λ_{ex} – Excitation Wavelength

EXPAR – Exponential Isothermal Amplification Reaction

Fc – Ferrocene

FRET – Förster Resonance Energy Transfer

G – Guanine

HPLC – High Performance Liquid Chromatography

HOMO – Highest Occupied Molecular Orbital

IC – Internal Conversion

IR – Infrared

ISC – Intersystem Crossing

LAMP – Loop-Mediated Isothermal Amplification

LNA – Locked Nucleic Acid

LOD – Limit of Detection

MALDI – Matrix Assisted Laser Desorption Ionisation

MB – Methylene Blue

MeOH – Methanol

miRNA – microRNA

MOF – Metal-Organic Framework

mRNA – Messenger RNA

MS – Mass Spectrometry

m/z – Mass (m) to Charge (z) ratio

NGS – Next Generation Sequencing

NMR – Nuclear Magnetic Resonance

PBS – Phosphate Buffered Saline

PCR – Polymerase Chain Reaction

PEG – Polyethylene Glycol

PNA – Peptide Nucleic Acid

qPCR – quantitative Polymerase Chain Reaction

R_f – Retention Factor

RFU – Relative Fluorescence Units

RNA – Ribonucleic Acid

rRNA – Ribosomal RNA

RP – Reversed Phase

RT – Room Temperature

SAM – Self-Assembled Monolayer

SBU – Secondary Building Unit

SD – Standard Deviation

SEM – Scanning Electron Microscopy

SNP – Single Nucleotide Polymorphism

SNV – Single Nucleotide Variant

SWV – Square Wave Voltammogram

T – Thymine

TCA – Trichloroacetic Acid

TCEP – Tris(2-carboxyethyl) Phosphine

TEAA – Triethylammonium acetate

THF – Tetrahydrofuran

TLC – Thin Layer Chromatography

T_m – Thermal Melting Temperature

TOC – Time of Flight

UNA – Unlocked Nucleic Acid

UV – Ultraviolet

UV/Vis – Ultraviolet/Visible

Chapter 1: Introduction

1.1. Nucleic Acids: Structure, Stability, and Function

1.1.1. Nucleotide Structure

Nucleic acids are biopolymers that play an essential role in all known organisms. There are two main types of nucleic acid: deoxyribonucleic acid (DNA) and ribonucleic acid (RNA). The monomers of nucleic acids are nucleotides. A standalone nucleotide (Figure 1.1) consists of a pentose sugar ring, a nitrogenous base, and one to three phosphate groups.[1,2] In DNA, the pentose sugar is deoxyribose, whilst in RNA, the pentose sugar is ribose. The pentose sugar consists of five carbon atoms labelled 1′ through to 5′. The base attaches to the 1′ carbon *via* a glycosidic bond and the phosphate group attaches to the 5′ carbon. Attachment of the base to the 1′ carbon results in the formation of a nucleoside. Attachment of one to three phosphate groups to the nucleoside results in the formation of a nucleotide.

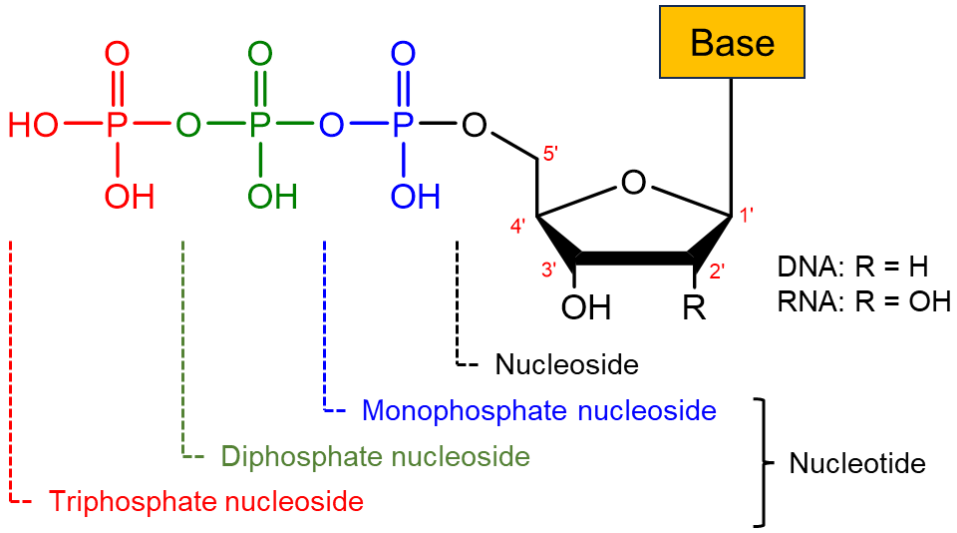

Figure 1.1: Nucleotide structure.

Five main nitrogenous bases are found in nature (Figure 1.2).[1,2] Adenine and guanine are the bicyclic purine bases, whereas cytosine, thymine, and uracil are the monocyclic pyrimidine

bases. Adenine, guanine, cytosine, and thymine are present in DNA. In RNA, uracil replaces thymine.

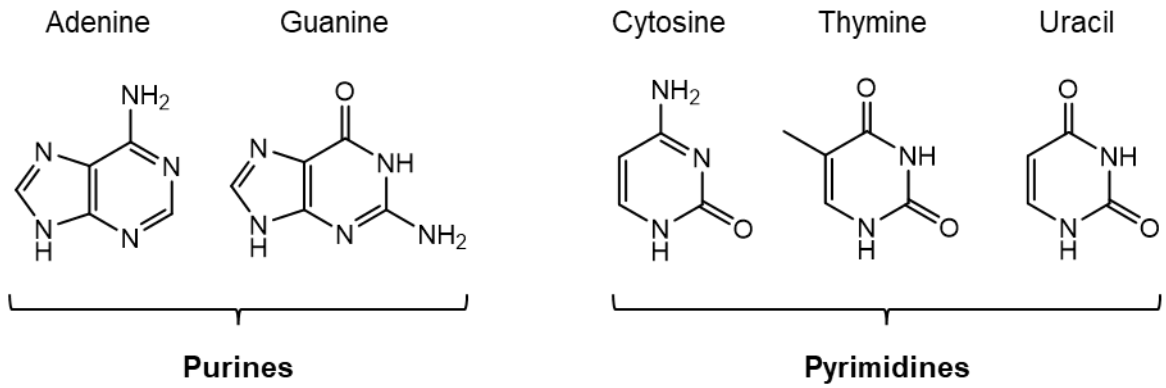

Figure 1.2: Nitrogenous base structures. Adenine, guanine, cytosine, and thymine are present in DNA; uracil replaces thymine in RNA.

1.1.2. Double-Helix Structure

Nucleotide monomers link together to form DNA or RNA strands (Figure 1.3).[1,2] The phosphate group attached to the 5′ carbon atom undergoes a condensation reaction with the 3′ hydroxyl group of another nucleotide to form a phosphodiester bond. Under physiological conditions, the hydroxyls on the phosphate groups are deprotonated, imparting a negative charge to the nucleic acid. The arrangement of nucleotides in a nucleic acid sequence is depicted linearly, starting with the nucleotide at the 5′ end and ending with the nucleotide at the 3′ end. Two complementary nucleic acid strands can bind together to form a duplexed double-helix structure. The two strands are held together by hydrogen bonding between the bases: two hydrogen bonds between adenine and thymine/uracil, and three hydrogen bonds between cytosine and guanine. The two strands run antiparallel to each other, with one strand running from 5′ to 3′ and other running from 3′ to 5′.

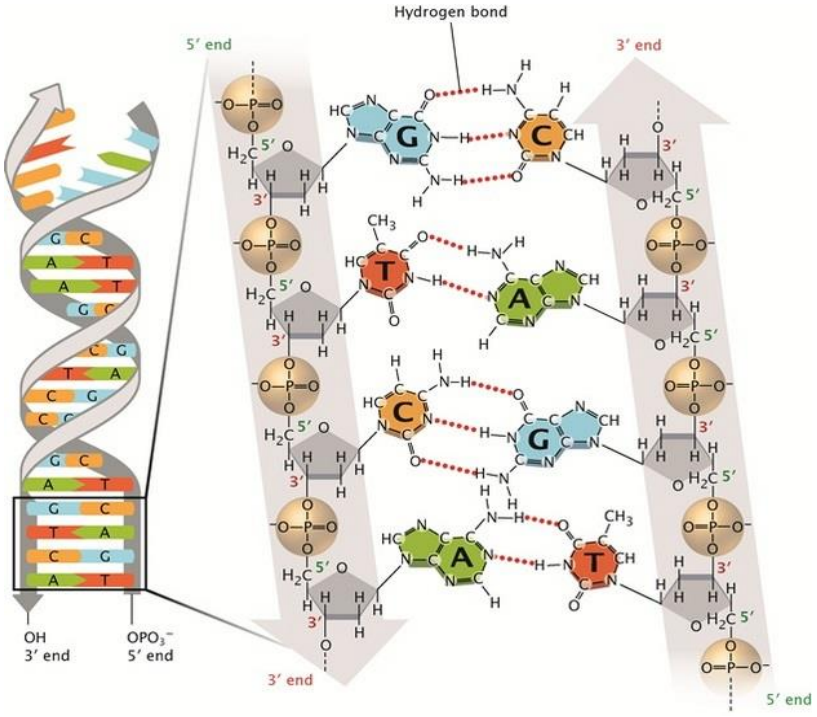

Figure 1.3: : The double-helix structure of DNA, with the hydrogen bonding between bases displayed. (Taken from reference 3.)

Three main double-helix DNA structures are known to exist in nature: B-form, A-form, and Z-form (Figure 1.4).[1,2] B-form DNA is the dominant structure present in the genome of cells, and is characterised by its right-handed helical twist and alternating major and minor grooves. A-form DNA also exhibits a right-handed helical twist and major and minor grooves, whilst possessing a larger helix diameter and base pairs that are more tilted relative to the helical axis compared with B-form DNA. Z-form DNA is markedly different from the B- and A- forms, exhibiting a left-handed helical twist, repeating units of not one, but two base pairs, and a zig-zagging instead of a smooth line connecting the phosphorus atoms in the phosphodiester backbone. RNA can also form double-helix structures. RNA is typically found single-stranded in nature but an RNA strand can duplex with itself and also form heterogeneous duplexes with complementary DNA. Duplexed RNA does not adopt a B-form structure[1] and has instead been found to adopt varieties of A-form[4] and Z-form[5] structures dependent on base sequence and salt concentration.

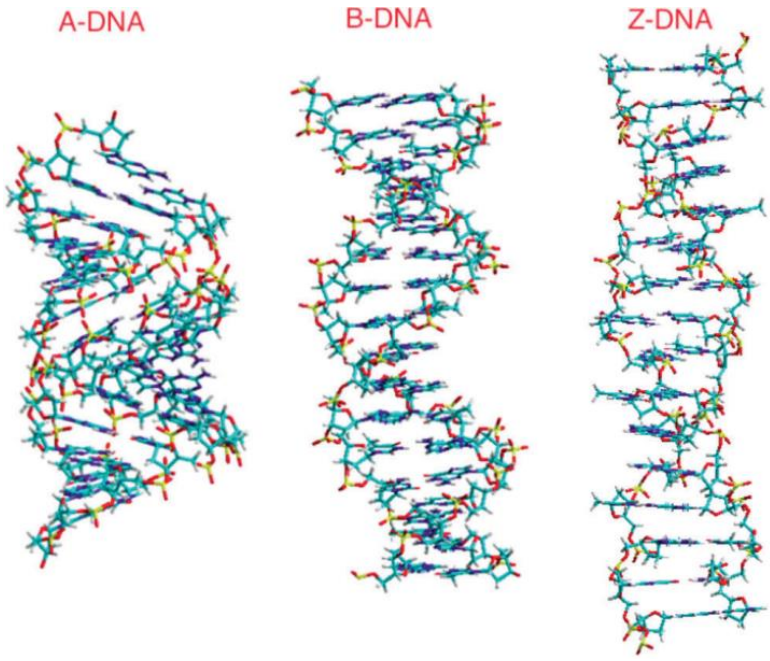

Figure 1.4: Molecular structures of the three double-helix DNA structures found in nature: A-DNA, B-DNA, and Z-DNA. (Taken from reference 6.)

1.1.3. Duplex Stability

The stability of a double-stranded DNA duplex is determined by several factors. Maximum stability is achieved when complementary base-pairing is perfect. Mismatches present in shorter duplexes have a significant negative effect on duplex stability, with certain mismatches (notably A-A, T-T, C-T, and C-A) being particularly impactful.[7,8] Base stacking, whereby interactions between the aromatic bases results in net attraction between adjacent stacked nucleotides, produces an even greater stabilising effect than fully complementary base-pairing.[9] Environmental factors such as salt composition/concentration and temperature also have a significant effect on duplex stability.[1,10] Cations such as alkaline earth metal ions have a stabilising effect on DNA duplexes by negating the negative charges lining the phosphodiester backbones and thus minimising repulsive electrostatic interactions between two duplexed strands. RNA duplexes are predominantly forced into the more rigid A-form by the 2′ hydroxyl groups, enhancing their thermal stability relative to the less rigid B-form DNA tends to adopt.[11]

However, the 2′ hydroxyl makes RNA more susceptible to hydrolysis reactions, making RNA less chemically stable than DNA.[2]

1.1.4. Biological Function of Nucleic Acids

The primary function of nucleic acids is the storage and transmission of genetic information.[1,2] Most organisms have a DNA-based genome but many viruses have RNA-based genomes. A gene is a section of an organism's genome that codes for a protein. The sequence of bases in a gene dictates the order in which amino acids are pieced together to form proteins, which play an integral role in the growth, function, and reproduction of all known organisms. A gene is first transcribed into messenger RNA (mRNA) which consists of the sequence of bases in the gene in RNA form. The ribosome then reads the genetic code carried by the mRNA and translates it into a protein (Figure 1.5).

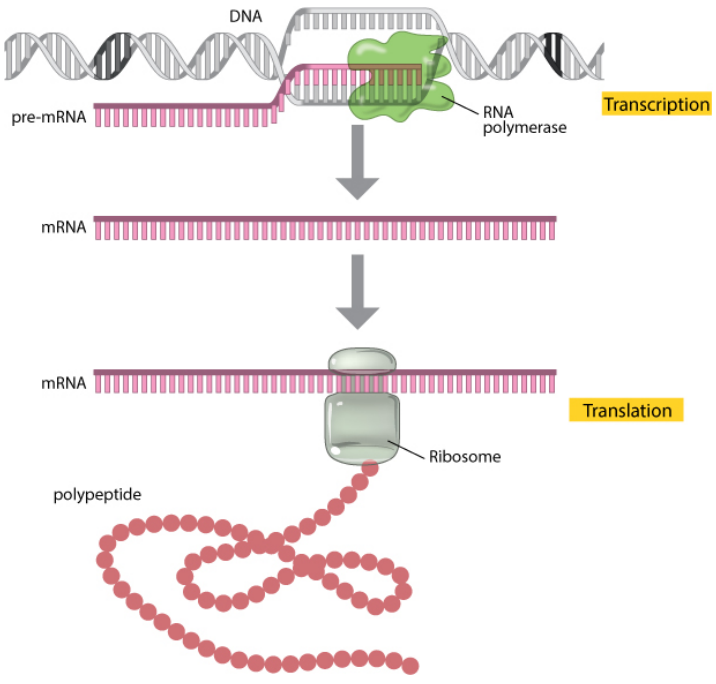

Figure 1.5: The synthesis of a polypeptide (protein) *via* transcription and translation. (Taken from reference 12.)

Although the storage and transmission of genetic information is the primary function of nucleic acids, they also perform other biological processes. RNA in particular adopts a diverse array of forms and undertakes a multitude of functions. Over half of the ribosome itself consists of ribosomal RNA (rRNA)[13] and RNA in the form of ribozymes act as biocatalysts for various biochemical reactions.[14] microRNAs (miRNAs), short (17–25 bases) noncoding RNA sequences, modulate gene expression post-transcriptionally and their dysregulation plays an important role in many diseases.[15] Long noncoding RNA, sequences of RNA more than 200 bases long that do not code for any proteins, are abundant in organisms and affect processes varying from transcription regulation to chromosomal stability.[16]

1.2. Nucleic Acids as Biomarkers

1.2.1. Cell-Free Nucleic Acids

Nucleic acids that exist outside of cells are termed cell-free (cf) nucleic acids.[17] Cf-DNA is fragmented DNA that is present in bodily fluids and mostly remains double-stranded.[18] Fragment lengths vary greatly and depend on their origin: cf-DNA released *via* apoptosis (controlled cell death) are approximately 70–200 base pairs in length, whilst cf-DNA released *via* necrosis (cellular death caused by cell injury) can be thousands of base pairs long.[18] Degradation and clearance of cf-DNA occurs in the blood (by DNA-degrading enzymes) and organs (liver, kidney, spleen, and lymph nodes), with the half-life of cf-DNA typically ranging from several minutes to two hours.[18] Cf-DNA has particular diagnostic and prognostic value for cancer patients, with higher cf-DNA levels in the blood indicative of more advanced tumour progression.[19,20] Cf-DNA also acts as a biomarker for a multitude of other diseases and conditions, including autoimmune diseases,[21] organ transplantation acceptance,[22] and stroke severity.[23]

Extracellular miRNAs are present in significant quantities in almost all bodily fluids, including blood, saliva, urine, and even tears.[24] Although single-stranded, miRNAs seldom exist in isolation and are usually bound to proteins or encapsulated within exosomes or microvesicles.[25] Because of their conjugation with proteins and the protection afforded by lipid bilayers, extracellular miRNAs are relatively stable and can remain in a bodily fluid for significantly longer than a typical cf-DNA fragment.[25] Although the biological function of extracellular miRNAs is not yet completely understood, there is a broad consensus that inter-cell signalling relating to gene expression is their primary biological function.[26] As with cf-DNA, extracellular miRNAs act as biomarkers for a host of different cancers.[27] Approximately 70% of known miRNAs are expressed in the brain[28] and, as such, multiple central nervous system disorders have been associated with miRNA dysregulation.[29] Extracellular miRNAs have also been identified as biomarkers for a variety of other diseases and conditions, including diabetes,[30] cardiovascular disease,[31] and viral infections.[32]

1.2.2. Single Nucleotide Variants

Single nucleotide variants (SNVs) are positions in the genome in which a single nucleotide or base pair is altered. Here, 'SNV' is used as an umbrella term and includes alterations such as single nucleotide polymorphisms (SNPs), point deletions, and epigenetic mutations. Figure 1.6 shows an SNP in which a single nucleotide (and its paired nucleotide) is changed from one duplexed DNA strand to the other. SNPs are defined as base pair variations at specific points in the germline DNA that occur in >1% of the population.[33] Although many have no effect on the encoded proteins, many others do affect the phenotypic expression of the genome and some are directly or indirectly linked to certain diseases.[34] Examples include SNPs associated with increased risk of Alzheimer's Disease,[35] cancer susceptibility,[36] and the body's response to fighting off infectious diseases.[37]

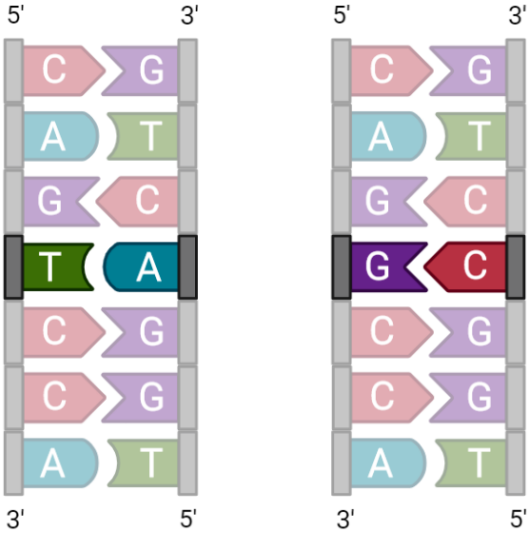

Figure 1.6: A SNP, with the relevant bases highlighted. The T–A base pair in the left duplex is replaced by a G–C base pair in the right duplex.

Epigenetic SNVs involve the natural modification of specific locations in the genome and are crucial in controlling genome regulation and expression.[38] The methylation of cytosine at the C5 position to produce 5-methylcytosine (5mC, Figure 1.7) is the prime example of an epigenetic mutation. In eukaryotic genomes, 5mC is mostly found in CpG dinucleotides (a cytosine followed by a guanine in the 5′ to 3′ direction) and affects gene regulation, DNA repair, and chromosome structure.[39] Localised hyper-methylation[40] and genome-wide hypo-methylation[41] have been associated with cancer, and therefore 5mC can act as a cancer biomarker dependent on its location in the genome. Dozens of other naturally occurring modified DNA bases have been discovered,[42] and their importance to the functioning of the genome is underlined by the army of enzymes dedicated to their formation and regulation.[43] Given their fundamental biological significance, the identification of epigenetic mutations will help to advance our understanding in the roles they play in normal genomic functioning and abnormal genomic pathology.

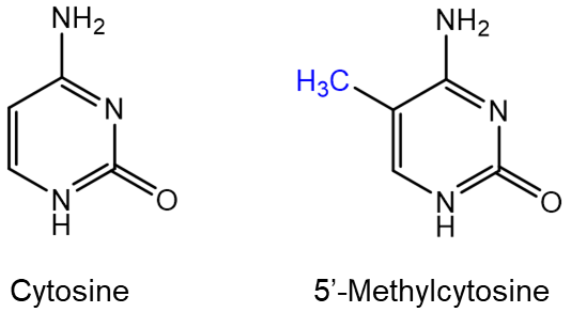

Figure 1.7: Structures of cytosine (left) and 5mC (right), with the additional methyl group in blue.

1.3. Modified Nucleic Acids

Nature's ability to alter the basic building blocks of nucleic acids to increase their functionality can and has been replicated in the laboratory. Artificially modifying nucleic acids seeks to impart added properties whilst retaining those that makes them so useful, namely their molecular recognition and structural stability. Modifications to a nucleic acid are intended to impart various properties, the most common being sensing ability (fluorescent and electrochemical), resistance to enzymatic degradation, and therapeutic properties. Different parts of the structure of a nucleic acid can be modified, examples of which are discussed below.

1.3.1. Base Modification

Artificial modification of the bases varies from relatively minor adjustments to complete replacement with unrelated groups. The N7 and C8 sites of purines, and the C5 site of pyrimidines, are often modified as they do not participate in base-pairing and are more synthetically accessible.[44] Examples of more limited alterations include modified bases such as 6-hydroxylaminopurine, in which the replacement of one of the amino hydrogen atoms with a hydroxyl group in adenine (Figure 1.8, left) imparts mutagenic properties owing to its ambivalent coding capacity.[45] The mutagenicity of 6-hydroxylaminopurine is such that it has been investigated for its antibacterial properties in an effort to develop novel antibiotics.[46] Other

simple synthetically modified bases include 2-aminopurine, in which the amine in adenine is moved to the 2-position of the purine ring (Figure 1.8, right). This simple alteration imparts fluorescent properties not observed with canonical bases and has been used to probe nucleic acid structures.[47]

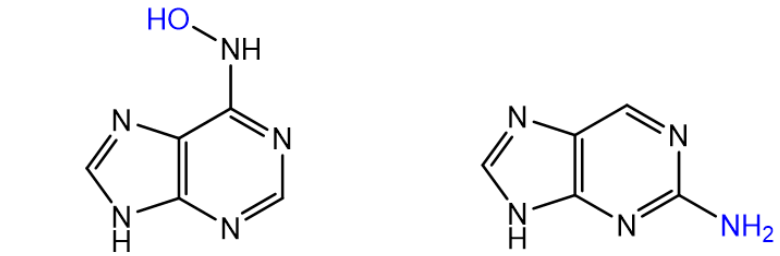

6-N-Hydroxylaminopurine 2-Aminopurine

Figure 1.8: Structures of 6-N-hydroxylaminopurine (left) and 2-aminopurine (right), with the modified components highlighted in blue.

More complex base modifications include adding larger groups to the base. Azide-alkyne click chemistry provides a simple route for the labelling of bases with fluorescent and redox-active labels, peptides, and other reporter groups under relatively mild conditions.[48] An illustrative example is the formation of fluorescent coumarin dye conjugates using bases modified with terminal alkynes reported by Seela and coworkers (Figure 1.9).[49] Starting with non-fluorescent precursors, the formation of strongly fluorescent 1,2,3-triazole conjugates in the presence of a copper catalyst can be used for the visualisation of DNA in solution or *in vivo*. Functional groups can also be attached to the bases by other means, including using amide,[50,51] alkene,[51,52] and alkyne[51,52] linkers.

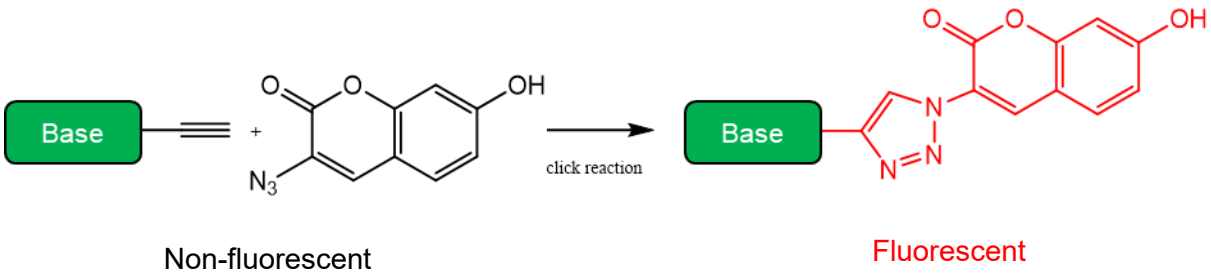

Figure 1.9: Click reaction reported by Seela and coworkers generating a fluorescent nucleoside analogue from non-fluorescent precursors. (Adapted from reference 49.)

More drastic still is the replacement of the bases entirely. Whereas modified bases still often retain their ability to base-pair, replacement will usually prevent this and have a correspondingly negative impact on duplex stability. In return, replacement of the bases and their relatively limited properties with more active groups offers enhanced functionality.[53] An early example is the incorporation of polycyclic aromatic hydrocarbons such as naphthalene, phenanthrene and pyrene reported by Kool and coworkers.[54] In addition to their fluorescent properties, the planar hydrophobic DNA base analogues exhibited stacking that was even more favourable than the stacking interactions observed between natural bases.[55] More recently, Kool and coworkers have developed phenethnylpyrene base analogues which, when adjacent to one another, produced green excimer fluorescence (Figure 1.10).[56] Upon irradiation at 365 nm, the alkynyl groups underwent cycloaddition and a rapid colour change to blue occurred. When combined with a redshifted dye acceptor (the cyanine dye Cy3) a colour change of orange to blue was observed in both the test tube and in human kidney cells.

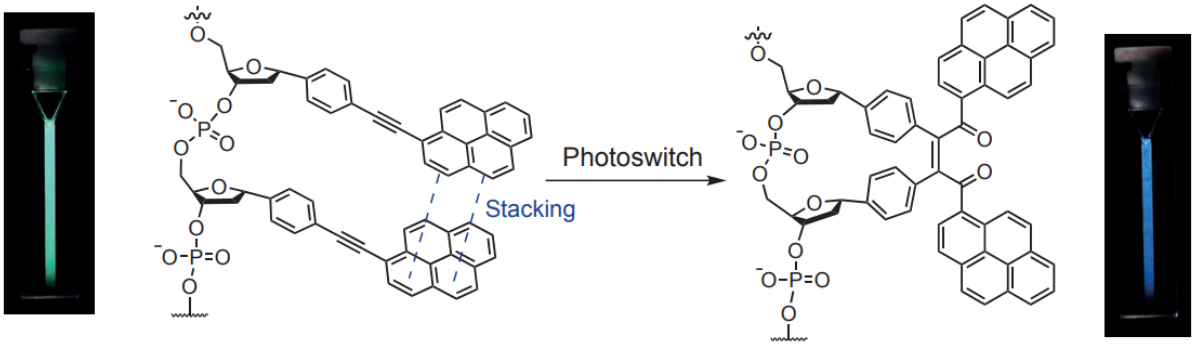

Figure 1.10: Photoreaction of adjacent phenethnylpyrene DNA base analogues resulting in a colour change of green to blue. (Taken from reference 56.)

1.3.2. Sugar Ring Modification

Modification of the sugar ring often occurs at the 2′ and 4′ carbon atoms. A key example are locked nucleic acids (LNAs), in which a methylene bridge links a 2′ oxygen atom with the 4′ carbon atom (Figure 1.11, left). LNAs exhibit a high resistance to nucleases, with even one strategically located LNA nucleotide in a sequence of otherwise natural nucleotides significantly decreasing rates of enzymatic degradation.[57,58] LNA-containing oligonucleotides also exhibit a high affinity for complementary DNA and RNA, with LNA/DNA and LNA/RNA hybrid duplexes adopting the rigid A-form conformation and having accordingly high thermal stabilities.[59] Even simple modifications of the 2′ carbon atom such as methoxy and fluorine substituents (Figure 1.11, middle) confer protective properties against nucleases.[60,61] Breakage of the sugar ring between the 2′ and 3′ carbons forms an unlocked nucleic acid (UNA) structure (Figure 1.11, right). Incorporation of UNA nucleotides increases the flexibility of an oligonucleotide, however at the expense of the thermal stability of duplexes it forms with complementary DNA/RNA.[62]

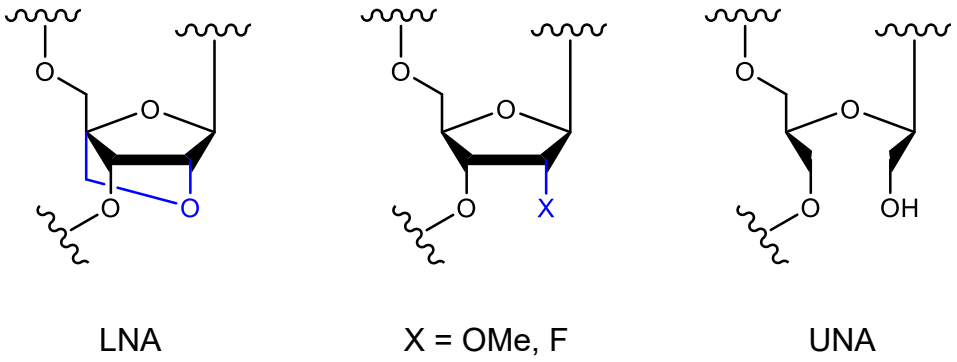

Figure 1.11: Structures of LNA (left), 2C' substituted nucleic acid (middle) and UNA (right).

Removal of the sugar ring whilst leaving the phosphodiester backbone intact has also been reported. Threoninol mimics the 3′ and 5′ hydroxyl groups, and the 3-carbon spacer between them, of a natural sugar ring (Figure 1.12) and can be incorporated into an oligonucleotide using phosphoramidite chemistry (discussed in detail in Chapter 2). A functional group can be attached *via* the amine to effectively replace an entire nucleoside. Because of the two chiral centres present in threoninol, the orientation of the reporting group within the oligonucleotide and the duplexes it forms can be changed depending on the isomer chosen. Using certain isomers of threoninol, Tucker and coworkers incorporated the fluorescent group anthracene into DNA probes.[63,64] The anthracene produced a different fluorescent response depending on the base opposite in the probe–target duplex, which allowed for the discrimination between different base pair mismatches. Threoninol and similar moieties have been used to incorporate a range of functional groups into DNA for purposes as varied as nick sealing,[65] photo-cross-linking,[66] and chiral sensing.[67]

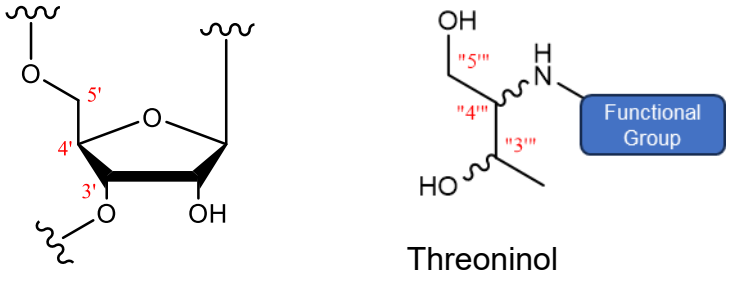

Figure 1.12: Structures of an unmodified DNA sugar ring (left) and threoninol (right), with the analogous carbons

Another key example of modified nucleic acids in which entire nucleosides are replaced are the metal cyclidene complexes also reported by Tucker and coworkers.[68] Macrocyclic cyclidene complexes with a Cu^{2+} or Ni^{2+} central cation, first synthesised by Kowalski and coworkers,[69,70] were incorporated into DNA in either a tagged or a linked system (Figure 1.13). In the tagged system (Figure 1.13, left) the core structure of the phosphodiester backbone was essentially left intact, with three carbon atoms separating the phosphate groups and the cyclidene itself protruding into the space a normal nucleoside would occupy. In the linked system (Figure 1.13, right) the cyclidene was effectively built into the backbone, occupying the space that multiple phosphate groups would occupy in a normal oligonucleotide. In the tagged system, the planar cyclidene was found to be able to intercalate into the duplex formed with complementary DNA. The redox-active Cu^{2+} and Ni^{2+} cations allowed for the generation of an electrochemical signal. The (*R*)-isomer of the Cu^{2+} cyclidene (CuCy) in the tagged system was able to discriminate electrochemically between all four bases in a sequence of target DNA. CuCy and its base-discriminating ability is discussed in detail in subsequent chapters and forms the basis of much of this thesis.

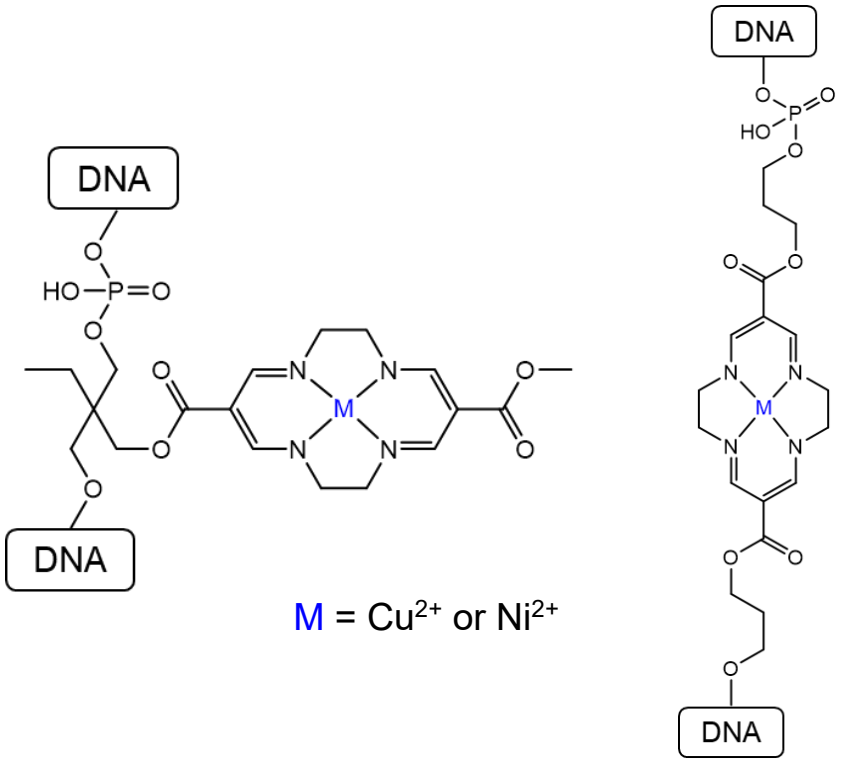

Figure 1.13: Structures of the tagged (left) and linked (right) metal cyclidene complexes reported by Tucker and coworkers. (Adapted from reference 68.)

1.3.3. Phosphate Backbone Modification

One example of a modified nucleic acid backbone has already been presented in the form of the linked cyclidene system discussed in section 1.3.2. However, as the name suggests, the cyclidene acted more as part of a chain linking two separate oligonucleotides together and inhibited base-pairing with a single complementary DNA target. Other modifications alter the natural phosphodiester backbone whilst still allowing the modified oligonucleotide to base-pair with a complementary nucleic acid. Simple modifications such as phosphorothioate DNA and phosphoroamidate DNA (Figure 1.14, left) alter the phosphate groups themselves. In phosphorothioate DNA, a non-bridging oxygen atom is replaced with a sulphur atom, and in phosphoroamidate DNA, a bridging oxygen atom is replaced with a nitrogen atom. As with many of the sugar modifications discussed above, a key benefit of such phosphate modifications is the enhanced resistance to nuclease degradation that they confer.[71,72] Additionally, both

phosphorothioate DNA and phosphoroamidate DNA exhibit increased binding affinities for their targets compared with unmodified DNA.[71,72] Peptide nucleic acids (PNAs) are DNA/RNA analogues that replace the phosphodiester backbone with repeating units of *N*-2-aminoethylglycine connected with peptide bonds (Figure 1.14, right). The uncharged backbone of PNA allows for stronger hybridisation with complementary DNA/RNA because of the lack of electrostatic repulsion.[73] PNAs also exhibit strong resistance to nuclease degradation and can therefore function *in vivo* for longer periods of time compared with analogous DNA/RNA oligonucleotides.[73]

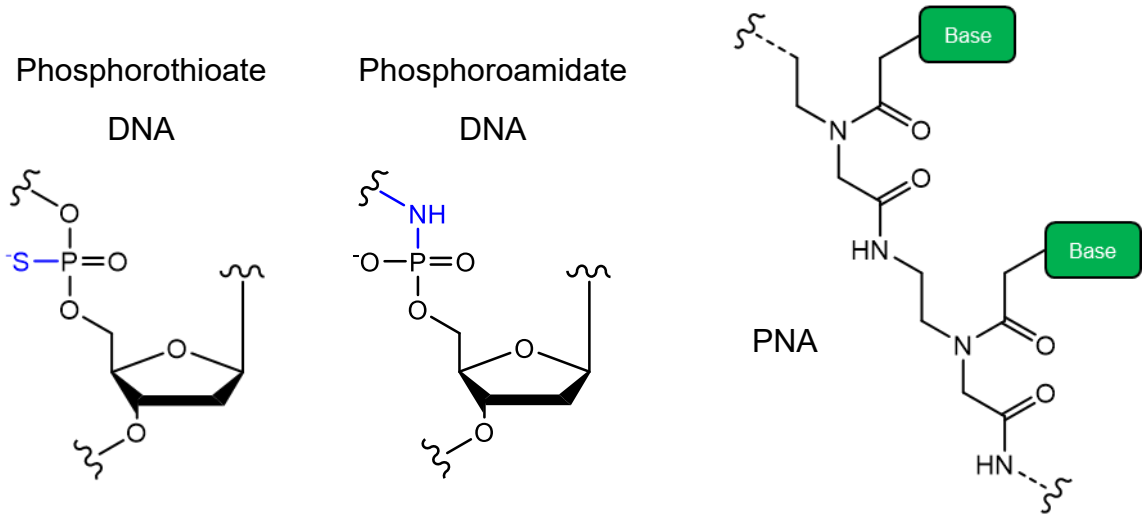

Figure 1.14: Structures of phosphorothioate and phosphoroamidate (left), and the structure of PNA (right).

1.3.4. Common Fluorescent and Electrochemical Modifications

A number of fluorophores are commonly incorporated into DNA for sensing or imaging applications. They are typically appended to the end of the oligonucleotide but can also be incorporated internally. Commercially, by far the most common use of fluorophore-labelled DNA is in real-time quantitative PCR (qPCR) as molecular beacon and TaqMan probes, the functioning of which is described in detail in section 1.4.1. These probes each incorporate a fluorescent reporter group and a quenching group. A fluorophore can act as either a reporter or

a quencher depending on the emission of its paired fluorophore. Common examples of DNA-modifying fluorophores used in real-time qPCR include FAM (6-carboxyfluorescein), TAMRA (6-carboxytetramethylrhodamine), and the cyanine family of dyes (Figure 1.15).

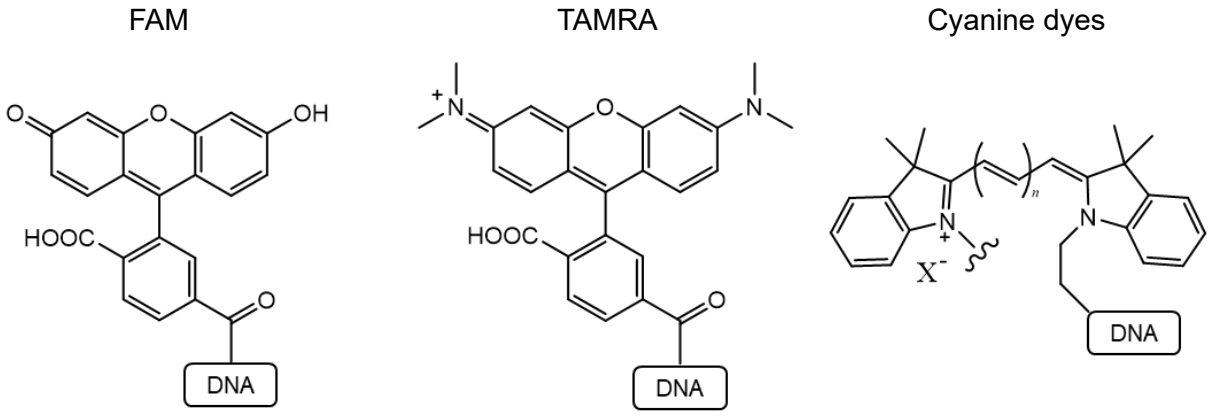

Figure 1.15: The fluorescent modifications FAM (left), TAMRA (middle), and cyanine dyes (right).

By comparison, no redox-modified nucleic acid is used as widely as fluorescent DNA probes are in qPCR. However, the last 25 years have seen the extensive reporting of the synthesis and application of redox-modified DNA, of which the cyclidene-modified DNA reported by Tucker and coworkers discussed above is an example.[68] The primary application of redox-modified DNA is the sensing of nucleic acids, key examples of which are discussed below in section 1.4.2. As with fluorophore-labelled DNA, a handful of electrochemical modifications are commonly used. In particular, methylene blue (MB) and ferrocene (Fc) are amongst the most popular. MB (Figure 1.16, left) undergoes a two electron and one proton transfer oxidation/reduction at physiological pH.[74] In addition to being covalently incorporated into an oligonucleotide, solution-based MB also interacts with single-stranded and double-stranded DNA differently and can therefore be used as a hybridisation indicator.[74] Fc consists of a central Fe^{2+} cation sandwiched between two cyclopentadienyl rings (Figure 1.16, right). The Fe^{2+} is d^6 and each cyclopentadienyl ring is allocated a single negative charge. Fc is redox-active owing

to the Fe^{2+}/Fe^{3+} redox couple, highly stable, and easily functionalised.[75] Fc and its incorporation into DNA is used extensively throughout this thesis and is discussed further in subsequent chapters.

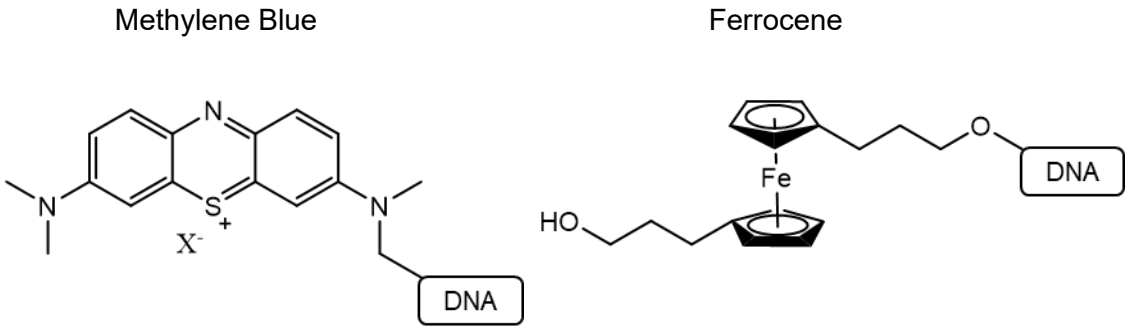

Figure 1.16: The electrochemical modifications methylene blue (left) and ferrocene (right).

1.4. Sensing Nucleic Acids

1.4.1. Fluorescence-Based Nucleic Acid Sensing

Real-time qPCR is the commercially dominant method for the detection and quantification of nucleic acids. In real-time qPCR, a variety of fluorescent reporters are used to signal the presence of a target nucleic acid. These include a host of dyes that intercalate into double-stranded DNA, of which one of the most commonly used is SYBR Green I (Figure 1.17).[76] SYBR Green I belongs to the cyanine dye family and is excited at 480 nm and emits at 520 nm. Once intercalated into double-stranded DNA, the mobility of SYBR Green I is greatly reduced, causing more of its energy, when excited, to be released as fluorescence. Therefore, in the presence of SYBR Green I, more double-stranded DNA results in increased fluorescent emission. SYBR Green I is thus used to monitor the amplification of double-stranded DNA as signalled by an increase in fluorescence. Real-time qPCR plots (cycle number versus fluorescent signal) can then be used to absolutely or relatively quantify a nucleic acid target. The major drawback to SYBR Green I and other intercalating dyes is that they bind to double-

stranded DNA in a largely non-specific manner.[77] Although not usually a problem during PCR amplification, owing to the vast majority of double-stranded DNA being amplified from target DNA, additional testing is sometimes required to confirm that the amplicon generated is the product of the target nucleic acid.

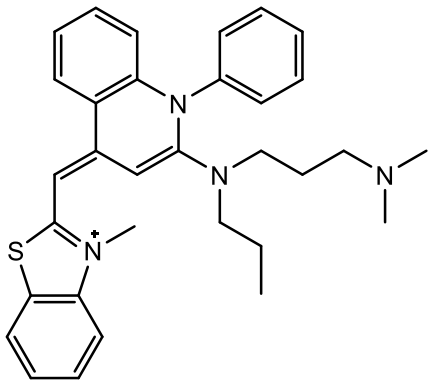

Figure 1.17: Structure of SYBR Green I.

Reporters in the form of fluorophore-modified DNA offer a more specific mode of nucleic acid sensing. Fluorescent molecular beacons are DNA probes modified with a fluorescent reporter group at one end and a quenching group at the other (Figure 1.18).[78] In the unbound state molecular beacons partially hybridise with themselves to form a hairpin structure that brings the reporter and quencher into close proximity, quenching fluorescent emission. In the presence of target nucleic acid the molecular beacon unfolds and binds with the target to form the thermodynamically more stable probe–target duplex, removing the reporter and quencher from close proximity to one another and thus resulting in increased fluorescent emission. In a real-time qPCR run employing a molecular beacon specific to the target nucleic acid, fluorescence increases as more amplified DNA is produced. Unlike intercalating dyes, molecular beacons are specific to the target and therefore an increase in fluorescence should only be observed if said target is present. However, there is the risk of molecular beacons

unfolding due to non-specific interactions[79] and also the presence of nucleases resulting in probe degradation,[80] both events leading to false positives.

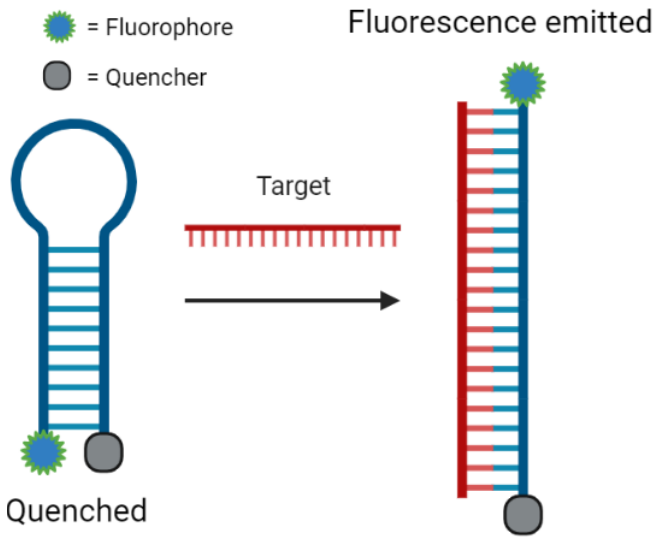

Figure 1.18: Schematic diagram of the functioning of a fluorescent molecular beacon.

The Taqman assay is another fluorescently-labelled DNA probe commonly used as a reporter group in real-time qPCR.[81] Like molecular beacons, Taqman probes are modified with a fluorescent reporter group at one end and a quenching group at the other (Figure 1.19). The probes are short enough such that the reporter is quenched whilst the probe is intact. The probes are also designed to bind specifically to a section of the target DNA being amplified. Taq polymerase, with its 5′ to 3′ exonuclease activity, cleaves the Taqman probe as it synthesises the target DNA, separating the reporter from the quencher and resulting in an increase in fluorescence. As more target DNA is amplified, more Taqman probe is cleaved and more fluorescent emission is observed. Unlike molecular beacons, the functioning of Taqman probes is dependent on the exonuclease activity of Taq polymerase and therefore can only be used in a real-time qPCR setup. However, as the design of Taqman probes does not need to facilitate

structures such as hairpins, shorter sequences can be used and moieties such as minor groove binders can be appended to increase the binding affinity to the target sequence.[82,83]

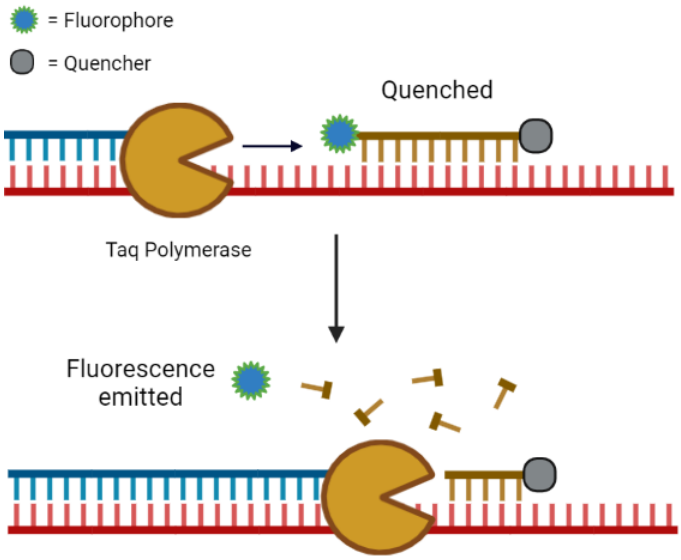

Figure 1.19: Schematic diagram of the functioning of a Taqman probe.

Other methods employing fluorescence are also used to sense nucleic acids. Microarrays typically involve running fluorescently labelled target nucleic acids (or copies/analogues of) across a plate containing microscopic pores with DNA probes immobilised within them.[84] The probes capture complementary labelled target nucleic acids and after a washing step the fluorescent signal of each pore corresponds to the amount of target captured. Gene expression analysis, whereby RNA is extracted from cells and used to determine which genes are ultimately being translated into proteins, has been the primary application of microarrays.[84,85] Sequencing methods, recently spearheaded by some variants of Next Generating Sequencing (NGS) technologies and their use of fluorescently-modified nucleotides, can also be used to sense nucleic acids.[86,87] They are ideal for determining the exact make-up of nucleic acids known or thought to be biomarkers of disease. However, microarrays and sequencing technologies have not supplanted real-time qPCR in detecting and quantifying nucleic acids and have instead been

employed in more niche applications. Furthermore, all of the fluorescent methods discussed above – real-time qPCR, microarrays, and sequencing technologies – remain the province of well-equipped labs and require specialist training to operate.

1.4.2. Electrochemical Nucleic Acid Sensing

Electrochemical nucleic acid sensors have the potential to improve on the weaknesses of fluorescent-based sensors, with results often produced in minutes, limited training and equipment required, and high sensitivities reported without the use of target amplification.[88,89] Typically, electrochemical nucleic acid sensors involve DNA probes modified with redox labels such as MB and Fc. The probes are usually immobilised onto the surface of an electrode to form self-assembled monolayers (SAMs), which are discussed in detail in Chapter 2. Probe–target binding modulates the electrochemical output of the redox labels to enable the sensing of the target. Amongst the simplest examples are redox-modified hairpin probes.[90,91] In their most basic form, the unbound probe adopts a hairpin conformation that holds a redox label close to the electrode surface, resulting in efficient electron transfer (Figure 1.20). Binding of the target removes the redox label from close proximity to the electrode surface, resulting in reduced electron transfer and a drop in current signal. More recent adaptations include the cleaving of the hairpin using the target-triggered nonspecific DNA cleaving activity of CRISPR/Cas12a proteins[92] and target-catalysed hairpin assembly.[93]

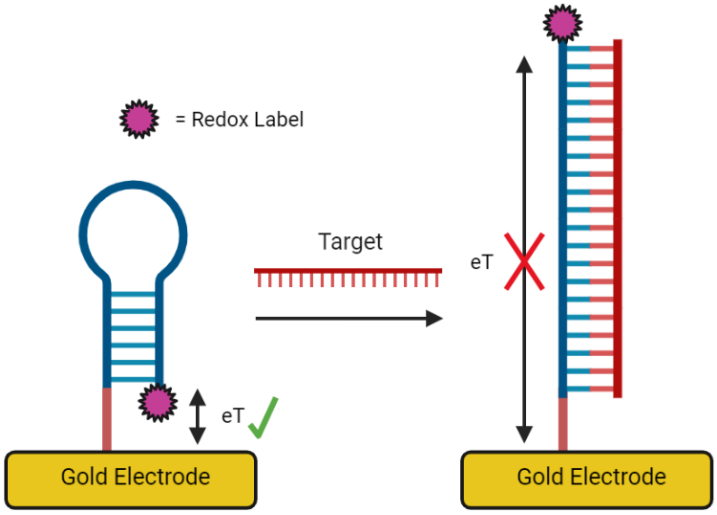

Figure 1.20: Schematic diagram of the functioning of a redox-modified hairpin probe.

Alternatively, other sensors have functioned by the probe's bringing a redox label closer to the electrode surface. Plaxco and coworkers' DNA 'pseudoknot' unravelled in the presence of target DNA to allow the MB to more easily reach the electrode surface (Figure 1.21).[94] The pseudoknot was also tested by sensing target spiked into blood serum, making it one of the minority of electrochemical sensors reported to have been tested with a physiologically relevant medium. Similarly, Ricci and coworker's sensor involved a probe that formed a triplex structure with target DNA *via* Watson-Crick and Hoogsteen interactions, bringing the attached MB closer to the electrode surface and generating an increased signal.[95]

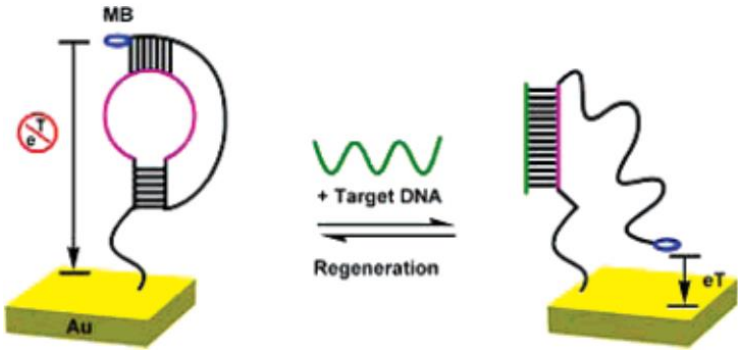

Figure 1.21: Plaxco and coworkers' pseudoknot. (Taken from reference 94.)

Multiple probes have been employed in the same sensor. Lai and Yu's involved a capture probe and a MB-modified signal probe, both surface-immobilised (Figure 1.22).[96] In the absence of target DNA both probes partially hybridised, removing the MB from the electrode surface. In the presence of target DNA the signal probe was displaced and formed a hairpin structure, bringing the MB closer to the electrode surface and generating an increased current signal. As with the pseudoknot described above, the sensor was also tested by sensing target in (diluted) blood serum. Plaxco and coworkers reported on a similar sensor but with the MB-modified signal probe not surface-immobilised and instead remaining partially hybridised to the surface-immobilised capture probe with and without target present.[97] The sensor reported an impressive limit of detection (LOD) of 0.4 pM.

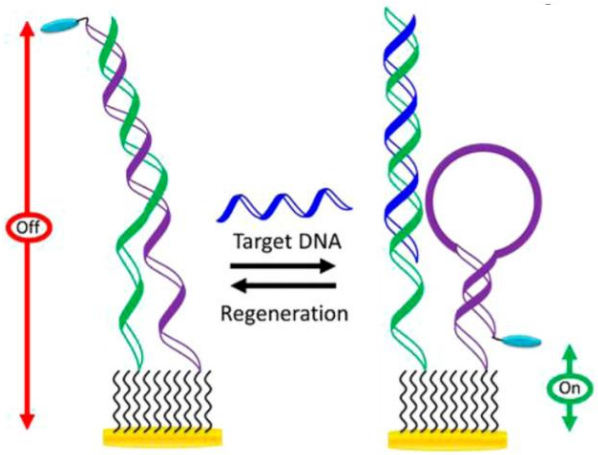

Figure 1.22: Lai and Yu's surface-immobilised capture and signal probes. (Taken from reference 96.)

Other sensors have employed multiple redox labels. Ellington and coworkers reported on a simple hairpin sensor modified with an additional Fc at its surface-bound end in addition to a MB at the 5′ terminal end (Figure 1.23).[98] Whilst the MB was removed from the electrode surface upon target binding, Fc remained relatively unmoved and therefore produced a constant current signal with and without target. This enabled a ratiometric sensing mechanism whereby

the current of the MB was divided by the current of the Fc, which proved more reproducible than using just the MB alone. Another benefit of having a constant redox signal acting as an internal reference is the assurance it brings regarding sensor integrity: if the reference signal remains constant, this indicates that the probes remain attached to the electrode surface. Using a ratiometric sensing mechanism can also account for signal drift, provided the two current signals drift in concert and the difference between them remains constant.[99]

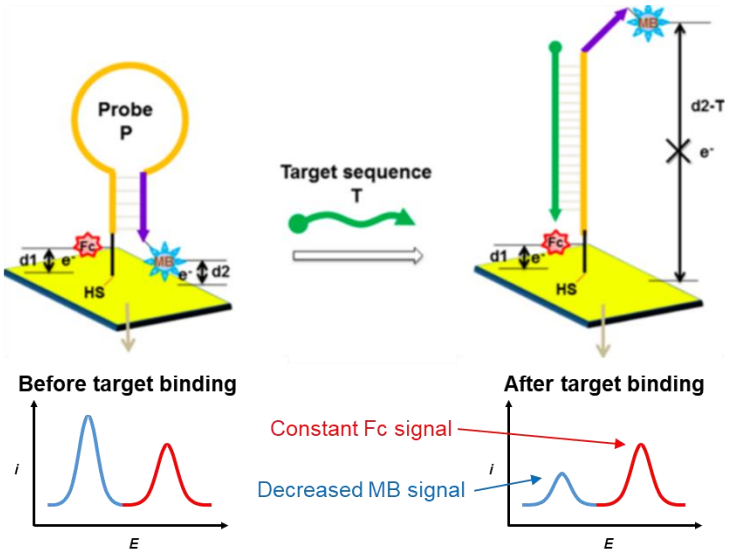

Figure 1.23: Ellington and coworkers ratiometric sensor with a dual-modified probe in which the Fc acted as a constant internal reference. (Taken and adapted from reference 98.)

Other sensors employing multiple redox labels involve a ratiometric sensing mechanism in which both signals change upon target addition. Lai and Yang's sensor adapted the capture/signal probes discussed above by modifying the capture probe with a MB and the signal probe with a Fc (Figure 1.24).[100] Upon target binding to the capture probe, Fc was able to move closer to the electrode whilst MB moved further away. Similarly, Chen and coworkers' sensor employed a surface-immobilised MB-modified signal probe partially hybridised to a Fc-modified capture probe.[101] Upon a miRNA target binding to the Fc-modified capture probe and floating away, the signal probe formed a hairpin structure which brought the MB closer to the

electrode surface, achieving a remarkably low LOD of 2.3 fM. Ratiometric sensing mechanisms in which two redox signals change upon target addition should result in larger and more definitive changes than those in which just one redox signal changes, potentially enhancing sensitivity. However, the lack of a constant internal reference means that sensor integrity may be harder to assess.

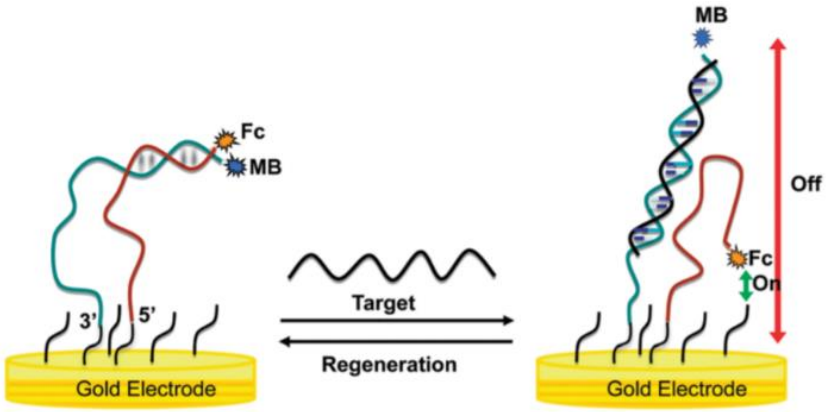

Figure 1.24: Lai and Yang's ratiometric sensor in which both the MB and Fc signals changed upon target addition. (Taken from reference 100.)

1.5. Summary

Nucleic acids are essential to the functioning of all known organisms. Although their primary function is the storage and transmission of genetic information, they also perform other essential biological tasks such as biocatalytic and cellular signalling activities. Nucleic acids act as biomarkers for certain diseases and conditions. In particular, being able to quantify the presence of cf-DNA and extracellular miRNAs, and detect the presence of SNVs, offers valuable diagnostic and prognostic information. Nucleic acids have been extensively modified in the lab in an attempt to enhance their functionality whilst maintaining their intrinsic useful properties, namely their molecular recognition capability and structural stability. Modifications ranging from minor base alterations to complete replacement of nucleosides and the phosphodiester backbone have been reported. The functionalities that nucleic acid modification most often

seeks to impart include fluorescent and electrochemical properties, resistance to nuclease degradation, and enhanced target binding affinities. Fluorophore-labelled nucleic acids and nucleotides currently play essential roles in commercially dominant sensing and sequencing technologies, usually in tandem with PCR amplification. Sensing using redox-modified nucleic acids offers an alternative sensing modality, with potential improvements over fluorescent-based systems including faster readout times, amplification-free sensing, and greater synchronisation with our increasingly digital, device-led world.

1.6. References

1. G. M. Blackburn, J. K. Watts, M. Egli and M. J. Gait, *Nucleic Acids in Chemistry and Biology*, Royal Society of Chemistry, Cambridge, 2022.
2. D. Voet and J. G. Voet, *Biochemistry*, Wiley & Sons, New York, 2011.
3. Nature, https://www.nature.com/scitable/topicpage/discovery-of-dna-structure-and-function-watson-397/, (accessed January 2023).
4. Y. Tanaka, S. Fujii, H. Hiroaki, T. Sakata, T. Tanaka, S. Uesugi, K.-i. Tomita and Y. Kyogoku, *Nucleic Acids Res.*, 1999, **27**, 949-955.
5. K. Hall, P. Cruz, I. Tinoco Jr, T. M. Jovin and J. H. Van De Sande, *Nature*, 1984, **311**, 584-586.
6. B. R. Wood, *Chemical Society Reviews*, 2016, **45**, 1980-1998.
7. R. B. Wallace, J. Shaffer, R. F. Murphy, J. Bonner, T. Hirose and K. Itakura, *Nucleic Acids Res.*, 1979, **6**, 3543-3557.
8. S. Ikuta, K. Takagi, R. B. Wallace and K. Itakura, *Nucleic Acids Res.*, 1987, **15**, 797-811.
9. P. Yakovchuk, E. Protozanova and M. D. Frank-Kamenetskii, *Nucleic Acids Res.*, 2006, **34**, 564-574.
10. A. Singh and N. Singh, *Phys. A (Amsterdam, Neth.)*, 2015, **419**, 328-334.
11. S. Wang and E. T. Kool, *Biochemistry*, 1995, **34**, 4125-4132.
12. Nature, https://www.nature.com/scitable/topicpage/translation-dna-to-mrna-to-protein-393/, (accessed January 2023).
13. H. F. Noller, *Annu. Rev. Biochem.*, 1984, **53**, 119-162.
14. J. A. Doudna and T. R. Cech, *Nature*, 2002, **418**, 222-228.
15. Y. Huang, X. J. Shen, Q. Zou, S. P. Wang, S. M. Tang and G. Z. Zhang, *J. Physiol. Biochem.*, 2011, **67**, 129-139.
16. K. C. Wang and H. Y. Chang, *Mol. Cell*, 2011, **43**, 904-914.
17. M. Szilágyi, O. Pös, É. Márton, G. Buglyó, B. Soltész, J. Keserű, A. Penyige, T. Szemes and B. Nagy, *Int. J. Mol. Sci.*, 2020, **21**, 6827.
18. A. Kustanovich, R. Schwartz, T. Peretz and A. Grinshpun, *Cancer Biol. Ther.*, 2019, **20**, 1057-1067.
19. H. Schwarzenbach, D. S. B. Hoon and K. Pantel, *Nat. Rev. Cancer*, 2011, **11**, 426-437.
20. S. Volik, M. Alcaide, R. D. Morin and C. Collins, *Mol. Cancer Res.*, 2016, **14**, 898-908.

21. B. Duvvuri and C. Lood, *Front. Immunol.*, 2019, **10**, 502.
22. E. Gielis, K. Ledeganck, D. Winter, J. Del Favero, J.-L. Bosmans, F. Claas, D. Abramowicz and M. Eikmans, *Am. J. Transplant.*, 2015, **15**, 2541-2551.
23. K. V. Glebova, N. N. Veiko, A. A. Nikonov, L. N. Porokhovnik and S. V. Kostuyk, *Crit. Rev. Clin. Lab. Sci.*, 2018, **55**, 55-70.
24. J. A. Weber, D. H. Baxter, S. L. Zhang, D. Y. Huang, K. H. Huang, M. J. Lee, D. J. Galas and K. Wang, *Clin. Chem.*, 2010, **56**, 1733-1741.
25. A. Turchinovich, L. Weiz, A. Langheinz and B. Burwinkel, *Nucleic Acids Res.*, 2011, **39**, 7223-7233.
26. J. A. Makarova, M. U. Shkurnikov, D. Wicklein, T. Lange, T. R. Samatov, A. A. Turchinovich and A. G. Tonevitsky, *Prog. Histochem. Cytochem.*, 2016, **51**, 33-49.
27. G. Di Leva and C. M. Croce, *Curr. Opin. Genet. Dev.*, 2013, **23**, 3-11.
28. X. W. Cao, G. Yeo, A. R. Muotri, T. Kuwabara and F. H. Gage, *Annu. Rev. Neurosci.*, 2006, **29**, 77-103.
29. K. F. Meza-Sosa, D. Valle-García, G. Pedraza-Alva and L. Pérez-Martínez, *J. Neurosci. Res.*, 2012, **90**, 1-12.
30. H. Zhu and S. W. Leung, *Diabetologia*, 2015, **58**, 900-911.
31. A. Kaur, S. T. Mackin, K. Schlosser, F. L. Wong, M. Elharram, C. Delles, D. J. Stewart, N. Dayan, T. Landry and L. Pilote, *Cardiovasc. Res.*, 2020, **116**, 1113-1124.
32. L. Tribolet, E. Kerr, C. Cowled, A. G. Bean, C. R. Stewart, M. Dearnley and R. J. Farr, *Frontiers in Microbiology*, 2020, DOI: 10.3389/fmicb.2020.01197.
33. R. Karki, D. Pandya, R. C. Elston and C. Ferlini, *BMC Med. Genomics*, 2015, **8**, 37.
34. A. A. Komar, *Single Nucleotide Polymorphisms*, Springer, New York, 2009.
35. H. Li, S. Wetten, L. Li, P. L. S. Jean, R. Upmanyu, L. Surh, D. Hosford, M. R. Barnes, J. D. Briley and M. Borrie, *Arch. Neurol.*, 2008, **65**, 45-53.
36. N. Deng, H. Zhou, H. Fan and Y. Yuan, *Oncotarget*, 2017, **8**, 110635-110649.
37. N. W. Schröder and R. R. Schumann, *Lancet Infect. Dis.*, 2005, **5**, 156-164.
38. G. Egger, G. Liang, A. Aparicio and P. A. Jones, *Nature*, 2004, **429**, 457-463.
39. M. Ehrlich and R. Y.-H. Wang, *Science*, 1981, **212**, 1350-1357.
40. J. F. Costello, M. C. Frühwald, D. J. Smiraglia, L. J. Rush, G. P. Robertson, X. Gao, F. A. Wright, J. D. Feramisco, P. Peltomäki and J. C. Lang, *Nat. Genet.*, 2000, **24**, 132-138.

41. M. A. Gama-Sosa, V. A. Slagel, R. W. Trewyn, R. Oxenhandler, K. C. Kuo, C. W. Gehrke and M. Ehrlich, *Nucleic Acids Res.*, 1983, **11**, 6883-6894.
42. A. J. Sood, C. Viner and M. M. Hoffman, *J. Cheminf.*, 2019, **11**, 1-10.
43. E.-A. Raiber, R. Hardisty, P. van Delft and S. Balasubramanian, *Nat. Rev. Chem.*, 2017, **1**, 1-13.
44. A. Shivalingam and T. Brown, *Biochem. Soc. Trans.*, 2016, **44**, 709-715.
45. M. T. Abdul-Masih and M. J. Bessman, *J. Biol. Chem.*, 1986, **261**, 2020-2026.
46. S. S. Krajewski, I. Isoz and J. Johansson, *Nucleic Acids Res.*, 2017, **45**, 1914-1924.
47. D. Ward, E. Reich and L. Stryer, *J. Biol. Chem.*, 1969, **244**, 1228-1237.
48. A. H. El-Sagheer and T. Brown, *Chem. Soc. Rev.*, 2010, **39**, 1388-1405.
49. F. Seela, V. R. Sirivolu and P. Chittepu, *Bioconjugate Chem.*, 2008, **19**, 211-224.
50. J. D. Vaught, C. Bock, J. Carter, T. Fitzwater, M. Otis, D. Schneider, J. Rolando, S. Waugh, S. K. Wilcox and B. E. Eaton, *J. Am. Chem. Soc.*, 2010, **132**, 4141-4151.
51. M. Kuwahara, J.-i. Nagashima, M. Hasegawa, T. Tamura, R. Kitagata, K. Hanawa, S.-i. Hososhima, T. Kasamatsu, H. Ozaki and H. Sawai, *Nucleic Acids Res.*, 2006, **34**, 5383-5394.
52. S. E. Lee, A. Sidorov, T. Gourlain, N. Mignet, S. J. Thorpe, J. A. Brazier, M. J. Dickman, D. P. Hornby, J. A. Grasby and D. M. Williams, *Nucleic Acids Res.*, 2001, **29**, 1565-1573.
53. E. T. Kool, *Acc. Chem. Res.*, 2002, **35**, 936-943.
54. R. X.-F. Ren, N. C. Chaudhuri, P. L. Paris, S. Rumney IV and E. T. Kool, *J. Am. Chem. Soc.*, 1996, **118**, 7671-7678.
55. K. M. Guckian, B. A. Schweitzer, R. X.-F. Ren, C. J. Sheils, D. C. Tahmassebi and E. T. Kool, *J. Am. Chem. Soc.*, 2000, **122**, 2213-2222.
56. K. M. Chan, D. K. Kölmel, S. Wang and E. T. Kool, *Angew. Chem.*, 2017, **129**, 6597-6601.
57. R. Crinelli, M. Bianchi, L. Gentilini and M. Magnani, *Nucleic Acids Res.*, 2002, **30**, 2435-2443.
58. D. A. Di Giusto and G. C. King, *Nucleic Acids Res.*, 2004, DOI: 10.1093/nar/gnh036.
59. B. Vester and J. Wengel, *Biochemistry*, 2004, **43**, 13233-13241.
60. V. Metelev, J. Lisziewicz and S. Agrawal, *Bioorg. Med. Chem. Lett.*, 1994, **4**, 2929-2934.

61. J. M. Layzer, A. P. McCaffrey, A. K. Tanner, Z. Huang, M. A. Kay and B. A. Sullenger, *RNA*, 2004, **10**, 766-771.
62. M. A. Campbell and J. Wengel, *Chem. Soc. Rev.*, 2011, **40**, 5680-5689.
63. J.-L. H. Duprey, Z.-y. Zhao, D. M. Bassani, J. Manchester, J. S. Vyle and J. H. Tucker, *Chem. Commun.*, 2011, **47**, 6629-6631.
64. J.-L. H. Duprey, D. M. Bassani, E. I. Hyde, C. Ludwig, A. Rodger, J. S. Vyle, J. Wilkie, Z.-Y. Zhao and J. H. Tucker, *Supramol. Chem.*, 2011, **23**, 273-277.
65. X. Liang, K. Fujioka and H. Asanuma, *Chem. - Eur. J.*, 2011, **17**, 10388-10396.
66. T. Sakamoto, Y. Tanaka and K. Fujimoto, *Org. Lett.*, 2015, **17**, 936-939.
67. H. Kashida, K. Nishikawa, Y. Ito, K. Murayama, I. Hayashi, T. Kakuta, T. Ogoshi and H. Asanuma, *Chem. - Eur. J.*, 2021, **27**, 14582-14585.
68. J. Duprey, J. Carr-Smith, S. L. Horswell, J. Kowalski and J. H. R. Tucker, *J. Am. Chem. Soc.*, 2016, **138**, 746-749.
69. A. Rybka, R. Kolinski, J. Kowalski, R. Szmigielski, S. Domagala, K. Wozniak, A. Wieckowska, R. Bilewicz and B. Korybut-Daszkiewicz, *Eur. J. Inorg. Chem.*, 2007, DOI: 10.1002/ejic.200600744.
70. U. E. Wawrzyniak, M. Woźny, J. Kowalski, S. Domagała, E. Maicka, R. Bilewicz, K. Woźniak and B. Korybut-Daszkiewicz, *Chem. - Eur. J.*, 2009, **15**, 149-157.
71. D. E. Volk and G. L. Lokesh, *Biomedicines*, 2017, **5**, 41.
72. N. K. Banavali and A. D. MacKerell, *Nucleic Acids Res.*, 2001, **29**, 3219-3230.
73. A. Gupta, A. Mishra and N. Puri, *J. Biotechnol.*, 2017, **259**, 148-159.
74. E. Farjami, L. Clima, K. V. Gothelf and E. E. Ferapontova, *Analyst*, 2010, **135**, 1443-1448.
75. D. R. Van Staveren and N. Metzler-Nolte, *Chem. Rev.*, 2004, **104**, 5931-5986.
76. C. T. Wittwer, M. G. Herrmann, A. A. Moss and R. P. Rasmussen, *Biotechniques*, 1997, **22**, 130-138.
77. S. Giglio, P. T. Monis and C. P. Saint, *Nucleic Acids Res.*, 2003, DOI: 10.1093/nar/gng135.
78. S. Tyagi and F. R. Kramer, *Nat. Biotechnol.*, 1996, **14**, 303-308.
79. P. Hardinge and J. A. Murray, *BMC Biotechnol.*, 2019, **19**, 1-15.
80. J. J. Li, R. Geyer and W. Tan, *Nucleic Acids Res.*, 2000, DOI: 10.1093/nar/28.11.e52.

81. P. M. Holland, R. D. Abramson, R. Watson and D. H. Gelfand, *Proc. Natl. Acad. Sci. U. S. A.*, 1991, **88**, 7276-7280.
82. I. Afonina, M. Reed, E. Lusby, I. Shishkina and Y. Belousov, *Biotechniques*, 2002, **32**, 940-949.
83. J. A. Garson, R. B. Ferns, P. R. Grant, S. Ijaz, E. Nastouli, R. Szypulska and R. S. Tedder, *J. Virol. Methods*, 2012, **186**, 157-160.
84. R. Bumgarner, *Curr. Protoc. Mol. Biol.*, 2013, DOI: 10.1002/0471142727.mb2201s101.
85. P. Baldi and G. W. Hatfield, *DNA Microarrays and Gene Expression: From Experiments to Data Analysis and Modeling*, Cambridge University Press, Cambridge, 2011.
86. J. P. Lopez, A. Diallo, C. Cruceanu, L. M. Fiori, S. Laboissiere, I. Guillet, J. Fontaine, J. Ragoussis, V. Benes, G. Turecki and C. Ernst, *BMC Med. Genomics*, 2015, DOI: 10.1186/s12920-015-0109-x.
87. E. J. Pietzak, A. Bagrodia, E. K. Cha, E. N. Drill, G. Iyer, S. Isharwal, I. Ostrovnaya, P. Baez, Q. Li, M. F. Berger, A. Zehir, N. Schultz, J. E. Rosenberg, D. F. Bajorin, G. Dalbagni, H. Al-Ahmadie, D. B. Solit and B. H. Bochner, *Eur. Urol.*, 2017, **72**, 952-959.
88. E. E. Ferapontova, *Annu. Rev. Anal. Chem.*, 2018, **11**, 197-218.
89. P. Gillespie, S. Ladame and D. O'Hare, *Analyst*, 2019, **144**, 114-129.
90. C. H. Fan, K. W. Plaxco and A. J. Heeger, *Proc. Natl. Acad. Sci. U. S. A.*, 2003, **100**, 9134-9137.
91. E. Farjami, L. Clima, K. Gothelf and E. E. Ferapontova, *Anal. Chem.*, 2011, **83**, 1594-1602.
92. D. Zhang, Y. Yan, H. Que, T. Yang, X. Cheng, S. Ding, X. Zhang and W. Cheng, *ACS Sens.*, 2020, **5**, 557-562.
93. Y. Qian, D. Tang, L. Du, Y. Zhang, L. Zhang and F. Gao, *Biosens. Bioelectron.*, 2015, **64**, 177-181.
94. Y. Xiao, X. G. Qu, K. W. Plaxco and A. J. Heeger, *J. Am. Chem. Soc.*, 2007, **129**, 11896.
95. A. Idili, A. Amodio, M. Vidonis, J. Feinberg-Somerson, M. Castronovo and F. Ricci, *Anal. Chem.*, 2014, **86**, 9013-9019.
96. Z. G. Yu and R. Y. Lai, *Anal. Chem.*, 2013, **85**, 3340-3346.

97. Y. Xiao, A. A. Lubin, B. R. Baker, K. W. Plaxco and A. J. Heeger, *Proc. Natl. Acad. Sci. U. S. A.*, 2006, **103**, 16677-16680.
98. Y. Du, B. J. Lim, B. L. Li, Y. S. Jiang, J. L. Sessler and A. D. Ellington, *Anal. Chem.*, 2014, **86**, 8010-8016.
99. H. Li, N. Arroyo-Curras, D. Kang, F. Ricci and K. W. Plaxco, *J. Am. Chem. Soc.*, 2016, **138**, 15809-15812.
100. W. W. Yang and R. Y. Lai, *Chem. Commun.*, 2012, **48**, 8703-8705.
101. L. P. Luo, L. L. Wang, L. P. Zeng, Y. R. Wang, Y. P. Weng, Y. J. Liao, T. T. Chen, Y. K. Xia, J. Zhang and J. H. Chen, *Talanta*, 2020, DOI: 10.1016/j.talanta.2019.120298.

Chapter 2: Techniques

2.1. Automated Solid-Phase DNA Synthesis

Solid-phase automated DNA synthesis is the process by which oligonucleotides of up to approximately 100 bases long may be synthesised on a solid support, most commonly using phosphoramidites as nucleobase monomers. Multiple approaches to the chemical synthesis of oligonucleotides have been developed over the last 70 years, including the H-phosphonate,[1] phosphotriester,[2] and phosphite triester[3] syntheses reported in the 1950s–1970s. However, it was Caruthers and coworkers' phosphoramidite chemistry[4] developed in the early 1980s that proved to be the most popular and which has now been automated to a significant degree. The most common form of solid support is controlled pore glass (CPG), with pore sizes of 500–1000 Å typically used. CPG-attached oligonucleotides are synthesised within the pores and therefore pore size is one factor that limits the length of the oligonucleotides being synthesised. Using solid supports allows for the use of large excesses of reagents and the easy removal of unreacted material and impurities, resulting in high-yielding couplings that do not require purification after each step.

2.1.1. Nucleobase Phosphoramidites

Oligonucleotide synthesis using phosphoramidite chemistry requires the phosphitylation of the 3′ sugar-based hydroxyl group and the protection of all of the other main nucleophilic sites (Figure 2.1). Solid-phase DNA synthesis occurs in the 3′→5′ direction as opposed to the 5′→3′ direction performed in Nature by DNA polymerases. The other main nucleophilic sites are the 5′ sugar-based hydroxyl group and the primary amines on the adenine, cytosine and guanine bases. A dimethoxytrityl (DMT) group is used to protect the 5′ hydroxyl moiety. The sensitivity of the DMT group to mildly acidic conditions means that it is easily removed at the beginning

of each coupling step to regenerate the 5′ hydroxyl group. Additionally, the absorbance arising from the distinct orange colour of the liberated cationic DMT can be quantified to assess the efficiency of each coupling step. The primary amines on the adenine, cytosine and guanine bases are typically protected with benzoyl (adenine and cytosine) and isobutyryl (guanine) protecting groups.[5] These remain in place throughout the entire DNA synthesis process and are only removed once the synthesis of the CPG-attached oligonucleotide has been completed. The first nucleoside is attached to the CPG by functionalising its 3′ hydroxyl group with a succinate linker.[6] The succinate linker is then activated and reacted with the amine-functionalised CPG resin to tether the nucleoside using an amide linking group.

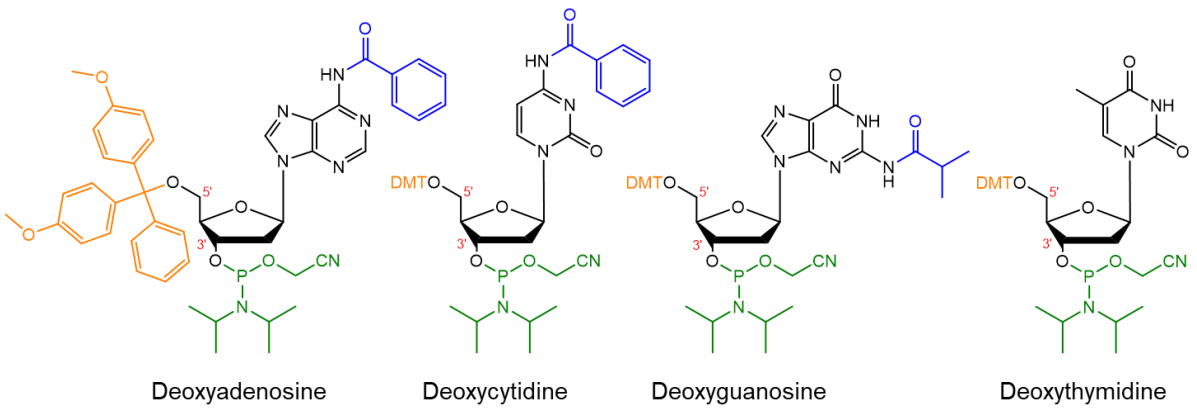

Figure 2.1: Structures of the protected nucleobases used in standard solid-phase DNA synthesis. Primary amines are protected using benzoyl and isobutyryl protecting groups (blue), the 5' hydroxyl group is protected using a DMT group (orange), and the 3' hydroxyl group is phosphitylated (green) to form the protected nucleobase.

2.1.2. DNA Synthesis Cycle

Scheme 2.1 shows the complete solid-phase DNA synthesis cycle.[6] The cycle repeats until the desired number and sequence of nucleobases (as programmed into the computer) have been added to the oligonucleotide.

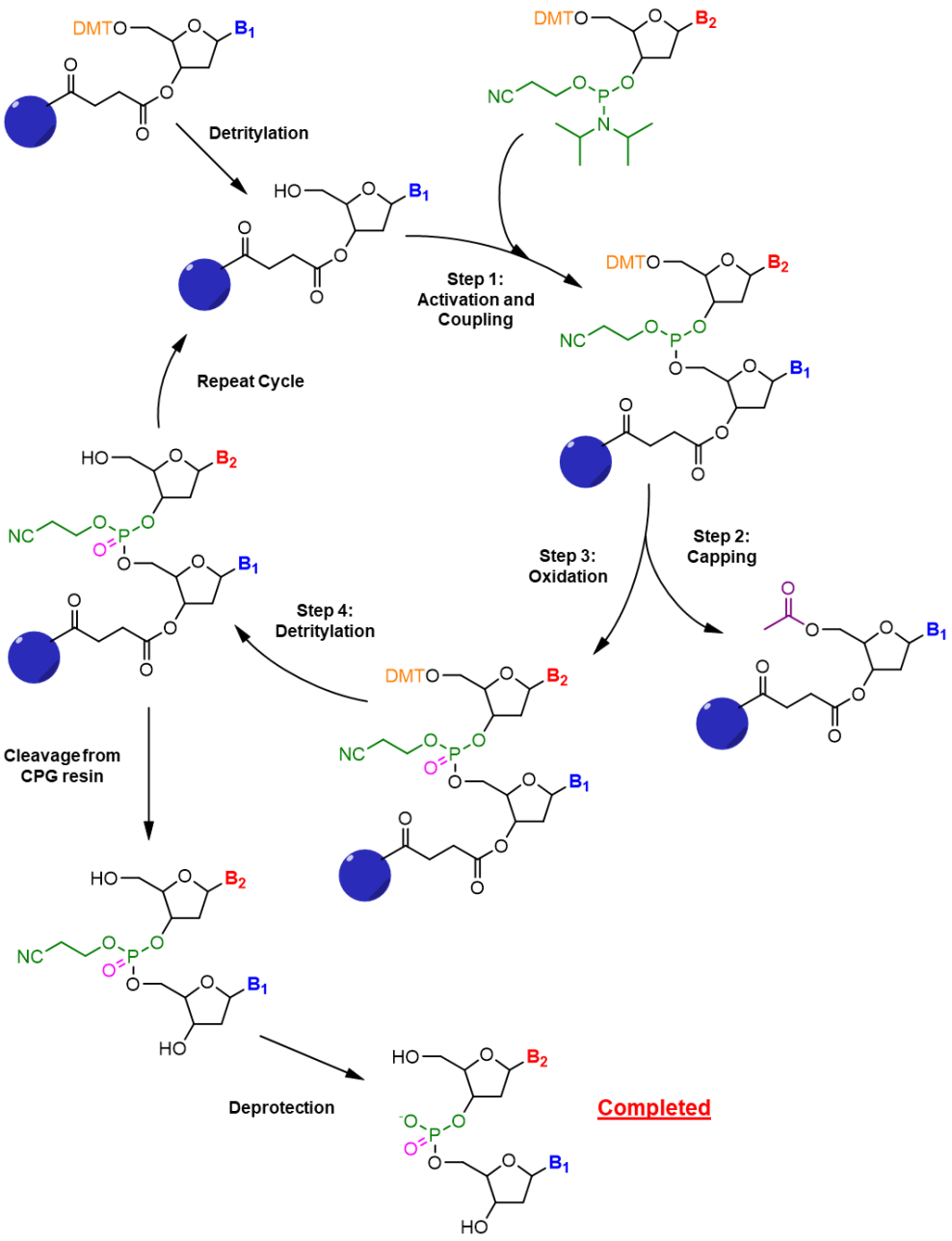

Scheme 2.1: The solid-phase DNA synthesis cycle.

Detritylation of the CPG-Attached Nucleoside. The beginning of the cycle involves the detritylation of the CPG-attached nucleoside at the 3′ end of the oligonucleotide to be synthesised. The DMT protecting group is removed using trichloroacetic acid (TCA) in DCM to regenerate the 5′ hydroxyl group.

Step 1: Activation and Coupling. The next nucleoside to be added is then introduced. It is first activated by protonating the diisopropylamino protecting group and converting it into a good leaving group using tetrazole in acetonitrile. The regenerated 5′ hydroxyl group on the CPG-attached nucleoside then reacts with the activated nucleoside phosphoramidite to form a phosphite triester.

Step 2: Capping. Although each coupling step is high yielding, they are not 100% efficient. Some 5′ hydroxyl groups remain unreacted and it is important they do not react in subsequent coupling steps to form failure oligonucleotides that are hard to separate from the desired oligonucleotide. A capping solution of acetic anhydride and N-methylimidazole is used to acetylate any unreacted 5′ hydroxyl groups, rendering them inert to subsequent coupling steps.

Step 3: Oxidation. The newly formed phosphite triester (P(III)) is oxidised to a phosphotriester (P(V)) using iodine in water and pyridine. The resultant phosphotriester is a DNA backbone with a cyanoethyl protecting group that prevents unwanted reactions at the phosphorus in the subsequent synthesis cycles.

Step 4: Detritylation. The DMT protecting group on the newly coupled nucleoside is removed using TCA in DCM to regenerate the 5′ hydroxyl group, and the synthesis cycle begins again at Step 1 until the desired oligonucleotide has been synthesised. As the liberated DMT cation absorbs at 495 nm, the absorbance intensity is measured at this stage to determine the efficiency of each coupling step.

Cleavage from CPG Resin and Deprotection. Once the desired oligonucleotide has been synthesised, it is cleaved from the CPG resin using concentrated aqueous ammonia. Now dissolved in the aqueous ammonia, the solution is heated at 60 ºC for six hours to remove the cyanoethyl protecting groups on the phosphotriester backbone and the acyl protecting groups

on the nucleobases. The aqueous ammonia is then evaporated to leave the desired oligonucleotide along with the shorter capped strands, ready to be purified.

2.1.3. Ultramild Conditions

The final steps of standard cleavage and deprotection are relatively harsh, and some modifications incorporated into DNA using solid-phase synthesis are sensitive to the heated ammonia solution employed. Different protecting groups can instead be used to protect the primary amines on the bases, as shown in Figure 2.2. These groups can be removed using a methanolic solution of potassium carbonate at RT.[6] The majority of the modified oligonucleotides synthesised in this work were done so using ultramild reagents and conditions, as described in Chapter 3.

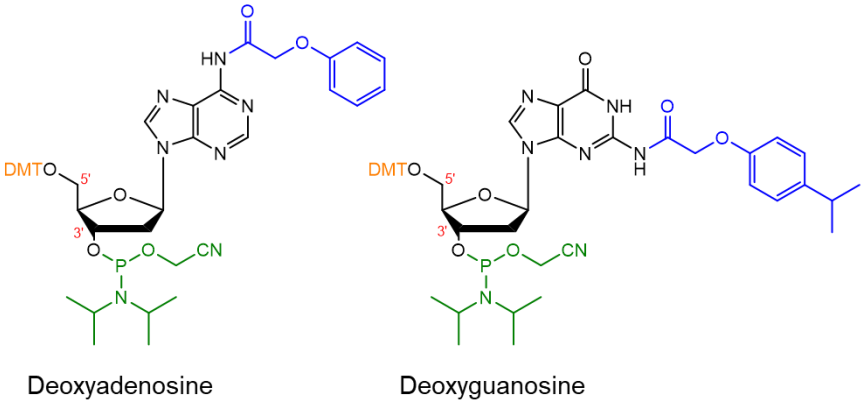

Figure 2.2: Structures of the protected nucleobases deoxyadenosine and deoxyguanosine used in ultramild solid-phase DNA synthesis. Primary amines are protected using phenoxyacetyl and isopropyl phenoxyacetyl protecting groups (blue), the 5' hydroxyl group is protected using a DMT group (orange), and the 3' hydroxyl is phosphitylated (green) to form the protected nucleobase.

2.2. High Performance Liquid Chromatography

After the DNA synthesis cycle has completed, the crude product contains the desired oligonucleotide along with the unwanted capped oligonucleotides and remaining impurities. High performance liquid chromatography (HPLC) is suitable for purifying crude mixtures

containing oligonucleotides of up to approximately 40 bases in length.[5,7] HPLC involves the pumping of the dissolved crude mixture through a HPLC column. The column is packed with a solid stationary phase, and a liquid mobile phase pumps the crude through the column at a high pressure. HPLC separates components in the crude product by each component interacting with the stationary phase differently. The eluent is monitored using a detector (typically UV/vis or fluorescent) that produces peaks when an analyte that absorbs at a set wavelength passes through.

2.2.1. Reversed-Phase High Performance Liquid Chromatography

Reversed phase- (RP-) HPLC is used to separate and purify short oligonucleotides based on differences in hydrophobicity.[7] Standard HPLC uses a hydrophilic stationary phase and a relatively non-polar mobile phase; RP-HPLC, on the other hand, uses a hydrophobic stationary phase and a relatively polar mobile phase. The stationary phase is made hydrophobic by coating with hydrocarbons of varying length, and the mobile phase consists of polar solvents such as water and acetonitrile. Oligonucleotides that have not been fully deprotected are more hydrophobic and will elute later. Chemical modification often significantly changes the overall hydrophobicity of an oligonucleotide, resulting in drastic differences in elution time between modified and unmodified DNA. In this work, aqueous triethylammonium acetate (TEAA) in the mobile phase is used which, upon interaction with the coating hydrocarbon chains, forces the oligonucleotides to interact more with the stationary phase *via* ion-pairing to increase peak resolution. Conditions in RP-HPLC must be carefully controlled to ensure effective separation.[7] The pH can affect the hydrophobicity of an oligonucleotide and must be adjusted appropriately. Secondary structures (such as hairpin loops) can affect the retention time of an oligonucleotide and this problem can be overcome by heating at 60 ^{o}C to ensure temporary denaturation. Longer oligonucleotides (>40 bases) are harder to separate using RP-HPLC. One solution is to leave

the DMT protecting group on the 5′ of the synthesised oligonucleotide, greatly increasing its hydrophobicity and therefore easily enabling its separation from failure sequences of similar length.

2.3. Mass Spectrometry

As the sequence and mass of a synthesised oligonucleotide is known, mass spectrometry can be used to confirm that the oligonucleotide has been synthesised correctly. Mass spectrometry measures ionised analytes by their mass to charge ratios (*m/z*). In simple terms, the sample is ionised and vaporised, accelerated by electric/magnetic fields, and hits a mass analyser where its *m/z* ratio is determined.[8] Each sample will consist of different ionised analytes that will be deflected more or less by the electric/magnetic fields depending on their *m/z* ratio.

2.3.1. Ionisation Methods

The two methods of ionisation used in the analysis of oligonucleotides are matrix assisted laser desorption ionisation (MALDI) and electrospray ionisation (ESI). MALDI involves the fixing of the sample in a matrix, with 3-hydroxypiclinic acid typically used for oligonucleotide analysis.[9] A laser pulse then vaporises the matrix, ionising the sample *via* protonation to produce predominantly singly charged species. ESI involves the dissolving of the sample in a volatile solvent, with the resulting solution then sprayed from a needle-injector.[10] ESI can either be negative mode (negatively charged analyte ions formed) or positive mode (positively charged analyte ions formed); negative mode ESI was used for the analysis of oligonucleotides in this thesis. As the spray accelerates towards the mass analyser, the solvent evaporates and the droplets continuously split under the effects of coulombic repulsion until solvent-free analyte ions are obtained. ESI typically results in multiply charged ionic species.

2.3.2. Data Analysis

As MALDI predominantly results in singly charged species *via* protonation, the molecular mass can be calculated by subtracting the mass of a proton from the *m/z* signal produced. ESI results in multiply charged species and therefore calculating the molecular mass from the *m/z* signals is more involved. The charge of the species giving rise to a *m/z* signal cluster is first determined. This is done by taking the inverse of the spacing between the *m/z* signals that comprise a cluster. For example, if the *m/z* signals of a cluster are 1532.04, 1532.38, 1532.71, *etc*. (these are taken from the raw mass spectrometry data produced for the oligonucleotide T2A, see Chapter 3), the spacing between them is approximately 1/3 and therefore the charge of the species giving rise to the cluster is –3. The *m/z* is then multiplied by the magnitude of the charge, with the magnitude of the charge then added onto the result (accounting for the removed protons that resulted in ionisation) to obtain the molecular mass on the deconvoluted spectrum. This processing of the raw ESI data is done computationally using a deconvolution algorithm. The software can be programmed to produce the exact mass or the molecular weight of the analyte; for this thesis, the exact mass of each oligonucleotide was determined and compared with the theoretical exact mass to confirm successful synthesis (see Chapter 7 for full details).

2.4. Thermal Melting

2.4.1. Ultraviolet Thermal Melting

The thermal melting temperature (T_m) of an oligonucleotide duplex is used as a measure of its stability: the higher the T_m, the higher its stability. Traditionally, ultraviolet (UV) light absorption has been used to track the denaturation of a duplex and determine its T_m.[11] The aromatic bases absorb UV light strongly at 260 nm. However, when shielded within a duplex, the bases absorb less UV light compared with when in a single-stranded environment. As such, UV light absorption increases as the temperature rises and duplexed DNA denatures into single

strands. The midpoint of the curve correlates with the temperature at which 50% of duplexes have denatured and is termed the T_m.

2.4.2. Fluorescent Thermal Melting

An alternative way to determine the thermal stability of a duplex is to use the fluorescent intercalating dye SYBR Green. In its free state in solution, the fluorescence of SYBR Green is quenched. Intercalating into double-stranded DNA restricts the movement of SYBR Green, resulting in a 1000-fold enhancement in fluorescence intensity compared with its free state.[12] In a thermal melting experiment using SYBR Green, fluorescence decreases as the temperature rises and the DNA denatures (Figure 2.3). As with the UV absorption approach, the T_m is determined from the midpoint of the curve. Intercalating SYBR Green also stabilises double-stranded DNA *via* electrostatic and stacking interactions, raising the T_m by several degrees.[12] Duplexes rich in G≡C base pairs have higher T_m values because greater energy is required to break the three hydrogen bonds than to break the two hydrogen bonds of A=T base pairs. The thermal stability of a duplex is sensitive to salt concentration, DNA concentration, and pH; all three must be kept constant to compare T_m values reliably. DNA modifications can have either a negative or a positive impact on the thermal stability of a duplex. For example, terminal cyanine dyes stabilise duplexes *via* stacking onto the adjacent base pair[13] whilst internal incorporations can disrupt the base stack and cause duplex destabilisation.

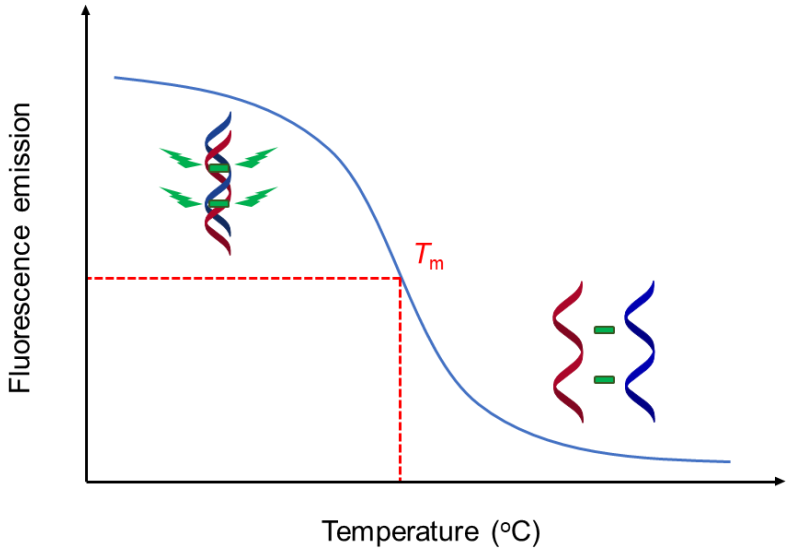

Figure 2.3: Schematic of the T_m determination of a duplex using SYBR Green. At lower temperatures, the SYBR Green intercalates into the duplex and produces fluorescence. At higher temperatures, the denaturation of the duplex releases the SYBR green which subsequently produces less fluorescence. The T_m is determined to be the maximum of the negative first derivative of the melting curve shown.

2.5. Ultraviolet Visible Spectroscopy

Ultraviolet/Visible (UV/Vis) spectroscopy involves the irradiation of a sample with light in the ultraviolet to visible range (approximately 200–800 nm) and recording the absorption profile.[14] UV/Vis light of a certain wavelength is absorbed by the sample whilst the rest is transmitted. Absorption of light excites the electrons in the sample, causing them to rise from a lower energy level to a higher energy level. The energy of the absorbed light correlates with the differences in energy between these energy levels. An absorption spectrum is measured which compares the initial intensity of light with the light that has passed through the sample, enabling the determination of the amount of light absorbed and at which wavelength. The wavelength at which the most light is absorbed is termed λ_{max}. UV/Vis spectroscopy offers a simple way of determining the concentration of a sample by application of the Beer-Lambert Law (Equation 2.1.).

Equation 2.1 Beer-Lambert Law.

$$A = \varepsilon c l$$

Where:

A = absorbance at λ_{max}

ε = molar extinction coefficient (M^{-1} cm^{-1})

c = concentration (M)

l = path length (cm)

2.5.1. Oligonucleotide Concentration Determination

UV/Vis spectroscopy is used to determine the concentration of an oligonucleotide sample. The aromatic bases absorb strongly at 260 nm owing to the π–π* transition.[15] By measuring the absorbance at 260 nm, the resulting number can be inputted into the Beer-Lambert Law to obtain the oligonucleotide concentration. The molar extinction coefficient of an unmodified oligonucleotide is dependent on the number and sequence of its constituent bases.[15,16] The molar extinction coefficient of a modified oligonucleotide is the sum of the modification plus sequence molar extinction coefficients. Most UV/Vis spectrometers have a set path length of 1 cm and generate optical density values (cm^{-1}) that equals the absorbance divided by 1 cm.

2.6. Fluorescence Spectroscopy

Whereas UV/Vis spectroscopy measures the absorbance of light, fluorescence spectroscopy measures the emission of light from excited samples. In fluorescence spectroscopy, the sample is irradiated with light of a specific wavelength that excites the electrons from the ground state to higher energy levels.[17] Figure 2.4 is a simplified version of the Jablonski diagram that depicts the transitions between energy levels which give rise to fluorescence. S_o is the ground state from which electrons are excited to the excited electronic singlet states S_1 and S_2. Within each

electronic state are multiple vibrational energy levels, and within each vibrational level are multiple rotational energy levels. Upon excitation, an electron can be promoted to any vibrational level within an excited electronic singlet state. The excited electron undergoes vibrational relaxation *via* the host molecule's colliding with other molecules, resulting in energy loss and a transition to lower energy levels. If two electronic states of the same spin multiplicity are close enough in energy such that their vibrational levels overlap, internal conversion (IC) can occur in which the excited electron non-radiatively transitions from a vibrational level of the higher electronic state (*e.g.*, S_2) to a vibrational level of the lower electronic state (*e.g.*, S_1). (The transition of an excited electron between electronic states with different spin multiplicities, for example from a singlet to a triplet state or *vice versa*, is known as intersystem crossing (ISC); ISC leads to phosphorescence, and both are not relevant to this work.) Once an electron has relaxed down to the lowest vibrational level of the first excited state S_1, it passes to any of the vibrational levels of the ground state S_o releasing a photon of light in the process – fluorescence.

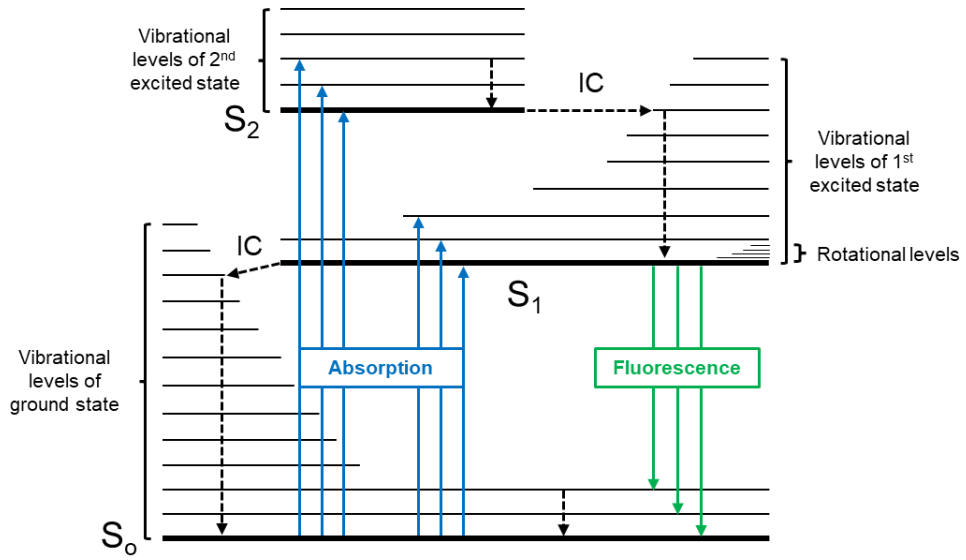

Figure 2.4: Simplified Jablonski diagram showing the absorption, internal conversion (IC), and fluorescence transitions between the relevant energy levels.

The light emitted as electrons fall from the lowest vibrational level of S_1 to any of the vibrational levels of S_o has a longer wavelength (lower energy) than the light that was absorbed and caused the excitation. This is because many electrons are initially excited to a vibrational level higher than the lowest vibrational level of S_1, and then non-radiatively de-excite *via* IC and vibrational relaxation before making the S_1 to S_o transition. This shift to longer wavelengths in the emitted light relative to the absorbed light is known as the Stokes shift, and plays an important role in assessing the fluorescent properties of a molecule.[17] Emission or excitation spectra can be produced using the technique of fluorescence spectroscopy. An emission spectrum uses a fixed excitation wavelength and the emitted light is measured across a range of wavelengths. An excitation spectrum uses a fixed emission wavelength and shows the wavelengths of light that are absorbed that give rise to the emission at the fixed wavelength.

2.7. Electrochemical Techniques

Faradaic electrochemistry is the study of chemical reactions involving the transfer of electrons between substances. A redox-active species is one that can be oxidised or reduced under certain conditions. The direct measurement of electrons that move from one substance or molecule to another is the basis of many electrochemical techniques.

2.7.1. Electrochemical Setup

The electrochemistry reported in this thesis was conducted using a three-electrode set up consisting of a gold working electrode, a Ag|AgCl reference electrode, and a platinum wire counter electrode (Figure 2.5A). The three electrodes are assembled in an electrochemical cell such that they are immersed in the electrolyte sensing solution and connected to a potentiostat (Figure 2.5B).

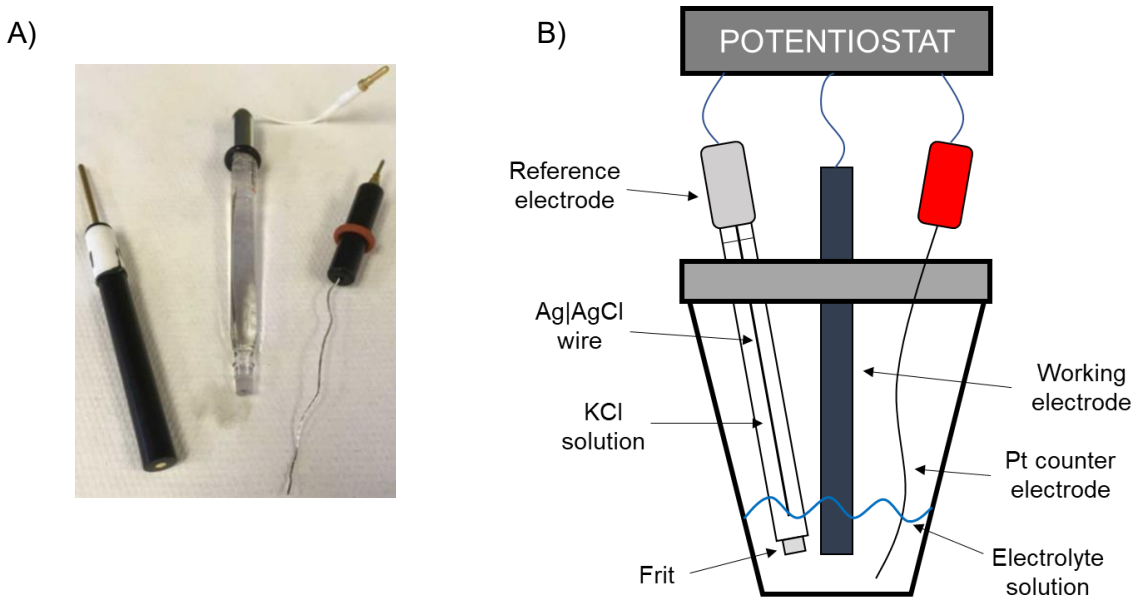

Figure 2.5: A) Pictures of the working electrode, with gold surface visible at the bottom (left), Ag|AgCl reference electrode (middle), platinum wire counter electrode (right). B) Electrochemical cell setup schematic diagram.

The surface of the working electrode that makes contact with the electrolyte solution is where the electrochemical activity being measured occurs. In the type of electrochemistry carried out in the present work, the material of the working electrode itself should be chemically and electrochemically inert under the conditions employed, criteria which gold satisfies. A voltage is applied between the working electrode and the Ag|AgCl reference electrode. The reference electrode is used to produce a stable, known potential such that when connected to the working electrode, the potential difference (voltage) between the two can be measured. A Ag|AgCl reference electrode consists of a Ag wire coated with AgCl and immersed in a 3 M KCl solution. The electrochemical reaction that occurs at the surface of the Ag|AgCl wire is shown in Figure 2.6 and has a potential of +0.197 V versus a standard hydrogen electrode.[18]

$$AgCl_{(s)} + e^- \rightleftharpoons Ag_{(s)} + Cl^-_{(aq)}$$

Figure 2.6: Electrochemical reaction occurring at the surface of a Ag|AgCl wire immersed in a saturated KCl solution.

The potential of this reaction is stable because the Cl^- concentration is essentially fixed. According to the Nernst equation (Equation 2.2), the potential of a reaction conducted under non-standard conditions is dependent on the reaction quotient (Q).[18] Q is equal to the activities of the products multiplied together divided by the activities of the reactants multiplied together. The activity of a substance is dependent on its concentration. As Cl^- is the only dissolved species present in the redox reaction occurring in a Ag|AgCl reference electrode (Figure 2.6), only its concentration will affect the potential of the reaction. And as the concentration of Cl^- is essentially fixed, this results in a highly stable potential making it well-suited for use as a reference.

Equation 2.2

$$E = E^o - \frac{RT}{nF} \ln (Q)$$

Where:

E = potential of reaction being measured (V)

E^o = standard potential of reaction being measured (V)

R = gas constant (8.314 J K^{-1} mol^{-1})

T = temperature (K)

n = number of electrons transferred in the redox process

F = Faraday's constant (96,485 C mol^{-1})

Q = reaction quotient, equal to activities of the products divided by activities of the reactants

The purpose of the platinum counter electrode is to complete the circuit and allow for the flow of current during electrochemical reactions.[18] This set-up avoids the flow of large currents through the reference electrode, which could alter its composition. If an oxidation occurs at the surface of the working electrode, then the electrons that are removed from the oxidised species

travel to the counter electrode where a complementary reduction takes place. Conversely, if a reduction occurs at the working electrode, a complementary oxidation takes place at the counter electrode. The surface area of the counter electrode is larger than the surface area of the working electrode to ensure that the current measured is reflective of the electrochemical processes occurring at the working electrode, and not those occurring at the counter electrode.[19]

2.7.2. Cyclic Voltammetry

Cyclic voltammetry is a technique that involves sweeping the potential of the working electrode from potential A to potential B and then back to potential A in a linear fashion (Figure 2.7).[20] An analyte will be oxidised in the forward sweep and, if it exhibits fully or partially electrochemical reversible behaviour, will be reduced in the reverse sweep. The movement of electrons travelling from/to the working electrode in the event of oxidation/reduction occurring at its surface is measured as current.

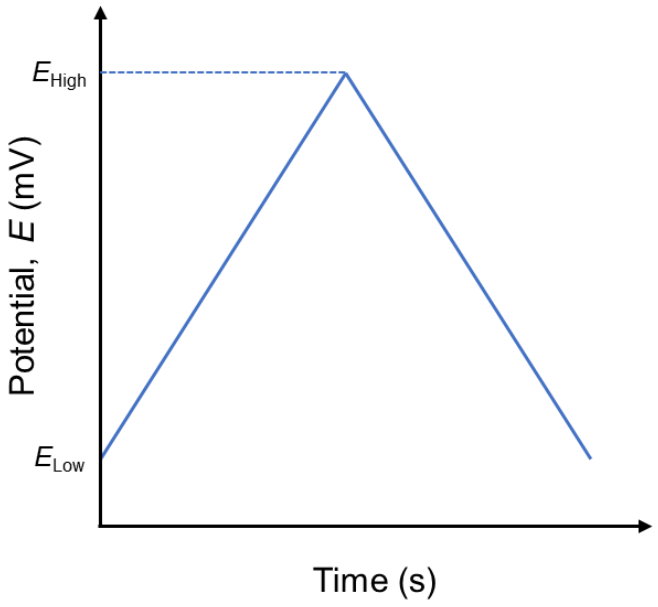

Figure 2.7: Cyclic voltammetry waveform.

Plotting the current measured (A) against the potential applied (mV) produces a cyclic voltammogram (CV). The analysis of a CV yields important information about the electrochemical characteristics of the analyte. Figure 2.8 shows the CV of a solution-based reversible redox process. The anodic (oxidation) and cathodic (reduction) peak currents are referred to as i_p^a and i_p^c, respectively. The potentials at which i_p^a and i_p^c occur are E_p^a and E_p^c, respectively, and indicate the potentials at which the maximum amount of redox activity is occurring. $E_{1/2}$ is the half-wave potential and is determined by taking the average of E_p^a and E_p^c. ΔE_p is the difference in potential between E_p^a and E_p^c.

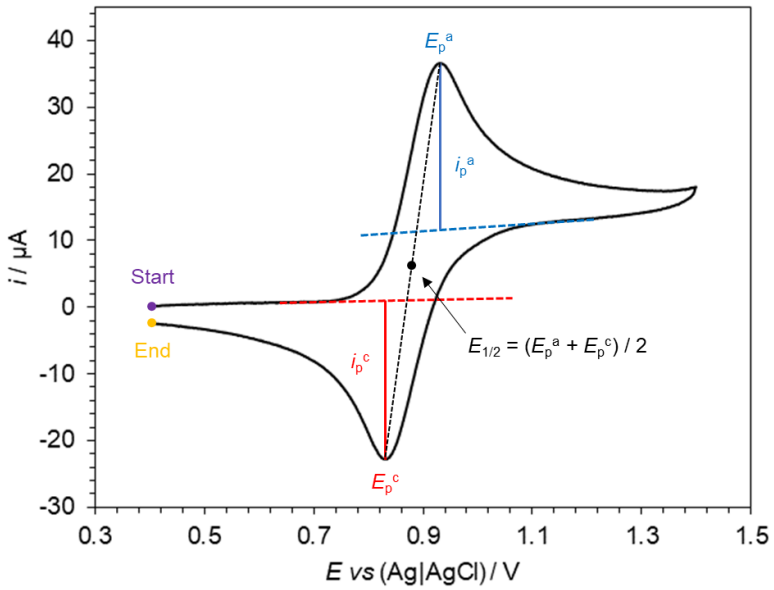

Figure 2.8: Annotated CV of a reversible solution-based redox process. i_p^a = anodic (oxidation) peak current, i_p^c = cathodic (reduction) peak current, E_p^a = anodic peak potential, E_p^c = cathodic peak potential, $E_{1/2}$ = half-wave potential.

For a solution-based species, full electrochemical reversibility must satisfy several criteria.[20,21] Firstly, ΔE_p is approximately $59/n$ mV at 25 °C, where n is the number of electrons transferred in the redox process. Secondly, the peak position should be invariant with potential sweep rate. Thirdly, the magnitude of the anodic and cathodic peak currents must be close to equal ($i_p^a/i_p^c = 1$), assuming that the diffusion coefficients of the oxidised and reduced forms are similar, because this indicates that for each analyte molecule oxidised, an equal number are

reduced back. Fourthly, a reversible solution-based redox process will produce currents that exhibit a linear, proportional relationship to the square root of the scan rate according to the Randles-Sevčik equation. For a redox process involving one electron at 25 ºC, the Randles-Sevčik equation equates to Equation 2.3 and is heavily influenced by the diffusion of oxidised and reduced species to and from the electrode surface, accounted for by the diffusion coefficient (*D*).

Equation 2.3

$$i_p = 2.69 \times 10^5 A D^{\frac{1}{2}} C v^{\frac{1}{2}}$$

Where:

A = electrochemical working electrode surface area (cm^2)

D = diffusion coefficient ($cm^2\ s^{-1}$)

C = analyte concentration ($mol\ cm^{-3}$)

v = scan rate ($V\ s^{-1}$)

For a surface-anchored redox-active moiety, the diffusion of the redox-active species to and from the electrode surface does not occur. Therefore, the electrochemical behaviour of a reversible surface-based redox process differs significantly from that of a reversible solution-based redox process.[21] Firstly, ΔE_p of a reversible surface-based redox process should theoretically be 0. In practice, factors such as kinetics and solution resistance deviates ΔE_p from 0, with values of approximately 10 mV typical. Secondly, a reversible surface-based redox process will exhibit a linear, proportional relationship to scan rate (not the square root of scan rate as it is for a reversible solution-based redox process) according to equation 2.4.[21] A reversible surface-based redox process will however exhibit $i_p^a/i_p^c = 1$.

Equation 2.4

$$i_p = \frac{n^2F^2}{4RT} vA\Gamma$$

Where:

A and v are the same as in Equation 2.3

n, F, R, and T are the same as in Equation 2.2

Γ = surface concentration of surface-bound species (mol cm^{-2})

Using Equation 2.4, it is possible to determine the surface coverage (Γ) of a redox-active surface-bound species in mol cm^{-2}. First, the electrochemical surface area of the electrode must be determined. The electrochemical surface area refers to the area of the electrode that can facilitate electrochemical activity and is not the same as the geometric surface area of the electrode. Submerging a bare gold electrode in an acidic solution causes a gold oxide layer to form.[22] The charge required to remove this oxide layer electrochemically is given by the charge corresponding to the reduction peak at ~900 mV of the gold electrode in acid, as shown in Figure 2.9. This can then be divided by the literature value[22] of 390 μC cm^{-2} for the removal of an oxide layer from a gold surface to obtain the electrochemically active surface area of any gold working electrode in cm^2.

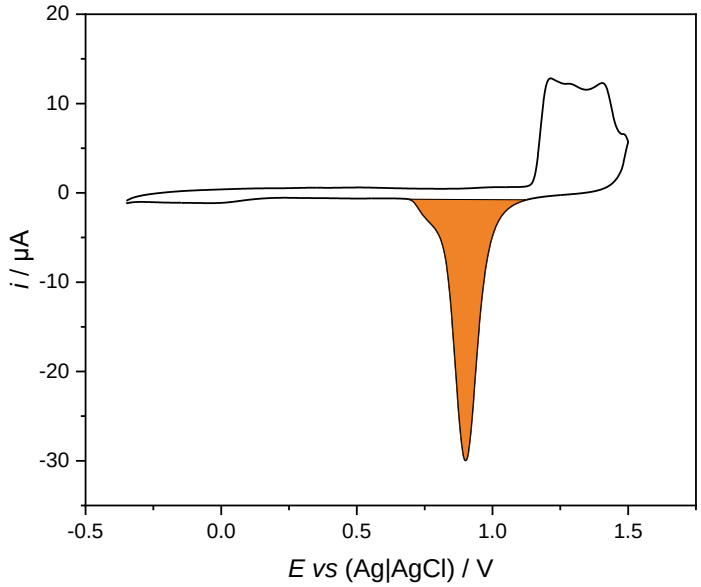

Figure 2.9: CV of a gold electrode in 0.5 M H_2SO_4, scan rate = 500 mV s^{-1}. The orange peak is the current produced by the reduction of the gold oxide layer.

Once the electrochemically active surface area of an electrode has been calculated, the coverage of a redox-active species bound to its surface can be determined. This can be done either by using the current produced by the redox species and Equation 2.4, or using the charge produced by the redox species and Equation 2.5.[21]

Equation 2.5

$$Q = nFA\Gamma$$

Q = charge (µC)

All components are the same as in Equations 2.2 and 2.4

2.7.3. Square Wave Voltammetry

Square wave voltammetry is a technique that combines a square wave and staircase waveforms (Figure 2.10).[21] The current is sampled twice in each cycle, once immediately before stepping the potential in one direction (forward current sample, i_f) and once immediately before stepping the potential in the other direction (reverse current sample, i_r).

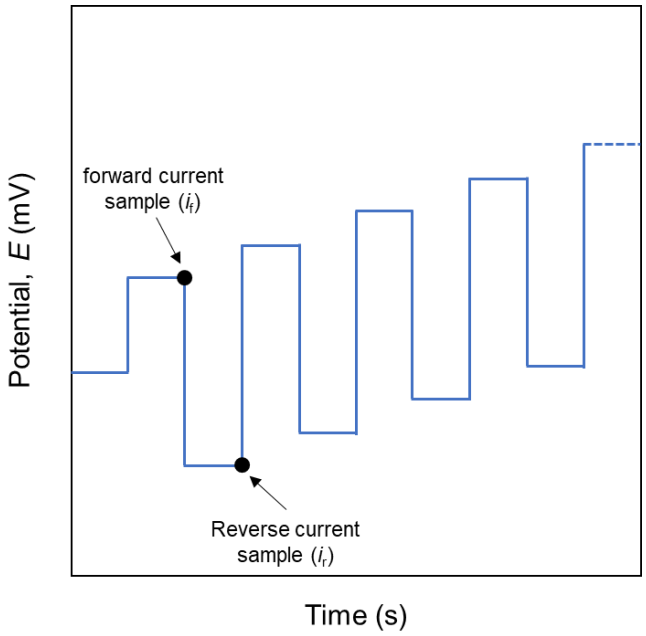

Figure 2.10: Square wave voltammetry waveform.

The current plotted on the square wave voltammogram (SWV) is the difference between i_f and i_r according to equation 2.6. The enhanced current obtained by essentially combining the two samplings contributes to the increased sensitivity of square wave voltammetry compared with other electrochemical techniques. Additionally, the subtraction of i_r from i_f results in the effective rejection of background capacitive current, further enhancing sensitivity.

Equation 2.6

$$\Delta i = i_f - i_r$$

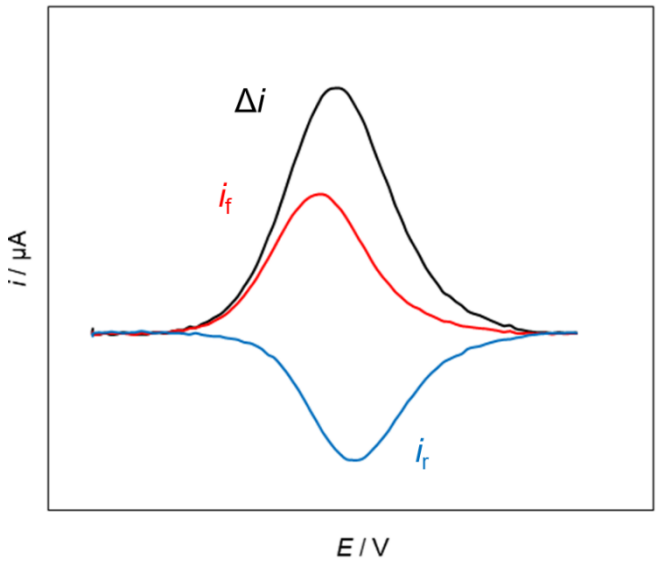

Figure 2.11: An example SWV, showing the forward current sample (i_f) and reverse current sample (i_r) traces and the resulting difference in current (Δi) which is then plotted.

2.8. Self-Assembled Monolayer Formation

As briefly mentioned in Chapter 1, the formation of SAMs is a commonly used technique in the field of DNA electrochemistry. A SAM is a single layer of molecules that spontaneously arrange themselves on a surface.[23] Originally involving relatively simple organic molecules, it was not long before DNA was being used to form SAMs.[24] DNA modified with a terminal linking modification that reacts with the surface results in the formation of a SAM. One of the most popular combinations is DNA modified with a terminal thiol modification that reacts with a gold surface to form a covalently tethered DNA monolayer (Figure 2.12). The DNA is initially synthesised with a 3′ terminal disulphide modification, which is less reactive than a thiol and is more suitable for long-term storage. Prior to SAM formation, the disulphide is reduced to a thiol using tris(2-carboxyethyl) phosphine (TCEP). The thiol-modified DNA is then incubated with a polished and cleaned gold electrode surface during which a gold-sulphur bond is formed. The spaces in between probes are then backfilled with 6-mercapto-1-hexanol to prevent unwanted adsorption of contaminants. Backfilling with 6-mercapto-1-hexanol has also been shown to aid in the formation of well-ordered SAMs.[25] By immobilising a DNA probe onto the surface of an electrode, far less probe is required and the sensitivity of the sensor can be improved.

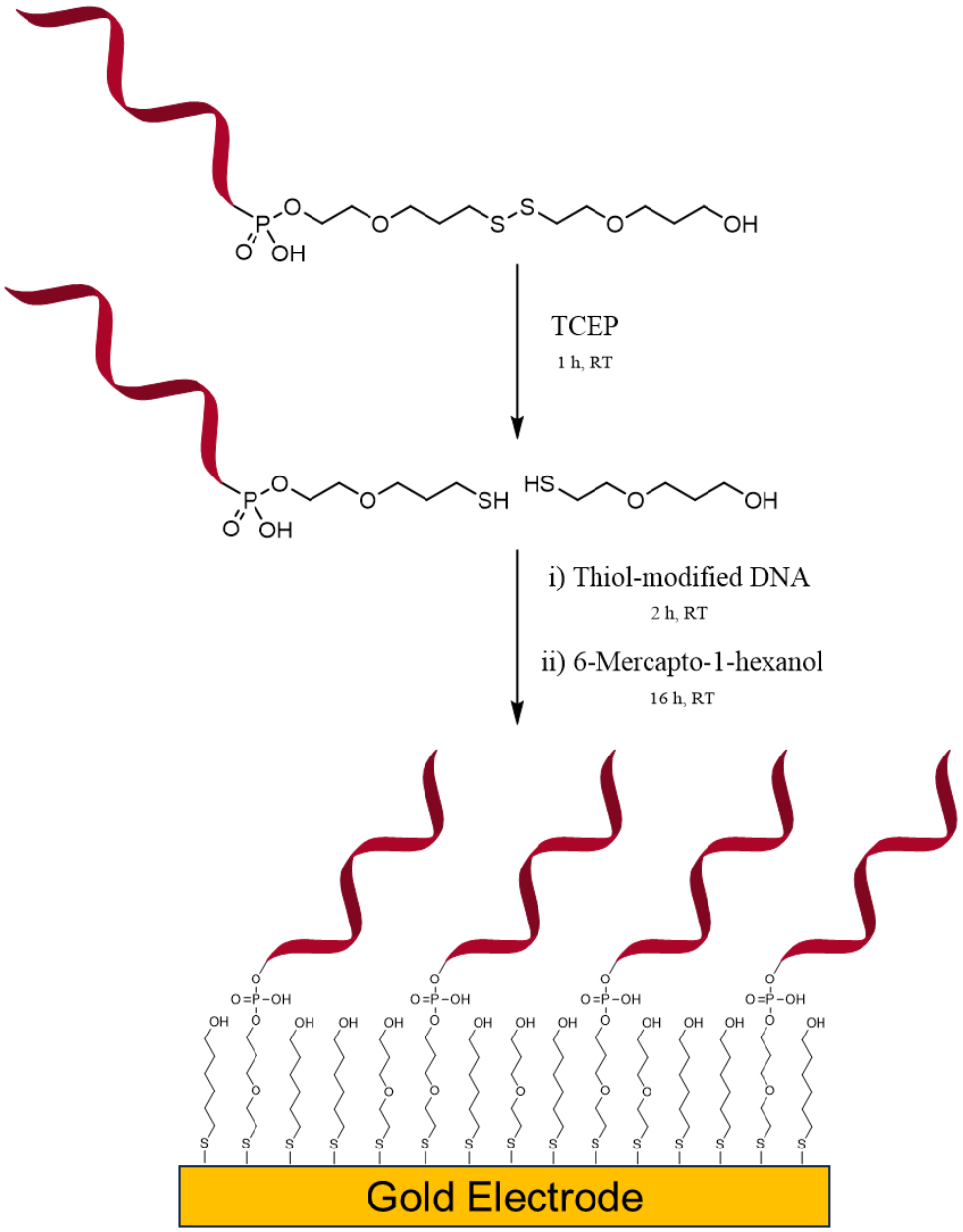

Figure 2.12: SAM formation procedure. The disulphide-modified DNA is reduced to form thiol-modified DNA. Together with 6-Mercapto-1-hexanol, incubation on top of the gold electrode surface results in the formation of a self-assembled DNA mixed monolayer.

2.9. Confocal Fluorescence Microscopy

Confocal fluorescence microscopy is used to obtain images of fluorescently labelled samples and is utilised extensively in the study of the distribution and interaction of specific molecules within biological systems.[26] The setup and functioning of a confocal fluorescent microscope is shown in Figure 2.13. First, the fluorescently labelled sample is immobilised onto a microscope slide. Light from a laser is then filtered such that only the wavelength of light that excites the labelling fluorophore passes through. The filtered light is then reflected towards the sample by a dichroic mirror and focused onto a specific point of the sample by an objective lens (this is in contrast to widefield microscopy in which the entire sample is illuminated by the exciting light[27]). The fluorophore is then excited which causes it to emit light (fluorescence). The emitted light is not reflected by the dichroic mirror and instead passes through, owing to its slightly longer wavelength than the exciting light that was reflected. The emitted light then passes through an emission filter which filters out wavelengths of light not emitted from the fluorophore. The filtered emitted light then encounters a pinhole aperture, which only allows light originating from a specific focal plane cutting through the sample to pass through to the detector. The laser is then scanned across the sample, point by point, collecting a pixel of information with each scan to build up an image of the sample. As only light produced close to the focal plane can pass through the pinhole aperture, the optical resolution of the image generated (particularly in terms of sample depth) is superior to a comparative image generated using widefield microscopy.[26]

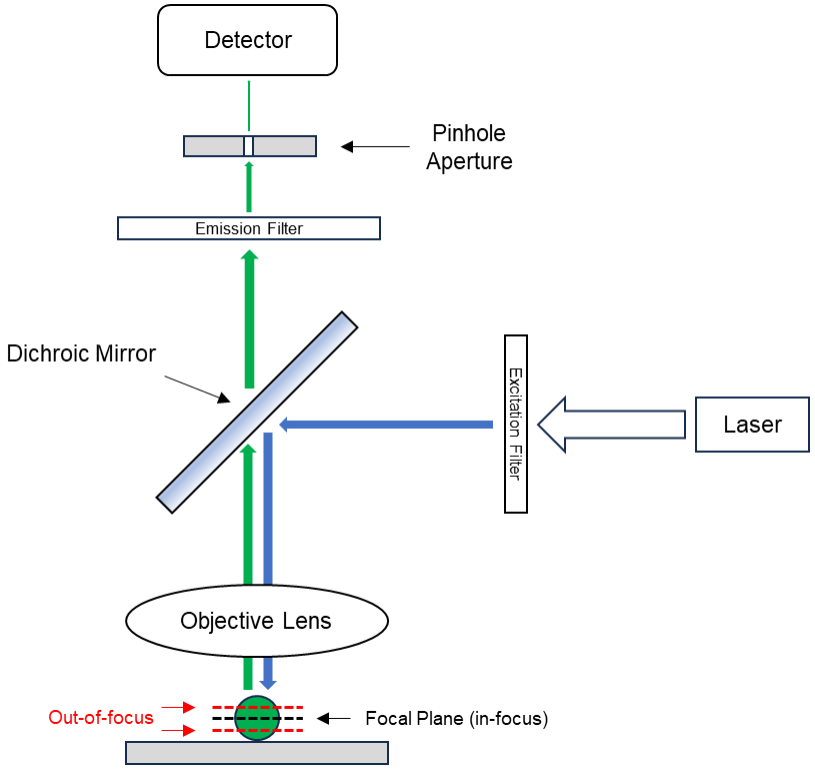

Figure 2.13: Schematic diagram showing the key components of a confocal fluorescence microscopy setup.

2.10. References

1. A. Michelson and A. R. Todd, *J. Chem. Soc.*, 1955, 2632-2638.
2. R. L. Letsinger and K. K. Ogilvie, *J. Am. Chem. Soc.*, 1969, **91**, 3350-3355.
3. R. Letsinger, J. Finnan, G. Heavner and W. Lunsford, *J. Am. Chem. Soc.*, 1975, **97**, 3278-3279.
4. S. Beaucage and M. Caruthers, *Tetrahedron Lett.*, 1981, **22**, 1859-1862.
5. G. M. Blackburn, J. K. Watts, M. Egli and M. J. Gait, *Nucleic Acids in Chemistry and Biology*, Royal Society of Chemistry, Cambridge, 2022.
6. ATDBio, https://atdbio.com/nucleic-acids-book/Solid-phase-oligonucleotide-synthesis, (accessed February 2023).
7. ATDBio, https://atdbio.com/nucleic-acids-book/Purification-of-oligonucleotides, (accessed February 2023).
8. J. Rajawat and G. Jhingan, *Data Processing Handbook for Complex Biological Data Sources*, Elsevier, London, 2019, ch. 1, pp. 1-20.
9. L. Haff, P. Juhasz, S. Martin, M. Roskey, I. Smirnov, W. Stanick, M. Vestal and K. Waddell, *Analusis*, 1998, **26**, 26-30.
10. C. S. Ho, C. Lam, M. H. Chan, R. Cheung, L. Law, L. Lit, K. Ng, M. Suen and H. Tai, *The Clinical Biochemist Reviews*, 2003, **24**, 3.
11. R. Thomas, *Gene*, 1993, **135**, 77-79.
12. A. I. Dragan, R. Pavlovic, J. B. McGivney, J. R. Casas-Finet, E. S. Bishop, R. J. Strouse, M. A. Schenerman and C. D. Geddes, *J. Fluoresc.*, 2012, **22**, 1189-1199.
13. B. G. Moreira, Y. You and R. Owczarzy, *Biophys. Chem.*, 2015, **198**, 36-44.
14. H.-H. Perkampus, *UV-VIS Spectroscopy and its Applications*, Springer Science & Business Media, 2013, ch. 2, pp. 3-9.
15. S. R. Gallagher and P. R. Desjardins, *Curr. Protoc. Mol. Biol.*, 2006, **76**, 1-21.
16. IDT Technologies, https://eu.idtdna.com/calc/analyzer, (accessed February 2023).
17. J. R. Albani, *Principles and Applications of Fluorescence Spectroscopy*, John Wiley & Sons, Oxford, 2008, ch. 7, pp. 88-114.
18. C. G. Zoski, *Handbook of Electrochemistry*, Elsevier, 2006.
19. W. R. Browne, *Electrochemistry*, Oxford Chemistry Primers, Oxford, 2018.
20. N. Elgrishi, K. J. Rountree, B. D. McCarthy, E. S. Rountree, T. T. Eisenhart and J. L. Dempsey, *J. Chem. Educ.*, 2018, **95**, 197-206.

21. A. J. Bard, L. R. Faulkner and H. S. White, *Electrochemical Methods: Fundamentals and Applications*, John Wiley & Sons, Oxford, 2022.
22. S. Trasatti and O. A. Petrii, *J. Electroanal. Chem.*, 1992, **327**, 353-376.
23. A. Ulman, *Chemical Reviews*, 1996, **96**, 1533-1554.
24. L. A. Chrisey, G. U. Lee and C. E. O'Ferrall, *Nucleic Acids Res.*, 1996, **24**, 3031-3039.
25. F. Ricci, N. Zari, F. Caprio, S. Recine, A. Amine, D. Moscone, G. Palleschi and K. W. Plaxco, *Bioelectrochemistry*, 2009, **76**, 208-213.
26. M. Muller, *Introduction to Confocal Fluorescence Microscopy*, SPIE press, Bellingham, 2006, ch. 1, pp. 1-23.
27. M. J. Sanderson, I. Smith, I. Parker and M. D. Bootman, *Cold Spring Harbor Protocols*, 2014, DOI: 10.1101/pdb.top071795.

Chapter 3: Synthesis and Characterisation of Redox Labels and Modified DNA

3.1. Introduction

This chapter details the design, synthesis, purification and characterisation of a library of modified oligonucleotides. The uses of these modified oligonucleotides are detailed in Chapters 4–6. A brief overview of the modifications incorporated into DNA is given in this introduction. Then, the syntheses of the phosphoramidite versions of two of these modifications – CuCy and Fc – followed by the design, synthesis, purification, and characterisation of the modified oligonucleotides are described.

3.1.1. Electrochemical Modifications

As described in Chapter 1, CuCy (Figure 3.1, left) is a copper-containing complex belonging to a family of redox-active, DNA-intercalating macrocycles first synthesised by Kowalski and coworkers.[1,2] The Cu^{2+} cation is d^9 and the surrounding tetradentate cyclidene macrocycle adopts a square planar conformation. Tucker and coworkers developed the system by incorporating CuCy into DNA using automated DNA synthesis and investigating its ability to discriminate between bases (*i.e.*, SNVs) at the position opposite the CuCy in a probe–target duplex.[3] Also described in Chapter 1, Fc (Figure 3.1, right) is an iron-containing complex which has been commonly used as a DNA modification owing to its stability, ease of functionalisation and well-studied redox activity. Fc-modified DNA has been used to directly sense nucleic acids, with the change in the Fc redox signal signifying the detection of a target.[4-6] Fc has also been used as one part of a ratiometric sensing mechanism, either remaining constant[7] or changing[8-10] upon the addition of a target nucleic acid.

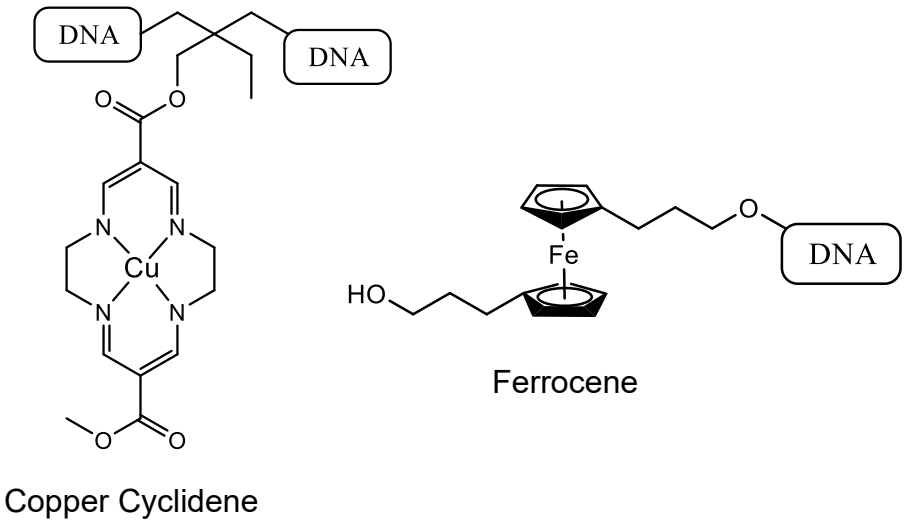

Figure 3.1: CuCy incorporated internally into DNA (left) and Fc incorporated at the 5' end of DNA (right).

3.1.2. Linking Modifications

Linking modifications such as disulphides and alkynes (Figure 3.2) are designed to react under certain conditions to link the modified oligonucleotide to entities such as reporter groups or surfaces. The disulphide can be reduced to a thiol, which can then react with gold to covalently tether the oligonucleotide to the surface to create a SAM as described in Chapter 2. Alkynes can react with an azide *via* copper-catalysed click chemistry to form a cyclic 1,4-triazole linker, coupling the alkyne-modified oligonucleotide to another group. Copper-catalysed azide-alkyne cycloaddition reactions have been used to modify and functionalise a range of biomolecules, including DNA,[11] peptides[12] and carbohydrates.[13]

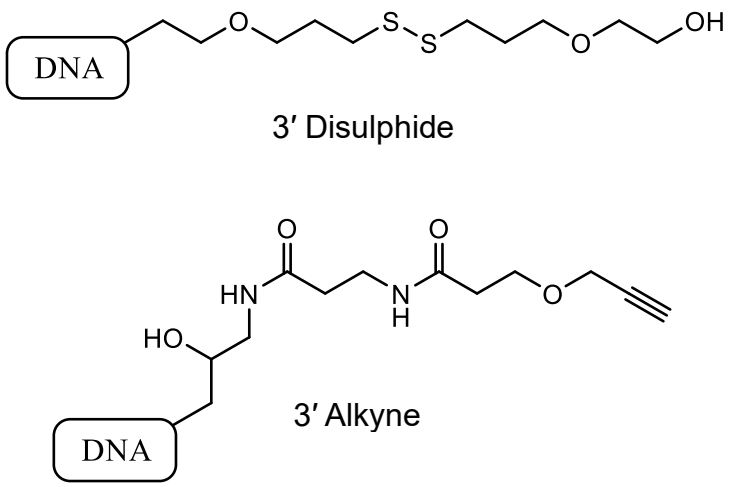

Figure 3.2: 3' disulphide (top) and 3' alkyne linker (bottom) modifications.

3.1.3. Fluorescent Modifications

Cy3 and Cy5 (Figure 3.3) belong to the cyanine dye family and have commonly been used for biological labelling.[14-16] Cy3 and Cy5 are classified as closed cyanines due to the two heterocycles at the ends of the polymethine chain[17] and have excitation/emission wavelengths of approximately 554/570 nm and 650/670 nm, respectively. Due to the overlap between the excitation/emission spectra of Cy3 and Cy5, Förster resonance energy transfer (FRET) can occur between the two fluorophores. FRET is the process that occurs when an excited donor fluorophore non-radiatively transfers energy to an acceptor fluorophore at distances between 0.5–10 nm[18] and is described in detail in Chapter 6.

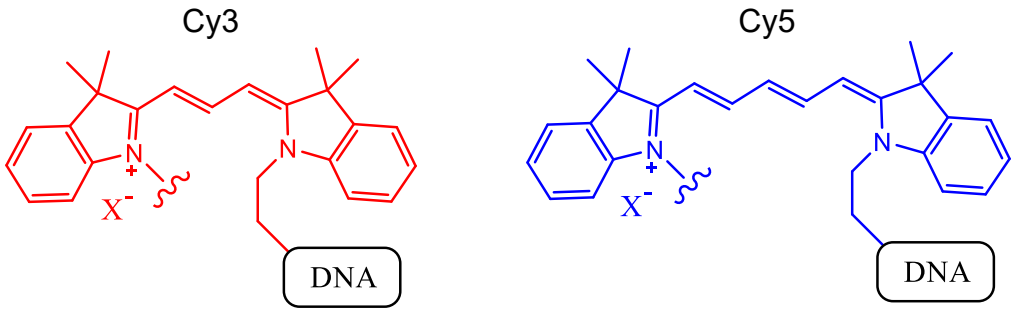

Figure 3.3: Structures of the cyanine dyes Cy3 (left) and Cy5 (right) attached to DNA at the 5' end.

3.1.4. Spacer Modifications

C3 spacers can be incorporated into DNA, resulting in the removal of a nucleoside whilst maintaining the structural integrity of the phosphodiester backbone (Figure 3.4, top). C3 spacer-modified oligonucleotides have been used to investigate how removal of nucleosides affects enzyme activity on DNA[19] and to probe the function of individual nucleotides in DNAzymes (DNA oligonucleotides capable of catalysing specific chemical reactions).[20] Longer spacers are also used to modify DNA, with polyethylene glycol (PEG) spacers particularly common. PEG spacers consist of any number of ethylene glycol units (Figure 3.4, bottom) and can extend the modified oligonucleotide to many times its original length.[21]

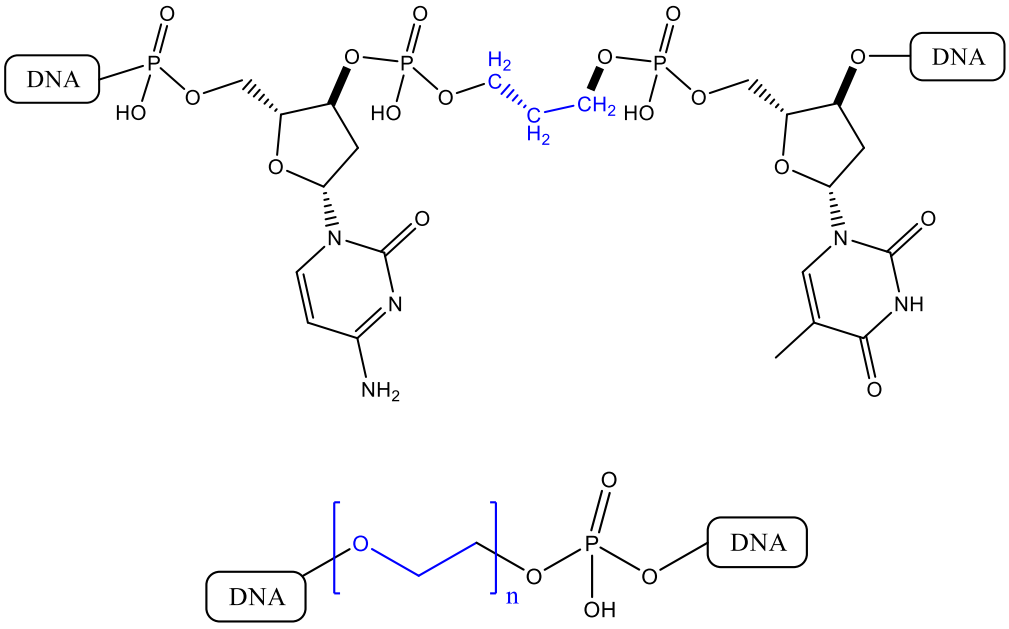

Figure 3.4: Top: structure of DNA modified with a C3 spacer (highlighted in blue) which removes an entire nucleoside. Bottom: structure of DNA modified with a PEG spacer (highlighted in blue). For the P18 spacer used in this thesis, n = 6.

3.2. Redox Label Synthesis

3.2.1. Copper Cyclidene Macrocycle Phosphoramidite Synthesis

The first step was the synthesis of the two 'halves' of the macrocycle in the form of methyl diformylacetate **2**, according to procedures reported by Knutson and coworkers (scheme 3.1).[22]

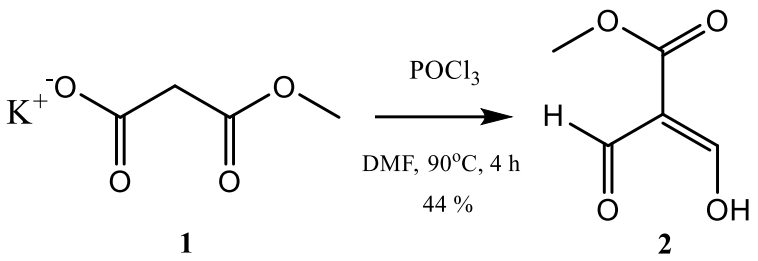

Scheme 3.1: Synthesis of methyl diformylacetate **2**.

The key intermediate steps during the synthesis of **2** are shown in Scheme 3.2.[22] First, phosphorus oxychloride reacted with DMF to form the Vilsmeier reagent. Potassium monomethyl malonate then reacted with the Vilsmeier reagent to form **2a**, before further reaction with another equivalent of Vilsmeier reagent to form **2c** via **2b**. Under basic conditions a formylation event occurred to give **2d** before an acidic workup produced the product **2**, which was collected by vacuum distillation with a yield of 44%. Although traces of impurities were visible in the NMR spectrum, further purification was deemed impractical and the product was reacted on as-was. Several factors contributed to the low yield. The vacuum distillation had to be carefully controlled so as to not lose any product, including cooling the collection vessel in a dry-ice acetone bath; even removal of solvent on the rotary evaporator was done cautiously to prevent product evaporation. To ensure efficient formation of the Vilsmeier reagent, dried DMF and fresh phosphorus oxychloride had to be used. The product **2** was found to be unstable

in acidic conditions for extended periods and therefore extraction following the acidification had to be done promptly.

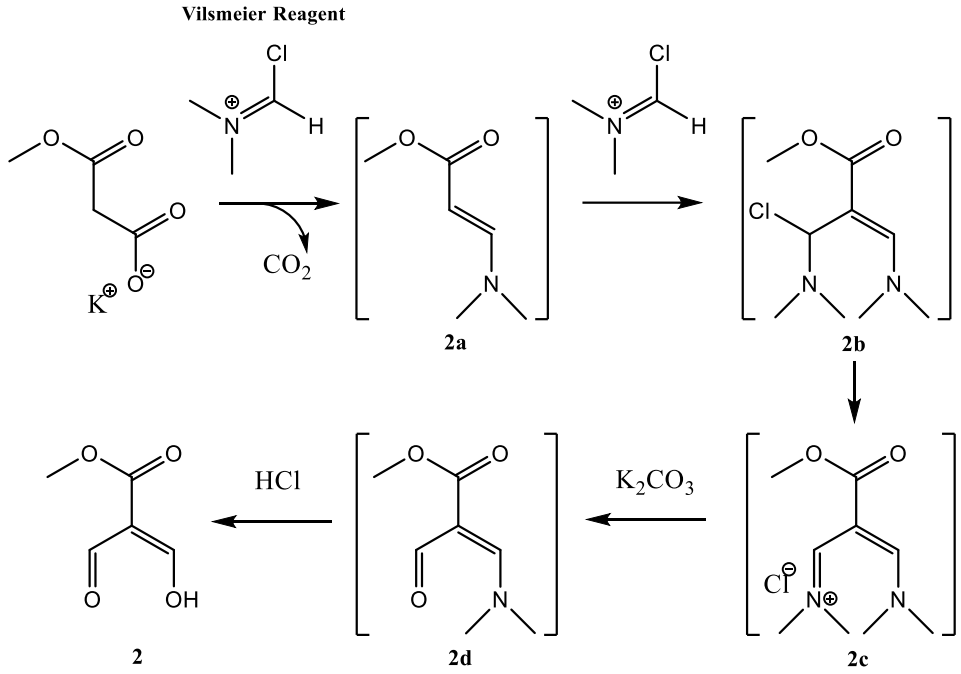

Scheme 3.2: Intermediate steps formed during the synthesis of methyl diformylacetate **2**. (Adapted from reference 22.)

The next step was the synthesis of the 14-membered cyclidene macrocycle **3** (Scheme 3.3) according to procedures reported by Takamura and coworkers.[23] Ethylenediamine was diluted in methanol before being added dropwise slowly to a solution of **2** in methanol. High dilution methods are commonly employed in the syntheses of macrocycle complexes to avoid unwanted polymerisation.[24,25] An alteration to Takamura and coworkers' procedure in this work was the increase in reaction time from 6 h to 18 h, which significantly increased the yield. Despite the increased reaction time, the modest yield of 51% reflects the competing side-reactions that detracted from product formation. When recrystallising the crude product to collect the pure product, multiple batches were harvested over several days. Given more time, the yield could

have been increased by harvesting more batches; however, the amount collected was more than sufficient for subsequent syntheses.

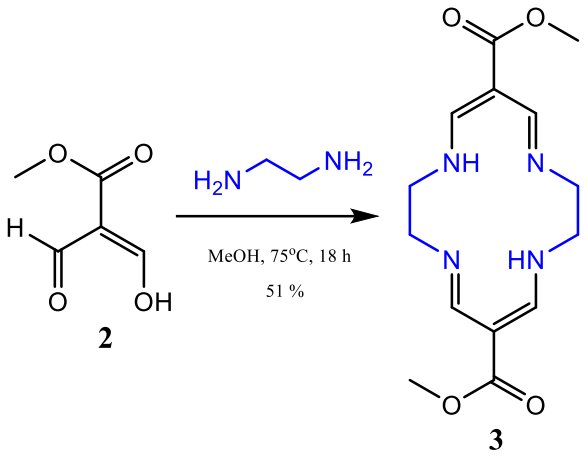

Scheme 3.3: Synthesis of the cyclidene macrocycle **3**.

Copper was then introduced to **3** to produce the copper cyclidene macrocycle **4** (Scheme 3.4). Formation of the product was observed soon after the reaction mixture was heated by the onset of a deep red colour. The Cu^{2+} cation with a d^9 configuration sits at the centre of the macrocycle, which adopts a square planar conformation. This rendered **4** (and its subsequent synthetic derivatives) paramagnetic, because of the lone unpaired electron in the HOMO ($d_{x^2-y^2}$), meaning NMR spectroscopy could not be used in their analyses. The reaction was high yielding and completed quickly, with the product crashing out of solution as a red solid. No purification was required as no traces of impurities were visible upon thin layer chromatography (TLC) analysis.

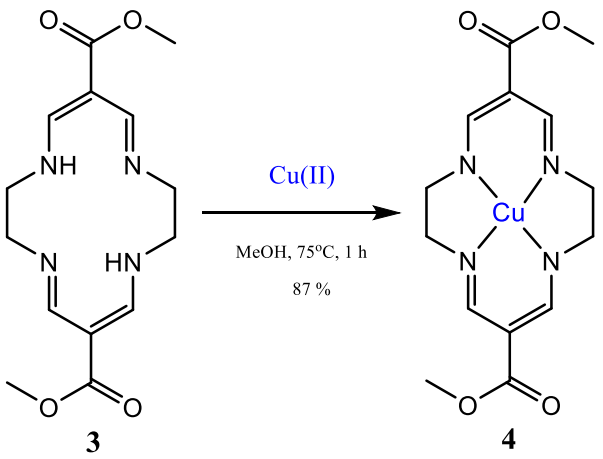

Scheme 3.4: Synthesis of the copper cyclidene macrocycle **4**.

Modification of one of the ester groups on **4** to form the diol **6** was then undertaken (Scheme 3.5). The first stage was the transesterification of both esters using a sodium catalyst and trimethylolpropane. The reaction time of 72 h was three times as long as that reported by Tucker and coworkers[3] owing to incomplete transesterification after 24 h. Once complete formation of the bis-diol **5** was confirmed by TLC, the reaction temperature was reduced to 80 °C and methanol added. The reaction mixture was then carefully monitored with TLC, until it was judged that the spot for the mono-diol **6** was at its most intense, and then quenched, after approximately 24 h. After precipitating the crude containing unreacted **4**, mono-diol **6**, and bis-diol **5**, the constituents were easily separated using column chromatography owing to the significant differences in polarity afforded by 0/1/2 hydroxyl groups. The low yield of 39% reflects the careful balancing act between waiting too long to quench after methanol addition (over-formation of **4**) versus not waiting long enough (under-reaction of **5**).

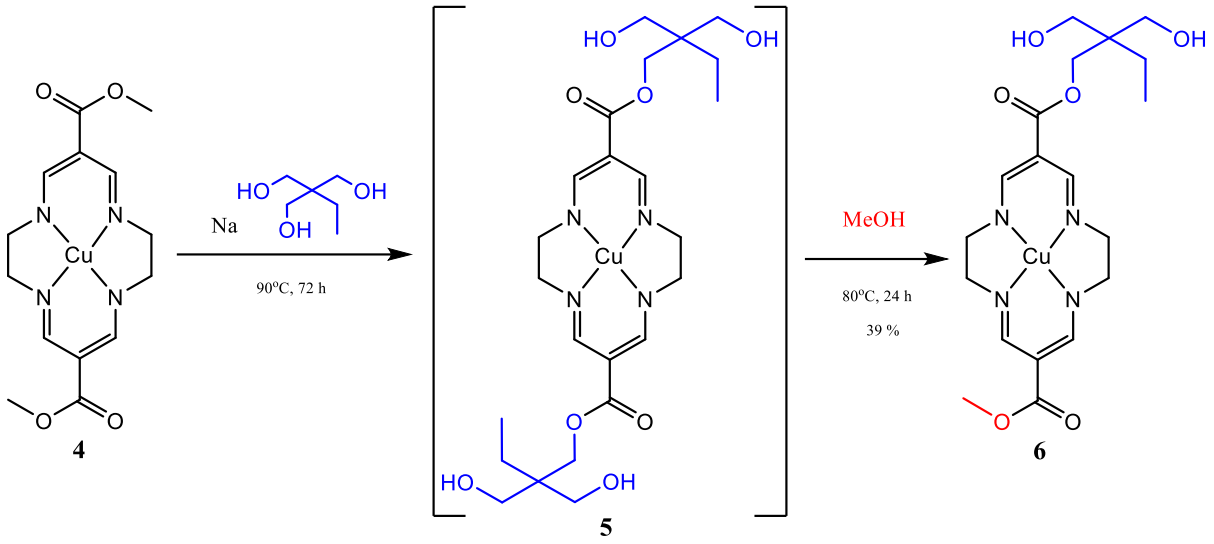

Scheme 3.5: Synthesis of the copper cyclidene mono-diol **6** *via* the bis-diol **5**.

One of the hydroxyl groups in **6** was then protected with a DMT protecting group (Scheme 3.6) prior to phosphitylation. To prevent excessive formation of the thermodynamic bis-substituted product, the reaction was conducted at room temperature with only 1.2 molar equivalents of DMTCl. The DMT protecting group is used in DNA synthesis because of its sensitivity to mild acidic conditions and therefore easy removal for each coupling step. During purification of the DMT-protected product **7** using column chromatography, this sensitivity to acidic conditions necessitated the use of triethylamine to neutralise the mildly acidic silica gel. The low yield of 41% is again reflective of the inevitable formation of bis-substituted side product and the retention of unreacted diol **6**. Both the bis-substituted side product and starting material **6** were collected, as the former could be regenerated back into **6** using glacial acetic acid and the latter could be reacted again. It was at this stage that a stereogenic centre was formed (highlighted with an asterix in Scheme 3.6.), which had important effects on the purification and sensing properties of the CuCy-modified DNA.

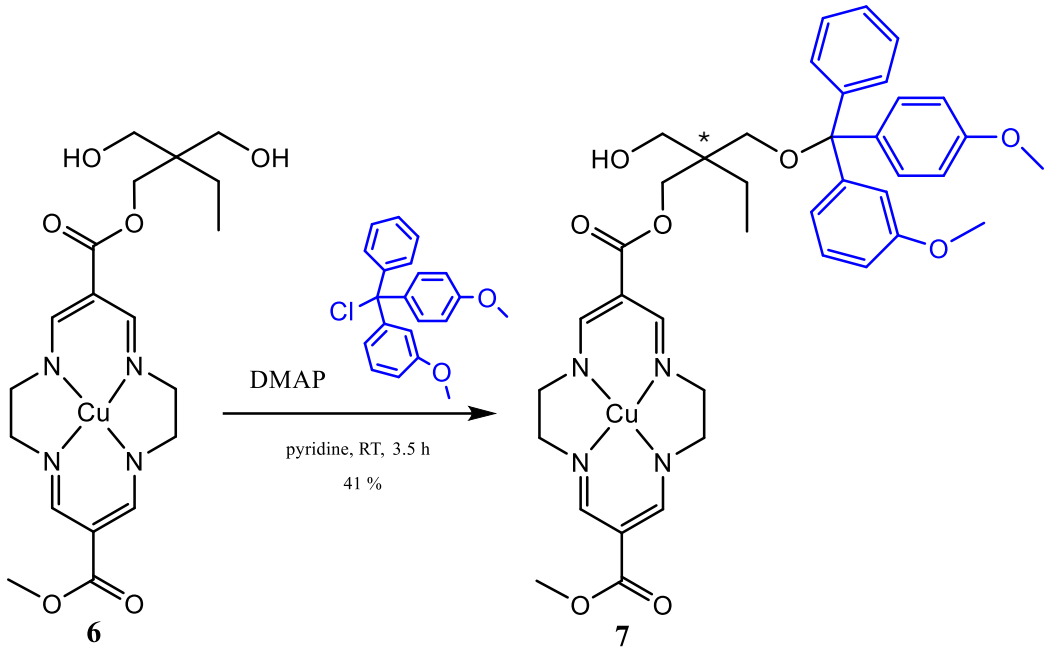

Scheme 3.6: Protection of one of the hydroxyl groups on **6** using a DMT protecting group. The * highlights the stereogenic centre.

Finally, phosphitylation of **7** was conducted by reaction of the remaining hydroxyl group with 2-cyanoethyl *N*,*N*-diisopropylchlorophosphoramidite and *N*,*N*-diisopropylethylamine (DIPEA) in dry dichloromethane (Scheme 3.7). The P(III) in the resultant phosphoramidite **8** is easily oxidised to P(V), an event that must be prevented as P(V) is incompatible with automated DNA synthesis. To minimise any P(III) to P(V) oxidation, all reagents were thoroughly deoxygenated prior to use. As with the previous tritylation step, triethylamine was used during purification to neutralise the mildly acidic silica gel and prevent removal of the DMT protecting group.

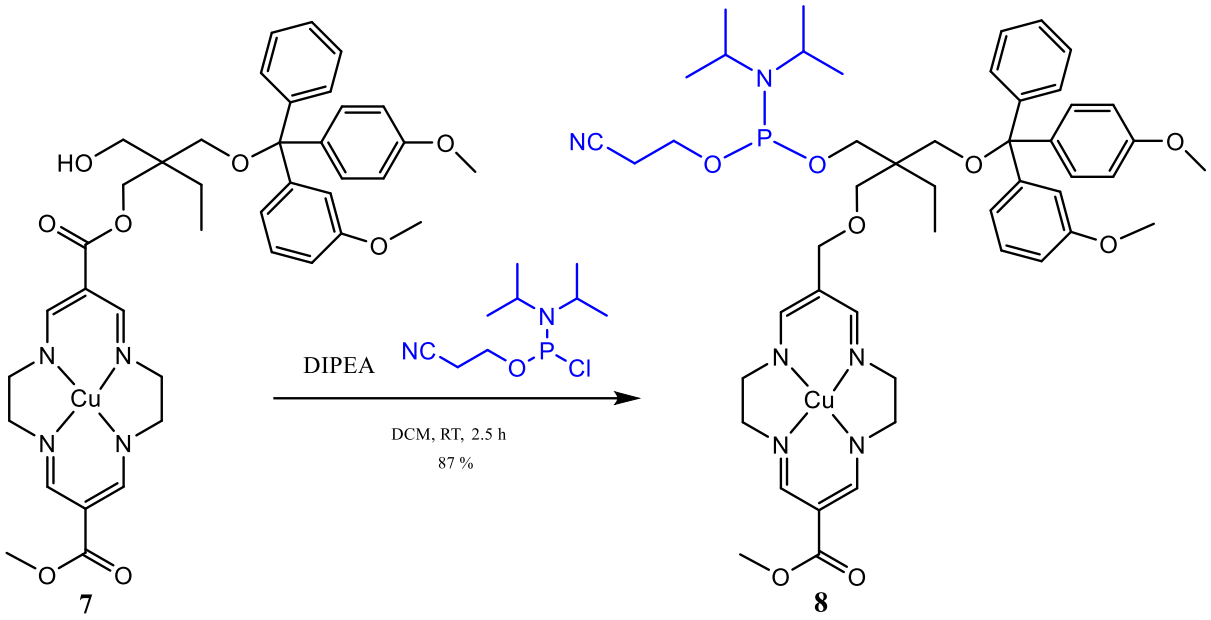

Scheme 3.7: Phosphitylation of **7** to form the copper cyclidene macrocycle phosphoramidite **8**.

3.2.2. Ferrocene Phosphoramidite Synthesis

The synthesis of the Fc phosphoramidite **15** is shown in Scheme 3.8 and is adapted from the procedures published by Ihara and coworkers.[26] Although the process involves several steps, the synthesis of **15** is more straightforward than the synthesis of the CuCy phosphoramidite **8** and the procedures more established within the Tucker group. Therefore, only a brief overview will be provided here. The synthesis of **15** follows the same route as for all phosphoramidite reagents intended for automated DNA synthesis: *i.e.* the generation of the diol (**13**) which is tritylated (**14**) and then phosphitylated (**15**). Yields for all steps were reasonable except for the synthesis of the diester **11** and tritylated Fc **14**. The former could most likely be improved with the use of fresher NaH and the latter is typically low-yielding due to the formation of bis-substituted side product and the retention of unreacted starting material. Starting on a 3 g scale and with an overall yield of 9%, a sufficient amount of **15** was synthesised to perform dozens of couplings on the automated DNA synthesiser.

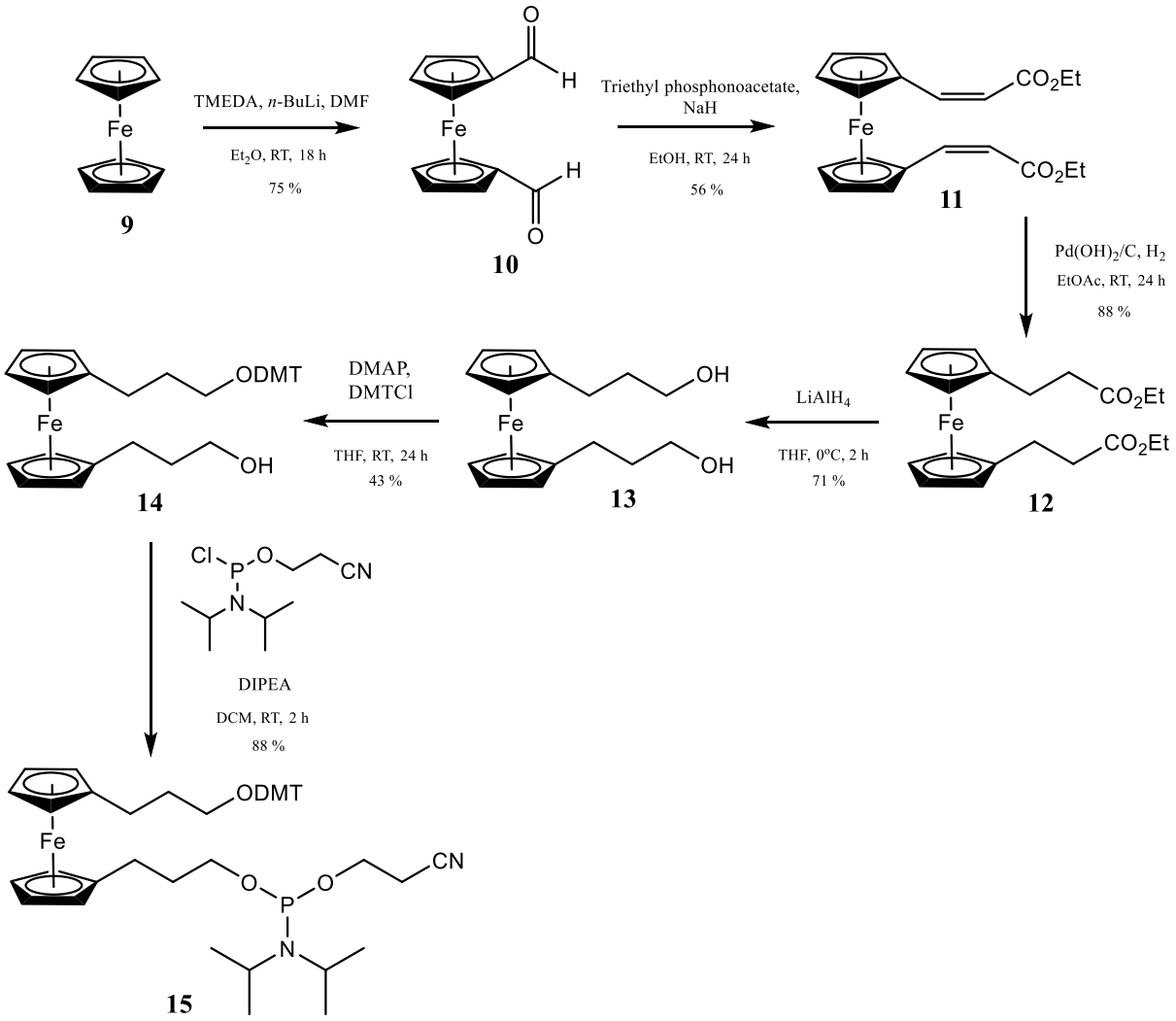

Scheme 3.8: Synthesis of the Fc phosphoramidite **15**.

3.3. Oligonucleotide Probe Synthesis

3.3.1. General Design Considerations

All modified oligonucleotides synthesised and used are shown in Table 3.1. Within the Tucker group a standard in-house test sequence (**T1unmod**, sometimes colloquially referred to as the "NINA" sequence) has been used for a number of years (Table 3.1). It has been thoroughly studied[3,27] and was thus used as the basis for all modified oligonucleotides not based on clinically relevant sequences. Probe oligonucleotides that were based on clinically relevant

sequences (**B1**, **K1**, **E1**, **N1**, **miR135-1**) consisted of base sequences complementary to the 'real-life' target sequence in question.

Table 3.1: The standard in-house test sequence used within the group for a number of years (**T1unmod**) and the modified oligonucleotides synthesised for this thesis. X = CuCy; F = Fc; S = disulphide; C3 = C3 spacer; P18 = P18 spacer; Z = alkyne; Cy3 = Cyanine 3; Cy5 = Cyanine 5.

Oligonucleotide	5′ – Sequence – 3′
T1unmod	TGG ACT CTC TCA ATG
T1	F TGG ACT CXC TCA ATG S
(*S*)-T1	F TGG ACT CXC TCA ATG S
CuCyMid	TGG ACT CXC TCA ATG S
B1	F AGA TTT CXC TGT AGC S
K1	F TAC GCC AXC AGC TCC S
E1	F AAA CCT TXA ACA CCA S
N1	F ACA CCA TXA GTG GGT S
miR135-1	F TCA CAT AGG AAT XAA AAG CCA TA S
CuCy5′	X TGG ACT CTC TCA ATG S
CuCy3′	TGG ACT CTC TCA ATG X S
FcMid	TGG ACT CFC TCA ATG S
Fc5′	F TGG ACT CTC TCA ATG S
Fc3′	TGG ACT CTC TCA ATG F S
CuCy5′-30mer	X TGG ACT CTC TCA ATG TGG ACT CTC TCA ATG S
Fc5′-30mer	F TGG ACT CTC TCA ATG TGG ACT CTC TCA ATG S
T1-21mer	F CAT TGG ACT CXC TCA ATG TAC S
B1-30mer	F GGA CCC ACT CCA TCG AGA TTT CXC TGT AGC S
CuCyMid_C3-2	TGG ACT CXC C3CA ATG S
CuCyMid_C3+2	TGG ACC3 CXC TCA ATG S
T2A_C3-2	CAT TGC3 GAG AGT CCA
T2A_C3+2	CAT TGA GAG C3GT CCA
DNA-Cy3	Cy3 TGG ACT CTC TCA ATG TTT Z
DNA-Cy5	Cy5 CAT TGA GAG AGT CCA TTT Z
DNA-Cy3-Ext	Cy3 TGG ACT CTC TCA ATG TTT TTT P18 Z
DNA-Cy5-Ext	Cy5 CAT TGA GAG AGT CCA TTT TTT P18 Z

The ability of the CuCy to discriminate between bases at the position opposite in the probe–target duplex had previously been investigated in free solution when it had been incorporated internally at the eighth position within the probe oligonucleotide.[3,28] Accordingly for this work, involving surface-based SNV sensing (Chapter 4), the CuCy was also placed at the same position. Where CuCy was placed internally but not at the centre of the probe, this was done firstly to match the location of a base that differentiated two closely related miRNA targets

(**miR135-1**), and secondly to keep the relative position of CuCy to the electrode surface constant whilst extending probe length in an attempt to increase sensitivity (**B1-30mer**) (Chapter 5). CuCy was also placed at the 5′ end (**CuCy5′**) and after the disulphide at the 3′ end (**CuCy3′**) to investigate whether different bases around it would affect its sensing capabilities (Chapter 5). Fc, for this work mostly used to generate an internal reference signal, was usually placed at the 5′ end of oligonucleotides in which it was incorporated. Being at the end of a probe oligonucleotide, it was intended for the Fc to be relatively unaffected by probe–target duplex formation and therefore for it to produce a constant current (Chapters 4 and 5). Where Fc was not placed at the 5′ end (**FcMid** and **Fc3′**), this was to investigate the impact of the modification location on the current produced (Chapter 5).

The linker modifications 3′ disulphide and 3′ alkyne were placed at the 3′ end of the oligonucleotides whenever they were incorporated. Being at the 3′ end, CPG-attached versions of each could be readily purchased and on which the rest of the oligonucleotide would be then synthesised in the 3′ to 5′ fashion demanded by automated DNA synthesis.

C3 spacer modifications were placed internally at positions that might affect any through-DNA electron transport occurring between the CuCy and the electrode (Chapter 5). P18 spacer modifications were placed in **DNA-Cy3-Ext** and **DNA-Cy5-Ext** immediately after the 3′ alkyne modifications to extend the lengths of the oligonucleotides in an effort to facilitate hybridisation once attached to MOFs (Chapter 6).

For the studies involving MOFs (Chapter 6), Cy3 and Cy5 were placed at the 5′ end of the oligonucleotides, with the intention that the Cy3-modified DNA would hybridise with the complementary Cy5-modified DNA after being attached to their respective MOFs. The

resultant duplex would have the fluorophores separated by 15 base pairs – a distance capable of facilitating FRET.

All "unmodified" target oligonucleotides used are shown in Table 3.2. Bases that sit opposite the CuCy in the relevant probe–target duplexes are highlighted in red. For example, targets for the **B1** probe, **B2A** and **B2T**, are identical bar the adenine/thymine switch at position 8. Although all probe oligonucleotides made were modified DNA, several RNA targets were bought commercially to investigate RNA sensing. The DNA target **T2ran** and the RNA target 23RNAran consisted of random bases not complementary to any probe and were used to assess specificity.

Table 3.2: Target and unmodified oligonucleotides. Bases highlighted in red sit opposite CuCy in the duplexes formed with complementary CuCy-modified probes. mC = methylated cytosine.

Oligonucleotide	5′ – Sequence – 3′
T2A	CAT TGA GAG AGT CCA
T2C	CAT TGA GCG AGT CCA
T2G	CAT TGA GGG AGT CCA
T2T	CAT TGA GTG AGT CCA
T25mC	CAT TGA GmCG AGT CCA
T2ran	ACA GCT TCA TGG AAG
T1unmod	TGG ACT CTC TCA ATG
B2A	GCT ACA GAG AAA TCT
B2T	GCT ACA GTG AAA TCT
K2A	GGA GCT GAT GGC GTA
K2G	GGA GCT GGT GGC GTA
K2T	GGA GCT GTT GGC GTA
E2A	TGG TGT TAA AGG TTT
E2G	TGG TGT TGA AGG TTT
N2A	ACC CAC TAA TGG TGT
N2T	ACC CAC TTA TGG TGT
21T2T	GTA CAT TGA GAG AGT CCA ATG
30B2T	GCT ACA GTG AAA TCT CGA TGG AGT GGG TCC
T2A_mm-2	CAT TGT GAG AGT CCA
T2A_mm+2	CAT TGA GAG TGT CCA
16T2A5′	ACA TTG AGA GAG TCC A
16T2T5′	TCA TTG AGA GAG TCC A
16T2A3′	CAT TGA GAG AGT CCA A
16T2T3′	CAT TGA GAG AGT CCA T
RNA_T2A	CAU UGA GAG AGU CCA

RNA_T2U	CAU UGA GUG AGU CCA
RNA_T2ran	AUG GGC AUU CCG AUC
miR135b-5p	UAU GGC UUU UCA UUC CUA UGU GA
miR135a-5p	UAU GGC UUU UUA UUC CUA UGU GA
23RNAran	UAC CCU GUA GAU CCG AAU UUG UG

3.3.2. Oligonucleotide Synthesis

Oligonucleotides were synthesised using solid-phase automated DNA synthesis (see section 7.2 for full details). They could either be synthesised using 'standard' or 'ultramild' conditions, the latter being used when a modification was considered not able to withstand the comparatively harsher standard conditions. When employing ultramild conditions, ultramild variants of the oxidiser, activator, capping reagent A and adenine/guanine phosphoramidites are used. Additionally, post-synthesis, instead of heating the crude oligonucleotides at 60 ºC for 6 h in concentrated ammonia to cleave them for the resin and remove the protecting groups, they are instead soaked in methanolic potassium carbonate overnight at RT to achieve the same result. However, not cleaving the oligonucleotides from the resin *in situ* on the column necessitates the use of an additional desalting column to remove the resin prior to HPLC purification, in addition to the standard use of a desalting column after HPLC purification. These factors – *i.e.* less-forcing conditions and the use of two desalting columns post-synthesis – result in ultramild conditions generally producing lower yields than standard conditions. Previous work in the Tucker group has shown that CuCy is not compatible with DNA synthesis using standard conditions.[3,28] As such, all CuCy-modified oligonucleotides were synthesised using ultramild conditions. As per the manufacturer's instructions, all Cy3- and Cy5-modified oligonucleotides were also synthesised using ultramild conditions. The remaining modifications are comparatively more stable and therefore all oligonucleotides *not* modified with CuCy/Cy3/Cy5 were synthesised using standard conditions.

When using freshly prepared samples in acetonitrile, the CuCy, Fc, and C3 and P18 spacer modifications gave stepwise yields for DNA coupling that were similar to those for the nucleobase phosphoramidites. However, Cy3 and Cy5 modifications exhibited significantly poorer coupling efficiencies, with Cy3 coupling particularly poorly at stepwise yields 70–80% lower than nucleobase phosphoramidites. This can be explained by the relatively low solubility of the two cyanine dyes in acetonitrile. The solubility of Cy3 in acetonitrile was so poor that dichloromethane (DCM) had to be used as an alternative solvent, as detailed in section 7.2.2.

3.3.3. Oligonucleotide Purification

Oligonucleotides were purified using semi-preparative RP-HPLC with an acetonitrile/triethylammonium acetate buffer eluent system (see section 7.3 for full details). The retention times and % purities as determined by analytical HPLC of the purified modified oligonucleotides are shown in Table 3.3. With the exception of the C3 spacer-modified and Cy3-/Cy5-modified oligonucleotides, all modified oligonucleotides were purified using a gradient increase of acetonitrile from 15–25% over 30 min. All unmodified oligonucleotides were purified by an increase of acetonitrile from 5–18% over 25 min. A detection wavelength of 260 nm was used for all oligonucleotides, in addition to 554 nm and 650 nm for Cy3- and Cy5-modified oligonucleotides, respectively.

Table 3.3: Analytical HPLC retention times and % purities as determined by integration of the HPLC peaks. S = disulphide; C3 = C3 spacer; alkyne = 3' alkyne; Cy3 = Cyanine 3; Cy5 = Cyanine 5; P18 = P18 spacer.

Oligonucleotide	Modifications	Retention time (min)	HPLC Purity (%)	
T1	CuCy, Fc, S	28.70	100	15–25% acetonitrile gradient over 30 min.
(*S*)-T1	CuCy, Fc, S	27.34	95.7	
CuCyMid	CuCy, S	15.11	98.8	
B1	CuCy, Fc, S	26.99	96.3	
K1	CuCy, Fc, S	28.59	95.8	
E1	CuCy, Fc, S	27.64	97.0	
N1	CuCy, Fc, S	26.04	96.2	
miR135-1	CuCy, Fc, S	26.53	100	
CuCy5′	CuCy, S	29.54	99.8	
CuCy3′	CuCy, S	31.61	98.9	
FcMid	Fc, S	22.67	96.8	
Fc5′	Fc, S	25.25	99.2	
Fc3′	Fc, S	28.34	99.9	
CuCy5′-30mer	CuCy, S	25.40	99.8	
Fc5′-30mer	Fc, S	21.60	100	
T1-21mer	CuCy, Fc, S	23.72	100	
B1-30mer	CuCy, Fc, S	20.69	100	
CuCyMid_C3-2	CuCy, C3, S	14.62	96.7	
CuCyMid_C3+2	CuCy, C3, S	15.12	95.5	
T2A_C3-2	C3	16.41	99.3	Different acetonitrile gradients.
T2A_C3+2	C3	16.73	99.1	
DNA-Cy3	Cy3, alkyne	32.11	98.5	
DNA-Cy5	Cy5, alkyne	23.21	100	
DNA-Cy3-Ext	Cy3, P18, alkyne	30.89	100	
DNA-Cy5-Ext	Cy5, P18, alkyne	22.27	100	

Incorporation of all modifications increased RP-HPLC retention times. Unmodified oligonucleotides had retention times of between 12–17 min using relatively less acetonitrile, whilst most modified oligonucleotides had retention times of at least 20 min using relatively more acetonitrile. The increased retention times indicate that the modifications interact more with the comparatively non-polar, hydrophobic stationary phase. Owing to the formation of a

stereogenic centre during the synthesis of the CuCy phosphoramidite, its incorporation into DNA resulted in two diastereomers for each CuCy-modified oligonucleotide (Figure 3.6). This was also observed in previous work involving CuCy-modified DNA,[3,28] in addition to anthracene-modified DNA which similarly possessed a stereogenic centre.[29] The (*R*)-isomer eluted shortly after the (*S*)-isomer, indicating that the CuCy interacts more with the stationary phase when adopting the (*R*) over the (*S*) conformation. As the two diastereomers exhibited different electrochemical sensing capabilities,[3] the two were separated out for each CuCy-modified oligonucleotide. All reported CuCy-modified oligonucleotides incorporated the (*R*)-isomer, except for **(*S*)-T1** which incorporated the (*S*)-isomer. The differences in electrochemical sensing between the CuCy (*S*)- and (*R*)-isomers are reported and discussed in Chapter 5.

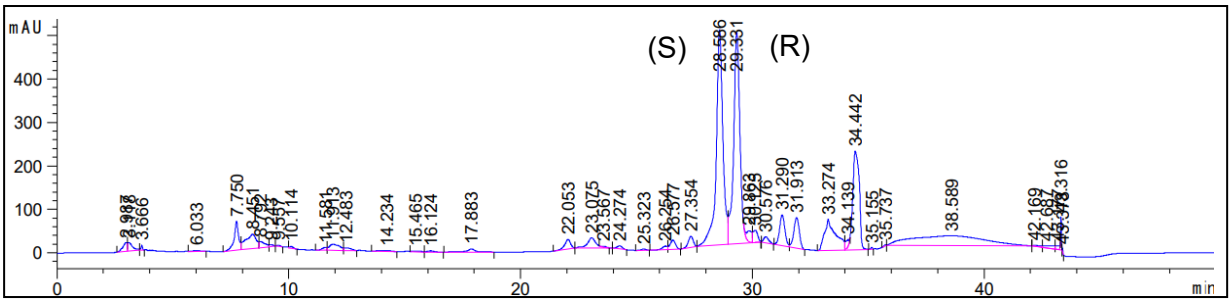

Figure 3.6: Analytical HPLC of crude CuCy5' prior to purification. The two main peaks correspond to the (*S*)- and (*R*)-isomers. Detector wavelength 260 nm.

The location of the CuCy within the modified oligonucleotide had a remarkably large impact on retention time (Figure 3.7). Incorporating CuCy at the 5′ end (**CuCy5′**) or towards the 3′ end (**CuCy3′**) resulted in retention times of around 28–29 min. Incorporating the CuCy in the middle of the oligonucleotide (**CuCyMid**) instead resulted in a retention time of 15 min. Such drastic differences in retention times reflects the different extents to which CuCy is exposed and therefore its interaction with the stationary phase: it is less exposed when incorporated internally and more exposed when incorporated at or near the ends.

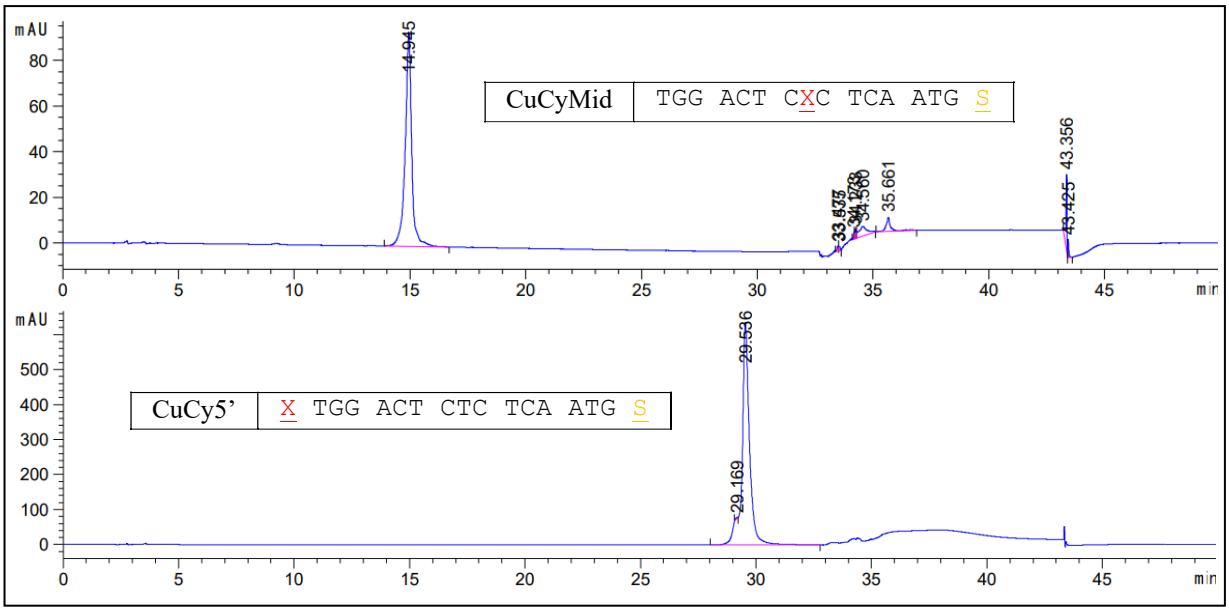

Figure 3.7: Analytical HPLCs of purified **CuCyMid** (top) and CuCy5' (bottom). The same acetonitrile:buffer gradient (15–25% acetonitrile over 30 min) was used for each. Detector wavelength 260 nm. Sequences are shown 5' to 3'. X = CuCy, S = disulphide.

A similar trend in retention times was observed when Fc was incorporated at or near the strand ends (**Fc5′** and **Fc3′**) compared with when it was incorporated in the middle (**FcMid**), albeit with smaller differences (Table 3.3). This suggests that the Fc is comparatively more exposed than CuCy regardless of its position in the oligonucleotide, which might be expected given that Fc does not lend itself to stacking between nucleobases as comfortably as the planar CuCy moiety. For oligonucleotides modified with both CuCy and Fc, addition of the Fc at the 5′ end increased their retention times by around 14 min, indicative of the increased hydrophobicity of the strands. Removal of a nucleoside using a C3 spacer to produce the modified oligonucleotides **T2A_C3-2** and **T2A_C3+2** resulted in only marginally increased retention times versus the unmodified analogue (**T2A**) using the same HPLC method. Notwithstanding the slightly different eluent conditions (see section 7.3), the oligonucleotides modified with Cy3/Cy5 and an alkyne group at the 3′ end (**DNA-Cy3** and **DNA-Cy5**), had relatively long retention times in accordance with the hydrophobicity of the added groups, with

incorporation of a P18 spacer and three additional thymine bases to create **DNA-Cy3-Ext** and **DNA-Cy5-Ext** resulting in marginal decreases in retention times.

3.3.4. Oligonucleotide Characterisation and Quantification

Analytical RP-HPLC was used to check purity, with any oligonucleotides less than 95% pure purified again using semi-preparative RP-HPLC. Electrospray ionisation mass spectrometry was used to confirm that the desired oligonucleotide had been synthesised, with the results for the modified oligonucleotides shown in Table 3.4. All oligonucleotides matched their predicted exact masses with the exception of **E1**, which had a mass 15 units greater than predicted. This was seen with other CuCy-modified oligonucleotides and had been attributed to oxidised CuCy and the additional presence of an oxygen atom ($(M-H)^-$ ion).[28] Although **E1** (as well as all other CuCy-modified oligonucleotides) was recorded as being synthesised using ultramild reagents, the inadvertent addition of an oxygen atom to the Cu^{2+} cation could have been caused by improper preparation of the CuCy phosphoramidite solution or the accidental loading of a standard reagent (oxidiser) onto the DNA synthesiser. The effects of the additional oxygen on the electrochemical properties of **E1** are discussed in Chapter 4. After purification and characterisation, oligonucleotide quantification was achieved by application of UV/Vis spectroscopy and the Beer Lambert Law (see section 7.4 for full details.).

Table 3.4: Modified oligonucleotide negative mode electrospray ionisation mass spectrometry results. * indicates the inadvertent oxidation of the CuCy.

Oligonucleotide	Calculated Exact Mass	Observed Exact Mass
T1	5465.88	5466.06
(*S*)-T1	5465.88	5466.56
CuCyMid	5101.93	5102.30
B1	5480.00	5480.79
K1	5396.00	5396.43
E1	5397.95	5412.43*
N1	5514.95	5515.40
miR135-1	7970.40	7971.31
CuCy5′	5405.93	5406.36
CuCy3′	5405.93	5406.40
FcMid	4932.85	4932.81
Fc5′	5236.89	5237.01
Fc3′	5236.89	5236.85
CuCy5′-30mer	10008.67	10010.44
Fc5′-30mer	9839.64	9839.32
T1-21mer	7278.23	7278.42
B1-30mer	10038.68	10040.30
CuCyMid_C3-2	4921.83	4921.82
CuCyMid_C3+2	4921.83	4921.82
T2A_C3-2	4423.77	4424.17
T2A_C3+2	4423.77	4424.17
DNA-Cy3	6294.26	6293.20
DNA-Cy5	6378.31	6377.27
DNA-Cy3-Ext	7549.52	7549.41
DNA-Cy5-Ext	7633.56	7633.44

3.4. References

1. A. Rybka, R. Kolinski, J. Kowalski, R. Szmigielski, S. Domagala, K. Wozniak, A. Wieckowska, R. Bilewicz and B. Korybut-Daszkiewicz, *Eur. J. Inorg. Chem.*, 2007, DOI: 10.1002/ejic.200600744.
2. U. E. Wawrzyniak, M. Woźny, J. Kowalski, S. Domagała, E. Maicka, R. Bilewicz, K. Woźniak and B. Korybut-Daszkiewicz, *Chem. - Eur. J.*, 2009, **15**, 149-157.
3. J. Duprey, J. Carr-Smith, S. L. Horswell, J. Kowalski and J. H. R. Tucker, *J. Am. Chem. Soc.*, 2016, **138**, 746-749.
4. C. H. Fan, K. W. Plaxco and A. J. Heeger, *Proc. Natl. Acad. Sci. U. S. A.*, 2003, **100**, 9134-9137.
5. T. Ihara, Y. Maruo, S. Takenaka and M. Takagi, *Nucleic Acids Res.*, 1996, **24**, 4273-4280.
6. M. J.-R. Mayreli Ortiz, Vasso Skouridou, Diana Machado, Miguel Viveiros, Taane G. Clark, Anna Simonova, David Kodr, Michal Hocek, and Ciara K. O'Sullivan, *ACS Sens.*, 2021, DOI: 10.1021/acssensors.1c01710.
7. Y. Du, B. J. Lim, B. L. Li, Y. S. Jiang, J. L. Sessler and A. D. Ellington, *Anal. Chem.*, 2014, **86**, 8010-8016.
8. L. P. Luo, L. L. Wang, L. P. Zeng, Y. R. Wang, Y. P. Weng, Y. J. Liao, T. T. Chen, Y. K. Xia, J. Zhang and J. H. Chen, *Talanta*, 2020, DOI: 10.1016/j.talanta.2019.120298.
9. E. H. Xiong, X. H. Zhang, Y. Q. Liu, J. W. Zhou, P. Yu, X. Y. Li and J. H. Chen, *Anal. Chem.*, 2015, **87**, 7291-7296.
10. F. L. Gao, L. Du, Y. Zhang, D. Q. Tang and Y. Du, *Anal. Chim. Acta*, 2015, **883**, 67-73.
11. A. H. El-Sagheer and T. Brown, *Chem. Soc. Rev.*, 2010, **39**, 1388-1405.
12. A. A. Ahmad Fuaad, F. Azmi, M. Skwarczynski and I. Toth, *Molecules*, 2013, **18**, 13148-13174.
13. X.-P. He, Y.-L. Zeng, Y. Zang, J. Li, R. A. Field and G.-R. Chen, *Carbohydr. Res.*, 2016, **429**, 1-22.
14. M. Lipowska, G. Patonay and L. Strekowski, *Synth. Commun.*, 1993, **23**, 3087-3094.
15. A. Fegan, P. S. Shirude and S. Balasubramanian, *Chem. Commun.*, 2008, DOI: 10.1039/B801629A.
16. J. W. Park, Y. Kim, K.-J. Lee and D. J. Kim, *Bioconjugate Chem.*, 2012, **23**, 350-362.

17. H. Shindy, *Dyes Pigm.*, 2017, **145**, 505-513.
18. R. M. Clegg, *Laboratory Techniques in Biochemistry and Molecular Biology*, Elsevier, 2009, vol. 33, ch. 1, pp. 1-57.
19. Y. Wang, M. T. T. Ng, T. Zhou, X. Li, C. H. Tan and T. Li, *Bioorg. Med. Chem. Lett.*, 2008, **18**, 3597-3602.
20. B. Wang, L. Cao, W. Chiuman, Y. Li and Z. Xi, *Biochemistry*, 2010, **49**, 7553-7562.
21. S. Wang, S. S. Park, C. T. Buru, H. Lin, P.-C. Chen, E. W. Roth, O. K. Farha and C. A. Mirkin, *Nat. Commun.*, 2020, **11**, 2495.
22. M. Nakane, H. Gollman, C. R. Hutchinson and P. L. Knutson, *J. Org. Chem.*, 1980, **45**, 2536-2538.
23. S. Takamura, T. Yoshimiya, S. Kameyama, A. Nishida, H. Yamamoto and M. Noguchi, *Synthesis*, 2000, **5**, 637-639.
24. P. Ruggli, *Eur. J. Org. Chem*, 1912, **392**, 92-100.
25. K. Ziegler, H. Eberle and H. Ohlinger, *Eur. J. Org. Chem*, 1933, **504**, 94-130.
26. T. Ihara, D. Sasahara, M. Shimizu and A. Jyo, *Supramol. Chem.*, 2009, **21**, 207-217.
27. J.-L. H. Duprey, D. M. Bassani, E. I. Hyde, G. Jonusauskas, C. Ludwig, A. Rodger, N. Spencer, J. S. Vyle, J. Wilkie and Z.-Y. Zhao, *Org. Biomol. Chem.*, 2018, **16**, 6576-6585.
28. E. Wilkinson, PhD thesis, University of Birmingham, 2020.
29. J. Manchester, D. M. Bassani, J.-L. H. Duprey, L. Giordano, J. S. Vyle, Z.-y. Zhao and J. H. Tucker, *J. Am. Chem. Soc.*, 2012, **134**, 10791-10794.

Chapter 4: Electrochemical Sensing of Single Nucleotide Variants Using Redox-Modified DNA Probes

4.1. Introduction

As discussed in Chapter 1, a SNV is the overarching term for a change at a single locus (*i.e.*, nucleobase) in a nucleic acid sequence, with those that are present in germline DNA (and in at least 1% of the population) denoted SNPs. Many SNVs have been shown to alter gene expression and/or change the structure and functioning of encoded proteins, potentially resulting in disease. Because of this, SNVs are of great diagnostic value and several methods have been developed or adapted to sense them. This chapter focuses on the electrochemical detection of SNVs using surface-immobilised probes, with the main focus on canonical nucleobase changes.

4.1.1. Fluorescent Intercalators and Reporter/Quencher Probes for Single Nucleotide Variant Sensing

A variety of fluorescence-based methods have been employed to sense SNVs. The products of specially designed real-time qPCR runs, in which allele-specific primers result in different rates of amplification in wild-type/mutant targets, can be analysed by melting curve analysis using intercalating dyes such as SYBR Green I.[1,2] Fluorescent molecular beacons have also been used to detect SNVs, typically when used with real-time qPCR.[3,4] The assays involve multiple molecular beacons, each labelled with a different fluorophore/quencher pair, that unravel and bind only to perfectly matched sections of the target. The molecular beacons are designed to bind to the section of the target that contains the SNV, with the sequence of each beacon identical bar the base opposite the SNV site. Amplification of just one target, in the

presence of the multiple molecular beacons, results in a fluorogenic response only from the beacon that perfectly matches the target (Figure 4.1). In a similar fashion, Taqman probes have also been used to sense SNVs, with multiple probes designed to be cleaved and produce different fluorogenic responses depending on which target is being amplified.[5,6]

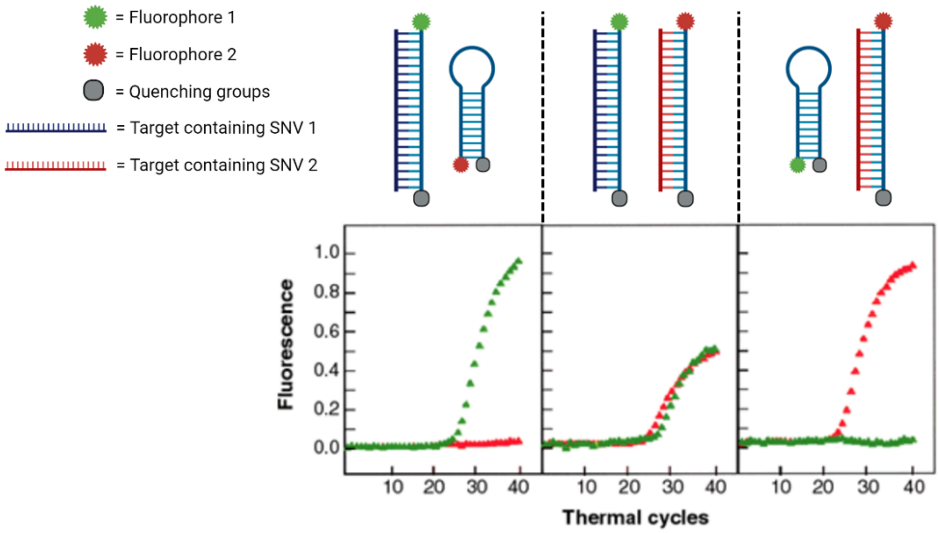

Figure 4.1: Fluorogenic responses specific to the molecular beacons that perfectly matched the target being amplified, as reported by Kramer and coworkers. The left and right plots are the result of only wild-type and mutant targets being amplified, respectively; the middle plot is the result of both wild-type and mutant targets being amplified. (Adapted from reference 3.)

Although these fluorescence-based methods are commercially dominant in the sensing of SNVs, they suffer from several drawbacks. As intercalating dyes such as SYBR Green I interact non-specifically with double-stranded DNA,[7] the primers must be carefully designed to ensure that the correct amplicons are produced on which to carry out the melting curve analyses. Molecular beacons, with their susceptibility to non-specific interactions,[8] must be carefully designed to avoid giving false positives, particularly if those used to discriminate between SNVs differ by only one base. The same logic applies to Taqman probes, which additionally are also dependent on the activity of Taq polymerase and therefore must be used in a PCR-based setup (a restriction that does not apply to molecular beacons, which can be used in SNV-sensing setups that do not involve target amplification[9]). Furthermore, molecular beacons,

Taqman probes, and any other method of SNV sensing that involves labelling fluorophores, are also restricted by the number of fluorophores/quenchers available. Multiple, simultaneous sensing of SNVs (*i.e.*, multiplexing) is possible to some extent but is limited by the useable window of the electromagnetic spectrum.[10] Any involvement of PCR also results in challenges in terms of speed (a typical real-time qPCR run takes 1–2 hours to complete[11]) and improving the accessibility of the method to those without specialist training and well-equipped labs.

4.1.2. Fluorescent Microarrays and Sequencing Technologies for Single Nucleotide Variant Sensing and Mapping

Other fluorescence-based methods have also been used to sense SNVs. SNV microarrays are a variant of DNA microarrays that involve capture probes which are specific to the wild-type and possible mutant targets.[12] Depending on the type of SNV microarray used, fluorescently-labelled signal probes or nucleotides are used to identify the base at a known SNV location. The data are then analysed computationally to determine quantitively the prevalence of a particular SNV. One major drawback to SNV arrays is that they can only interrogate known SNV locations and thus require prior genomic information.[13] Sequencing technologies, most prominently some NGS methods and their use of fluorescently-labelled nucleotides, offer one of the best ways of mapping unknown SNVs in a genome.[13-15] New SNVs are located by comparing multiple sequences and identifying consistent differences at certain points.[13,16] As with SNV microarrays, the data collected by NGS technologies require extensive computational processing. Both SNV microarrays and NGS also typically involve PCR amplification.[12,16] Furthermore, neither SNV arrays or NGS tend to be suitable for point-of-care diagnostics, with run times taking hours to days and extensive training and well-equipped laboratories essential.[12,13,16]

4.1.3. Electrochemical Mismatch Detection

Electrochemical sensing of SNVs offers an alternative read-out method to fluorescence. To demonstrate specificity, some sensors have been tested with targets containing mismatches: the more mismatches present in the target, the weaker the readout signals that result. Using this approach, targets containing one or more mismatches can be identified versus perfectly matched targets. Plaxco and coworkers reported on a sensor which used a triple-stem DNA probe specifically designed for single mismatch (*i.e.*, SNV) detection.[17] The surface-immobilised probe was modified with a MB at its terminal end and contained three stem loop structures in its unbound conformation (Figure 4.2). A section of the probe was complementary to perfectly matched target DNA. Upon target binding, the three stem-loop structures unravelled, bringing the MB closer to the electrode surface which resulted in an increased current signal. Because of the large thermodynamic changes involved in the unravelling of the three stem-loop structures, the probe was highly sensitive to mismatches. Probes involving one stem-loop structure (*i.e.*, classic redox-modified molecular beacons) are not as sensitive to mismatches, but still produce current signals that negatively correlate with the number of mismatched base pairs in the probe–target duplex.[18]

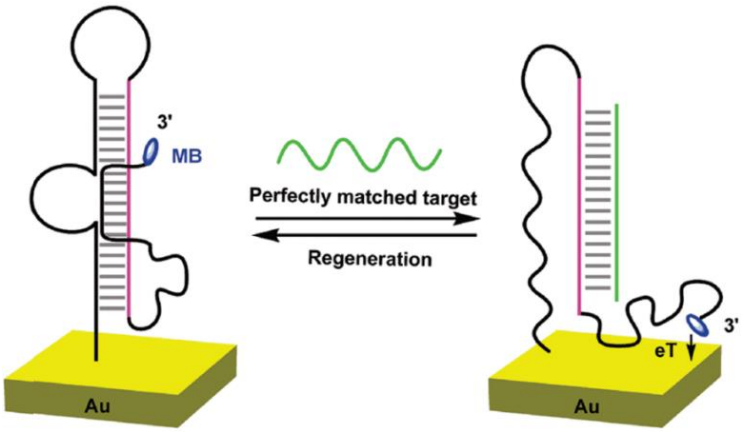

Figure 4.2: Plaxco and coworkers' triple-stem DNA probe designed for SNV detection. (Taken from reference 17.)

A variety of other sensors that use redox-modified DNA probes have also been used to discriminate between perfectly matched and mismatched targets, based on the same principle: that perfectly matched targets are thermodynamically favoured to form probe–target duplexes over mismatched targets and thus induce larger changes in current signals.[19-21] However, this approach has several drawbacks. Whilst the presence of mismatches can be detected, their specific locations in the target are hard to pinpoint. Additionally, the changes in current signals induced by targets containing one, two, three, *etc*. mismatches are often overlapping and hard to differentiate. Most importantly, from a SNV-sensing perspective, is that the nature of the mismatches are hard to interrogate as it is not easy to determine whether a mismatch is, for example, an A–G or an A–C mismatch – a distinction that can be vital when identifying clinically relevant SNVs.

4.1.4. Electrochemical Enzymatic Single Nucleotide Variant Sensing

Several electrochemical sensors have been designed to interrogate the specific nature of SNVs. An important subset of these use DNA polymerase or ligation enzymes whose activity occurs in a SNV-specific manner. A common setup includes a DNA primer probe, surface-immobilised at the 5′ end, that captures a SNV-containing target strand. On the partially hybridised primer probe–target duplex that results, enzymatic extension that incorporates redox-modified nucleotides signifies the presence of a particular base at the SNV location (Figure 4.3).

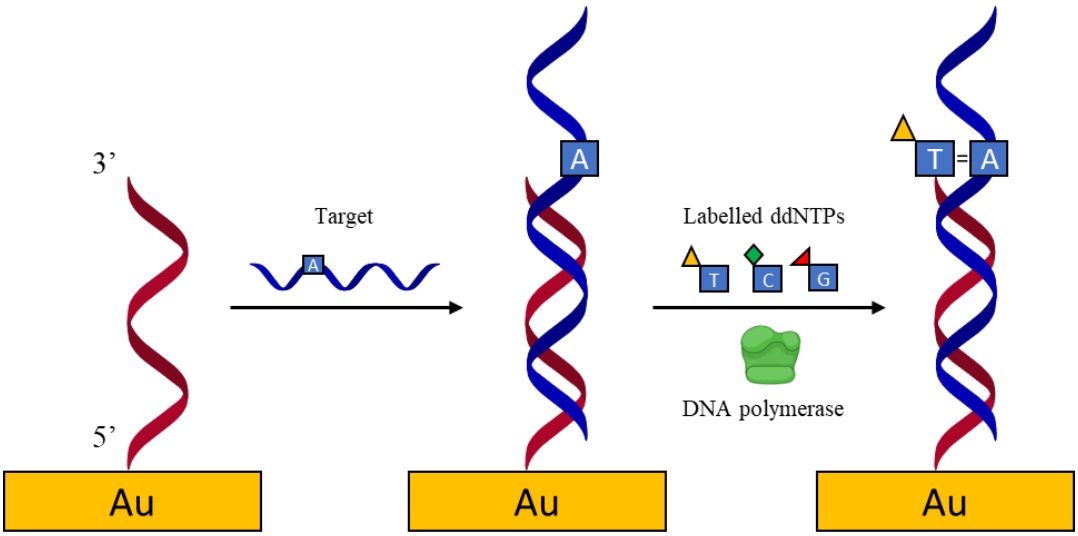

Figure 4.3: Schematic diagram of a sensor employing a primer DNA probe capturing a SNV-containing target strand, with a DNA polymerase enzyme then conducting a single-base extension with a redox-modified ddNTP in a SNV-dependent manner. A washing step followed by electrochemical interrogation identifies the redox-modified ddNTP remaining and thus the nucleobase present at the SNV location.

Ortiz and coworkers used dideoxynucleotides (ddNTPs, nucleotides that lack a 3′ hydroxyl group and thus inhibit further elongation after their addition by DNA polymerase) modified with common redox labels such as Fc and MB,[22] whilst O'Sullivan and coworkers used ddNTPs modified with polyoxymetalates.[23] Hocek and coworkers instead used Fc-modified nucleotides that did possess 3′ hydroxyl groups, with Fc-containing elongation products forming only on the primer that matched the SNV present in the target strand.[24] Other sensors have used DNA ligase enzymes, which similarly only activated in a SNV-specific manner to result in measurable current signal changes.[25,26] The major benefit of sensors that use DNA polymerase/ligase enzymes is the unequivocal nature of the results: enzymatic extension/ligation will only occur if a certain SNV is present. However, the very use of enzymes brings with it complications, with optimal temperature/pH windows required together with the ever-present threat of denaturation.

4.1.5. Electrochemical Ratiometric Single Nucleotide Variant Sensing

Only one example of electrochemical ratiometric SNV sensing can be found in the literature. Xiang and coworkers reported on a dual-tagged MB-/Fc-modified probe structure that underwent an amplification cycle in the presence of perfectly matched target (Figure 4.4).[27] Without the target present, a Fc-modified capture probe (Fc-CP in Figure 4.4) was bound to a MB-modified surface-immobilised oligonucleotide (MB-HP) by Watson-Crick base pairing in addition to Hoogsteen base pairing. Addition of the target (mp53) resulted in mp53 binding to Fc-CP, removing the Fc from the electrode surface and thus decreasing its current. MB-HP then formed a hairpin structure, bringing the MB closer to the electrode surface and thus increasing its current. Measuring the ratiometric change of the two currents resulted in more reproducible and sensitive sensing compared to measuring the change in either current individually. An additional oligonucleotide (AS-HP) was used to displace the mp53 in the mp53–Fc-CP duplex so that mp53 was free to initiate the cycle again. Changing one base in the target resulted in no current change taking place, enabling SNV detection. Although the amplification mechanism resulted in an exceptionally low limit of detection (LOD) in the fM range, drawbacks to the sensor include an inability both to locate the mutation within the target and to distinguish between different SNVs.

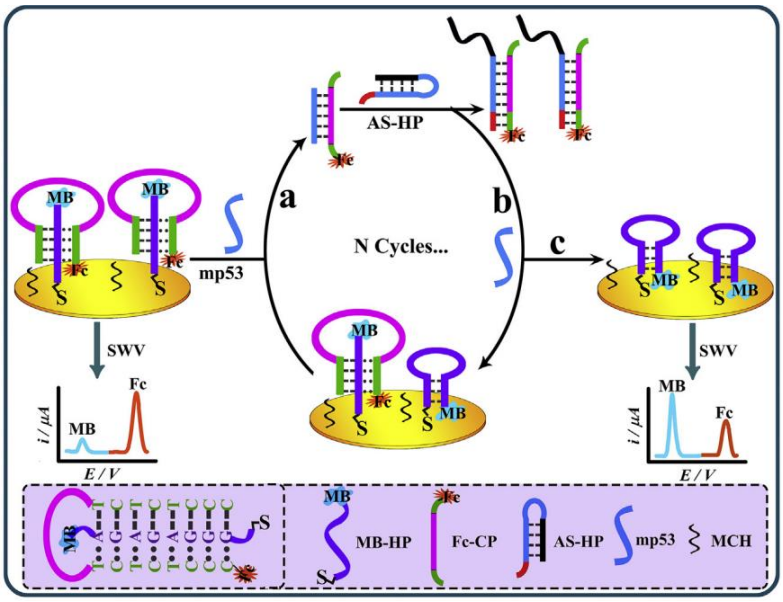

Figure 4.4: Xiang and coworkers' electrochemical ratiometric SNV sensor. The target mp53 is recycled resulting in the detachment of the Fc-modified hairpin from the electrode surface (decreasing Fc current) and the formation of a MB-modified hairpin at the electrode surface (increasing MB current). (Taken from reference 27.)

4.1.6. Electrochemical Copper Macrocycle Single Nucleotide Variant Sensing

Tucker and coworkers created a probe capable of electrochemically interrogating the specific nature of a SNV without the use of enzymes.[28] The planar, redox-active CuCy replaced one nucleoside and could intercalate into the probe–target duplex (Figure 4.5). In a solution-based setup, probe–target hybridisation resulted in a decrease in the CuCy's current as a result of its being within the duplex, where it was less able to facilitate electron transfer. Furthermore, the probe was able to discriminate between all four bases (*i.e.*, SNVs) at the position opposite the CuCy in the probe–target duplex. A proposed reason for this discriminatory ability was that the CuCy was buried deeper into the duplex to a greater or lesser extent depending on the size of the base opposite. Unlike other electrochemical sensors discussed previously, which typically employed probes that underwent large conformational changes upon target binding, more subtle shifts in the CuCy's position resulted in pronounced sensing differences that enabled the observed SNV sensing.

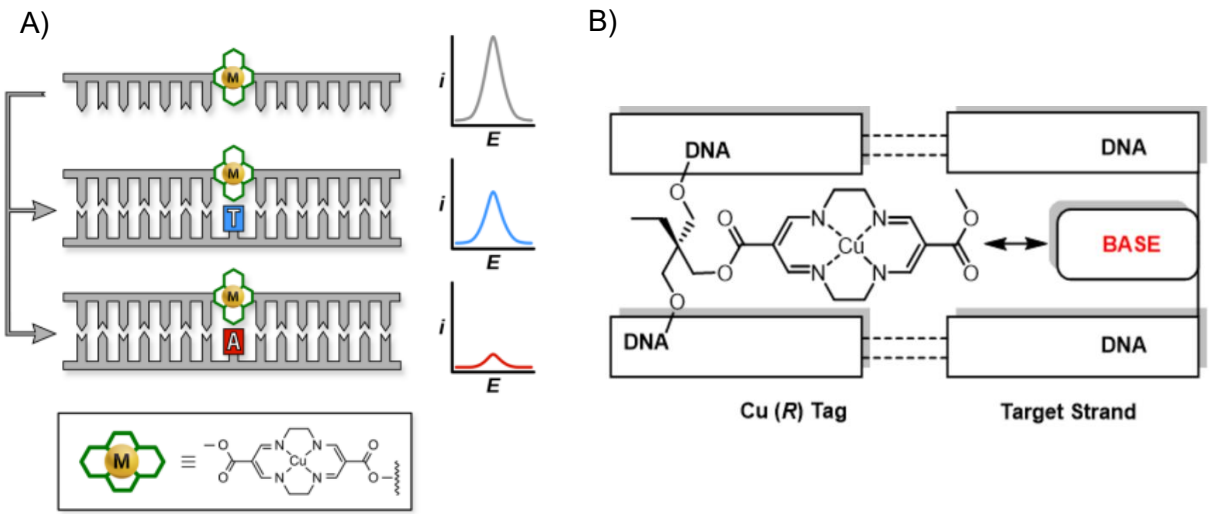

Figure 4.5: A) Tucker and coworkers' CuCy-modified probe exhibiting SNV discrimination. B) Schematic showing the interaction between the incorporated CuCy and the base opposite. (Taken from reference 28.)

4.2. Chapter Aims

The aim of this chapter is to sense clinically relevant SNVs using dual-labelled CuCy-/Fc-modified probes. Previous work in the group carried out by Dr Edward Wilkinson[29] focused on developing the solution-based CuCy-modified probe reported by Tucker and coworkers[28] in two main ways: 1) the surface-immobilisation of the probes to form SAMs and 2) the incorporation of a second redox label (Fc) into the probe to enable a ratiometric sensing mechanism. The main focus of this chapter is to further the development and understanding of this dual-labelled probe, in addition to its application in the sensing of clinically relevant SNVs. Having made the probes (described in Chapter 3), the first objective was to form SAMs and characterise the DNA-modified electrode surfaces. In particular, the electrochemical properties and probe packing densities of newly-formed SAMs were to be determined to aid in the interpretation of subsequent sensing results. The second objective was to determine the key sensing properties of the probe, namely stability, sensitivity and regeneration capability. These are fundamental characteristics of any nucleic acid sensor, regardless of any specialisation in SNV sensing. The third objective was to sense SNVs in a test sequence in addition to cancer-

related SNVs (BRAFV600E and KRAS G12V/G12D mutations), COVID19-related SNVs (E484K and N501Y mutations), and epigenetic nucleobase changes (cytosine to 5-methylcytosine). If successful, the results would provide the foundation for further development, understanding, and potential deployment of the sensor.

4.3. Probe Design and Self-Assembled Monolayer Formation

4.3.1. Probe Design and Function

The basic design and function of the CuCy-/Fc-modified (CuCyFc) probes is depicted in Figure 4.6. CuCy is incorporated centrally into the backbone of the probe oligonucleotide, replacing an entire nucleoside. Fc and a disulphide, whilst both also incorporated into the backbone of the probe, are added at the 5′ and 3′ ends respectively and do not replace any nucleotides. The probes form SAMs on the surface of gold electrodes *via* sulphur–gold chemistry. As with the solution-based setup,[28] probe–target binding induces the reduction of the CuCy current, which is attributed to inhibition of electron transfer between the CuCy and the electrode when the former is within a duplex. The amount by which the CuCy current is reduced is dependent on the base opposite in the probe–target duplex, enabling SNV sensing. The Fc, being at the end of the probe, is relatively unaffected by probe–target binding and therefore produces a constant current that is used as an internal reference. Prior to addition of the target, the disorder within the single-stranded system is larger than in the target-added double-stranded system, on account of the presence of more rigid, less flexible probe–target duplexes in the latter.

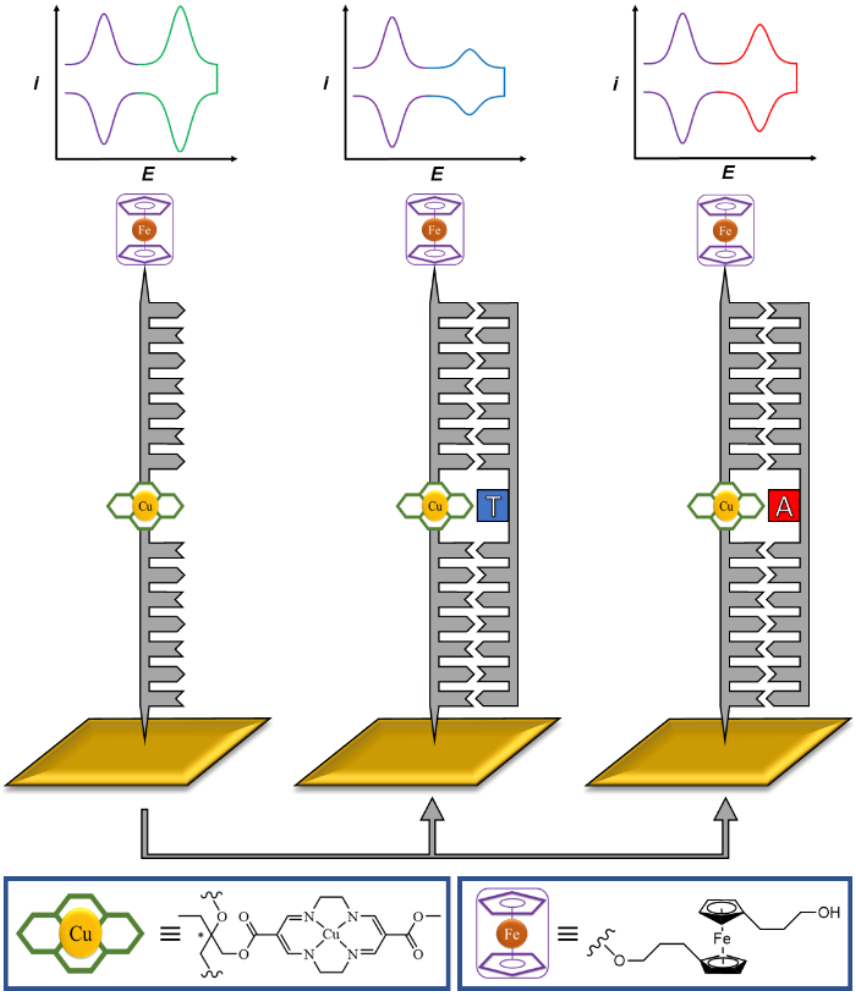

Figure 4.6: Schematic representation of a dual-labelled DNA probe used in this work, containing redox-active CuCy (* denotes stereogenic centre) and Fc complexes, and the effect of hybridisation with target DNA on its electrochemical properties.

Probe sequences and target sequences used in this chapter are shown in Table 4.1 and Table 4.2, respectively. **T1**, **(*S*)-T1** and **T1unmod** are based on the standard in-house test sequence used in the Tucker group. The sequences of all the other probe oligonucleotides are based on sections of the human genome which contain clinically relevant SNVs. The target sequences are complementary to their respective probes, with the base opposite the CuCy in the probe–target duplexes varied.

Table 4.1: Probe sequences used in this chapter. X = CuCy; F = Fc; S = disulphide.

Oligonucleotide	5′ – Sequence – 3′
T1	F TGG ACT CXC TCA ATG S
(*S*)-T1	F TGG ACT CXC TCA ATG S
CuCyMid	TGG ACT CXC TCA ATG S
B1	F AGA TTT CXC TGT AGC S
K1	F TAC GCC AXC AGC TCC S
E1	F AAA CCT TXA ACA CCA S
N1	F ACA CCA TXA GTG GGT S
T1unmod	TGG ACT CTC TCA ATG

Table 4.2: Target sequences used in this chapter. Bases highlighted in red sit opposite the CuCy in the probe–target duplexes formed. mC = 5-methylcytosine.

Oligonucleotide	5′ – Sequence – 3′
T2A	CAT TGA GAG AGT CCA
T2C	CAT TGA GCG AGT CCA
T2G	CAT TGA GGG AGT CCA
T2T	CAT TGA GTG AGT CCA
T25mC	CAT TGA GmCG AGT CCA
T2ran	ACA GCT TCA TGG AAG
B2A	GCT ACA GAG AAA TCT
B2T	GCT ACA GTG AAA TCT
K2A	GGA GCT GAT GGC GTA
K2G	GGA GCT GGT GGC GTA
K2T	GGA GCT GTT GGC GTA
E2A	TGG TGT TAA AGG TTT
E2G	TGG TGT TGA AGG TTT
N2A	ACC CAC TAA TGG TGT
N2T	ACC CAC TTA TGG TGT

4.3.2. Confirming Self-Assembled Monolayer Formation

Four gold electrodes were used, each with a diameter of 2 mm. Cyclic voltammetry was used to confirm that the probes formed SAMs on the gold electrodes. Figure 4.7A shows CVs recorded using the **T1** probe at various scan rates, with Figure 4.7B confirming a linear relationship between the Fc current and the scan rate. As detailed in section 2.7.2, a linear scan rate dependence provides evidence that the electrochemical activity is occurring at the surface of the electrode without any diffusion of the redox-active species, and thus it is used as evidence

for SAM formation. Although the use of TCEP ensures the reduction of the disulphide to a thiol and therefore enables the sulphur–gold reaction, DNA-modified electrodes prepared without the use of TCEP also resulted in the formation of SAMs, albeit of poorer quality (see Appendix 8.2.1.). Disulphide adsorption onto gold surfaces is known,[30] but reducing to thiols results in a greater extent of sulphur–gold reactions and therefore greater probe coverage of the electrode.

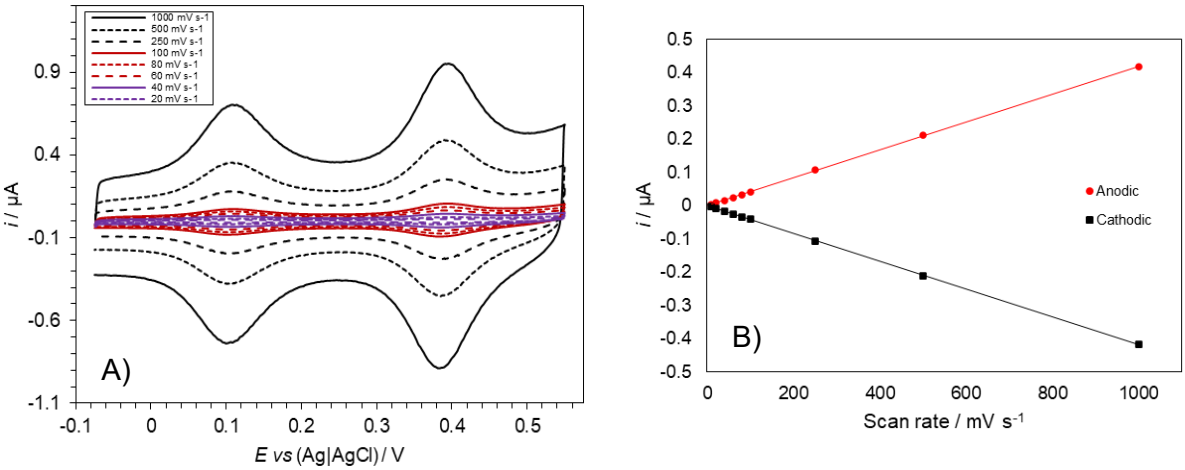

Figure 4.7: A) CVs of **T1** at various scan rates; in 10 mM sodium phosphate buffer (pH 7.0) 1 M $NaClO_4$. B) Dependence of the Fc currents on scan rate for **T1**, measured from the CVs shown in A.

4.3.3. Evaluating Probe Electrochemical Characteristics

$E_{1/2}$, ΔE_p and i_p^a/i_p^c values for the CuCy and Fc in the SAMs formed by the probe oligonucleotides are shown in Table 4.3 and Table 4.4, respectively. $E_{1/2}$ values were approximately 400 mV for CuCy and 110 mV for Fc, resulting in two non-overlapping yet relatively close redox signals. A spread in the $E_{1/2}$ values of 19 mV for CuCy and 15 mV for Fc indicated that the free energy changes of the electron transfer reactions differed slightly from probe to probe. The sequence of bases is known to affect the flexibility of double-stranded DNA.[31] Although single-stranded, one possibility is that the different sequences of the probe oligonucleotides affects their ability to flex and allow the redox labels to reach the electrode surface. Of note is the 12 mV difference in $E_{1/2}$ between the CuCy in **T1** (the (*R*)-isomer) and

the CuCy in **(*S*)-T1** (the (*S*)-isomer). As the sequences of **T1** and **(*S*)-T1** are identical, the difference in $E_{1/2}$ must be explained by the precise position of the CuCy affecting its redox behaviour. ΔE_p for CuCy and Fc in the probe oligonucleotides were 11 mV or less, typical of surface-bound electrochemical species.[32] The exception was the CuCy in **N1**, with a ΔE_p value of 24 mV, suggesting slower reaction kinetics. Although unclear why this was the case, the CuCy in **N1** also had the most positive $E_{1/2}$ value, which normally suggests oxidation is less thermodynamically favourable. The inadvertent addition of an oxygen atom to the Cu^{2+} cation in E1 described in Chapter 3 had little effect on the CuCy's $E_{1/2}$, ΔE_p and $i_{p,}{}^a/i_{p,}{}^c$ values relative to the majority of other probes. However, its presence was evident in the slight distortion of the current peaks (see section 4.6.). The $i_p{}^a/i_p{}^c$ values obtained for CuCy were below 1, which may be attributed in part to the proximity of CuCy's redox activity to the edge of the usable potential window, as well as the challenge of accurately extrapolating a baseline for the cathodic peak. The redox activity of Fc was comfortably within the useable potential window and therefore both its anodic and cathodic peaks were easy to analyse, so its $i_p{}^a/i_p{}^c$ values were close to unity.

Table 4.3. Electrochemical properties of the **CuCy** in SAMs formed by the probe oligonucleotides on gold electrodes. All values are determined from at least three CVs (1000 mV s^{-1}).

Probe	$E_{1/2}$ / mV	ΔE_p / mV	$i_p{}^a/i_p{}^c$
T1	395 (± 3)	10 (± 1)	0.87 (± 0.04)
(*S*)-T1	407 (± 2)	9 (± 1)	0.91 (± 0.02)
CuCyMid	398 (± 3)	8 (± 2)	0.90 (± 0.03)
B1	396 (± 3)	9 (± 1)	0.89 (± 0.01)
K1	406 (± 1)	11 (± 3)	0.91 (± 0.02)
E1	399 (± 2)	9 (± 2)	0.88 (± 0.02)
N1	414 (± 2)	24 (± 4)	0.84 (± 0.03)

Table 4.4. Electrochemical properties of the **Fc** in SAMs formed by the probe oligonucleotides on gold electrodes. All values are determined from at least three CVs (1000 mV s^{-1}).

Probe	$E_{1/2}$ / mV	ΔE_p / mV	i_p^a/i_p^c
T1	116 (± 1)	9 (± 2)	0.99 (± 0.01)
***(S)*-T1**	117 (± 2)	7 (± 1)	0.99 (± 0.01)
B1	105 (± 1)	7 (± 1)	0.98 (± 0.01)
K1	113 (± 1)	6 (± 1)	0.98 (± 0.02)
E1	102 (± 1)	5 (± 1)	1.00 (± 0.01)
N1	109 (± 1)	6 (± 1)	0.99 (± 0.01)

4.3.4. Probe Surface Coverage

After determining the electrochemical surface areas of the gold electrodes (see section 2.7.2.), probe packing densities following SAM formation were calculated. SAMs formed using redox-modified DNA offer an advantage in calculating surface coverages over those formed using unmodified DNA, in that the charge associated with the redox process is directly proportional to the number of strands immobilised at the surface. In this case, as each probe oligonucleotide contains one CuCy and one Fc, calculating the number of either redox label at the electrode surface allowed for the direct quantification of the surface molecular density of probes. Using Equation 4.1.[32] and the charge of the CuCy-produced anodic peak, the coverage of the **T1** probe was calculated to be approximately $(1.9 \pm 0.4) \times 10^{-11}$ mol cm^{-2}. This equated to approximately 1.1×10^{13} probe molecules per cm^2 of electrochemically active electrode. These values are broadly within the range of surface coverages reported for other DNA-modified gold electrodes.[33]

Equation 4.1.

$$Q = nFA\Gamma$$

Where:

Q = charge (μC)

n = number of electrons transferred in the redox process

F = Faraday's constant (96,485 C mol^{-1})

A = microscopic electrochemical surface area (cm^2)

Γ = surface coverage (mol cm^{-2})

For SAMs formed using unmodified DNA, surface coverage is often calculated by saturating with a charge-compensating redox marker (usually $[Ru(NH_3)_6]^{3+}$).[34,35] The saturating amount of redox marker is directly proportional to the number of phosphate groups and therefore the number of DNA strands forming the SAM. An attempt to measure the surface coverage of a SAM formed with **T1** probe using this method proved unsuccessful as the saturating concentration of $[Ru(NH_3)_6]^{3+}$ could not be reached (see Appendix 8.2.1.), likely due to incomplete SAM formation allowing the redox marker to reach the electrode surface.

4.3.5. Electrochemical Electrode Roughening

Part of the SAM preparation procedure involved the use of chronoamperometry to subject the electrode surface to a relatively positive potential in order to remove any contaminants prior to SAM formation. Chronoamperometry is a simple electrochemical technique that subjects the electrode to a set potential for a period of time. All electrodes were subjected to 2 V for 5 s followed by –0.35 V for 10 s in 0.5 M H_2SO_4 as part of the cleaning procedure. In addition to the removal of contaminants, using these potentials roughened the surfaces of the electrodes and increased their electrochemical surface areas (see Appendix 8.2.1.). Electrochemical

roughening is used by Plaxco and coworkers to increase the signalling of sensors involving redox-modified surface-immobilised DNA probes.[33,36] Larger electrode surface areas allows for the attachment of more probes which improves signal-to-noise ratios. The mechanism of electrochemical roughening in acid involves the dissolution of small areas of gold from the initially smooth electrode surface which results in roughened nanostructures.[36] Figure 4.8 compares the electrochemical activity of SAMs formed after the gold electrode was subjected to 2 V followed by –0.35 V (the standard chronoamperometry step used throughout this thesis, that resulted in some electrode roughening) versus 3.25 V followed by –0.35 V (only used here to highlight the effect of increased electrode roughening). Significantly larger peaks were observed with the SAM formed on the rougher surface owing to the increased number of attached probes. Unless otherwise stated, all SAMs for this work were formed on gold electrodes that had been subjected to 2 V in H_2SO_4 as detailed in section 7.6.2. This was to ensure that SAM formation was consistent with the procedures followed previously in the group.[29,37] However, the ability to form SAMs which produce larger redox signals may be of use, particularly when sensing in complex media and the resulting need to maximise signal-to-noise ratios.

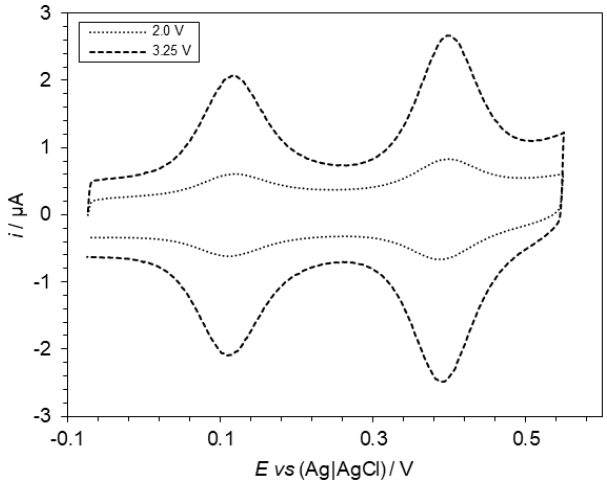

Figure 4.8: CVs of **T1** on electrodes subjected to 2 V (some electrochemical roughening) and 3.25 V (more electrochemical roughening) prior to SAM formation; in 10 mM sodium phosphate buffer (pH 7.0) 1 M $NaClO_4$, scan rates = 1000 mV s^{-1}.

4.4. Thermal Melting Studies

Thermal melting studies were conducted to assess how the modifications and varying the base opposite the CuCy affected duplex stability. SYBR Green I was used which increased the T_m values by way of its intercalation into DNA stabilising the duplexes, as detailed in section 2.4.2.[38] Table 4.5 shows the T_m values for the probes based on the in-house testing sequence and Table 4.6 shows the T_m values for the probes based on clinically relevant SNVs.

Table 4.5. Thermal melting temperatures for the probes based on the in-house testing sequence when duplexed with equimolar equivalents of unmodified complementary targets with the base opposite the CuCy varied. [DNA] = 10 μM in 10 mM sodium phosphate buffer pH 7.0, 100 mM NaCl.

Base Opposite CuCy	T1 / ºC	(*S*)-T1 / ºC	CuCyMid / ºC
A	57.5 (± 0.5)	63.5 (± 1.0)	60.0 (± 0.5)
C	60.5 (± 0.5)	66.0 (± 0.5)	62.5 (± 0.5)
G	58.5 (± 0.5)	63.0 (± 0.5)	60.0 (± 0.5)
T	60.0 (± 0.5)	65.0 (± 0.5)	62.0 (±0.5)
5mC	60.5 (± 0.5)	-	-

Table 4.6. Thermal melting temperatures for the probes based on clinically relevant SNVs when duplexed with equimolar equivalents of unmodified complementary targets with the base opposite the CuCy varied. [DNA] = 10 μM in 10 mM sodium phosphate buffer pH 7.0, 100 mM NaCl.

Base Opposite CuCy	B1 / ºC	K1 / ºC	E1 / ºC	N1 / ºC
A	55.5 (± 1.0)	69.5 (± 0.5)	57.5 (± 1.0)	53.0 (± 0.5)
C	-	-	-	-
G	-	68.0 (± 0.5)	59.0 (± 1.0)	-
T	60.5 (± 1.0)	66.5 (± 0.5)	-	55.5 (± 0.5)

Purines opposite the CuCy instead of pyrimidines tended to reduce duplex stability. This was found previously in CuCy-modified DNA and may be explained by the larger size of the purines, which then clash more with the CuCy to form less stable duplexes.[28,29] However, duplexes formed with the **K1** probe showed the reverse, with the purines adenine and guanine opposite the CuCy resulting in more stable duplexes than those formed with the pyrimidine

thymine opposite the CuCy. This indicated that the interaction with the base opposite the CuCy is not the only interaction that affects duplex stability, with the bases above and below the CuCy in the base stack also likely to affect its position and therefore the structural integrity of the duplex. The (*R*)-isomer of CuCy was previously modelled to disrupt the bases around it more so than the (*S*)-isomer (Figure 4.9),[28] which further indicates that interactions with all bases in the local environment of CuCy should be considered. As with previous studies, the (*S*)-isomer of CuCy in **(*S*)-T1** resulted in more stable duplexes than the (*R*)-isomer. This again supports the previous modelling predicting that the (*S*)-isomer fits better into the base stack than the (*R*)-isomer. Addition of the Fc at the 5′ end caused a minor reduction in duplex stability, as indicated by the slightly higher T_m values for **CuCyMid** compared to **T1**. This is surprising given Fc's terminal position, however the impact was modest and had no effect on probe sensing capabilities.

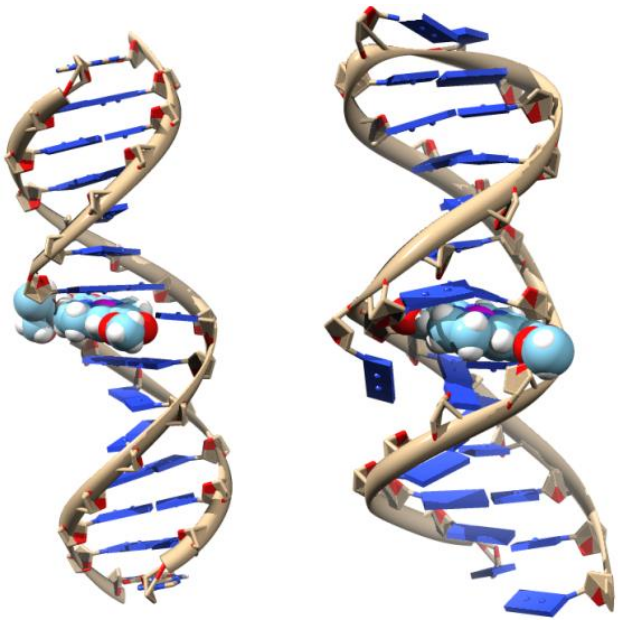

Table 4.9. Models of the (*S*)-isomer (left) and (*R*)-isomer (right) of CuCy in CuCy-modified DNA intercalating into probe–target duplexes formed with **T2A**. (Taken from reference 28.)

4.5. Key Properties and Sensing

4.5.1. Ratiometric Sensing

Incorporation of Fc at the 5′ end of the probes enables a dual-signal ratiometric sensing mechanism. The presence of an oxidation peak and a reduction peak for each redox label presents a choice: which of the anodic (oxidation) or cathodic (reduction) currents are used to determine the CuCy:Fc current ratio? As discussed in section 4.3.3., whilst the i_p^a/i_p^c values for Fc were approximately 1, the i_p^a/i_p^c values for CuCy varied from 0.84 to 0.91. Part of the reason for the variance in the CuCy i_p^a/i_p^c values was the difficulty in extrapolating an accurate baseline for the cathodic peak (Figure 4.10).

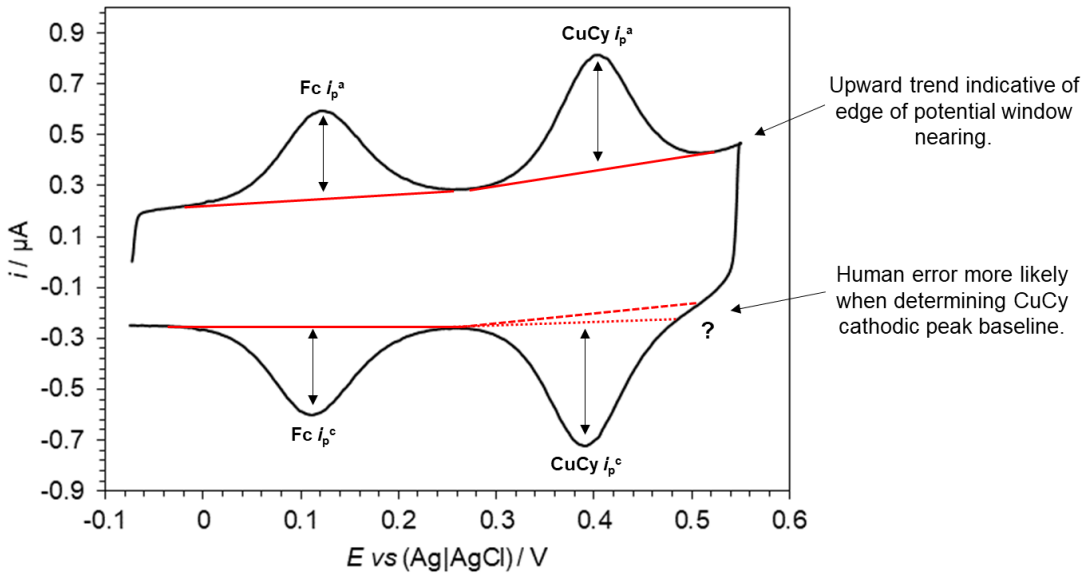

Figure 4.10: Cyclic voltammogram of **T1** showing the relevant peak currents; in 10 mM sodium phosphate buffer (pH 7.0) 1 M $NaClO_4$, scan rate = 1000 mV s^{-1}.

When manually drawing the baseline, there is a relatively high chance that two different people would draw two slightly different baselines. Conversely, extrapolating a baseline for the anodic CuCy peak was deemed to be less open to interpretation and therefore more

reproducible. As such, all CuCy:Fc current ratios reported in this work are derived from the anodic currents only (Equation 4.2.).

Equation 4.2.

$$\text{CuCy: Fc current ratio} = \frac{\text{CuCy } i_{\text{p}^{\text{a}}}}{\text{Fc } i_{\text{p}^{\text{a}}}}$$

To demonstrate the enhanced reproducibility of the ratiometric setup, the initial peak current of CuCy was compared with the initial CuCy:Fc current ratios over 20 individual measurements (Figure 4.11). Using the CuCy anodic current alone resulted in considerable variation with an average of 0.417 µA and a standard deviation (SD) of 0.099 µA. Using the CuCy:Fc current ratio resulted in significantly less variation with an average of 1.385 and a SD of 0.059. As with other sensors employing a dual-signal approach,[39,40] the ratiometric readout proved more reproducible than relying on a single current alone. An additional benefit of using the Fc as an internal reference is the ability to attribute the reduction in CuCy current to probe–target binding instead of probe detachment, as the latter would also result in the reduction of the Fc current.

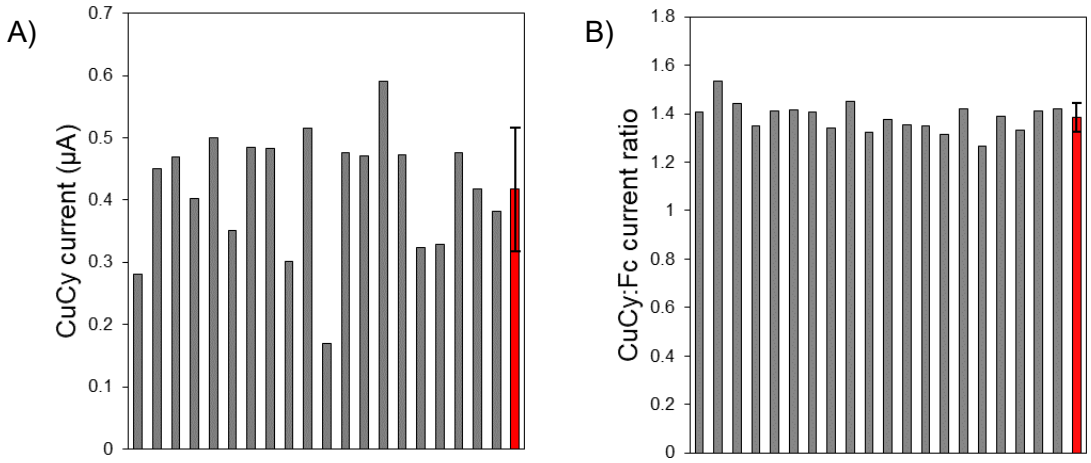

Figure 4.11: Comparison between the reliance on initial CuCy anodic current alone with **CuCyMid** (A) versus initial CuCy:Fc current ratio with **T1** (B). All currents are those recorded prior to target addition. Red bars represent the average values for the 20 measurements. Error bars represent SD.

4.5.2. Detection of Binding Events and Selectivity

Figure 4.12 shows the effect of adding complementary **T2T** target (A) and non-complementary **T2ran** target (B) to the surface-immobilised **T1** probe. Addition of the complementary **T2T** resulted in the reduction of the CuCy current whilst the Fc current remained relatively unchanged. Allowing for more time after target addition resulted in a larger CuCy current reduction as more targets bound to more probes. 60 minutes was deemed the longest time a point-of-care sensor should take to generate a result, given that PCR-based methods typically take at least 1–2 hours.[11] Selectivity was assessed by addition of non-complementary **T2ran**. At a relatively high target concentration of 1 µM, a minimal change in the CuCy current and no change in the Fc current was observed. The small change in the CuCy current can be attributed to non-specific binding, especially given the high target concentration used.

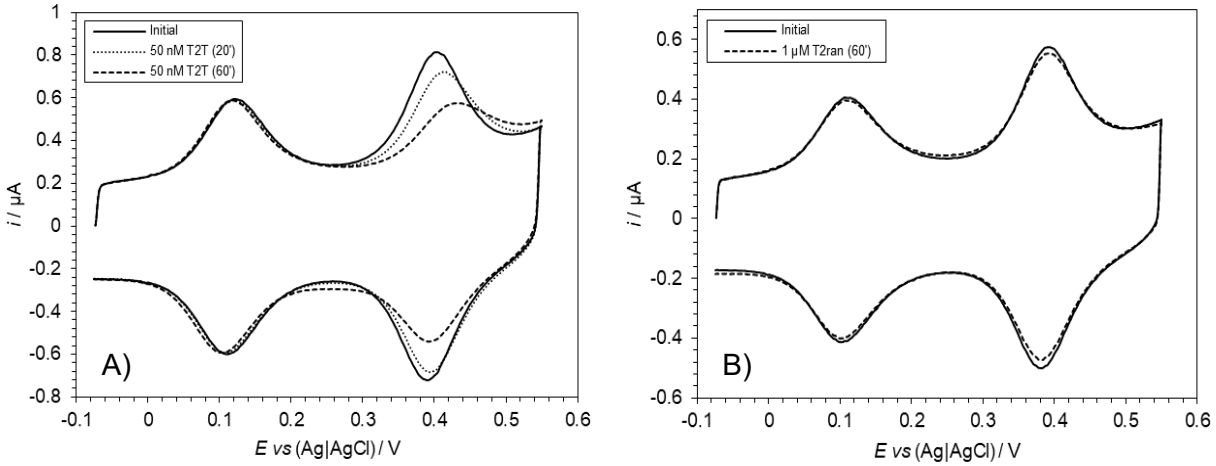

Figure 4.12: A) CVs of **T1** before (solid line), 20 minutes after (dotted line), and 60 minutes after (dashed line) **T2T** target addition; [**T2T**] = 50 nM. CVs of **T1** before (solid line) and 60 minutes after (dashed line) **T2ran** target addition; [**T2ran**] = 1 µM. In 10 mM sodium phosphate buffer (pH 7.0) 1 M $NaClO_4$, scan rates = 1000 mV s^{-1}.

4.5.3. Electrochemical Stability Studies

As discussed in sections 2.7.2 and 4.3.2, evidence for SAM formation is obtained by plotting current versus scan rate. The initial sensing protocol (Figure 4.13) involved measuring a series

of CVs prior to and after target addition to confirm that the SAM remained intact throughout the time it was under investigation.

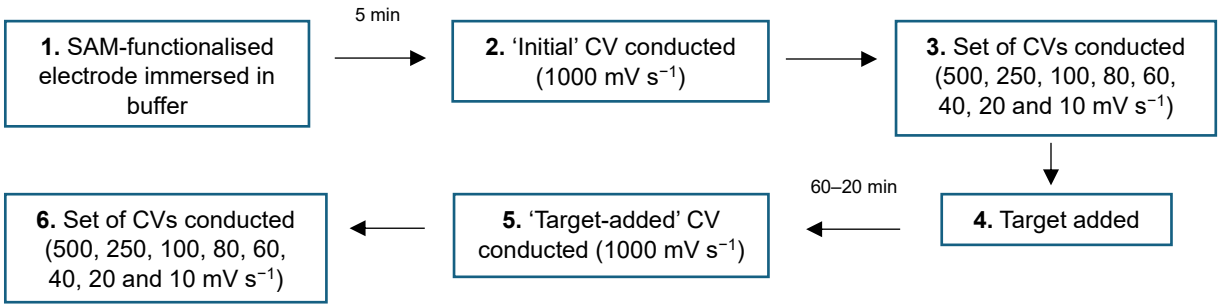

Figure 4.13: Initial sensing protocol.

However, it became apparent that measuring a series of CVs (steps 3 and 6 in Figure 4.13) was affecting the CuCy currents. A CV set consisted of CVs at scan rates of 500, 250, 100, 80, 60, 40, 20 and 10 mV s^{-1}. As seen in Figure 4.14, the completion of one set of CVs following this protocol significantly reduced the CuCy current whilst leaving the Fc current unchanged. To confirm that the sensing CVs conducted at a scan rate of 1000 mV s^{-1} were not affecting the CuCy current, five 1000 mV s^{-1} CVs were conducted over a 25 minute period which showed no impact on the CuCy current (see Appendix 8.2.3.).

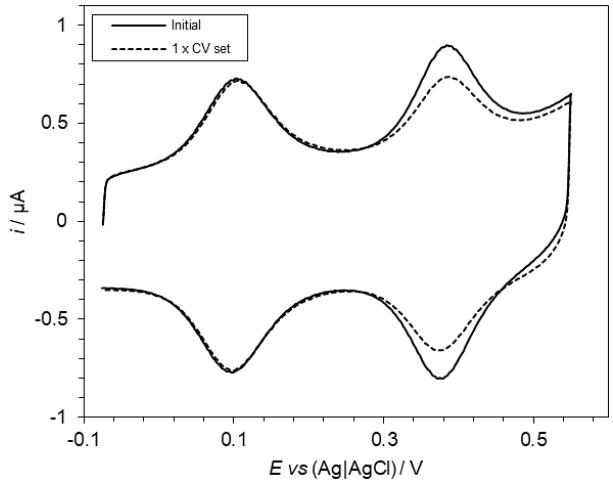

Figure 4.14: CVs of **T1** before (solid line) and after (dashed line) one set of CVs according to the initial sensing protocol; in 10 mM sodium phosphate buffer (pH 7.0) 1 M $NaClO_4$, scan rates = 1000 mV s^{-1}.

Next, the extent to which the sets of CVs were affecting the CuCy currents was investigated. Specifically, it was important to determine whether the CuCy currents reached a constant value or continued to decrease with further sets of CVs. Figure 4.15 shows that the CuCy currents continued to decrease with each CV set, up to a total of 10. Whilst it is possible that a levelling out of the CuCy currents could occur beyond 10 sets of CVs, even that many takes a considerable amount of time to complete and therefore achieving such a plateau would be impractical. Regardless, it was shown that the CV sets were inadvertently reducing the CuCy currents and therefore the sensing protocol had to be changed. Why the sets of CVs reduce the CuCy currents is not yet understood. A conformational change in the probes was considered but the continued reduction in CuCy currents with further CV sets implies that the Cu^{2+} centre itself is electrochemically unstable at the potentials used and for the lengths of time employed.

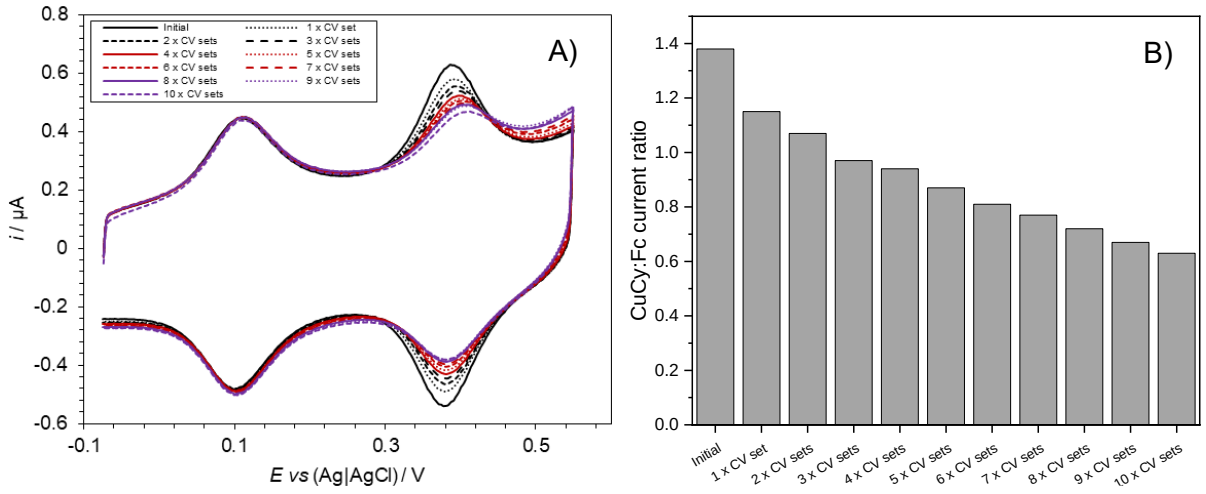

Figure 4.15: A) CVs of **T1** taken after sets of CVs; in 10 mM sodium phosphate buffer (pH 7.0) 1 M $NaClO_4$, scan rates = 1000 mV s^{-1}. B) CuCy:Fc current ratios derived from the CVs shown in (A).

Once it had been established that full CV sets (cycling between –75 and 550 mV) affected the CuCy currents, it was investigated whether only cycling over the Fc's redox potentials could be used to determine the relationship between current and scan rate. A 'half-CV' set involves 8 CVs at the same scan rates as a standard CV set, but each CV cycles between –75 and 240 mV

instead of between –75 and 550 mV. Using 'half-CV' sets, the CuCy's redox potentials are not reached. Half-CV sets were found not to affect the CuCy currents and therefore left the CuCy:Fc current ratios unchanged (Figure 4.16). Confirmation of SAM formation was thereafter obtained using half-CV sets.

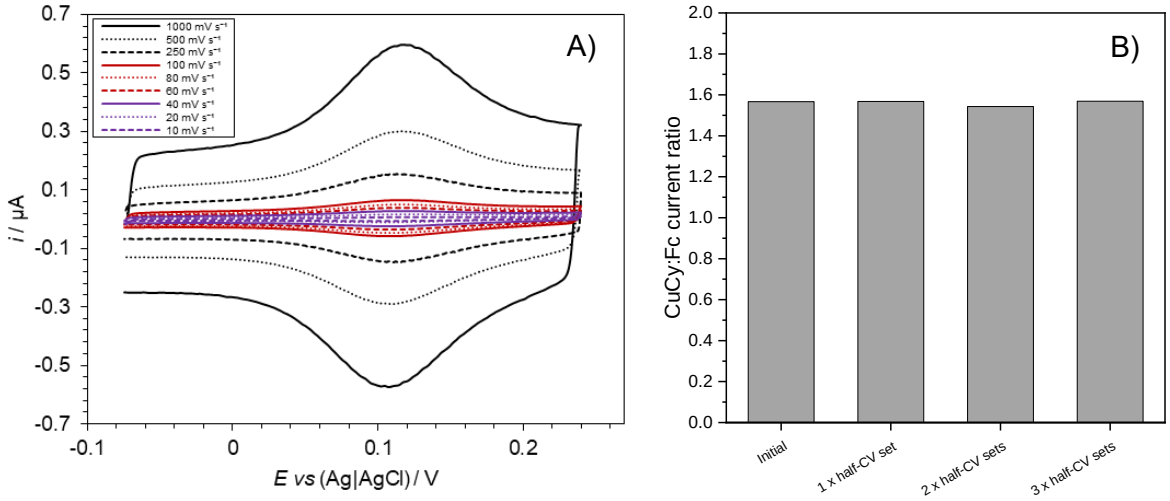

Figure 4.16: A) Half-CVs of **T1** cycling over the Fc's redox potentials; in 10 mM sodium phosphate buffer (pH 7.0) 1 M $NaClO_4$. B) CuCy:Fc current ratios derived from CVs taken before and after half-CV sets.

4.5.4. Limit of Detection

The ideal nucleic acid sensor would be able to sense targets without the need for target amplification. Physiological concentrations of cf-DNA are typically reported in ng mL^{-1} [41,42] and the equivalent concentrations in molarity (mol dm^{-3}) cannot be determined accurately, owing to the varying molecular weights of each fragment. miRNAs, with their known sequences and therefore known molecular weights, offer a better route for estimating a target LOD in terms of concentration. Concentrations of extracellular miRNAs are typically reported in copies of miRNA per unit of volume[43,44] or ΔCt.[42,45] Tewari and coworkers determined the concentrations of several blood-based cancer-related and non-cancer-related miRNAs in copies per µL.[43] In healthy subjects, the relatively abundant non-cancer-related miRNAs miR-16 and miR-24 were found in concentrations of approximately 100,000 copies per µL of plasma. Using

the molecular weights of each miRNA, 100,000 copies per μL of plasma is equivalent to approximately 166 pM. Given miR-16 and miR-24 are relatively abundant miRNAs, with most others determined to be present at concentrations orders of magnitude lower,[43,44] a sensor with a LOD in the fM–pM range could theoretically sense miRNAs at physiologically relevant concentrations without the need for target amplification.

As a result of the electrochemical stability studies, the true LOD, without the effects of the CV sets, had to be determined. The **T1** probe was tested with sequentially lower amounts of the target **T2T**, starting with a relatively high concentration of 1 μM and ending when only a minimal sensing response was observed (Figure 4.17). **T2T** was chosen as the target to investigate the LOD as previous studies had identified that a thymine opposite the CuCy in the probe–target duplex resulted in the largest reduction in CuCy current.[29] Measurements were taken 20 minutes and 60 minutes after target addition, revealing that at lower target concentrations a longer incubation time resulted in larger CuCy:Fc current ratio % changes. This can be explained given that solutions containing fewer targets should take longer to encounter and bind a set number of probes than solutions containing more targets. At a target concentration of 1 μM, a minimal change was observed between the two time points, indicating that an equilibrium had been reached no longer than 20 minutes after target addition.

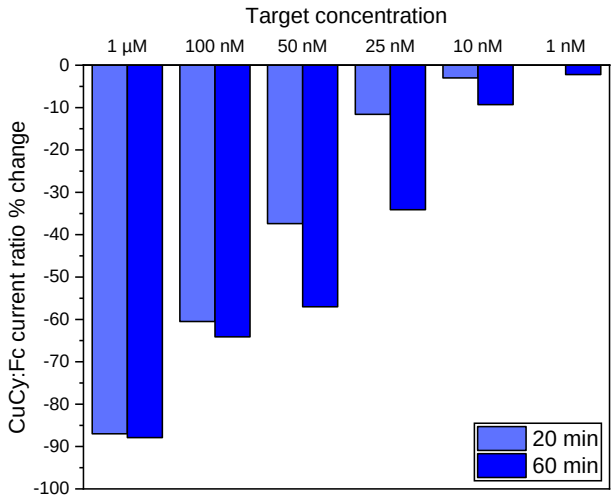

Figure 4.17: % changes in **T1**'s CuCy:Fc current ratio 20 minutes (light blue) and 60 minutes (dark blue) after addition of varying concentrations of target **T2T**; in 10 mM sodium phosphate buffer (pH 7.0) 1 M $NaClO_4$, scan rates = 1000 mV s^{-1}.

Once 10 nM and 1 nM target concentrations were identified as the concentrations at which minimal sensing responses were observed, repeat measurements were conducted at 60 minutes after target addition to confirm the LOD (Figure 4.18). At 1 nM target concentration, the small CuCy:Fc current ratio % changes were often indistinguishable from no % change at all (see Appendix 8.2.4.), as represented by the error overlapping with 0% change. The LOD was therefore determined to be 10 nM, as this was the concentration at which a sensing response could be reproducibly distinguished from no % change at all.

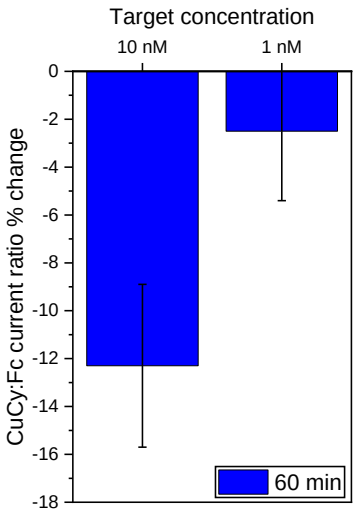

Figure 4.18: % changes in **T1**'s CuCy:Fc current ratio 60 minutes after target **T2T** addition at concentrations of 10 nM and 1 nM; in 10 mM sodium phosphate buffer (pH 7.0) 1 M $NaClO_4$, scan rates = 1000 mV s^{-1}. Error bars represent SD.

A LOD of 10 nM is estimated to be at least two orders of magnitudes short of being able to sense clinically relevant nucleic acids at physiological concentrations, as discussed above. Comparable sensors in the literature employing redox-modified surface-immobilised DNA probes report a wide range of LODs. Sensors using simple hairpin probes that removed a redox-label from the electrode surface upon target binding reported LODs from 10 pM to 1 nM;[46,47] those using probes that moved a redox-label closer to the electrode surface upon target binding reported LODs from 400 fM to 2 nM;[48-51] and those using dual-labelled probes that employed ratiometric sensing mechanisms reported LODs from 2.3 fM to 1 μM.[39,52,53] The probes used in all of these sensors underwent large conformational changes that drastically changed the position of the reporting redox label(s) relative to the electrode surface upon target binding, which may account for some of the lower LODs. By contrast, the position of the CuCy relative to the electrode surface undergoes a less drastic change upon target binding. Stulz and coworkers' cobalt porphyrin-modified probe, which is similar to CuCy-modified probes in that target binding induces a relatively small change in the redox-label's position relative to the electrode surface, reported a LOD of 10 fM.[54]

Relating probe packing density to LOD provides useful context. As discussed above, the surface coverage for SAMs formed with the **T1** probe was calculated to be $(1.9 \pm 0.4) \times 10^{-11}$ mol cm^{-2}. Electrochemically active electrode surface areas were approximately 0.021 cm^2. Therefore, a typical **T1** SAM has *ca* 0.4 pmol of probes attached to the electrode surface which equates to *ca* 2.4×10^{11} probes. A 1.5 mL solution (the standard sensing volume used, see section 7.6.3.) containing target at a concentration of 10 nM contains *ca* 9×10^{12} target molecules. Therefore, a 10 nM target solution contains almost two orders of magnitude more targets than is theoretically needed to bind to every probe and saturate the sensor. That the sensor is not saturated, even though many more targets are present than are needed to

theoretically do so, is likely because of the repulsive electrostatic and steric effects experienced by DNA immobilised onto gold surfaces.[55,56] Travas-Sejdic and coworkers' comparison of DNA probes versus PNA probes provides an illustrative example of the repulsive electrostatic forces experienced by DNA at the surface of an electrode.[56] Using a $Fe(CN)_6^{3-/4-}$ redox couple, the charged DNA probes had a LOD of 2.9 nM when sensing DNA target, whereas the uncharged PNA probes had a LOD of 7.8 pM sensing the same DNA target – a 371-fold increase in sensitivity.

Conversely, solutions containing fewer target molecules than are needed to theoretically saturate the sensor must generate signals that are large enough to overcome the 'bulk' signal. For example, initial efforts to sense 10 fM **T2T** target using the **T1** probe and the updated sensing protocol (see section 4.5.3.) proved unsuccessful: the reduced current produced by the CuCy tags in the *ca* 9,000,000 probe–target duplexes (the maximum number that could theoretically form in a 1.5 mL 10 fM target solution) could not register above the normal current produced by the CuCy tags in the remaining (*ca* 2.4×10^{11}) unbound probe molecules.

4.5.5. Probe Regeneration

Sensors that can be reused offer clear advantages over single-use devices. Those that use surface-immobilised DNA probes face the challenge of ensuring effective probe–target duplex denaturation whilst minimising SAM destruction. Previous work had investigated soaking in urea solutions to regenerate CuCy-modified probes with limited success.[29] Instead, sonication (known to be effective for even significantly longer double-stranded DNA fragments[57]) in ultrapure water was found to more reliably regenerate the probes after sensing target. Figure 4.19A shows the regeneration of the **T1** probe by sonication in ultrapure water for 60 seconds after sensing **T2T** target for a total of 3.5 cycles, with the associated CuCy:Fc current ratios shown in Figure 4.19B. Repeated sonication regenerations did remove some probes from the

surface, as evidenced by the slight decreases in the Fc and CuCy currents with each cycle. However, regeneration by sonication proved to be inconsistent, with some SAMs remaining relatively intact (*e.g.*, Figure 4.19A) and others seeing much more significant probe detachment (see Appendix 8.2.5.).

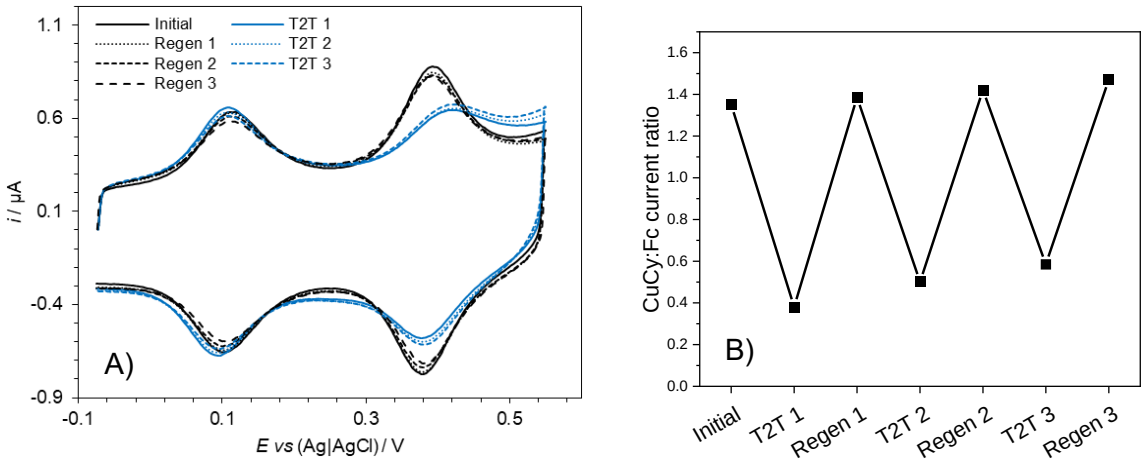

Figure 4.19: A) Regeneration of **T1** after incubation with **T2T** target (100 nM, 60 min) by sonication in ultrapure water for 60 seconds; in 10 mM sodium phosphate buffer (pH 7.0) 1 M $NaClO_4$, scan rates = 1000 mV s^{-1}. B) CuCy:Fc current ratios derived from the CVs shown in A.

Simple rinsing with ultrapure water has been reported to denature surface-immobilised double-stranded DNA.[18,58] Figure 4.20A shows the regeneration of the **T1** probe by rinsing under a stream of ultrapure water for 60 seconds after sensing **T2T** target for a total of 3.5 cycles, with the associated CuCy:Fc current ratios shown in Figure 4.20B. To more effectively evaluate the rinsing regeneration method, a higher target concentration was used (1 µM versus 100 nM) to maximise the number of probe–target duplexes formed. Compared with regeneration by sonication, regeneration by rinsing resulted in less probe detachment as evidenced by the more stable Fc and CuCy currents. Crucially, regeneration by rinsing also proved more consistent, with minimal destruction observed from SAM to SAM. However, with both methods some degree of probe detachment was observed. In these scenarios, the ratiometric sensing mechanism proves vital to the reusability of the sensor. Using just the CuCy

current alone, it is not clear whether partial or full regeneration of the probe has occurred, as a regenerated current smaller than the initial current may be due to partial regeneration or probe detachment. Alternatively, as probe detachment results in the same number of CuCys and Fcs being removed from the surface, the initial and regenerated CuCy:Fc current ratios should remain equal, which therefore makes it easier to distinguish between partial or full regeneration.

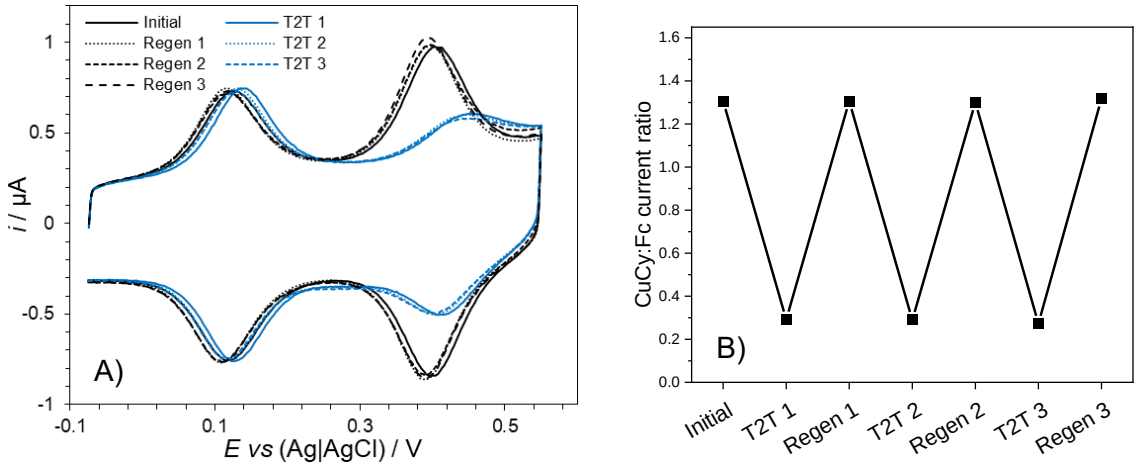

Figure 4.20: A) Regeneration of **T1** after incubation with **T2T** target (1 µM, 10 min) by rinsing in ultrapure water for 60 seconds; in 10 mM sodium phosphate buffer (pH 7.0) 1 M $NaClO_4$, scan rates = 1000 mV s^{-1}. B) CuCy:Fc current ratios derived from the CVs shown in A.

4.6. Electrochemical Single Nucleotide Variant Sensing

4.6.1. Test Probe

Table 4.7: Probe sequence (**T1**) and target sequences (T2X). X = CuCy; F = Fc; S = disulphide. Bases highlighted in red sit opposite the CuCy in the probe–target duplexes formed.

Oligonucleotide	5′ – Sequence – 3′
T1	F TGG ACT CXC TCA ATG S
T2T	CAT TGA GTG AGT CCA
T2A	CAT TGA GAG AGT CCA
T2G	CAT TGA GGG AGT CCA
T2C	CAT TGA GCG AGT CCA

SNV sensing and interrogation was firstly investigated using the test probe **T1**. Figure 4.21 shows the CuCy:Fc current ratio % changes induced by the four targets listed in Table 4.7 at 50

nM, and Figure 4.22 shows the associated representative CVs (see Appendix 8.2.6. for the processed anodic traces used to determine CuCy:Fc current ratios). The successful discrimination by surface-immobilised **T1** between **T2A**, **T2C** and **T2T**/**T2G** at a target concentration of 50 nM represents a thousand-fold increase in sensitivity compared with the solution-based setup previously reported.[28] However, unlike the solution-based setup, the surface-immobilised **T1** was unable to distinguish between all four canonical bases as **T2T** and **T2G** produced CuCy:Fc current ratio % changes within the margin of error. Investigations into the mechanism of SNV sensing using CuCy-modified DNA and the differences in sensing behaviour to the solution-based CuCy-modified probe previously reported[28] are discussed in more detail in Chapter 5.

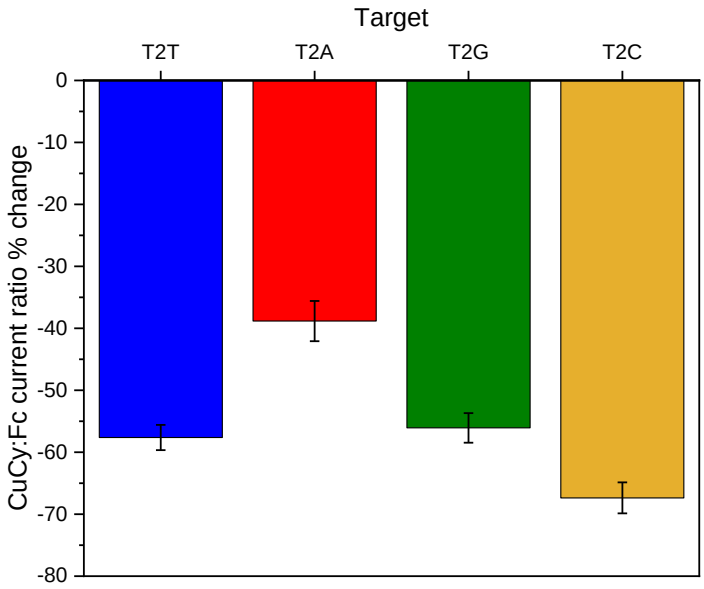

Figure 4.21: CuCy:Fc current ratio % changes for **T1** 60 minutes after target addition. Error bars represent SD. [Target] = 50 nM in 10 mM sodium phosphate buffer (pH 7.0) 1 M $NaClO_4$, scan rates = 1000 mV s^{-1}.

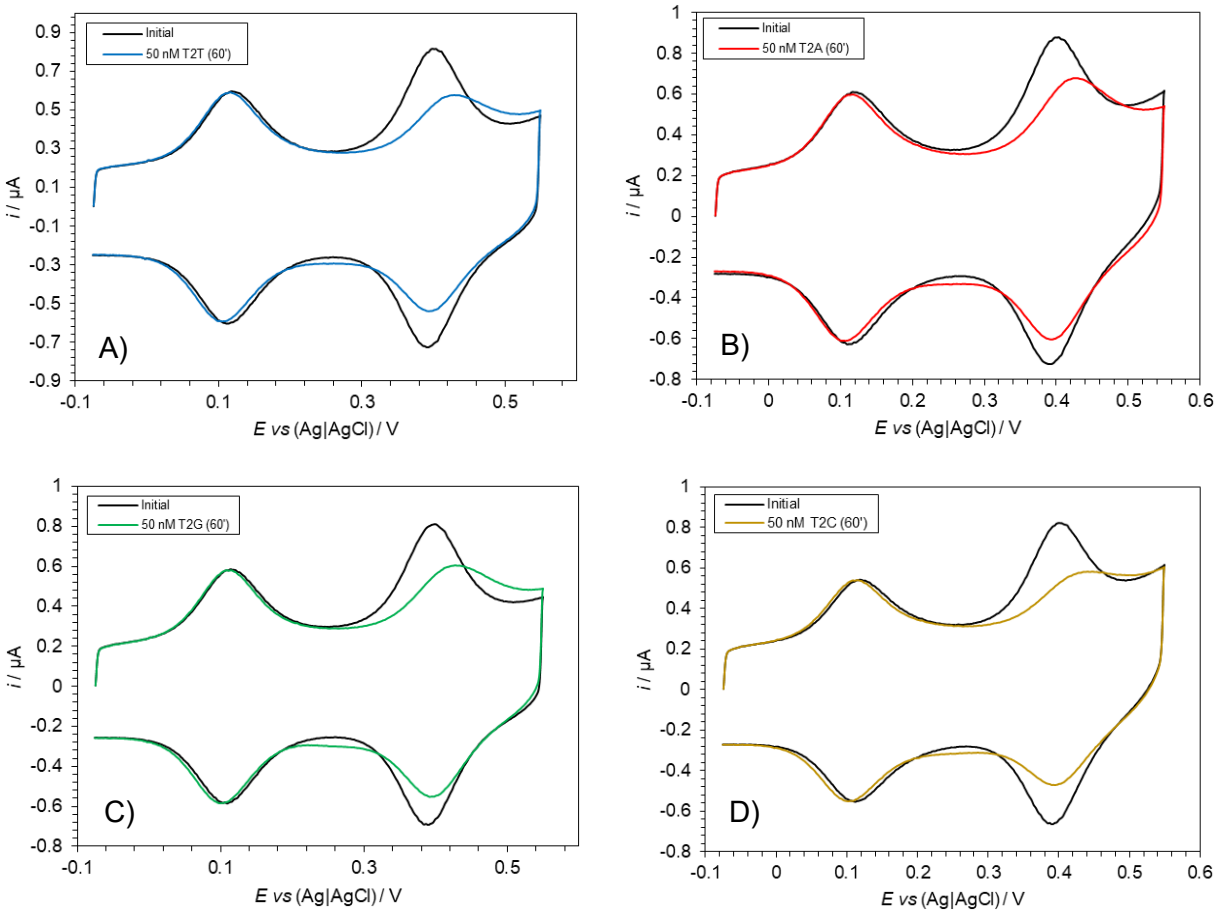

Figure 4.22: Representative CVs of **T1** sensing targets **T2T** (A), **T2A** (B), **T2G** (C) and **T2C** (D), [target] = 50 nM; in 10 mM sodium phosphate buffer (pH 7.0) 1 M $NaClO_4$, scan rates = 1000 mV s^{-1}.

4.6.2. Cancer-Based Probes

Table 4.8: Probe sequences (**B1**, **K1**) and target sequences (B2X, K2X). X = CuCy; F = Fc; S = disulphide. Bases highlighted in red sit opposite the CuCy in the probe–target duplexes formed.

Oligonucleotide	5′ – Sequence – 3′
B1	F AGA TTT CXC TGT AGC S
B2T	GCT ACA GTG AAA TCT
B2A	GCT ACA GAG AAA TCT
K1	F TAC GCC AXC AGC TCC S
K2T	GGA GCT GTT GGC GTA
K2A	GGA GCT GAT GGC GTA
K2G	GGA GCT GGT GGC GTA

Next, the **B1** and **K1** probes (Table 4.8) based on cancer-related SNV mutations were tested. The **B1** probe is based on the BRAF V600E mutation (thymine to adenine) in the BRAF

oncogene that is associated with various cancers.[59-61] The **K1** probe is based on the KRAS G12V (guanine to thymine) and KRAS G12D (guanine to adenine) mutations located at the same position in the KRAS oncogene, which are also associated with various cancers.[62-64] **B1** was able to discriminate between **B2T** and **B2A** at a target concentration of 50 nM (Figure 4.23, left). As with **T1**, having a thymine opposite the CuCy in the duplex resulted in a bigger reduction in the CuCy:Fc current ratio than adenine. **K1** was able to identify **K2T**, but was unable to discriminate between **K2A** and **K2G** (Figure 4.23, right). Unlike with **T1** and **B1** and their respective targets, the sensing of the purine targets **K2A** and **K2G** using **K1** resulted in larger CuCy:Fc current ratio % changes compared with the sensing of the pyrimidine target **K2T**. This further indicated that the base opposite in the probe–target duplex was not the sole determinant of the CuCy's electrochemical behaviour.

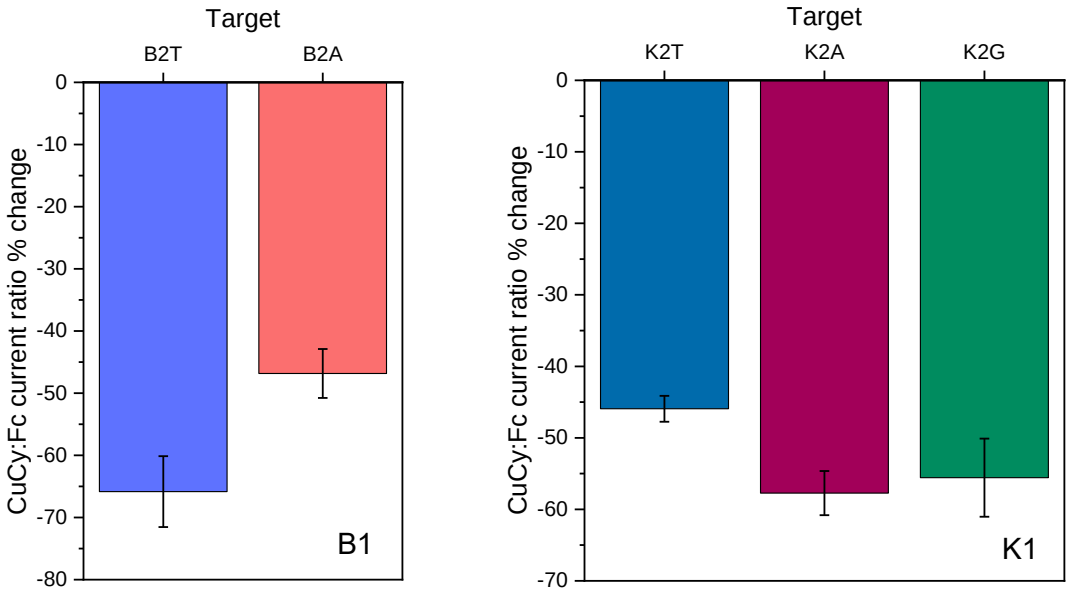

Figure 4.23: CuCy:Fc current ratio % changes for **B1** (left) and **K1** (right) 60 minutes after target addition. Error bars represent SD. [Target] = 50 nM in 10 mM sodium phosphate buffer (pH 7.0) 1 M $NaClO_4$, scan rates = 1000 mV s^{-1}.

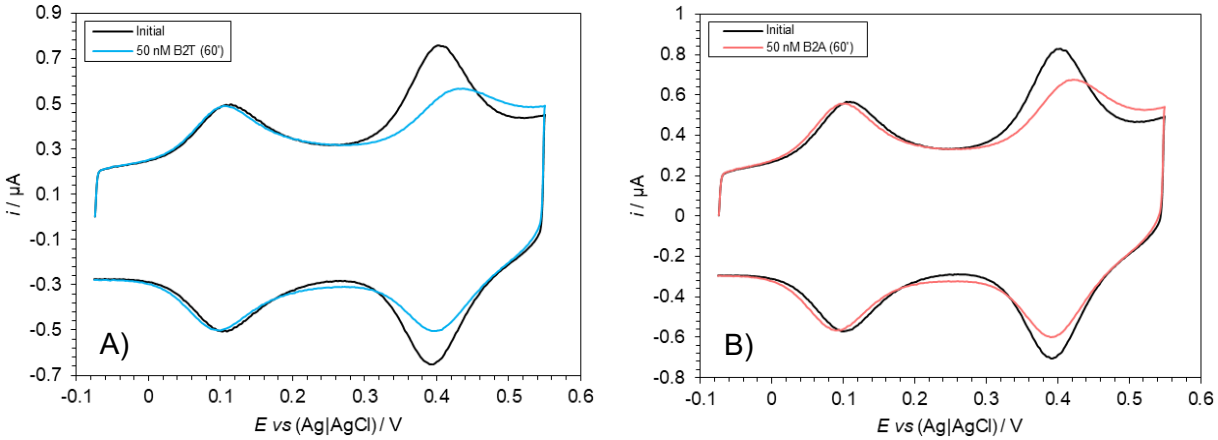

Figure 4.24: Representative CVs of **B1** sensing targets **B2T** (A) and **B2A** (B); in 10 mM sodium phosphate buffer (pH 7.0) 1 M $NaClO_4$, scan rates = 1000 mV s^{-1}.

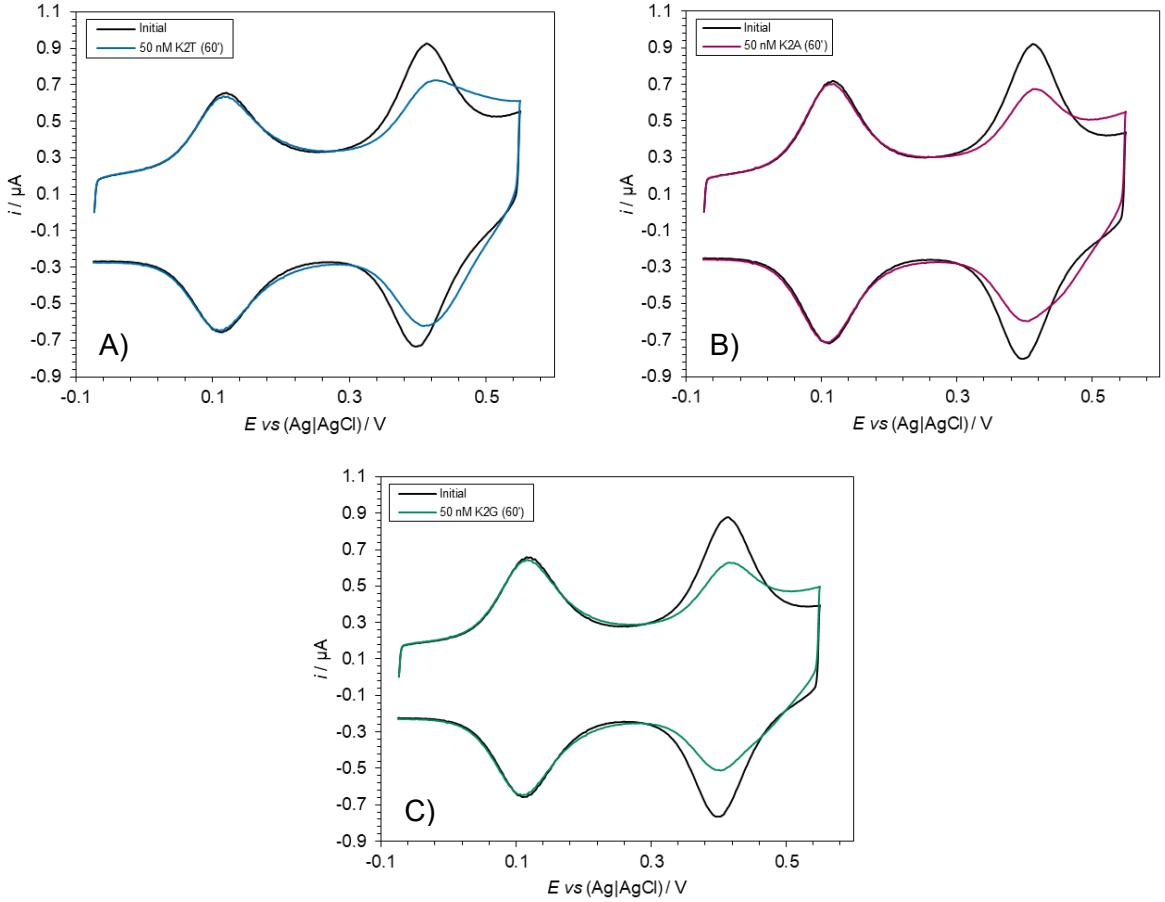

Figure 4.25: Representative CVs of **K1** sensing targets **K2T** (A), **K2A** (B) and **K2G** (C); in 10 mM sodium phosphate buffer (pH 7.0) 1 M $NaClO_4$, scan rates = 1000 mV s^{-1}.

4.6.3. COVID-19-Based Probes

Table 4.9: Probe sequences (**E1**, **N1**) and target sequences (E2X, N2X). X = CuCy; F = Fc; S = disulphide. Bases highlighted in red sit opposite the CuCy in the probe–target duplexes formed.

Oligonucleotide	5′ – Sequence – 3′
E1	F AAA CCT TXA ACA CCA S
E2A	TGG TGT TAA AGG TTT
E2G	TGG TGT TGA AGG TTT
N1	F ACA CCA TXA GTG GGT S
N2T	ACC CAC TTA TGG TGT
N2A	ACC CAC TAA TGG TGT

The **E1** and **N1** probes (Table 4.9) are based on SNV mutations in the gene of the COVID-19 genome that encodes the spike protein. **E1** is based on the E484K mutation (guanine to adenine) that substitutes a glutamate for a lysine at position 484 in the spike protein and confers enhanced resistance to antibody neutralisation effectiveness.[65] **N1** is based on the N501Y mutation (adenine to uracil in the RNA-based COVID-19 genome; adenine to thymine in the amplified reverse transcription PCR product) that substitutes an asparagine for a tyrosine at position 501 in the spike protein, resulting in enhanced viral transmissibility.[66] **E1** was able to discriminate between **E2A** and **E2G**, with a drastic difference in the CuCy:Fc current ratio % changes induced by each target (Figure 4.26, left). In particular, **E2G** resulted in a very large reduction in the CuCy current which easily enabled **E2A**/**E2G** discrimination. This was despite the inadvertent addition of an oxygen to the Cu^{2+} cation, as described in Chapter 3. The effect of the oxygen is evident in the slight distortion of the CuCy current peak and the reduction in the CuCy:Fc current ratio to ~1, compared with all other SNV CuCy-/Fc-modified probes which exhibited ratios of at least 1.2. **N1** was also able to discriminate between **N2T** and **N2A**, albeit with a smaller difference in the % changes induced by each target (Figure 4.26, right). Although COVID-19 possesses an RNA-based genome, and the targets sensed were DNA, hybrid nucleic acid duplexation is well established and is employed in other sensors involving redox-modified

nucleic acid probes.[53,67,68] Indeed, RNA sensing using the CuCy-/Fc-modified probes reported here is described in Chapter 5.

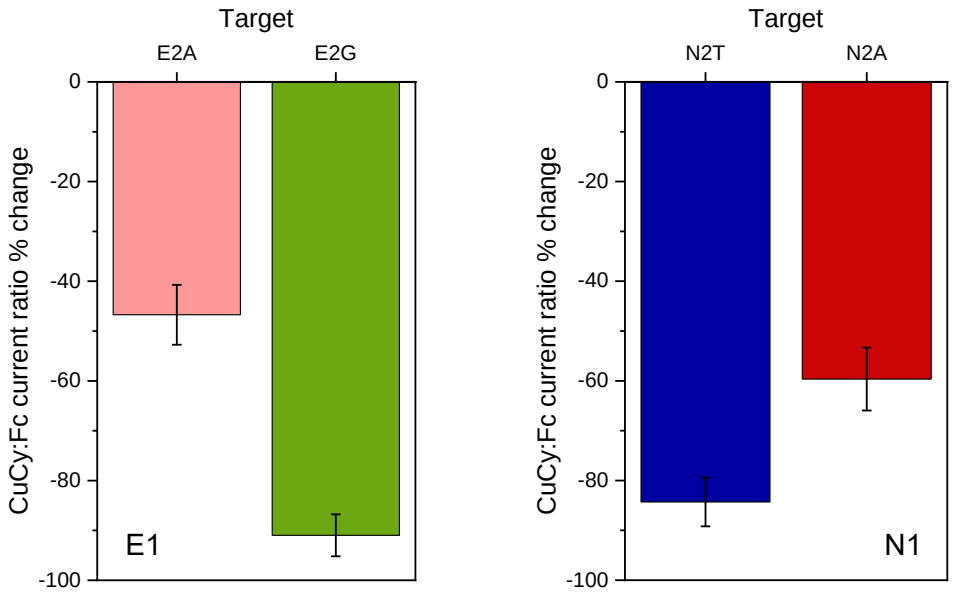

Figure 4.26: CuCy:Fc current ratio % changes for **E1** (left) and **N1** (right) 60 minutes after target addition. Error bars represent SD. [Target] = 50 nM in 10 mM sodium phosphate buffer (pH 7.0) 1 M $NaClO_4$, scan rates = 1000 mV s^{-1}.

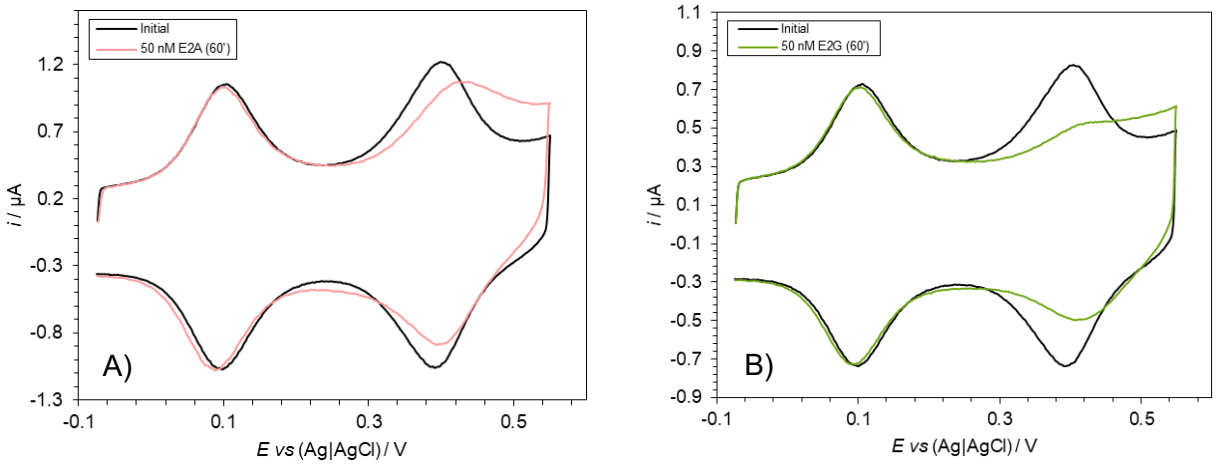

Figure 4.27: Representative CVs of **E1** sensing targets **E2A** (A) and **E2G** (B); in 10 mM sodium phosphate buffer (pH 7.0) 1 M $NaClO_4$, scan rates = 1000 mV s^{-1}.

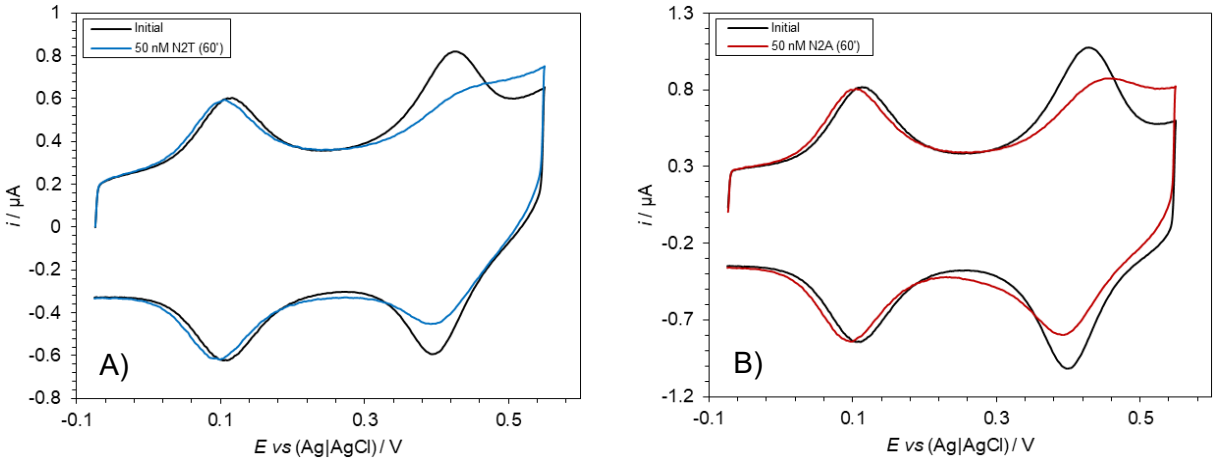

Figure 4.28: Representative CVs of **N1** sensing targets **N2T** (A) and **N2A** (B); in 10 mM sodium phosphate buffer (pH 7.0) 1 M $NaClO_4$, scan rates = 1000 mV s^{-1}.

4.6.4. Methylated Cytosine

Table 4.10: Probe sequence (**T1**) and target sequences (**T2C**, **T25mC**). X = CuCy; F = Fc; S = disulphide; mC = 5-methylcytosine. Bases highlighted in red sit opposite the CuCy in the probe–target duplexes formed.

Oligonucleotide	5′ – Sequence – 3′
T1	F TGG ACT CXC TCA ATG S
T2C	CAT TGA GCG AGT CCA
T25mC	CAT TGA GmCG AGT CCA

5-methylcytosine (5mC) is a methylated form of the canonical DNA base cytosine. In mammals, around 1% of cytosine residues are methylated[69] and abnormal DNA methylation is heavily implicated in human cancers.[70,71] It was investigated whether the CuCy within these DNA probes could discriminate between cytosine and 5mC at the position opposite in the probe–target duplex at a target concentration of 50 nM. Although the difference in CuCy:Fc current ratio % changes induced by targets **T2C** and **T25mC** were small and the error almost overlapped (Figure 4.29), **T1** could nonetheless discriminate between the non-methylated and methylated forms of cytosine. The small difference in % change induced by each target was to be expected, given the relatively minor structural difference between **T2C** and **T25mC**. However, the CuCy proved just sensitive enough that even such a small alteration resulted in a reproducible change to its electrochemical behaviour.

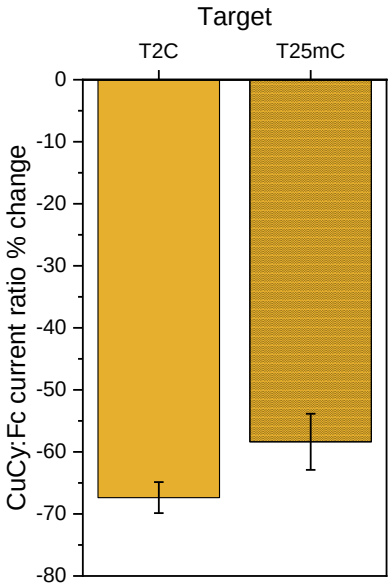

Figure 4.29: CuCy:Fc current ratio % changes for **T1** 60 minutes after target addition. Error bars represent SD. [Target] = 50 nM in 10 mM sodium phosphate buffer (pH 7.0) 1 M $NaClO_4$, scan rates = 1000 mV s^{-1}.

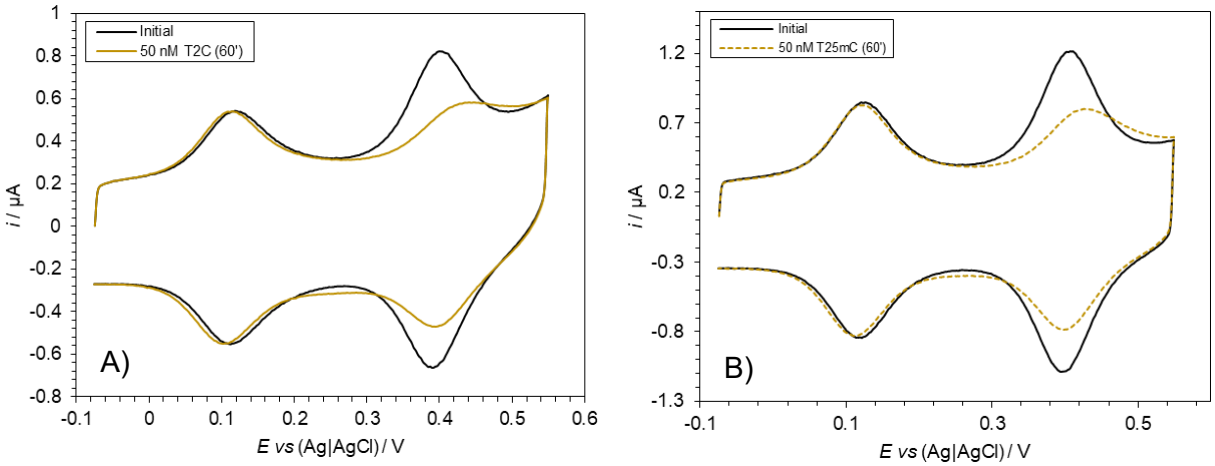

Figure 4.30: Representative CVs of **T1** sensing targets **T2C** (A) and **T25mC** (B); in 10 mM sodium phosphate buffer (pH 7.0) 1 M $NaClO_4$, scan rates = 1000 mV s^{-1}.

4.7. Conclusions and Future Work

Probe oligonucleotides synthesised in Chapter 3 were investigated and used to sense clinically relevant SNVs. The test probe **T1** was able to discriminate between adenine, cytosine, and thymine/guanine within target strands at a concentration of 50 nM in addition to being able to discriminate between cytosine and methylated cytosine. The probes **B1**, **K1**, **E1** and **N1**, based on cancer- or COVID-19-related SNVs, were able to discriminate between their relevant mutations with the exception of **K1** detecting the KRAS G12D (guanine to adenine) mutation. The CuCy-/Fc-modified probes reported are only the second example of electrochemical ratiometric SNV sensing in the literature and are the first that exhibit the combined properties of mutation location (by strategic placement of the CuCy), SNV discrimination, and probe regeneration. Whilst the ability to detect and interrogate the nature of SNVs using CuCy-modified probes has been demonstrated, the underlying mechanism for this capability is yet to be fully understood. Outstanding questions include whether kinetics plays an important role in the SNV discrimination mechanism and why the sensing behaviour of solution-based probes[28] differs from the surface-immobilised probes reported here, both of which are investigated in Chapter 5. Expansion of potential targets, including to other clinically relevant SNVs and RNA targets, is a natural progression and is also investigated in Chapter 5.

Key properties of the probes which are universal to all nucleic acid sensors, namely stability, sensitivity and regeneration capability, were investigated. The Cu^{2+} cation at the centre of CuCy was found to be unstable when subjected to prolonged periods of relatively positive potentials. Such periods of positive potentials had been previously used as part of the sensing procedure to confirm that the SAM remained intact throughout, but they had inadvertently reduced the CuCy current that ultimately resulted in an incorrect LOD determination.[29] The true LOD, without any inadvertent reduction of the CuCy current, was determined to be 10 nM for the test

probe **T1**. This concentration is higher than the fM–pM range required to theoretically sense clinically relevant nucleic acids without target amplification, and efforts to improve the LOD are described in Chapter 5. Regeneration of the probe was achieved using two methods, sonication and rinsing. Although sonication was generally successful, it frequently led to substantial SAM destruction, whereas rinsing was better tolerated. The ratiometric sensing mechanism proved essential to any regeneration method and was also demonstrated to improve signal reproducibility.

4.8. References

1. A. C. Papp, J. K. Pinsonneault, G. Cooke and W. Sadée, *Biotechniques*, 2003, **34**, 1068-1072.
2. S. Germer and R. Higuchi, *Genome Res.*, 1999, **9**, 72-78.
3. L. G. Kostrikis, S. Tyagi, M. M. Mhlanga, D. D. Ho and F. R. Kramer, *Science*, 1998, **279**, 1228-1229.
4. S. A. Marras, F. R. Kramer and S. Tyagi, *Genet. Anal.: Biomol. Eng.*, 1999, **14**, 151-156.
5. K. J. Livak, J. Marmaro and J. A. Todd, *Nat. Genet.*, 1995, **9**, 341-342.
6. F. E. A. McGuigan and S. H. Ralston, *Psychiatr. Genet.*, 2002, **12**, 133-136.
7. S. Giglio, P. T. Monis and C. P. Saint, *Nucleic Acids Res.*, 2003, **31**, e136.
8. P. Hardinge and J. A. Murray, *BMC Biotechnol.*, 2019, **19**, 1-15.
9. Q. Guo, Z. Bai, Y. Liu and Q. Sun, *Biosens. Bioelectron.*, 2016, **77**, 107-110.
10. P.-Y. Kwok and X. Chen, *Curr. Issues Mol. Biol.*, 2003, **5**, 43-60.
11. S. A. Bustin, *Biomol. Detect. Quantif.*, 2017, **12**, 10-14.
12. T. LaFramboise, *Nucleic Acids Res.*, 2009, **37**, 4181-4193.
13. Y. Jian and M. Li, *Journal of Bio-X Research*, 2021, **4**, 1-9.
14. C. Ding and S. Jin, in *Single Nucleotide Polymorphisms: Methods and Protocols*, Springer, 2nd edn, 2009, ch. 16, pp. 245-254.
15. S. Kumar, T. W. Banks and S. Cloutier, *Int. J. Plant Genomics*, 2012, DOI: 10.1155/2012/831460.
16. S. Yohe and B. Thyagarajan, *Arch. Pathol. Lab. Med.*, 2017, **141**, 1544-1557.
17. Y. Xiao, X. H. Lou, T. Uzawa, K. J. I. Plakos, K. W. Plaxco and H. T. Soh, *J. Am. Chem. Soc.*, 2009, **131**, 15311-15316.
18. A. A. Lubin, R. Y. Lai, B. R. Baker, A. J. Heeger and K. W. Plaxco, *Anal. Chem.*, 2006, **78**, 5671-5677.
19. Z. Ge, H. Pei, L. Wang, S. Song and C. Fan, *Sci. China: Chem.*, 2011, **54**, 1273-1276.
20. Z. G. Yu and R. Y. Lai, *Chem. Commun.*, 2012, **48**, 10523-10525.
21. N. Hong, L. Cheng, B. G. Wei, C. D. Chen, L. L. He, D. R. Kong, J. X. Ceng, H. F. Cui and H. Fan, *Biosens. Bioelectron.*, 2017, **91**, 110-114.
22. A. M. Debela, S. Thorimbert, B. Hasenknopf, C. O'Sullivan and M. Ortiz, *Chem. Commun.*, 2016, **52**, 757-759.

23. N. Chahin, L. A. Uribe, A. M. Debela, S. Thorimbert, B. Hasenknopf, M. Ortiz, I. Katakis and C. K. O'Sullivan, *Biosens. Bioelectron.*, 2018, **117**, 201-206.
24. M. J.-R. Mayreli Ortiz, Vasso Skouridou, Diana Machado, Miguel Viveiros, Taane G. Clark, Anna Simonova, David Kodr, Michal Hocek and Ciara K. O'Sullivan, *ACS Sens.*, 2021, DOI: 10.1021/acssensors.1c01710.
25. Y. Wan, R. Lao, G. Liu, S. Song, L. Wang, D. Li and C. Fan, *J. Phys. Chem. B*, 2010, **114**, 6703-6706.
26. Z. S. Wu, J. H. Jiang, G. L. Shen and R. Q. Yu, *Hum. Mutat.*, 2007, **28**, 630-637.
27. B. Dou, J. Li, B. Jiang, R. Yuan and Y. Xiang, *Anal. Chim. Acta*, 2018, **1038**, 166-172.
28. J. Duprey, J. Carr-Smith, S. L. Horswell, J. Kowalski and J. H. R. Tucker, *J. Am. Chem. Soc.*, 2016, **138**, 746-749.
29. E. Wilkinson, PhD thesis, University of Birmingham, 2020.
30. P. Ionita, A. Caragheorgheopol, B. C. Gilbert and V. Chechik, *Langmuir*, 2004, **20**, 11536-11544.
31. V. Ortiz and J. J. de Pablo, *Phys. Rev. Lett.*, 2011, **106**, 238107.
32. A. J. Bard, L. R. Faulkner and H. S. White, *Electrochemical Methods: Fundamentals and Applications*, Wiley & Sons, 2022.
33. P. Dauphin-Ducharme, N. Arroyo-Curras and K. W. Plaxco, *J. Am. Chem. Soc.*, 2019, **141**, 1304-1311.
34. A. B. Steel, T. M. Herne and M. J. Tarlov, *Anal. Chem.*, 1998, **70**, 4670-4677.
35. H. Z. Yu, C. Y. Luo, C. G. Sankar and D. Sen, *Anal. Chem.*, 2003, **75**, 3902-3907.
36. N. Arroyo-Currás, K. Scida, K. L. Ploense, T. E. Kippin and K. W. Plaxco, *Anal. Chem.*, 2017, **89**, 12185-12191.
37. H. Roberts, PhD thesis, University of Birmingham, 2018.
38. K. M. Ririe, R. P. Rasmussen and C. T. Wittwer, *Anal. Biochem.*, 1997, **245**, 154-160.
39. Y. Du, B. J. Lim, B. L. Li, Y. S. Jiang, J. L. Sessler and A. D. Ellington, *Anal. Chem.*, 2014, **86**, 8010-8016.
40. H. Li, N. Arroyo-Curras, D. Kang, F. Ricci and K. W. Plaxco, *J. Am. Chem. Soc.*, 2016, **138**, 15809-15812.
41. A. Kustanovich, R. Schwartz, T. Peretz and A. Grinshpun, *Cancer Biol. Ther.*, 2019, **20**, 1057-1067.

42. J. A. Weber, D. H. Baxter, S. L. Zhang, D. Y. Huang, K. H. Huang, M. J. Lee, D. J. Galas and K. Wang, *Clin. Chem.*, 2010, **56**, 1733-1741.
43. P. S. Mitchell, R. K. Parkin, E. M. Kroh, B. R. Fritz, S. K. Wyman, E. L. Pogosova-Agadjanyan, A. Peterson, J. Noteboom, K. C. O'Briant, A. Allen, D. W. Lin, N. Urban, C. W. Drescher, B. S. Knudsen, D. L. Stirewalt, R. Gentleman, R. L. Vessella, P. S. Nelson, D. B. Martin and M. Tewari, *Proc. Natl. Acad. Sci. U. S. A.*, 2008, **105**, 10513-10518.
44. J. Ma, N. Li, M. Guarnera and F. Jiang, *Biomarker Insights*, 2013, DOI: 10.4137/BMI.S13154.
45. C. Glinge, S. Clauss, K. Boddum, R. Jabbari, J. Jabbari, B. Risgaard, P. Tomsits, B. Hildebrand, S. Kääb and R. Wakili, *PloS One*, 2017, DOI: 10.1371/journal.pone.0167969.
46. C. H. Fan, K. W. Plaxco and A. J. Heeger, *Proc. Natl. Acad. Sci. U. S. A.*, 2003, **100**, 9134-9137.
47. E. Farjami, L. Clima, K. Gothelf and E. E. Ferapontova, *Anal. Chem.*, 2011, **83**, 1594-1602.
48. Y. Xiao, A. A. Lubin, B. R. Baker, K. W. Plaxco and A. J. Heeger, *Proc. Natl. Acad. Sci. U. S. A.*, 2006, **103**, 16677-16680.
49. Y. Xiao, X. G. Qu, K. W. Plaxco and A. J. Heeger, *J. Am. Chem. Soc.*, 2007, **129**, 11896-11897.
50. Z. G. Yu and R. Y. Lai, *Anal. Chem.*, 2013, **85**, 3340-3346.
51. A. Idili, A. Amodio, M. Vidonis, J. Feinberg-Somerson, M. Castronovo and F. Ricci, *Anal. Chem.*, 2014, **86**, 9013-9019.
52. W. W. Yang and R. Y. Lai, *Chem. Commun.*, 2012, **48**, 8703-8705.
53. L. P. Luo, L. L. Wang, L. P. Zeng, Y. R. Wang, Y. P. Weng, Y. J. Liao, T. T. Chen, Y. K. Xia, J. Zhang and J. H. Chen, *Talanta*, 2020, DOI: 10.1016/j.talanta.2019.120298.
54. I. Grabowska, D. G. Singleton, A. Stachyra, A. Gora-Sochacka, A. Sirko, W. Zagorski-Ostoja, H. Radecka, E. Stulz and J. Radecki, *Chem. Commun.*, 2014, **50**, 4196-4199.
55. F. Xu, A. M. Pellino and W. Knoll, *Thin Solid Films*, 2008, **516**, 8634-8639.
56. B. Zhu and J. Travas-Sejdic, *Analyst*, 2018, **143**, 687-694.
57. X. Wang, H. J. Lim and A. Son, *Environmental Health and Toxicology*, 2014, DOI: 10.5620/eht.2014.29.e2014007.

58. P. Gong and R. Levicky, *Proc. Natl. Acad. Sci. U. S. A.*, 2008, **105**, 5301-5306.
59. M. Xing, A. S. Alzahrani, K. A. Carson, D. Viola, R. Elisei, B. Bendlova, L. Yip, C. Mian, F. Vianello and R. M. Tuttle, *Jama*, 2013, **309**, 1493-1501.
60. K. J. Kurppa, J. Catón, P. R. Morgan, A. Ristimäki, B. Ruhin, J. Kellokoski, K. Elenius and K. Heikinheimo, *The Journal of Pathology*, 2014, **232**, 492-498.
61. B. K. Kleinschmidt-DeMasters, D. L. Aisner, D. K. Birks and N. K. Foreman, *The American Journal of Surgical Pathology*, 2013, **37**, 685-698.
62. S. Renaud, P. E. Falcoz, M. Schaeffer, D. Guenot, B. Romain, A. Olland, J. Reeb, N. Santelmo, M. P. Chenard, M. Legrain, A. C. Voegeli, M. Beau-Faller and G. Massard, *Br. J. Cancer*, 2015, **113**, 1206-1215.
63. L. Johnson, K. Mercer, D. Greenbaum, R. T. Bronson, D. Crowley, D. A. Tuveson and T. Jacks, *Nature*, 2001, **410**, 1111-1116.
64. I. A. Prior, P. D. Lewis and C. Mattos, *Cancer Res.*, 2012, **72**, 2457-2467.
65. S. Jangra, C. J. Ye, R. Rathnasinghe, D. Stadlbauer, F. Krammer, V. Simon, L. Martinez-Sobrido, A. Garcia-Sastre and M. Schotsaert, *Lancet Microbe*, 2021, **2**, E283-E284.
66. Y. Liu, J. Y. Liu, K. S. Plante, J. A. Plante, X. P. Xie, X. W. Zhang, Z. Q. Ku, Z. Q. An, D. Scharton, C. Schindewolf, S. G. Widen, V. D. Menachery, P. Y. Shi and S. C. Weaver, *Nature*, 2022, **602**, 294-299.
67. R. Tavallaie, J. McCarroll, M. Le Grand, N. Ariotti, W. Schuhmann, E. Bakker, R. D. Tilley, D. B. Hibbert, M. Kavallaris and J. J. Gooding, *Nat. Nanotechnol.*, 2018, **13**, 1066-1071.
68. R. B. Jamal, T. Vitasovic, U. Gosewinkel and E. E. Ferapontova, *Biosens. Bioelectron.*, 2023, 115214.
69. M. Ehrlich and R. Y.-H. Wang, *Science*, 1981, **212**, 1350-1357.
70. M. Ehrlich, *Epigenomics*, 2009, **1**, 239-259.
71. S. B. Baylin and J. G. Herman, *Trends Genet.*, 2000, **16**, 168-174.

Chapter 5: Efforts to Understand, Enhance, and Expand the Sensing of Nucleic Acids Using Redox-Modified DNA Probes

5.1. Overview and Chapter Aims

Chapter 4 detailed the use of CuCy-/Fc-modified probes to sense DNA targets and interrogate the nature of clinically relevant SNVs. Whilst largely successful, the results have raised new questions and presented routes to pursue in enhancing the probe's capabilities. The ability of the CuCy to discriminate between SNVs was clearly demonstrated in Chapter 4. However, important questions, including how the CuCy can discriminate between SNVs and why the surface-immobilised CuCy-/Fc-modified probes exhibit differences in sensing behaviour to their solution-based predecessors, remained unanswered.

The first objective of this chapter was to investigate the mechanism behind the SNV sensing using the CuCy-/Fc-modified probes. Furthermore, the LOD of 10 nM for probe **T1** was at least two orders of magnitude short of being able to theoretically sense clinically relevant nucleic acid targets at physiological concentrations. The second objective was to try to improve the sensitivity of the CuCy-/Fc-modified probes using new probes and different electrochemical techniques. Finally, demonstrating the ability of CuCy-/Fc-modified probes to sense RNA targets would considerably enhance their versatility. In particular, the sensing of miRNA targets, with their suitable length of ~20 nucleotides and closely related miRNAs often differing by only one base, offered the perfect target subset to test the probe's capabilities. Additionally, the ability to sense in more complex media containing biological contaminants would further enhance the practical usability of the CuCy-/Fc-modified probes. The third objective was to sense clinically relevant RNA targets in solutions containing bodily fluids.

5.2. Investigations into the Single Nucleotide Variant Sensing Mechanism

5.2.1. Sensing with (*S*)-T1

Probe **(*S*)-T1** exhibited markedly different electrochemical sensing and thermodynamic properties to its diastereomer **T1**. As discussed in Chapter 4, duplexes formed using **(*S*)-T1** exhibited significantly greater thermal stabilities than duplexes formed using **T1**. This was attributed to the fitting of the (*S*)-isomer of CuCy into the base stack with less disruption to surrounding bases than the (*R*)-isomer, as indicated by previous computational modelling.[1] As well as a difference in duplex stabilities, there was also a difference in sensing signal, as **(*S*)-T1** produced substantially larger CuCy:Fc current ratio % changes than **T1** when sensing equivalent amounts of target (Figure 5.1). However, SNV discrimination using **(*S*)-T1** proved harder with similar CuCy:Fc current ratio % changes produced for each base, which was also previously the case with the solution-based CuCy-modified probe.[1] These results indicate that even relatively modest adjustments to the CuCy's position within the base-pair stack can have a major impact on the properties of the probe–target duplex.

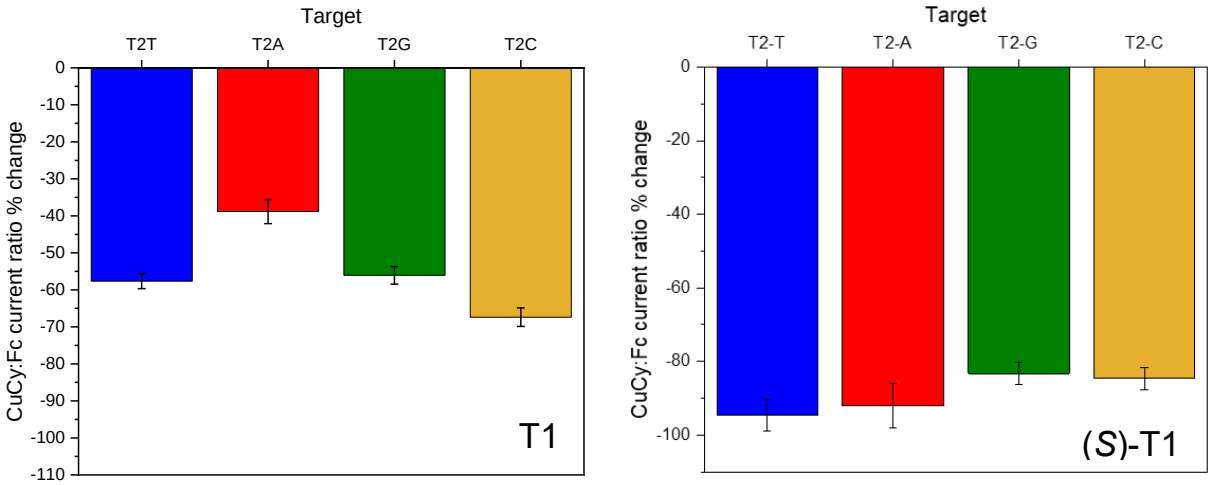

Figure 5.1: CuCy:Fc current ratio % changes for **T1** (left) and **(*S*)-T1** (right) when sensing each of the four canonical bases opposite the CuCy 60 minutes after target addition. Error bars represent SD. [Target] = 50 nM in 10 mM sodium phosphate buffer (pH 7.0) 1 M $NaClO_4$, scan rates = 1000 mV s^{-1}.

5.2.2. Duplex Stability and Electrochemical Current Signal Correlation

The surface-immobilised **T1** probe's base-discriminating ability appeared to be affected by the size of the base opposite the CuCy in the probe–target duplex. The smaller pyrimidine bases (cytosine and thymine) on average induced larger CuCy:Fc current ratio % changes than the bulkier purine bases (adenine and guanine). Previously, it had been hypothesised that the CuCy more easily accommodated a pyrimidine rather than a purine alongside it, with the latter case resulting in the CuCy burying itself deeper into the duplex at the expense of the purine opposite.[1] T_m results indeed indicated that the CuCy in the **T1** probe could more easily accommodate a pyrimidine over a purine in the base stack, with slightly higher values for the pyrimidine targets **T2T** (60.0 ± 0.5 °C) and **T2C** (60.5 ± 0.5 °C) than the purine targets **T2A** (57.5 ± 0.5 °C) and **T2G** (58.5 ± 0.5 °C). It was noted that, although the differences in T_m values were small, there was a positive correlation between duplex stability and CuCy:Fc current ratio % change: the higher the T_m, the bigger the % change. This trend was consistent across all of the probes used to sense SNVs (Figures 5.2 and 5.3) and will be incorporated into the proposed mechanism for the SNV discrimination observed, discussed below.

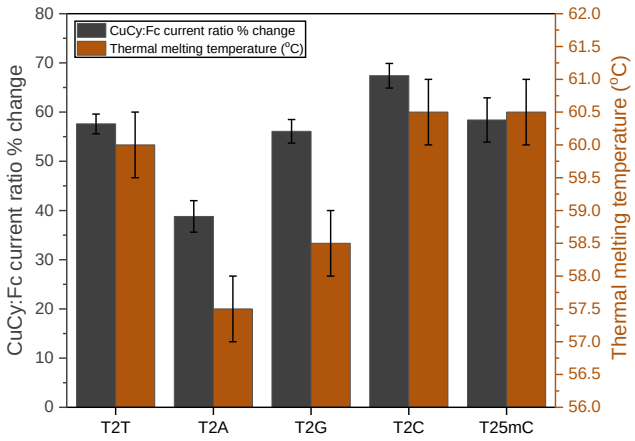

Figure 5.2: CuCy:Fc current ratio % changes plotted along with thermal melting temperatures of targets with **T1**. Sensing target concentration = 50 nM. Error bars represent SD.

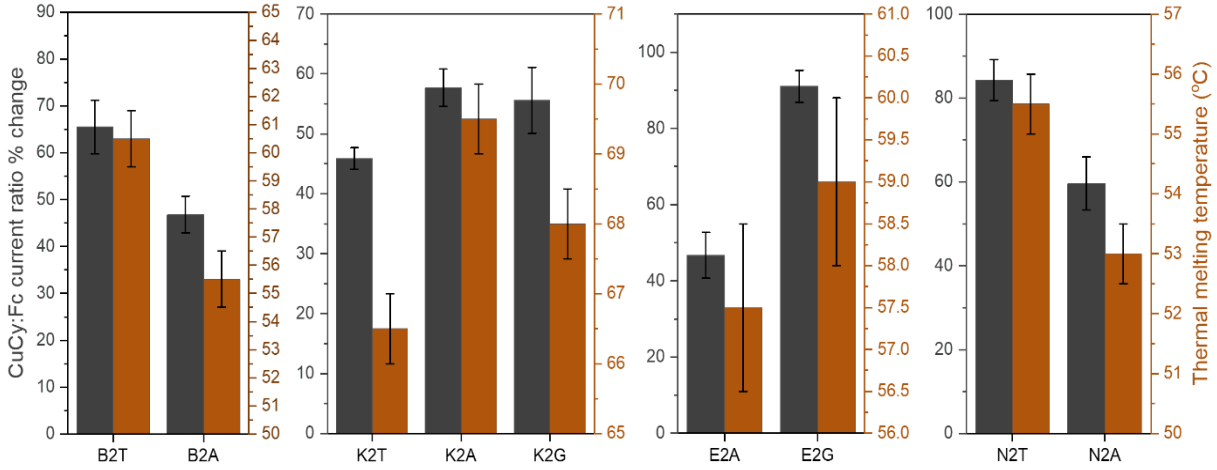

Figure 5.3: CuCy:Fc current ratio % changes along with thermal melting temperatures of targets with their respective probes. Sensing target concentration = 50 nM. Error bars represent SD.

5.2.3. Target Saturation and SAMs Assembled from Pre-Formed Duplexes

As has been discussed in the LOD studies reported in Chapter 4, even 10 nM target solutions contain almost two orders of magnitude more target molecules than is theoretically needed to saturate the sensor. Additionally, increasing target concentration and the time allowed for probe–target binding resulted in larger CuCy:Fc current ratio % changes, indicating that more probes were being bound at higher target concentrations. Given that at a target concentration of 50 nM (the concentration used for the SNV sensing reported in Chapter 4) not all probes were bound to target, this opened up the possibility that certain targets were binding to the probes more so than others, leading to different current changes at the end of the 60 minute sensing period. This possibility was strengthened by the positive correlation between duplex stability and CuCy:Fc current ratio % change, discussed above. To ensure that every probe was bound to target, experiments using very high target concentrations were conducted in an effort to saturate the sensor. If the SNV sensing differences persisted even after every probe was bound to target, then an entirely thermodynamic mechanistic explanation for the SNV discrimination observed could be discounted.

Sensing 1 µM **T2T** and **T2A** targets using the **T1** probe (Figures 5.4 and 5.5) showed that after 20 minutes no further change in the CuCy:Fc current ratio occurred, indicating that an equilibrium had been reached in which no more probe–target duplexes could be formed. Crucially, the difference in CuCy:Fc current ratios induced by **T2T** and **T2A** persisted at 1 µM target concentration and mirrored the discrimination observed at 50 nM. However, despite the high target concentration and no change in CuCy:Fc current ratio between 20 and 60 minutes, it could not be completely proven that every probe was bound to target.

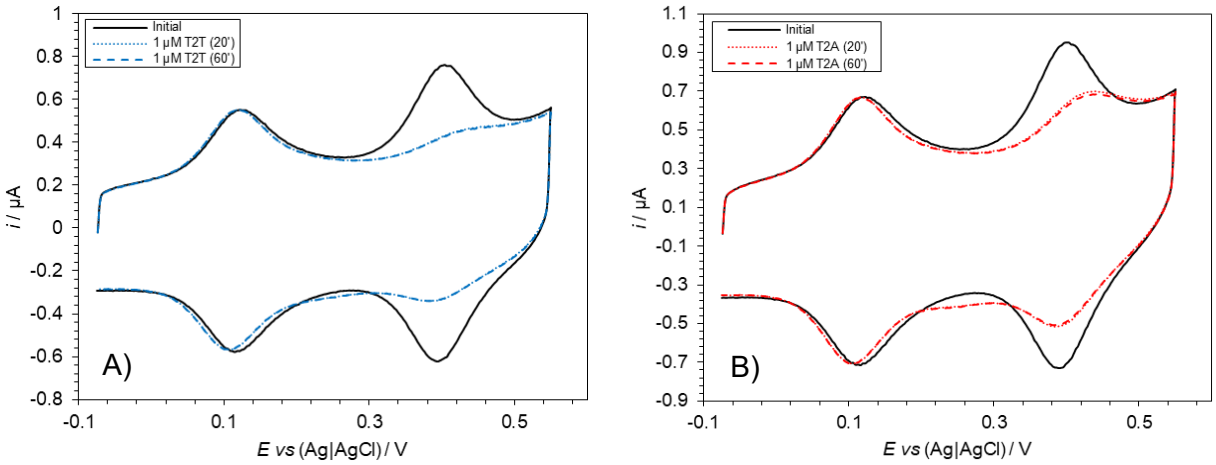

Figure 5.4: CVs of **T1** sensing 1 µM **T2T** (A) and 1 µM **T2A** (B) 20 minutes and 60 minutes after target addition; in 10 mM sodium phosphate buffer (pH 7) 1 M $NaClO_4$, scan rates = 1000 mV s^{-1}.

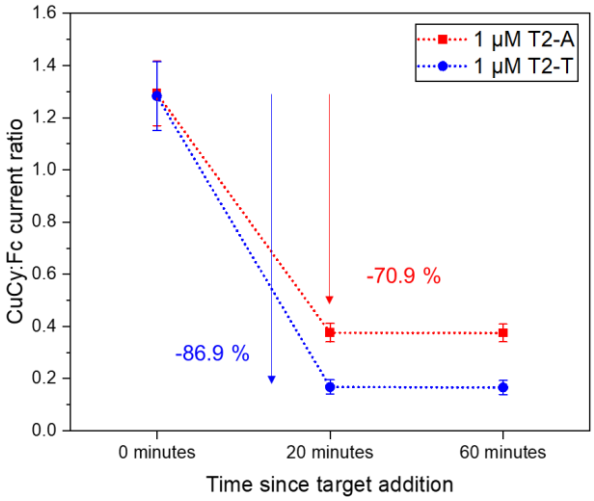

Figure 5.5: CuCy:Fc current ratio % changes using **T1** sensing 1 µM **T2A** (red squares) and 1 µM **T2T** (blue circles) 20 minutes and 60 minutes after target addition. No % change between 20 and 60 minutes indicates an equilibrium had been reached before the 20 minute time point. Error bars represent SD. CVs conducted in 10 mM sodium phosphate buffer (pH 7.0) 1 M $NaClO_4$, scan rates = 1000 mV s^{-1}.

Next, sensing was conducted at an even higher target concentration (3 µM). Again, the difference in CuCy:Fc current ratio % changes induced by the targets **T2T** and **T2A** persisted (Figures 5.6 and 5.7), albeit with a smaller difference compared with 50 nM and 1 µM target concentrations. It was also noted that the % changes were larger than when sensing 1 µM target. This indicated that even at a high target concentration of 1 µM, not every probe was bound and that adding more target resulted in slightly increased probe–target duplex formation. This may be explained by considering the bound:unbound probe ratio as an equilibrium. As previously discussed, at all target concentrations studied here, many times more target molecules are present in solution than are needed to theoretically saturate the sensor (*i.e.*, where all probes at the electrode surface are duplexed to target). That some probes remain unbound can be attributed to the repulsive electrostatic and steric effects experienced by DNA immobilised onto surfaces.[2-4] Increasing target concentration counters these repulsive forces, shifting the equilibrium in favour of more bound probes. Evidence for this can be seen in the different CuCy:Fc current ratio % changes induced by 1 µM versus 3 µM target concentrations, despite the fact that at each concentration no current ratio changes were observed between 20 and 60 minutes, indicating that an equilibrium had been reached.

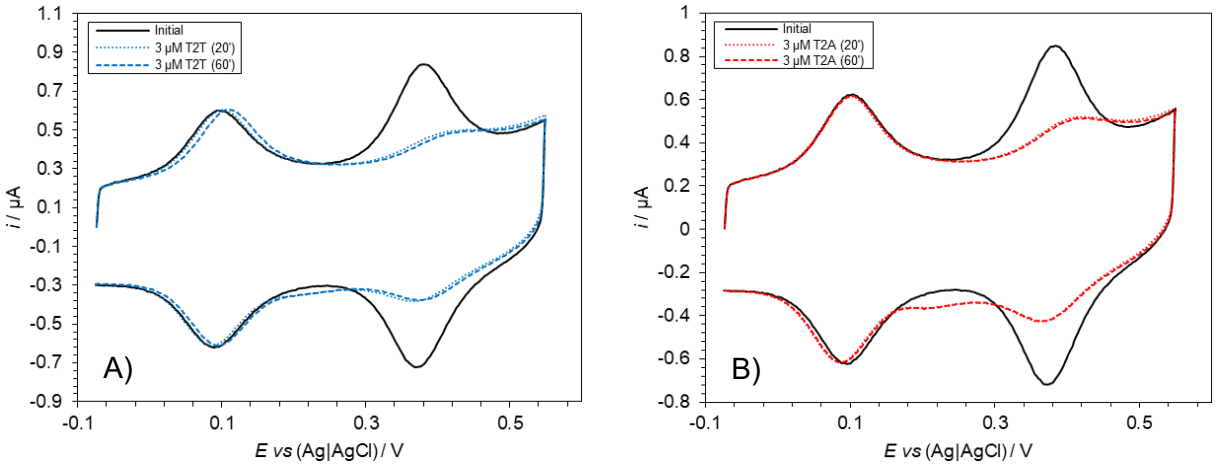

Figure 5.6: CVs of **T1** sensing 3 µM **T2T** (A) and 3 µM **T2A** (B) 20 minutes and 60 minutes after target addition; in 10 mM sodium phosphate buffer (pH 7) 1 M $NaClO_4$, scan rates = 1000 mV s^{-1}.

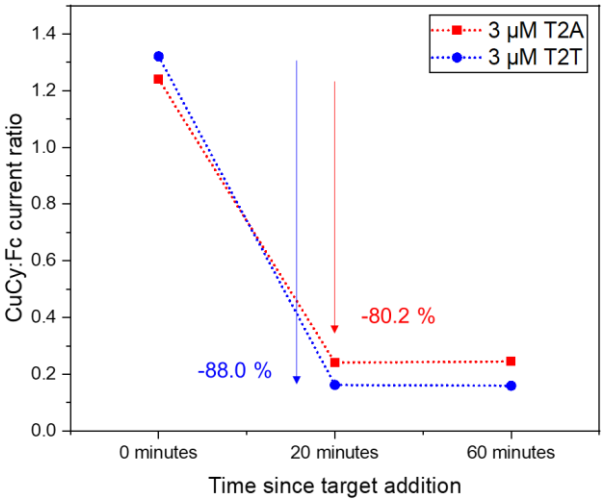

Figure 5.7: CuCy:Fc current ratio % changes using **T1** sensing 3 μM **T2A** (red) and 3 μM **T2T** (blue) 20 minutes and 60 minutes after target addition. No % change between 20 and 60 minutes indicates an equilibrium had been reached before the 20 minute time point. CVs conducted in 10 mM sodium phosphate buffer (pH 7.0) 1 M $NaClO_4$, scan rates = 1000 mV s^{-1}.

Although likely that the vast majority of probes were bound to target at the extremely high concentration of 3 μM, further experiments were conducted using SAMs assembled from preformed duplexes in an effort to maximise the proportion of bound probes. To preform the duplexes, large amounts of probe and target (10 μM and 15 μM, respectively) were incubated together for one hour in solution according to procedures published by Ferapontova and coworkers (Figure 5.8, see section 7.6.2. for full details).[5] Due to the significantly higher amount of probe required for preformed duplex SAM assembly, the abundant mono-modified **CuCyMid** probe was used instead of **T1**. Current (μA) was converted into current density (μA cm^{-2}) to account for the differences in electrochemically active surface area between electrodes.

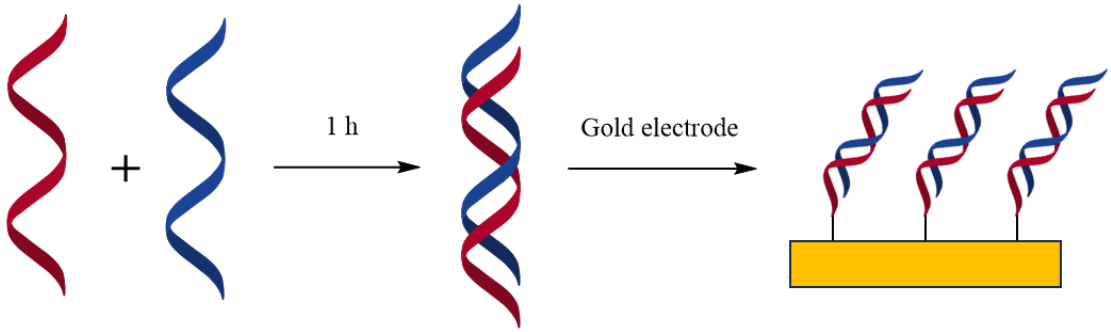

Figure 5.8: Simplified procedure of SAM formation using preformed duplexes.

Using SAMs assembled from preformed duplexes, T opposite the CuCy once again resulted in a smaller CuCy current signal (2.8 μA cm^{-2}) than with A opposite (5.3 μA cm^{-2}) (Figure 5.9). Additionally, SAMs assembled from duplexes preformed using a heating and annealing step to ensure maximum duplex formation also resulted in **T2T** producing a smaller CuCy current signal compared with **T2A** (see Appendix 8.3.4.).

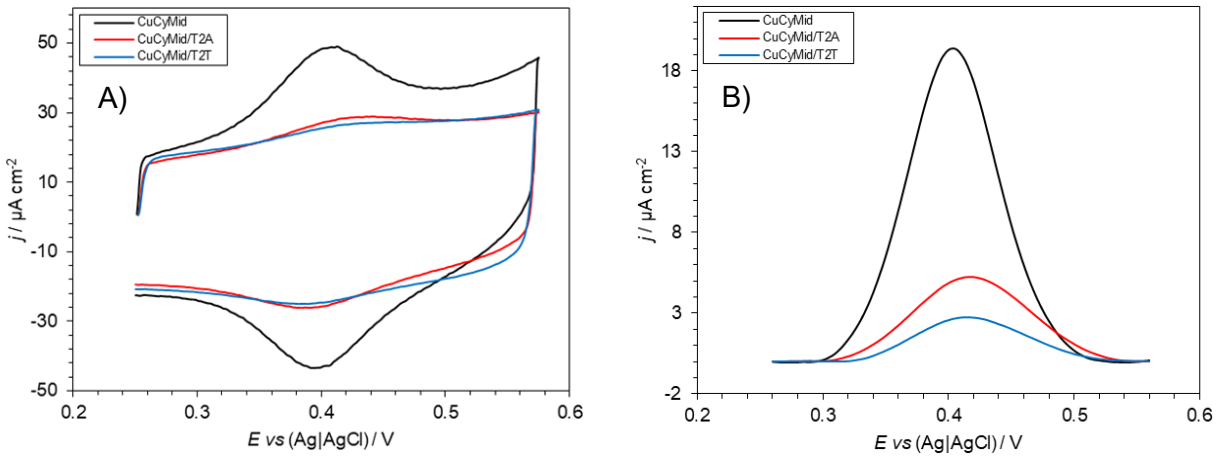

Figure 5.9: A) CV of **CuCyMid** alone (black), with **T2A** (red) and with **T2T** (blue), using SAMs assembled from preformed duplexes according to procedures published by Ferapontova and coworkers;[5] in 10 mM sodium phosphate buffer (pH 7) 1 M $NaClO_4$, scan rates = 1000 mV s^{-1}. B) normalised and background-corrected anodic traces of the CVs shown on the left.

The consistent differences between **T2T** and **T2A** target at both very high target concentrations and in SAMs assembled from preformed duplexes indicates that the SNV discrimination observed is not the result of an entirely thermodynamic mechanism. However, given that at 50 nM target concentration a significant proportion of probes remained unbound and that there is a positive correlation between duplex stability and CuCy:Fc current ratio % change, it is likely that the precise position of the CuCy within the probe–target duplex is not the only factor accounting for the SNV discrimination achieved in Chapter 4. Specifically, it would be expected that a more thermodynamically stable duplex would form to a greater extent than a slightly less thermodynamically stable duplex, notwithstanding that the differences in melting temperature (albeit for duplexes in solution) are very small. The magnitude of this

extent is difficult to quantify, but it is likely to be magnified at the surface of a DNA-modified electrode in which significant repulsive electrostatic and steric forces act against probe–target hybridisation[2-4] and where a significant proportion of probes remain unbound.

5.2.4. Proposed SNV Sensing Mechanism and Solution Versus Surface Differences

Given the clear and reproducible (*S*)- versus (*R*)-isomer probe sensing differences at various target concentrations, backed up by saturation and preformed duplex studies, the correlation with the thermal melting data, and work reported previously on analogous solution-based probes,[1] the mechanism for the SNV discrimination achieved using the surface-immobilised probes reported here is proposed to be a combination of two factors: 1) the precise position of the CuCy within the probe–target duplex, as dictated by the bases around it, significantly affecting its current; and 2) targets having different binding profiles according to the differences in thermodynamic stabilities of the probe–target duplexes.

Regarding the first factor, the hypothesis that the average position of the CuCy is affected by the identity of the base opposite, which in turn affects its current signal, was first derived from the electrochemical sensing, thermal melting, and computational modelling studies conducted for the solution-based work.[1] These indicated that the larger purine bases opposite the CuCy result in more distorted duplexes and lower T_m values due to the purines being pushed out of the duplex at the expense of the CuCy, which becomes more embedded. This in turn would reduce the rate of electron transfer from the less exposed CuCy, resulting in a lower current. Conversely, a smaller pyrimidine base opposite the CuCy was posited to result in less clashing, with the CuCy not burying as far into the duplex. This in turn would result in a relatively faster rate of electron transfer from the more exposed CuCy, resulting in a higher current. However, despite the same trend in T_m values observed for the CuCy-modified probe reported previously[1] and the **T1** probe reported here (the only difference between the two probes

being the Fc and disulphide modifications appended to the 5′ and 3′ ends of **T1**, respectively), the current signal trend for purine and pyrimidine targets is reversed upon surface-immobilisation: the pyrimidine targets now give a larger average current reduction than the purine targets (Figure 5.10).

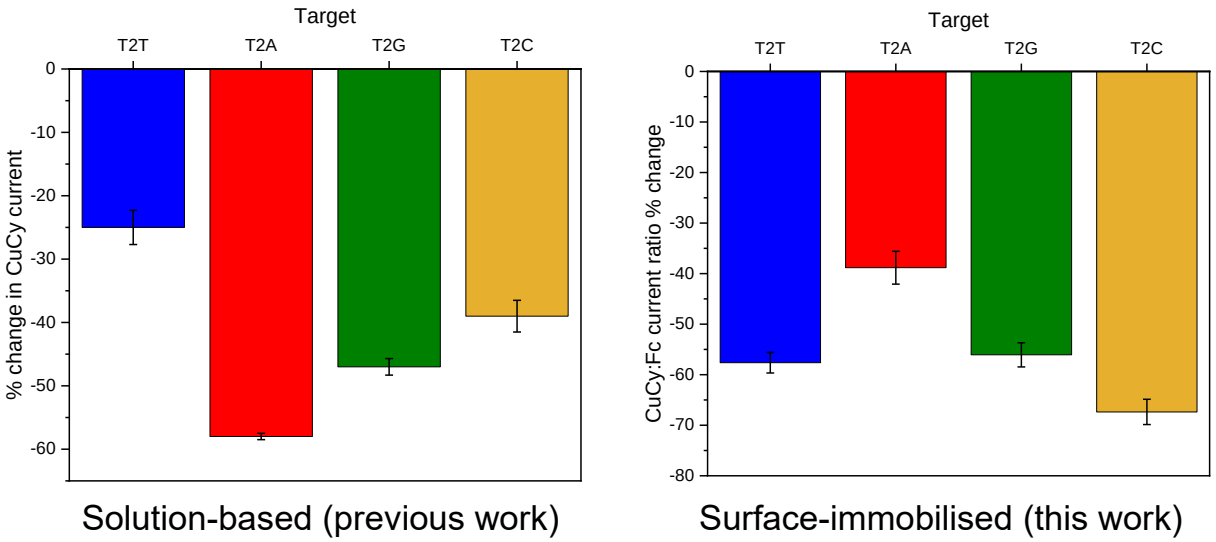

Figure 5.10: % change in CuCy current induced by each base in the solution-based work reported previously[1] (left) and the CuCy:Fc current ratio % changes for **T1** induced by each base (right). Error bars represent SD.

Whilst this inversion is difficult to rationalise, there are key differences between the solution-based sensing reported previously[1] and the surface-immobilised sensing reported here. DNA immobilised at the surface of an electrode is in an environment that is markedly different to DNA in solution. This is illustrated by the differences in hybridisation behaviour between solution-based and surface-immobilised DNA, with electrostatic and steric forces playing more significant roles at the surface.[2-4] Given in particular the substantial concentration of electrostatic forces at DNA-modified electrode surfaces, one possibility is that the average position the CuCy adopts in a surface-immobilised duplex is slightly different to the position it adopts in a solution-based duplex, both otherwise containing the same sequences. As illustrated by the contrast between **T1** and **(*S*)-T1**, even small changes to the CuCy's position may result

in significant sensing differences. Another important difference is the use of square wave voltammetry for the solution-based work[1] versus the use of cyclic voltammetry for the surface-immobilised work presented here. As is reported below in section 5.3.3., different signals can be produced for the same system using either square wave or cyclic voltammetry, and the use of different electrochemical techniques may have contributed to the solution-based versus surface-immobilised sensing differences observed.

Another key difference between the solution-based sensing reported previously[1] and the surface-immobilised sensing reported here is that in the solution-based work the vast majority of probes would be expected to be bound to target, whereas the target saturation studies reported in section 5.2.3. showed that at a 50 nM target concentration, a significant proportion of surface-immobilised probes remained unbound. It is reasonable to infer, that in an environment in which a significant proportion of probes remain unbound, that there will be a higher relative population of duplexes with higher stability forming than those with lower stability. Thus, the second factor – that certain targets bind to probes more than others over the 60 minute sensing period – accounts for the likely thermodynamic contribution to the SNV discrimination observed and is supported by the positive correlation between duplex stability and CuCy:Fc current ratio % change discussed in section 5.2.2.

5.2.5. Through-DNA Charge Transport Studies

Another theory was also proposed as a possible explanation for the observed solution-based versus surface-immobilised sensing differences. Different modes of electron transfer between the CuCy and electrode in solution-based duplexes versus surface-immobilised duplexes were considered. In both solution-based and surface-immobilised duplexes, contact-mediated electron transfer can occur: if the CuCy or Fc approaches close enough to the electrode surface, an electron can tunnel from one to the other. Electrons have been shown to tunnel over distances

of 1–3 nm,[6] including up to 2.5–3 nm through proteins on relevant timescales.[7,8] Figure 5.11 shows that, with the 6-mercapto-1-hexanol layer being a maximum of 1.6 nm thick, direct contact-mediated electron transfer can occur from the redox labels to the electrode (and *vice versa*) upon flexing of the probes.

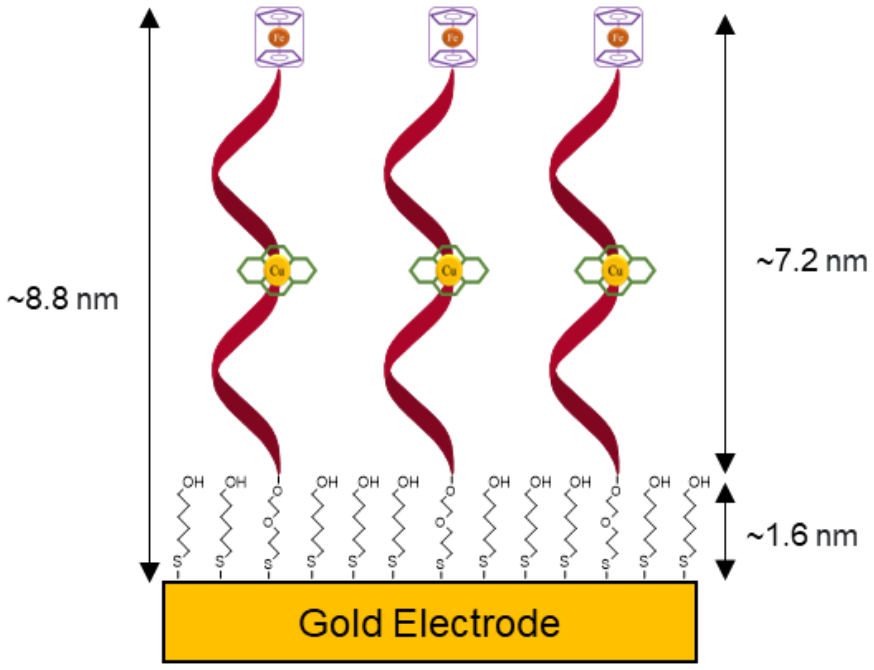

Figure 5.11: Schematic representation of a mixed SAM comprised of a **T1**-length probe and 6-mercapto-1-hexanol drawn approximately to scale length-wise.

An alternative mode of electron transfer is only relevant to surface-immobilised duplexes. Through-DNA electron transfer, most prominently championed by Barton[9-11] and Ferapontova,[5,12] amongst others, posits that double-stranded DNA can act as a molecular wire with delocalised electrons passing directly through the base-stack of well-matched strands. Experiments involving redox-modified, surface-immobilised DNA (Figure 5.12) have been used to investigate the transfer of electrons between the redox label and the electrode. Interruptions to the base stack, whether in the form of mismatches,[10,13] abasic sites,[14,15] or DNA-binding proteins,[16] have been found to attenuate the transfer of electrons and thus is provided as evidence for electron transfer through double-stranded DNA.

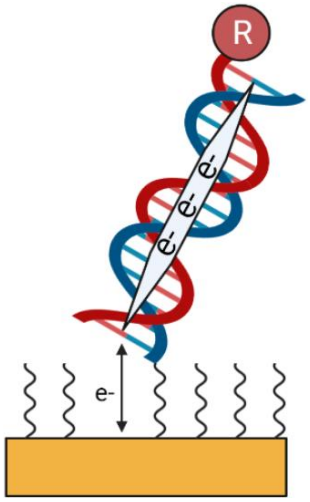

Figure 5.12: Schematic representation of through-DNA electron transfer occurring between a redox label and a gold electrode.

Relating to the CuCy-/Fc-modified probes reported here, through-DNA electron transport between the CuCy and the electrode was thought to possibly be occurring. If so, then the CuCy burying itself more deeply into the duplex may hinder electron transfer when the duplex is solution-based (through-DNA transfer irrelevant, contact-mediated transfer impeded) but increase the rate of through-DNA electron transfer when the duplex is surface-immobilised (through-DNA transfer relevant, contact-mediated transfer still impeded). This would explain the pyrimidine/purine sensing inversion between the solution-based CuCy-modified probe and surface-immobilised **T1** probes: when opposite a purine, the CuCy's current is relatively less reduced as a new electron transport mechanism (through-DNA) becomes available when surface-immobilised. Investigating whether through-DNA electron transport was occurring through surface-immobilised CuCy-modified probes was therefore deemed to be of importance to the work reported here as well as a potentially useful contribution to the field of DNA electronics.

To investigate whether meaningful through-DNA electron transfer was occurring between the CuCy and the electrode, mismatches and abasic sites were introduced into the base stack in a fashion similar to that reported by Ferapontova[13] and Slinker.[14] Using the **CuCyMid**, **CuCyMid_C3+2** and **CuCyMid_C3-2** probes and their respective targets (Table 5.1), a T–T mismatch or an abasic site was introduced either 'in-between' the CuCy and the electrode or 'above' the CuCy with respect to the electrode (Figure 5.13). If meaningful through-DNA electron transfer was occurring, it was thought that the interruption in-between the CuCy and the electrode would result in a smaller CuCy current than the interruption *not* in-between the CuCy and the electrode.

Table 5.1: The **CuCyMid**, **CuCyMid_C3+2**, and **CuCyMid_C3-2** probes and their respective targets used to form duplexes in which a mismatch or abasic site is 'in-between' (-2) or 'above' (+2) the CuCy and the electrode. Bases highlighted in blue/purple sit opposite one another in the probe–target duplex; bases highlighted in red sit opposite the CuCy in the probe–target duplex. X = CuCy; C3 = C3 spacer; S = disulphide.

Oligonucleotide	5′ – Sequence – 3′
CuCyMid	TGG ACT CXC TCA ATG S
T2A_mm+2	CAT TGA GAG TGT CCA
T2A_mm-2	CAT TGT GAG AGT CCA
CuCyMid_C3+2	TGG ACC3 CXC TCA ATG S
T2A_C3+2	CAT TGA GAG C3GT CCA
CuCyMid_C3-2	TGG ACT CXC C3CA ATG S
T2A_C3-2	CAT TGC3 GAG AGT CCA

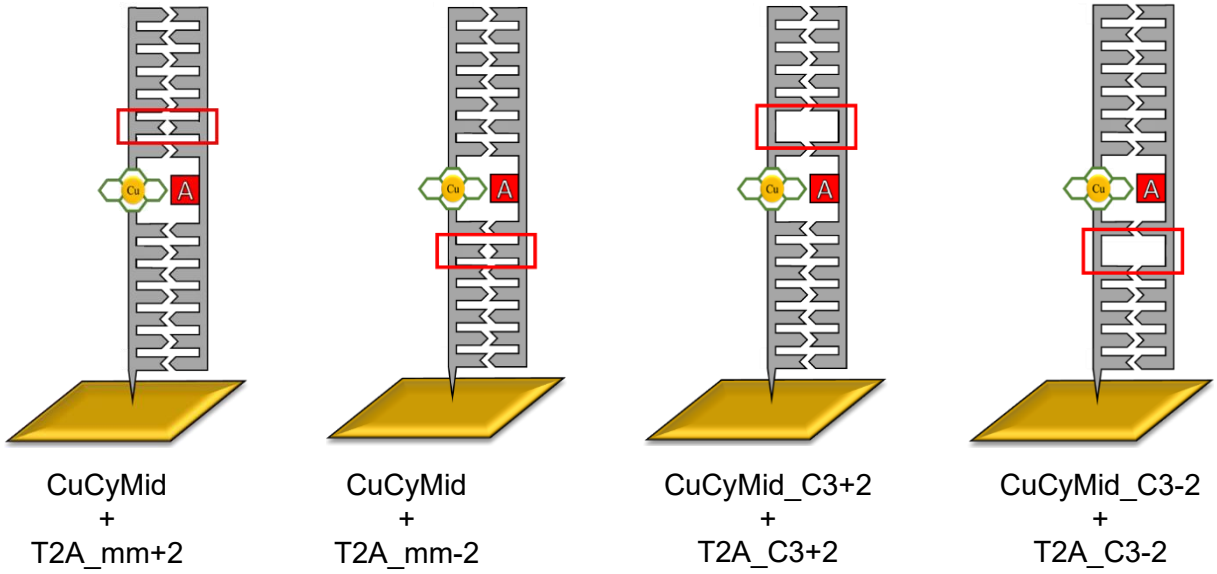

Figure 5.13: Schematic diagrams of duplexes formed with the oligonucleotides in Table 5.1 in which a mismatch or abasic site (highlighted red) is 'in-between' (-2) or 'above' (+2) the CuCy and the electrode.

Contrary to expectations, introduction of an interruption above the CuCy with respect to the electrode (A and C in Figure 5.14) resulted in a greater decrease in current compared with when an interruption was introduced in-between the CuCy and the electrode (B and D in Figure 5.14). (See Appendix 8.3.3. for all extrapolated anodic traces of the CVs shown in the main text.) As before when using the mono-modified **CuCyMid** probe without the additional Fc (thus negating the ability to perform ratiometric sensing), to compare the CVs, current (i, μA) was converted into current density (j, μA cm^{-2}) by dividing by the electrochemically active surface area of each electrode. Why the interruptions placed between the CuCy and the electrode resulted in smaller decreases in current is not clear. One possibility is that, although the nature of the respective interruptions were identical (both either a T–T mismatch or an abasic site replacing a T–A base pair), their different positions had a non-identical impact on the position of the nearby CuCy – a property that has been shown to affect the current it produces. However, evidence for the CuCy adopting different positions depending on the position of the same interruption was not found in the thermal melting data, as the T_m values were within error of

one another (see Appendix 8.3.2.) Alternatively, the location of the interruption may affect the flexibility of the probe and therefore the ease with which the CuCy can reach the electrode surface. In either case, the difference in the CuCy currents would be explained by the impact on contact-mediated electron transfer and not through-DNA transfer.

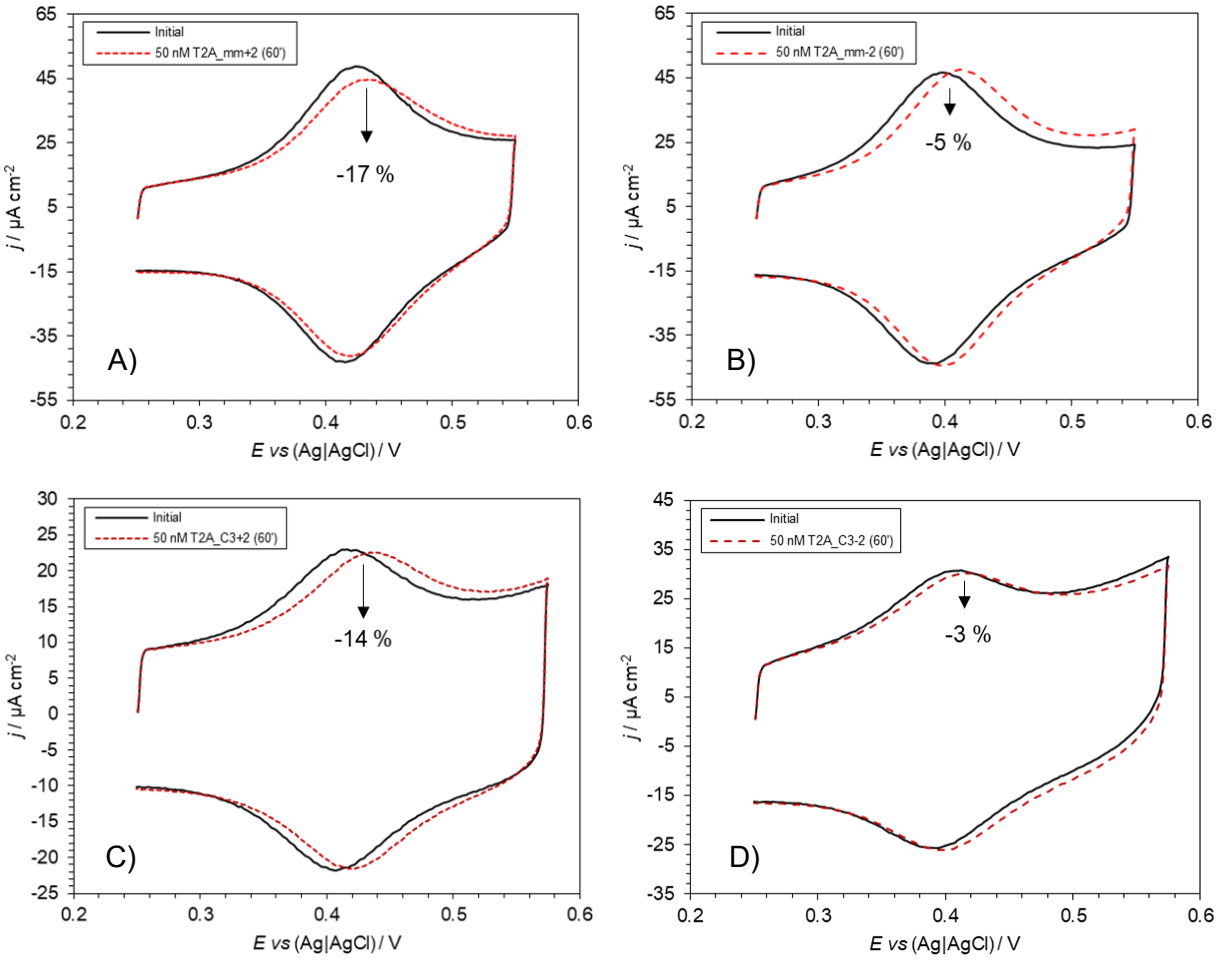

Figure 5.14: CVs of the probes with their respective targets (50 nM) shown in Table 5.1: A) mismatch above CuCy; B) mismatch in-between CuCy and electrode; C) abasic site above CuCy; D) abasic site in-between CuCy and electrode. %s shown are the reductions in the CuCy anodic current 60 minutes after target addition. In 10 mM sodium phosphate buffer (pH 7.0) 1 M $NaClO_4$, scan rates = 1000 mV s^{-1}.

The SAMs used for Figure 5.14 were assembled according to the standard procedures and consisted of single-stranded probes to which target was subsequently added (see section 7.6.3. for full details). However, much of the literature reporting on electron transport through surface-immobilised DNA involved SAMs assembled from preformed duplexes.[5,13,14] As Barton and

coworkers convincingly argued[11] in their response to Plaxco and coworkers' assertion[17] that electron transfer from surface-immobilised DNA is a contact-mediated process, not duplexing the DNA prior to surface-immobilisation may result in more disorderly SAMs in which contact-mediated electron transfer dominates. Therefore, experiments using SAMs assembled from preformed duplexes were conducted in a similar fashion to those reported in section 5.2.3.

Figure 5.15 shows CVs of SAMs assembled from preformed duplexes of **CuCyMid** with either **T2A**, **T2A_mm-2**, or **T2A_mm+2**. A SAM assembled using just **CuCyMid** probe alone is also shown for comparison. Once again, placing the interruption above the CuCy with respect to the electrode resulted in a smaller CuCy current: the mismatch above the CuCy resulted in a current density of 1.2 μA cm^{-2}, whereas the mismatch in-between the CuCy and the electrode resulted in a current density of 4.2 μA cm^{-2} (comparable to a current density of 3.8 μA cm^{-2} produced by the **CuCyMid**/**T2A** duplex). The placement of an interruption above the CuCy relative to the electrode resulting in a smaller CuCy current was therefore consistent across two different systems (mismatches versus abasic sites) and two different SAM-assembly procedures.

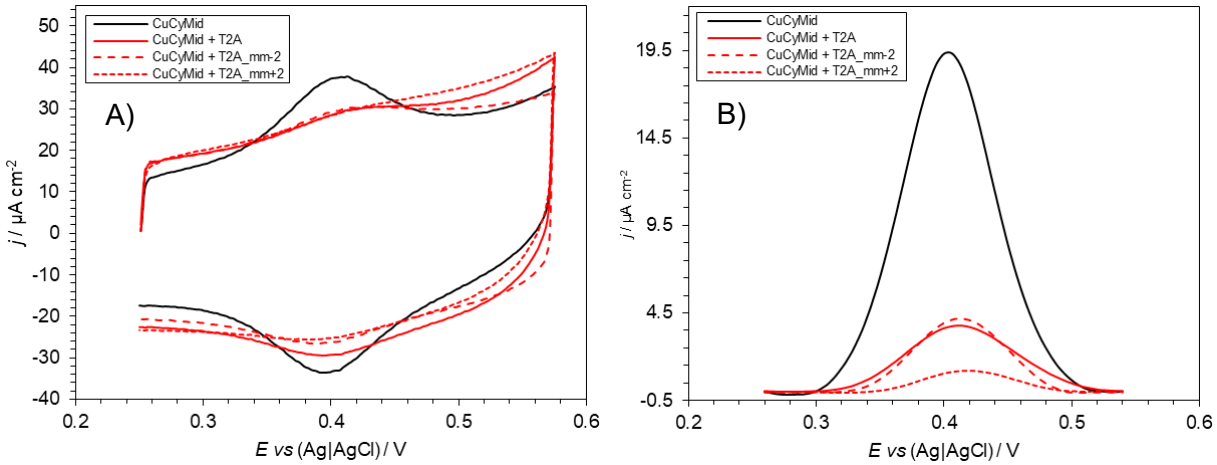

Figure 5.15: A) Overlaid CVs using preformed duplexes of the probes and their respective targets shown in Table 5.1; in 10 mM sodium phosphate buffer (pH 7.0) 1 M $NaClO_4$, scan rates = 1000 mV s^{-1}. B) Overlaid and background-corrected anodic traces of the cyclic voltammograms shown on the left.

These experiments produced no evidence of meaningful through-DNA electron transport in surface-immobilised CuCy-modified DNA. Therefore, the theory that through-DNA electron transport could explain the purine/pyrimidine sensing inversion going from solution-based to surface-immobilised CuCy-modified probes was not pursued further. This does not mean that through-DNA electron transport is not occurring in the systems reported here, and further experiments are needed. An important factor to consider when investigating through-DNA electron transport in surface-immobilised DNA is the angle at which the DNA sits relative to the electrode surface. It has been shown that a potential of +0.4 V (versus Ag|AgCl) forces the surface-immobilised DNA to lie flat on the electrode surface as it attracts the negatively charged phosphodiester backbone (Figure 5.16, right).[18,19] The $E_{1/2}$ value for the CuCy of *ca* +0.4 V (versus Ag|AgCl) suggests that the probes are likely lying close to the electrode surface when the CV reaches the CuCy redox potential, which would aid direct contact-mediated electron transfer. Through-DNA electron transport would be expected to play a less significant role in DNA lying flat on the electrode surface versus DNA forced to adopt a more upright position. Much of the literature investigating through-DNA electron transport uses redox labels such as MB,[11,12] Nile Blue,[9,14] or daunomycin[10], which all have $E_{1/2}$ values negative of 0 V (versus Ag|AgCl). At these potentials, electrostatic repulsion would force the DNA into a more upright position in which any through-DNA electron transport would play a more significant role.

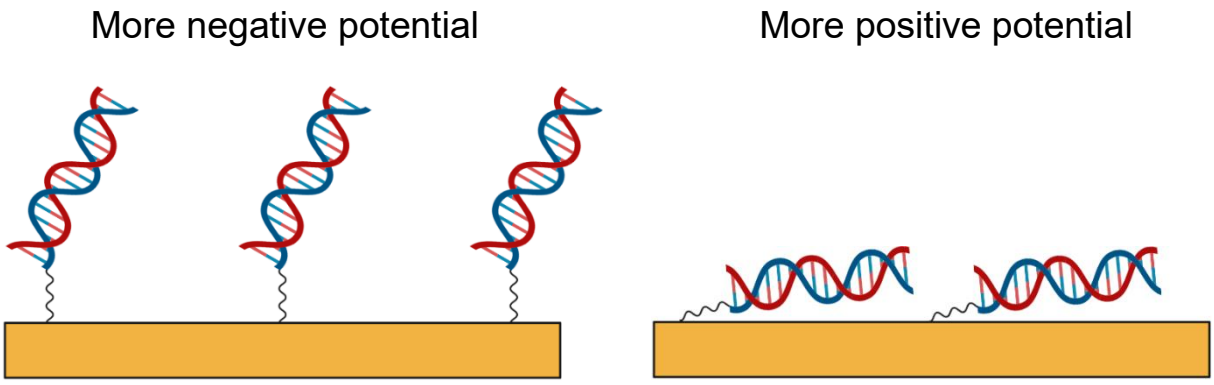

Figure 5.16: Schematic diagram of the different angles at which surface-immobilised DNA orientates itself with respect to the gold electrode depending on the applied potential.

5.3. Efforts to Enhance the Sensing of CuCy-/Fc-Modified Probes

5.3.1. Increasing Probe Sensitivity

The 10 nM LOD that was determined for probe **T1** was far short of what is required to sense clinically relevant nucleic acids at physiological concentrations, as discussed in Chapter 4. One approach to improving the sensitivity was to increase the length of the probes and the targets they were sensing. Shorter duplexes with fewer base pairs are thermodynamically less stable than longer duplexes with more base pairs. It was proposed that the enhanced thermodynamic stability of longer probe–target duplexes might favour more targets being captured and hence increase the probe's sensitivity.

Table 5.2 shows the sequences of the longer probes and their respective targets used in an attempt to improve sensitivity. **T1-21mer** is an extension of **T1** with 3 extra bases on each end. **B1-30mer** is an extension of **B1** with 15 bases added on the 5′ end prior to incorporation of Fc. The CuCy in **T1-21mer** is therefore slightly further away from the electrode than the CuCy in **T1**, whereas the CuCy in **B1-30mer** is the same distance from the electrode as the CuCy in **B1**. (See section 5.3.2. for an investigation into the effect that redox label sequence position has on electrochemical output.)

Table 5.2: The longer probes and their respective targets. X = CuCy; F = ferrocene; S = disulphide.

Oligonucleotide	5′ – Sequence – 3′
T1-21mer	F CAT TGG ACT CXC TCA ATG TAC S
21T2T	GTA CAT TGA GTG AGT CCA ATG
B1-30mer	F GGA CCC ACT CCA TCG AGA TTT CXC TGT AGC S
30B2T	GCT ACA GTG AAA TCT CGA TGG AGT GGG TCC

As predicted, the thermal stabilities of the longer probe–target duplexes were greatly enhanced relative to their shorter counterparts, with T_m values of 68.0 ºC and 75.0 ºC for **T1-21mer** and **B1-30mer**, respectively (versus 60.0 ºC and 60.5 ºC for **T1** and **B1**, respectively). However, the more thermodynamically stable duplexes failed to translate into significantly improved sensitivity, with **T1-21mer** sensing 1 nM target resulting in a −5.2(± 2.2)% change in CuCy:Fc current ratio and **B1-30mer** resulting in a −3.1(± 2.4)% change (Figure 5.17), versus **T1**'s −2.5(± 2.9)% change. An explanation can be found in the increased electrostatic repulsion and steric crowding at the electrode surface brought about by the longer oligonucleotides, which is likely to offset the more favourable thermodynamics. Possible solutions to accommodate for the downsides of longer probes/targets whilst harnessing the more stable duplexes they form include the use of longer linkers[20] that have been shown to enhance hybridisation efficiency and/or the use of PNA probes[21] which exhibit decreased electrostatic repulsion upon target hybridisation.

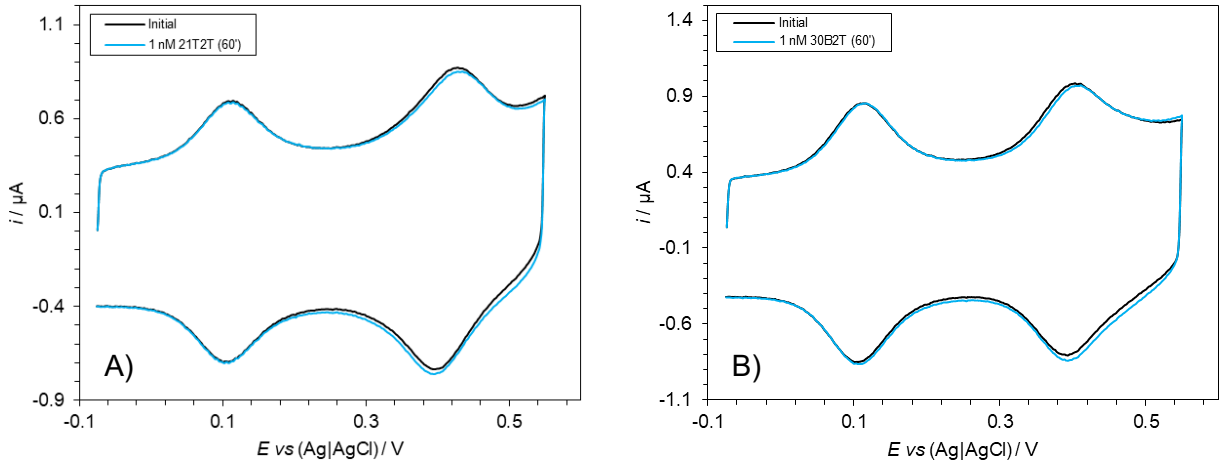

Figure 5.17: CVs of **T1-21mer** (A) and **B1-30mer** (B) sensing 1 nM **21T2T** and **30B2T** target, respectively; in 10 mM sodium phosphate buffer (pH 7) 1 M $NaClO_4$, scan rates = 1000 mV s^{-1}.

Other efforts to enhance the sensitivity of CuCy-/Fc-modified probes included sensing with **(*S*)-T1** and sensing in Mg^{2+}-containing solutions. As discussed in section 5.2.1., sensing 50 nM target with **(*S*)-T1** (containing the (*S*)-isomer of CuCy), resulted in significantly larger CuCy:Fc current ratio % changes than sensing with **T1** (containing the (*R*)-isomer of CuCy). It was thought that a similar increase in % change may be observed at a lower target concentration. The standard sensing solution used (10 mM sodium phosphate buffer (pH 7.0), 1 M $NaClO_4$) contains Na^+ cations that aid in the formation of probe–target duplexes by lining the negatively charged phosphodiester backbones and mitigating the repulsive electrostatic forces associated with DNA hybridisation. Divalent Mg^{2+} cations have been shown[22] to be more effective at duplex stabilisation than monovalent Na^+ cations, and it was thought that sensing in a solution containing 1 M $Mg(ClO_4)_2$ instead of 1 M $NaClO_4$ might favour the capture of more targets and hence increase the probe's sensitivity. However, both approaches – sensing with **(*S*)-T1** and in Mg^{2+}-containing solutions – failed to significantly increase the sensitivity at 1 nM target concentration compared with **T1** sensing in the standard solution (see Appendix 8.3.6.). Clearly, the repulsive forces inhibiting a shift in the bound:unbound probe ratio were too strong to be overcome by the approaches described.

5.3.2. Modification Sequence Position and Effect on Electrochemical Signal

Studies were then conducted to investigate the effect that changing the sequence position of the redox label within the probe had on the electrochemical signal produced. Initially, it was thought that moving the redox label may result in a current signal that was more affected by target binding and could therefore enhance sensitivity. It was also recognised that moving the CuCy within the probe could aid in investigating the SNV sensing mechanism, particularly whether bases above and below the CuCy were influential.

Gooding and coworkers moved a MB redox label within a 23mer probe and found that a terminal position furthest from the electrode resulted in the largest current, whilst the position closest to the electrode resulted in the smallest.[23] Additionally, upon target addition, the largest current change was observed when MB was located at the terminal position, and the smallest change observed when MB was located closest to the electrode. Previous work by Gooding and coworkers attributed the smaller currents observed for redox labels located closer to the electrode surface to a limitation in ion accessibility.[24] Mayer and coworkers similarly found that a MB located at the terminal end furthest from the electrode performed better than when MB was located close to the electrode (albeit when sensing a protein and not complementary DNA).[25]

To investigate the impact that modification sequence position had in the CuCy-/Fc-modified DNA systems reported here, a selection of oligonucleotides were synthesised that shifted the position of the redox label (Table 5.3). CuCy or Fc was incorporated at the 3′ end immediately after the disulphide modification (**CuCy3′** and **Fc3′**), internally (**CuCyMid** and **FcMid**), at the 5′ terminal end (**CuCy5′** and **Fc5′**), and at the 5′ end of longer probes (**CuCy5′-30mer** and **Fc5′-30mer**).

Table 5.3: Probes used to investigate impact of modification sequence position on electrochemical behaviour. X = CuCy; F = ferrocene; S = disulphide.

Oligonucleotide	5′ – Sequence – 3′
CuCyMid	TGG ACT CXC TCA ATG S
CuCy5′	X TGG ACT CTC TCA ATG S
CuCy3′	TGG ACT CTC TCA ATG X S
CuCy5′-30mer	X TGG ACT CTC TCA ATG TGG ACT CTC TCA ATG S
FcMid	TGG ACT CFC TCA ATG S
Fc5′	F TGG ACT CTC TCA ATG S
Fc3′	TGG ACT CTC TCA ATG F S
Fc5′-30mer	F TGG ACT CTC TCA ATG TGG ACT CTC TCA ATG S

Table 5.4: Targets used to investigate impact of modification sequence position on electrochemical behaviour. Bases highlighted in red sit opposite CuCy in the duplexes formed with complementary CuCy-modified probes.

Oligonucleotide	5′ – Sequence – 3′
T2A	CAT TGA GAG AGT CCA
T2T	CAT TGA GTG AGT CCA
16T2A5′	ACA TTG AGA GAG TCC A
16T2T5′	TCA TTG AGA GAG TCC A
16T2A3′	CAT TGA GAG AGT CCA A
16T2T3′	CAT TGA GAG AGT CCA T

Contrary to Gooding and coworkers' work discussed above, shifting the Fc in the shorter probes (**Fc5′**, **FcMid**, and **Fc3′**) resulted in minimal differences in the initial signals produced (Figure 5.18) with current densities ranging from 9.6–11.6 μA cm^{-2}. Fc incorporated at the 5′ end of the longer probe **Fc5′-30mer** resulted in an even smaller current density of 7.4 μA cm^{-2} (see Appendix 8.3.7.). It was posited that the longer length of **Fc5′-30mer** likely resulted in more inter-probe interactions which would reduce the Fc's access to the electrode surface. The differences from the findings of Gooding and coworkers (that moving the redox label closer to the 5′ end resulted in larger currents) is likely due to the different redox labels used (Fc versus MB). Addition of target had minimal effect on the signals produced by **Fc5′** and **Fc3′** (Figure 5.18 left and right, respectively), which was expected given the terminal positions of the Fcs incorporated meant that they were out of the way of the DNA hybridisation occurring. Addition

of **T2A** target had a more significant impact on the signal produced by **FcMid** (Figure 5.18, middle), with the current density reduced by −15.8% and ΔE_p increasing by +20 mV. Again, this was expected given the internal incorporation of Fc in **FcMid** meaning that its current signal was more affected by probe–target hybridisation.

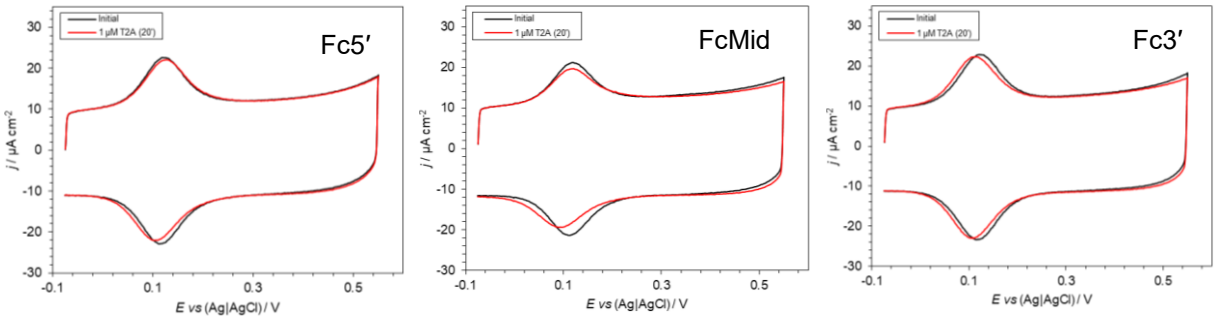

Figure 5.18: Initial CVs of **Fc5'**, **FcMid** and **Fc3'** (black lines) sensing 1 μM **T2A** (red lines); in 10 mM sodium phosphate buffer (pH 7.0) 1 M $NaClO_4$, scan rates = 1000 mV s^{-1}.

In contrast, shifting the CuCy sequence position did result in differences in the initial currents produced. Moving the CuCy closer to the terminal 5′ end of the shorter probes resulted in larger current densities, with CuCy at the 5′ end (**CuCy5′**; Figure 5.19, left) resulting in an average of 21.8 μA cm^{-2}, CuCy in the middle (**CuCyMid**; Figure 5.19, middle) resulting in an average of 16.9 μA cm^{-2}, and CuCy at the 3′ end (**CuCy3′**; Figure 5.19, right) resulting in an average of 13.6 μA cm^{-2}. This matched the effect that Gooding[23] and Mayer[25] observed with MB and may indicate that CuCy's electrochemical behaviour is more similar to MB than Fc's is to MB. However, incorporating CuCy at the 5′ end of the longer probe **CuCy5′-30mer** resulted in the smallest current density of 7.5 μA cm^{-2} (see Appendix 8.3.7.), likely due to the aforementioned predicted increase in inter-probe interactions. Target was added to the shorter CuCy-modified probes such that in the resulting duplexes, the CuCy either had a T (Figure 5.19, top) or an A (Figure 5.19, bottom) placed opposite. This was to investigate whether the SNV

discrimination could still be achieved at the extremities of the probe where there were no bases either above (**CuCy5′**) or below (**CuCy3′**) the CuCy–base pair, relative to the electrode surface. Target addition was also used to investigate whether the sensitivity of CuCy-modified probes could be improved by changing the sequence position of CuCy.

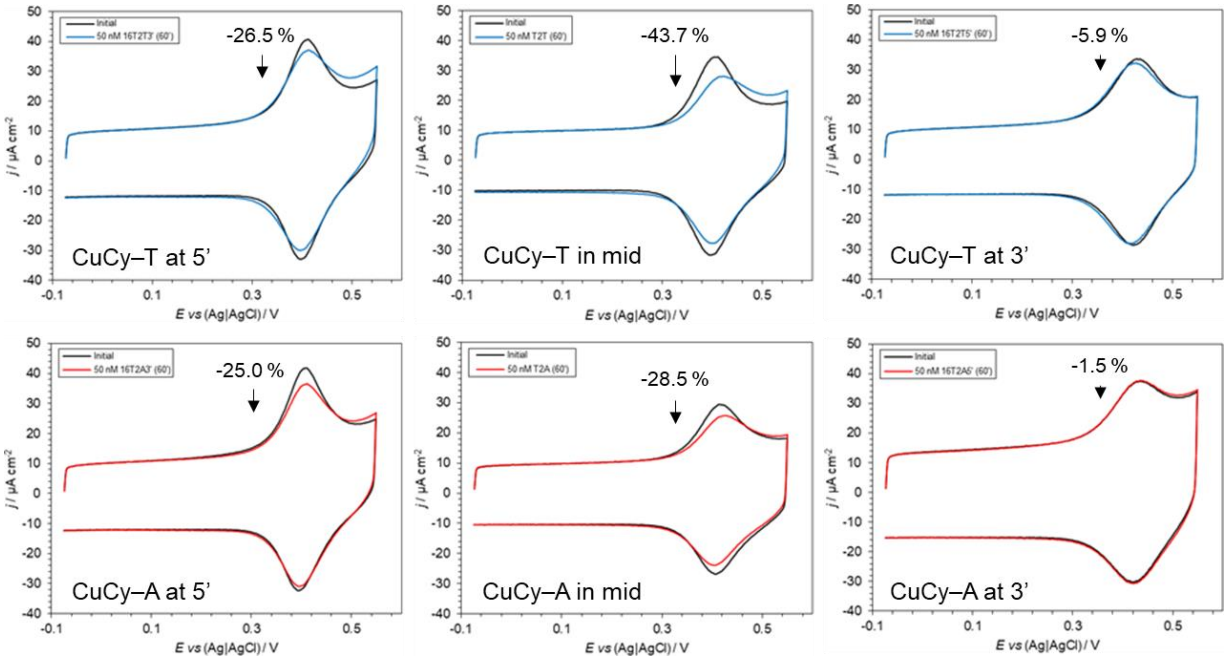

Figure 5.19: CVs of **CuCy5'** (left), **CuCyMid** (middle) and **CuCy3'** (right) sensing the targets (50 nM) in Table 5.4 such that either T (top) or A (bottom) placed opposite the CuCy in the probe–target duplex; in 10 mM sodium phosphate buffer (pH 7.0) 1 M $NaClO_4$, scan rates = 1000 mV s^{-1}. 5' and 3' in the CV labels refers to the probe.

As anticipated, the CuCy located internally clearly distinguished between T and A with current density % changes of –43.7% and –28.5%, respectively (Figure 5.19, middle). However, when the CuCy was located at either end of the probe, it could not clearly distinguish between T and A. CuCy located at 5′ resulted in current density % changes of –26.5% and –25.0% for T and A, respectively (Figure 5.19, left); CuCy located at 3′ resulted in current density % changes of –5.9% and –1.5% for T and A, respectively (Figure 5.19, left). Whilst T induced a larger % change than A at all three CuCy positions, the smaller differences at the 5′ and 3′ ends of the probe indicates that the bases above and below the CuCy likely affect its conformational

position within the duplex and therefore its ability to discriminate between SNVs. These results also showed that changing the position of the CuCy did not result in improved sensitivity, with smaller current density % changes when the CuCy was moved closer to or further from the electrode surface.

The thermal stabilities of the duplexes formed using **CuCy5′** and **CuCy3′** with either T or A opposite the CuCy were not significantly different. For **CuCy5′**, T opposite (**16T2T3′** target) resulted in a T_m of 64.0 (± 0.5) ºC whilst A opposite (**16T2A3′** target) resulted in a T_m of 65.5 (± 1.5) ºC; for **CuCy3′**, T opposite (**16T2T5′** target) resulted in a T_m of 63.0 (± 0.5) ºC whilst A opposite (**16T2A5′** target) resulted in a T_m of 63.5 (± 0.5) ºC. In contrast, the thermal stabilities of the duplexes formed using **CuCyMid** with T or A opposite the CuCy were significantly different, with T opposite resulting in a T_m of 62.0 (± 0.5) ºC and A opposite resulting in a T_m of 60.0 (± 0.5) ºC. The thermal melting studies indicated that the positions of the CuCy when at the 5′ or 3′ end of the probe have a similar impact on duplex stability regardless of the base opposite. It can therefore be inferred that different bases opposite the CuCy when they are located at the end of a probe–target duplex do not force the CuCy to adopt significantly different conformational positions, contributing to the similar current depletions observed. Conversely, when CuCy is incorporated internally, it is proposed that having base pairs above and below the CuCy forces it to adopt different conformational positions dependent on the set of surrounding bases that significantly affect its exposure to the electrode surface and thus contributes to SNV discrimination.

5.3.3. Square Wave Voltammetry: Initial Studies

As discussed in Chapter 2, square wave voltammetry is a pulse voltammetry technique that combines staircase and square waveforms designed to reject background currents.[26] It is also considered to be a particularly sensitive electrochemical technique[26,27] and therefore it was

thought that its use might improve the sensitivity of the CuCy-/Fc-modified probes reported here. Although previous work in the group had achieved SNV sensing differences using surface-immobilised CuCy-/Fc-modified DNA probes and square wave voltammetry, the results were inconsistent, with initial SWVs that differed from electrode to electrode and Fc currents that changed dramatically upon target addition.[28] Efforts to achieve ratiometric and more sensitive sensing using square wave voltammetry are detailed below.

Initial studies focused on repeating the SNV sensing with **T1** using square wave voltammetry instead of cyclic voltammetry. Figure 5.20 shows SWVs of **T1** sensing 50 nM target DNA in which the base opposite the CuCy was varied between the four canonical bases. The first observation noted was the small size of the initial Fc current peak at *ca* 0.12 V relative to the larger initial CuCy current peak at *ca* 0.4 V. Even more striking was the significant increase in the Fc current upon target addition. Both of these behaviours were in stark contrast to the behaviour of Fc when using cyclic voltammetry, for which its reproducibility and stability made it a suitable internal reference signal. The behaviour of the CuCy was more in line with what was expected, in that its initial current reduced upon target addition in a base-dependent manner similar to previous work using square wave voltammetry[28] and to work reported here using cyclic voltammetry (Chapter 4).

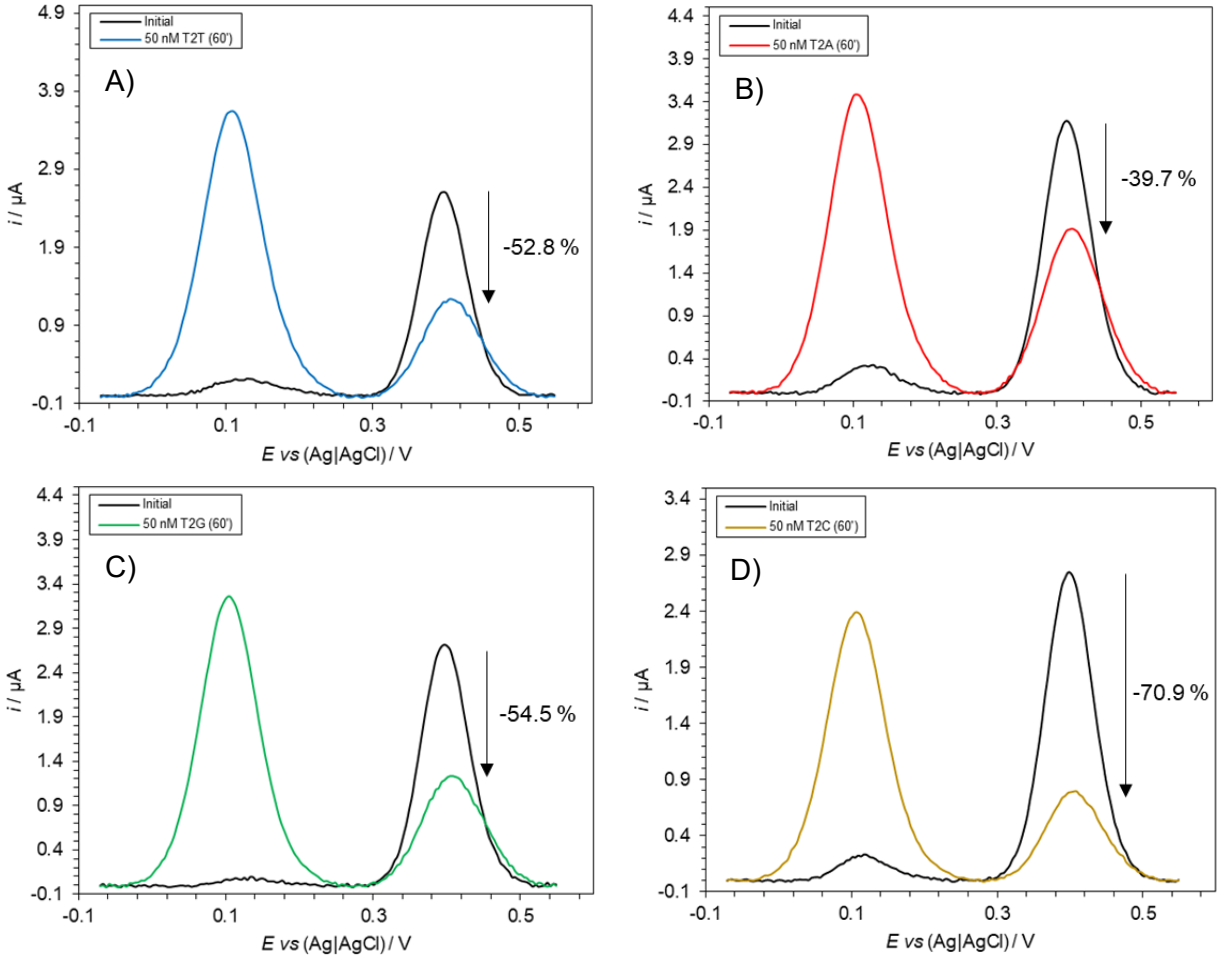

Figure 5.20: SWVs of **T1** sensing 50 nM **T2T** (A), **T2A** (B), **T2G** (C) and **T2C** (D) 60 minutes after target addition; in 10 mM sodium phosphate buffer (pH 7.0) 1 M $NaClO_4$, frequency = 200 Hz, amplitude = 25 mV, step = 1 mV. %s shown are the reduction in CuCy current.

5.3.4. Square Wave Voltammetry: Buffer/Electrolyte Studies

Previous work in the group had noted the impact of different buffer/electrolyte solutions on CVs and SWVs.[28,29] In particular, the initial Fc current had previously been affected by the composition of the buffer/electrolyte solution.[28] First, it was investigated whether the currents produced using square wave voltammetry remained stable prior to target addition in the standard 10 mM sodium phosphate 1 M $NaClO_4$ buffer/electrolyte solution used thus far. Figure 5.21 shows CVs and SWVs of **T1** recorded every five minutes prior to target addition, followed by a CV and a SWV recorded 20 minutes after target addition. The CVs showed relatively stable

CuCy and Fc currents, with the CuCy:Fc current ratios remaining constant up until target addition. In contrast, the SWVs showed the CuCy current increasing with every 5 minutes until target addition, followed by a decrease in the CuCy current and a large increase in the Fc current following target addition. Although it is not fully understood why the CuCy current increases over time, it is likely that subtle rearrangements of the SAM post-submersion in the sensing solution is detected with the more sensitive square wave voltammetry and not with the less sensitive cyclic voltammetry. Subsequent experiments showed less drastic but still significant (>20%) increases in the CuCy current over time. The changing CuCy current and small Fc current prior to target addition made the standard 10 mM sodium phosphate 1 M $NaClO_4$ buffer/electrolyte solution unsuitable for use with square wave voltammetry.

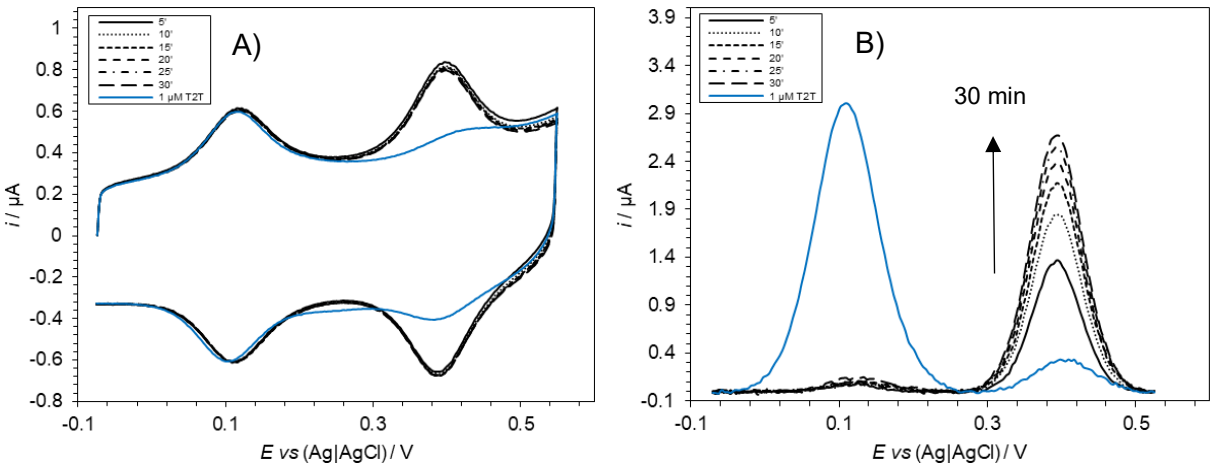

Figure 5.21: A) CVs of **T1** over 30 minutes (black lines) followed by addition of **T2T** target (1 µM) and a further waiting period of 20 minutes (blue line); in 10 mM sodium phosphate buffer (pH 7.0) 1 M $NaClO_4$, scan rates = 1000 mV s^{-1}. B) SWVs measured at the same time as the CVs taken in (A); frequency = 200 Hz, amplitude = 25 mV, step = 1 mV.

Alternative buffer/electrolyte solutions for stable initial CuCy and Fc currents were then investigated. Other groups reporting on square wave voltammetry sensing with redox-modified DNA have used a number of different buffer/electrolyte solutions.[30-33] A selection of these were then tested using **T1** (Figures 5.22–5.24). Every one of the four buffer/electrolyte solutions tested (including the standard 10 mM sodium phosphate 1 M $NaClO_4$) resulted in stable CVs

over the 30 minute period prior to target addition. Only two buffer/electrolyte solutions resulted in reasonably stable SWVs: 10 mM TrisHCl (pH 7.0) 100 mM NaCl (Figure 5.22), and 90 mM sodium citrate (pH 7.0) 90 mM NaCl (Figure 5.23). These two solutions also resulted in relatively prominent initial Fc currents, and therefore they were selected for further square wave voltammetry studies. However, even with these there were small changes to the initial currents within 5–10 minutes and, therefore, all subsequent sensing using square wave voltammetry extended the equilibration time to 15 minutes before the initial SWV was recorded.

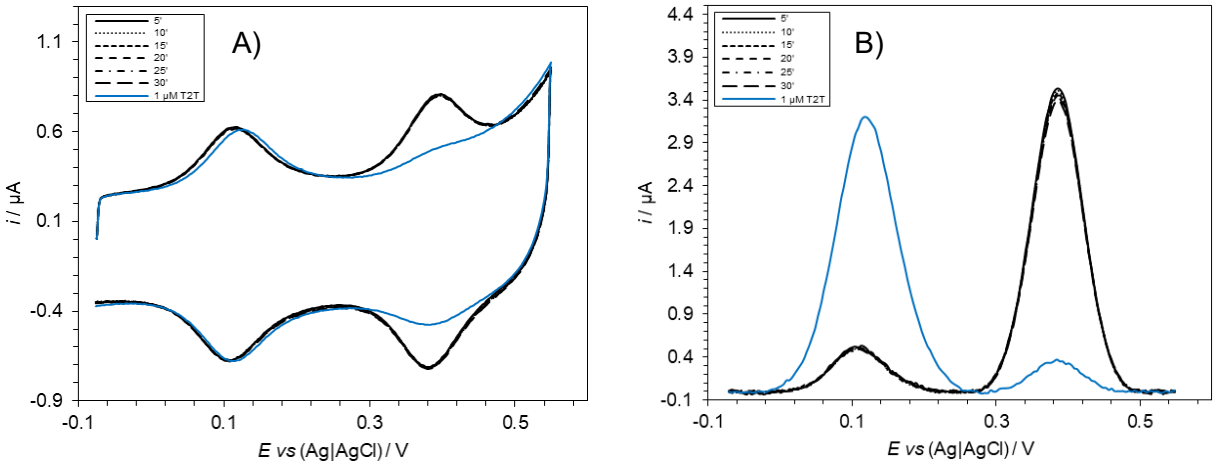

Figure 5.22: A) CVs of **T1** over 30 minutes (black lines) followed by addition of **T2T** target (1 µM) and a waiting period of 20 minutes (blue line); in 10 mM TrisHCl buffer (pH 7.0) 100 mM NaCl, scan rates = 1000 mV s^{-1}. B) SWVs measured at the same time as the CVs taken in (A); frequency = 200 Hz, amplitude = 25 mV, step = 1 mV.

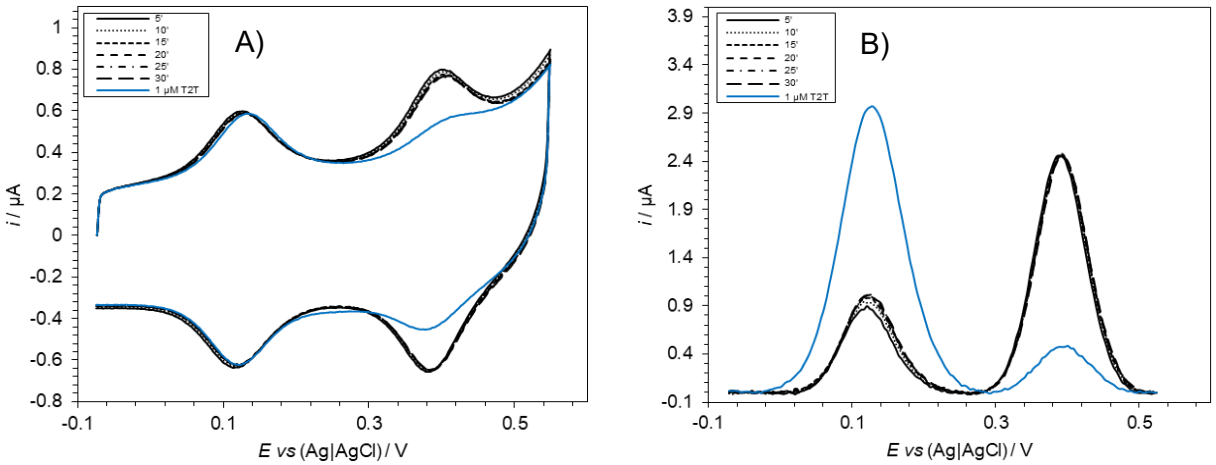

Figure 5.23: A) CVs of **T1** over 30 minutes (black lines) followed by addition of **T2T** target (1 µM) and a waiting period of 20 minutes (blue line); in 90 mM sodium citrate buffer (pH 7.0) 90 mM NaCl, scan rates = 1000 mV s^{-1}. B) SWVs measured at the same time as the CVs taken in (A); frequency = 200 Hz, amplitude = 25 mV, step = 1 mV.

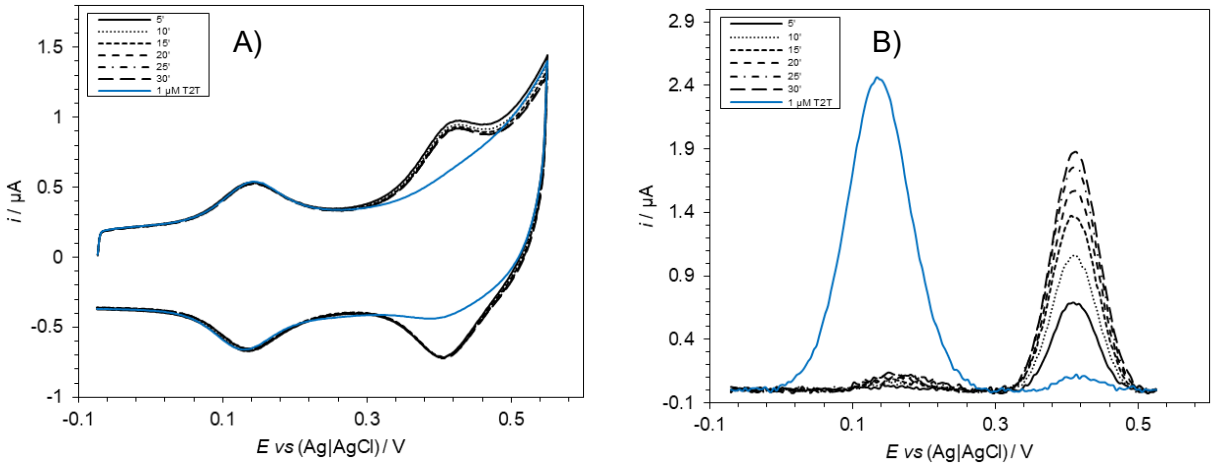

Figure 5.24: A) CVs of **T1** over 30 minutes (black lines) followed by addition of **T2T** target (1 µM) and a waiting period of 20 minutes (blue line); in 10 mM PBS (pH 7.4) 500 mM NaCl 2.7 mM KCl, scan rates = 1000 mV s^{-1}. B) SWVs measured at the same time as the CVs taken in (A); frequency = 200 Hz, amplitude = 25 mV, step = 1 mV.

A noticeable feature of the CVs shown in Figures 5.22–5.24 is the upward tailing effect towards more positive potentials. This was attributed to the presence of Cl^- anions, with a larger concentration of chloride-containing salts resulting in steeper tailing (*e.g.*, Figure 5.24). Chloride has been shown to adsorb onto gold surfaces[34] and likely affects the mechanism of the gold oxidation. Thanks to the combined staircase and square waveform used by square wave voltammetry, the tailing was not observed in the SWVs.

5.3.5. Square Wave Voltammetry: Frequency and Amplitude Studies

Attention then turned to the mystery of the increasing Fc current upon target addition. To confirm that the increasing Fc current was caused by target binding, the probe **Fc5′** was incubated with high concentrations (1 µM) of either complementary **T2T** or non-complementary **T2ran** (Table 5.5). For both the complementary **T2A** and the non-complementary **T2ran**, the Fc current in the CVs remained largely unchanged (Figure 5.25, left). This was expected given Fc's terminal position, meaning it was relatively unaffected by probe–target binding. In contrast, the SWVs showed significant differences, with the complementary **T2A** resulting in the previously observed large increase in the Fc current whilst

the non-complementary **T2ran** resulted in only a negligible increase (Figure 5.25, right). These experiments showed that it was the formation of the probe–target duplex that resulted in the increase in the Fc current upon complementary target addition seen using square wave voltammetry.

Table 5.5: Probe **Fc5'** and targets **T2A** and **T2ran**. F = Fc; S = disulphide.

Oligonucleotide	5′ – Sequence – 3′
Fc5′	F TGG ACT CTC TCA ATG S
T2A	CAT TGA GAG AGT CCA
T2ran	ACA GCT TCA TGG AAG

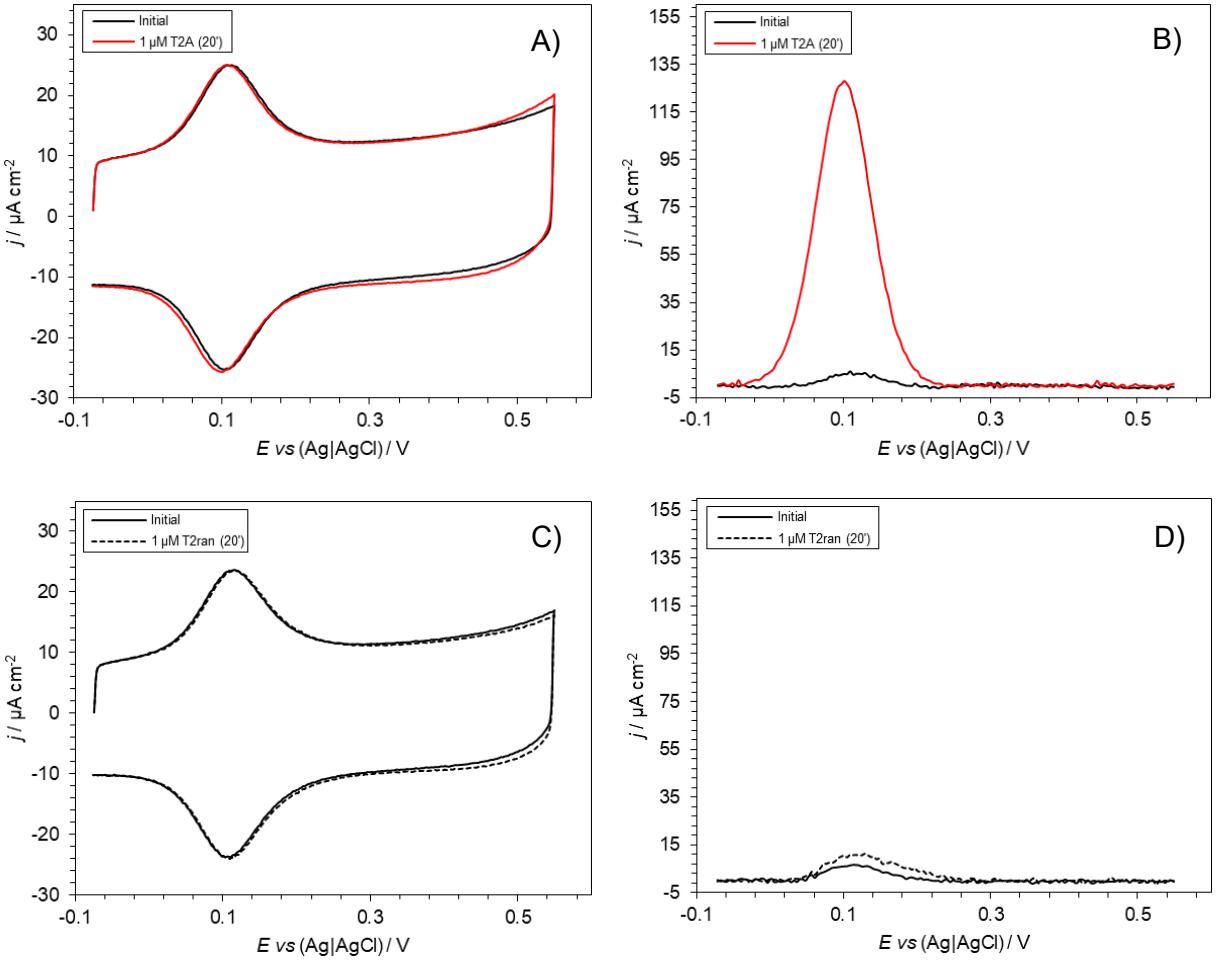

Figure 5.25: CVs (left) and SWVs (right) of **Fc5'** sensing complementary **T2A** target (1 µM; A, B) and non-complementary **T2ran** target (1 µM; C, D); in 10 mM sodium phosphate buffer (pH 7.0) 1 M $NaClO_4$; scan rates = 1000 mV s^{-1} (CVs); frequency = 200 Hz, amplitude = 25 mV, step = 1 mV (SWVs).

An explanation for the observed electrochemical behaviour of the Fc on surface-immobilised DNA probes in square wave voltammetry experiments has been reported by Plaxco and coworkers.[35,36] They detailed the relationship between electron transfer rates and the square wave frequency employed. In square wave voltammetry, the current is sampled twice at the end of each potential pulse within one cycle (Figure 5.26). Therefore, the current measured at the sample points is highly dependent on the speed of the electron transfer reaction. If the electron transfer rate is high, then the current may have depleted by the time the current is sampled; if the rate is slower, then the current is more likely to be higher when the current is sampled. By increasing the frequency of a SWV (*i.e.*, increasing the number of pulses per second), the length of time elapsing before the current is sampled is shortened.

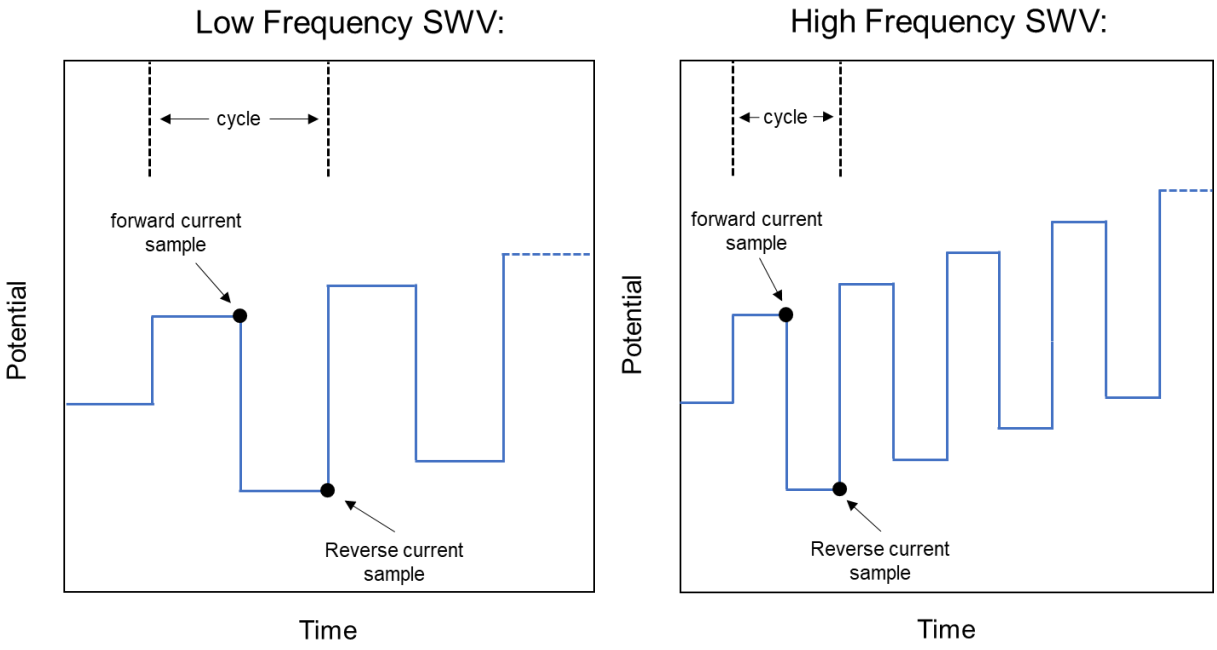

Figure 5.26: Waveform schematics of a lower frequency SWV (left) and a higher frequency SWV (right). Adapted from reference 35.

This knowledge can be applied to SWVs shown in Figure 5.25. When **Fc5′** is unbound, the electron transfer rate of the Fc is faster owing to the relative flexibility of a single-stranded probe, which allows the Fc to more easily reach the electrode surface. In the initial SWVs

shown, the frequency was such that the Fc current had mostly depleted by the time the current was sampled and therefore only a small Fc current peak was observed. When the **Fc5′** is target-bound, the electron transfer rate of the Fc is slower owing to the relative inflexibility of the double-stranded probe–target duplex. In the **T2A**-added SWV shown (Figure 5.25B), the Fc-produced current had therefore not depleted as much by the time the current was sampled and thus a larger Fc current peak was observed. This phenomenon also explains the square wave voltammetry behaviour of the Fc in probe **T1** and all other Fc-modified oligonucleotides. For the CuCy in **T1**, its large initial current is evidence of a slower electron transfer rate relative to Fc, whether that be inherent to CuCy or due to its internal incorporation within the strand. The observed reduction in the CuCy current upon target addition might then be explained by duplex formation somehow increasing the electron transfer rate to an extent that the current had depleted by the time it was sampled. However, as evidenced by the CVs, the CuCy current reduction can instead be attributed to duplex formation inhibiting electron transfer between the CuCy and the electrode such that the current is significantly lower at the time of sampling.

Using the two suitable buffer/electrolyte solutions identified in section 5.3.4., combinations of the square wave voltammetry parameters frequency and amplitude were investigated in a fashion similar to Plaxco and coworkers.[35,36] The aim was to identify a combination that resulted in a stable Fc current so that it could be used as a constant signal in a ratiometric sensing mechanism, as it had done using cyclic voltammetry. Figure 5.27 shows the initial (top) and target-added (bottom) SWVs of **T1** recorded at different frequency and amplitude combinations in 10 mM TrisHCl (pH 7.0) 100 mM NaCl (see Appendix 8.3.8. for the analogous sensing in 90 mM Na citrate (pH 7.0) 90 mM NaCl).

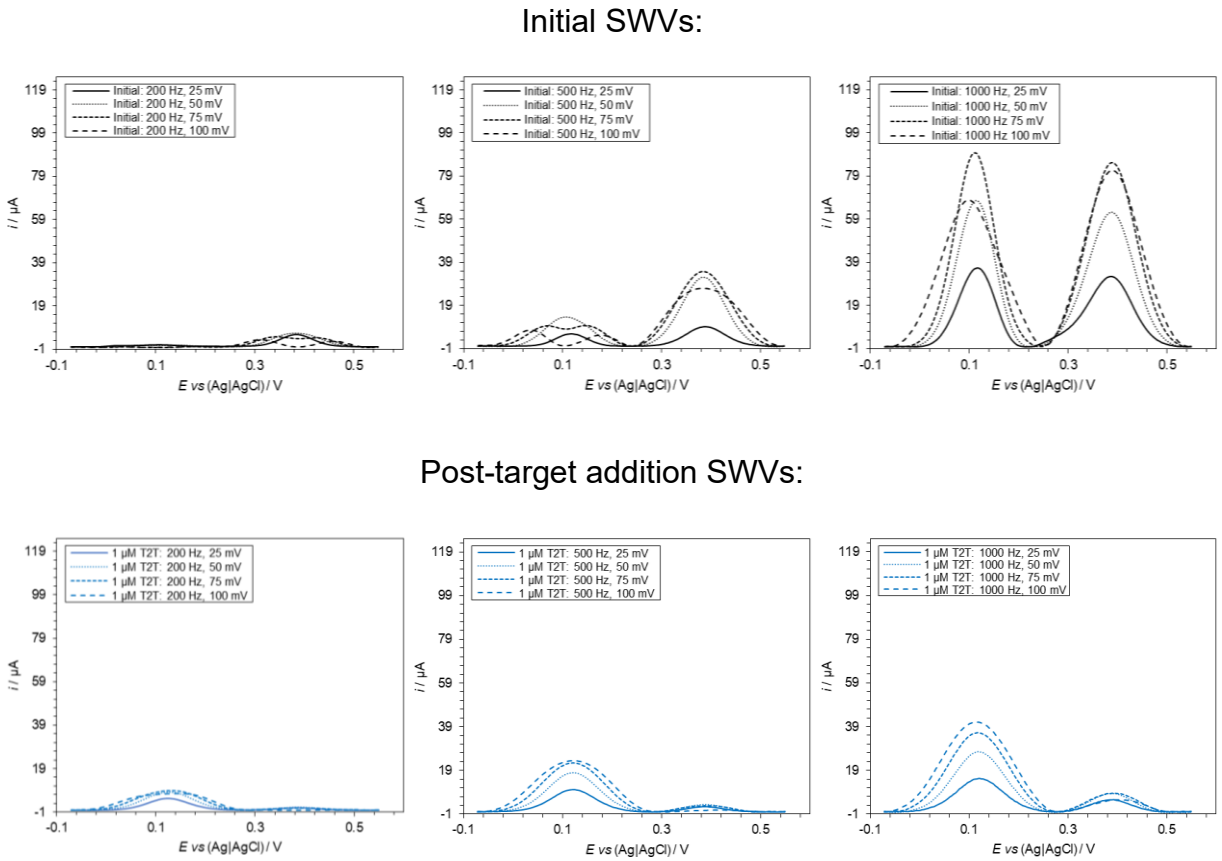

Figure 5.27: Initial SWVs (top) and target-added SWVs (1 µM, bottom) of **T1** recorded at different frequency and amplitude combinations; in 10 mM TrisHCl buffer (pH 7.0) 100 mM NaCl.

All possible combinations of frequencies 200/500/1000 Hz and amplitudes 25/50/75/100 mV were tested. None of the frequency/amplitude combinations resulted in a Fc current that remained as constant as it had done when using cyclic voltammetry. The only frequency/amplitude combination that resulted in a Fc current that remained even somewhat stable before and after target addition was a frequency of 500 Hz and an amplitude of 50 mV in 10 mM TrisHCl (pH 7.0) 100 mM NaCl (Figure 5.28). Further studies using this combination of frequency, amplitude, and buffer/electrolyte solution were undertaken in an effort to achieve ratiometric sensing with a constant reference signal.

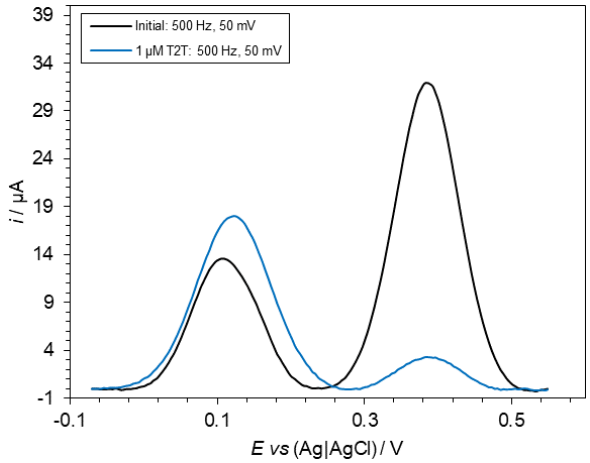

Figure 5.28: SWVs of **T1** sensing 1 µM **T2T** using a frequency of 500 Hz and an amplitude of 50 mV; in 10 mM TrisHCl buffer (pH 7.0) 100 mM NaCl, step = 1 mV.

The SNV sensing previously observed using cyclic voltammetry was again achieved using square wave voltammetry with this 500 Hz/50 mV combination. When only assessing the CuCy current, cytosine induced the largest CuCy current % change, followed by thymine/guanine, and then adenine (Figure 5.29) – the same order as observed when using cyclic voltammetry. However, the Fc currents remained relatively unstable upon target addition and even the starting CuCy:Fc current ratios varied significantly from SAM to SAM. As with the increasing CuCy currents prior to target addition in some buffer/electrolyte solutions (section 5.3.4.), the unpredictability of the Fc's signal is difficult to explain. The increased sensitivity of square wave voltammetry as a technique, and its comparatively complex (compared to cyclic voltammetry) waveform and sampling regime, is likely to factor in the explanation. Given time and material constraints, further efforts to investigate frequency/amplitude combinations that would result in stable, reproducible Fc currents were not pursued. However it is possible that a suitable combination does exist and therefore further experiments may prove fruitful. Indeed, Plaxco and coworkers' work on the optimisation of square wave voltammetry parameters for sensing with redox-modified DNA encompassed significantly larger frequency ranges.[36]

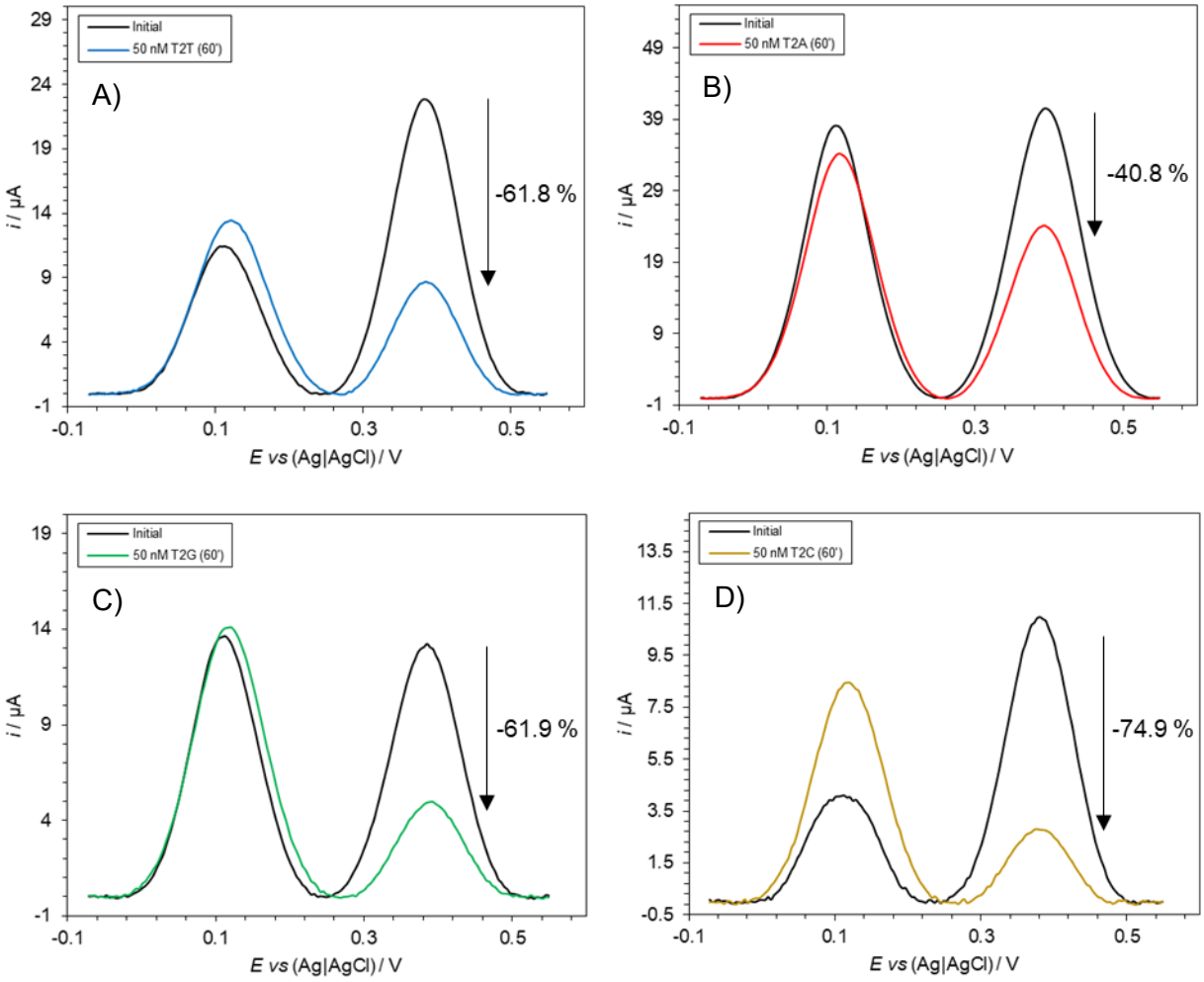

Figure 5.29: SWVs of **T1** sensing 50 nM **T2T** (A), **T2A** (B), **T2G** (C), and **T2C** (D) using a frequency of 500 Hz and an amplitude of 50 mV; in 10 mM TrisHCl buffer (pH 7.0) 100 mM NaCl, step = 1 mV. %s shown are the reduction in CuCy current.

One final approach using square wave voltammetry was considered. If the Fc current were to change upon target addition, then this might be used as one part of a ratiometric sensing mechanism in which both signals change. Fc has played this role before in other sensors employing a ratiometric sensing mechanism.[37,38] Given that two signals changing produce a greater combined signal change than just one (Figure 5.30A), it was thought that identifying the frequency/amplitude combination that induced the largest combined current change might aid in improving the probe's sensitivity. Figure 5.30B shows the magnitude of the combined CuCy and Fc current % changes when **T1** sensed **T2T** target at a concentration of 1 µM. Amplitudes of 75 and 100 mV at frequencies of 200 and 500 Hz were not considered due to the

peak splitting of the initial Fc current (Figure 5.27). A frequency of 200 Hz resulted in the largest overall combined current % changes, largely due to the relatively small initial Fc current significantly increasing upon target addition as seen in Figure 5.30A. Of the SWVs conducted at 200 Hz, an amplitude of 50 mV resulted in the largest combined current % change (1082%) and this was the combination chosen in an attempt to improve probe sensitivity.

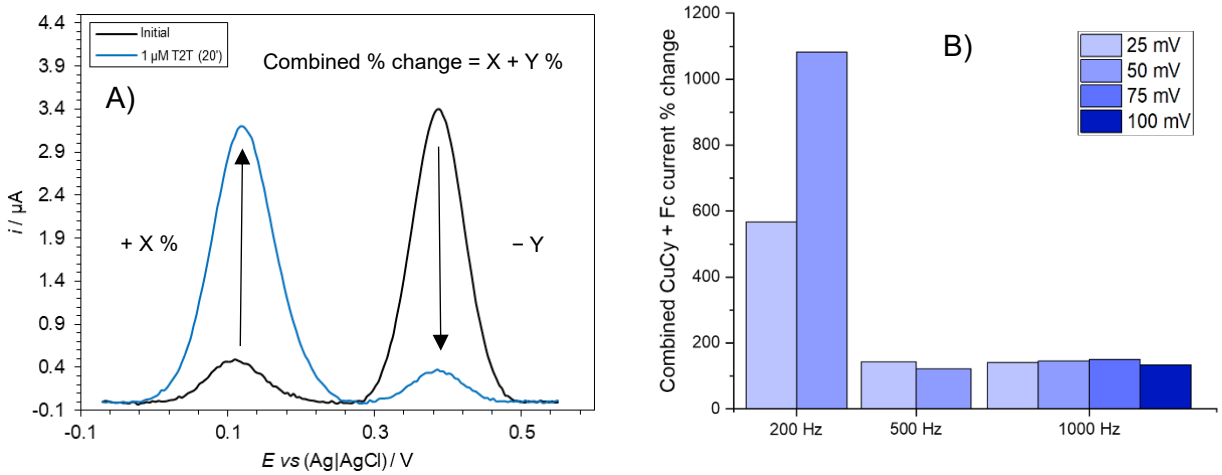

Figure 5.30: A) SWV of **T1** sensing 1 µM **T2T** using a frequency of 200 Hz and an amplitude of 25 mV, denoting the Fc and CuCy current changes as X and Y %, respectively. B) The magnitude of the combined CuCy and Fc current % change when **T1** sensed 1 µM **T2T** 20 minutes after target addition using square wave voltammetry at different frequencies and amplitudes. All SWVs for this figure were conducted in 10 mM TrisHCl buffer (pH 7.0) 100 mM NaCl, step = 1 mV.

T1 sensing 1 nM **T2T** target using the 200 Hz/50 mV frequency/amplitude combination resulted in a small decrease in the CuCy current and an even smaller increase in the Fc current (Figure 5.31A). Combining these current % changes resulted in an average combined % change of 16.9%, significantly higher than the 2.6% CuCy:Fc current ratio % change achieved when sensing the same target concentration using cyclic voltammetry under the same conditions (Figure 5.31B). However, sensing at a target concentration of 100 pM resulted in no significant change in the combined current % change (Appendix 8.3.8.). Whilst the improvement in sensitivity was welcome, it was acknowledged that a more fundamental change in probe function and design is needed to sense nucleic acids at physiologically relevant concentrations.

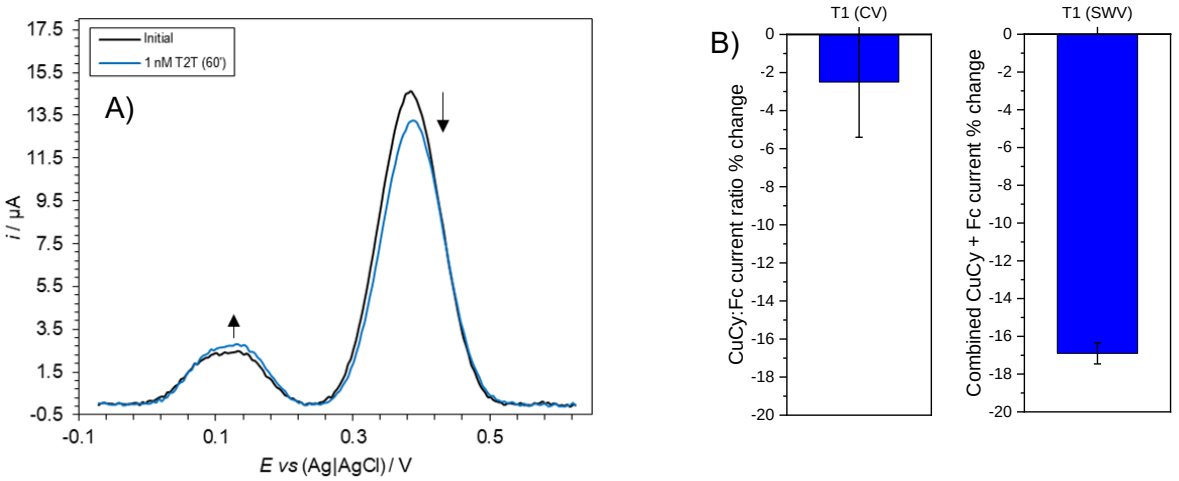

Figure 5.31: A) SWVs of **T1** sensing 1 nM **T2T** 60 minutes after target addition; in 10 mM TrisHCl buffer (pH 7.0) 100 mM NaCl, frequency = 200 Hz, amplitude = 50 mV, step = 1 mV. B) Comparison between **T1** sensing 1 nM **T2T** 60 minutes after target addition using cyclic voltammetry (left; measuring the CuCy:Fc current % change) and square wave voltammetry (right, measuring the combined CuCy + Fc current % change); error bars represent SD.

5.3.6. Differential Pulse Voltammetry Studies

Differential pulse voltammetry is another pulse technique also commonly used with electrochemical nucleic acid sensors.[39-41] It has a similar waveform to square wave voltammetry and it offers comparable advantages over linear voltammetry techniques in terms of suppression of background currents and enhanced sensitivity.[42] How the CuCy-/Fc-modified probes could respond to this alternative pulse technique was therefore investigated. Figure 5.32 shows differential pulse voltammograms (DPVs) of **T1** sensing either complementary **T2A** target (A) or non-complementary **T2ran** target (B) at a concentration of 1 µM. In the initial DPVs, no current was observed for either CuCy or Fc. This can again be explained by applying Plaxco and coworkers' theory,[35,36] as discussed in section 5.3.5. In the unbound state, the current of both the CuCy and the Fc had depleted by the time the current was sampled at the end of each pulse. Upon probe–target duplex formation, the electron transfer rate between the CuCy and the electrode was reduced such that when the current was sampled, the CuCy current had not yet fully depleted and was therefore increased. As Fc current was still not observed after probe–target duplex formation, this meant that, despite the electron transfer rate between the Fc and

the electrode becoming slower (owing to the relative inflexibility of double-stranded DNA), the rate was still fast enough for the Fc current to have depleted by the time the current was sampled. Changing the frequency of the DPV would change when the current is sampled and would result in different behaviours of the CuCy and Fc currents, as it did with the SWVs. However, as with the sets of CVs discussed in Chapter 4, the act of taking the DPVs subjected the SAM-modified electrodes to lengthier periods of more positive potential at which the CuCy was electrochemically unstable (Figure 5.33). As recording the DPV itself inadvertently reduced the CuCy current, no further studies were made using differential pulse voltammetry.

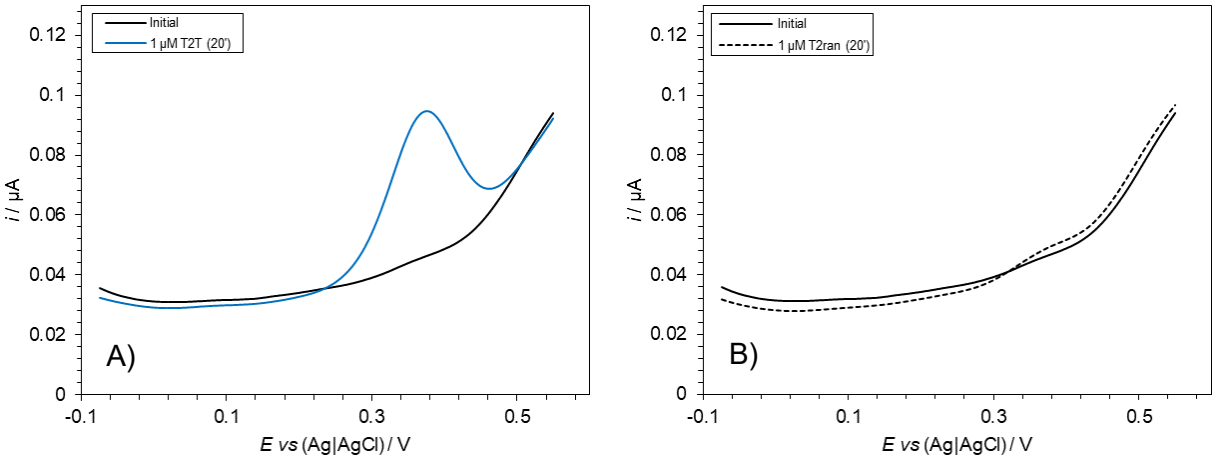

Figure 5.32: DPVs of **T1** sensing 1 µM complementary **T2T** target (A) and 1 µM non-complementary **T2ran** target (B); in 10 mM sodium phosphate buffer (pH 7.0) 1 M $NaClO_4$, pulse width = 50 ms, pulse period = 200 ms, amplitude = 50 mV, step = 1 mV.

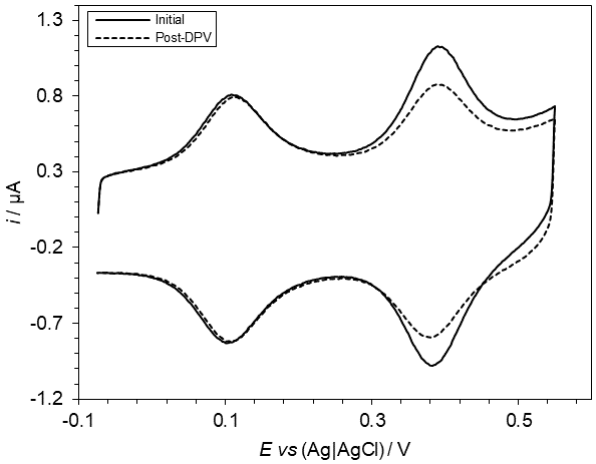

Figure 5.33: A) CVs of **T1** taken before a DPV was taken (solid line) and after a DPV was taken (dashed line). Completing the DPV (conditions same as Figure 5.32) subjected the SAM-modified electrode to minutes of relatively positive potential under which the CuCy was not electrochemically stable, as evidenced by the reduction in its current. CVs recorded in 10 mM sodium phosphate buffer (pH 7.0) 1 M $NaClO_4$, scan rates = 1000 mV s^{-1}.

5.4. Expanding Sensing to RNA Targets and Complex Media

5.4.1. Sensing RNA Targets

DNA binds well to complementary RNA to form hybrid duplexes. Many groups have specifically reported the sensing of RNA targets using unmodified and modified DNA probes, particularly in recent years with the surging interest in the diagnostic value of miRNAs.[43-47] In theory, most sensors in which DNA probes capture nucleic acids can sense RNA as well as DNA targets. The same logic applied to the CuCy-/Fc-modified probes reported here and, therefore, RNA analogues (Table 5.6) of the DNA targets **T2A** and **T2T** were sensed using **T1**.

Table 5.6: RNA target oligonucleotides sensed using the probe **T1**. Bases highlighted in red sit opposite the CuCy in the probe–target duplex. X = CuCy; F = ferrocene; S = disulphide.

Oligonucleotide	5′ – Sequence – 3′
T1	F TGG ACT CXC TCA ATG S
RNA_T2A	CAU UGA GAG AGU CCA
RNA_T2U	CAU UGA GUG AGU CCA

As expected, **T1** bound to the RNA targets with each inducing a significant CuCy:Fc current ratio % change (Figure 5.34). The peculiar appearance of the CuCy redox peaks after target addition is noteworthy. Their broader, less defined shape hints at different electrochemical behaviours of the CuCy within a hybrid versus a homogenous duplex. Nevertheless, **T1** still discriminated between uracil and adenine opposite the CuCy in the probe–target duplex with CuCy:Fc current ratio % changes of –69.2% and –47.3%, respectively (Figure 5.35), proving that CuCy-modified DNA probes could sense SNVs in RNA targets. This mirrored the SNV sensing in the analogous DNA targets, for which thymine resulted in a larger CuCy:Fc current ratio % change than adenine (section 4.6.1.). Thermal melting data indicated that the homogenous **T1**–**T2T** and **T1**–**T2A** duplexes (T_ms of 60.0 ± 0.5 °C and 57.5 ± 0.5 °C, respectively) had higher thermal stabilities than their analogous hybrid **T1**–**RNA_T2U** and **T1**–**RNA_T2A** duplexes (T_ms of 55.5 ± 0.5 °C and 53.0 ± 0.5 °C, respectively). The thermal stabilities of the probe–target duplexes again correlated with the CuCy:Fc current ratio % change, with the more stable **T1**–**RNA_T2U** duplex resulting in a larger % change than the less stable **T1**–**RNA_T2A** duplex.

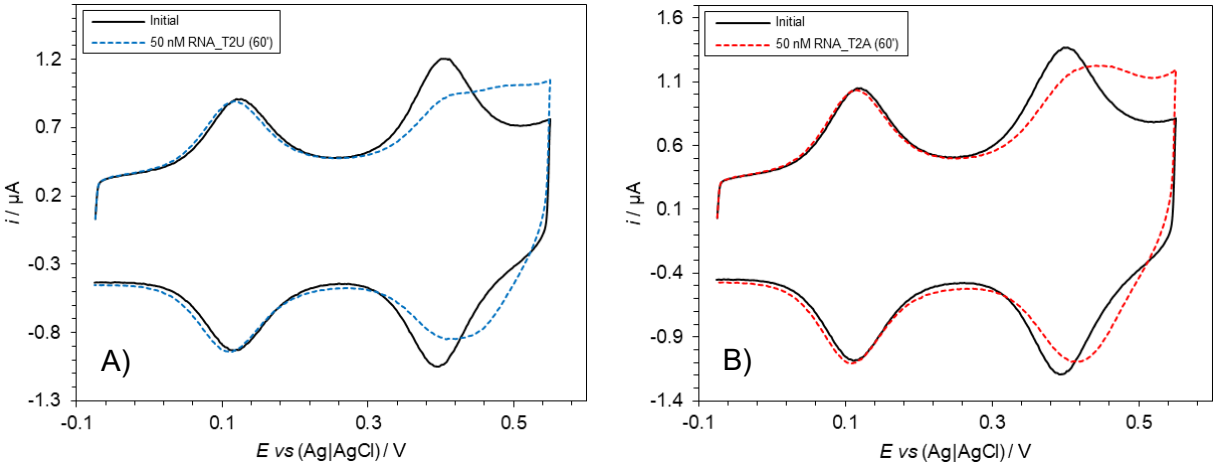

Figure 5.34: CVs of **T1** sensing 50 nM **RNA_T2U** (A) and 50 nM **RNA_T2A** (B) 60 minutes after target addition; in 10 mM sodium phosphate buffer (pH 7.0) 1 M $NaClO_4$, scan rates = 1000 mV s^{-1}.

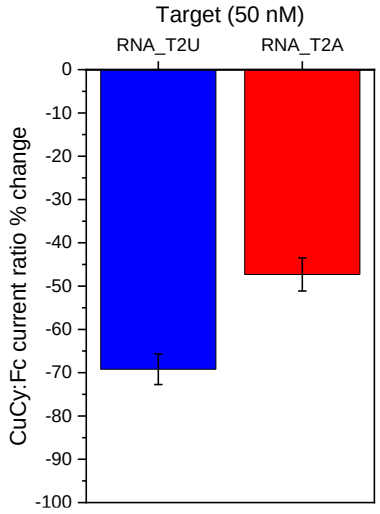

Figure 5.35: CuCy:Fc current ratio % changes for **T1** sensing the RNA targets **RNA_T2U** and **RNA_T2A** 60 minutes after target addition. Error bars represent SD. [Target] = 50 nM in 10 mM sodium phosphate buffer (pH 7.0) 1 M $NaClO_4$, scan rates = 1000 mV s^{-1}.

5.4.2. Sensing in Complex Media

Thus far, all sensing reported has been conducted in pure buffer/electrolyte solutions. A commercially viable point-of-care sensor needs to be able to sense in more complex media. Serum and saliva were chosen as the complex media to test the CuCy-/Fc-modified probe, given their abundance of nucleic acid biomarkers.[48,49] Electrochemical nucleic acid sensors have been commonly tested with samples diluted with buffer/electrolyte solutions.[45,50,51] Sample dilution helps to improve the electrochemical signals by reducing the concentration of interfering species and increasing the concentration of current-carrying electrolytes. Starting with a pure buffer/electrolyte solution and then diluting with human saliva or serum, different dilutions were investigated to establish a suitable dilution level. Figure 5.36 shows the CVs measured of **T1** in solutions of buffer/electrolyte solution diluted with saliva (see Appendix 8.3.10. for **T1** in buffer/electrolyte solutions diluted with human serum). Dilutions of 50% and 90% with saliva or serum resulted in significant distortion of the CVs. A dilution of 10% resulted in only minimal difference to the CV taken in pure buffer/electrolyte solution.

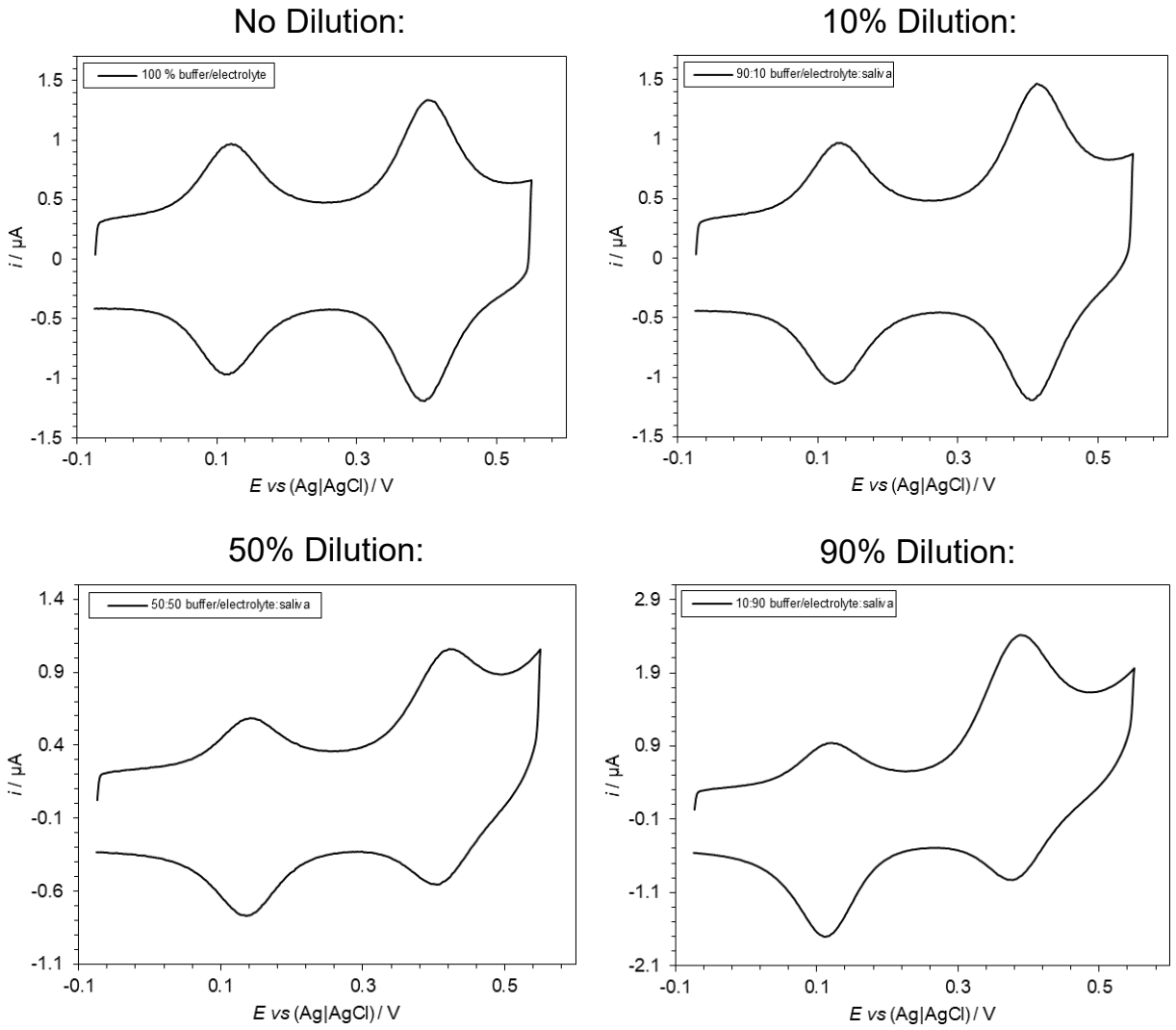

Figure 5.36: CVs of **T1** in solutions of buffer/electrolyte solutions (10 mM sodium phosphate buffer (pH 7.0) 1 M $NaClO_4$) diluted with human saliva. Ratios shown are volume. Scan rates = 1000 mV s^{-1}.

The stability of the **T1** probe when incubated in a saliva-containing solution was also assessed. Figure 5.37A shows CVs of **T1** recorded in a 50:50 buffer/electrolyte:saliva solution initially and after 16 hours, followed by addition of **T2T** target (1 µM) to the same solution. The current signals remained largely unchanged, as reflected in the stable CuCy:Fc current ratios (Figure 5.37B), and effective sensing of target was achieved despite the high % of saliva. However, the level of distortion induced in the CVs by sensing in 50% or 90% saliva or serum resulted in inconsistent starting CuCy:Fc current ratios. Therefore, 10% dilution was chosen as

the most suitable dilution level given that the minimal distortion of the CVs resulted in more consistent starting CVs.

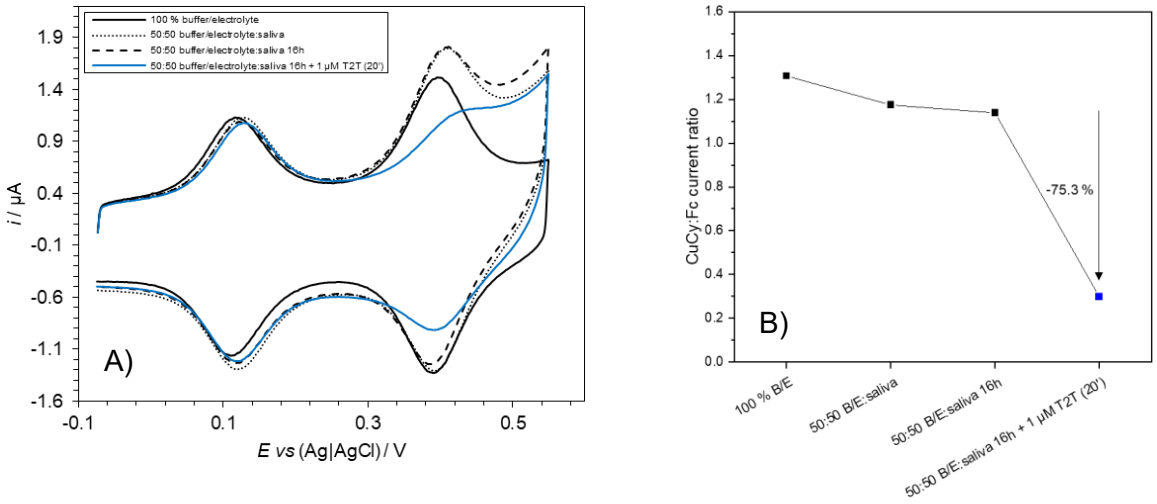

Figure 5.37: A) CVs of **T1** in pure buffer/electrolyte solution (solid black line), then placed in a 50:50 buffer/electrolyte:saliva solution (dotted line), then left for 16 hours in the same 50:50 buffer/electrolyte:saliva solution (dashed line), then 20 minutes after **T2T** target addition (1 µM) to the same 50:50 buffer/electrolyte:saliva solution (solid blue line); pure buffer/electrolyte solution = 10 mM sodium phosphate buffer (pH 7.0) 1 M $NaClO_4$, scan rates = 1000 mV s^{-1}. B) CuCy:Fc current ratios of the CVs shown in A.

5.4.3. miR135-1 Probe Studies

A probe based on an appropriate miRNA was then synthesised and tested. Belli and coworkers have identified **miR135b-5p** (Table 5.7) as a physical trauma biomarker found in human saliva.[52] **miR135a-5p** is a closely related miRNA to **miR135b-5p** that differs by only one base[53] and has not been identified as a trauma biomarker. The **miR135-1** probe (Table 5.7) was created firstly to sense the miRNA trauma biomarker **miR135b-5p**, and secondly to distinguish between **miR135b-5p** (confirmed trauma biomarker) and the closely related **miR135a-5p** (not a trauma biomarker). The non-complementary RNA target **23RNAran** was also used to demonstrate the selectivity of **miR135-1**.

Table 5.7: Probe **miR135-1** and associated RNA targets. Bases highlighted in red sit opposite the CuCy in the probe–target duplex. X = CuCy; F = ferrocene; S = disulphide.

Oligonucleotide	5′ – Sequence – 3′
miR135-1	F TCA CAT AGG AAT XAA AAG CCA TA S
miR135b-5p	UAU GGC UUU UCA UUC CUA UGU GA
miR135a-5p	UAU GGC UUU UUA UUC CUA UGU GA
23RNAran	UAC CCU GUA GAU CCG AAU UUG UG

First, it was determined whether **miR135-1** could distinguish between **miR135b-5p** and **miR135a-5p** in a pure buffer/electrolyte solution. Figure 5.38 shows **miR135-1** sensing both targets in the standard 10 mM sodium phosphate buffer (pH 7.0) 1 M $NaClO_4$ solution. Each target induced a reduction in the CuCy current large enough to almost eliminate the anodic peak in a manner indistinguishable from one another. As the bases being substituted are both similarly sized pyrimidines, the position the CuCy adopts in each probe–target duplex is likely to be similar, which would therefore contribute to the comparable currents observed. T_m results showed that each target forms a similarly stable duplex with **miR135-1** (**miR135b-5p** = 59 ± 0.5 °C, and **miR135a-5p** = 58.5 ± 0.5 °C), also indicating that the CuCy adopts a similar position in each duplex.

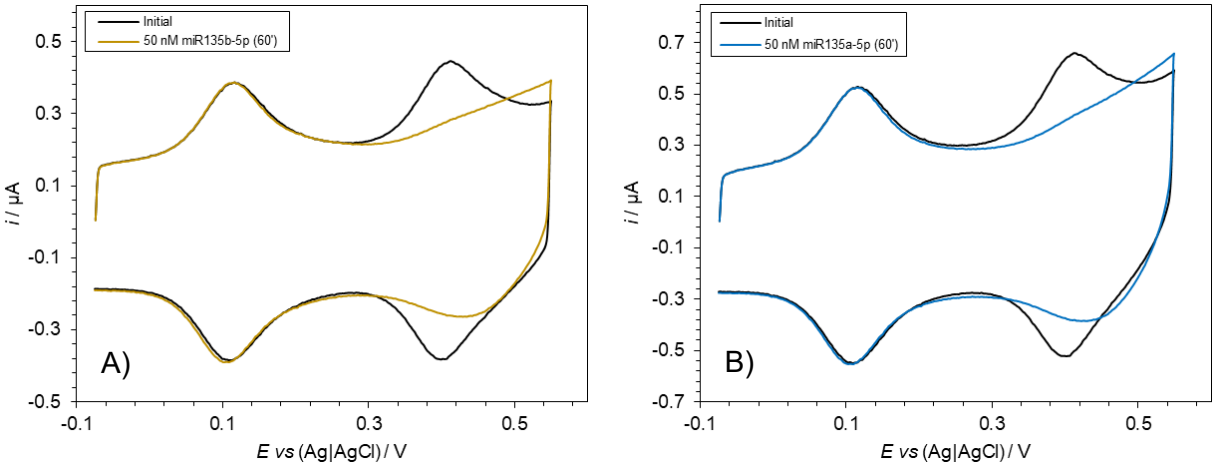

Figure 5.38: CVs of **miR135-1** sensing 50 nM **miR135b-5p** (A) and 50 nM **miR135a-5p** (B); in 10 mM sodium phosphate buffer (pH 7.0) 1 M $NaClO_4$; scan rates = 1000 mV s^{-1}.

These studies indicated that **miR135-1** could not distinguish between the closely related miRNAs **miR135b-5p** (trauma biomarker) and **miR135a-5p** (not a trauma biomarker). However, as was observed with the cancer- and COVID-19-related mutations sensed in Chapter 4, SNV discrimination using CuCy-modified DNA probes is sequence dependent and other miRNAs differing by one base likely could be distinguished from one another. The selectivity of **miR135-1** was also demonstrated by incubating with the non-complementary target **23RNAran** at a high concentration (1 μM), resulting in a negligible CuCy:Fc current ratio % change (Figure 5.39).

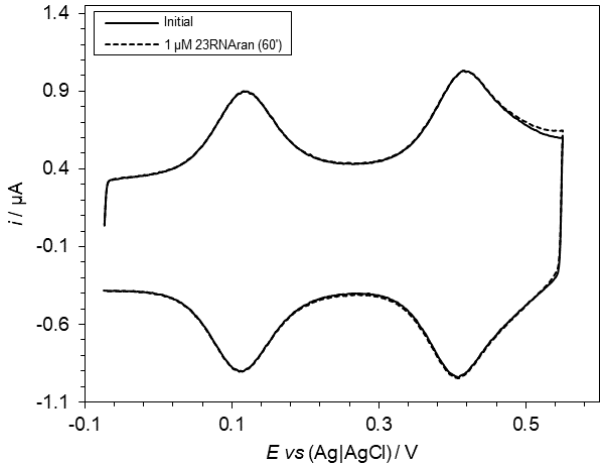

Figure 5.39: CVs of **miR135-1** sensing non-complementary 1 μM **23RNAran** target; in 10 mM sodium phosphate buffer (pH 7.0) 1 M $NaClO_4$; scan rates = 1000 mV s^{-1}.

Sensing of the trauma biomarker **miR135b-5p** in complex media was then investigated. As before, saliva- and serum-containing solutions were chosen for sensing. Following on from the studies discussed in section 5.4.2., a 10% dilution of buffer/electrolyte solution with either saliva or serum was chosen as a suitable dilution level. Figure 5.40 shows the sensing of **miR135b-5p** in saliva- and serum-containing solutions, with CuCy:Fc current ratio % changes of –100% and –83%, respectively. Little difference was observed compared with the analogous

sensing in pure buffer/electrolyte solutions (Figure 5.38), proving that the probe could function in the presence of significant levels of biological contaminants.

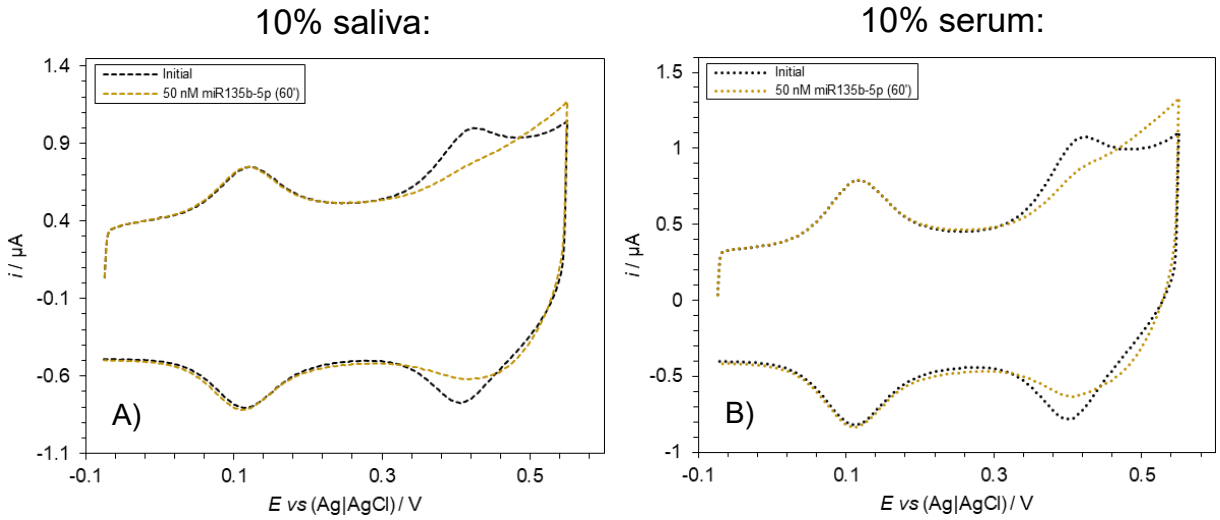

Figure **5.40**: CVs of **miR135-1** sensing 50 nM **miR135b-5p** in 90:10 buffer/electrolyte:saliva (A) and 90:10 buffer/electrolyte:serum (B); buffer/electrolyte = 10 mM sodium phosphate buffer (pH 7.0) 1 M $NaClO_4$, scan rates = 1000 mV s^{-1}.

Sensing at lower target concentrations was then conducted in the saliva- and serum-containing solutions to establish whether the biological contaminants interfered with the sensing of smaller quantities of target. It was noted that the magnitude of the reduction in CuCy current induced by the **miR135b-5p** and **miR135a-5p** targets at 50 nM was larger than the reduction observed for the analogous sensing of RNA targets using **T1** (section 5.4.1.) and most DNA targets using the SNV probes (Chapter 4). Therefore, a target concentration of 1 nM was chosen to see if the **miR135-1** probe could improve on the minimal (–2.6%) change in CuCy:Fc current ratio achieved by **T1** sensing DNA **T2T** target using cyclic voltammetry (Chapter 4). Figure 5.41 shows the CVs of **miR135-1** sensing 1 nM **miR135b-5p** target in saliva- and serum-containing solutions. CuCy:Fc current ratio % changes of –10.7% and –6.1% in the saliva- and serum-containing solutions, respectively, were an improvement on the –2.6% CuCy:Fc current ratio % change for the analogous sensing using **T1** probe and **T2T** target. The results showed

that the biological contaminants present did not interfere with the sensing of lower quantities of target. However, given the fM-range LOD required theoretically to sense most miRNAs at physiological concentrations (as discussed in Chapter 4), the marginal improvement in sensitivity of the **miR135-1** probe only highlighted the need for the fundamental change in probe function and design required to sense miRNAs without target amplification.

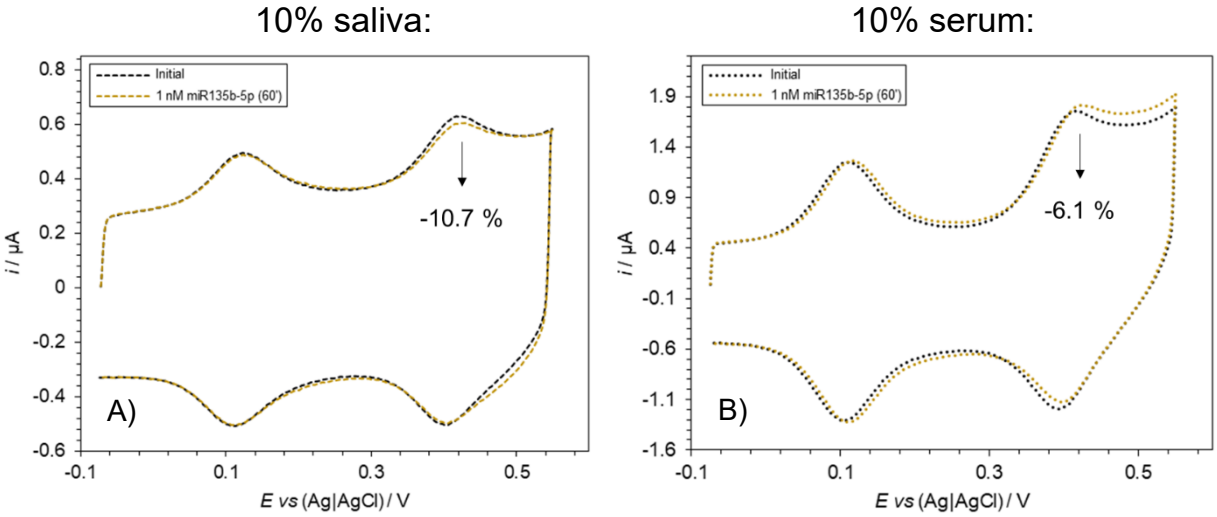

Figure 5.41: CVs of **miR135-1** sensing 1 nM **miR135b-5p** in 90:10 buffer/electrolyte:saliva (A) and 90:10 buffer/electrolyte:serum (B); buffer/electrolyte = 10 mM sodium phosphate buffer (pH 7.0) 1 M $NaClO_4$, scan rates = 1000 mV s^{-1}. %s shown are the CuCy:Fc current ratio % changes upon target addition.

5.5. Conclusions and Future Work

To conclude, the SNV sensing mechanism for the surface-immobilised CuCy-modified probes is proposed to be a combination of two factors: 1) the precise position of the CuCy within the probe–target duplex, dictated by the bases around it, significantly affecting the current it produces; and 2) targets that form more thermodynamically stable probe–target duplexes forming to a greater extent in the sensing period allowed than targets that form less stable probe–target duplexes. Regarding the first factor, previous work involving solution-based CuCy-modified probes,[1] the stark sensing differences between the (*S*)- and (*R*)-isomers of

CuCy, and persistent SNV sensing differences at very high target concentrations and with SAMs assembled from preformed duplexes, make a compelling case that the CuCy's conformational position within the duplex is a significant factor in the sensing mechanism. Future work could include the use of X-ray crystallography, long used to investigate new nucleic acid structures,[54] to probe duplex distortion as well as the CuCy's position and the extent of its intercalation in CuCy-modified DNA. However, crystallography would only be able to provide structural information for solution-based duplexes and would not be able to determine whether the CuCy adopted a different position in surface-immobilised duplexes.

Regarding the second factor, having shown that at a 50 nM target concentration a significant proportion of probes remain unbound at a surface, it would be expected that there would be a higher relative population of more thermodynamically stable probe–target duplexes over less thermodynamically stable duplexes. The observation that larger CuCy current reductions with the solution-based test probe sequence are observed with purines compared to pyrimidines,[1] whereas the opposite is true with the analogous surface-immobilised **T1** probe, remains difficult to rationalise. The explanation is likely to factor in the significant differences between the two setups, including the use of different electrochemical techniques and the differences in electrostatic and steric forces acting on surface-immobilised versus solution-based duplexes. No evidence of through-DNA electron transport was produced for the surface-immobilised CuCy-modified DNA studied. However, as the CuCy-modified DNA is likely to be electrostatically attracted to the electrode at the redox potential of the CuCy, contact-mediated electron transfer may be an important factor and could mask any through-DNA electron transport that occurs. Future work could include the determination of the angle at which the CuCy-modified DNA is orientated relative to the electrode surface at the redox potentials involved using atomic force microscopy.[18,19]

Square wave voltammetry could not replicate the reliable ratiometric SNV sensing achieved using cyclic voltammetry, but its use did enhance the sensitivity of the CuCy-/Fc-modified probes. Longer probes did not enhance sensitivity. Changing the sequence position of the CuCy within the probe demonstrated that SNV sensing is affected by the bases above and below the CuCy. Efforts to improve the sensitivity of the CuCy-/Fc-modified probe highlight the need to enhance the design of the sensor. This enhancement would likely be in the form of pairing the electrochemical setup with a target amplification mechanism to produce target in at least nM quantities. Whilst PCR amplification would be suitable, faster isothermal alternatives such as loop-mediated isothermal amplification (LAMP)[55] and exponential isothermal amplification reaction (EXPAR)[56] could achieve faster overall readout times. Ultimately, engineering would be required to fuse the electrochemical and target amplification aspects together to form a device that used the CuCy's SNV sensing capabilities.

The CuCy-/Fc-modified probes can sense RNA targets as well as DNA targets. Sensing in complex solutions containing biological contaminants was achieved using a suitable dilution level. Combining these two strands of investigation, the physical trauma salivary miRNA biomarker **miR135b-5p** was sensed in saliva- and serum-containing solutions at a target concentration of 1 nM. Future work on CuCy-/Fc-modified probes should include a continued focus on the sensing of miRNAs. Their ideal length of ~20 nucleotides, single-stranded nature, and high durability makes them the ideal target for electrochemical sensors that use surface-immobilised nucleic acid probes. Although in this instance the SNV discrimination between **miR135b-5p** and **miR135a-5p** was unsuccessful, there remain many other sets of closely related miRNAs that differ by only one base.[53] A miRNA-focused setup that combines the electrochemical SNV sensing reported here and a signal/target amplification mechanism would potentially lead to a commercially viable sensor.

5.6. References

1. J. Duprey, J. Carr-Smith, S. L. Horswell, J. Kowalski and J. H. R. Tucker, *J. Am. Chem. Soc.*, 2016, **138**, 746-749.
2. L. Vanjur, T. Carzaniga, L. Casiraghi, M. Chiari, G. Zanchetta and M. Buscaglia, *Biophys. J.*, 2020, **119**, 989-1001.
3. F. Xu, A. M. Pellino and W. Knoll, *Thin Solid Films*, 2008, **516**, 8634-8639.
4. W. Q. Qiao, H. C. Chiang, H. Xie and R. Levicky, *Chem. Commun.*, 2015, **51**, 17245-17248.
5. L. Kekedy-Nagy and E. E. Ferapontova, *Angew. Chem., Int. Ed.*, 2019, **58**, 3048-3052.
6. R. G. Lemer and G. L. Trigg, *Encyclopedia of Physics*, VCH Publishers, 1991.
7. J. R. Winkler and H. B. Gray, *J. Am. Chem. Soc.*, 2014, **136**, 2930-2939.
8. A. Stuchebrukhov, *Laser Phys.*, 2010, **20**, 125-138.
9. J. D. Slinker, N. B. Muren, S. E. Renfrew and J. K. Barton, *Nat. Chem.*, 2011, **3**, 228-233.
10. S. O. Kelley, N. M. Jackson, M. G. Hill and J. K. Barton, *Angew. Chem., Int. Ed.*, 1999, **38**, 941-945.
11. A. Nano, A. L. Furst, M. G. Hill and J. K. Barton, *J. Am. Chem. Soc.*, 2021, **143**, 11631-11640.
12. A. Abi and E. E. Ferapontova, *J. Am. Chem. Soc.*, 2012, **134**, 14499-14507.
13. C. G. Pheeney and J. K. Barton, *Langmuir*, 2012, **28**, 7063-7070.
14. M. A. McWilliams, R. Bhui, D. W. Taylor and J. D. Slinker, *J. Am. Chem. Soc.*, 2015, **137**, 11150-11155.
15. M. C. DeRosa, A. Sancar and J. K. Barton, *Proc. Natl. Acad. Sci. U. S. A.*, 2005, **102**, 10788-10792.
16. E. M. Boon, J. E. Salas and J. K. Barton, *Nat. Biotechnol.*, 2002, **20**, 282-286.
17. P. Dauphin-Ducharme, N. Arroyo-Curras and K. W. Plaxco, *J. Am. Chem. Soc.*, 2019, **141**, 1304-1311.
18. U. Rant, K. Arinaga, S. Fujita, N. Yokoyama, G. Abstreiter and M. Tornow, *Nano Lett.*, 2004, **4**, 2441-2445.
19. S. O. Kelley, J. K. Barton, N. M. Jackson, L. D. McPherson, A. B. Potter, E. M. Spain, M. J. Allen and M. G. Hill, *Langmuir*, 1998, **14**, 6781-6784.
20. E. L. Wong, E. Chow and J. J. Gooding, *Langmuir*, 2005, **21**, 6957-6965.

21. R. P. Singh, B.-K. Oh and J.-W. Choi, *Bioelectrochemistry*, 2010, **79**, 153-161.
22. T. Špringer, H. Šípová, H. Vaisocherová, J. Štěpánek and J. Homola, *Nucleic Acids Res.*, 2010, **38**, 7343-7351.
23. S. M. Silva, S. Hoque, V. R. Goncales and J. J. Gooding, *Electroanalysis*, 2018, **30**, 1529-1535.
24. S. M. Silva, R. Tavallaie, V. R. Gonçales, R. H. Utama, M. B. Kashi, D. B. Hibbert, R. D. Tilley and J. J. Gooding, *Langmuir*, 2018, **34**, 1249-1255.
25. M. D. Mayer and R. Y. Lai, *Talanta*, 2018, **189**, 585-591.
26. J. G. Osteryoung and R. A. Osteryoung, *Anal. Chem.*, 1985, **57**, 101-110.
27. L. Ramaley and M. S. Krause, *Anal. Chem.*, 1969, **41**, 1362-1365.
28. E. Wilkinson, PhD thesis, University of Birmingham, 2020.
29. H. Roberts, PhD thesis, University of Birmingham, 2018.
30. Y. Du, B. J. Lim, B. L. Li, Y. S. Jiang, J. L. Sessler and A. D. Ellington, *Anal. Chem.*, 2014, **86**, 8010-8016.
31. A. Idili, A. Amodio, M. Vidonis, J. Feinberg-Somerson, M. Castronovo and F. Ricci, *Anal. Chem.*, 2014, **86**, 9013-9019.
32. I. Grabowska, D. G. Singleton, A. Stachyra, A. Gora-Sochacka, A. Sirko, W. Zagorski-Ostoja, H. Radecka, E. Stulz and J. Radecki, *Chem. Commun.*, 2014, **50**, 4196-4199.
33. F. Xia, R. J. White, X. L. Zuo, A. Patterson, Y. Xiao, D. Kang, X. Gong, K. W. Plaxco and A. J. Heeger, *J. Am. Chem. Soc.*, 2010, **132**, 14346-14348.
34. Z. Shi and J. Lipkowski, *J. Electroanal. Chem.*, 1996, **403**, 225-239.
35. R. J. White and K. W. Plaxco, *Anal. Chem.*, 2010, **82**, 73-76.
36. P. Dauphin-Ducharme and K. W. Plaxco, *Anal. Chem.*, 2016, **88**, 11654-11662.
37. C. Y. Deng, X. M. Pi, P. Qian, X. Q. Chen, W. M. Wu and J. Xiang, *Anal. Chem.*, 2017, **89**, 966-973.
38. F. L. Gao, L. Du, Y. Zhang, D. Q. Tang and Y. Du, *Anal. Chim. Acta*, 2015, **883**, 67-73.
39. Y. K. Ye, Y. Q. Liu, S. D. He, X. Xu, X. D. Cao, Y. W. Ye and H. S. Zheng, *Sens. Actuators, B*, 2018, **272**, 53-59.
40. Y. L. Chu, B. Cai, Y. Ma, M. G. Zhao, Z. Z. Ye and J. Y. Huang, *RSC Adv.*, 2016, **6**, 22673-22678.

41. M. Azimzadeh, M. Rahaie, N. Nasirizadeh and H. Naderi-Manesh, *Anal. Methods*, 2015, **7**, 9495-9503.
42. W. F. Sokol and D. H. Evans, *Anal. Chem.*, 1981, **53**, 578-580.
43. R. B. Jamal, T. Vitasovic, U. Gosewinkel and E. E. Ferapontova, *Biosens. Bioelectron.*, 2023, **228**, 115214.
44. L. P. Luo, L. L. Wang, L. P. Zeng, Y. R. Wang, Y. P. Weng, Y. J. Liao, T. T. Chen, Y. K. Xia, J. Zhang and J. H. Chen, *Talanta*, 2020, DOI: 10.1016/j.talanta.2019.120298.
45. R. Tavallaie, J. McCarroll, M. Le Grand, N. Ariotti, W. Schuhmann, E. Bakker, R. D. Tilley, D. B. Hibbert, M. Kavallaris and J. J. Gooding, *Nat. Nanotechnol.*, 2018, **13**, 1066-1071.
46. S. Han, W. Y. Liu, S. Yang and R. S. Wang, *ACS Omega*, 2019, **4**, 11025-11031.
47. L. Tian, K. Qian, J. Qi, Q. Liu, C. Yao, W. Song and Y. Wang, *Biosens. Bioelectron.*, 2018, **99**, 564-570.
48. H. Schwarzenbach, D. S. B. Hoon and K. Pantel, *Nat. Rev. Cancer*, 2011, **11**, 426-437.
49. J. A. Weber, D. H. Baxter, S. L. Zhang, D. Y. Huang, K. H. Huang, M. J. Lee, D. J. Galas and K. Wang, *Clin. Chem.*, 2010, **56**, 1733-1741.
50. A. R. Cardoso, F. T. C. Moreira, R. Fernandes and M. G. F. Sales, *Biosens. Bioelectron.*, 2016, **80**, 621-630.
51. B. Jeong, Y. J. Kim and J. Y. Jeong, *J. Electroanal. Chem.*, 2019, **846**, 113127.
52. V. Di Pietro, E. Porto, M. Ragusa, C. Barbagallo, D. Davies, M. Forcione, A. Logan, C. Di Pietro, M. Purrello, M. Grey, D. Hammond, V. Sawlani, A. K. Barbey and A. Belli, *Front. Mol. Neurosci.*, 2018, DOI: 10.3389/fnmol.2018.00290.
53. miRBase, https://www.mirbase.org/, (accessed March 2023).
54. M. Egli, *Curr. Opin. Chem. Biol.*, 2004, **8**, 580-591.
55. Y. Li, P. Fan, S. Zhou and L. Zhang, *Microb. Pathog.*, 2017, **107**, 54-61.
56. M. S. Reid, X. C. Le and H. Zhang, *Angew. Chem., Int. Ed.*, 2018, **57**, 11856-11866.

Chapter 6: Functionalisation of Metal-Organic Frameworks with Fluorescently-Modified DNA

6.1. Introduction

6.1.1. Structure of MOFs

Metal-organic frameworks (MOFs) form a class of crystalline materials that are composed of metal ions or clusters connected through multidentate organic linkers to form an extended repeating framework.[1,2] The most notable properties of MOFs are their high surface areas and permanent porosities, with surface areas of 7000 m^2 g^{-1} being reported.[3] The properties of MOFs can be almost endlessly tuned owing to the vast numbers of different metal nodes and organic linkers that can be combined together.[1,2] Hoskins and Robson synthesised the first MOF-like structures in 1989, reporting on materials formed from simple uncharged ligands connecting lone metal centres.[4] The term MOF was first used by Yaghi and coworkers[5] in 1995 and the field has since expanded significantly, with over 99,075 MOF crystal structures archived in the Cambridge Structural Database as of 2020.[6]

MOF structures can be described in terms of four structure levels (Figure 6.1).[7] The first level consists of the basic units of the MOF: the metal nodes and organic linkers. Multivalent metal ions are typically used but monovalent ions have also been used. The organic linkers are usually alkyl chains or ring-based structures from which multiple carboxyl or amine groups extend. The second level comprises secondary building units (SBUs) that consist of multiple organic linkers coordinated around a single metal ion or cluster to form the simplest repeated unit of the MOF structure. The third level, the internal framework, is formed by linking the SBUs together. This third level includes the pores and cages from which MOFs derive their unique properties. The fourth level is the morphology (shape, size and orientation) of the MOF

crystal. Whereas the first three structure levels are largely determined by the metal nodes and organic linkers used, the morphology of a MOF crystal is affected by the conditions and any additional reagents (such as therapeutics intended to be encapsulated) used during synthesis.

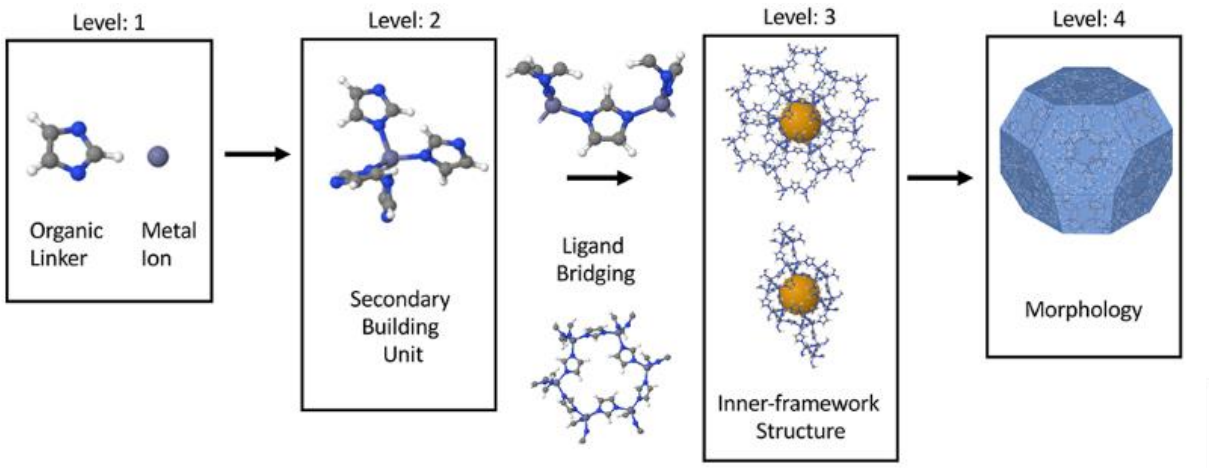

Figure 6.1: Schematic diagrams of the composition of MOFs and their structure levels. Level 1 consists of the basic units: the organic linker and metal nodes (ions or clusters). Level 2 is the secondary building unit (SBU), which is the simplest repeated unit of the MOF. Level 3 is the inner-framework structure, which is the extended lattice of the MOF. Level 4 is the morphology of the MOF particles. (Taken from reference 7.)

6.1.2. Applications of MOFs

The applications of MOFs are mostly derived from their large surface areas and high permanent porosities. MOFs are commonly employed as adsorbents to capture various different compounds, from heavy metals and pharmaceuticals to smaller molecules such as H_2 and O_2 found in water, fuels, and air.[8-10] In addition to their capture, contaminants can also be detected with MOFs designed to produce a luminescent response upon the binding of a certain target.[11] Heavy metal removal from waste water streams is a key MOF application. Zhong and coworkers reported on the modification of the robust MOF-808 with ethylenediaminetetraacetic acid (EDTA) groups that were able to adsorb 22 different metal ions at high removal efficiencies in multi-component systems (Figure 6.2).[12] The EDTA-functionalised MOF-808 is a good example of how the properties of a known MOF (MOF-808 was first reported in 2014[13]) can

be tuned and improved using relatively modest modifications. The selective separation and capture of small molecules is another key MOF application. Hong-Cai Zhou and coworkers reported on the MOF PCN-17 that exhibited selected adsorption of H_2 and O_2 over N_2 and CO.[14] By restricting the pore window size to 3.5 Å using sulfate bridges, the larger N_2 and CO molecules (determined by their kinetic diameters) were excluded whilst the smaller H_2 and O_2 molecules were captured. The authors posited potential uses in fuel-cell and ammonia synthesis applications. Such examples serve to illustrate the capability of MOFs to treat our evermore polluted water systems[15] and potentially enhance existing and developing processes.

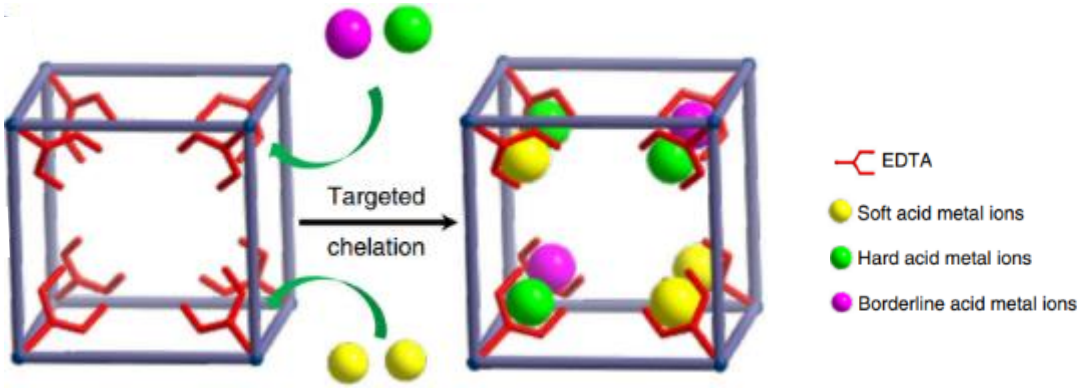

Figure 6.2: Schematic diagram of EDTA-functionalised MOF-808 capturing metal ions. (Taken and adapted from reference 12.)

The high surface areas, permanent porosities, and tuneable components of MOFs have also led to their application as catalysts.[16,17] Advantages of using MOFs over more traditional catalysts includes their large internal surface areas allowing for high catalytic reaction rates per unit volume and the ability to modify MOFs with complementary catalytic groups.[17] Selected examples of reactions catalysed by MOFs include hydrogenation,[18,19] oligomerisation,[20,21] and alkylation[22] reactions – all important industrial processes. An illustrative example of a MOF directly catalysing a reaction is provided by Nguyen and coworkers' series of M-MOF-184 MOFs used to catalyse the cycloaddition of CO_2 to epoxides (Figure 6.3A).[23] The zinc-based

MOF Zn-MOF-184 was found to exhibit the best catalytic properties and a mechanism involving the activation of the epoxide *via* direct interaction with the Zn sites was proposed. An example of a MOF hosting a catalyst, and therefore enabling the catalytic process, is Farha and coworkers' NU-1000 MOF that occluded copper nanoparticles, which facilitated the partial hydrogenation of acetylene to ethylene (Figure 6.3B).[18] The pores of NU-1000 fixed the copper nanoparticles in place, which then more efficiently converted acetylene to ethylene compared with a copper on zirconia control. However, the generally inferior stability of MOFs compared with inorganic solids and the difficulty in removing unwanted organic deposits without destroying the organic linkers pose practical limitations on the use of MOFs as catalysts.[17] Nonetheless, their immense potential means that MOF catalysis is an active and growing area of research.

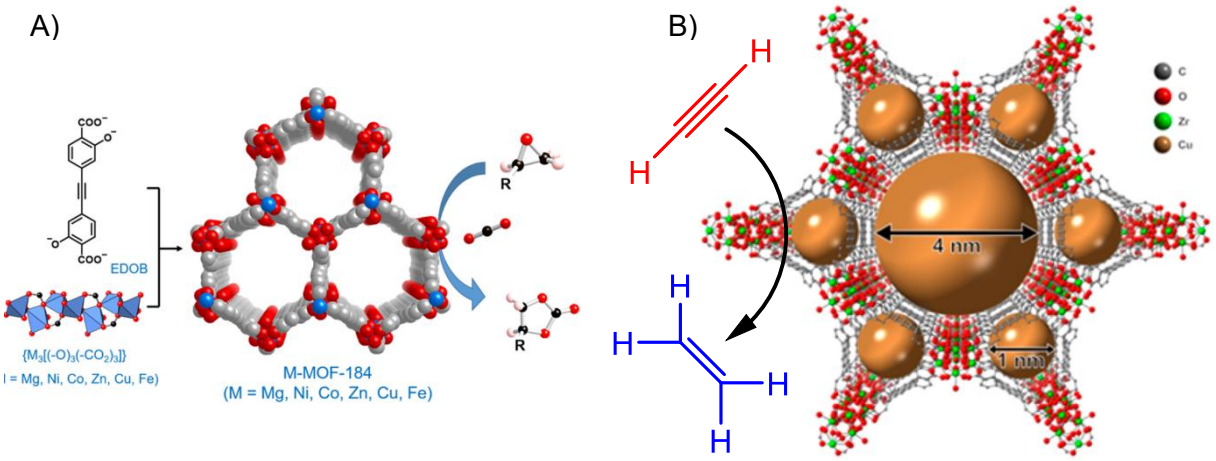

Figure 6.3: A) Schematic diagram of an M-MOF-184 MOF catalysing the cycloaddition of CO_2 to an epoxide. (Taken from reference 23.) B) Schematic diagram of an NU-1000 MOF incorporating copper nanoparticles within its pores and used to hydrogenate acetylene to ethylene. (Taken and adapted from reference 18.)

6.1.3. Post-Synthetic DNA-Functionalisation of MOFs

MOFs can be post-synthetically modified and functionalised in various ways, including metal-based, ligand-based, and guest-based modification of the parent MOF.[24] Most relevant to this chapter is the functionalisation of MOFs with DNA, which over the last decade has been

reported by multiple groups. Mirkin and coworkers reported on the first MOF structure covalently functionalised with DNA (Figure 6.4) in 2014.[25] Azide-containing linkers reacted with dibenzylcyclooctyne- (DBCO) modified DNA *via* copper-free strained alkyne click chemistry to functionalise UiO-66-N_3 MOF nanoparticles. The DNA was modified with the dyes TAMRA or FAM and therefore the functionalised MOFs were highly fluorescent when imaged using confocal microscopy. Gold nanoparticles functionalised with complementary DNA were found to bind to the DNA-functionalised MOFs but no experiments were conducted attempting to bind different DNA-functionalised MOFs together *via* complementary base pairing. The DNA was found to create a steric and electrostatic barrier that aided in the cellular uptake of functionalised MOFs, with promising implications from a drug-delivery perspective.

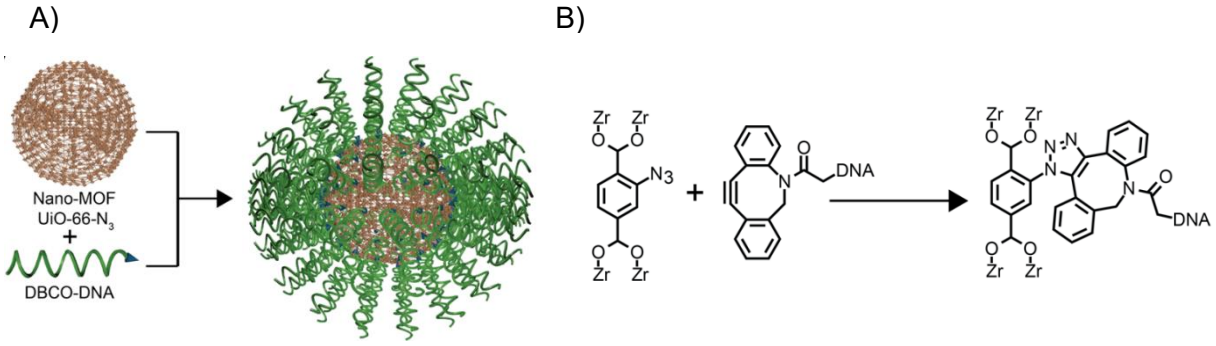

Figure 6.4: A) Schematic diagram of the MOF UiO-66-N_3 being functionalised with DBCO-DNA. B) Copper-free strained alkyne click chemistry used to covalently tether the DNA to the MOF. (Taken and adapted from reference 25.)

Since 2014, more groups have reported covalent DNA-functionalisation of MOFs and associated applications. Willner and coworkers reported on a Zn-based MOF functionalised with DNA that formed a quadruplex structure at pH 5.5 and denatured into single-stranded DNA at pH 7.4 (Figure 6.5).[26] The fluorescent dye rhodamine 6G was loaded into the pores of the MOF and locked in at pH 5.5 by the surrounding quadruplex structures. At pH 7.4, the quadruplex structures denatured, allowing the loaded rhodamine 6G to be released. Farha and

coworkers similarly reported on the encapsulation of insulin in a Zr-based MOF that was subsequently functionalised using 3′ terminal phosphate-modified DNA.[27] As with Mirkin and coworkers' 2014 report described above, the DNA-functionalised MOFs were able to traverse the membranes of mammalian cells and release their insulin cargo. However, there appeared to be no specific trigger for the release of insulin once inside the cell, leading to the possibility that significant quantities were released prior to cellular uptake. A DNA-functionalised MOF combining efficient cellular uptake and stimulated cargo release has the potential to make a powerful drug delivery mechanism.

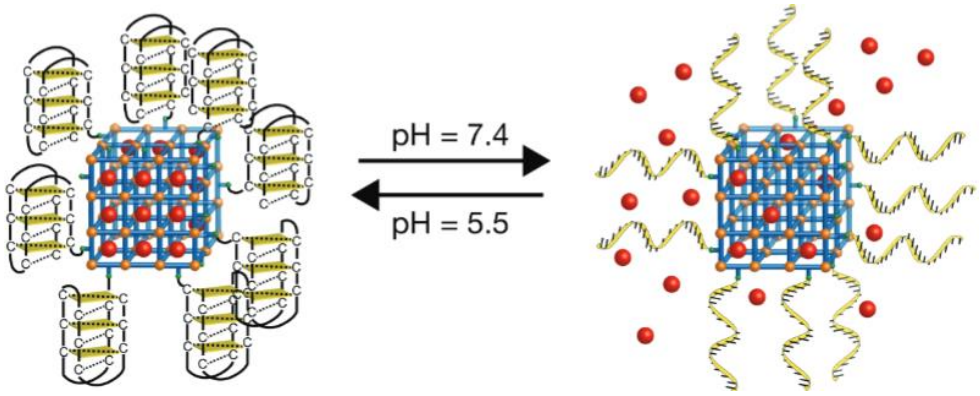

Figure 6.5: Schematic diagram of rhodamine 6G (red) being released from a MOF upon raising the pH to 7.4 and the resulting denaturation of the DNA quadruplex structures. (Taken from reference 26.)

Other groups have reported on the binding of DNA-functionalised MOFs to other entities functionalised with complementary DNA. As mentioned above, Mirkin and coworkers' initial report on DNA-functionalised MOFs described its binding to DNA-functionalised gold nanoparticles.[25] Li and coworkers similarly reported on a DNA-functionalised PCN-224 MOF that could bind to smaller gold nanoparticles functionalised with complementary DNA (Figure 6.6).[28] Their aim in doing so was to confirm that the DNA still retained the ability to hybridise, with the delivery of cancer cell-targeting aptamers being the primary purpose of the DNA-functionalised MOF. Cha and coworkers also reported on a DNA-functionalised PCN-224 MOF

that could bind to DNA-functionalised gold nanoparticles, with the resulting MOF–nanoparticle superstructures able to produce singlet oxygen species in greater amounts than unfunctionalised mixtures of PCN-224 MOF and gold nanoparticles.[29]

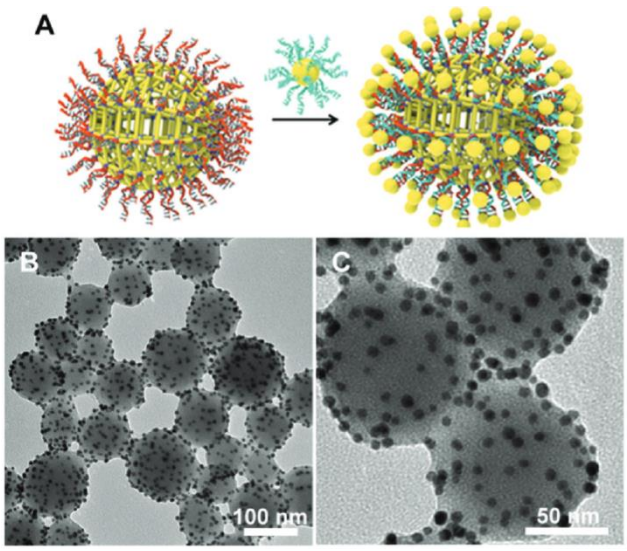

Figure 6.6: A) Schematic diagram of DNA-functionalised PCN-224 MOF nanoparticles binding to gold nanoparticles functionalised with complementary DNA. B, C) Transmission electron microscopy images of the DNA-functionalised nanoparticles (black) binding to the DNA-functionalised PCN-224 MOF nanoparticles (grey). (Taken from reference 28.)

Mirkin and coworkers' report on DNA-functionalised UiO-66 MOF nanoparticles forming MOF superlattices is the only report in the literature of DNA-functionalised MOFs binding together *via* DNA hybridisation (Figure 6.7).[30] Prior to DNA functionalisation, the surfaces of the MOFs were passivated by a layer of azide-modified PEG polymers, with which the DBCO-modified DNA reacted *via* copper-free click chemistry. Linker DNA of programmable length, containing single-stranded end sections and a duplexed internal section, was used to control interparticle distances and hybridised with the MOF-attached DBCO DNA at one of its ends. The other 'sticky' end could then hybridise with complementary sticky ends attached to other MOF nanoparticles, thus forming the superlattice structure. By modifying the length and sequence of the DNA components described, different sets of superlattices with altered properties were formed in a programmable fashion. Whilst binary MOF nanoparticle–gold

nanoparticle superlattices were formed (similar to the work of Li[28] and Cha[29] described above), no binary MOF superlattices consisting of two different types of MOF were reported. There is yet to be a report in the literature of different DNA-functionalised MOFs, each with different properties, binding together *via* DNA hybridisation.

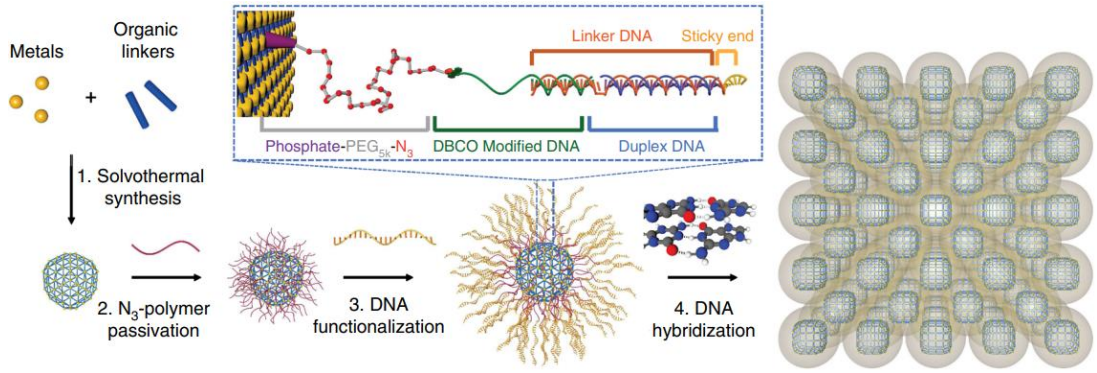

Figure 6.7: Schematic diagram of the functionalisation of UiO-66 MOFs nanoparticles with DNA and their subsequent arrangement into a MOF superlattice *via* DNA hybridisation. (Taken from reference 30.)

6.1.4. Förster Resonance Energy Transfer

FRET is the process that occurs when an excited donor fluorophore non-radiatively transfers energy to an acceptor fluorophore at distances between 0.5–10 nm (Figure 6.8).[31] Efficient FRET depends on the spectral overlap in the excitation/emission spectra, close proximity, and correct orientation of the fluorophores involved.[31] The efficiency of FRET transfer is inversely proportional to the sixth power of the distance between two fluorophores[31] and is therefore highly sensitive to changes in distance. FRET has been used in a number of applications. TaqMan probes incorporating two FRET-capable fluorophores can be used for nucleic acid detection in real-time qPCR.[32] FRET can also be used to detect the hybridisation of complementary donor- and acceptor-labelled DNA,[33] which has then been used to determine the structural integrity of duplexes delivered into live cells.[34] Many different fluorophore pairs

can be used to facilitate FRET. Cy3 and Cy5 are commonly used owing to their high FRET efficiency, simple incorporation into DNA, and relatively low photobleaching rates.

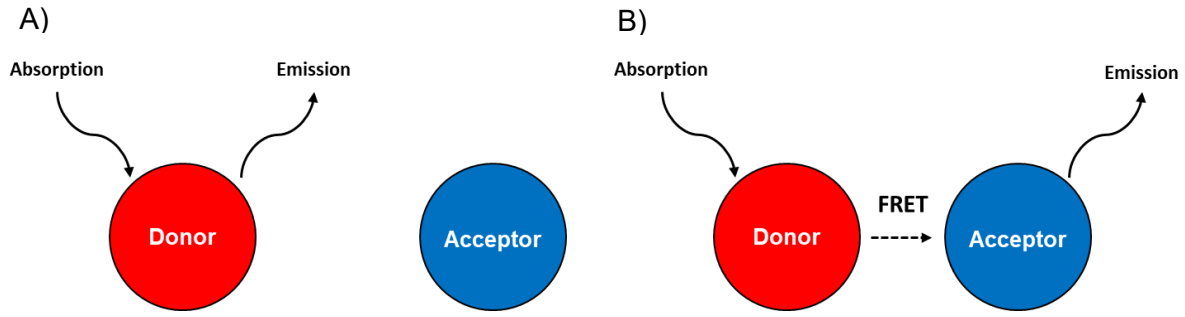

Figure 6.8: Schematic diagrams of A) a donor and an acceptor fluorophore not close enough to facilitate FRET; and B) a donor and an acceptor fluorophore that are close enough to facilitate FRET.

6.2. Chapter Aims

The aim of this chapter is to functionalise two different MOFs with complementary fluorescently-modified DNA and bind the DNA-functionalised MOFs together *via* DNA hybridisation (Figure 6.9). The formation of a heterogenous MOF structure interconnected by duplexed DNA may allow for the combination of desirable MOF properties in a single material. As described above, several groups have bound DNA-functionalised MOFs to DNA-functionalised gold nanoparticles and Mirkin and coworkers have combined DNA-functionalised MOFs into homogenous crystal superlattice structures,[30] but no group has combined together different MOFs functionalised with complementary DNA. The functionalising DNA used in this work will be modified with the fluorophores Cy3 or Cy5, with the syntheses of the Cy3-/Cy5-modified DNA having been described in Chapter 3. The purpose of the labelling fluorophores is to firstly confirm the successful DNA-functionalisation of the MOFs, and secondly to confirm the hybridisation of the modified DNA oligonucleotides both pre- and post-MOF attachment using FRET.

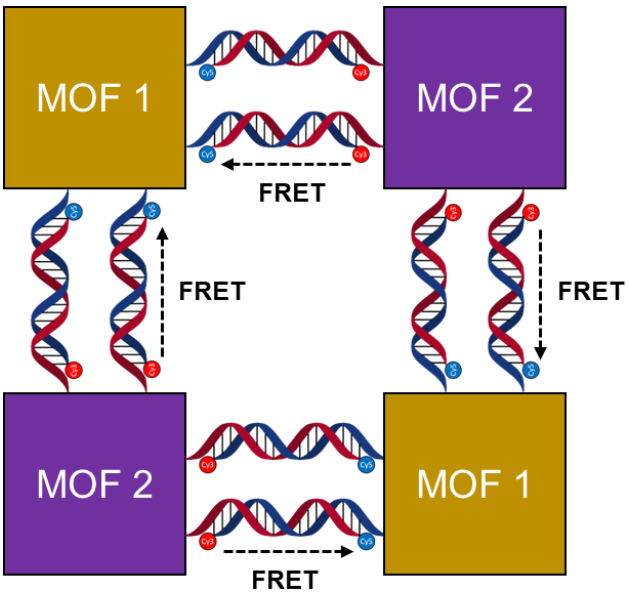

Figure 6.9: Simplified schematic diagram depicting the aim of this chapter. Different MOFs are functionalised with complementary DNA modified with either Cy3 (red circles) or Cy5 (blue circles). The DNA-functionalised MOFs bind together *via* DNA hybridisation, bringing the Cy3 and Cy5 fluorophores close enough to facilitate FRET and thus confirm successful hybridisation.

6.3. Design and Pre-MOF Functionalisation Studies of DNA Probes

6.3.1. DNA Probe Design

Table 6.1: Fluorescently-modified DNA oligonucleotides. Cy3 = Cyanine 3; Cy5 = Cyanine 5; Z = alkyne; P18 = PEG18 spacer.

Oligonucleotide	5′ – Sequence – 3′
DNA-Cy3	Cy3 TGG ACT CTC TCA ATG TTT Z
DNA-Cy5	Cy5 CAT TGA GAG AGT CCA TTT Z
DNA-Cy3-Ext	Cy3 TGG ACT CTC TCA ATG TTT TTT P18 Z
DNA-Cy5-Ext	Cy5 CAT TGA GAG AGT CCA TTT TTT P18 Z

Four DNA oligonucleotides modified with Cy3 or Cy5 were synthesised (Table 6.1). **DNA-Cy3** is based on the in-house test sequence (NINA) used in the group with Cy3 incorporated at the 5′ end and three thymines followed by an alkyne modification at the 3′ end. **DNA-Cy5** is complementary to **DNA-Cy3** and has a Cy5 incorporated at the 5′ end as well as three thymines and an alkyne modification at the 3′ end. The duplex formed from **DNA-Cy3** and **DNA-Cy5** is shown in Figure 6.10. Cy3 and Cy5 are separated by a distance of approximately 5.1 nm and

are therefore within range to facilitate FRET. The three unbound thymines at one end of each probe were incorporated to act as a spacer and provide some distance between the DNA and the MOF. The terminal alkynes were designed to react with the azide-functionalised linkers of the MOFs *via* copper-catalysed click chemistry and covalently attach the DNA. **DNA-Cy3-Ext** and **DNA-Cy5-Ext** were the same as their shorter analogues bar the incorporation of a PEG spacer and three extra thymines, both features designed to add even more distance between the DNA and the MOFs. These longer oligonucleotides were synthesised to test whether having more distance between the DNA and the MOF allowed for better DNA hybridisation post-MOF functionalisation.

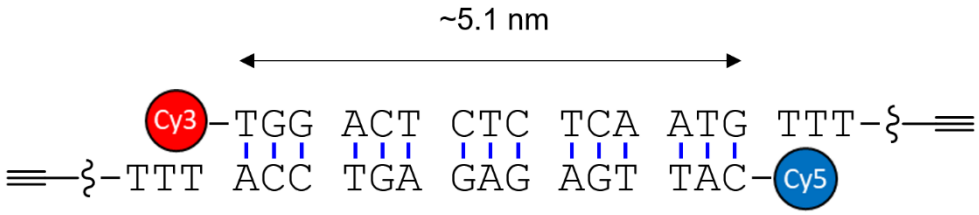

Figure 6.10: Schematic diagram of the **DNA-Cy3**/**DNA-Cy5** duplex. Cy3 and Cy5 are separated by a distance of <10 nm, and therefore are capable of facilitating FRET.

6.3.2. Thermal Melting Studies

Thermal melting studies were conducted to assess the impact that the Cy3 and Cy5 modifications had on duplex stability. As the success of the design depended on the binding of the Cy3-/Cy5-modified oligonucleotides, it was important to determine that the fluorophores did not have a prohibitively negative impact on hybridisation.

Table 6.2. Thermal melting temperatures for the Cy3-/Cy5-modified oligonucleotides duplexed with each other and unmodified complementary sequences. Error shown is SD from three repeats. [DNA] = 10 μM in 10 mM sodium phosphate buffer pH 7.0, 100 mM NaCl.

Duplex	T_m (°C)
DNA-Cy3 / DNA-Cy5	68.0 (± 1.5)
DNA-Cy3 / T2A	64.0 (± 1.0)
T1unmod / DNA-Cy5	67.5 (± 1.0)
T1unmod / T2A	64.5 (± 0.5)
DNA-Cy3-Ext / DNA-Cy5-Ext	69.5 (± 1.5)
DNA-Cy3-Ext / T2A	63.0 (± 1.0)
T1unmod / DNA-Cy5-Ext	66.0 (± 1.5)

Table 6.2 shows the T_m values for the Cy3-/Cy5-modified oligonucleotides shown in Table 6.1. The Cy3- and Cy5-modified oligonucleotides were duplexed with each other as well as with the complementary unmodified strands **T2A** and **T1unmod**. The most thermally stable duplexes were the ones in which both oligonucleotides were modified with Cy3 or Cy5. Terminal cyanine modifications are known to stack onto the adjacent base pair and stabilise the duplex,[35] thus explaining why the Cy3- and Cy5-containing duplexes were the most stable. Having an unpaired base opposite the Cy3 or Cy5 in the duplex, as is the case with the duplexes reported here, has an additive effect on stabilisation and further increases thermal stability.[35] Cy5 resulted in more stabilisation than Cy3, with the **T1unmod**/**DNA-Cy5** and **T1unmod**/**DNA-Cy5-Ext** duplexes exhibiting greater thermal stabilities than their analogous **DNA-Cy3**/**T2A** and **DNA-Cy3-Ext**/**T2A** duplexes, respectively.

It was noted that duplexes containing Cy3- and Cy5-modified oligonucleotides resulted in less fluorescence emission (measured in relative fluorescence units, RFU) than duplexes not containing Cy3 and/or Cy5 (Figure 6.11). As discussed in Chapter 2, SYBR Green dye was used to monitor DNA denaturation *via* fluorescence. The most likely explanation for the reduced fluorescence of mixtures containing Cy3-/Cy5-modified oligonucleotides is that Cy3 and Cy5 have a quenching effect on SYBR Green. That the emissive range of SYBR Green (approximately 490–650 nm with a maximum of 520 nm) overlaps with the peak excitation

wavelengths of Cy3 and Cy5 (554 nm and 650 nm, respectively) increases the likelihood of this possibility. An effect of the reduced fluorescence was the decreased signal-to-noise ratio in the plots of the negative first derivatives of the melting curves versus temperature, the maxima of which correspond to the T_m of the duplex (see Appendix 8.4.1.). As such, the errors associated with the T_m values for the Cy3- and Cy5-containing duplexes presented in Table 6.2 were larger than would typically be expected. Nevertheless, these thermal melting studies showed that the Cy3 and Cy5 modifications did not inhibit DNA hybridisation and in fact increased duplex stability.

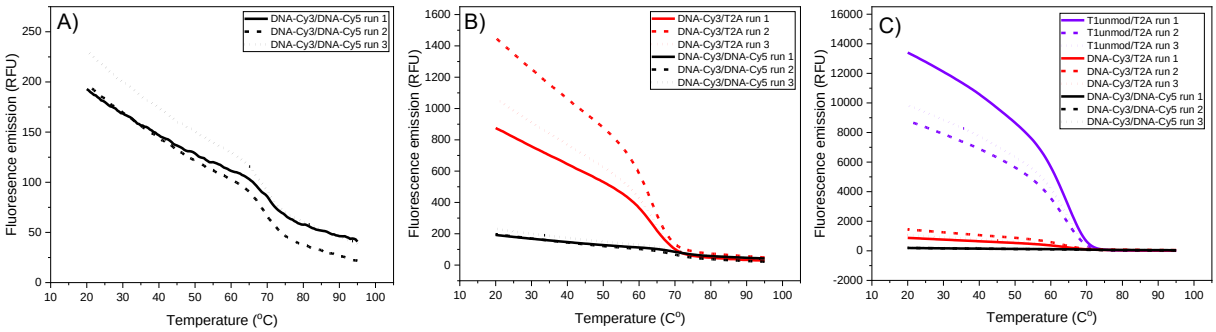

Figure 6.11: Comparison of fluorescence emission between three sets of duplexes: **DNA-Cy3/DNA-Cy5** (black), **DNA-Cy3/T2A** (red), **T1unmod/T2A** (purple). Duplexes containing Cy3 and/or Cy5 resulted in lower fluorescence emission. [DNA] = 10 μM for each oligo. Spectra measured in sodium phosphate buffer pH 7.0, 100 mM NaCl, 1 μL SYBR Green dye. λ_{ex} = 497 nm.

6.3.3. Fluorescence Spectroscopy

Fluorescence spectroscopy was then used to determine the presence and efficiency of FRET in Cy3-/Cy5-modified duplexes in aqueous solution at neutral pH. Firstly, excitation and emission spectra of **DNA-Cy3** and **DNA-Cy5** were measured separately (Figure 6.12). The overlap in the emission of **DNA-Cy3** and the excitation of **DNA-Cy5** demonstrates the suitability of Cy3 and Cy5 as a FRET pair, even when incorporated into DNA. No differences were observed in the excitation and emission spectra of **DNA-Cy3-Ext** and **DNA-Cy5-Ext**

compared with the spectra of **DNA-Cy3** and **DNA-Cy5** shown in Figure 6.12 (see Appendix 8.4.2.).

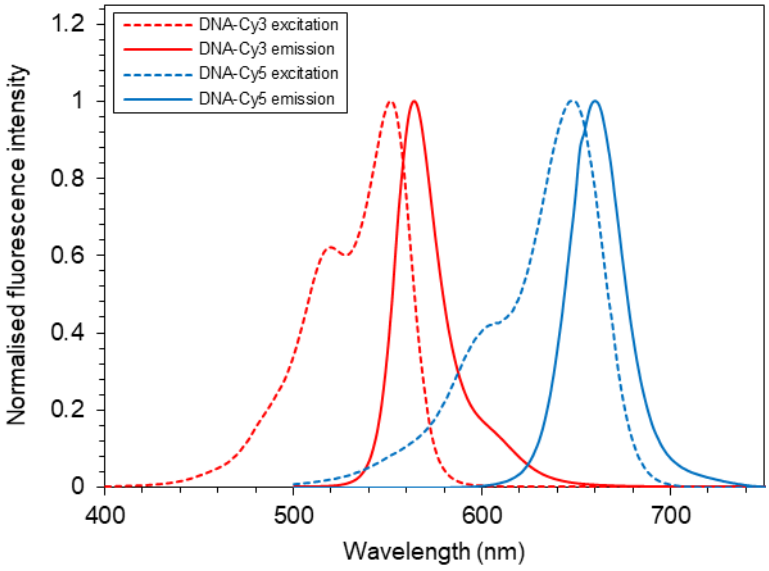

Figure 6.12: Normalised excitation and emission spectra of **DNA-Cy3** and **DNA-Cy5**. The overlap in the emission of **DNA-Cy3** and the excitation of **DNA-Cy5** demonstrates the suitability of Cy3 and Cy5 as a FRET pair. [DNA] = 1 μM. Measured in sodium phosphate buffer pH 7.0, 100 mM NaCl. **DNA-Cy3** λ_{ex} = 554 nm, λ_{em} = 570 nm; **DNA-Cy5** λ_{ex} = 650 nm, λ_{em} = 665 nm.

Evidence of FRET was then sought by titrating in **DNA-Cy5** into a 1 μM solution of **DNA-Cy3** (Figure 6.13). FRET occurs when the donor fluorophore (Cy3) is excited and non-radiatively transfers energy to the acceptor fluorophore (Cy5). As such, the titration solutions were excited at the excitation wavelength of Cy3 (554 nm) and the emissions at approximately 570 nm (Cy3 emission) and 665 nm (Cy5 emission) were monitored. Titrating in **DNA-Cy5** resulted in significant quenching of the emission at 570 nm and a small increase in the emission at 665 nm, both of which are indicative of FRET. Identical behaviour was observed with the longer oligonucleotides **DNA-Cy3-Ext** and **DNA-Cy5-Ext** (see Appendix 8.4.2.). No further quenching or increase in emission was observed after more than one molar equivalent of **DNA-Cy5** was added, consistent with 1:1 duplex formation. The excitation spectrum of a solution containing equimolar amounts of **DNA-Cy3** and **DNA-Cy5**, holding the emission at 665 nm,

revealed the presence of an extra peak at approximately 554 nm (see Appendix 8.4.2.) to confirm further the presence of FRET.

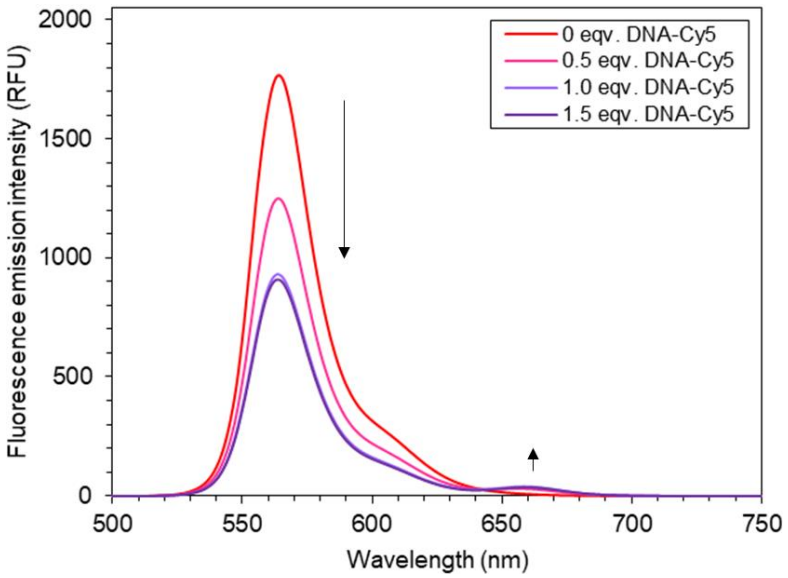

Figure 6.13: Emission spectra of **DNA-Cy5** being titrated into a solution of **DNA-Cy3** (1 μM). The decrease in emission at 570 nm is indicative of the quenching of the Cy3 fluorescence by Cy5, and the small increase in emission at 660 nm is the result of FRET from the Cy3 to the Cy5. Recorded in sodium phosphate buffer pH 7.0, 100 mM NaCl. λ_{ex} = 554 nm. Spectra have been background-subtracted using a spectrum of **DNA-Cy5** excited at 554 nm to account for the direct excitation of Cy5.

However, whilst the quenching of the Cy3 emission was pronounced, the increase in the Cy5 emission was very small. The quenching of the Cy3 signal implies that at least one part of FRET, the non-radiative transfer of energy from the donor to the acceptor fluorophore, was present. That the subsequent emission from the excited Cy5 was so small may indicate that another quenching process was at play. In a closely related system previously reported by the Tucker group involving Cy3- and Cy5-modified DNA forming a duplex and facilitating FRET, the quenching of the Cy3 emission was similarly pronounced but the increase in emission at 665 nm was much larger.[34] The difference in the system reported here is the presence of unpaired thymines and an alkyne modification near the Cy5 once the duplex has formed, which may affect its emission. Somoza and coworkers reported that unpaired sequences with high

pyrimidine content adjacent to a terminal Cy5 – as is the case here – resulted in significantly less fluorescence than sequences with high purine content,[36] providing an explanation for the smaller than expected increase in Cy5 emission observed. Regardless, the FRET was deemed large enough to be detected using confocal fluorescence microscopy in subsequent experiments.

6.4. MOF Synthesis and Characterisation

A Hf-based MOF and a Zr-based MOF were synthesised. All MOF synthesis and characterisation reported in this thesis was conducted by Dr Sarah Griffin in the Champness group at the University of Birmingham. The Hf and Zr MOFs were UiO-68, a well-studied structure with potential industrial applications.[37] Being the same UiO-68 structure, it could be expected that the Hf and Zr MOFs would have similar properties. However, changing the metal comprising the metal nodes has been shown to change the properties of a MOF[38,39] and therefore the Hf and Zr MOFs synthesised were deemed to be suitable proof-of-concept starting points. UiO-68 MOFs consist of metal-oxo-hydroxo clusters ($M_6O_4(OH)_4$, where M is the metal cation) that form the SBUs. The clusters are linked together by the bridging ligands to form the inner-framework structure of the MOF (Figure 6.14). For the Hf and Zr UiO-68 MOFs used in this work, azide-functionalised dicarboxylate bridging ligands were used in order to facilitate the post-synthetic attachment of Cy3-/Cy5-modified DNA *via* copper-catalysed click chemistry.

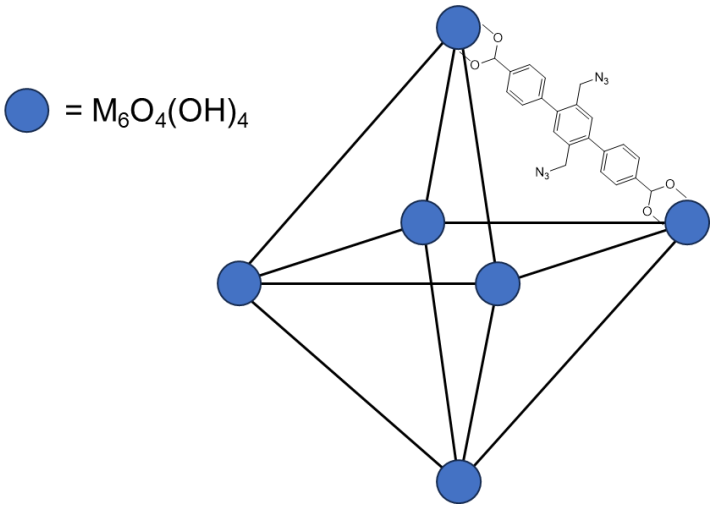

Figure 6.14: Inner-framework structure of the Hf and Zr UiO-68 MOFs used for this work. M = Hf or Zr. One azide-functionalised dicarboxylate bridging ligand is shown.

Powder X-Ray diffraction (PXRD) was used to confirm the structure of the MOFs. Each MOF structure diffracts X-rays in a unique way, with each peak corresponding to a specific set of crystallographic planes within the material.[40] Figure 6.15 shows the measured PXRD pattern of the Hf UiO-68 MOF compared with a simulated pattern of a UiO-68 MOF. The peaks matched well, confirming the UiO-68 structure. Both the Hf and Zr UiO-68 MOFs produced similar PXRD patterns, as changing one atom type for another in a material that otherwise retains its crystal structure will have a minimal impact on the pattern produced.[40]

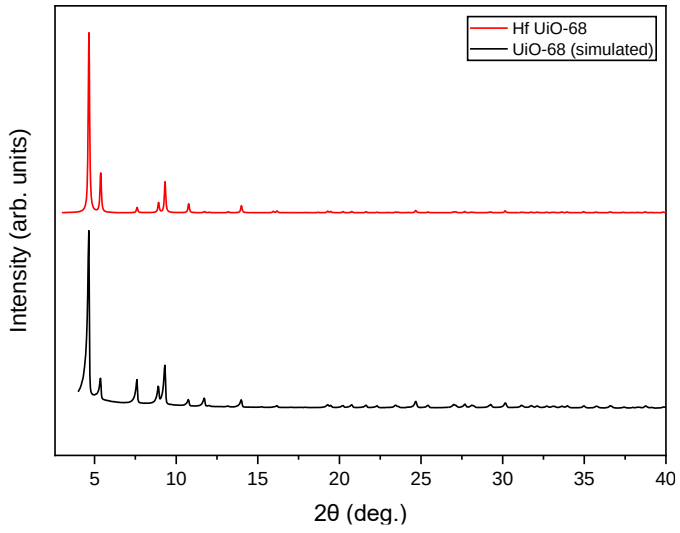

Figure 6.15: PXRD pattern of the Hf UiO-68 MOF synthesised (red) versus the simulated pattern of a UiO-68 MOF (black).

Two crystal sizes of each of the Hf and Zr UiO-68 MOFs were synthesised, a larger version (**Hf-B** and **Zr-B**) and a smaller version (**Hf-S** and **Zr-S**). The smaller versions were synthesised in addition to the larger versions as it was thought that hybridisation between MOF-attached DNA would be more likely to succeed if the MOFs themselves were smaller. The larger versions of each MOF were imaged under a microscope and estimated to be approximately 50–100 µm in size (Figure 6.16, left). The smaller versions of each MOF were imaged using scanning electron microscopy (SEM) and estimated to be approximately 3–10 µm in size (Figure 6.16, right). These sizes were further confirmed by the subsequent confocal microscopy imaging reported below.

Larger MOFs (50–100 µm) imaged using visible light microscopy:

Smaller MOFs (3–10 µm) imaged using SEM:

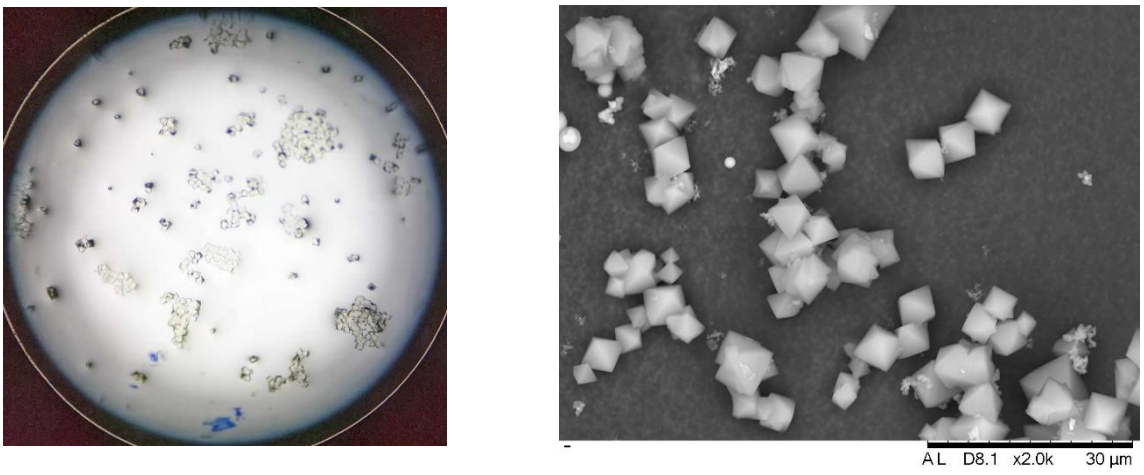

Figure 6.16: Larger version of Hf UiO-68 MOF (**Hf-B**) imaged using visible light microscopy (left) and smaller version of Hf UiO-68 MOF (**Hf-S**) imaged using SEM (right).

6.5. DNA Functionalisation and Confocal Imaging

6.5.1. DNA Functionalisation of MOFs

The MOFs were functionalised using a copper-catalysed azide-alkyne cycloaddition (CuAAC), a type of 'click chemistry' reaction. CuAAC allows for the conjugation of two

groups by the formation of a triazole linker. The reaction is highly selective with only the 1,4-isomer synthesised. Copper acts as a catalyst and is regenerated at the end of a reaction cycle that involves a dicopper mechanism.[41] CuAAC and other click chemistry reactions have been used to modify and functionalise a range of biomolecules, including DNA,[42] peptides,[43] and carbohydrates.[44] For this work, the azide-functionalised dicarboxylate bridging ligands reacted with the alkyne-modified DNA to attach the DNA covalently to the MOF (Scheme 6.1).

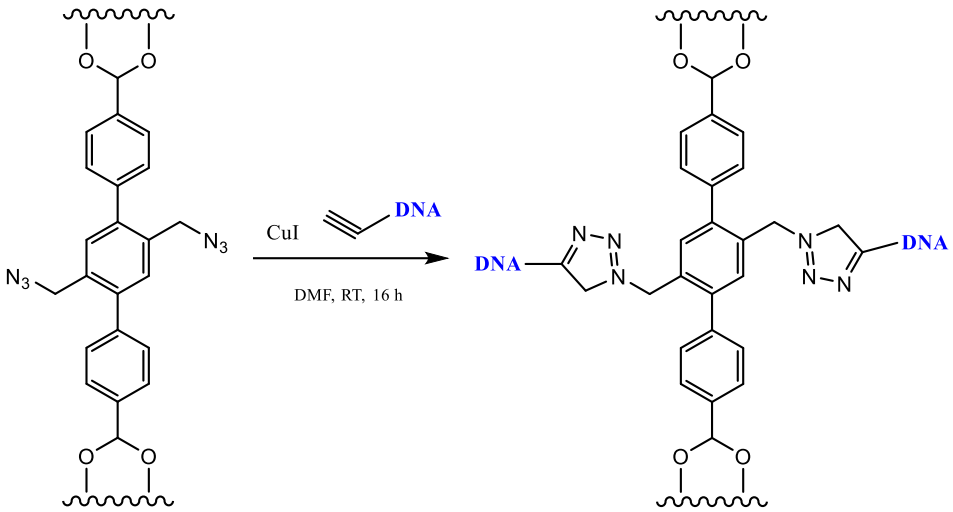

Scheme 6.1: CuAAC of DNA onto the azide-functionalised dicarboxylate bridging ligand.

To confirm that the CuAAC reaction had succeeded and that the DNA had attached, confocal fluorescent microscopy was used to compare control MOFs that had not undergone the functionalisation procedure with MOFs that had been functionalised. All confocal fluorescent microscopy reported in this thesis was conducted by Stanimir Tashev in the Herten group at the University of Birmingham. The unfunctionalised MOFs **Hf-B** and **Zr-B** (A and C in Figure 6.17) show little to no emission when excited with the 532 nm and 640 nm lasers, respectively. These lasers were chosen as their wavelengths were closest to the peak excitation wavelengths of Cy3 (λ_{ex} = 554 nm) and Cy5 (λ_{ex} = 650 nm) out of the lasers available. Conversely, **Hf-B** functionalised with **DNA-Cy3** (B in Figure 6.17) and **Zr-B** functionalised with **DNA-Cy5** (D

and Figure 6.17) showed clear emission from around their edges when excited using the same lasers, indicating successful functionalisation with DNA. As expected, only the edges of the functionalised MOFs were emissive as the DNA was too big to penetrate and attach further in. (However, a confocal image adjusted such that the focal plane passed through the periphery of a functionalised MOF would show a shape filled with emission.) The Hf-based MOFs exhibited small amounts of autofluorescence when excited using the 532 nm laser, as seen in Figure 6.17A.

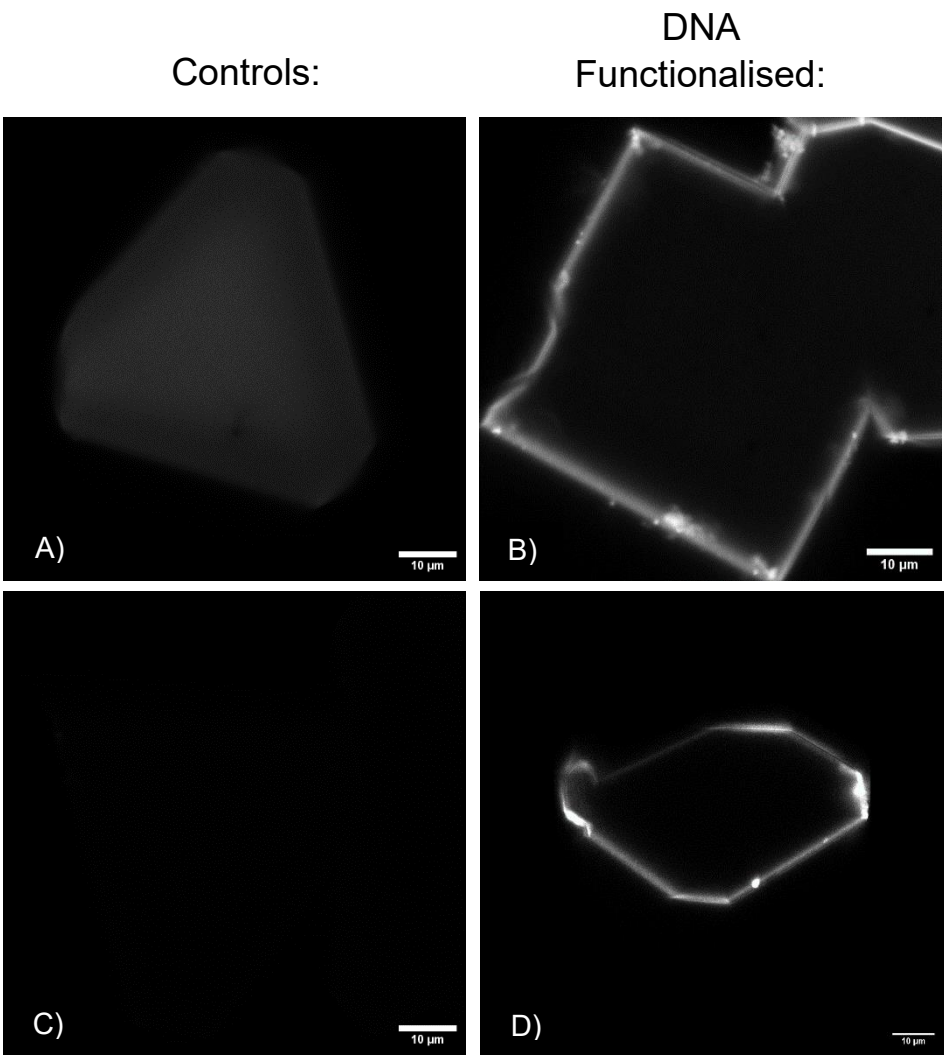

Figure 6.17: Confocal images of unfunctionalised **Hf-B** (A) and **Zr-B** (C), and **DNA-Cy3–Hf-B** (B) and **DNA-Cy5–Zr-B** (D). A and B excited with the 532 nm laser, C and D excited with the 640 nm laser. Emission collected for all images is the total emission.

6.5.2. DNA-Functionalised MOF Binding Efforts

Having confirmed successful functionalisation of the MOFs, efforts then turned to hybridisation. Figure 6.18 shows confocal images of the same area in a sample of **DNA-Cy3**–**Hf-B** mixed with **DNA-Cy5**–**Zr-B** in Milli-Q water containing 100 mM NaCl, excited using different lasers. When excited with the 532 nm laser, emission from a **DNA-Cy3**–**Hf-B** crystal is observed (A); when excited with the 640 nm laser, emission from **DNA-Cy5**–**Zr-B** is observed (B). Image C is a composite of images A and B with false colourings. However, no hybridisation and joining of the MOFs was observed under the confocal microscope. As no joining of MOFs was observed, the presence of FRET was not tested for by exciting with the 532 nm laser and detecting only the fluorescence emitted within the emission range of Cy5.

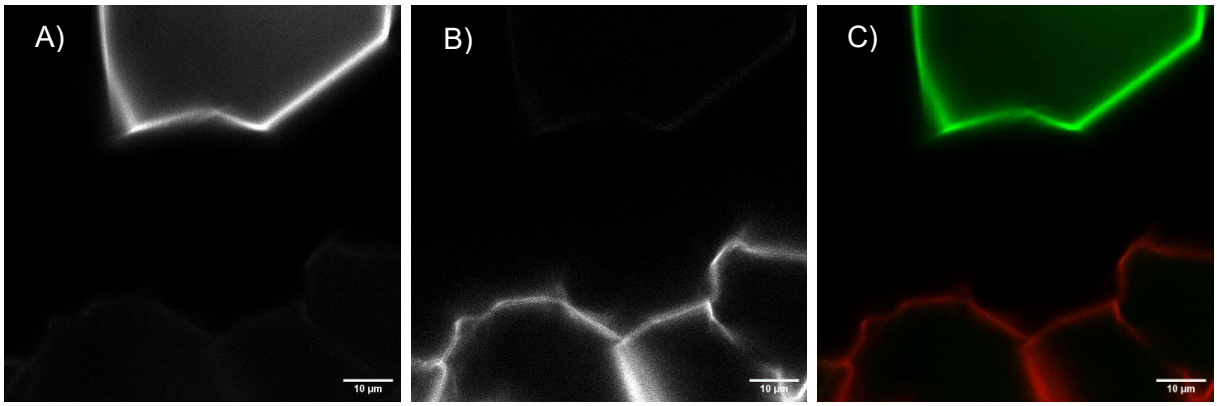

Figure 6.18: Confocal images of the same area in a sample of **DNA-Cy3**–**Hf-B** mixed with **DNA-Cy5**–**Zr-B** (Milli-Q water, 100 mM NaCl), excited using different lasers. A) Excited with the 532 nm laser, showing emission from **DNA-Cy3**–**Hf-B**; B) Excited with the 640 nm laser, showing emission from **DNA-Cy5**–**Zr-B**; C) Composite image combining images A and B, with emission caused by excitation with the 532 nm laser coloured green, and emission caused by excitation with the 640 nm laser coloured red. Emission collected for all images is the total emission.

The main reason proposed for the failed hybridisation between the MOF-attached DNA was that the MOFs used were too big relative to the DNA strands. **DNA-Cy3** and **DNA-Cy5** are at least 6 nm long accounting for the 18 nucleotides alone, whereas the crystals of **Hf-B** and **Zr-B** were typically dozens of µm in size. With their widths of approximately 6–12 µm, combining the smaller functionalised MOFs **Hf-S** and **Zr-S** was thought to increase the likelihood of

successful DNA hybridisation. However, just as with the larger MOFs, no evidence of significant fusing *via* DNA hybridisation was observed between **DNA-Cy3**–**Hf-S** and **DNA-Cy5**–**Zr-S**.

It was then investigated whether hybridisation could be observed between MOF-attached DNA and solution-based DNA. If the MOFs were so large that they inhibited significant DNA hybridisation, then solution-based DNA should be able to freely access the DNA attached to the surface of the MOF and FRET between the Cy3 and Cy5 fluorophores may be observed. Figure 6.19 shows samples of **DNA-Cy3**–**Hf-S** before and after addition of 50 nM solution-based **DNA-Cy5**. Emission was either measured in the green range (545–620 nm, corresponding to Cy3 emission) or the red range (650–720 nm, corresponding to Cy5 emission). For the images recorded after **DNA-Cy5** addition, each sample was washed to ensure that any free-floating (*i.e.*, non-duplexed) **DNA-Cy5** had been removed prior to imaging. Exciting with the 532 nm laser caused the MOF-attached Cy3 to fluoresce both before and after addition of the **DNA-Cy5** (images A and B in Figure 6.19). Exciting with the 640 nm laser prior to addition of the **DNA-Cy5** resulted in no emission, as there was no Cy5 to excite (image C in Figure 6.19). Exciting with the 640 nm laser after addition of the **DNA-Cy5** resulted in significant emission, indicating that the **DNA-Cy5** had hybridised with the MOF-attached **DNA-Cy3** (image D in Figure 6.19). These experiments showed that MOF-attached DNA could hybridise with complementary solution-based DNA, and that it was likely that the sheer bulk of the MOFs had previously inhibited any significant hybridisation between the MOF-attached **DNA-Cy3** and MOF-attached **DNA-Cy5**.

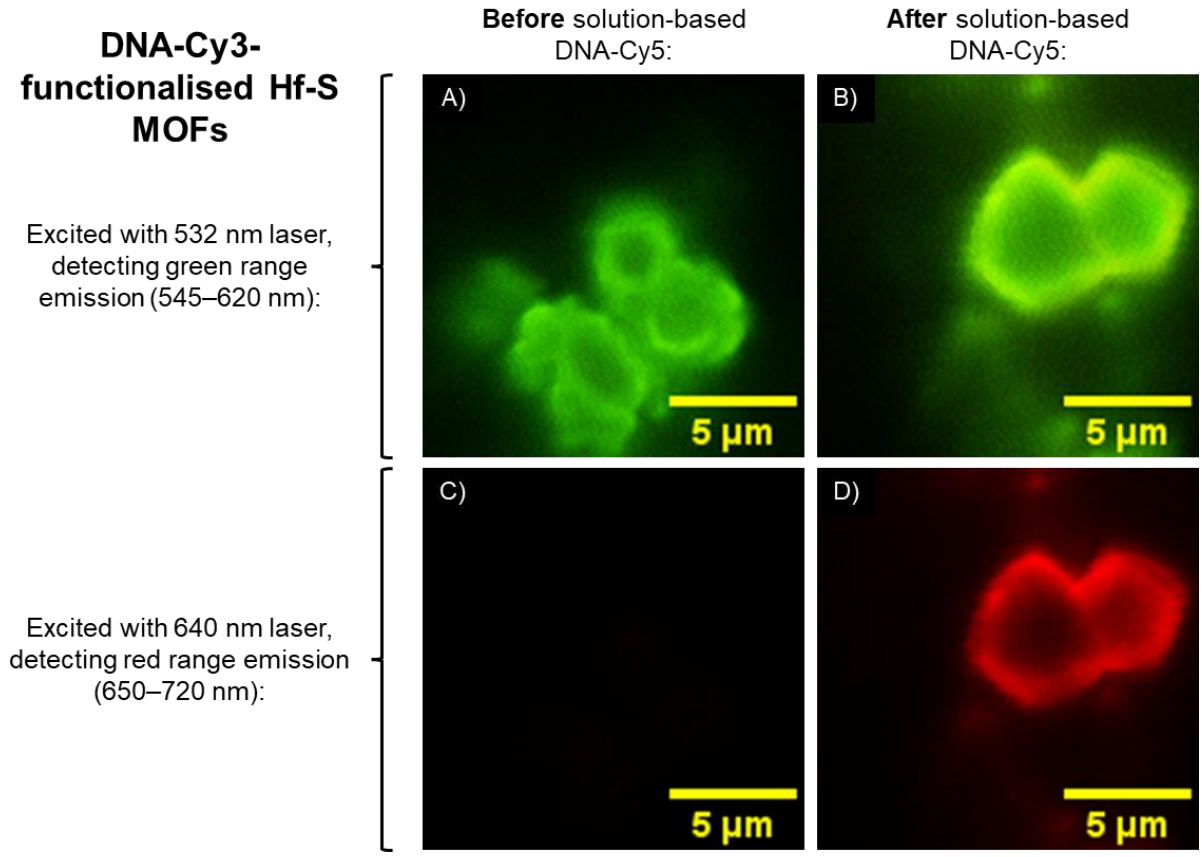

Figure 6.19: Confocal images of **DNA-Cy3–Hf-S**. Images A and C were taken before addition of solution-based **DNA-Cy5**; images B and D were recorded after addition of 50 nM solution-based **DNA-Cy5**. Images A and B show emission in the green range (mostly Cy3 emission) caused by excitation with the 532 nm laser. As expected, the Cy3 in the **DNA-Cy3** attached to the **Hf-S** produced significant emission. Images C and D show the emission in the red range (Cy5 emission) caused by excitation with the 640 nm laser. In image C, no emission is observed as no **DNA-Cy5** is present. In image D, emission is observed from the **DNA-Cy5** that has hybridised with the MOF-attached **DNA-Cy3**. MOF samples were washed after addition of the solution-based **DNA-Cy5** to remove free-floating DNA.

Evidence of FRET across these MOF-attached **DNA-Cy3**–**DNA-Cy5** duplexes was also investigated. Figure 6.20 shows confocal images of **DNA-Cy3**–**Hf-S** before (image A) and after (image B) addition of solution-based **DNA-Cy5**. As before, samples were washed after the addition of **DNA-Cy5** to remove any non-duplexed DNA. Emission in the red range was measured whilst exciting with the 532 nm laser. The emission observed in image A is the result of the small amount of emission released by Cy3 in the red region of the spectrum, as was observed in the solution fluorescence experiments described in section 6.3.3 (Figure 6.12). The relatively more intense emission observed in image B is a combination of three different processes. Firstly, there is the aforementioned small amount of Cy3 emission that falls within

the red range. Secondly, there is the small amount of Cy5 emission caused by direct excitation with the 532 nm laser, which again was observed in the solution fluorescence experiments. Thirdly, there is FRET caused by Cy3 being excited and transferring energy to Cy5 that subsequently emits fluorescence in the red range.

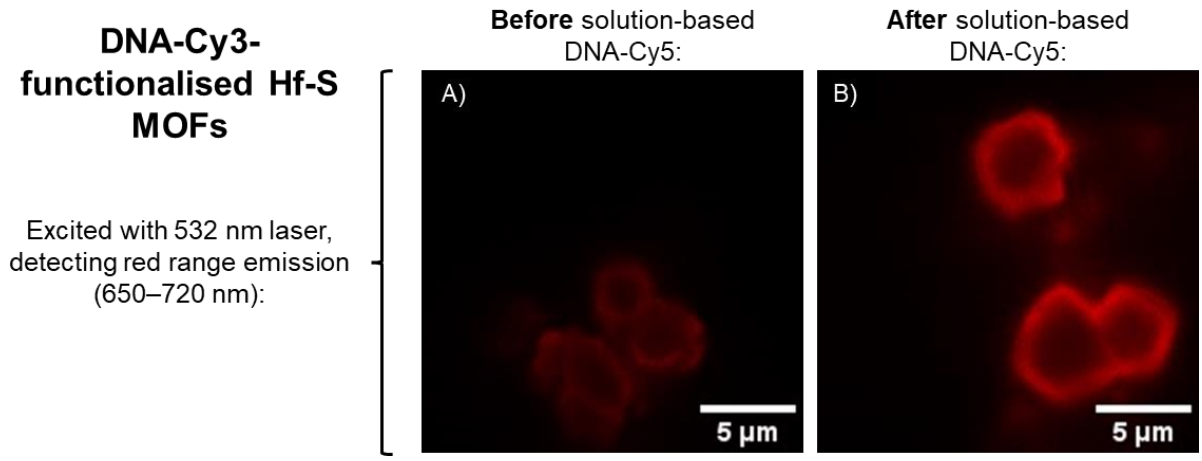

Figure 6.20: Confocal images of **DNA-Cy3–Hf-S** excited using the 532 nm laser and detecting the emission in the red range. Image A was recorded before solution-based **DNA-Cy5** was added and image B was recorded after solution-based **DNA-Cy5** was added (and any free-floating **DNA-Cy5** was washed away). The emission observed in image A is caused by the small amount of emission released in the red range by excitation of Cy3. The relatively more intense emission observed in image A is a combination of the aforementioned Cy3 emission, the small amount of Cy5 emission caused by direct excitation with the 532 nm laser, and Cy3 → Cy5 FRET.

Figure 6.21 shows a quantitative comparison between the ratio of emission in the red range to emission in the green range before and after addition of solution-based **DNA-Cy5** to **DNA-Cy3**–**Hf-S** MOFs. For each data set, the emission from nine separate images was measured. Matching what can be visually seen in Figure 6.20, the ratio of red range emission to green range emission increases after addition of the solution-based **DNA-Cy5** because of the reasons outlined above. However, it is hard to attribute how much of the increased red range emission is attributable to Cy3 → Cy5 FRET versus direct excitation of Cy5 with the 532 nm laser. Unlike the solution fluorescence experiments, it was not possible to create a comparable sample and background-subtract the emission produced by direct excitation of Cy5 with the 532 nm

laser. If the increase in Cy5 emission caused by FRET had been more pronounced, as was seen previously in similar Cy3-/Cy5-modified oligonucleotides to the ones used for this work,[34] then more of the increase in red range emission could be confidently attributed to Cy3 → Cy5 FRET. However, given that FRET was observed in the solution fluorescence experiments, it is reasonable to conclude that a significant portion of the increased Cy5 emission is attributable to Cy3 → Cy5 FRET.

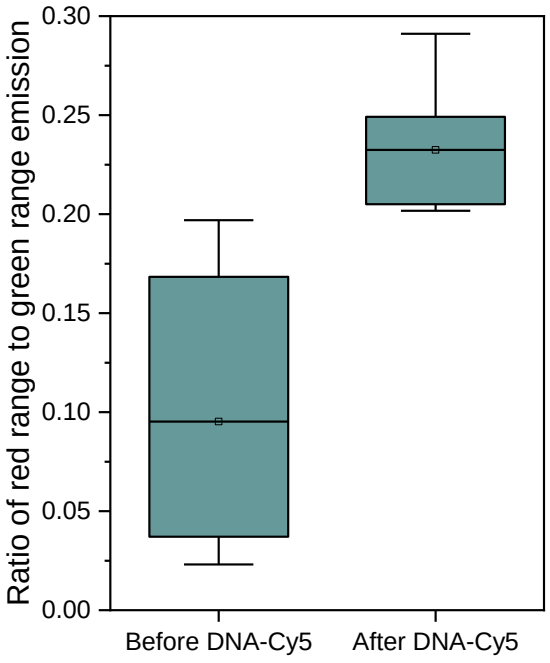

Figure 6.21: Box plots depicting the ratio of red range emission (650–720 nm) to green range emission (545–620 nm) for **DNA-Cy3–Hf-S** MOFs excited with the 532 nm laser before and after addition of solution-based **DNA-Cy5**. The data for each column consist of the emission measured for at least nine separate images. Each box represents the range in which the middle 25–75 % of values resided for each column, with the minimum/maximum ranges of values represented by the extending bars. The internal lines within each box represent the mean.

6.6. Conclusions and Future Work

Hf- and Zr-based MOFs were successfully functionalised with fluorescently-modified DNA using copper-catalysed click chemistry. Evidence of Cy3 → Cy5 FRET occurring across a MOF-attached duplex was also produced, which is the first example of DNA-functionalised

MOFs facilitating FRET reported in the literature. However, the binding together of different MOFs *via* DNA hybridisation and to confirm this using FRET was not achieved. The most likely reason for this is that the MOF crystals were too large relative to the functionalising DNA. Even the smaller MOF crystals used (**Hf-S** and **Zr-S**) were thousands of times larger than the functionalising **DNA-Cy3** and **DNA-Cy5** oligonucleotides. Due to time constraints, the longer **DNA-Cy3-Ext** and **DNA-Cy5-Ext** oligonucleotides were not studied. The next step should be to functionalise the **Hf-S** and **Zr-S** MOFs with the **DNA-Cy3-Ext** and **DNA-Cy5-Ext** oligonucleotides and determine whether the extra length can accommodate some binding between the MOF crystals. It is noteworthy that all of the reports discussed in section 6.1.3. detailing the binding of MOFs to gold nanoparticles or other same-type MOF crystals *via* DNA hybridisation exclusively employed nanosized MOF crystals. Future work could also involve the synthesis and DNA-functionalisation of MOF nanoparticles, with the aim of creating a heterogenous MOF structure interconnected by duplexed DNA. Fluorescently-modified DNA can still be used to confirm successful hybridisation of the MOF-attached DNA. However, optimisation of the DNA sequences should be undertaken. In particular, the replacement of unpaired pyrimidines with unpaired purines near to the Cy5 in the resultant duplex may aid in enhancing Cy5 FRET emission as per Somoza and coworkers' report.[36] Other FRET pairs could also be used in an attempt to maximise FRET emission.

6.7. References

1. H. Furukawa, K. E. Cordova, M. O'Keeffe and O. M. Yaghi, *Science*, 2013, DOI: 10.1126/science.1230444.
2. S. Kitagawa, *Chem. Soc. Rev.*, 2014, **43**, 5415-5418.
3. O. K. Farha, I. Eryazici, N. C. Jeong, B. G. Hauser, C. E. Wilmer, A. A. Sarjeant, R. Q. Snurr, S. T. Nguyen, A. O. z. r. Yazaydın and J. T. Hupp, *J. Am. Chem. Soc.*, 2012, **134**, 15016-15021.
4. B. F. Hoskins and R. Robson, *J. Am. Chem. Soc.*, 1989, **111**, 5962-5964.
5. O. M. Yaghi, G. Li and H. Li, *Nature*, 1995, **378**, 703-706.
6. P. Z. Moghadam, A. Li, X.-W. Liu, R. Bueno-Perez, S.-D. Wang, S. B. Wiggin, P. A. Wood and D. Fairen-Jimenez, *Chem. Sci.*, 2020, **11**, 8373-8387.
7. H. D. Lawson, S. P. Walton and C. Chan, *ACS Appl. Mater. Interfaces*, 2021, **13**, 7004-7020.
8. M. Mon, R. Bruno, J. Ferrando-Soria, D. Armentano and E. Pardo, *J. Mater. Chem. A*, 2018, **6**, 4912-4947.
9. N. A. Khan, Z. Hasan and S. H. Jhung, *J. Hazard. Mater.*, 2013, **244**, 444-456.
10. J.-R. Li, R. J. Kuppler and H.-C. Zhou, *Chem. Soc. Rev.*, 2009, **38**, 1477-1504.
11. G. L. Yang, X. L. Jiang, H. Xu and B. Zhao, *Small*, 2021, **17**, 2005327.
12. Y. Peng, H. Huang, Y. Zhang, C. Kang, S. Chen, L. Song, D. Liu and C. Zhong, *Nat. Commun.*, 2018, **9**, 187.
13. H. Furukawa, F. Gandara, Y.-B. Zhang, J. Jiang, W. L. Queen, M. R. Hudson and O. M. Yaghi, *J. Am. Chem. Soc.*, 2014, **136**, 4369-4381.
14. S. Ma, X. S. Wang, D. Yuan and H. C. Zhou, *Angew. Chem.*, 2008, **120**, 4198-4201.
15. M. Kumar, A. Gogoi, D. Kumari, R. Borah, P. Das, P. Mazumder and V. K. Tyagi, *J. Hazard., Toxic Radioact. Waste*, 2017, DOI: 10.1061/(ASCE)HZ.2153-5515.0000351.
16. A. Corma, H. Garcia and F. Llabrés i Xamena, *Chem. Rev.*, 2010, **110**, 4606-4655.
17. D. Yang and B. C. Gates, *ACS Catal.*, 2019, **9**, 1779-1798.
18. L. R. Redfern, Z. Li, X. Zhang and O. K. Farha, *ACS Appl. Nano Mater.*, 2018, **1**, 4413-4417.
19. S. P. Desai, J. Ye, J. Zheng, M. S. Ferrandon, T. E. Webber, A. E. Platero-Prats, J. Duan, P. Garcia-Holley, D. M. Camaioni and K. W. Chapman, *J. Am. Chem. Soc.*, 2018, **140**, 15309-15318.

20. J. Canivet, S. Aguado, Y. Schuurman and D. Farrusseng, *J. Am. Chem. Soc.*, 2013, **135**, 4195-4198.
21. C. A. Trickett, T. M. Osborn Popp, J. Su, C. Yan, J. Weisberg, A. Huq, P. Urban, J. Jiang, M. J. Kalmutzki and Q. Liu, *Nat. Chem.*, 2019, **11**, 170-176.
22. E. Rahmani and M. Rahmani, *Microporous Mesoporous Mater.*, 2017, **249**, 118-127.
23. Y. Tran, P. T. Nguyen, Q. T. Luong and K. D. Nguyen, *Inorg. Chem.*, 2020, **59**, 16747-16759.
24. S. Mandal, S. Natarajan, P. Mani and A. Pankajakshan, *Adv. Funct. Mater.*, 2021, **31**, 2006291.
25. W. Morris, W. E. Briley, E. Auyeung, M. D. Cabezas and C. A. Mirkin, *J. Am. Chem. Soc.*, 2014, **136**, 7261-7264.
26. J. S. Kahn, L. Freage, N. Enkin, M. A. A. Garcia and I. Willner, *Adv. Mater.*, 2017, **29**, 1602782.
27. S. Wang, Y. Chen, S. Wang, P. Li, C. A. Mirkin and O. K. Farha, *J. Am. Chem. Soc.*, 2019, **141**, 2215-2219.
28. W. Ning, Z. Di, Y. Yu, P. Zeng, C. Di, D. Chen, X. Kong, G. Nie, Y. Zhao and L. Li, *Small*, 2018, **14**, 1703812.
29. L. He, M. Brasino, C. Mao, S. Cho, W. Park, A. P. Goodwin and J. N. Cha, *Small*, 2017, **13**, 1700504.
30. S. Wang, S. S. Park, C. T. Buru, H. Lin, P.-C. Chen, E. W. Roth, O. K. Farha and C. A. Mirkin, *Nat. Commun.*, 2020, **11**, 2495.
31. R. M. Clegg, *Laboratory Techniques in Biochemistry and Molecular Biology*, Elsevier, 2009, vol. 33, ch. 1, pp. 1-57.
32. P. Jothikumar, V. Hill and J. Narayanan, *Biotechniques*, 2009, **46**, 519-524.
33. R. A. Cardullo, S. Agrawal, C. Flores, P. C. Zamecnik and D. E. Wolf, *Proc. Natl. Acad. Sci. U. S. A.*, 1988, **85**, 8790-8794.
34. R. A. Bamford, Z.-y. Zhao, N. A. Hotchin, I. B. Styles, G. B. Nash, J. H. Tucker and R. Bicknell, *PLoS One*, 2014, DOI: 10.1371/journal.pone.0095097.
35. B. G. Moreira, Y. You and R. Owczarzy, *Biophys. Chem.*, 2015, **198**, 36-44.
36. N. Kretschy, M. Sack and M. M. Somoza, *Bioconjugate Chem.*, 2016, **27**, 840-848.
37. X. Ye and D. Liu, *Cryst. Growth Des.*, 2021, **21**, 4780-4804.

38. S. Abednatanzi, P. G. Derakhshandeh, H. Depauw, F.-X. Coudert, H. Vrielinck, P. Van Der Voort and K. Leus, *Chem. Soc. Rev.*, 2019, **48**, 2535-2565.
39. M. Lalonde, W. Bury, O. Karagiaridi, Z. Brown, J. T. Hupp and O. K. Farha, *J. Mater. Chem. A*, 2013, **1**, 5453-5468.
40. S. A. Speakman, http://prism.mit.edu/xray/education/reading.html, (accessed June 2023).
41. V. O. Rodionov, V. V. Fokin and M. Finn, *Angew. Chem.*, 2005, **117**, 2250-2255.
42. A. H. El-Sagheer and T. Brown, *Chem. Soc. Rev.*, 2010, **39**, 1388-1405.
43. A. A. Ahmad Fuaad, F. Azmi, M. Skwarczynski and I. Toth, *Molecules*, 2013, **18**, 13148-13174.
44. X.-P. He, Y.-L. Zeng, Y. Zang, J. Li, R. A. Field and G.-R. Chen, *Carbohydr. Res.*, 2016, **429**, 1-22.

Chapter 7: Experimental

7.1. Chemical Syntheses

All chemicals and reagents were purchased from commercial suppliers and were used without further purification, unless otherwise stated. Column chromatography was performed using Merck grade 60 silica gel. NMR spectra were obtained on Bruker AVIII300 and AVIII400 spectrometers. NMR data were analysed using MestReNova v12.0.4.22023. Mass spectrometry data were obtained using Micromass LCT Electrospray Time-of-Flight or Synapt G2S spectrometers. IR data were obtained using a Varian 660-IR FT-IR spectrometer.

7.1.1. Copper Cyclidene Phosphoramidite Synthesis

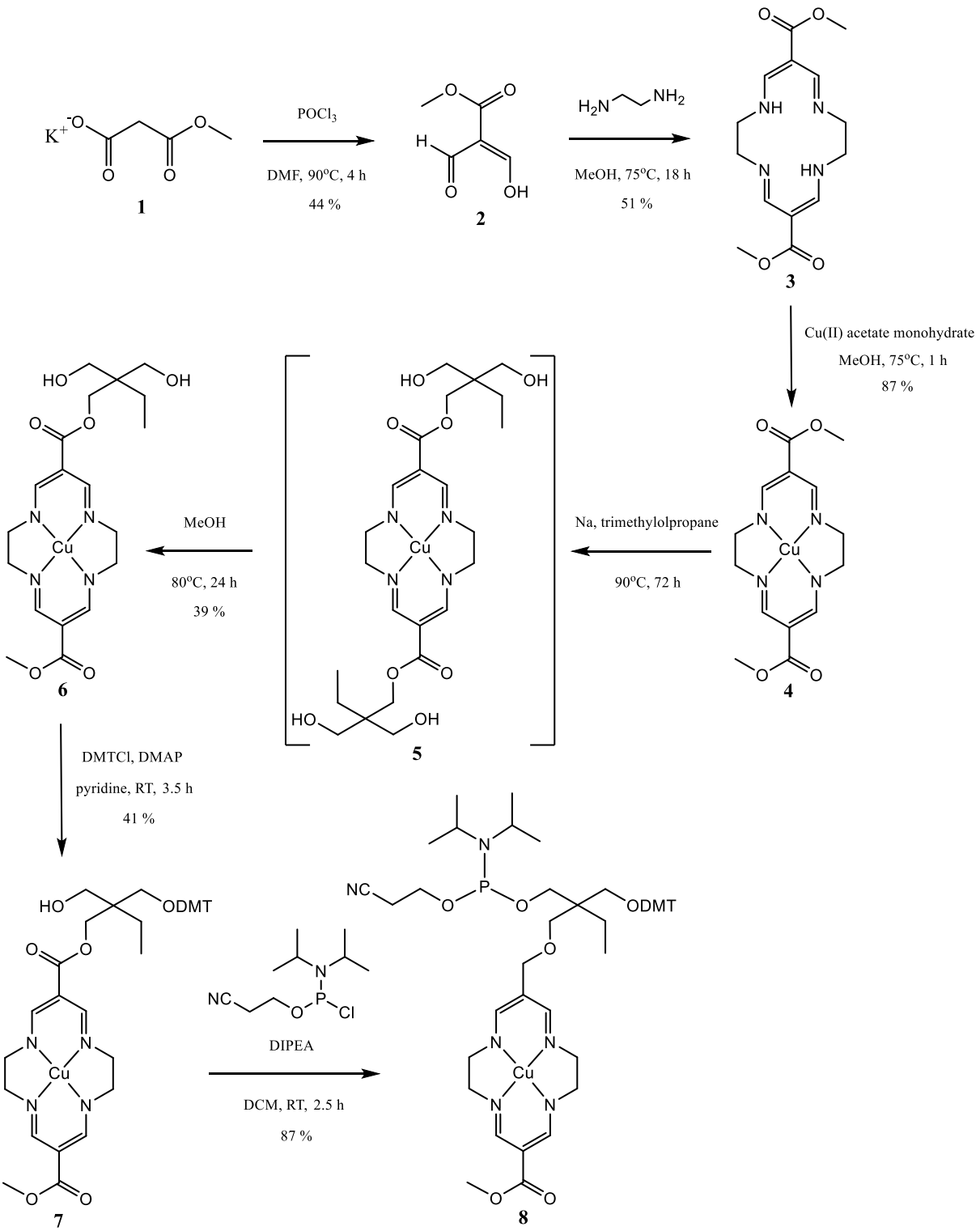

Methyl Diformylacetate (2)

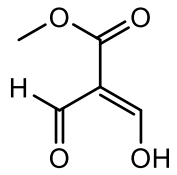

Known compound; characterisation matches literature data.[1] Phosphorus oxychloride (8.95 mL, 0.01 mol) was added dropwise to dry DMF (50 mL) before **1** (5.00 g, 32 mmol) was added in 10 equal portions over 30 min. The reaction mixture was heated at 90 °C at reflux for 4 hours. DMF was removed *via* vacuum distillation (vapours 55–60 °C) leaving a dark brown liquid. Ice (100 g) was added to the mixture, which was basified using saturated K_2CO_3 solution to pH 11. The resultant mixture was left to stir at RT for 16 hours. The mixture was washed with ethyl acetate (4 × 150 mL) and the organic residue removed before being saturated with KCl. Ice (50 g) was added, followed by cooling in an ice bath. The reaction mixture was acidified to pH 1 using conc. hydrochloric acid. Extraction using diethyl ether (10 × 200 mL) was conducted. 75% of the solvent was removed *in vacuo* and the remainder was washed with saturated aqueous KCl solution (100 mL). The reaction mixture was dried over Na_2SO_4 for 1 h and then filtered before the remaining solvent was removed *in vacuo* to leave a red-brown oil. Vacuum distillation produced the product **2** (vapours 58–60 °C) as a colourless liquid at RT (1.84 g, 14.2 mmol, 44%). ^{1}H NMR (300 MHz, $CDCl_3$): δ 12.22 (broad, 1H, O***H***), 9.06 (s, 2H, C***H***OC=C***H***), 3.75 (s, 3H, C***H***$_3$). ^{13}C NMR (101 MHz, $CDCl_3$): δ 186.5 (H***C***=O), 175.3 (C=***C***OH), 164.9 (***C***=O), 109.3 (***C***=COH), 51.7 (O***C***H$_3$). Mass spectrometry (MS) (TOF EI −ve) (*m/z*) calculated for $C_5H_6O_4$: 130.03 [M]; found: 130.02 [M], 129.02 $[M\text{-}H]^-$.

Cyclidene Macrocycle (3)

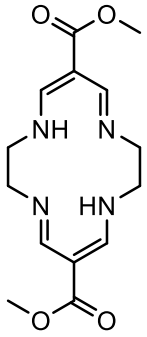

Known compound; characterisation matches literature data.[2] **2** (1.80 g, 13.9 mmol) was dissolved in dry methanol (50 mL). Ethylene diamine (1.04 mL, 15.6 mmol) was added dropwise. The reaction mixture was heated at 70 °C at reflux for 18 h under argon. Methanol was removed *in vacuo* leaving a honey-coloured oil, which was subsequently redissolved in a minimal amount of dry methanol and kept at –20 °C overnight. Recrystallised product **3**, in the form of cream-white crystals, was harvested *via* vacuum filtration (1.11 g, 3.61 mmol, 51%). ^{1}H NMR (300 MHz, $CDCl_3$): δ 12.62 (s, 2H, N***H***), 8.32 (d, *J* = 6.0 Hz, 4H, ***H***C=CC***H***), 3.75 (s, 6H, C***H***$_3$), 3.61 (s, 8H, C***H***$_2$C***H***$_2$). ^{13}C NMR (101 MHz, $CDCl_3$): δ 168.5 (***C***=O), 157.8 (H***C***=C***C***H), 94.9 (HC=***C***CH), 53.5 (N***C***H_2***C***H_2N), 50.8 (O***C***H_3). MS (TOF EI+) (*m/z*) calculated for $C_{14}H_{20}O_4N_4$: 308.15 [M]; found: 309.16 $[M+H]^+$.

Copper Cyclidene Macrocycle (4)

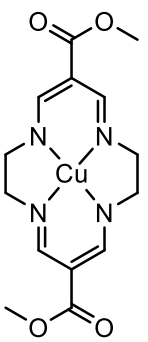

Known compound; characterisation matches literature data.[3] **3** (0.938 g, 3.04 mmol) was dissolved in dry methanol (75 mL) before copper acetate monohydrate (0.663 g, 3.32 mmol) was added. The reaction mixture was heated at 75 °C at reflux under argon for 1 h. Methanol was removed *in vacuo* and the crude product was redissolved in DCM (30 mL). The solution was washed with water (30 mL) and the organic phase dried over $MgSO_4$ and then filtered. DCM was removed *in vacuo* to produce **4** as dark pink crystals (0.976 g, 2.64 mmol, 87%). R_f = 0.49 (DCM w/ 5% methanol). MS (TOF EI+) (*m/z*) calculated for $C_{14}H_{18}N_4O_4Cu$: 369.06 [M]; found: 370.07 $[M+H]^+$.

Copper Cyclidene Diol (6)

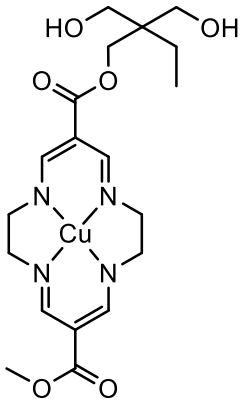

Known compound; characterisation matches literature data.[4] **4** (0.621 g, 1.68 mmol) was added to molten trimethylolpropane (23.1 g, 0.17 mol, m.p. 58 °C). Elemental sodium (0.41 g, 18 mmol) was added to the reaction mixture. After reacting at 90 °C at reflux under argon for 72 h the intermediate **5** was produced, evidenced by a single spot on a thin layer chromatography plate. The reaction mixture was allowed to cool to RT and methanol (16.5 mL, 0.41 mol) added, before being heated to 80 °C and refluxed for 24 h. The reaction mixture was quenched with water (66 mL) followed by ice-water (266 mL), before being left in the refrigerator at 4 °C overnight. A pink precipitate was collected by vacuum filtration and purified with column chromatography (silica; starting at 96:3:1 DCM:MeOH:NEt_3, finishing at 89:10:1

DCM:MeOH:NEt_3), collecting the second band to yield **6** as a pink solid (0.307 g, 0.65 mmol, 39%). R_f = 0.32 (DCM w/ 5% methanol). MS (TOF EI+) (*m/z*) calculated for $C_{19}H_{28}O_6N_4Cu$: 471.13 [M]; found: 472.14 $[M+H]^+$, 494.12 $[M+Na]^+$.

Monotrityl Copper Cyclidene Alcohol (7)

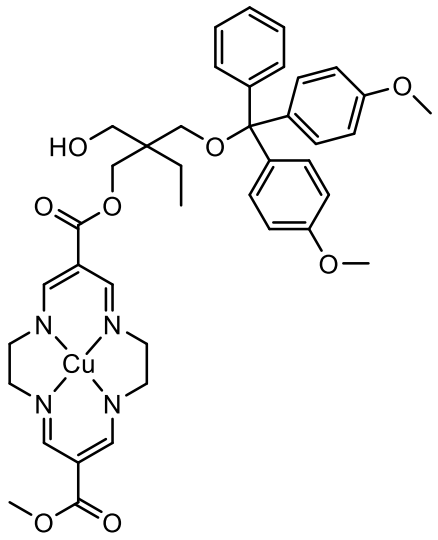

Known compound; characterisation matches literature data.[4] **6** (0.289 g, 0.61 mmol) was dissolved in dry pyridine (10 mL). 4-dimethylaminopyridine (0.011 g, 0.09 mmol) was added, followed by 4,4′-dimethoxytrityl chloride (0.251 g, 0.74 mmol) in 4 equal portions over 10 min. The reaction mixture was stirred at RT for 3.5 h under argon. Pyridine was removed *in vacuo* by coelution with toluene (3 × 10 mL). The crude product was purified with column chromatography (silica; 5:3 ethyl acetate:hexane w/ 1% NEt_3), collecting the second band to yield **7** as a red, foamy oil (0.194 g, 0.25 mmol, 41%). R_f = 0.27 (1:1 ethyl acetate:hexane). MS (TOF EI+) (*m/z*) calculated for $C_{40}H_{46}O_8N_4Cu$: 773.26 [M]; found: 773.26 $[M]^+$, 796.25 $[M+Na]^+$.

Monotrityl Copper Cyclidene Phosphoramidite (8)

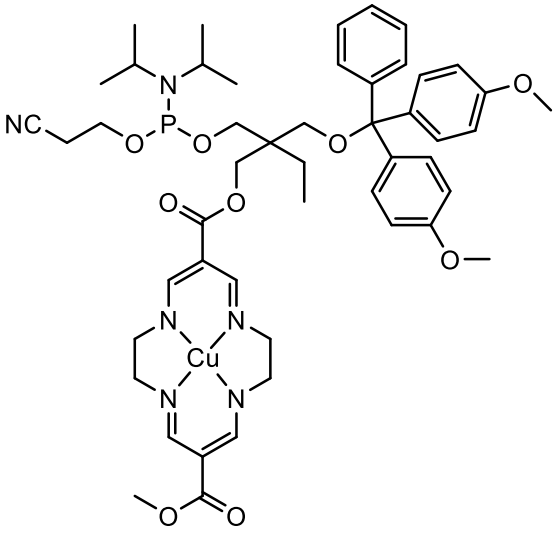

Known compound; characterisation matches literature data.[4] **7** (0.193 g, 0.25 mmol) was dissolved in dry DCM (10 mL). The solvent was removed *in vacuo* and this process was repeated twice before **7** was redissolved in dry DCM (10 mL). The reaction mixture was deoxygenated with argon and *N*,*N*-diisopropylethylamine (0.19 mL, 1.09 mmol) was added dropwise. 2-cyanoethoxy-*N*,*N*-diisopropylaminochlorophosphine (0.08 mL, 0.36 mmol) was added dropwise and the reaction mixture was stirred at RT for 2.5 hours under argon. The reaction was quenched with deoxygenated ethyl acetate (32 mL) and the resulting solution was washed with deoxygenated saturated $NaHCO_3$ solution (20 mL) and then deoxygenated brine (20 mL). The washed reaction mixture was dried over Na_2SO_4 and the desiccant filtered before the solvent was removed *in vacuo*. The crude product was purified with column chromatography using deoxygenated solvents (silica; 1:1 ethyl acetate:hexane w/ 1% NEt_3), collecting the one band to yield **8** as a red foamy oil (0.211 g, 0.22 mmol, 87%). R_f = 0.39 (1:1 ethyl acetate:hexane). Infrared (IR, cm^{-1}) υ: 2930 m (CH), 1736 w (CN), 1677 m (C=O). MS (TOF EI+) (*m/z*) calculated for $C_{49}H_{63}O_9N_4Cu$: 973.37 [M]; found: 973.37 $[M]^+$, 996.36 $[M+Na]^+$.

7.1.2. Ferrocene Phosphoramidite Synthesis

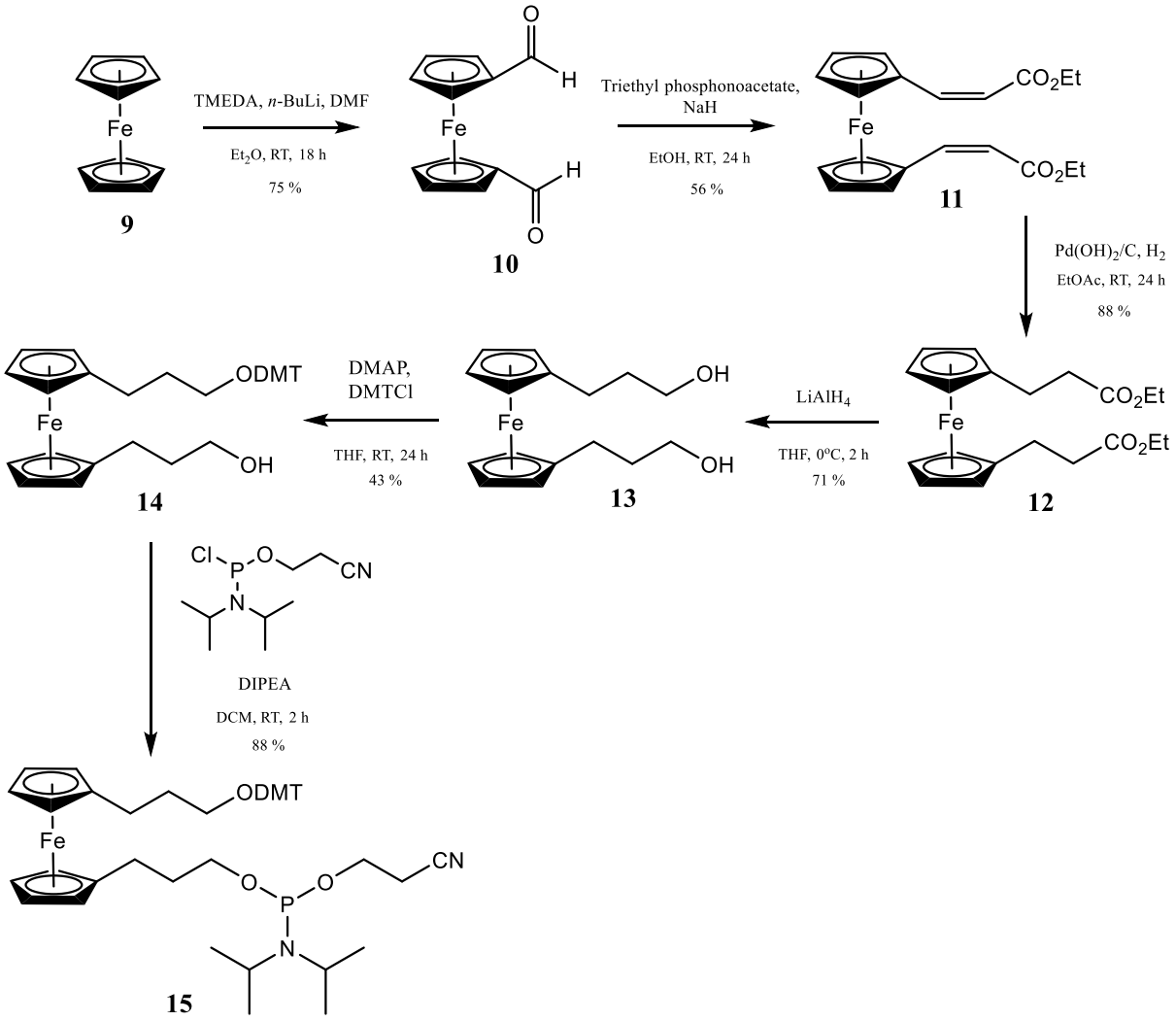

1,1-Bisformyl Ferrocene (10)

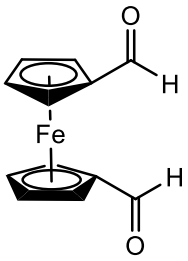

Known compound; characterisation matches literature data.[5] **9** (3.0 g, 16 mmol) was dissolved in dry diethyl ether (25 mL) and tetramethylethylenediamine (5.8 mL, 39 mmol) was

added to the solution. *n*-Butyllithium in hexane (2.5 M, 16.7 mL, 41.9 mmol) was added dropwise to the reaction mixture under argon. The reaction mixture was stirred at RT for 16 h under argon. The reaction mixture was cooled to –78 ºC before dry DMF (5.5 mL, 71 mmol) was added dropwise, followed by stirring for 10 min. The reaction mixture was allowed to warm to RT, followed by stirring for 2 h. The reaction was quenched with brine (20 mL) followed by extraction using DCM (3 × 20 mL), with the combined extractions dried over $MgSO_4$ before the desiccant was filtered. The crude product was purified with column chromatography (silica; 1:1 ethyl acetate:hexane), collecting the second band to yield **2** as a brown-red solid (2.91 g, 12.0 mmol, 75%). ^{1}H NMR (400 MHz, $CDCl_3$): δ 9.95 (s, 2H, C***H***O), 4.89 (t, *J* = 2.0 Hz, 4 H, Fc C***H***), 4.68 (t, *J* = 2.0 Hz, 4H, Fc C***H***). ^{13}C NMR (101 MHz, $CDCl_3$): δ 192.9 (***C***=O), 80.3 (Fc ***C***C=O), 74.2 (Fc ***C***H), 70.9 (Fc ***C***H). MS (TOF EI+) (*m/z*) calculated for $C_{12}H_{10}FeO_2$: 242.00 [M]; found: 242.29 $[M]^+$.

Ferrocene Unsaturated Diester (11)

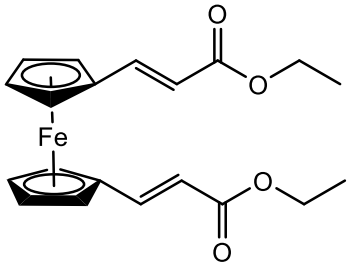

Known compound; characterisation matches literature data.[5] Triethyl phosphonoacetate (3.6 mL, 18 mmol) was dissolved in dry ethanol (10 mL). NaH (0.954 g, 35.8 mmol) was added to the solution under argon and the reaction mixture was stirred at RT for 2 h. **10** (1.44 g, 5.97 mmol) was dissolved in dry ethanol (10 mL) and the solution was added to the reaction mixture before being left to stir at RT for 23 h. The reaction mixture was quenched with water (15 mL). Extraction using ethyl acetate (5 × 10 mL) was conducted, with the organic components

combined and dried over $MgSO_4$ before the desiccant was filtered. The solvent was removed *in vacuo* and the crude product was purified with column chromatography (silica; 2:1 hexane:ethyl acetate), collecting the first band to yield **11** as a deep red solid (1.28 g, 3.34 mmol, 56%). ^{1}H NMR (400 MHz, $CDCl_3$): δ 7.40 (d, *J* = 15.8 Hz, 2H, Fc CC***H***), 5.98 (d, *J* = 15.8 Hz, 2H, C***H***CO_2), 4.45 (t, *J* = 1.9 Hz, 4H, Fc C***H***), 4.38 (t, *J* = 1.9 Hz, 4H, Fc C***H***), 4.22 (q, *J* = 7.1 Hz, 4H, OC***H***$_2$), 1.33 (t, *J* = 7.1 Hz, 6H, C***H***$_3$). ^{13}C NMR (101 MHz, $CDCl_3$): δ 166.9 (***C***=O), 144.0 (Fc C–***C***H=CH), 116.3 (Fc C–CH=***C***H), 80.0 (Fc ***C***–CH), 72.3 (Fc ***C***H), 69.8 (Fc ***C***H), 60.3 (O***C***H_2CH_3), 14.3 (***C***H_3). MS (TOF ASAP+) (*m/z*) calculated for $C_{20}H_{22}FeO_4$: 382.09 [M]; found: 382.09 [M^+].

Ferrocene Saturated Diester (12)

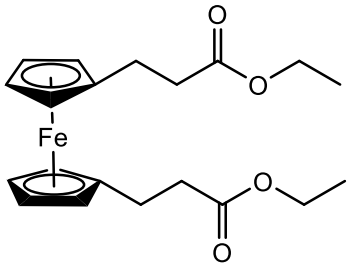

Known compound; characterisation matches literature data.[5] **11** (1.24 g, 3.23 mmol) was dissolved in dry ethyl acetate (20 mL). $Pd(OH)_2$ (5% wt. on carbon, 0.5 g) was added to the solution. The reaction mixture was stirred at RT for 22 h under a H_2 atmosphere. The reaction mixture was filtered through celite, dried over $MgSO_4$, and filtered again using filter paper. The solvent was removed *in vacuo* to yield **12** as an orange oil (1.10 g, 2.85 mmol, 88%). ^{1}H NMR (400 MHz, $CDCl_3$): δ 4.14 (q, *J* = 7.1 Hz, 4H, OC***H***$_2$), 4.01 (s, 8H, Fc C***H***), 2.68 – 2.63 (m, 4H, Fc CC***H***$_2$), 2.53 – 2.49 (m, 4H, C***H***$_2CO_2$), 1.26 (t, *J* = 7.2 Hz, 6H, C***H***$_3$). ^{13}C NMR (101 MHz, $CDCl_3$): δ 173.1 (***C***=O), 87.5 (Fc ***C***–CH_2), 68.6 (Fc ***C***H), 68.1 (Fc ***C***H), 60.4 (O***C***H_2CH_3), 35.9 (***C***H_2COO), 24.8 (Fc C–***C***H_2), 14.3 (***C***H_3). MS (TOF ASAP+) (*m/z*) calculated for $C_{20}H_{26}FeO_4$: 386.12 [M]; found: 386.12 [$M]^+$, 387.12 [$M+H]^+$.

Ferrocene Dipropanol (13)

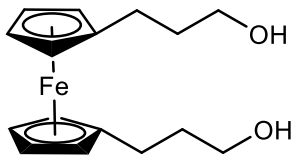

Known compound; characterisation matches literature data.[5] **12** (1.06 g, 2.75 mmol) was dissolved in dry tetrahydrofuran (20 mL). The solution was cooled to 0 °C and $LiAlH_4$ (1.0 M in tetrahydrofuran, 11.4 mL) was added dropwise under argon. The reaction mixture was stirred at 0 °C for 2 h under argon. The reaction mixture was quenched with saturated potassium tartrate solution (30 mL) and extracted using diethyl ether (4 × 10 mL). The organic components were combined and dried over $MgSO_4$. The solvent was removed *in vacuo* and the crude product was purified with column chromatography (silica; 1:1 ethyl acetate:hexane), collecting the one band to yield **13** as an orange oil (0.585 g, 1.94 mmol, 71%). ^{1}H NMR (400 MHz, $CDCl_3$): δ 4.01 (s, 8H, Fc C***H***), 3.67 (t, *J* = 5.4 Hz, 4H, C***H***$_2$OH), 2.42 (t, *J* = 7.9 Hz, 4H, Fc CC***H***$_2$), 1.77 (ddt, *J* = 9.3, 7.7, 6.4 Hz, 4H, Fc CCH_2C***H***$_2$), 1.33 (s, 2H, O***H***). ^{13}C NMR (101 MHz, $CDCl_3$): δ 88.5 (Fc ***C***–CH_2), 68.7 (Fc ***C***H), 68.0 (Fc ***C***H), 62.7 (***C***H_2OH), 34.4 (Fc C–CH_2***C***H_2), 25.7 (Fc C–***C***H_2). MS (TOF ASAP+) (*m/z*) calculated for $C_{16}H_{22}FeO_2$: 302.10 [M]; found: 303.11 $[M+H]^+$.

Monotrityl Ferrocene Alcohol (14)

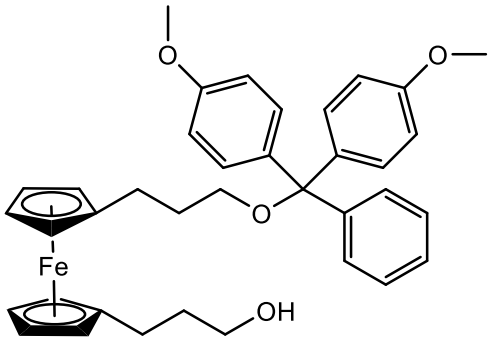

Known compound; characterisation matches literature data.[5] **13** (0.539 g, 1.78 mmol) was dissolved in dry tetrahydrofuran (20 mL) under argon. 4-dimethylaminopyridine (0.059 g, 0.05 mmol), *N*,*N*-diisopropylethylamine (0.33 mL, 0.19 mmol) and 4,4′-dimethoxytrityl chloride (0.492 g, 0.15 mmol) was added, and the reaction mixture was stirred at RT for 23 h under argon. The reaction mixture was quenched with saturated $NaHCO_3$ solution (20 mL). Extractions using DCM (3 × 20 mL) were conducted, with the organic components combined and dried over Na_2SO_4. The solvent was removed *in vacuo* and the crude product purified with column chromatography (silica; 2:1 hexane:ethyl acetate w/ 1% NEt_3), collecting the second band to yield **14** as a yellow oil (0.467 g, 0.77 mmol, 43%). ^{1}H NMR (400 MHz, $CDCl_3$): δ 7.48 – 7.18 (m, 9H, DMTr C***H***), 6.87 – 6.79 (m, 4H, DMTr C***H***), 4.02 – 3.90 (m, 8H, Fc C***H***), 3.80 (s, 6H, DMTr OC***H***$_3$), 3.65 (q, *J* = 6.0 Hz, 2H C***H***$_2$OH), 3.09 (t, *J* = 6.4 Hz, 2H C***H***$_2$ODMTr), 2.45 – 2.35 (m, 4H, Fc CC***H***$_2$), 1.88 – 1.70 (m, 4H, Fc CCH$_2$C***H***$_2$), O***H*** not observed. ^{13}C NMR (101 MHz, $CDCl_3$): δ 158.3 (Ph ***C***–O), 145.4 (Ph ***C***–C), 136.7 (Ph ***C***–C), 130.1 (Ph ***C***H), 128.2 (Ph ***C***H), 127.7 (Ph ***C***H), 126.6 (Ph ***C***H), 113.0 (Ph ***C***H), 89.0 (Fc ***C***–CH$_2$), 88.4 (Fc ***C***–CH$_2$), 85.8 (DMT ^{t}***C***–O), 68.6 (Fc ***C***H), 68.6 (Fc ***C***H), 67.9 (Fc ***C***H), 67.8 (Fc ***C***H), 63.1 (***C***H$_2$ODMT), 62.7 (***C***H$_2$OH), 55.2 (***C***H$_3$O), 34.2 (Fc C–CH$_2$***C***H$_2$), 31.4 (Fc C–CH$_2$***C***H$_2$), 26.0 (Fc C–***C***H$_2$), 25.8 (Fc C–***C***H$_2$). MS (TOF ASAP+) (*m/z*) calculated for $C_{37}H_{40}FeO_4$: 604.23 [M]; found: 604.23 $[M]^+$, 605.23 $[M+H]^+$.

Monotrityl Ferrocene Phosphoramidite (15)

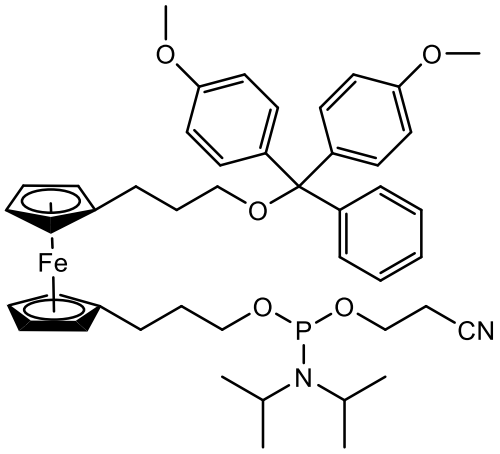

Known compound; characterisation matches literature data.[5] **14** (0.449 g, 0.74 mmol) was azeotroped with dry DCM (2 × 20 mL) then redissolved in dry DCM (10 mL) under argon. *N*,*N*–diisopropylethylamine (0.37 mL, 1.93 mmol) and 2-cyanoethoxy-*N*,*N*-diisopropylaminochlorophosphine (0.26 mL, 1.16 mmol) were added dropwise. The reaction mixture was stirred at RT for 2.5 h under argon. The reaction mixture was quenched with deoxygenated ethyl acetate (20 mL), then washed with deoxygenated saturated $NaHCO_3$ solution (20 mL) and deoxygenated brine (15 mL). The organic layer was dried over Na_2SO_4 and filtered. The solvent was removed *in vacuo* and the crude product purified with column chromatography using deoxygenated solvents (silica; 3:2 hexane:ethyl acetate w/ 1% NEt_3), collecting the one band to yield **15** as a yellow oil (0.525 g, 0.65 mmol, 88%). ^{1}H NMR (400 MHz, $CDCl_3$): δ 7.48 – 7.18 (m, 9H, DMTr C***H***), 6.86 – 6.80 (m, 4H, DMTr C***H***), 3.99 – 3.91 (m, 8H, Fc C***H***), 3.88 – 3.75 (m, 8H, DMTr OC***H***$_3$, C***H***$_2$CH$_2$CN), 3.72 – 3.55 (m, 4H, C***H***$_2$OP, NC***H***), 3.09 (t, *J* = 6.4 Hz, 2H, C***H***$_2$ODMTr), 2.61 (t, *J* = 6.6 Hz, 2H, C***H***$_2$CN), 2.44 – 2.34 (m, 4H, Fc CC***H***$_2$), 1.87 – 1.75 (m, 4H, Fc CCH$_2$C***H***$_2$), 1.18 (dd, *J* = 6.8, 4.7 Hz, 12H, C***H***$_3$). ^{31}P NMR (400 MHz, $CDCl_3$): δ 147.4. IR (cm^{-1}) υ: 3084 (CH), 2965 (CH). MS (TOF ASAP+) (*m/z*) calculated for $C_{46}H_{57}FeN_2O_5P$: 804.34 [M]; found: 804.34 $[M]^+$, 805.34 $[M+H]^+$.

7.2. Oligonucleotide Synthesis

All oligonucleotides were synthesised with an Applied Biosystems ABI 394 synthesiser. Unmodified strands were synthesised using standard reagents and conditions. Modified strands that incorporated CuCy, Cy3, or Cy5 modifications were synthesised using ultramild reagents and conditions. All other modified strands were synthesised using standard reagents and conditions.

7.2.1. Standard Synthesis

Bz-dA, iBu-dG, Ac-dC, dT, and C3 Spacer phosphoramidites from LGC Genomics, and Fc phosphoramidite compound **15**, were used for the standard synthesis of oligonucleotides. All phosphoramidites were dissolved in anhydrous acetonitrile (0.1 M) prior to synthesis. Oligonucleotides were synthesised on CPG solid support columns (1000 Å pore size) from Glen Research or LGC Genomics at a 1 μmol scale. Oligonucleotides with a 3′ disulphide modification were synthesised on a 3′-thiol-modifier 6 S-S CPG column from Glen Research; oligonucleotides with a canonical 3′ nucleoside were synthesised on a nucleoside-attached CPG column from LGC Genomics. 5′ DMT removal was achieved using trichloroacetic acid in DCM. Phosphoramidites were activated using 5-ethylthio-1H-tetrazole (0.5 M) in acetonitrile. Coupling times of 25 s and 10 min were used for the nucleosides and modifications (Fc and C3 spacer), respectively. Unreacted material was capped using acetic anhydride and methylimidazole. Iodine (0.1 M) in THF/pyridine/water (7:2:1) oxidised the phosphotriesters formed. Upon completion, each oligonucleotide was treated with aqueous ammonia (30%) for 1 h at RT followed by heating at 60 ºC for 6 h to cleave the strands from the resin and remove protecting groups. Solvent was removed *in vacuo* using a Thermo Scientific speed vac and the crude product was redissolved in Milli-Q water (0.9 mL) prior to purification.

7.2.2. Ultramild Synthesis

Pac-dA, iPr-Pac-dG, Ac-dC, dT, Cy3, Cy5, and 18PEG Spacer phosphoramidites from LGC genomics, CuCy phosphoramidite compound **8**, and Fc phosphoramidite compound **15**, were used for the ultramild synthesis of oligonucleotides. With the exception of Cy3, all phosphoramidites were dissolved in anhydrous acetonitrile (0.1 M) prior to synthesis. Cy3 phosphoramidite was instead dissolved in anhydrous DCM (0.1 M) according to the manufacturer's instructions. Oligonucleotides were synthesised on CPG solid support columns (1000 Å pore size) from Glen Research at a 1 μmol scale. Oligonucleotides with a 3′ disulphide modification were synthesised on a 3′-thiol-modifier 6 S-S CPG column from Glen Research; oligonucleotides with a 3′ alkyne modification were synthesised on a 3′-alkyne-modifier serinol CPG column from Glen Research. 5′ DMT removal was achieved using trichloroacetic acid in DCM. Phosphoramidites were activated using 5-ethylthio-1H-tetrazole (0.25 M) in acetonitrile. Coupling times of 25 s and 10 min were used for the nucleosides and modifications, respectively. Unreacted material was capped using acetic anhydride and methylimidazole. Iodine (0.02 M) in THF/pyridine/water (7:2:1) oxidised the phosphotriesters formed. Upon completion the oligo-attached resin was mixed with methanolic potassium carbonate (0.05 M, 1 mL) and left overnight to cleave the strands from the resin and remove protecting groups. The resulting solution was neutralised with acetic acid (6 μL) before the solvent was removed *in vacuo* using a Thermo Scientific speed vac. Milli-Q water (1 mL) was added to the remaining solid and the solution was desalted using a NAP-10 column from GE Healthcare to remove the resin and potassium carbonate prior to purification.

7.3. Oligonucleotide Purification

7.3.1. Purification of CuCy- and Fc-Modified Oligonucleotides

Oligonucleotide purification was performed with semi-preparative RP-HPLC on an Agilent Technologies 1260 Infinity using a Phenomenex Clarity 5 µm Oligo-RP LC 250 × 10 mm column. 0.9 mL of crude DNA solution was injected for each run and a flow rate of 3 mL min^{-1} was used. The absorbance at 260 nm was monitored for each run. A heated (60 ºC) solvent system was used consisting of 0.1 M TEAA buffer solution (in HPLC-grade water) and acetonitrile. The solvent gradient system used is shown in Table 7.1. Following HPLC purification, the solvent was removed *in vacuo* before the oligonucleotide was redissolved in Milli-Q water (1 mL). The resulting solution was then desalted using a NAP-10 column from GE Healthcare to elute 1.5 mL of purified oligonucleotide solution.

Table 7.1: Solvent gradient system used to purify CuCy- and Fc-modified oligonucleotides.

Time (min)	TEAA solution (%)	Acetonitrile (%)
0	85	15
30	75	25
30.01	0	100
40	0	100
40.01	85	15
50	85	15

7.3.2. Purification of Cy3- and Cy5-Modified Oligonucleotides

Purification procedures for Cy3- and Cy5-modified oligonucleotides were identical to those described in section 7.3.1., except for the different solvent gradient systems used. Cy3-modified oligonucleotides were purified using the gradient system shown in Table 7.2, and Cy5-modified oligonucleotides were purified using the gradient system shown in Table 7.3.

Table 7.2: Solvent gradient system used to purify Cy3-modified oligonucleotides.

Time (min)	TEAA solution (%)	Acetonitrile (%)
0	95	5
30	75	25
30.01	0	100
40	0	100
40.01	85	15
45	85	15

Table 7.3: Solvent gradient system used to purify Cy5-modified oligonucleotides.

Time (min)	TEAA solution (%)	Acetonitrile (%)
0	85	15
30	65	35
30.01	0	100
40	0	100
40.01	85	15
45	85	15

7.3.3. Purification of C3 Spacer-Modified and Unmodified Oligonucleotides

Purification procedures for C3 Spacer-modified and unmodified oligonucleotides were identical to those described in section 7.3.1., except for the different solvent gradient system used which is shown in Table 7.4.

Table 7.4: Solvent gradient system used to purify C3 Spacer-modified and unmodified oligonucleotides.

Time (min)	TEAA solution (%)	Acetonitrile (%)
0	95	5
25	82	18
30	0	100
40	0	100
40.01	95	5
45	95	5

7.4. Oligonucleotide Characterisation

Purity of the oligonucleotides was determined using analytical HPLC on either an Agilent Technologies 1260 Infinity (example trace shown in Figure 7.1, top) or a Thermo Fisher

Vanquish Core (example trace shown in Figure 7.1, bottom) using a Phenomenex Clarity 5 µm Oligo-RP LC 250 × 4.6 mm column, with the same solvent parameters as used for semi-preparative HPLC purification. Samples exhibiting >95% purity were deemed sufficiently pure for use. Negative mode electrospray mass spectrometry was performed using a Waters Xevo G2-XS spectrometer, with data collection and analysis conducted using Mass Lynx software. Oligonucleotide concentrations were determined by optical density at 260 nm using a Shimadzu BioSpecNano micro-volume UV-Vis spectrophotometer, with extinction coefficients obtained from Integrated DNA Technologies' OligoAnalyzer[6] and values of 3300 mol^{-1} cm^{-1} and 8294 mol^{-1} cm^{-1} at 260 nm used for Fc and CuCy, respectively.

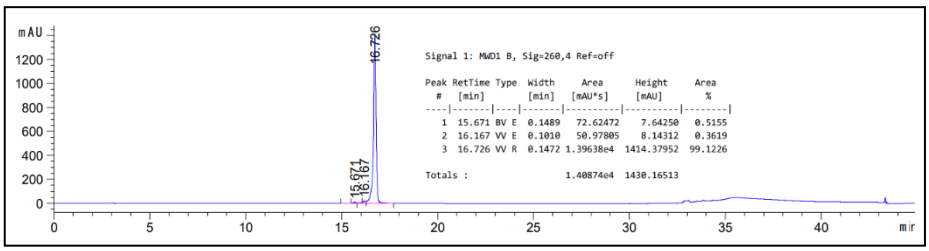

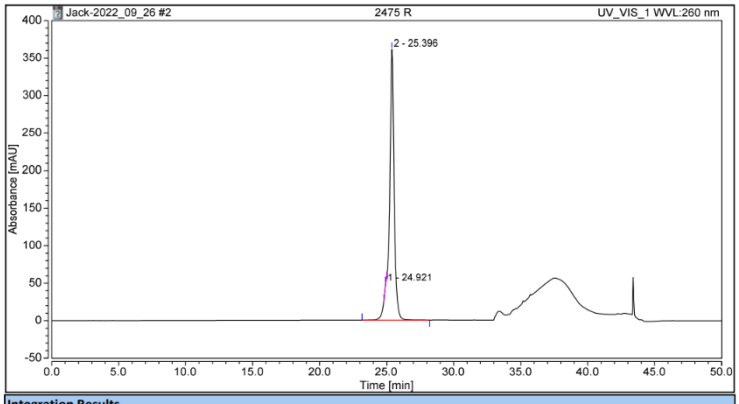

Integration Results							
No.	Peak Name	Retention Time min	Area mAU*min	Height mAU	Relative Area %	Relative Height %	Amount n.a.
1		24.921	0.347	2.650	0.23	0.73	n.a.
2		25.396	149.836	360.972	99.77	99.27	n.a.
Total:			**150.183**	**363.622**	**100.00**	**100.00**	

Figure 7.1: Example analytical HPLC traces produced using the Agilent Technologies 1260 Infinity (top) or the Thermo Fisher Vanquish Core (bottom).

7.5. Thermal Melting Studies

Samples of oligonucleotides were made to a concentration of 10 μM in 10 mM sodium phosphate buffer pH 7.0, 100 mM NaCl. 1 μL of 20× concentration SsoAdvanced Universal SYBR Green Supermix from Bio-Rad was added to 19 μL of each 10 μM oligonucleotide sample. Samples were heated from 20 ºC to 95 ºC and subsequently cooled from 95 ºC to 20 ºC at a rate of 1 ºC min^{-1} in a M550 double beam scanning UV/Vis spectrophotometer. T_m values were obtained from the maxima of the negative first derivative of the melting curve.

7.6. Electrochemistry

7.6.1. Equipment and Preparation

All cleaning and sensing procedures were conducted using a 3-electrode setup consisting of a BioAnalytical Systems Inc. EC Epsilon potentiostat, a C3 cell stand, a working electrode with a polycrystalline gold disc (2.0 mm diameter), a platinum wire counter electrode, and a Ag/AgCl reference electrode (3 M KCl). All water used (Milli-Q water) was purified using a Merck Millipore Elix-Gradient A10 system (resistivity > 18 μΩ cm, toc ≤ 5 ppb) for cleaning and solution preparation. Before use, the reference electrode was thoroughly rinsed with Milli-Q water and the counter electrode was flame annealed and rinsed with Milli-Q water. All solutions were deoxygenated with argon before use. All glassware was cleaned by soaking for several hours in a 1:1 mixture of ammonia (35%) and hydrogen peroxide (30%) before being thoroughly rinsed with Milli-Q water and left to soak overnight in Milli-Q water. After a final rinse with Milli-Q water the glassware was oven dried for several hours.

7.6.2. Self-Assembled Monolayer Preparation

The gold working electrodes were polished using a 1 μm diamond suspension for 3 min, followed by a 1 μm, 0.3 μm, and 0.05 μm alumina suspension for 3, 3, and 5 min, respectively. The electrodes were rinsed with Milli-Q water between each polish. Once polished, the electrodes were subjected to electrochemical cleaning in 0.5 M H_2SO_4: chronoamperometry (2 V for 5 seconds, –350 mV for 10 seconds) and cyclic voltammetry (4 V s^{-1}, 500 mV s^{-1}, and 100 mV s^{-1} for 20, 4, and 1 cycles, respectively; range –350 to 1500 mV). 2.0 μL of 100 μM purified probe oligonucleotide was reacted with 2.0 μL of 10 mM TCEP for 1 hour at RT, followed by dilution to 200 μL with 10 mM sodium phosphate buffer (pH 7.0) 1 M $NaClO_4$ solution. Polished and cleaned gold electrodes were soaked in the resulting 1 μM reduced probe oligonucleotide solution for 2 h followed by soaking in 2 mM 6-mercapto-1-hexanol solution for 16 h. Prior to use, the DNA-modified electrode was rinsed for 1 min under a stream of Milli-Q water.

SAM formation using preformed duplexes was conducted according to procedures adapted from Ferapontova and coworkers.[7] 10 μM of probe oligonucleotide was hybridised with 15 μM of complementary target DNA in 10 mM sodium phosphate buffer pH 7.0 1 M $NaClO_4$ and 0.05 mM TCEP, the solution volume totalling 50 μL. After 1 h at RT, a polished and cleaned gold electrode was soaked in the duplexed DNA solution for 16 h. The SAM-modified electrode was briefly rinsed with 10 mM sodium phosphate buffer (pH 7.0) 1 M $NaClO_4$ solution, before being soaked in 2 mM 6-mercapto-1-hexanol solution for 30 min. Prior to use, the electrode was removed from the 6-mercapto-1-hexanol solution, briefly rinsed with 10 mM sodium phosphate buffer (pH 7.0) 1 M $NaClO_4$ solution, and immediately used. An adaption of the above procedure was also conducted that incorporated a heating and annealing step to ensure maximum duplex formation. The adapted procedure was identical except that the probe

oligonucleotide–target DNA solution was heated from 20 ºC to 95 ºC and subsequently cooled from 95 ºC to 20 ºC at a rate of 1 ºC min^{-1} prior to being introduced to the gold electrode.

7.6.3. Electrochemical Sensing Procedure

The DNA-modified gold electrode was allowed to equilibrate in solution for 5 min before use. This was extended to 15 min for the square wave voltammetry experiments. After the equilibration period, the target was added directly to the sensing solution. Target-added voltammograms were recorded up to 1 h after target addition. A potential window of –75 to 550 mV was typically used, with occasionally smaller windows within that range used, depending on the probe. To assess the–relationship between current and scan rate, CVs were recorded at scan rates of 500, 250, 100, 80, 60, 40, 20 and 10 mV s^{-1}. For the ratiometric CuCy-/Fc-modified probes, the CuCy:Fc current ratio was calculated by dividing the CuCy anodic current by the Fc anodic current. CVs recorded at a scan rate of 1000 mV s^{-1} were used for CuCy:Fc current ratio determination. Data were analysed using OriginPro 2021b (Academic) software (Northampton, MA). To denature the probe–target duplexes and regenerate the sensor, the DNA-modified gold electrode was rinsed under a stream of Milli-Q water for 1 minute. If the CuCy:Fc current ratio had not returned to its initial value, a further 1 minute rinse was conducted.

7.7. Fluorescence Spectroscopy

The cuvette fluorescence spectroscopy experiments with the Cy3- and Cy5-modified oligonucleotides were conducted on a Jasco FP-8500 spectrofluorometer using a 1 mL quartz fluorescence cuvette at RT. Samples containing one oligonucleotide were allowed to equilibrate for 5 minutes before a fluorescence spectrum was recorded; samples containing two complementary oligonucleotides were allowed to hybridise for 20 minutes after mixing with a

pipette before a fluorescence spectrum was recorded. The spectrofluorometer parameters were scan speed = 200 nm min^{-1}, data interval = 1 nm, bandwidth = 5 nm, and sensitivity = medium.

7.8. MOF Synthesis and Characterisation

The MOFs used in Chapter 6 were synthesised and characterised by Dr Sarah Griffin in the Champness Group at the University of Birmingham.

7.8.1. MOF Synthesis

Single Crystal Zr and Hf UiO-68 Azide

Zirconium tetrachloride or hafnium tetrachloride (0.1 mmol), 2′,5′-bis(azidomethyl)[1,1′:4′,1″-terphenyl]-4,4″-dicarboxylic acid (0.1 mmol), and benzoic acid (2.0 mmol) were added to a 25 mL jar followed by DMF (3 mL). The solution was sonicated until all material had dissolved before being placed in the oven at 120 °C for 24 h. After cooling, single crystals were present on the walls of the jar. The solvent was removed *in vacuo* and the crystals were washed with DMF × 3 before drying *in vacuo* again.

Powdered Zr and Hf UiO-68 Azide

Zirconium tetrachloride or hafnium tetrachloride (0.23 mmol), 2′,5′-bis(azidomethyl)[1,1′:4′,1″-terphenyl]-4,4″-dicarboxylic acid (0.23 mmol), and L-proline (1.13 mmol) were added to a 25 mL jar followed by DMF (10 mL) and conc. hydrochloric acid (40 μL). The solution was sonicated until all material had dissolved before being placed in the oven at 120 °C for 24 h. After cooling, a light brown powder was present in the jar. The material was transferred into a centrifuge tube and washed with DMF × 3 and acetone × 3 before drying *in vacuo*.

Single Crystal Zn-MOF

Zinc nitrate hexahydrate (0.19 mmol) and 2′,5′-bis(azidomethyl)[1,1′:4′,1″-terphenyl]-4,4″-dicarboxylic acid (0.07 mmol) were added to a 25 mL jar followed by DMF (5 mL). The solution was sonicated until all material had dissolved before being placed in the oven at 80 °C overnight. After cooling, single crystals were present on the walls of the jar. The solvent was removed *in vacuo* and the crystals washed several times with fresh DMF and acetone before drying *in vacuo* again. The sample was then ground to a fine powder using a pestle and mortar.

7.8.2. MOF Characterisation

PXRD measurements were conducted at 298 K using either a Bruker D8 Advance diffractometer (λ (CuKα1) = 1.5406 Å), or a PANalytical Empyrean diffractometer (λ (CuKα1) = 1.5406 Å) mounted on either a welled or zero-background sample stage. PXRD patterns were calculated from single crystal structures using Mercury 3.10.1. SEM imaging was conducted using a Hitachi TM3030 tabletop microscope with powdered samples deposited into conductive carbon tabs.

7.8.3. DNA-Functionalisation of MOFs

DNA-functionalisation of MOFs was conducted in foil-covered glass vials. A 1 mL reaction mixture consisting of degassed DMF, 50 μM Cy3-/Cy5-modified DNA, 100 μL of MOF suspended in degassed DMF, and 1 mM $CuI.P(OEt)_3$ was left overnight on a mechanical shaker at RT. The solvent was removed *in vacuo* and the DNA-functionalised MOFs were washed with DMF and acetone until no further colour was observed in the washing solvents before drying *in vacuo* again.

7.9. Confocal Fluorescence Microscopy

The confocal fluorescence microscopy in Chapter 6 was conducted by Stanimir Tashev in the Herten group at the University of Birmingham.

7.9.1. Sample Preparation

MOF samples suspended in DMF were washed three times with Milli-Q water (100 mM NaCl) before being resuspended in Milli-Q water (100 mM NaCl) and heated at 60 °C for one hour. Parts of the sample were then pipetted onto a custom-made chamber made out of SYLGARD™ 184 Silicone Elastomer and a #1.5 coverslip (0.17 mm), which was previously washed in ethanol for 5 min and rinsed twice with Milli-Q water.

7.9.2. Confocal Microscope Setup

Imaging was conducted on a custom inverted microscope (Nikon Eclipse Ti; Nikon, Japan). 640 nm (LDH P-C-640B; PicoQuant, Germany) and 532 nm (P-FA-530XL; PicoQuant, Germany) picosecond pulsed lasers were directed to a 100 × 1.49 NA oil immersion objective (Apo TIRF; Nikon, Japan) by a four-band dichroic mirror (405, 488, 532, 640 nm). Emission signal was filtered by a quad-band notch filter (488/532/631–640 nm; AHF Analysetechnik). Out of focus light was blocked by a pinhole (100 μm diameter) in between two achromatic doublet lenses (f = 75 mm; Thorlabs). The emission was focused by an achromatic doublet lens (f = 150 mm; Thorlabs) before being split by three 50:50 beamsplitters (Thorlabs) onto four avalanche photo diode detectors (SPCM AQR-13; Perkin-Elmer, USA). Where red and green channels were separated this was done by placing a 685/70 band pass filter in the transmission path and a 582/75 bandpass filter in the reflection path after the first beam splitter.

7.9.3. Imaging and Analysis

Confocal images were recorded at 40 MHz with a pixel size of 100 nm and a dwell time of 50 µs. Imaging with the 640 nm laser was done with 4.2 kW/cm^2 and 532 nm excitation with 18.9 µW. Z-stacks were done with a distance between frames of 200 nm.

Raw data were converted into images using a custom Python script. For spectral unmixing the images were separated between the four avalanche photo diode detectors before being combined two-by-two into the red and the green channels using a custom Fiji code. For FRET detection Weka was used to segment the outside surfaces of the MOFs before using them as a mask for each channel separately.

7.10. References

1. M. Nakane, H. Gollman, C. R. Hutchinson and P. L. Knutson, *J. Org. Chem.*, 1980, **45**, 2536-2538.
2. S. Takamura, T. Yoshimiya, S. Kameyama, A. Nishida, H. Yamamoto and M. Noguchi, *Synthesis*, 2000, **5**, 637-639.
3. A. Rybka, R. Kolinski, J. Kowalski, R. Szmigielski, S. Domagala, K. Wozniak, A. Wieckowska, R. Bilewicz and B. Korybut-Daszkiewicz, *Eur. J. Inorg. Chem.*, 2007, DOI: 10.1002/ejic.200600744.
4. J. Duprey, J. Carr-Smith, S. L. Horswell, J. Kowalski and J. H. R. Tucker, *J. Am. Chem. Soc.*, 2016, **138**, 746-749.
5. T. Ihara, D. Sasahara, M. Shimizu and A. Jyo, *Supramol. Chem.*, 2009, **21**, 207-217.
6. IDT Technologies, https://eu.idtdna.com/calc/analyzer, (accessed June 2023).
7. L. Kekedy-Nagy and E. E. Ferapontova, *Angew. Chem., Int. Ed.*, 2019, **58**, 3048-3052.

8. Appendix

8.1. Modified Oligonucleotide Characterisation

T1

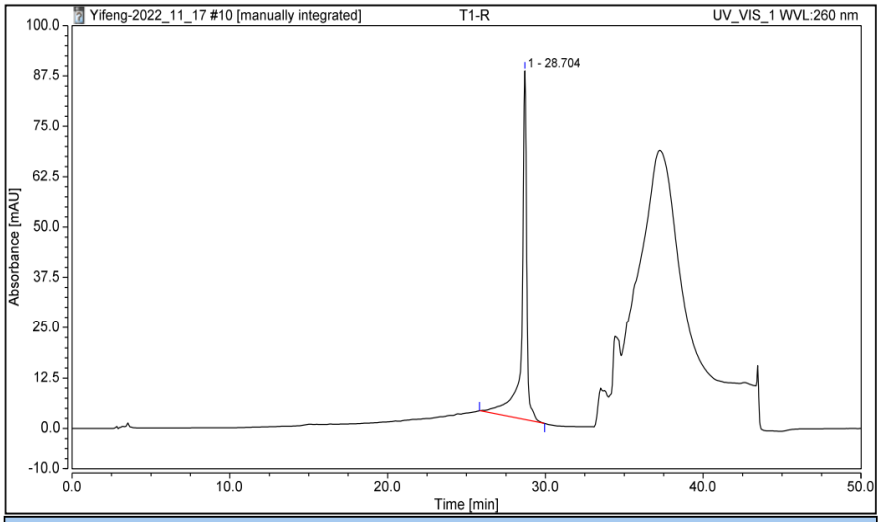

Integration Results							
No.	Peak Name	Retention Time min	Area mAU*min	Height mAU	Relative Area %	Relative Height %	Amount n.a.
1		28.704	31.692	86.559	100.00	100.00	n.a.
Total:			**31.692**	**86.559**	**100.00**	**100.00**	

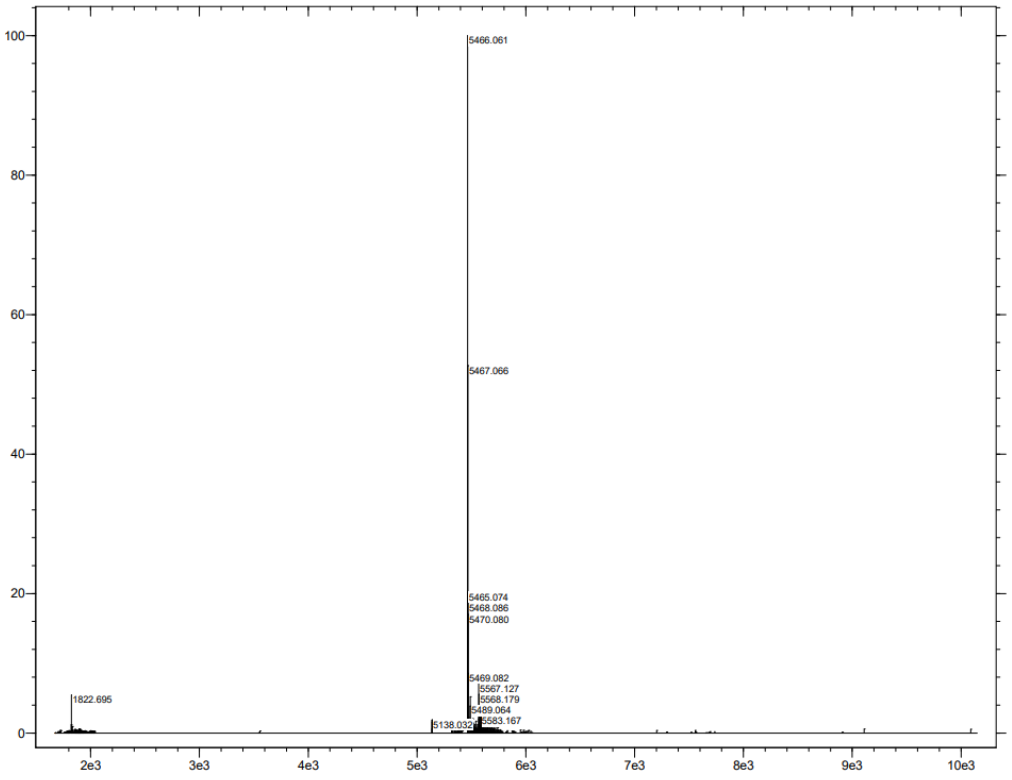

Figure 8.1: Analytical HPLC trace (top, detection wavelength = 260 nm) and processed mass spectrometry spectrum (bottom) for **T1**.

(*S*)-T1

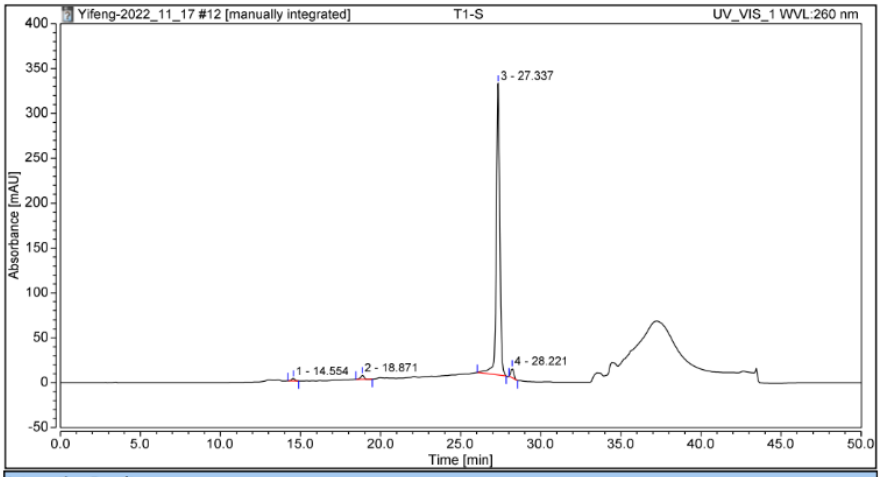

Integration Results

No.	Peak Name	Retention Time min	Area mAU*min	Height mAU	Relative Area %	Relative Height %	Amount n.a.
1		14.554	0.604	2.785	0.69	0.81	n.a.
2		18.871	0.985	4.716	1.13	1.37	n.a.
3		27.337	83.398	325.204	95.70	94.70	n.a.
4		28.221	2.161	10.704	2.48	3.12	n.a.
Total:			**87.148**	**343.409**	**100.00**	**100.00**	

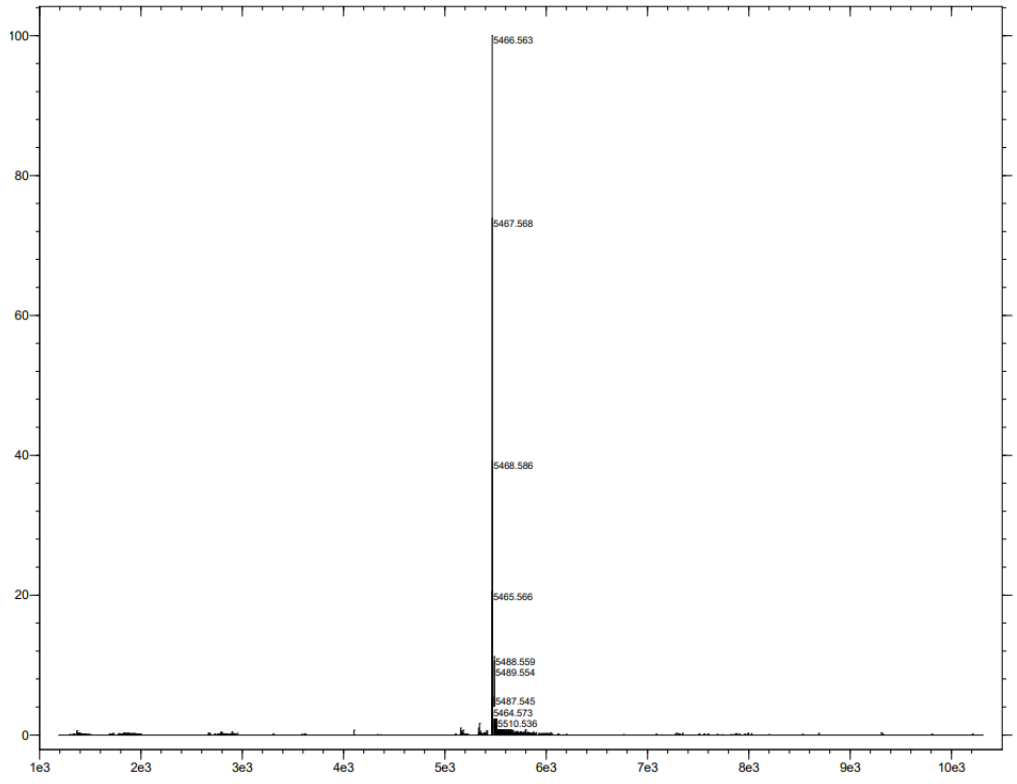

Figure 8.2: Analytical HPLC trace (top, detection wavelength = 260 nm) and processed mass spectrometry spectrum (bottom) for **(*S*)-T1**.

CuCyMid

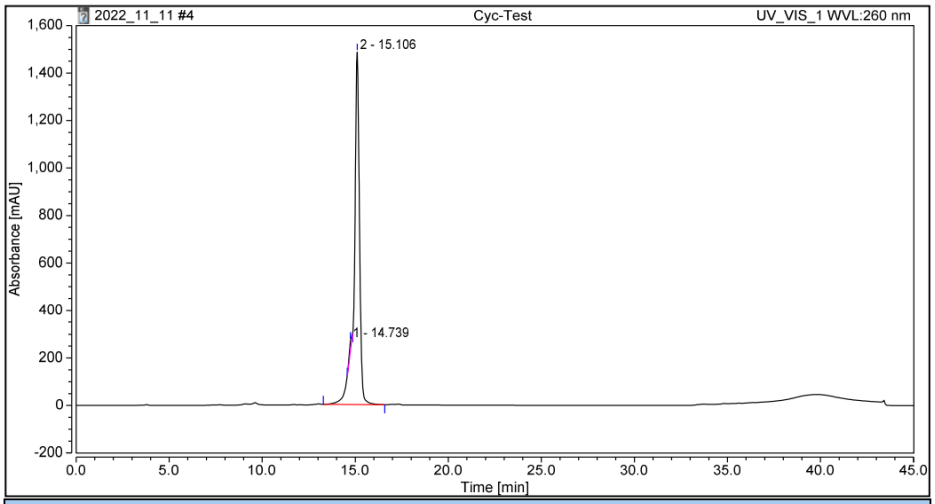

Integration Results

No.	Peak Name	Retention Time min	Area mAU*min	Height mAU	Relative Area %	Relative Height %	Amount n.a.
1		14.739	6.314	44.490	1.25	2.91	n.a.
2		15.106	500.014	1483.646	98.75	97.09	n.a.
Total:			**506.329**	**1528.136**	**100.00**	**100.00**	

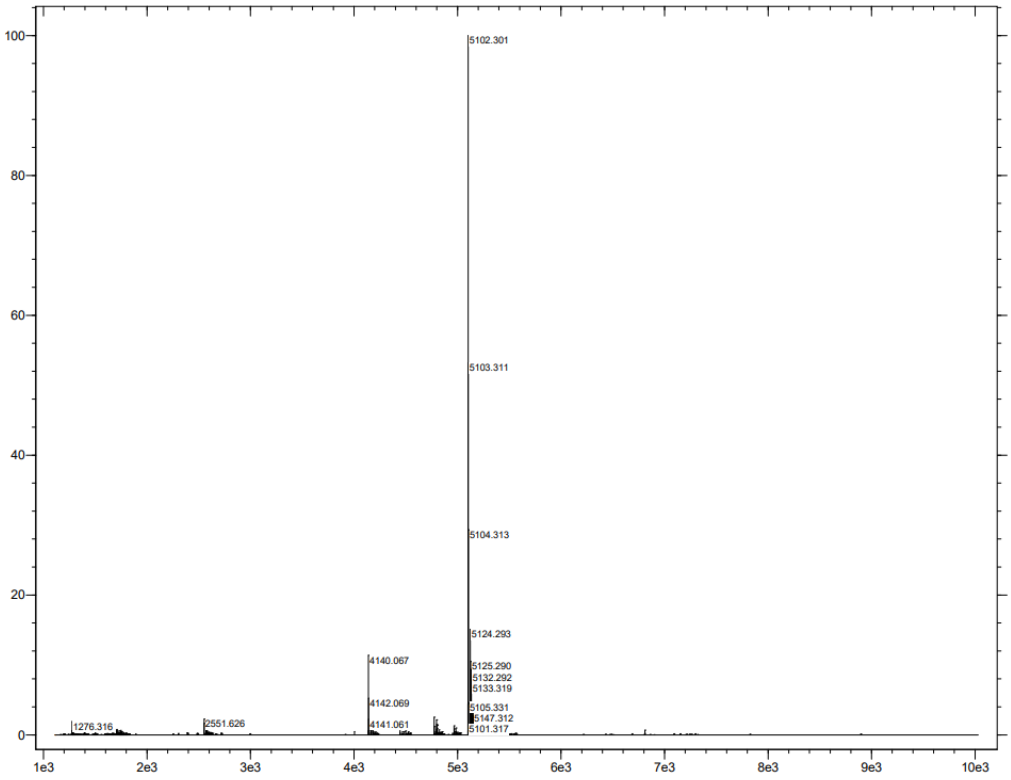

Figure 8.3: Analytical HPLC trace (top, detection wavelength = 260 nm) and processed mass spectrometry spectrum (bottom) for **CuCyMid**.

B1

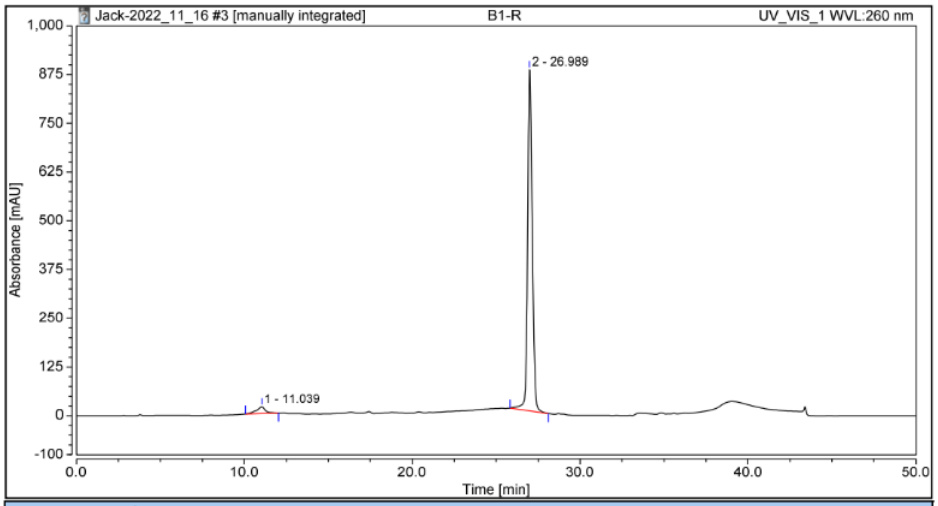

Integration Results

No.	Peak Name	Retention Time min	Area mAU*min	Height mAU	Relative Area %	Relative Height %	Amount n.a.
1		11.039	10.939	17.562	3.72	1.97	n.a.
2		26.989	282.972	875.292	96.28	98.03	n.a.
Total:			**293.910**	**892.855**	**100.00**	**100.00**	

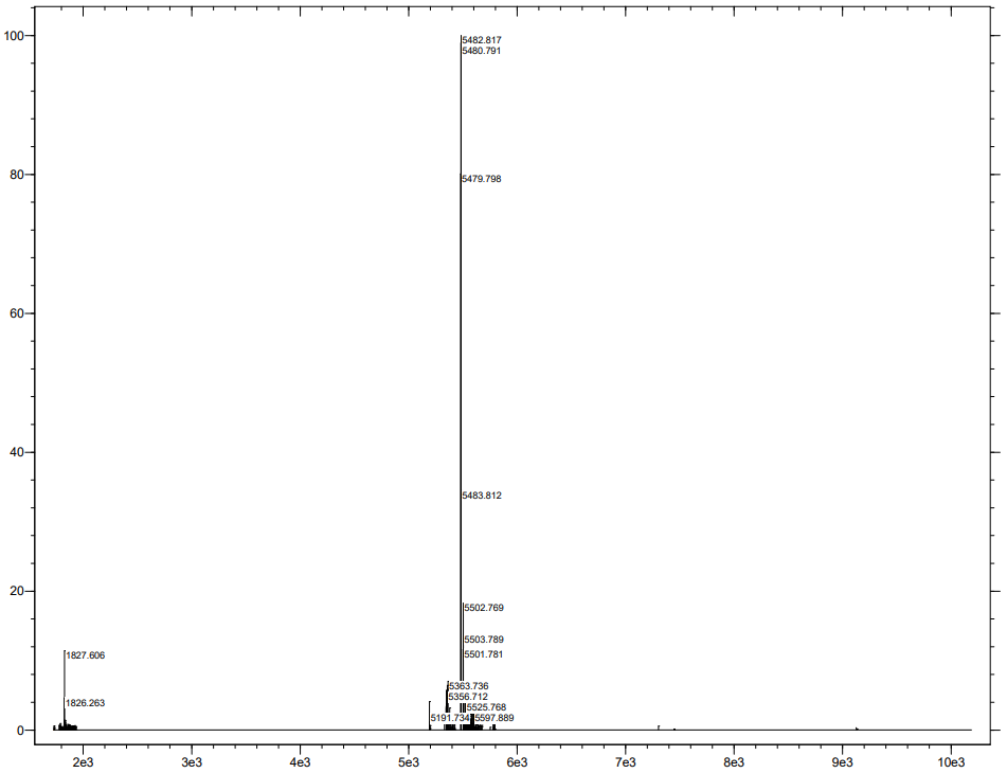

Figure 8.4: Analytical HPLC trace (top, detection wavelength = 260 nm) and processed mass spectrometry spectrum (bottom) for **B1**.

K1

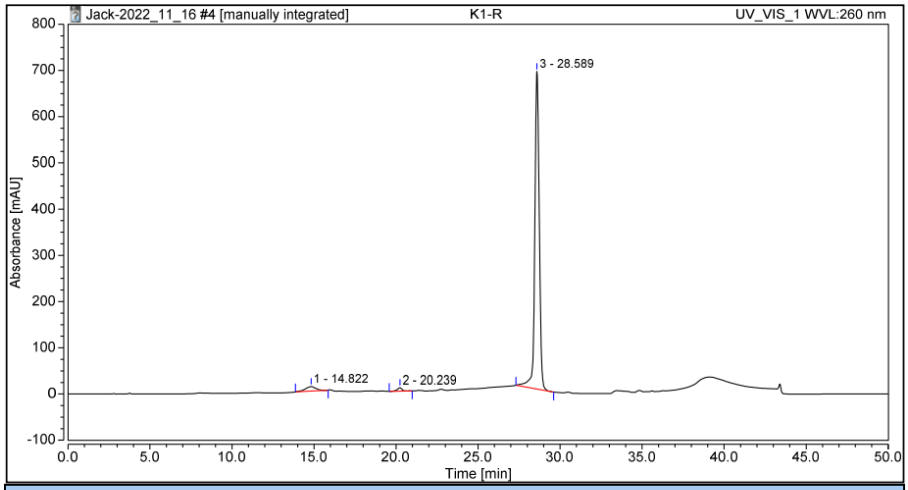

Integration Results

No.	Peak Name	Retention Time min	Area mAU*min	Height mAU	Relative Area %	Relative Height %	Amount n.a.
1		14.822	7.033	9.996	3.13	1.42	n.a.
2		20.239	2.491	7.731	1.11	1.10	n.a.
3		28.589	215.378	686.942	95.77	97.48	n.a.
Total:			**224.902**	**704.668**	**100.00**	**100.00**	

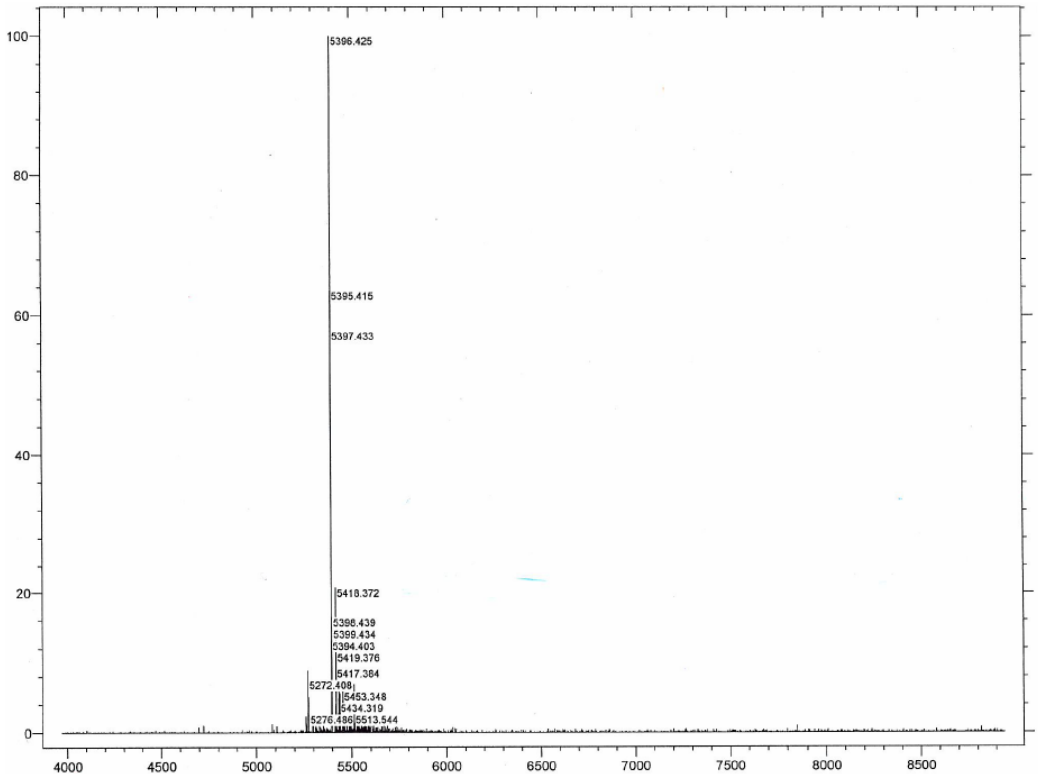

Figure 8.5: Analytical HPLC trace (top, detection wavelength = 260 nm) and processed mass spectrometry spectrum (bottom) for **K1**.

E1

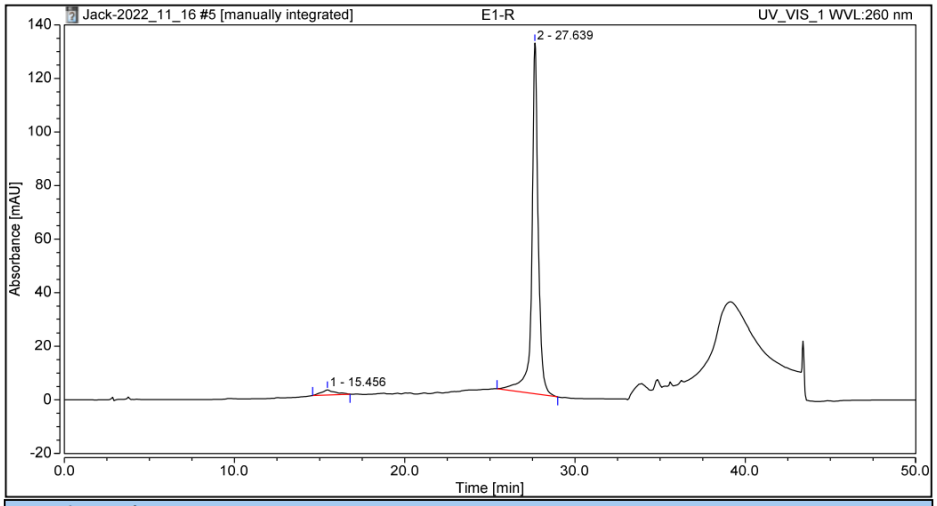

Integration Results

No.	Peak Name	Retention Time min	Area mAU*min	Height mAU	Relative Area %	Relative Height %	Amount n.a.
1		15.456	1.812	1.900	3.05	1.43	n.a.
2		27.639	57.607	130.945	96.95	98.57	n.a.
Total:			**59.419**	**132.845**	**100.00**	**100.00**	

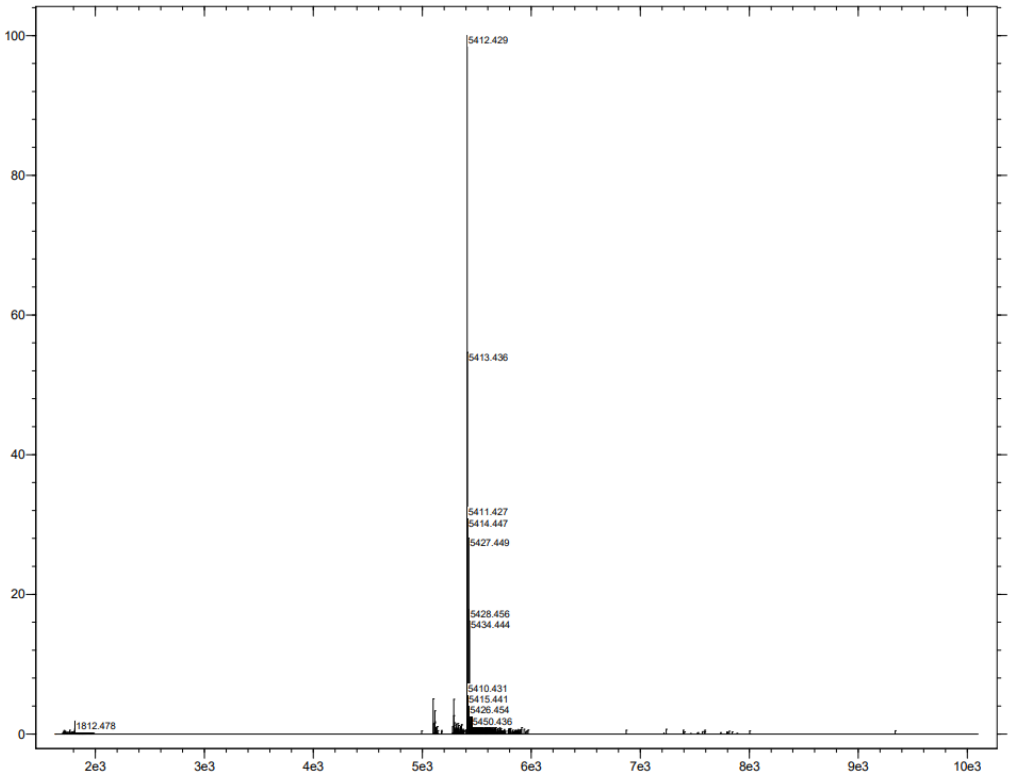

Figure 8.6: Analytical HPLC trace (top, detection wavelength = 260 nm) and processed mass spectrometry spectrum (bottom) for **E1**.

N1

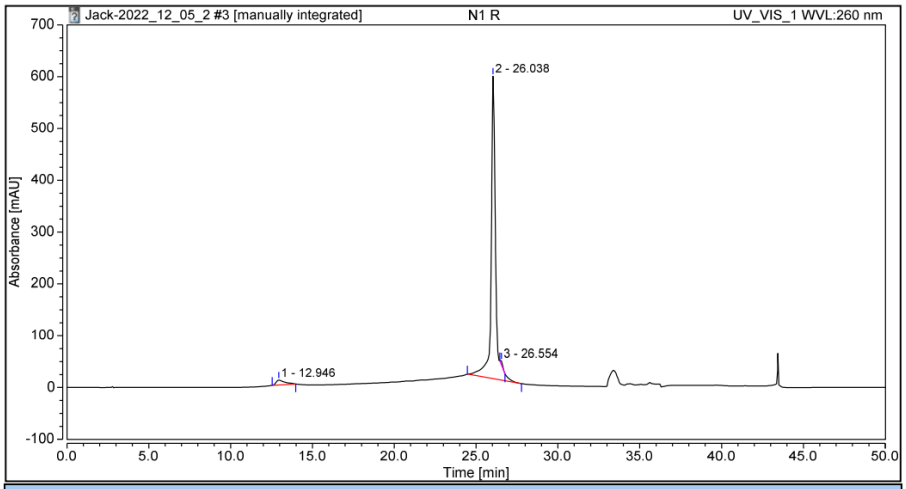

Integration Results

No.	Peak Name	Retention Time min	Area mAU*min	Height mAU	Relative Area %	Relative Height %	Amount n.a.
1		12.946	5.848	9.237	3.13	1.54	n.a.
2		26.038	179.656	583.716	96.23	97.11	n.a.
3		26.554	1.186	8.155	0.64	1.36	n.a.
Total:			**186.690**	**601.109**	**100.00**	**100.00**	

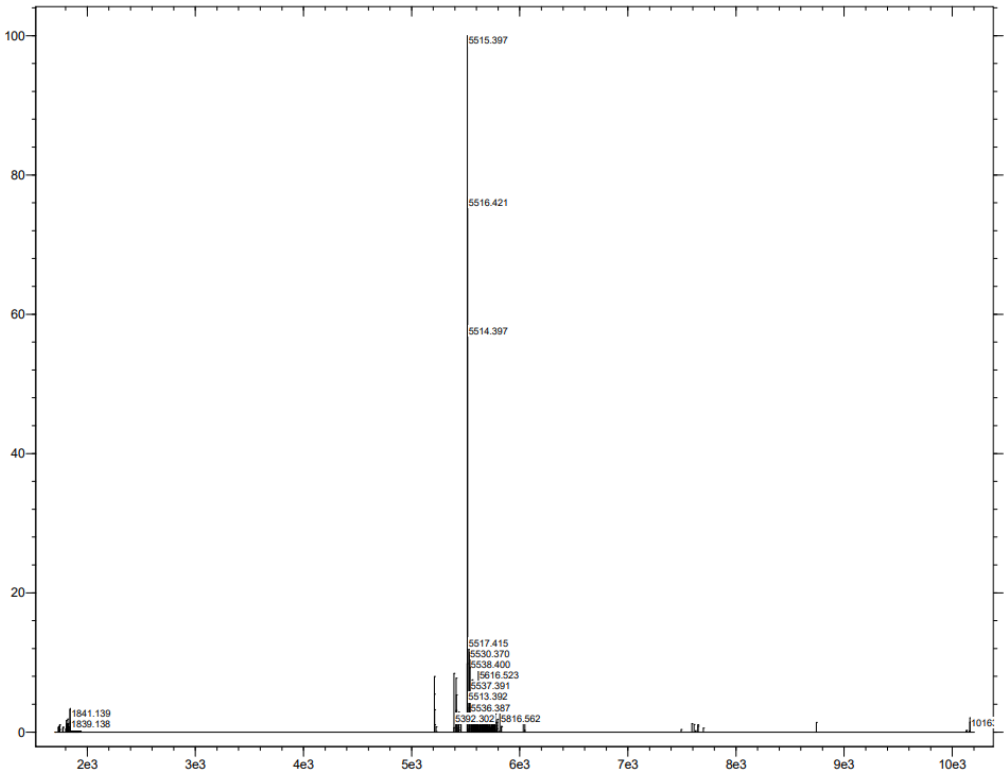

Figure 8.7: Analytical HPLC trace (top, detection wavelength = 260 nm) and processed mass spectrometry spectrum (bottom) for **N1**.

miR135-1

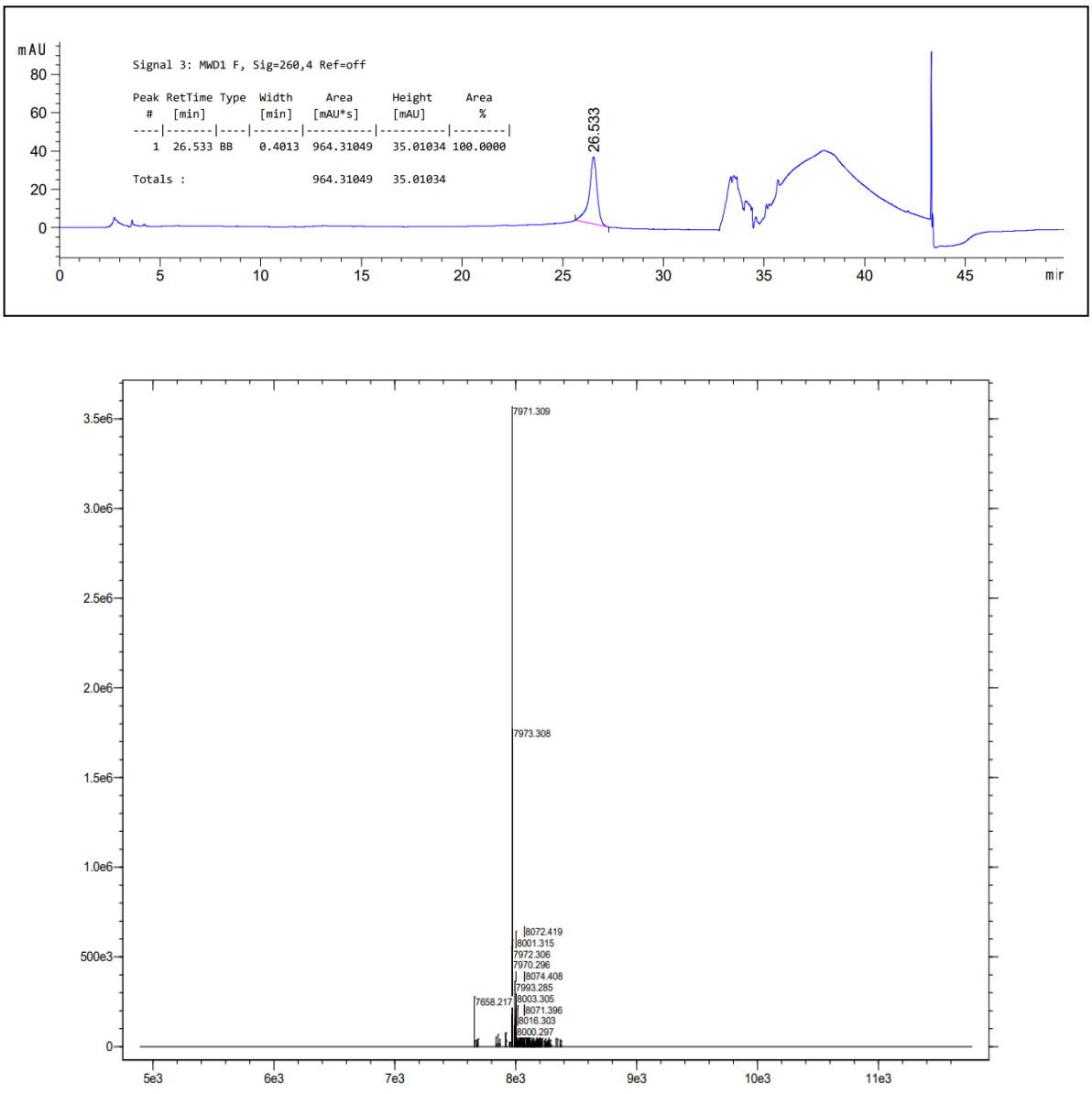

Figure 8.8: Analytical HPLC trace (top, detection wavelength = 260 nm) and processed mass spectrometry spectrum (bottom) for **miR135-1**.

CuCy5′

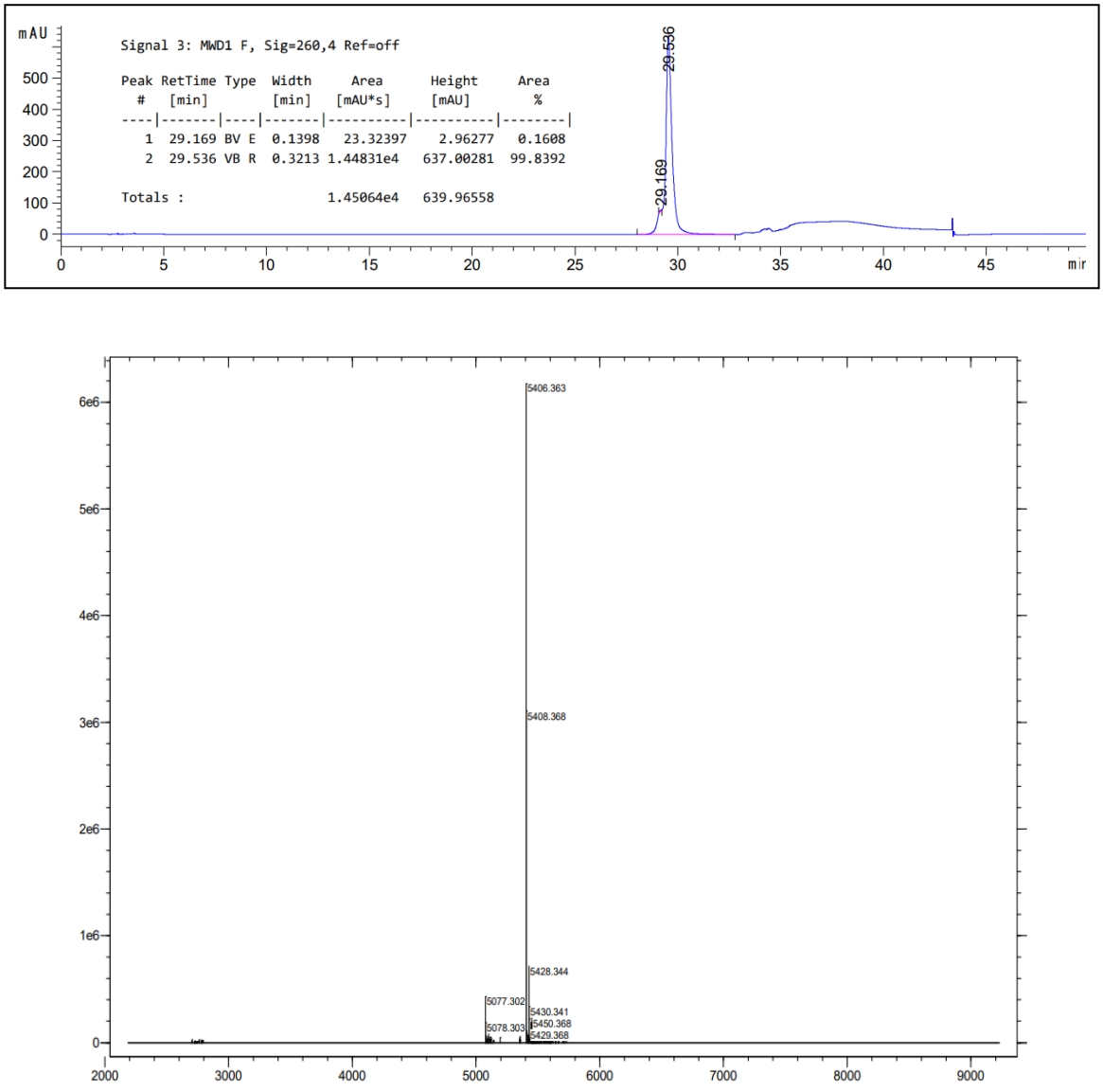

Figure 8.9: Analytical HPLC trace (top, detection wavelength = 260 nm) and processed mass spectrometry spectrum (bottom) for **CuCy5'**.

CuCy3′

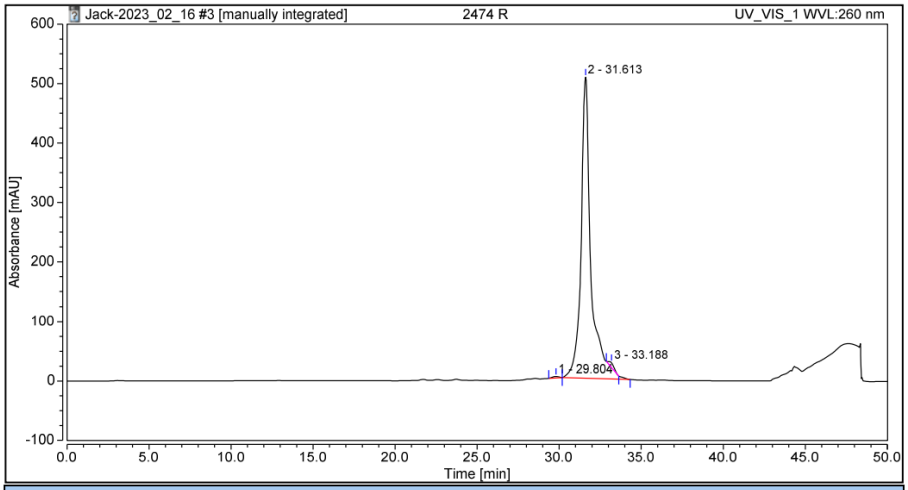

Integration Results

No.	Peak Name	Retention Time min	Area mAU*min	Height mAU	Relative Area %	Relative Height %	Amount n.a.
1		29.804	1.083	2.427	0.30	0.47	n.a.
2		31.613	354.765	506.073	98.93	97.98	n.a.
3		33.188	2.750	7.985	0.77	1.55	n.a.
Total:			**358.597**	**516.485**	**100.00**	**100.00**	

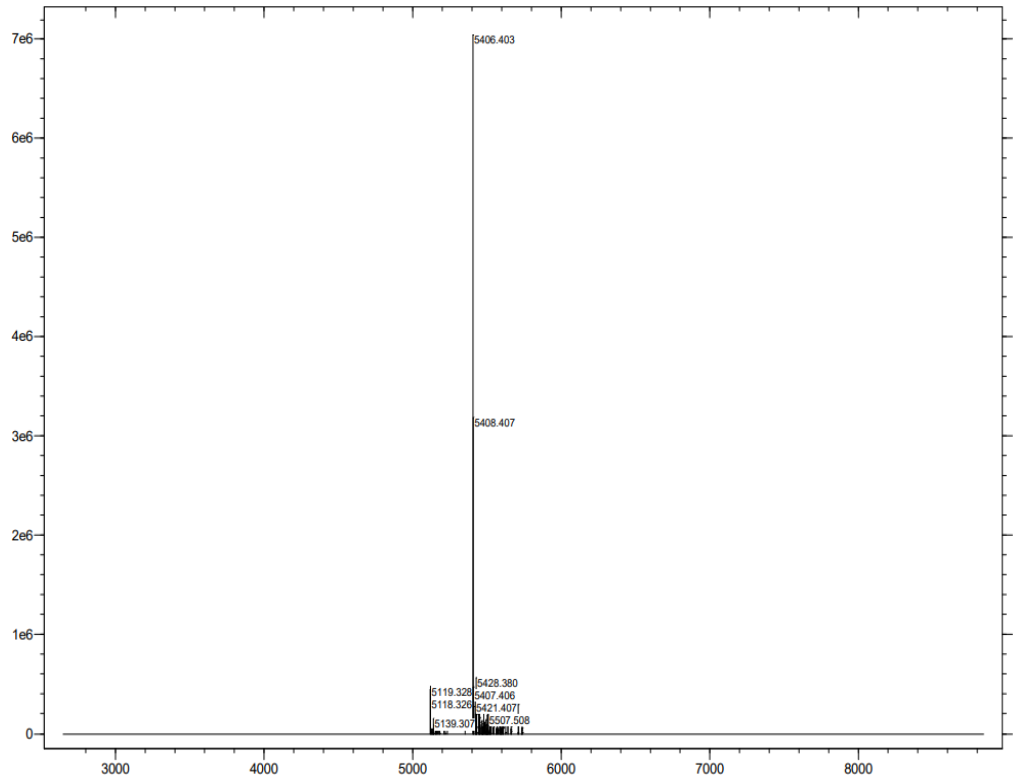

Figure 8.10: Analytical HPLC trace (top, detection wavelength = 260 nm) and processed mass spectrometry spectrum (bottom) for **CuCy3'**.

FcMid

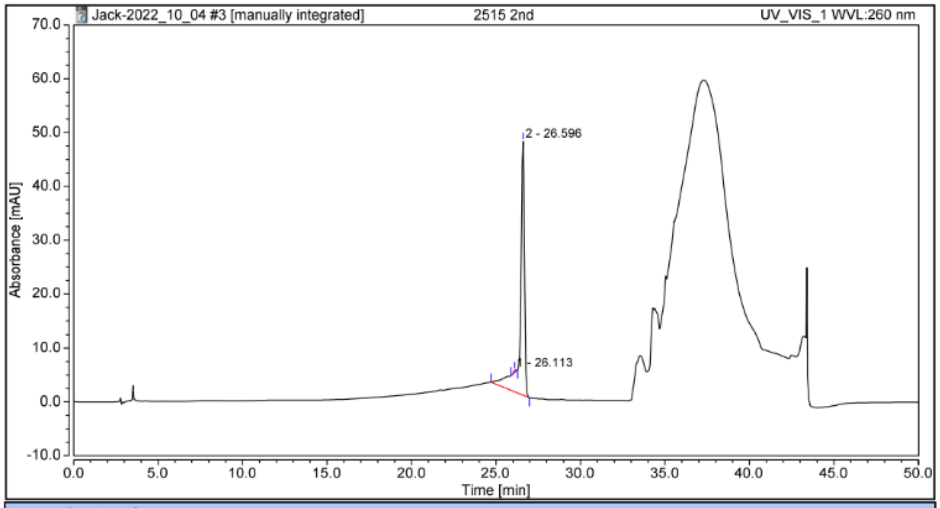

Integration Results

No.	Peak Name	Retention Time min	Area mAU*min	Height mAU	Relative Area %	Relative Height %	Amount n.a.
1		26.113	0.072	0.407	0.52	0.86	n.a.
2		26.596	13.690	47.104	99.48	99.14	n.a.
Total:			**13.762**	**47.511**	**100.00**	**100.00**	

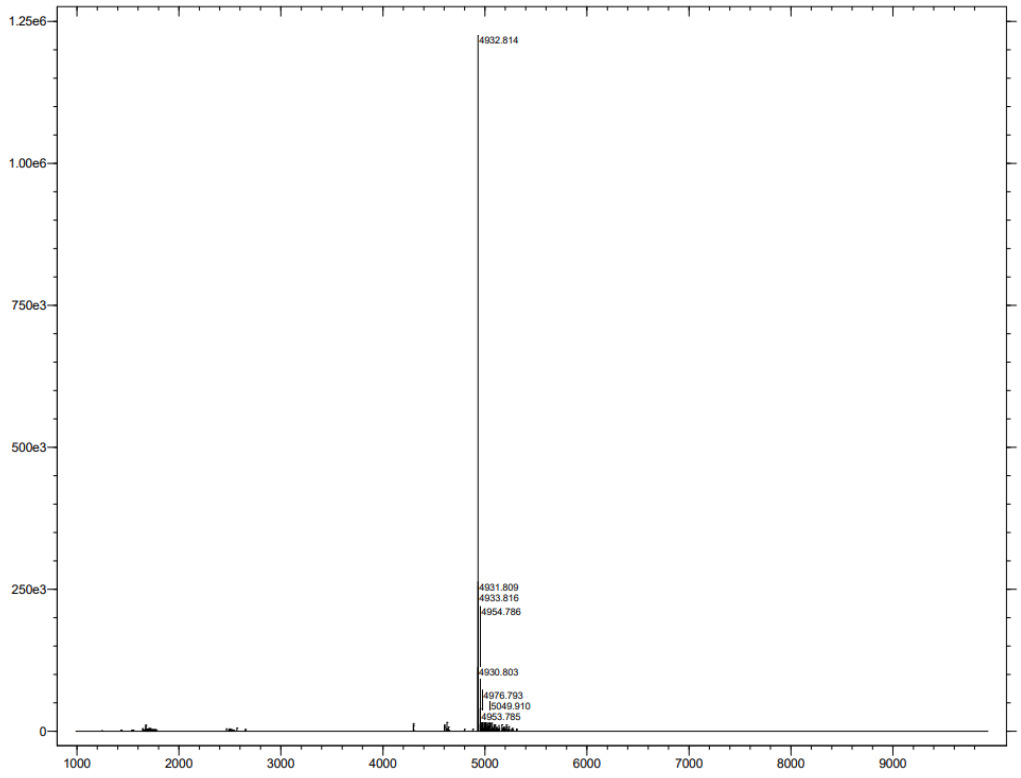

Figure 8.11: Analytical HPLC trace (top, detection wavelength = 260 nm) and processed mass spectrometry spectrum (bottom) for **FcMid**.

Fc5′

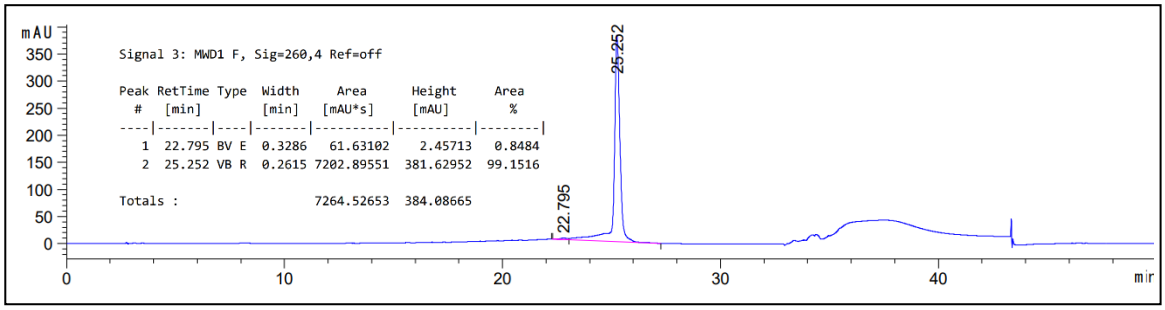

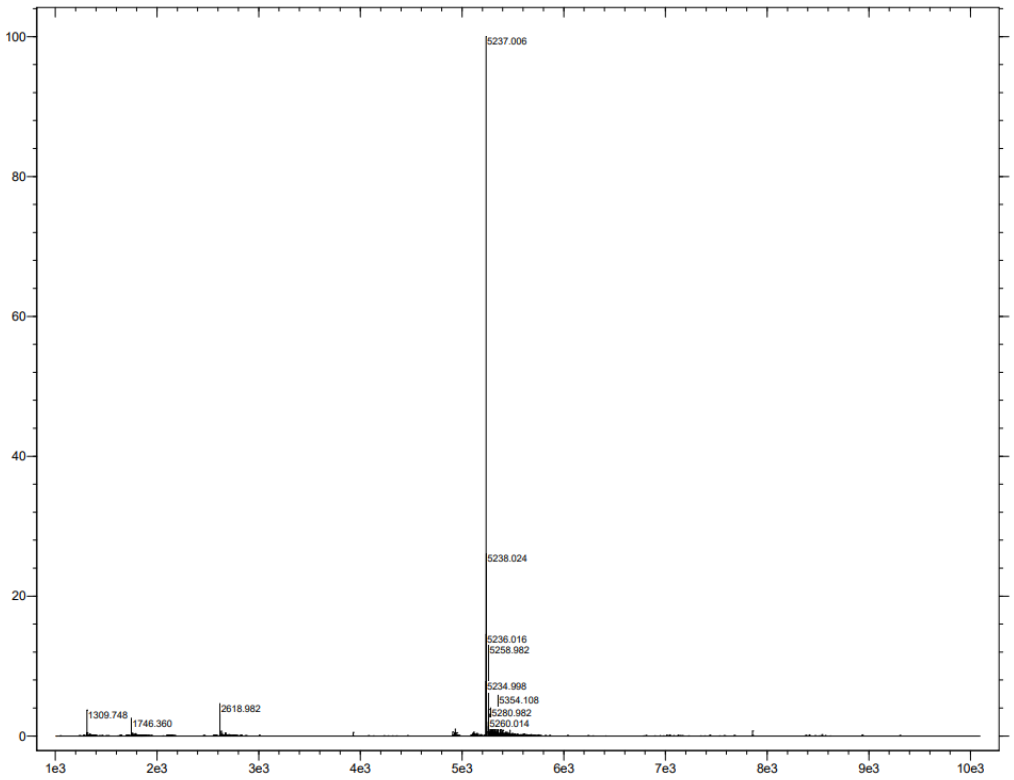

Figure 8.12: Analytical HPLC trace (top, detection wavelength = 260 nm) and processed mass spectrometry spectrum (bottom) for **Fc5'**.

Fc3′

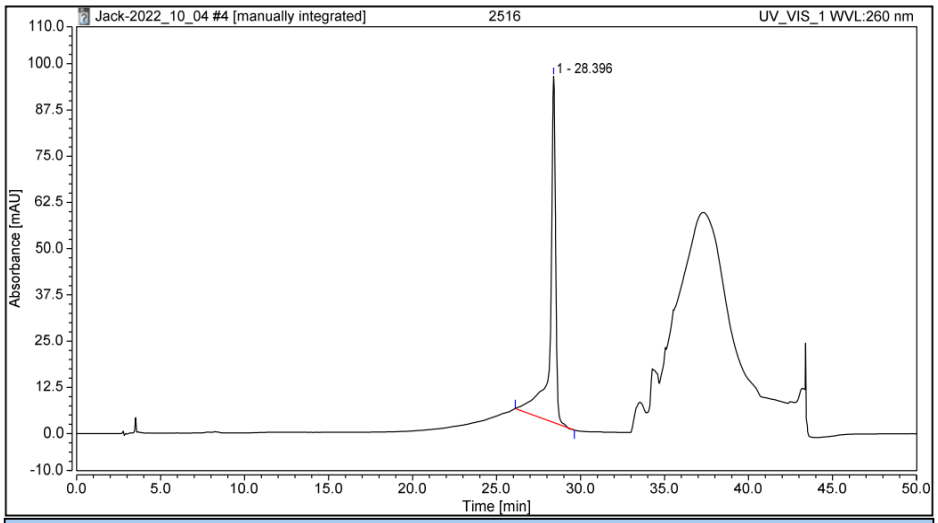

Integration Results							
No.	Peak Name	Retention Time min	Area mAU*min	Height mAU	Relative Area %	Relative Height %	Amount n.a.
1		28.396	34.834	93.572	100.00	100.00	n.a.
Total:			**34.834**	**93.572**	**100.00**	**100.00**	

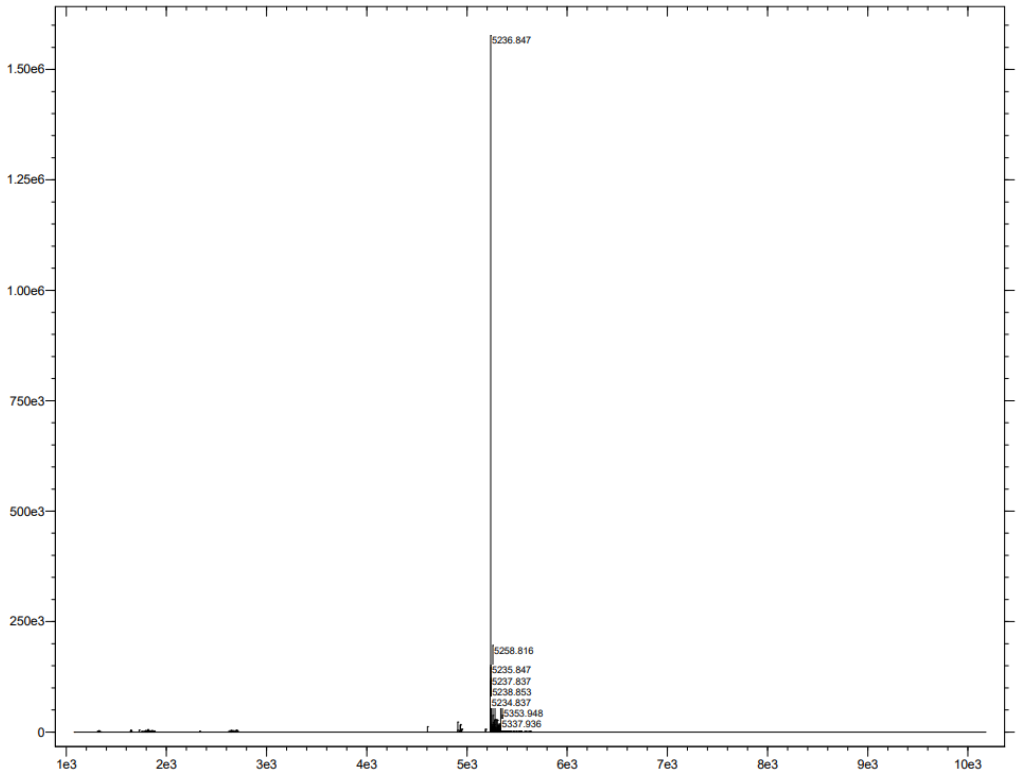

Figure 8.13: Analytical HPLC trace (top, detection wavelength = 260 nm) and processed mass spectrometry spectrum (bottom) for **Fc3'**.

CuCy5′-30mer

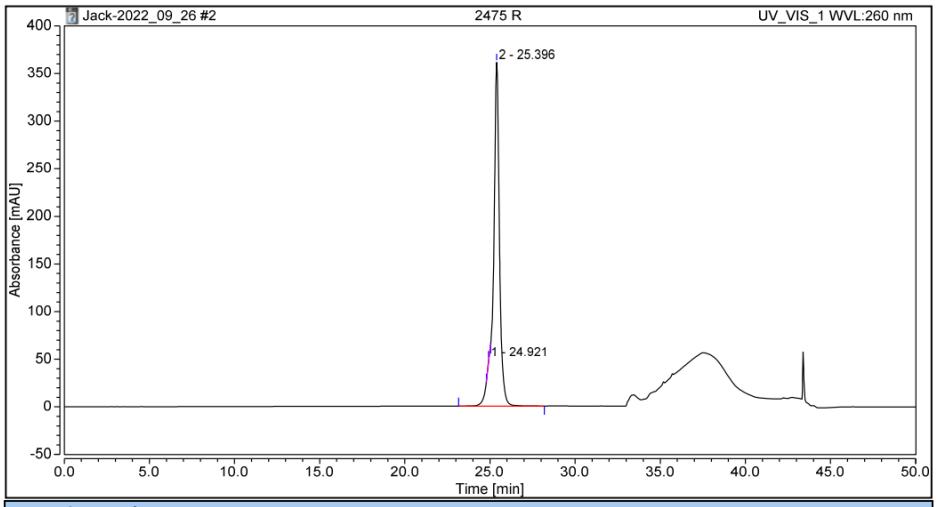

Integration Results							
No.	Peak Name	Retention Time min	Area mAU*min	Height mAU	Relative Area %	Relative Height %	Amount n.a.
1		24.921	0.347	2.650	0.23	0.73	n.a.
2		25.396	149.836	360.972	99.77	99.27	n.a.
Total:			**150.183**	**363.622**	**100.00**	**100.00**	

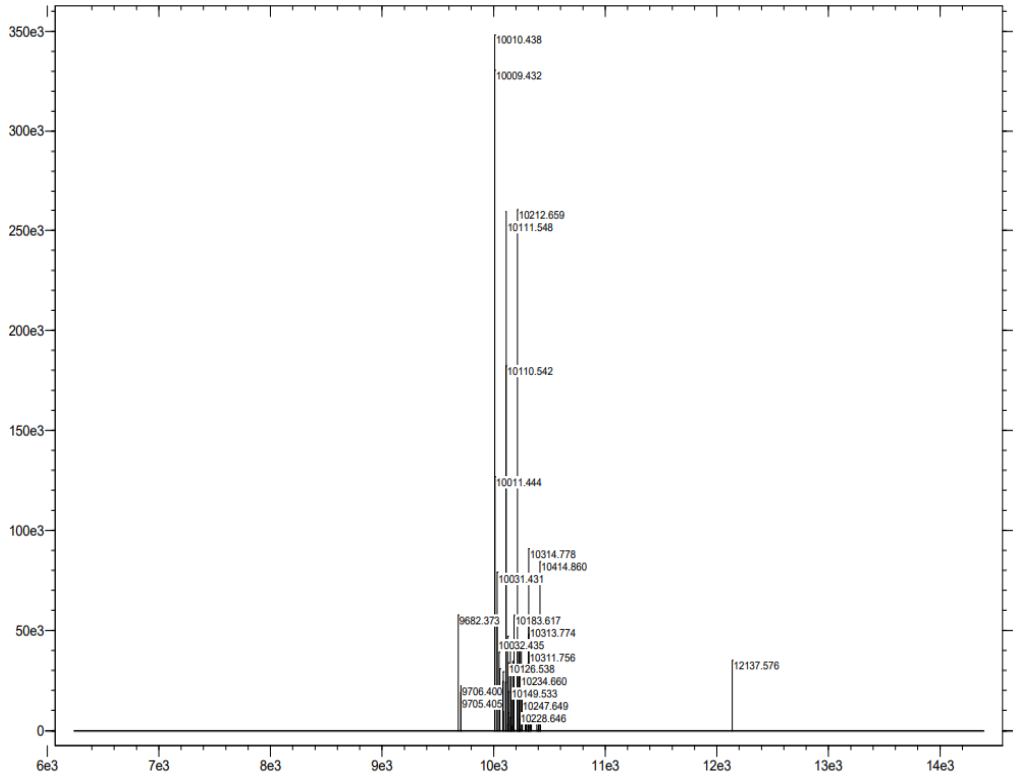

Figure 8.14: Analytical HPLC trace (top, detection wavelength = 260 nm) and processed mass spectrometry spectrum (bottom) for **CuCy5'-30mer**.

Fc5′-30mer

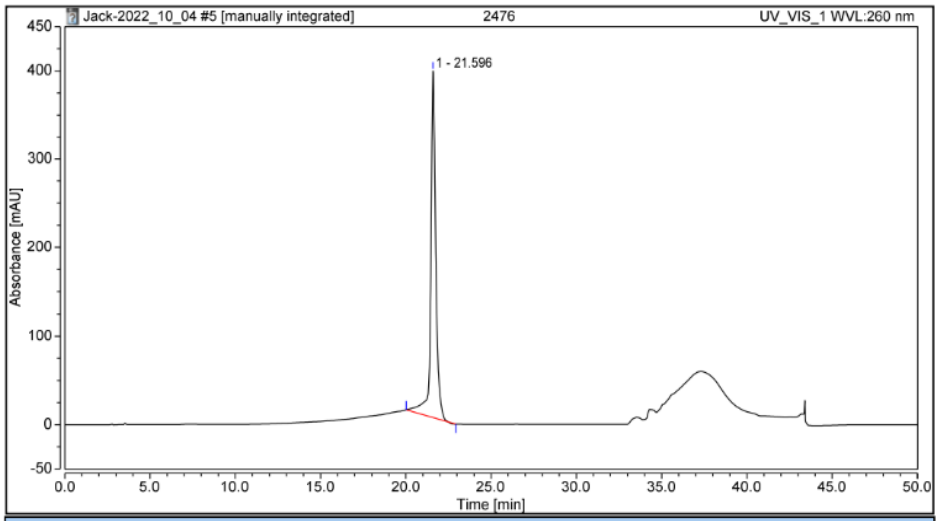

Integration Results

No.	Peak Name	Retention Time min	Area mAU*min	Height mAU	Relative Area %	Relative Height %	Amount n.a.
1		21.596	132.682	391.875	100.00	100.00	n.a.
Total:			**132.682**	**391.875**	**100.00**	**100.00**	

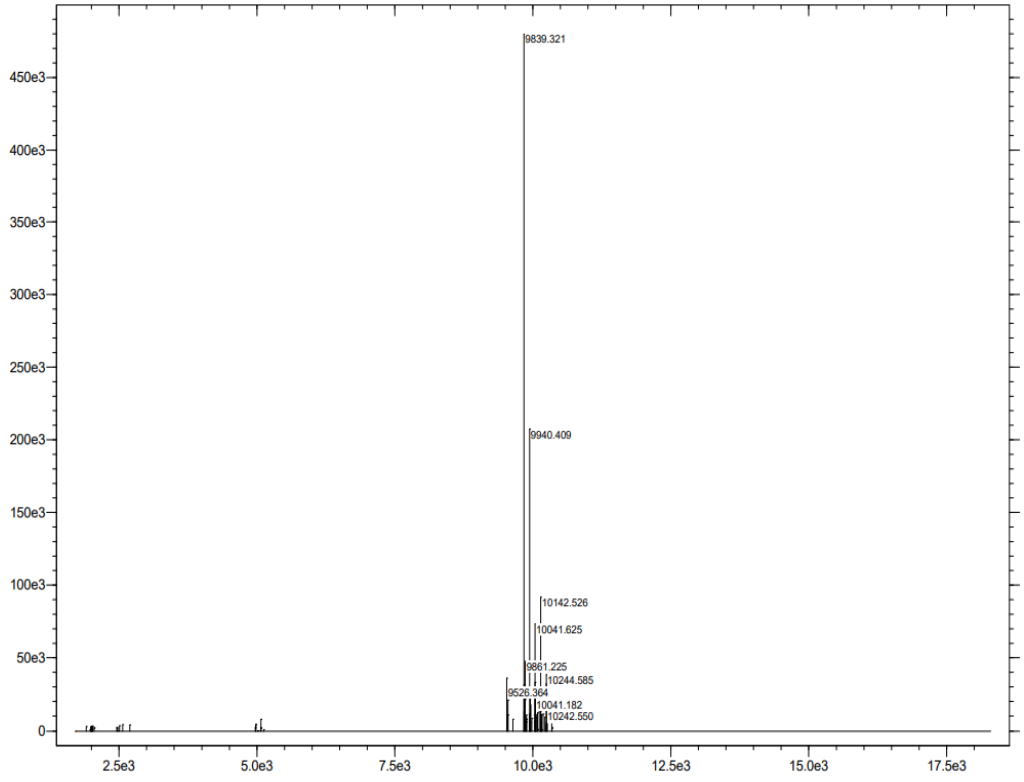

Figure 8.15: Analytical HPLC trace (top, detection wavelength = 260 nm) and processed mass spectrometry spectrum (bottom) for **Fc5'-30mer**.

T1-21mer

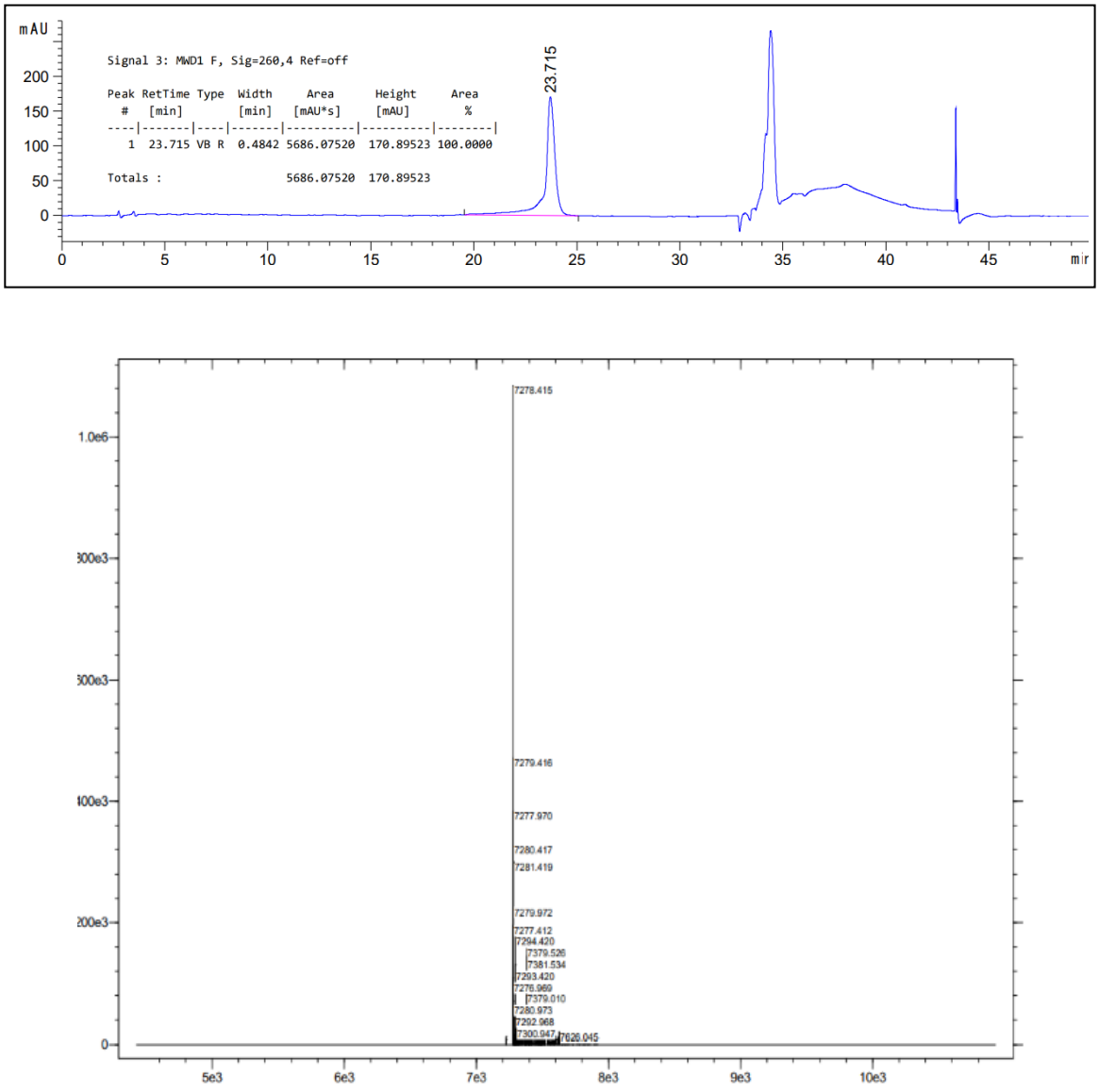

Figure 8.16: Analytical HPLC trace (top, detection wavelength = 260 nm) and processed mass spectrometry spectrum (bottom) for **T1-21mer**.

B1-30mer

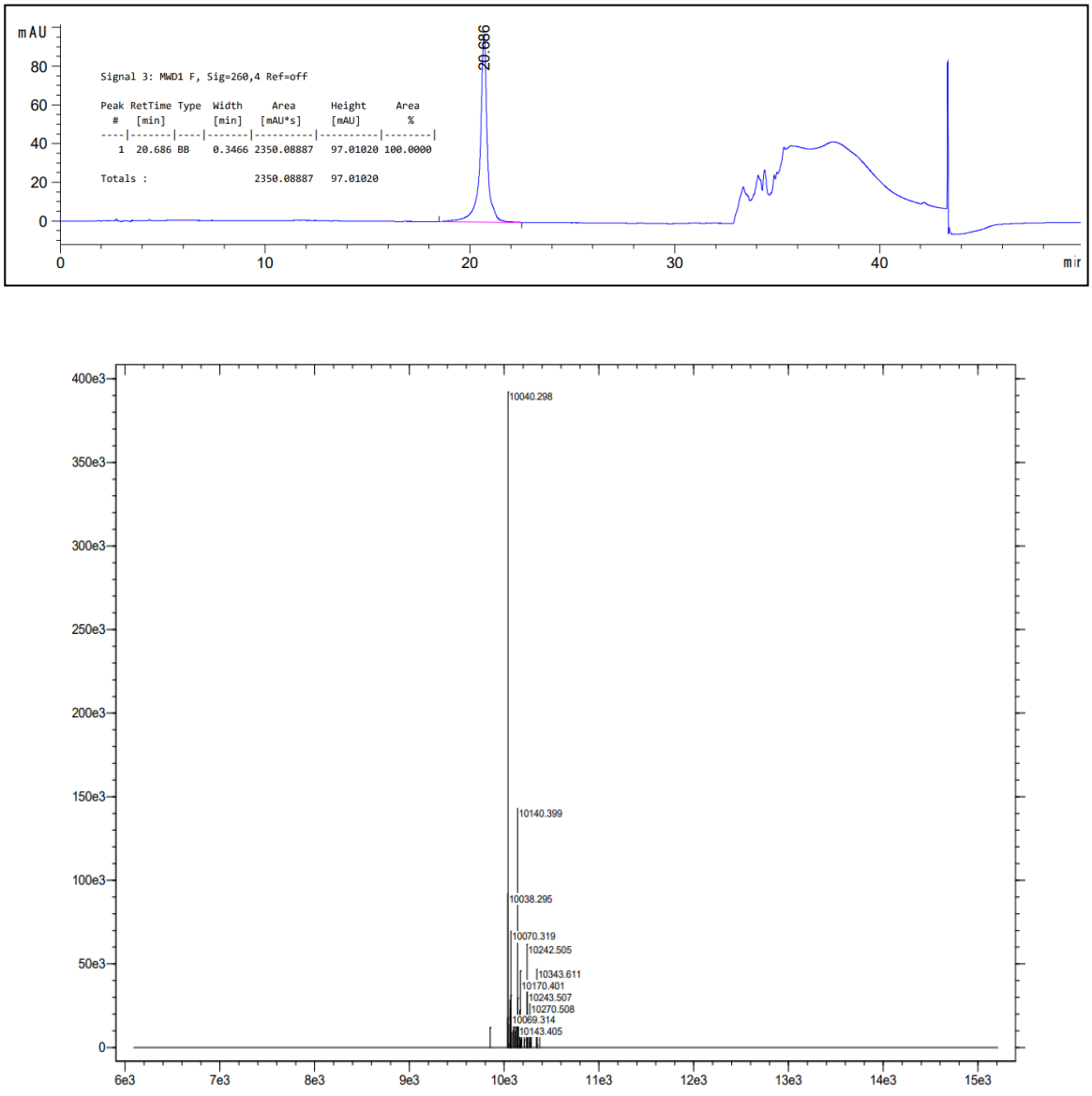

Figure 8.17: Analytical HPLC trace (top, detection wavelength = 260 nm) and processed mass spectrometry spectrum (bottom) for **B1-30mer**.

CuCyMid_C3-2

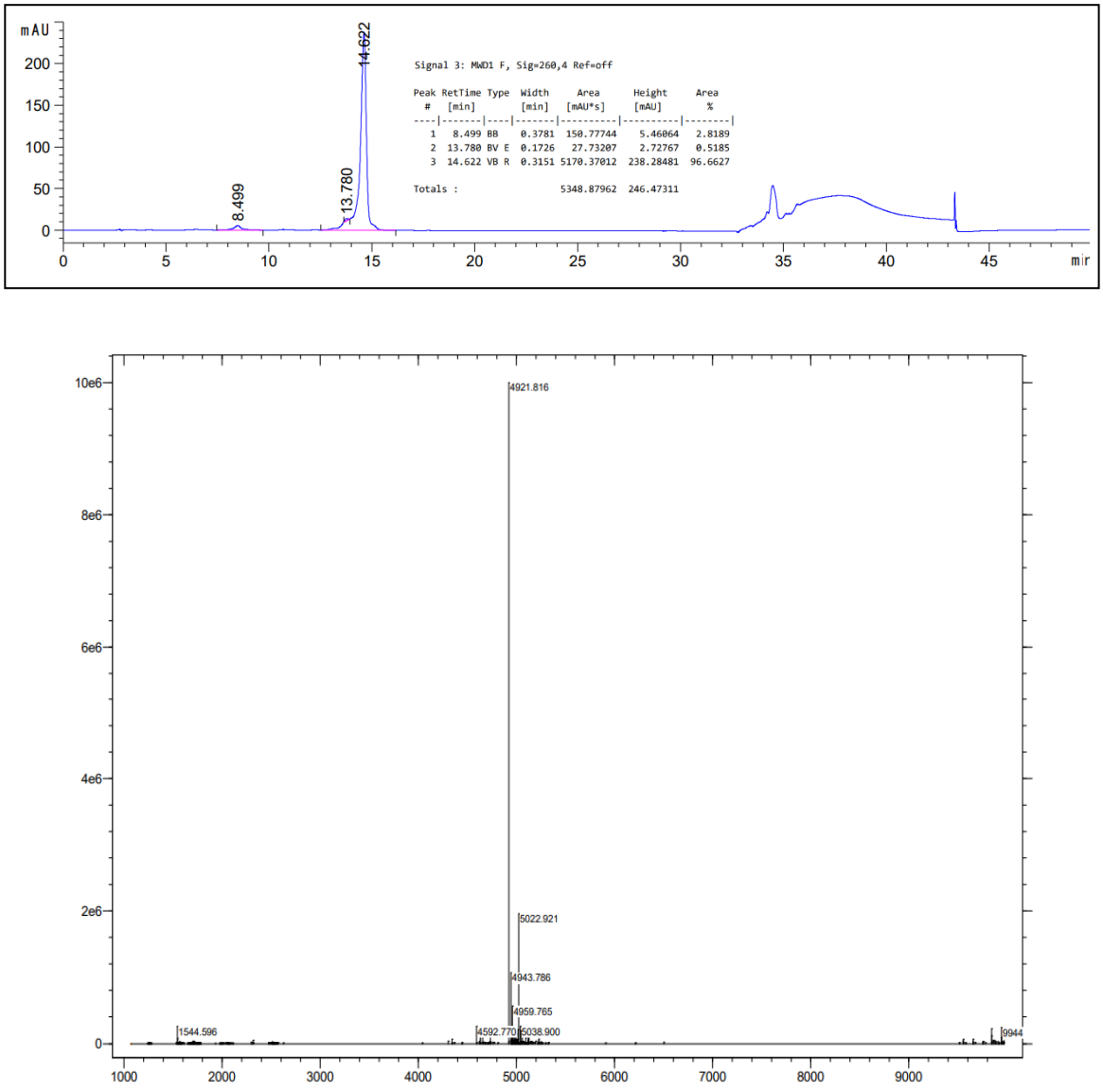

Figure 8.18: Analytical HPLC trace (top, detection wavelength = 260 nm) and processed mass spectrometry spectrum (bottom) for **CuCyMid_C3-2**.

CuCyMid_C3+2

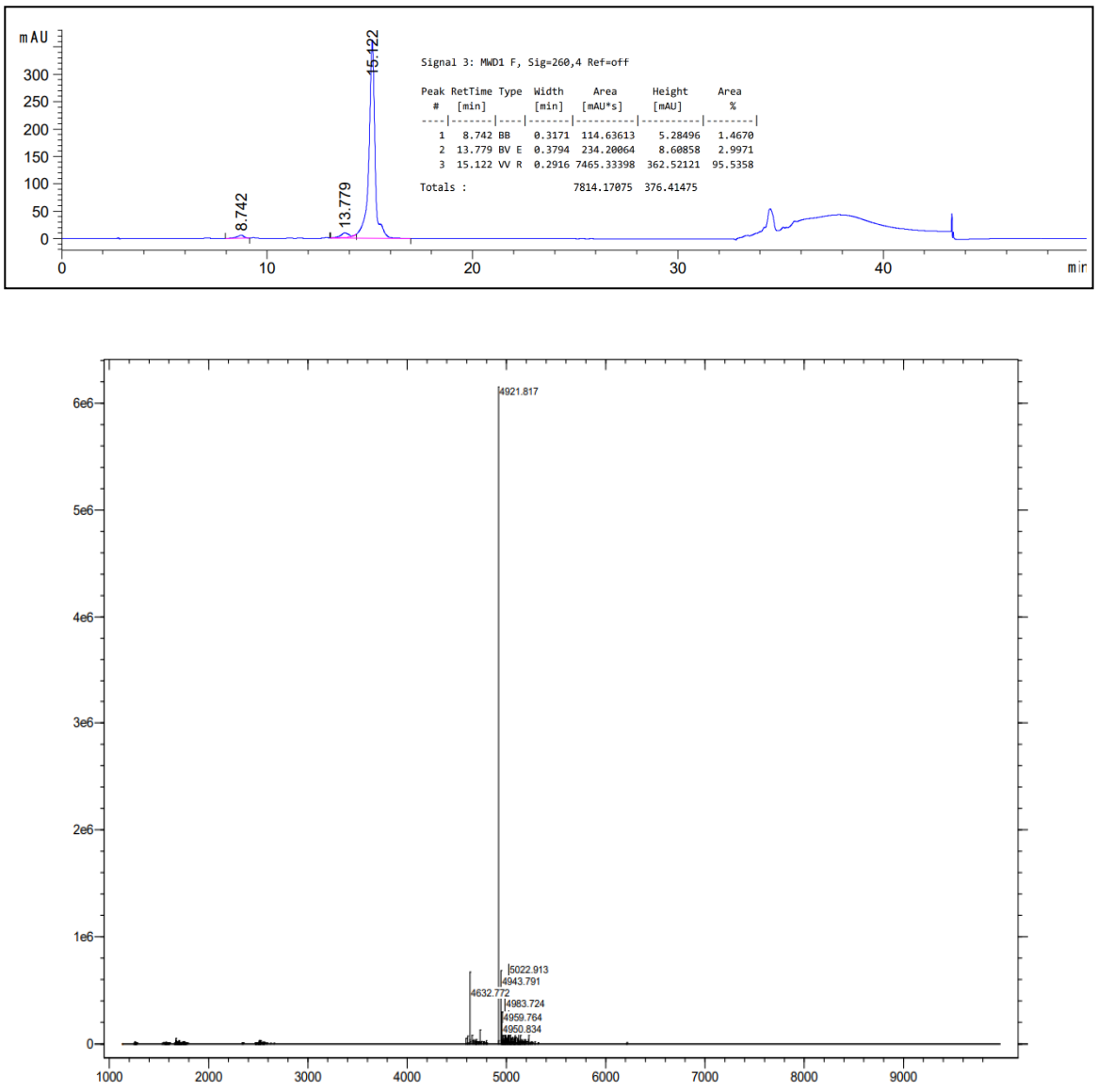

Figure 8.19: Analytical HPLC trace (top, detection wavelength = 260 nm) and processed mass spectrometry spectrum (bottom) for **CuCyMid_C3+2**.

T2A_C3-2

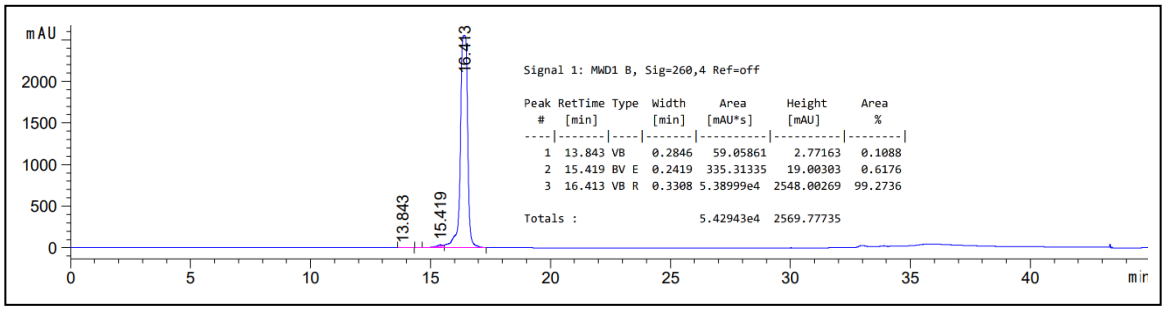

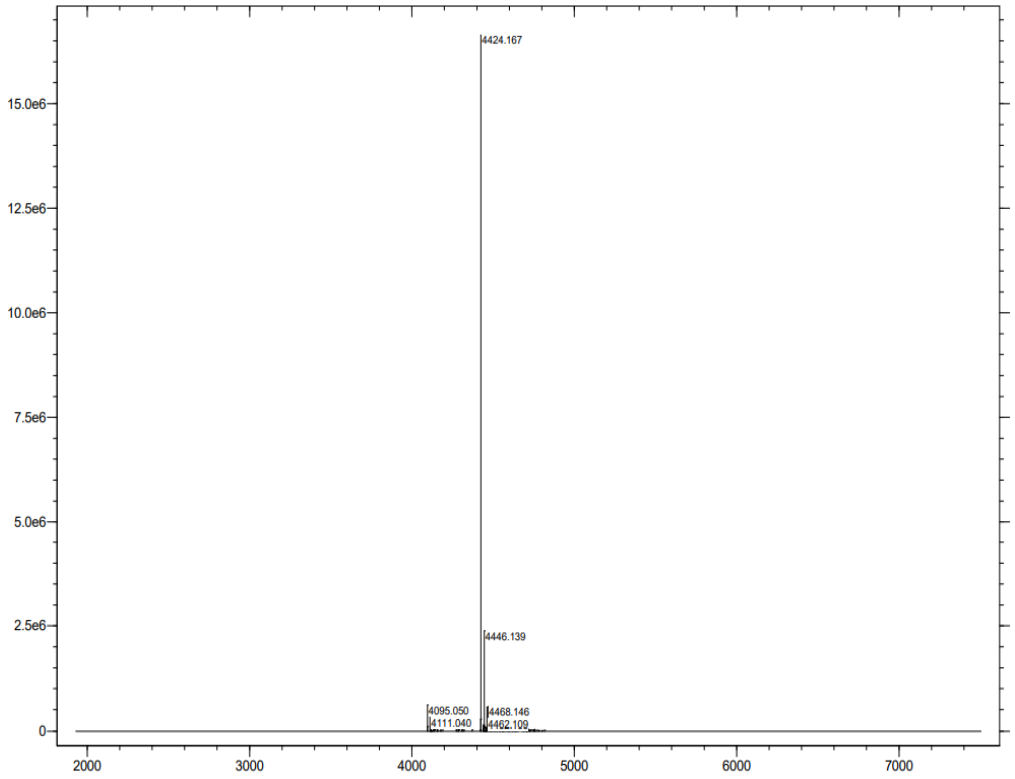

Figure 8.20: Analytical HPLC trace (top, detection wavelength = 260 nm) and processed mass spectrometry spectrum (bottom) for **T2A_C3-2**.

T2A_C3+2

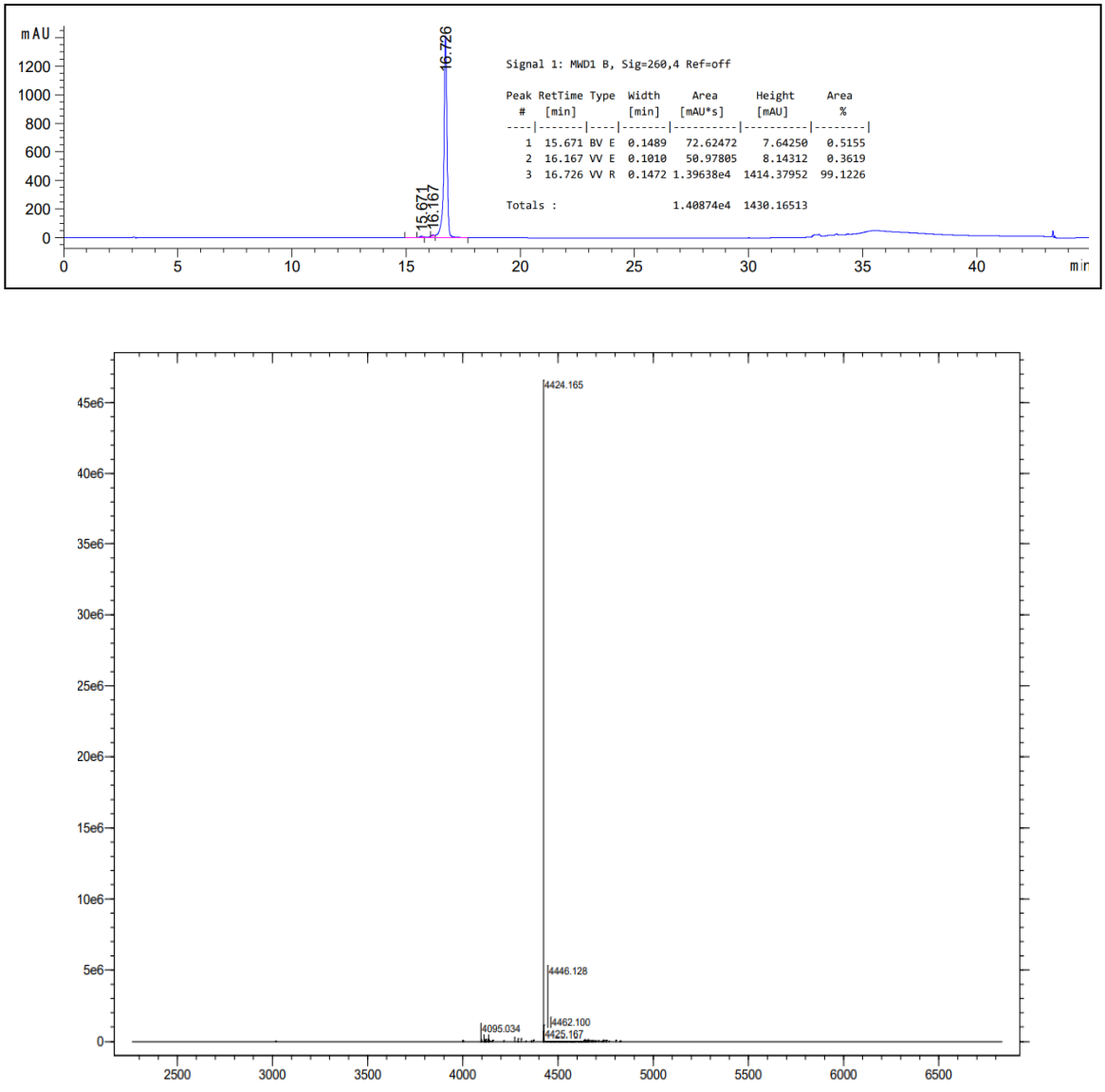

Figure 8.21: Analytical HPLC trace (top, detection wavelength = 260 nm) and processed mass spectrometry spectrum (bottom) for **T2A_C3+2**.

DNA-Cy3

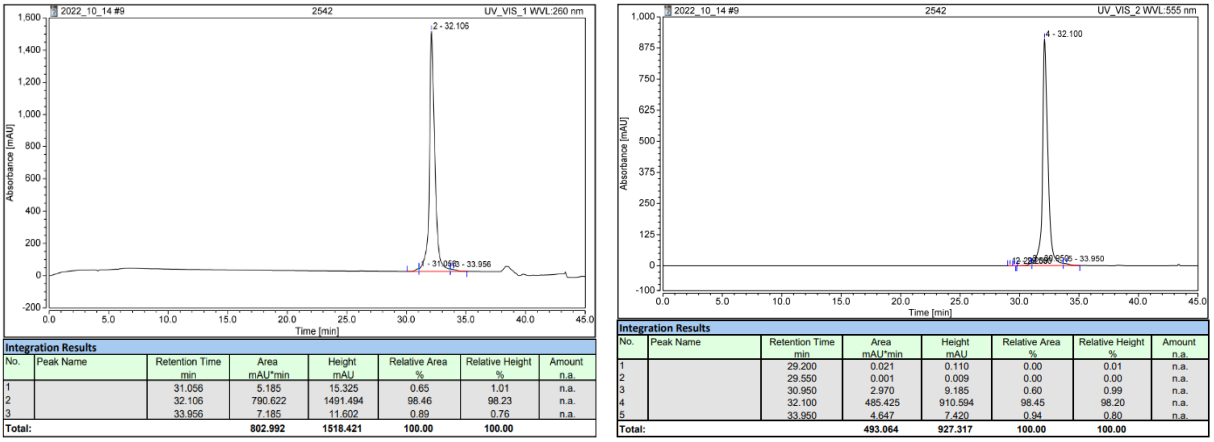

Integration Results

No.	Peak Name	Retention Time min	Area mAU*min	Height mAU	Relative Area %	Relative Height %	Amount n.a.
1		31.056	5.185	15.325	0.65	1.01	n.a.
2		32.106	790.622	1491.494	98.46	98.23	n.a.
3		33.956	7.185	11.602	0.89	0.76	n.a.
Total:			**802.992**	**1518.421**	**100.00**	**100.00**	

Integration Results

No.	Peak Name	Retention Time min	Area mAU*min	Height mAU	Relative Area %	Relative Height %	Amount n.a.
1		29.200	0.021	0.110	0.00	0.01	n.a.
2		29.550	0.001	0.009	0.00	0.00	n.a.
3		30.950	2.970	9.185	0.60	0.99	n.a.
4		32.100	485.425	910.594	98.45	98.20	n.a.
5		33.950	4.647	7.420	0.94	0.80	n.a.
Total:			**493.064**	**927.317**	**100.00**	**100.00**	

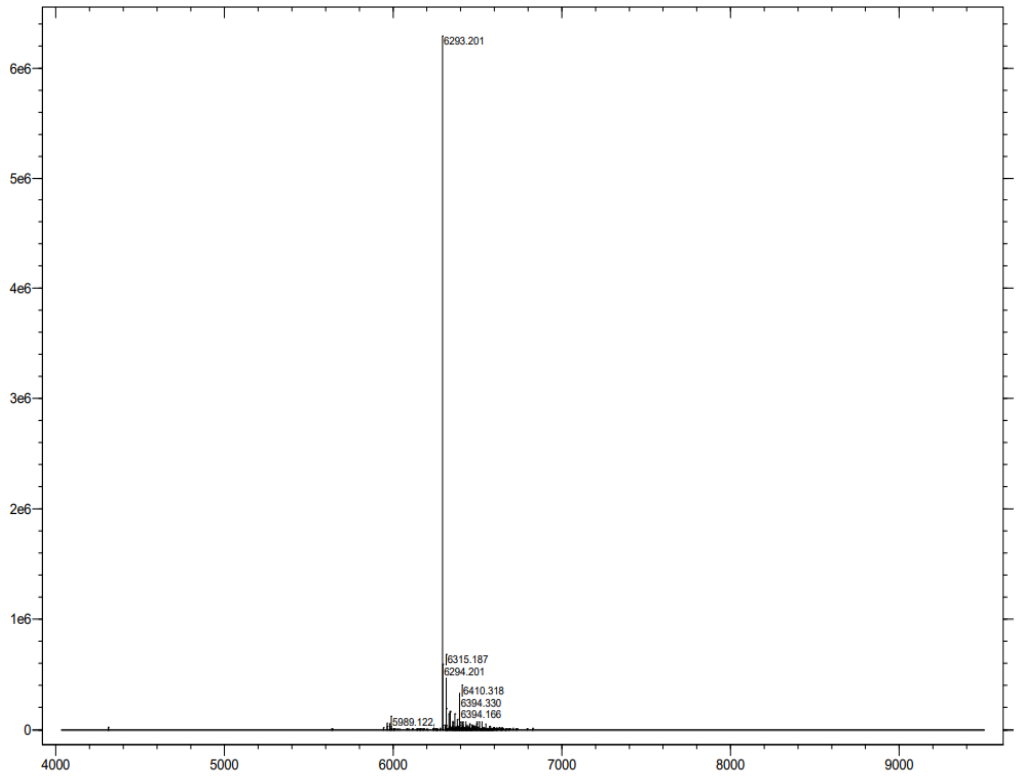

Figure 8.22: Analytical HPLC trace (top, detection wavelengths = 260 nm and 555 nm) and processed mass spectrometry spectrum (bottom) for **DNA-Cy3**.

DNA-Cy5

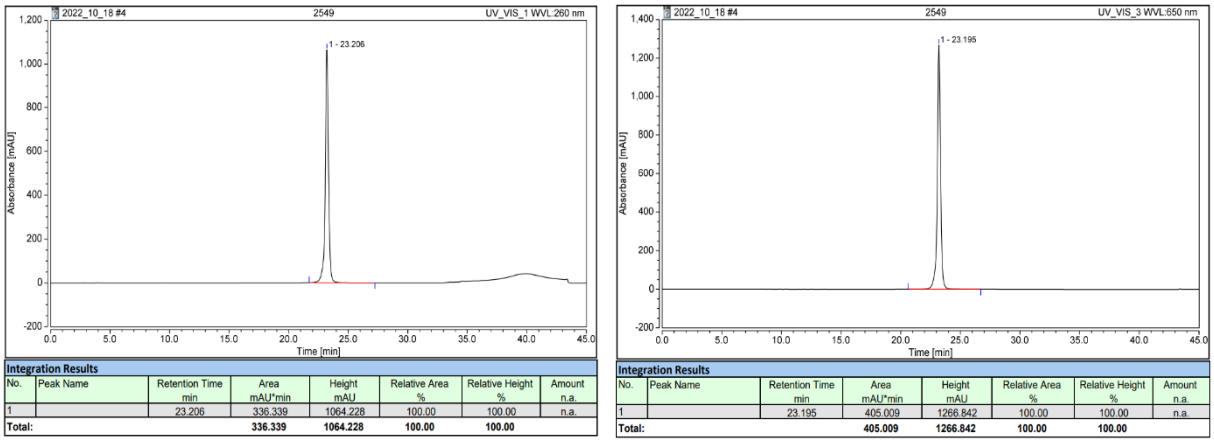

Integration Results

No.	Peak Name	Retention Time min	Area mAU*min	Height mAU	Relative Area %	Relative Height %	Amount n.a.
1		23.206	336.339	1064.228	100.00	100.00	n.a.
Total:			**336.339**	**1064.228**	**100.00**	**100.00**	

Integration Results

No.	Peak Name	Retention Time min	Area mAU*min	Height mAU	Relative Area %	Relative Height %	Amount n.a.
1		23.195	405.009	1266.842	100.00	100.00	n.a.
Total:			**405.009**	**1266.842**	**100.00**	**100.00**	

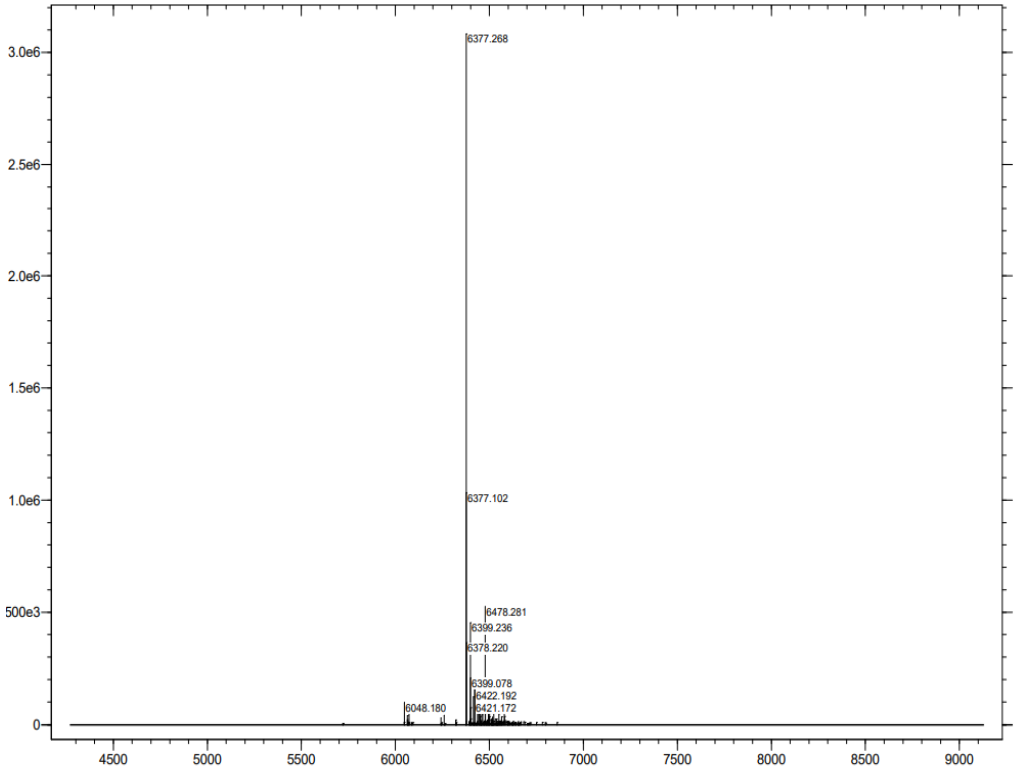

Figure 8.23: Analytical HPLC trace (top, detection wavelengths = 260 nm and 650 nm) and processed mass spectrometry spectrum (bottom) for **DNA-Cy5**.

DNA-Cy3-Ext

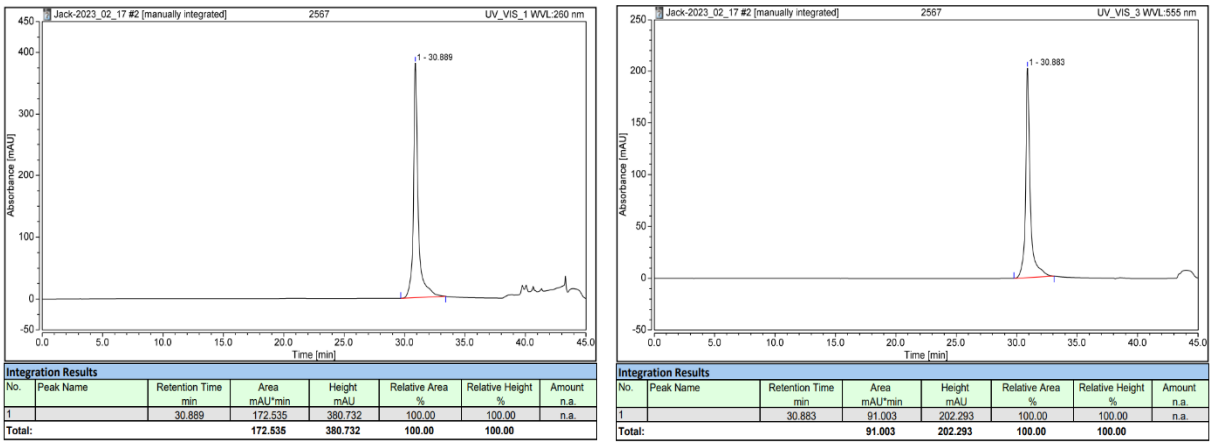

Integration Results

No.	Peak Name	Retention Time min	Area mAU*min	Height mAU	Relative Area %	Relative Height %	Amount n.a.
1		30.889	172.535	380.732	100.00	100.00	n.a.
Total:			**172.535**	**380.732**	**100.00**	**100.00**	

Integration Results

No.	Peak Name	Retention Time min	Area mAU*min	Height mAU	Relative Area %	Relative Height %	Amount n.a.
1		30.883	91.003	202.293	100.00	100.00	n.a.
Total:			**91.003**	**202.293**	**100.00**	**100.00**	

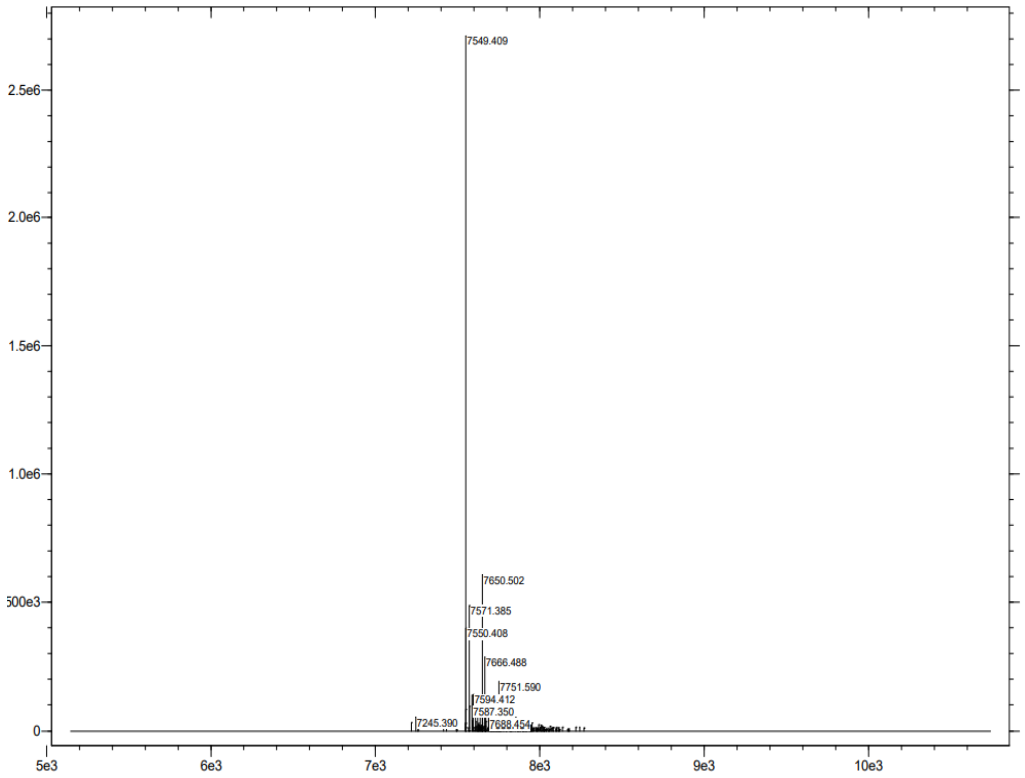

Figure 8.24: Analytical HPLC trace (top, detection wavelengths = 260 nm and 554 nm) and processed mass spectrometry spectrum (bottom) for **DNA-Cy3-Ext**.

DNA-Cy5-Ext

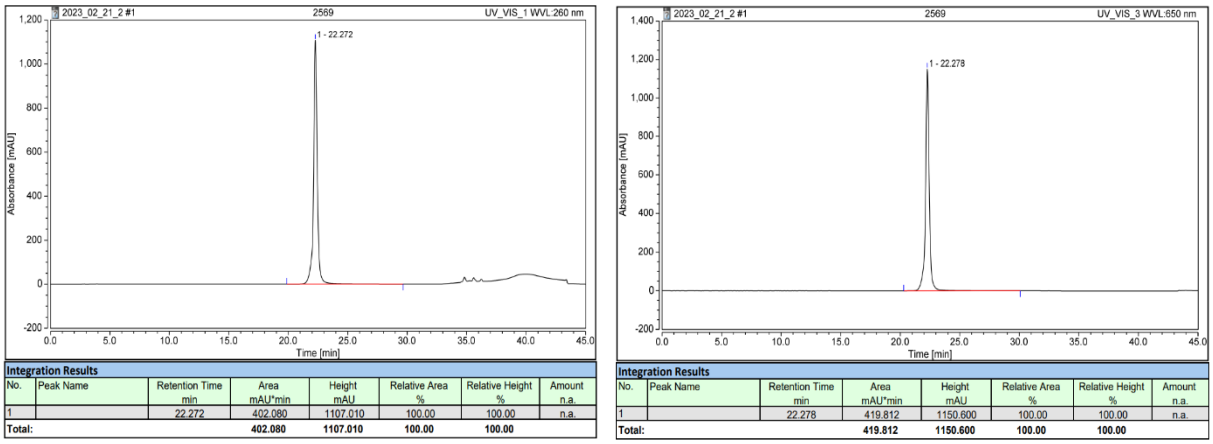

Integration Results

No.	Peak Name	Retention Time min	Area mAU*min	Height mAU	Relative Area %	Relative Height %	Amount n.a.
1		22.272	402.080	1107.010	100.00	100.00	n.a.
Total:			**402.080**	**1107.010**	**100.00**	**100.00**	

Integration Results

No.	Peak Name	Retention Time min	Area mAU*min	Height mAU	Relative Area %	Relative Height %	Amount n.a.
1		22.278	419.812	1150.600	100.00	100.00	n.a.
Total:			**419.812**	**1150.600**	**100.00**	**100.00**	

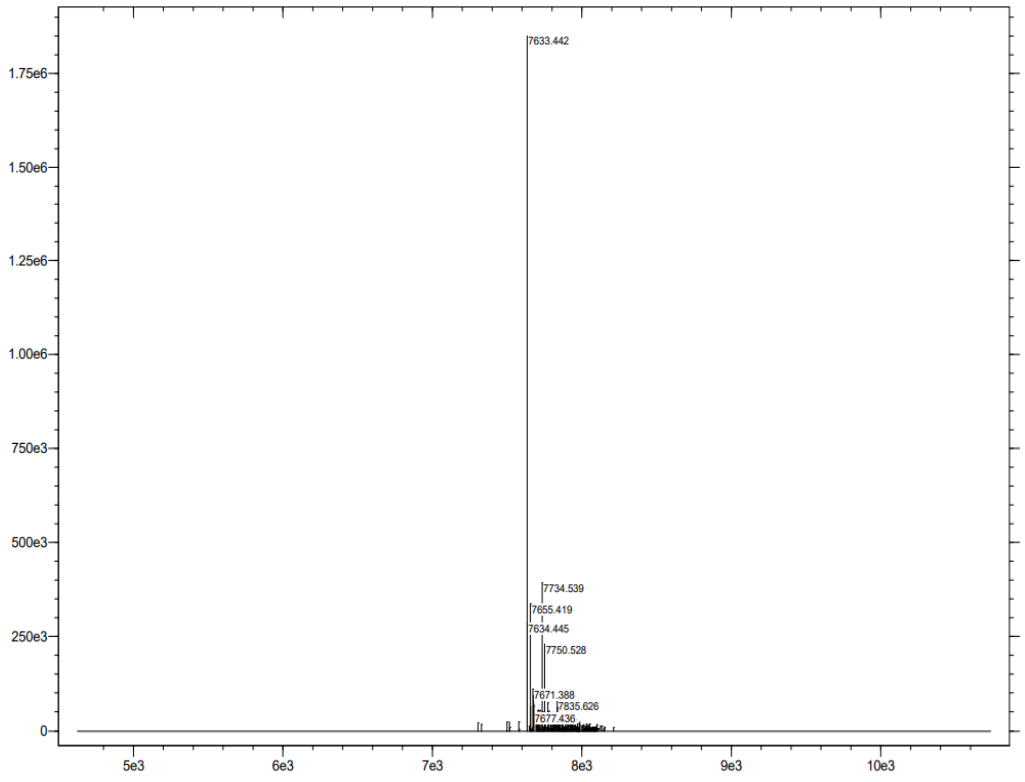

Figure 8.25: Analytical HPLC trace (top, detection wavelengths = 260 nm and 650 nm) and processed mass spectrometry spectrum (bottom) for **DNA-Cy5-Ext**.

8.2. Electrochemical Sensing of Single Point Variants Using Redox-Modified DNA Probes

8.2.1. Self-Assembled Monolayer Formation

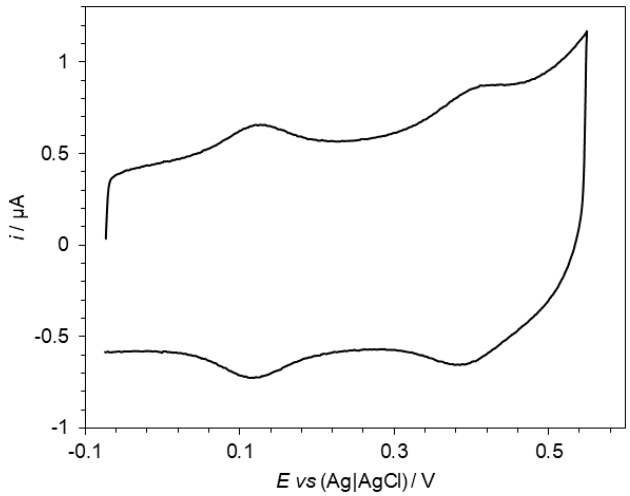

Figure 8.26: CV of **T1** after preparing the SAM without the use of TCEP; in 10 mM sodium phosphate buffer (pH 7.0) 1 M $NaClO_4$, scan rate = 1000 mV s^{-1}.

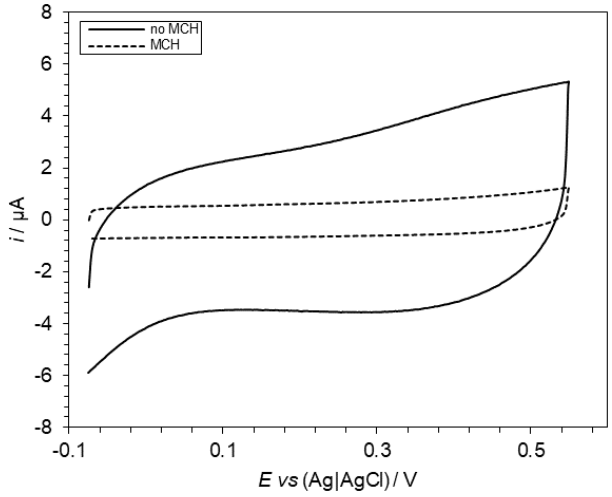

Figure 8.27: CV of a bare gold electrode (solid line) and a gold electrode passivated with 6-mercapto-1-hexanol (dashed line); in 10 mM sodium phosphate buffer (pH 7.0) 1 M $NaClO_4$, scan rate = 1000 mV s^{-1}.

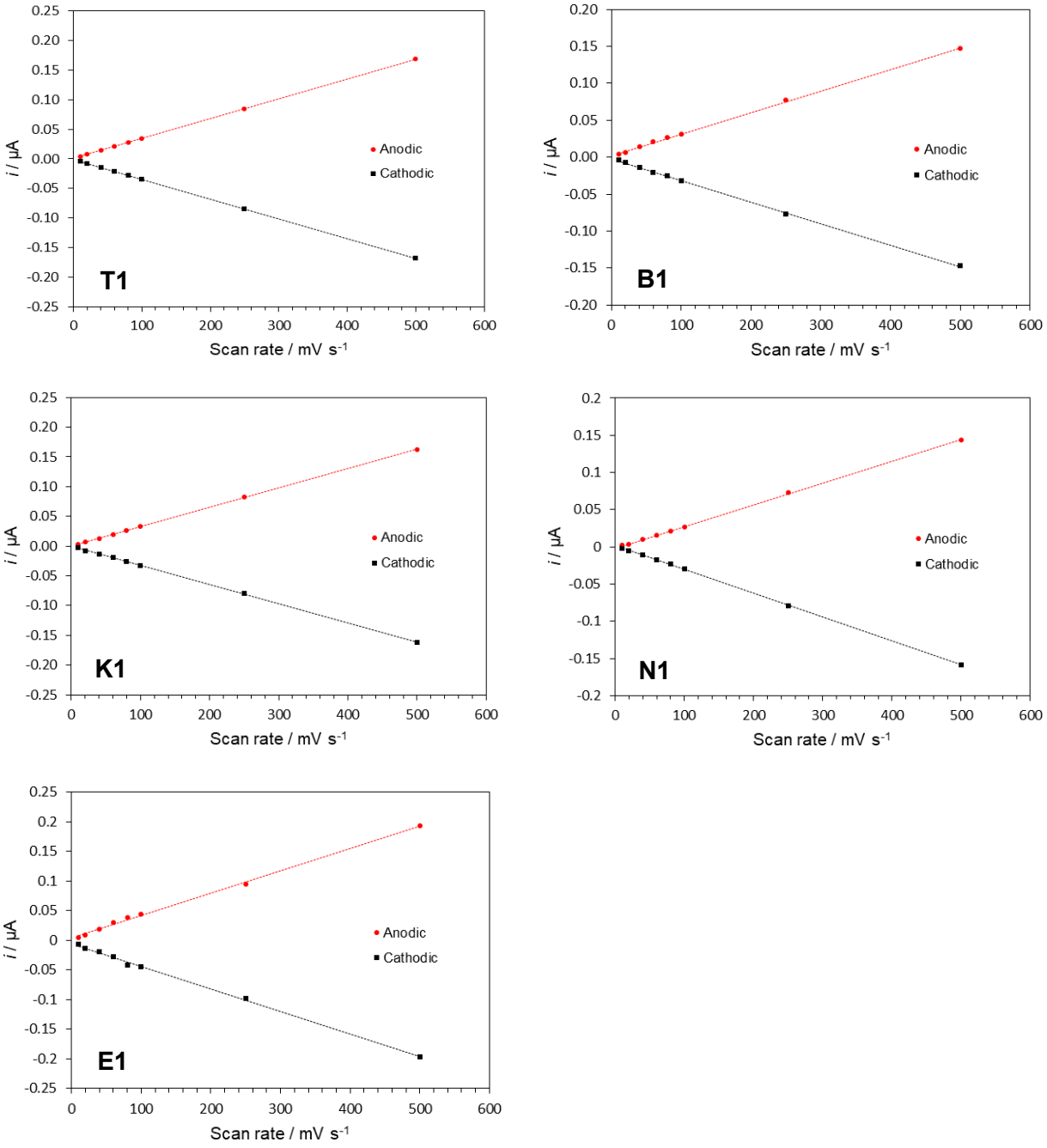

Figure 8.28: Dependence of the Fc currents on scan rate for the SPV sensing probe oligonucleotides; in 10 mM sodium phosphate buffer (pH 7.0) 1 M $NaClO_4$.

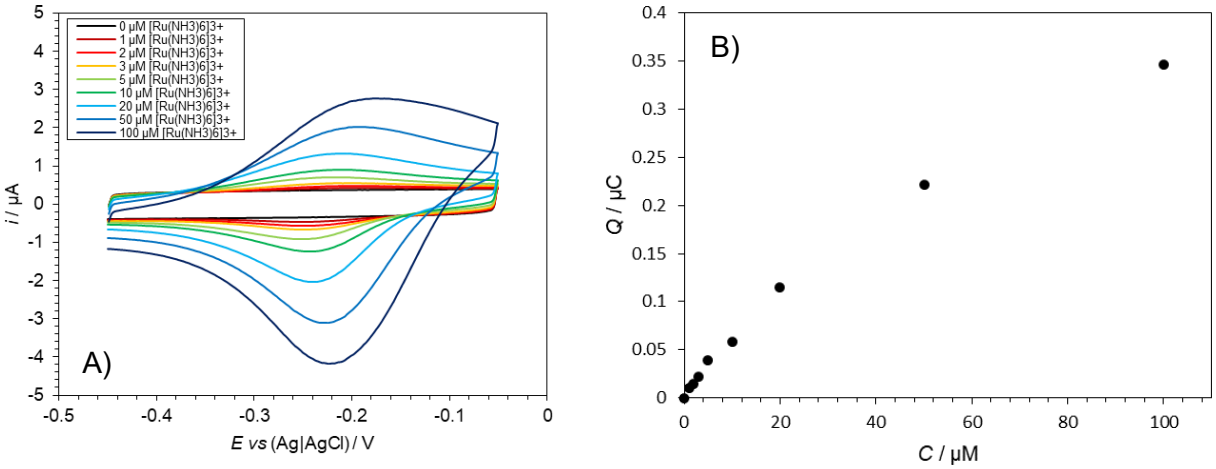

Figure 8.29: A) CVs of the **T1** probe with different amounts of $[Ru(NH_3)_6]^{3+}$ redox marker; in 10 mM Tris HCl buffer (pH 7.0) 100 mM NaCl, scan rates = 1000 mV s^{-1}. B) Plot of the concentration of $[Ru(NH_3)_6]^{3+}$ versus the charge of the cathodic peaks generated by $[Ru(NH_3)_6]^{3+}$ seen in A.

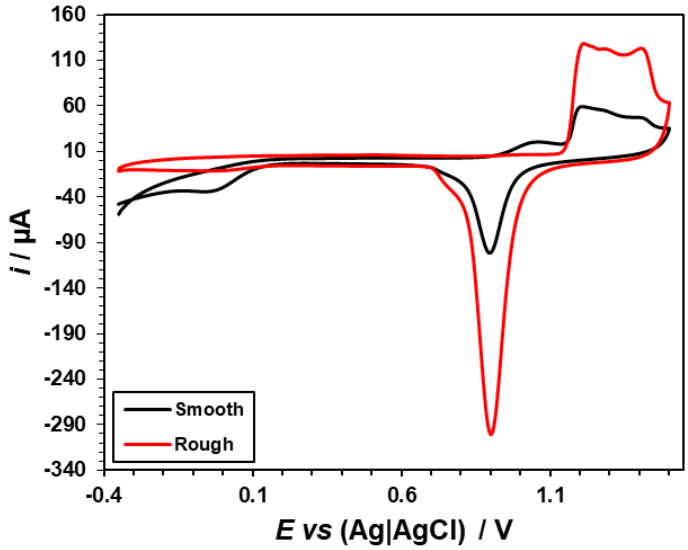

Figure 8.30: CVs of bare gold electrodes before electrochemical roughening (black) and after electrochemical roughening (red); in 0.5 M H_2SO_4, scan rates = 500 mV s^{-1}.

8.2.2. Single Point Variant Probe Thermal Melting Data

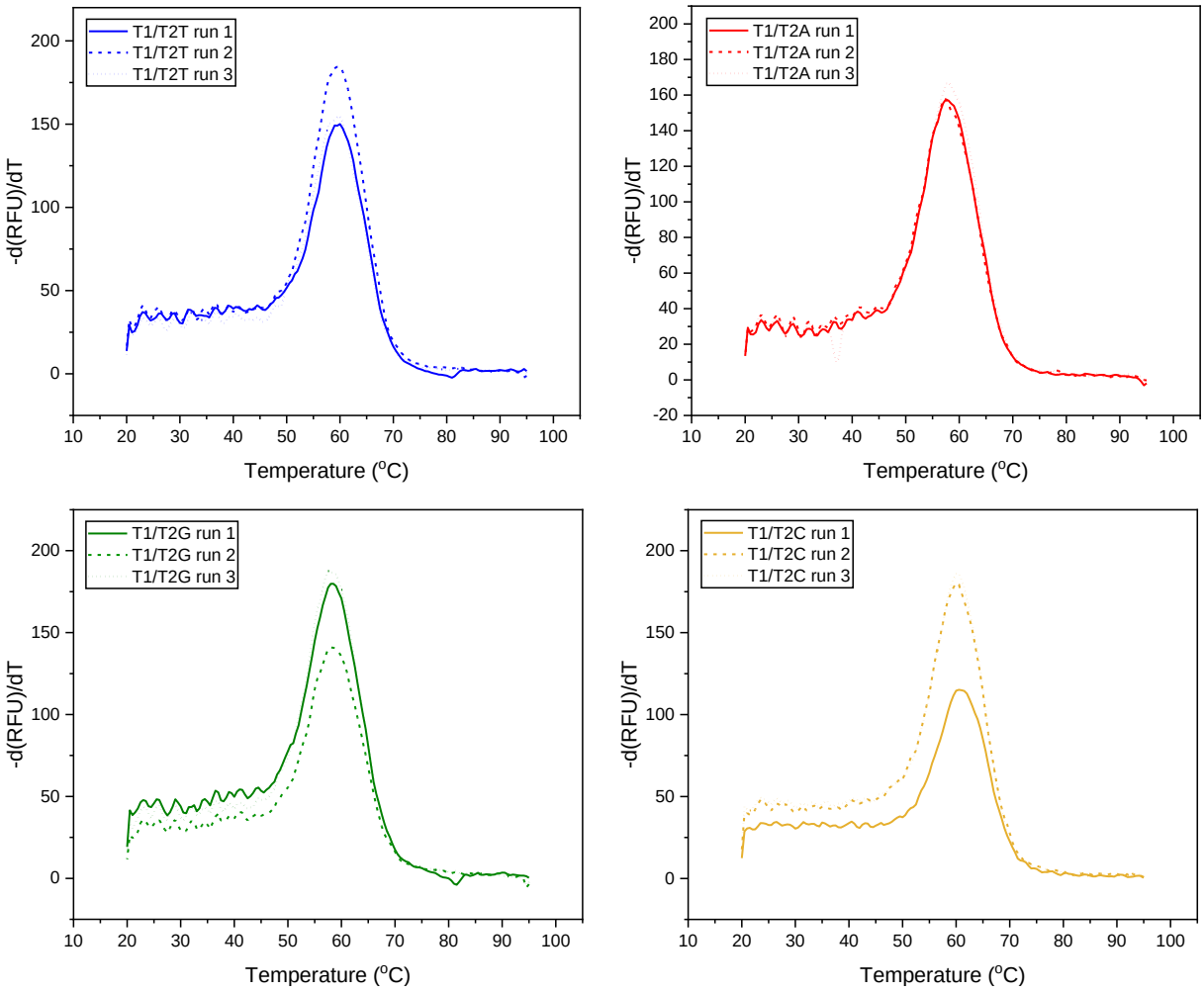

Figure 8.31: Thermal melting graphs for **T1**, plotting temperature of the oligonucleotide sample versus the negative rate of change in the relative fluorescence emission (RFU) of SYBR Green I.

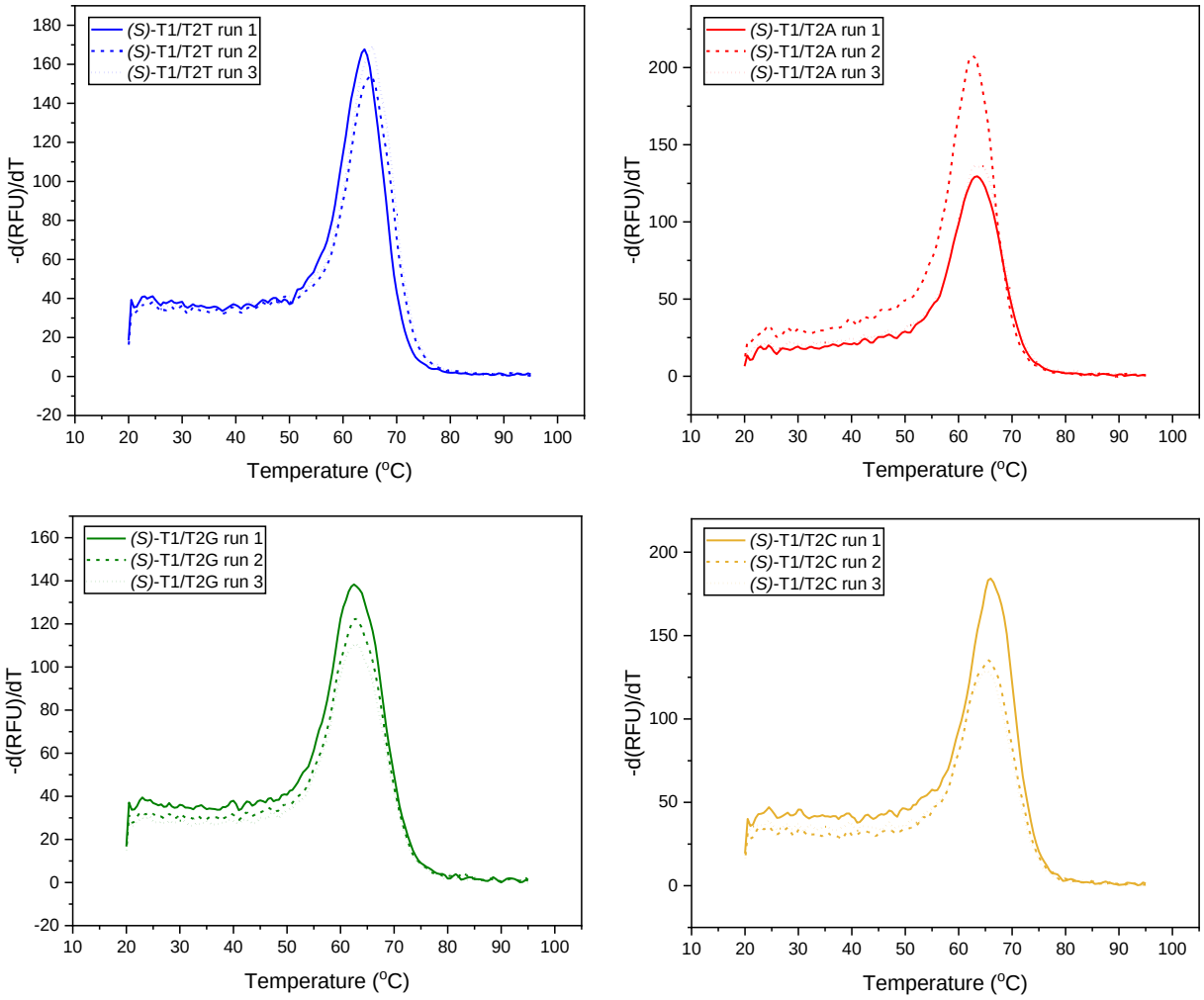

Figure 8.32: Thermal melting graphs for **(*S*)-T1**, plotting temperature of the oligonucleotide sample versus the negative rate of change in the RFU of SYBR Green I.

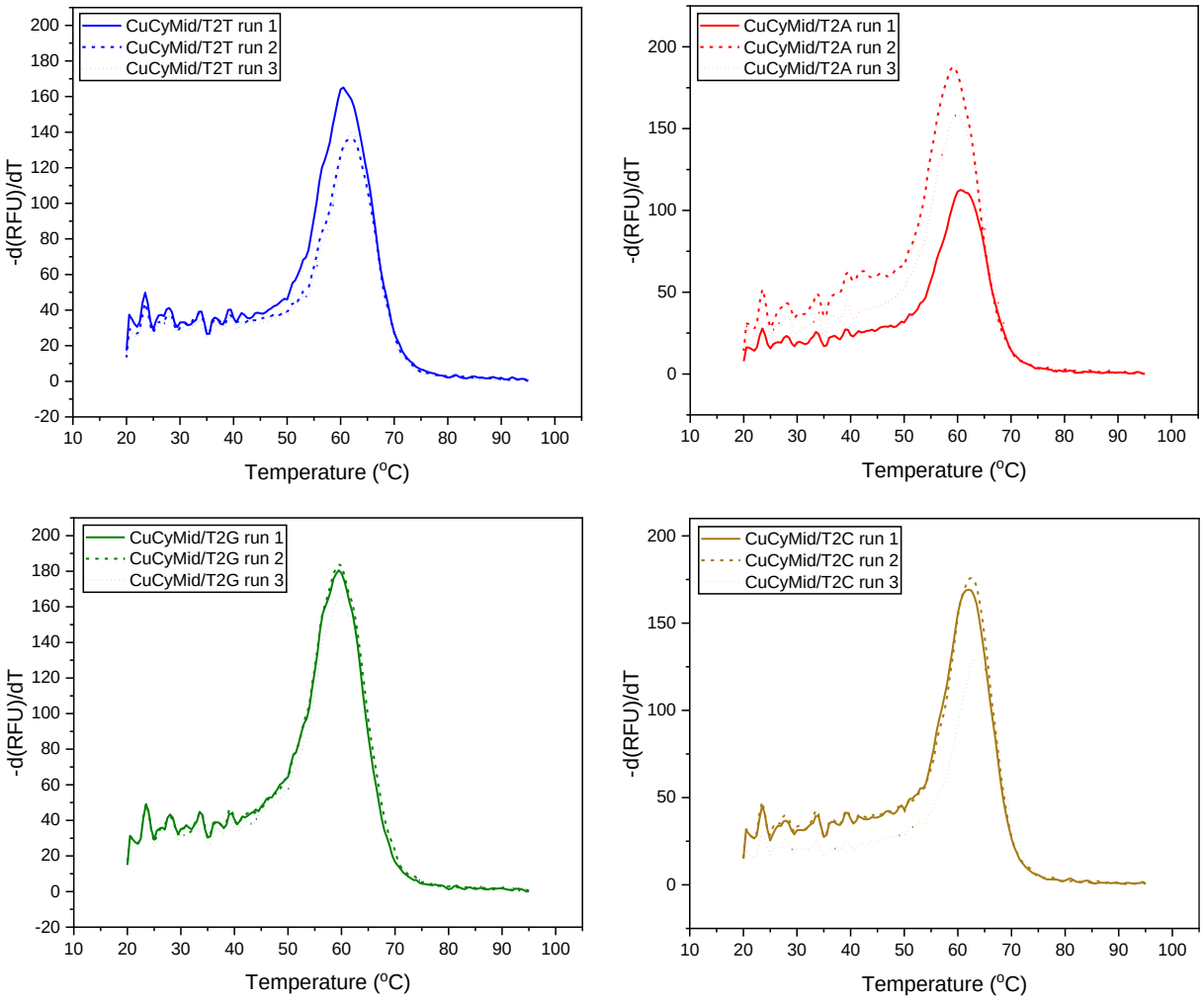

Figure 8.33: Thermal melting graphs for **CuCyMid**, plotting temperature of the oligonucleotide sample versus the negative rate of change in the RFU of SYBR Green I.

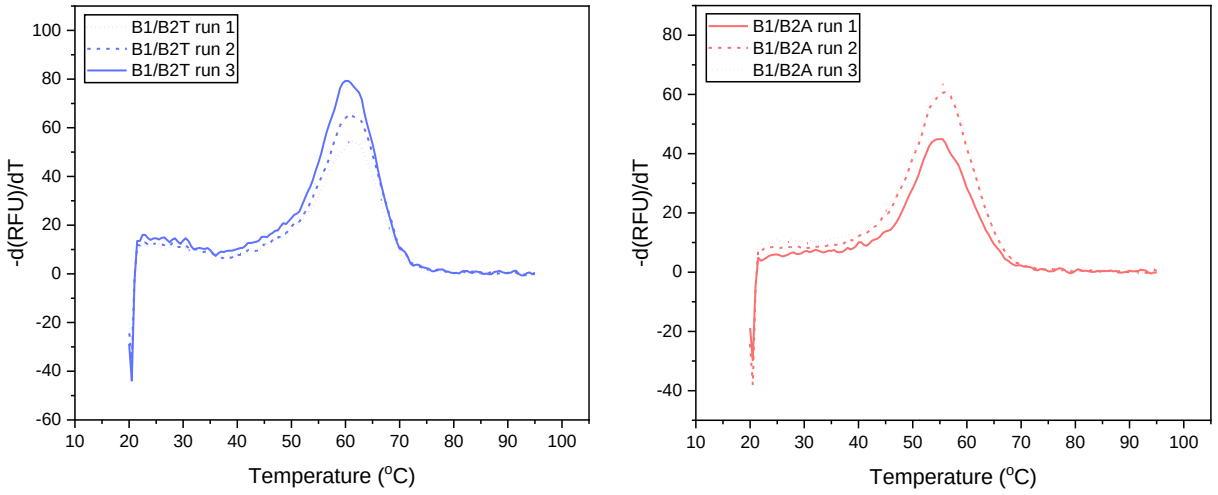

Figure 8.34: Thermal melting graphs for **B1**, plotting temperature of the oligonucleotide sample versus the negative rate of change in the RFU of SYBR Green I.

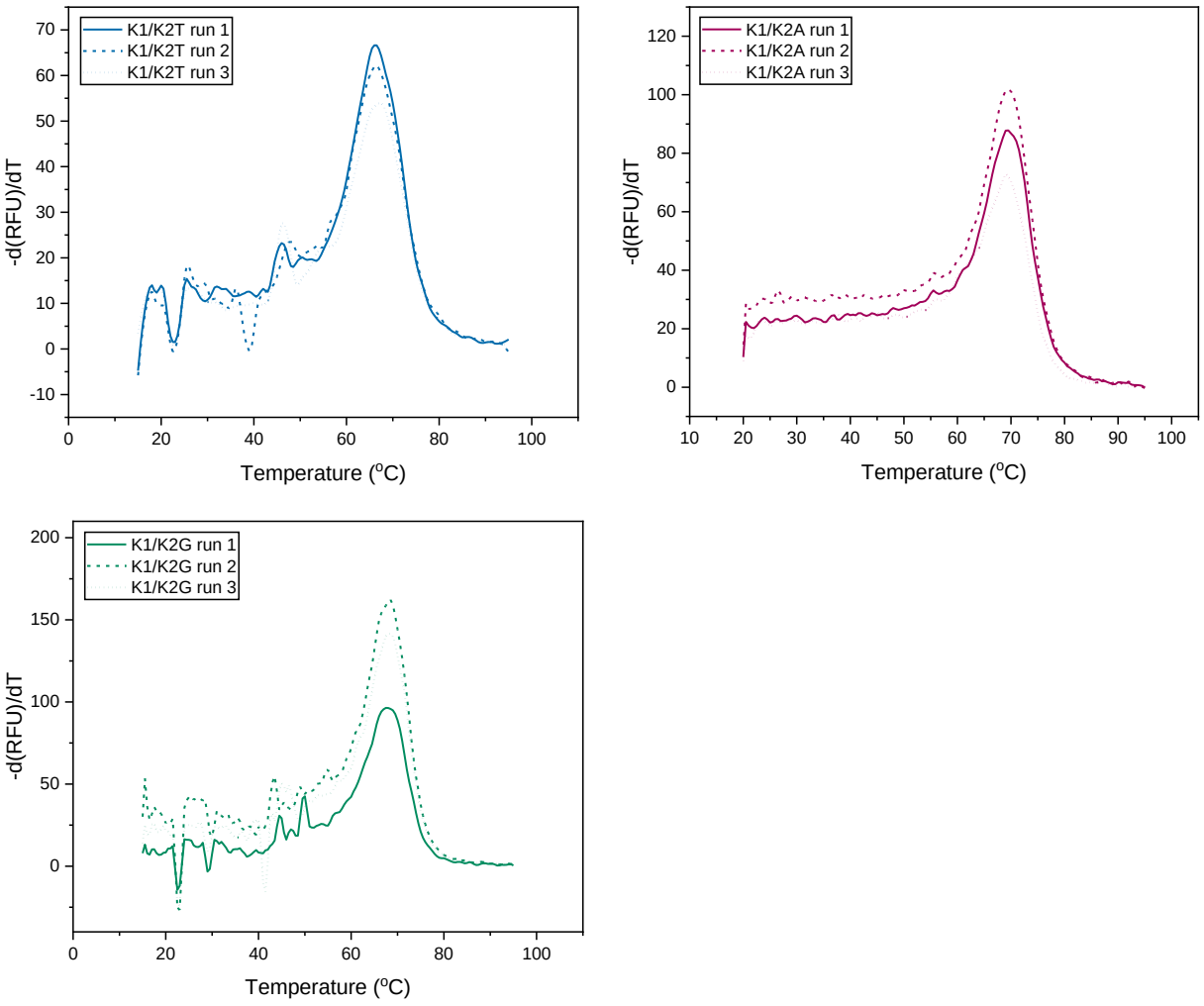

Figure 8.35: Thermal melting graphs for **K1**, plotting temperature of the oligonucleotide sample versus the negative rate of change in the RFU of SYBR Green I.

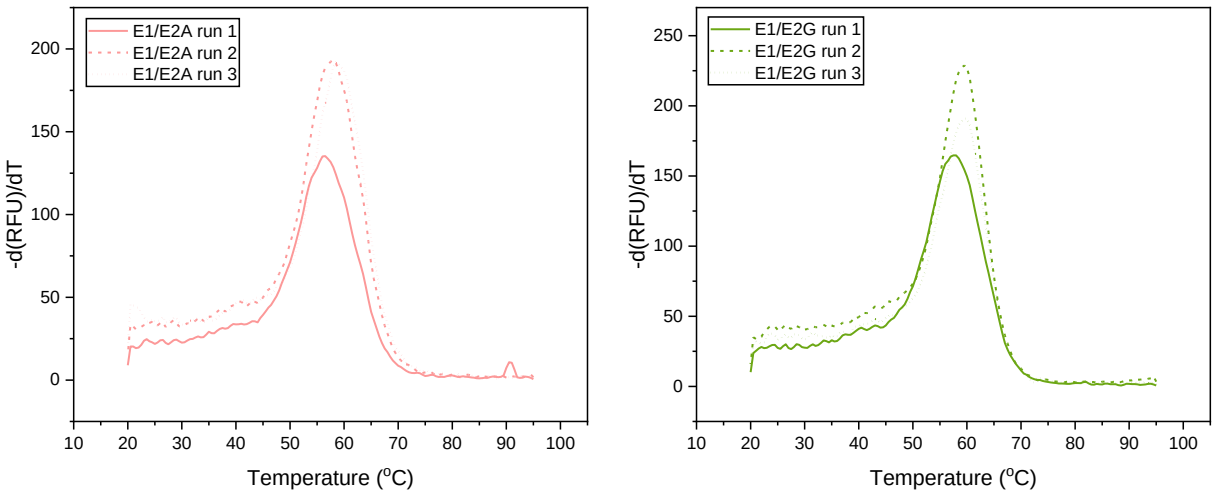

Figure 8.36: Thermal melting graphs for **E1**, plotting temperature of the oligonucleotide sample versus the negative rate of change in the RFU of SYBR Green I.

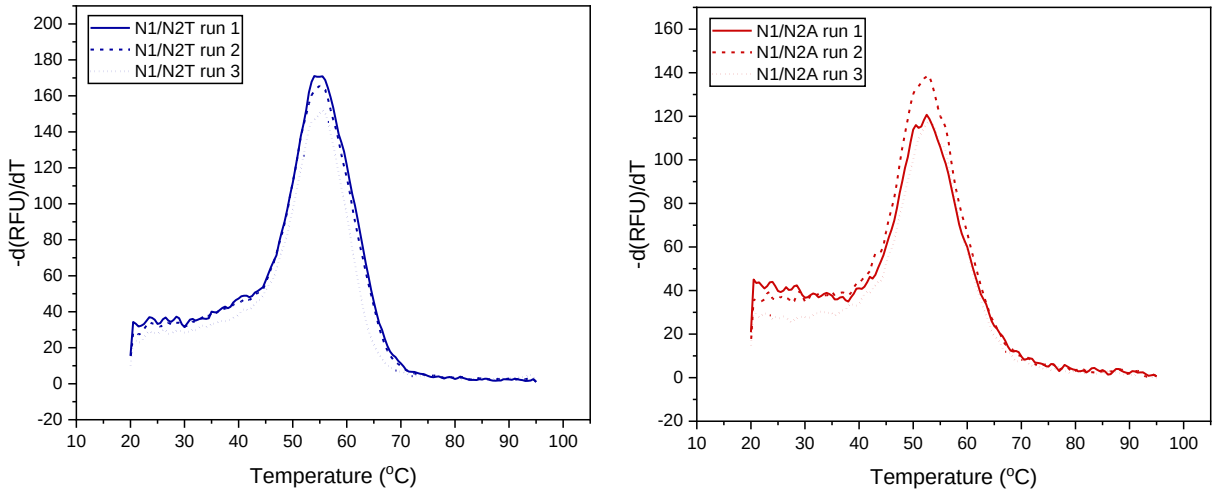

Figure 8.37: Thermal melting graphs for **N1**, plotting temperature of the oligonucleotide sample versus the negative rate of change in the RFU of SYBR Green I.

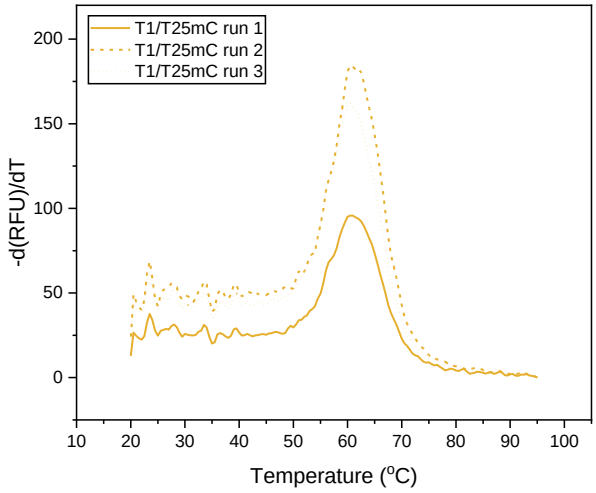

Figure 8.38: Thermal melting graphs for **T1** with **T25mC**, plotting temperature of the oligonucleotide sample versus the negative rate of change in the RFU of SYBR Green I.

8.2.3. Electrochemical Stability Cyclic Voltammograms

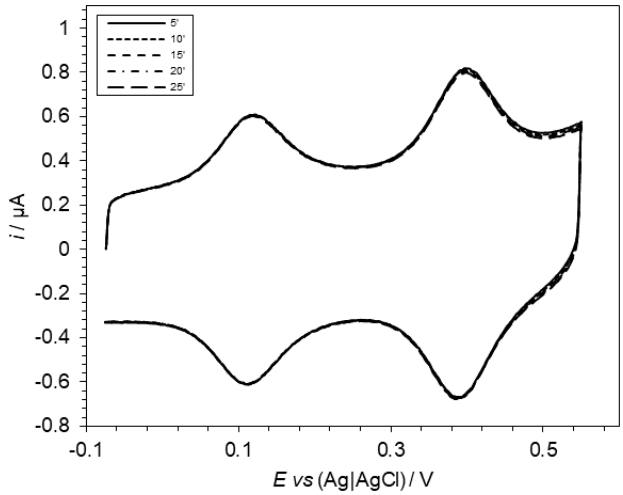

Figure 8.39: CVs of **T1** taken every five minutes, each at a scan rate of 1000 mV s^{-1} (the scan rate used for sensing). No significant change in either the Fc or the CuCy currents indicated that the sensing CVs themselves were not impacting the CuCy:Fc current ratios. Taken in 10 mM sodium phosphate buffer (pH 7.0) 1 M $NaClO_4$.

8.2.4. Limit of Detection Cyclic Voltammograms

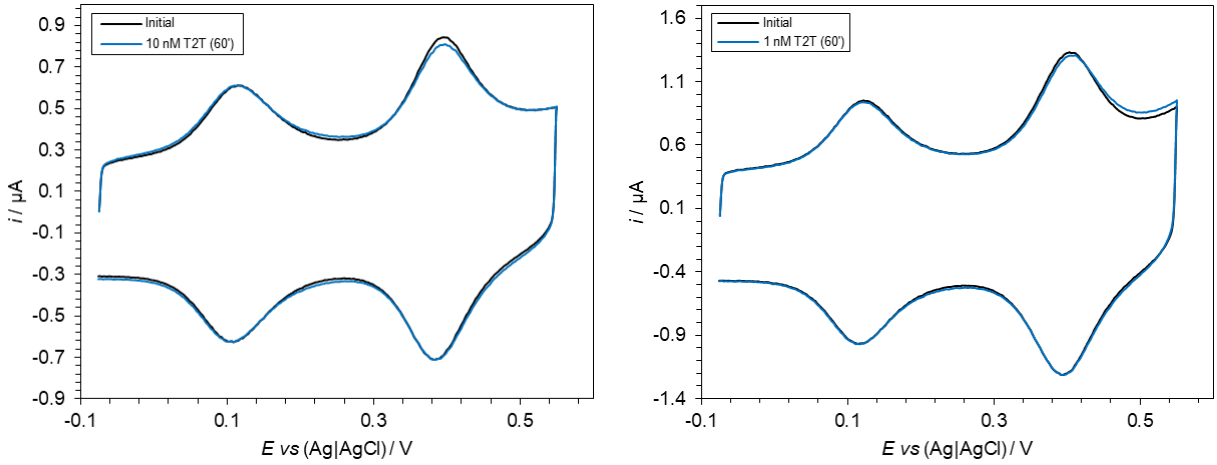

Figure 8.40: CVs of **T1** sensing 10 nM **T2T** (left) and 1 nM **T2T** (right); in 10 mM sodium phosphate buffer (pH 7.0) 1 M $NaClO_4$, scan rates = 1000 mV s^{-1}.

8.2.5. Destructive Probe Regeneration Using Sonication

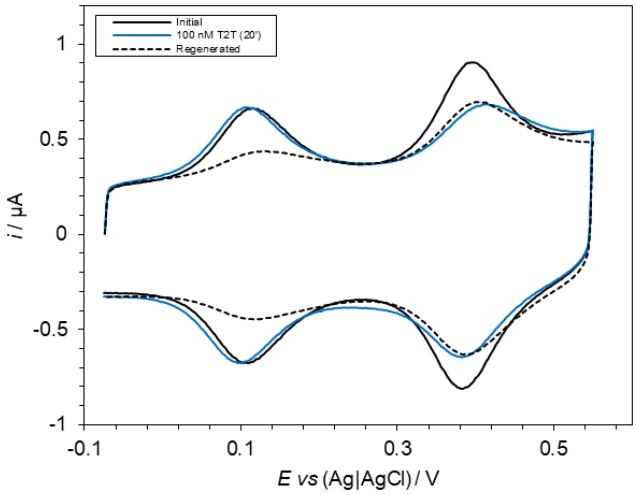

Figure 8.41: Destructive regeneration of **T1** by sonication in ultrapure water for 60 seconds, after incubation with **T2T** target (100 nM, 60 min); in 10 mM sodium phosphate buffer (pH 7.0) 1 M $NaClO_4$, scan rates = 1000 mV s^{-1}.

8.2.6. Electrochemical Single Point Variant Sensing

Table 8.1. Average CuCy:Fc current ratio % changes for the **T1**, **B1**, **K1**, **E1**, and **N1** probes when incubated with complementary targets that varied the base opposite the CuCy in the probe–target duplex. SD shown in brackets. [Target] = 50 nM, 10 mM sodium phosphate buffer (pH 7) 1 M $NaClO_4$, scan rates = 1000 mV s^{-1}.

Base Opposite CuCy	T1	B1	K1	E1	N1
T	–57.6 (± 2.0)	–65.8 (± 5.7)	–45.9 (± 1.8)	-	–84.3 (± 4.9)
A	–38.8 (± 3.2)	–46.8 (± 3.9)	–57.7 (± 3.1)	–46.7 (± 6.0)	–59.6 (± 6.3)
G	–56.1 (± 2.4)	-	–55.6 (± 5.5)	–91.0 (± 4.2)	-
C	–67.4 (± 2.5)	-	-	-	-
5mC	–58.4 (± 4.5)	-	-	-	-

Representative T1-T2X CVs and the processed anodic traces:

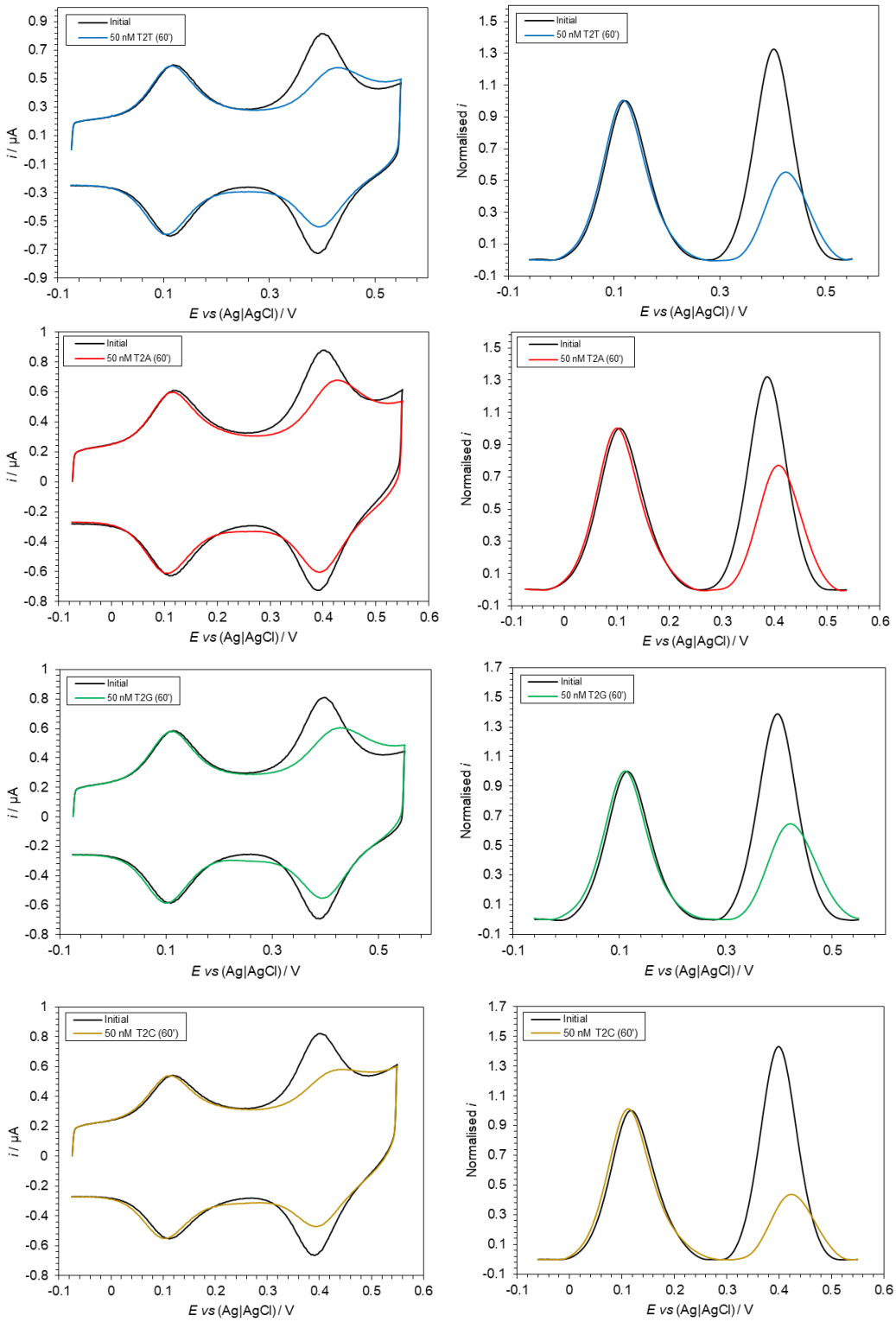

Figure 8.42: Left) Representative CVs of **T1** sensing targets (50 nM); in 10 mM sodium phosphate buffer (pH 7) 1 M $NaClO_4$, scan rates = 1000 mV s^{-1}. Right) normalised and background-corrected anodic traces of the CVs shown on the left.

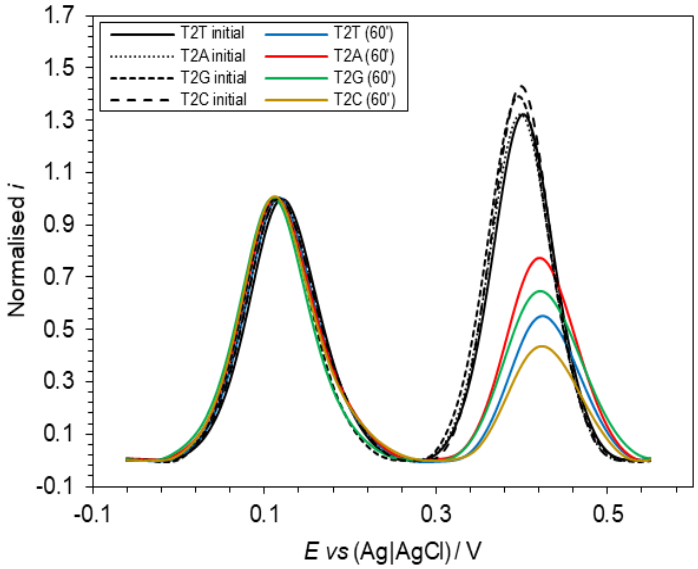

Figure 8.43: Overlaid normalised and background-corrected anodic traces of the CVs shown in Figure 8.42.

Representative B1-B2X CVs and the processed anodic traces:

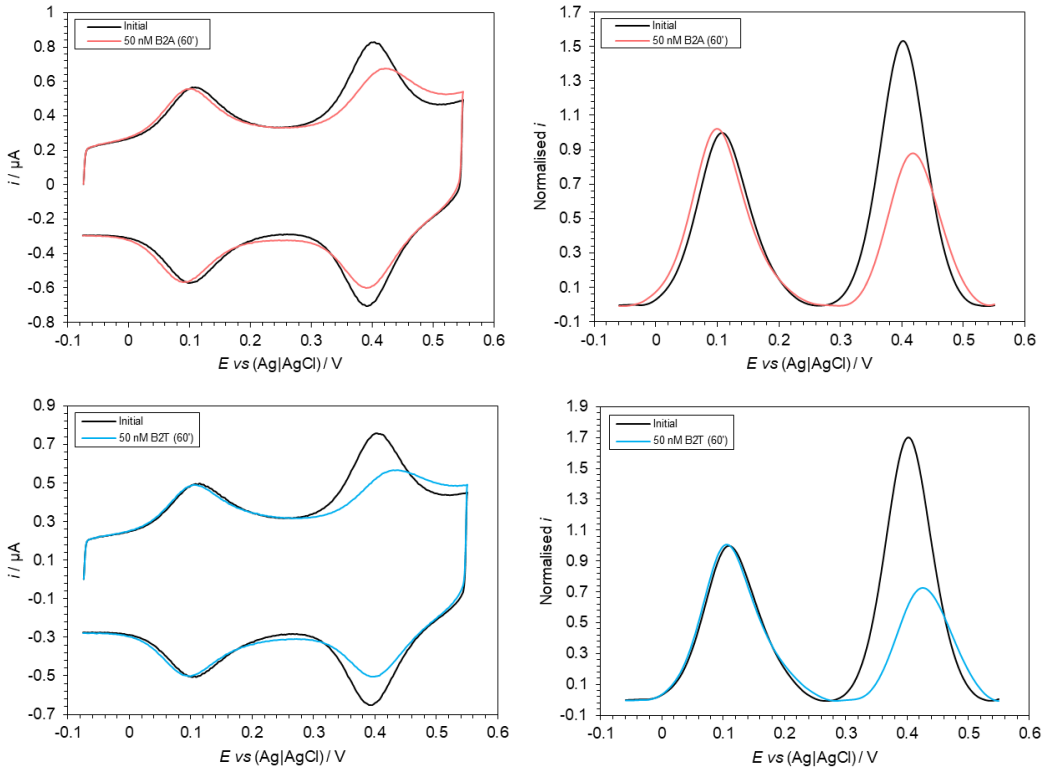

Figure 8.44: Left) Representative CVs of **B1** sensing targets (50 nM); in 10 mM sodium phosphate buffer (pH 7) 1 M $NaClO_4$, scan rates = 1000 mV s^{-1}. Right) normalised and background-corrected anodic traces of the CVs shown on the left.

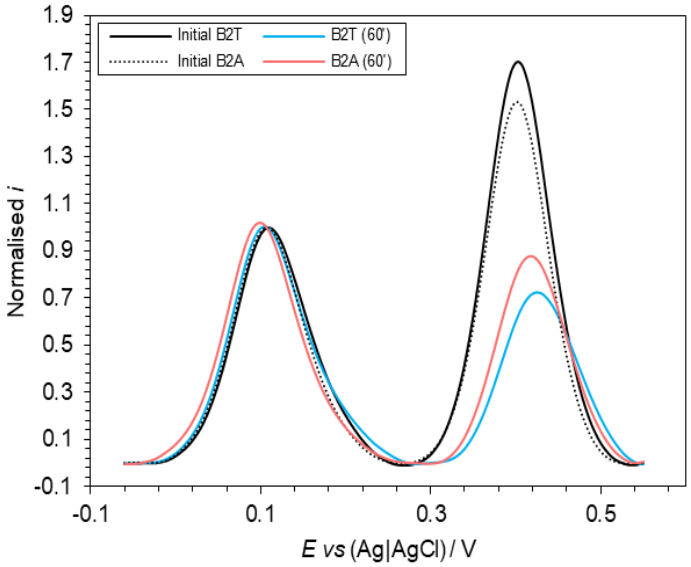

Figure 8.45: Overlaid normalised and background-corrected anodic traces of the CVs shown in Figure 8.44.

Representative K1-K2X CVs and the processed anodic traces:

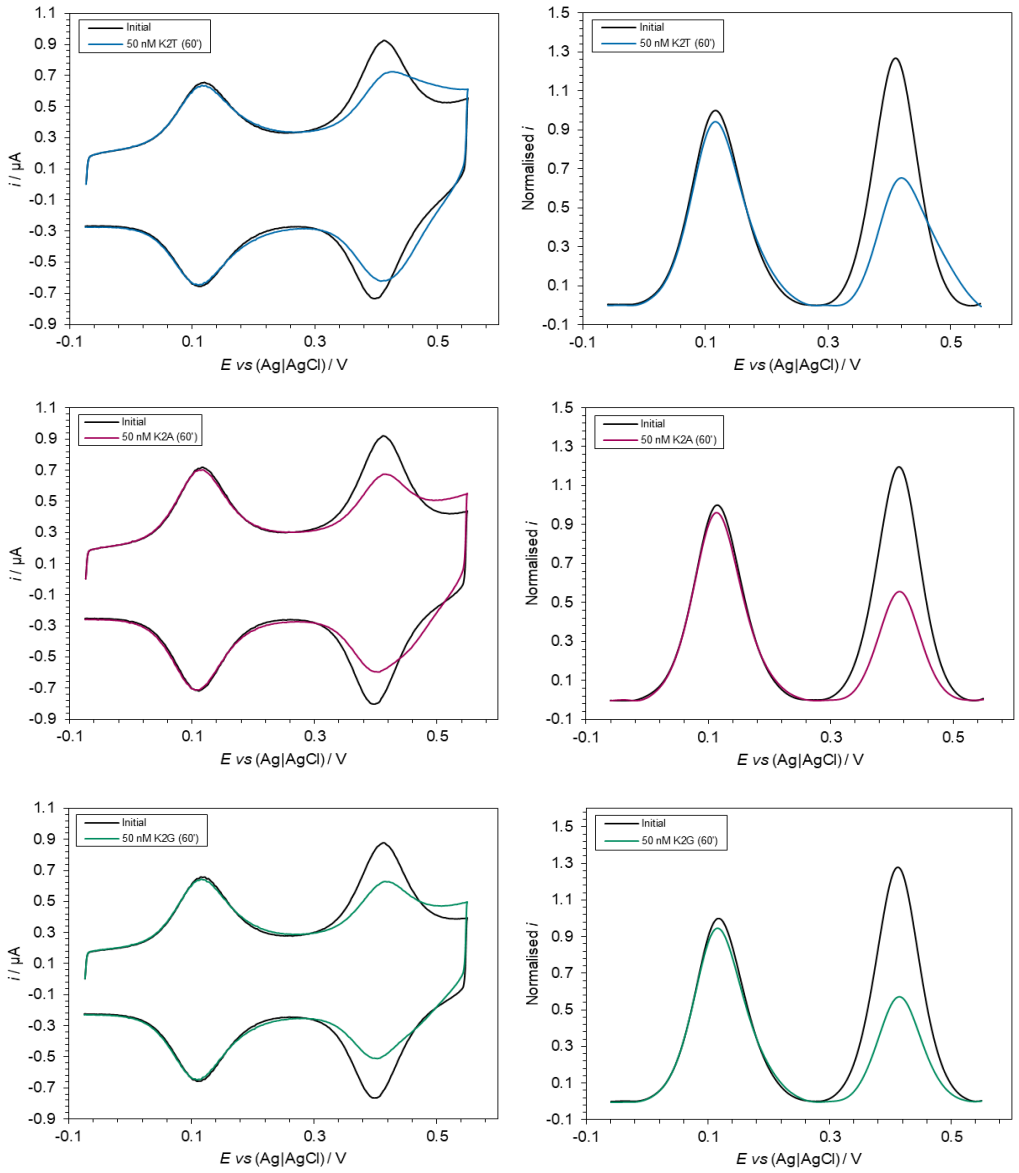

Figure 8.46: Left) Representative CVs of **K1** sensing targets (50 nM); in 10 mM sodium phosphate buffer (pH 7) 1 M $NaClO_4$, scan rates = 1000 mV s^{-1}. Right) normalised and background-corrected anodic traces of the CVs shown on the left.

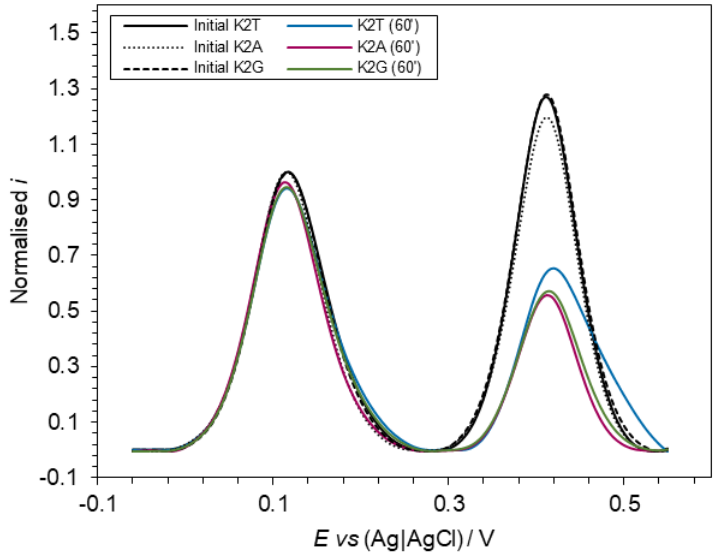

Figure 8.47: Overlaid normalised and background-corrected anodic traces of the CVs shown in Figure 8.46.

Representative E1-E2X CVs and the processed anodic traces:

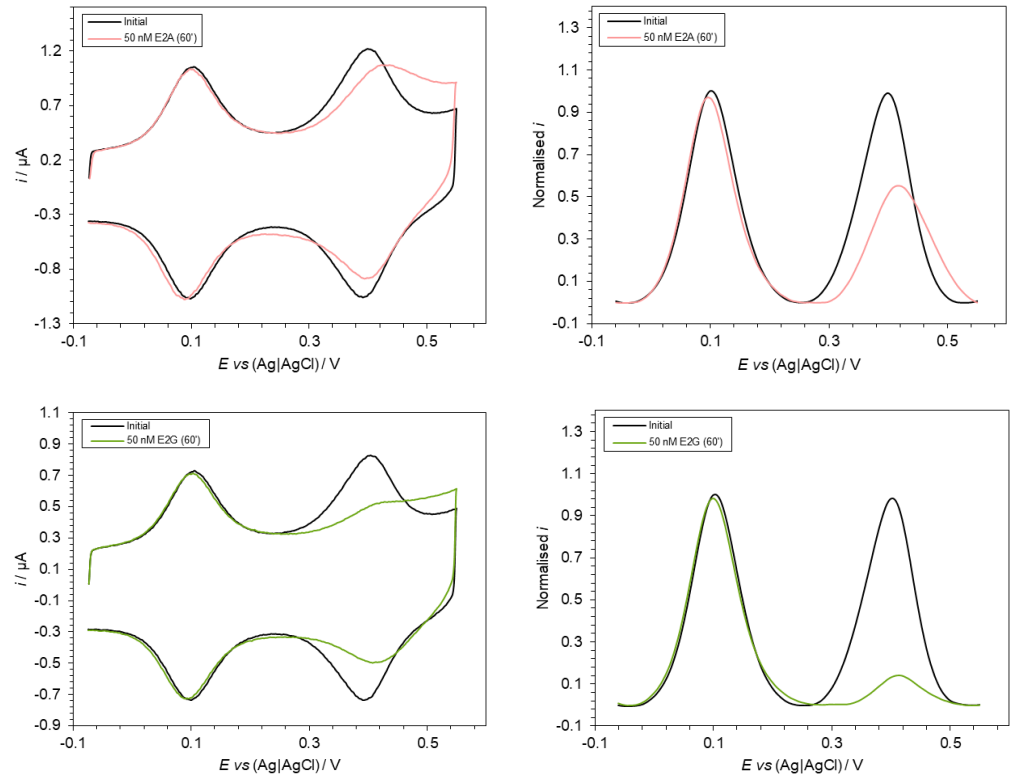

Figure 8.48: Left) Representative CVs of **E1** sensing targets (50 nM); in 10 mM sodium phosphate buffer (pH 7) 1 M $NaClO_4$, scan rates = 1000 mV s^{-1}. Right) normalised and background-corrected anodic traces of the CVs shown on the left.

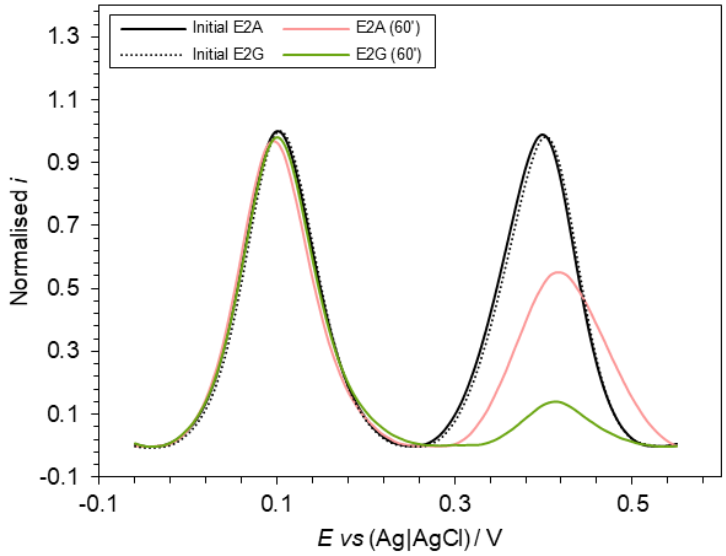

Figure 8.49: Overlaid normalised and background-corrected anodic traces of the CVs shown in Figure 8.48.

Representative N1-N2X CVs and the processed anodic traces:

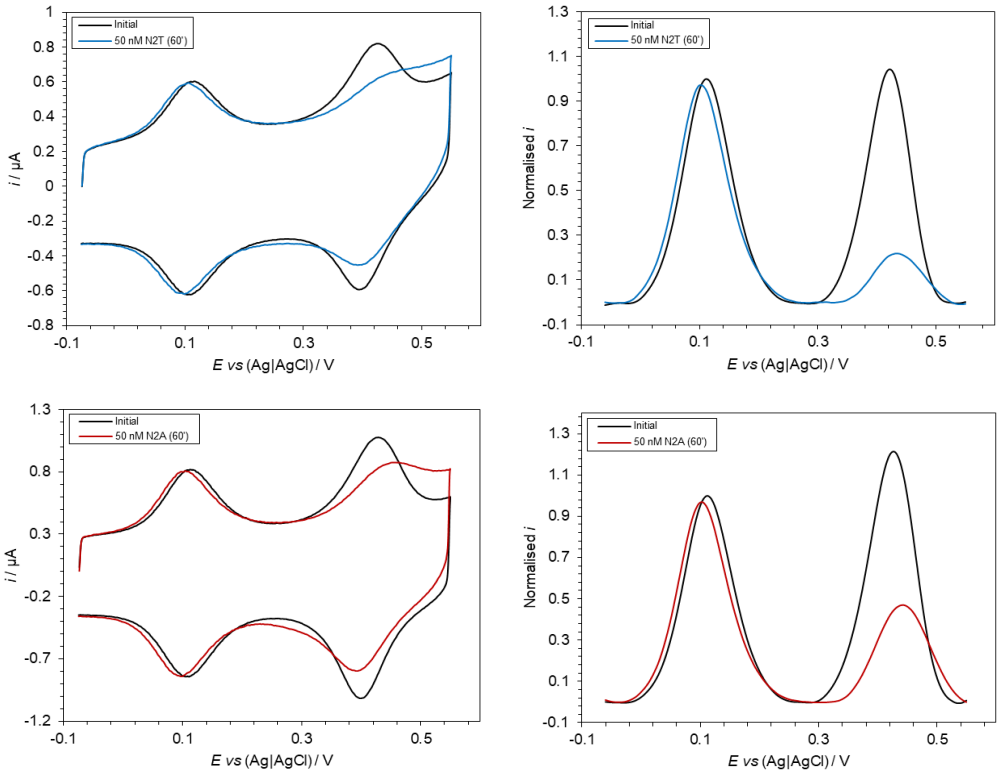

Figure 8.50: Left) Representative CVs of **N1** sensing targets (50 nM); in 10 mM sodium phosphate buffer (pH 7) 1 M $NaClO_4$, scan rates = 1000 mV s^{-1}. Right) normalised and background-corrected anodic traces of the CVs shown on the left.

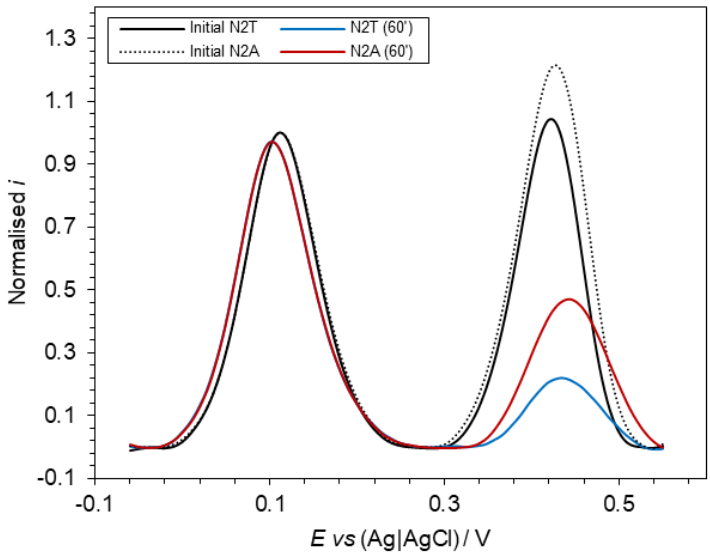

Figure 8.51: Overlaid normalised and background-corrected anodic traces of the CVs shown in Figure 8.50.

Representative T1 sensing T2C/T25mC CVs and the processed anodic traces:

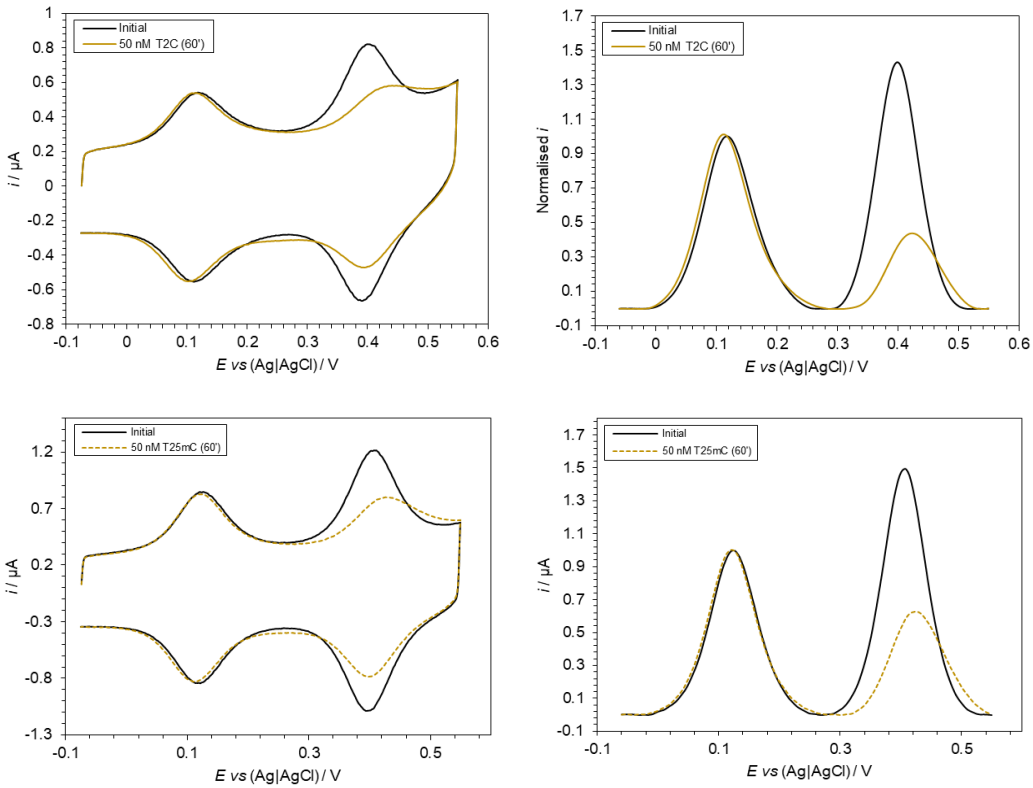

Figure 8.52: Left: Representative CVs of **T1** sensing targets (50 nM); in 10 mM sodium phosphate buffer (pH 7) 1 M $NaClO_4$, scan rates = 1000 mV s^{-1}. Right: normalised and background-corrected anodic traces of the CVs shown on the left.

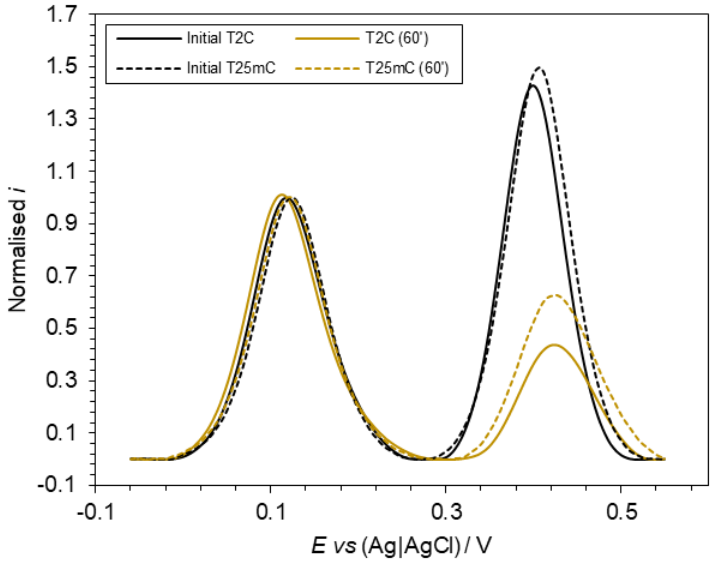

Figure 8.53: Overlaid normalised and background-corrected anodic traces of the CVs shown in Figure 8.52.

8.3. Efforts to Understand, Enhance, and Expand the Sensing of Nucleic Acids Using Redox-Modified DNA Probes

8.3.1. Representative (*S*)-T1 Sensing Cyclic Voltammograms

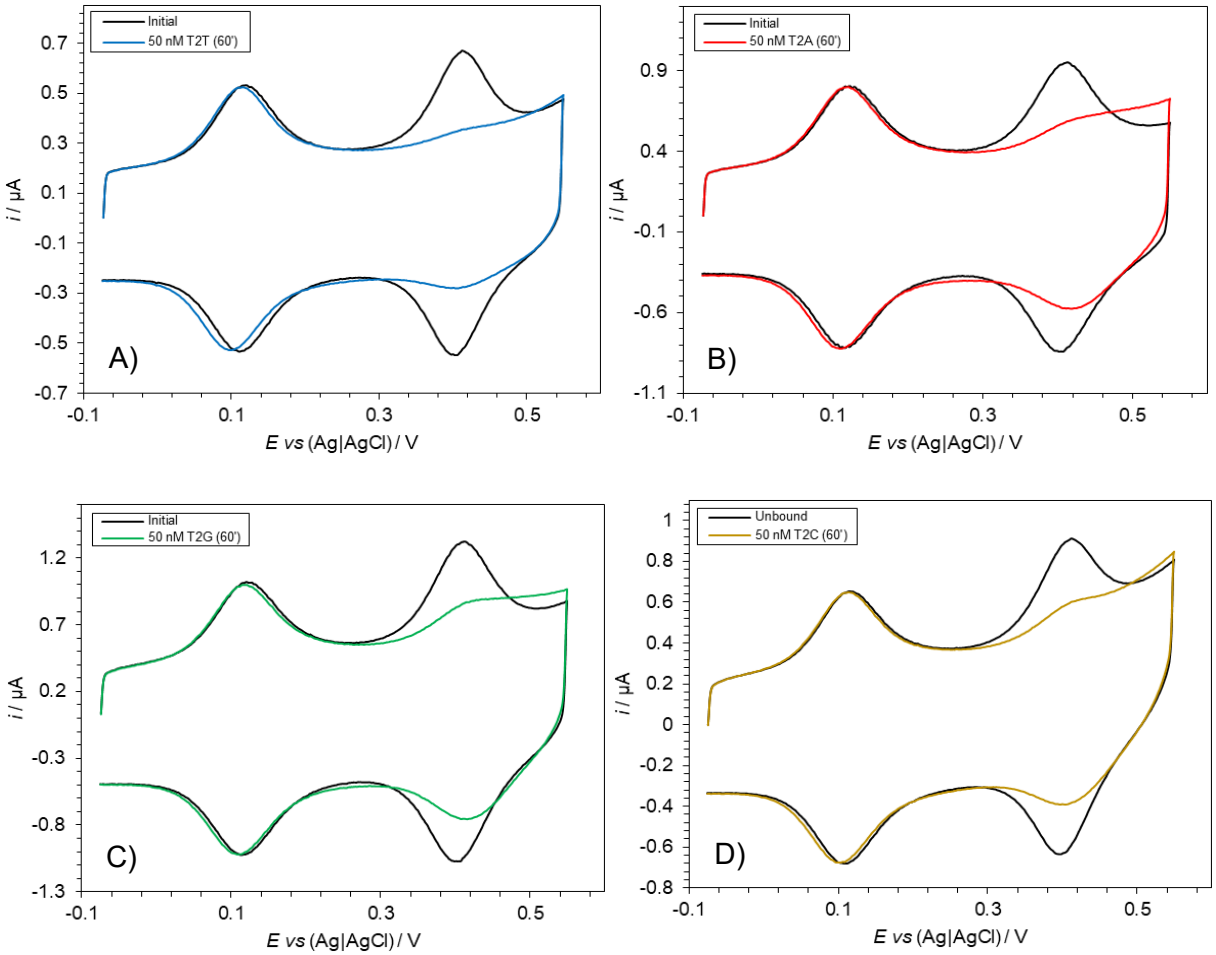

Figure 8.54: Representative CVs of **(*S*)-T1** sensing targets **T2T** (A), **T2A** (B), **T2G** (C) and **T2C** (D), [target] = 50 nM; in 10 mM sodium phosphate buffer (pH 7.0) 1 M $NaClO_4$, scan rates = 1000 mV s^{-1}.

8.3.2. Mismatched and Abasic Duplexes Thermal Melting Data

Table 8.2. Thermal melting temperatures of duplexes containing mismatches or abasic sites. [DNA] = 10 μM in 10 mM sodium phosphate buffer pH 7.0, 100 mM NaCl.

	CuCyMid / ºC	CuCyMid_C3+2 / ºC	CuCyMid_C3-2 / ºC
T2A_mm+2	50.5 (± 1.0)	-	-
T2A_mm-2	50.0 (± 0.5)	-	-
T2A_C3+2	-	55.5 (± 0.5)	-
T2A_C3-2	-	-	56 (± 0.5)

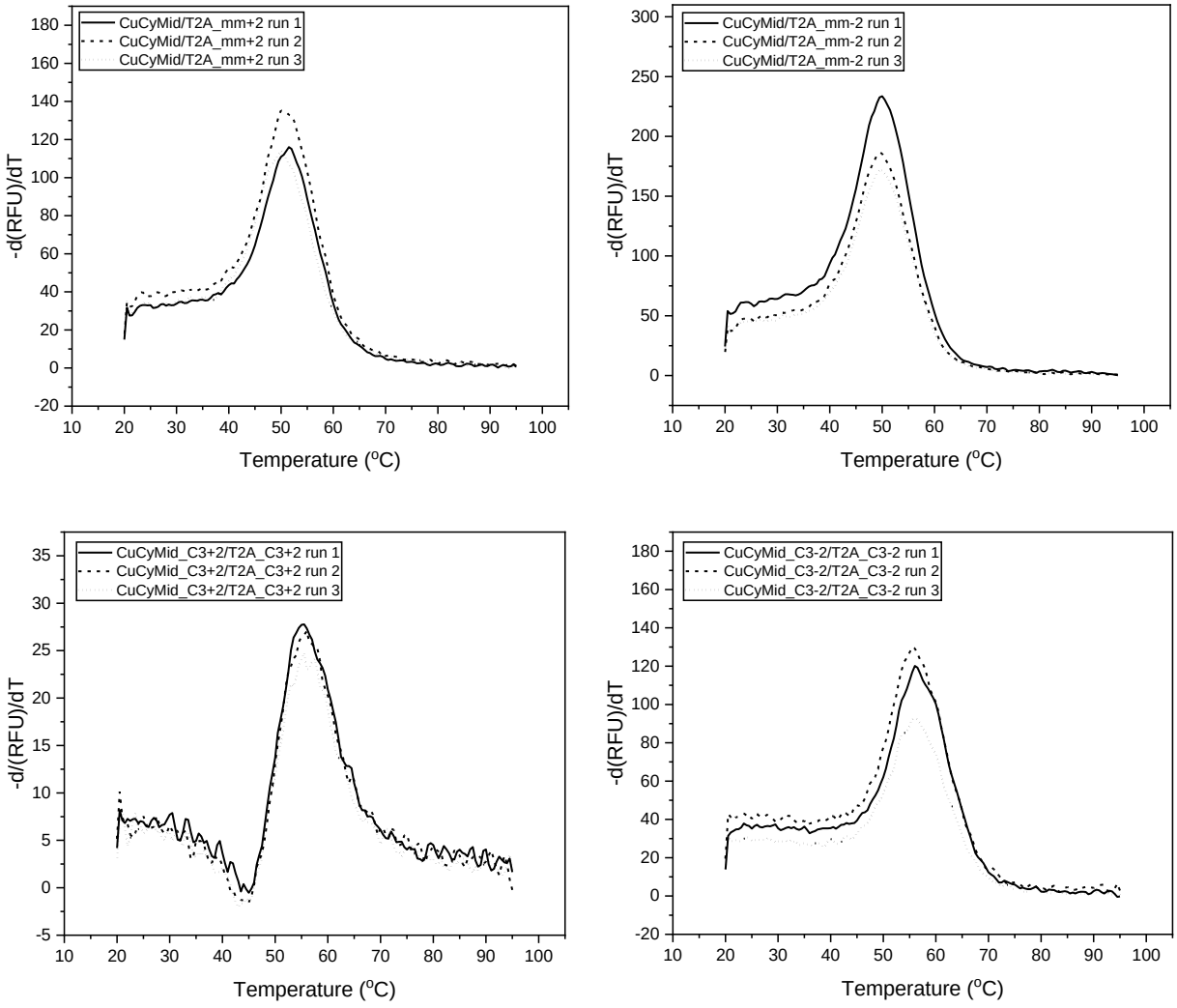

Figure 8.55: Thermal melting graphs for duplexes containing mismatches or abasic sites, plotting temperature of the oligonucleotide sample versus the negative rate of change in the RFU of SYBR Green I.

8.3.3. Mismatched and Abasic Duplexes Cyclic Voltammograms and the Processed Anodic Traces

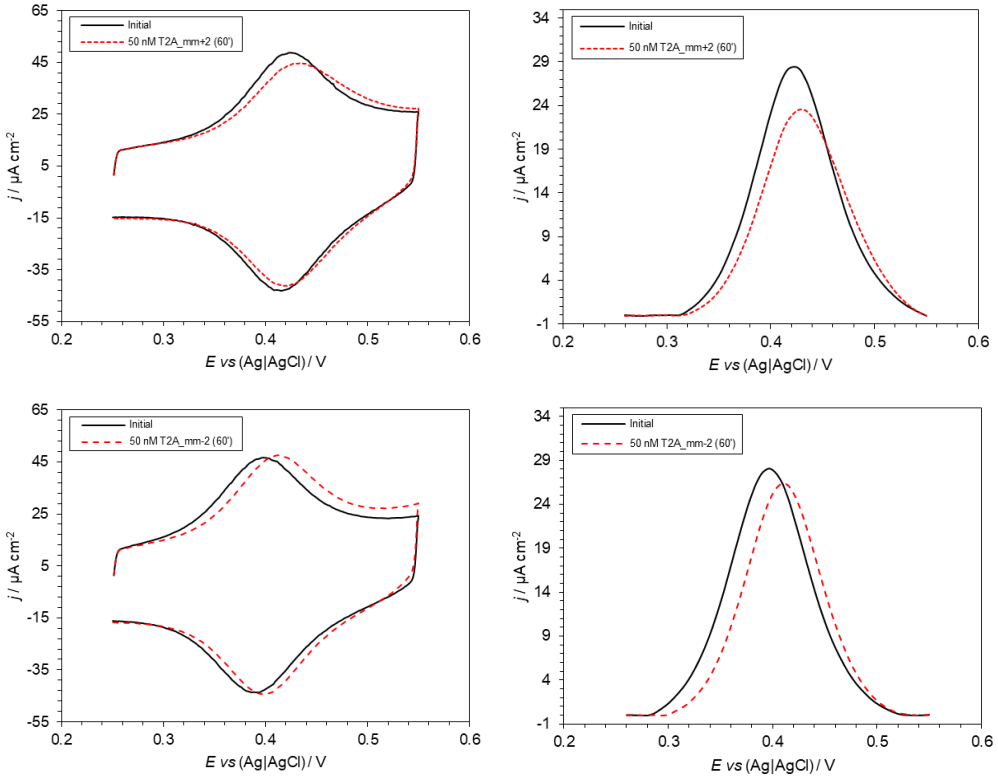

Figure 8.56: Left) CVs of **CuCyMid** sensing targets (50 nM) resulting in mismatch-containing duplexes; in 10 mM sodium phosphate buffer (pH 7) 1 M $NaClO_4$, scan rates = 1000 mV s^{-1}. Right) normalised and background-corrected anodic traces of the CVs shown on the left.

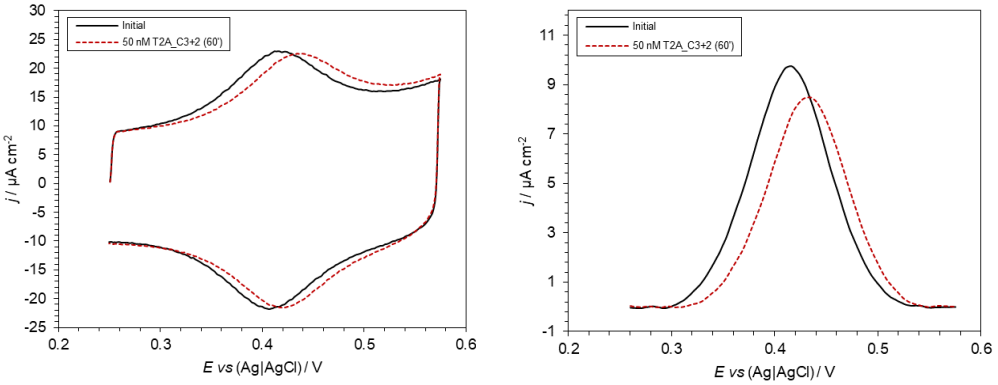

Figure 8.57: Left) CVs of **CuCyMid_C3+2** sensing target (50 nM) that resulted in abasic site-containing duplexes; in 10 mM sodium phosphate buffer (pH 7) 1 M $NaClO_4$, scan rates = 1000 mV s^{-1}. Right) normalised and background-corrected anodic traces of the CVs shown on the left.

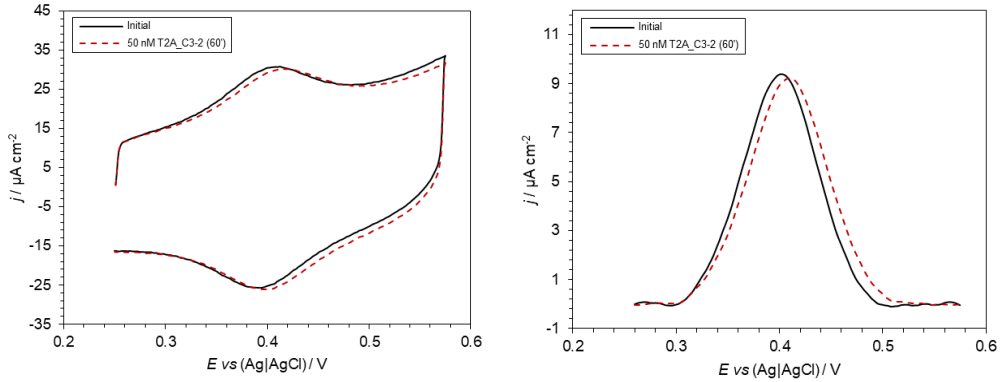

Figure 8.58: Left) CVs of **CuCyMid_C3-2** sensing target (50 nM) that resulted in abasic site-containing duplexes; in 10 mM sodium phosphate buffer (pH 7) 1 M $NaClO_4$, scan rates = 1000 mV s^{-1}. Right) normalised and background-corrected anodic traces of the CVs shown on the left.

8.3.4. High Target Concentration and Preformed Duplex SAM Cyclic Voltammograms

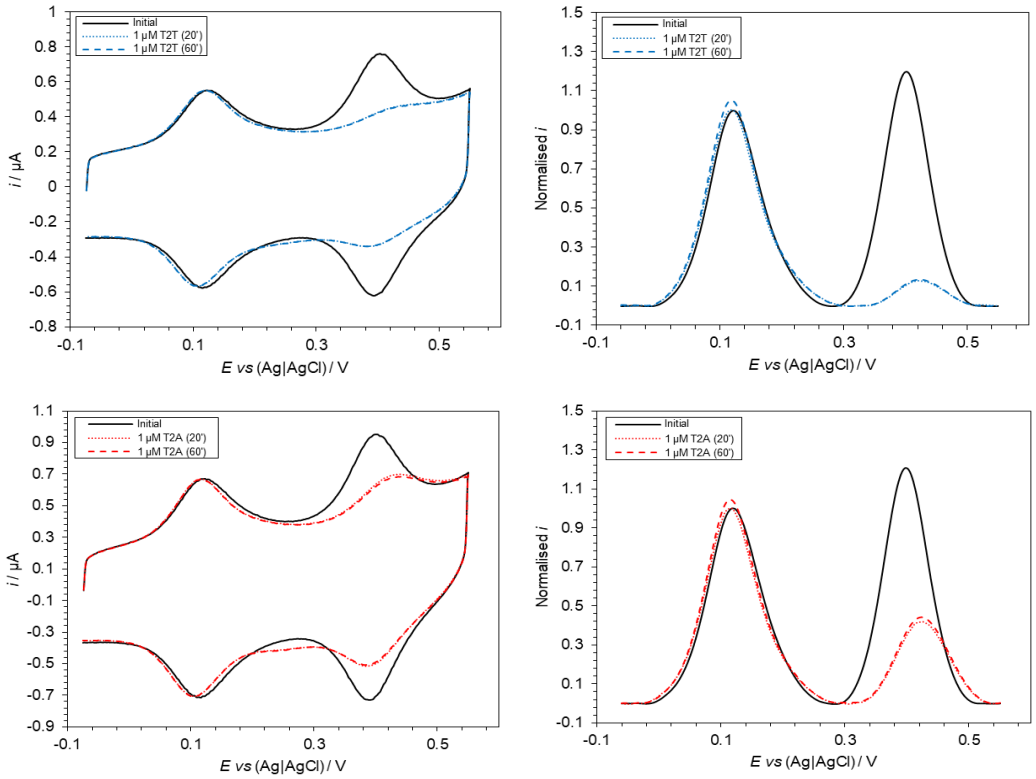

Figure 8.59: Left) Representative CVs of **T1** sensing 1 µM **T2T** (top) and 1 µM **T2A** (bottom) 20 minutes and 60 minutes after target addition; in 10 mM sodium phosphate buffer (pH 7) 1 M $NaClO_4$, scan rates = 1000 mV s^{-1}. Right) normalised and background-corrected anodic traces of the CVs shown on the left.

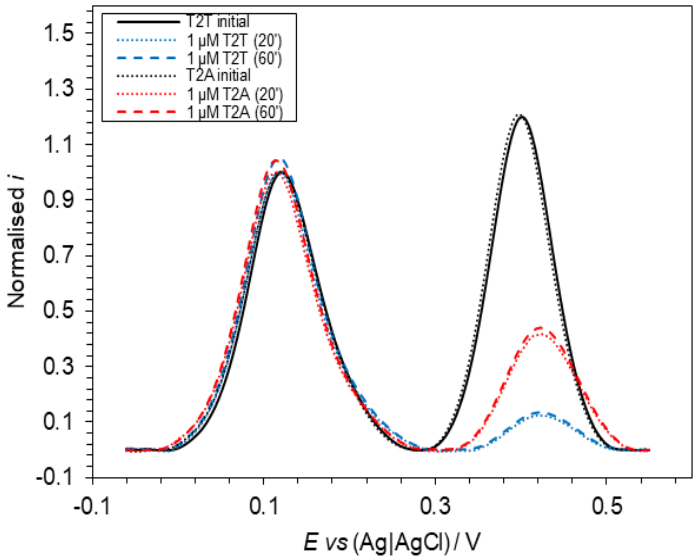

Figure 8.60: Overlaid normalised and background-corrected anodic traces of the CVs shown in Figure 8.59.

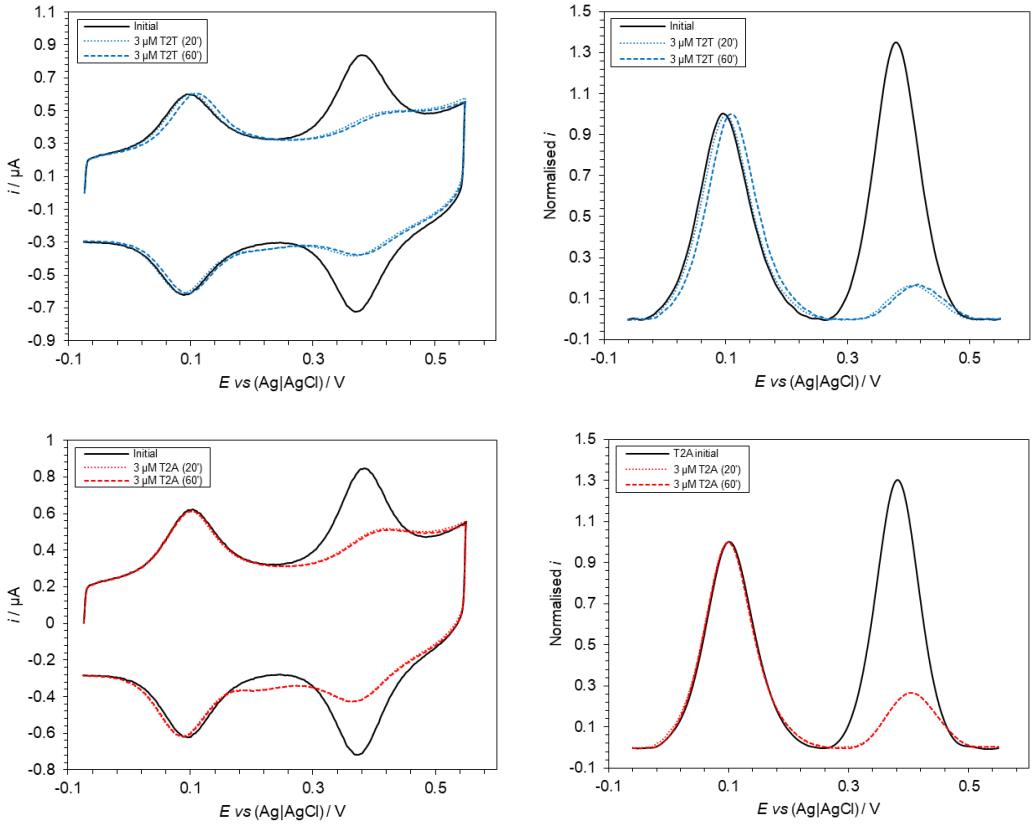

Figure 8.61: Left) Representative CVs of **T1** sensing 3 µM **T2T** (top) and 3 µM **T2A** (bottom) 20 minutes and 60 minutes after target addition; in 10 mM sodium phosphate buffer (pH 7) 1 M $NaClO_4$, scan rates = 1000 mV s^{-1}. Right) normalised and background-corrected anodic traces of the CVs shown on the left.

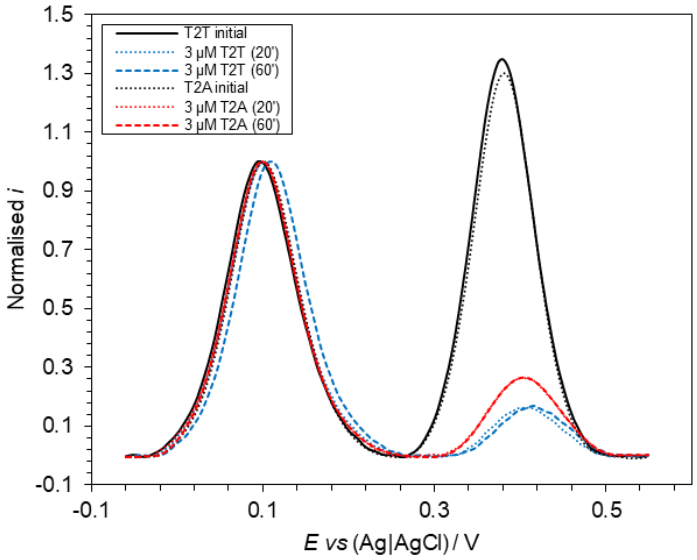

Figure 8.62: Overlaid normalised and background-corrected anodic traces of the CVs shown in Figure 8.61.

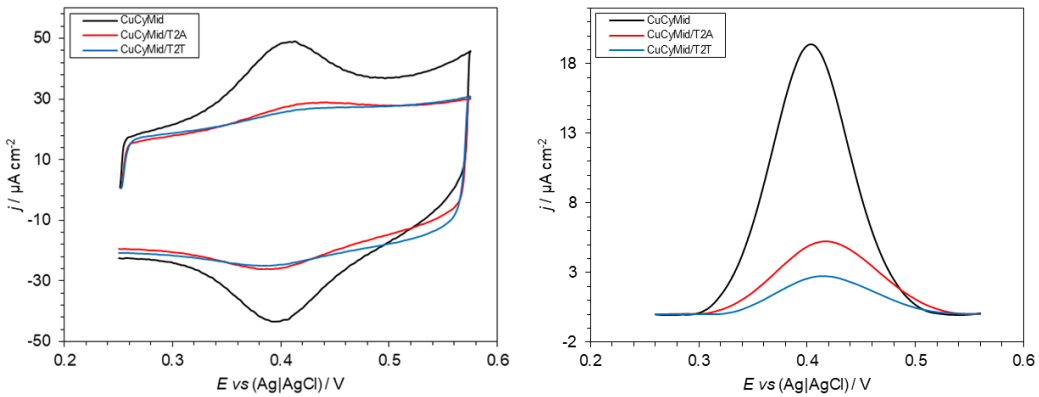

Figure 8.63: Left) CV of **CuCyMid** alone (black), with **T2A** (red) and with **T2T** (blue), using SAMs assembled from preformed duplexes; in 10 mM sodium phosphate buffer (pH 7) 1 M $NaClO_4$, scan rates = 1000 mV s^{-1}. Right) normalised and background-corrected anodic traces of the CVs shown on the left.

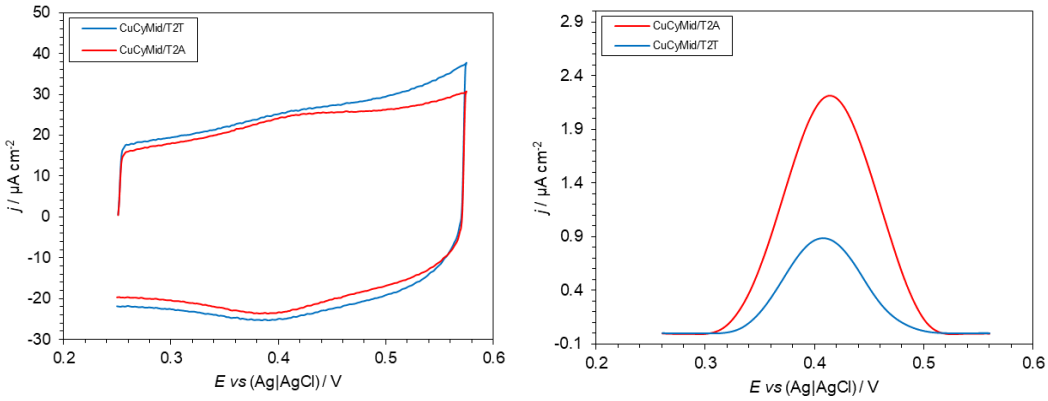

Figure 8.64: Left) CV of **CuCyMid** with **T2T** (blue) and with **T2A** (red), using SAMs assembled from preformed duplexes with a heating/annealing step (see section 7.6.2. for full details); in 10 mM sodium phosphate buffer (pH 7) 1 M $NaClO_4$, scan rates = 1000 mV s^{-1}. Right) normalised and background-corrected anodic traces of the CVs shown on the left.

8.3.5. T1-21mer and B1-30mer Thermal Melting Data and Cyclic Voltammograms

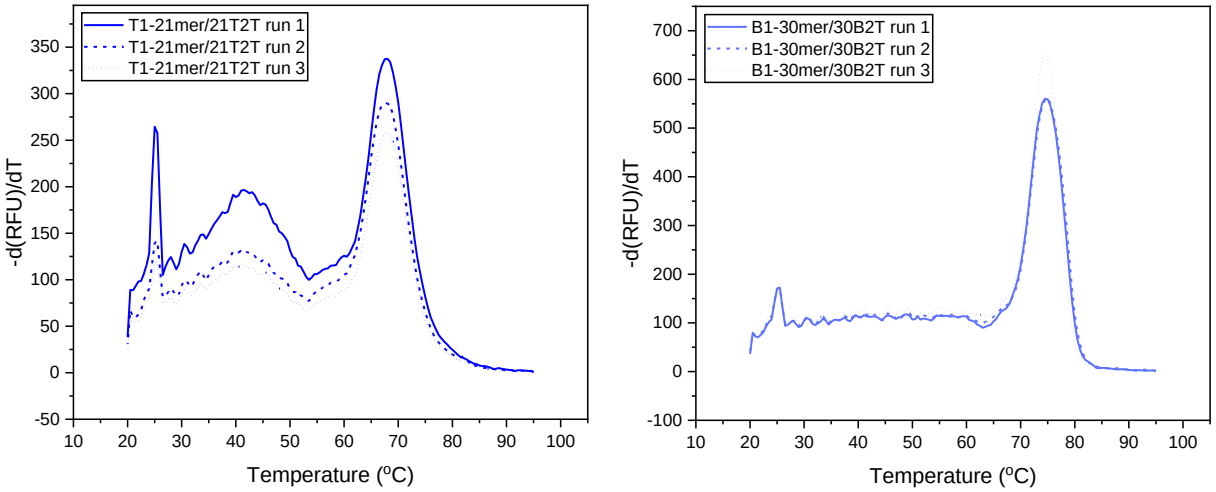

Figure 8.65: Thermal melting graphs for **T1-21mer** (left) and **B1-30mer** (right), plotting temperature of the oligonucleotide sample versus the negative rate of change in the relative fluorescence emission (RFU) of SYBR Green I.

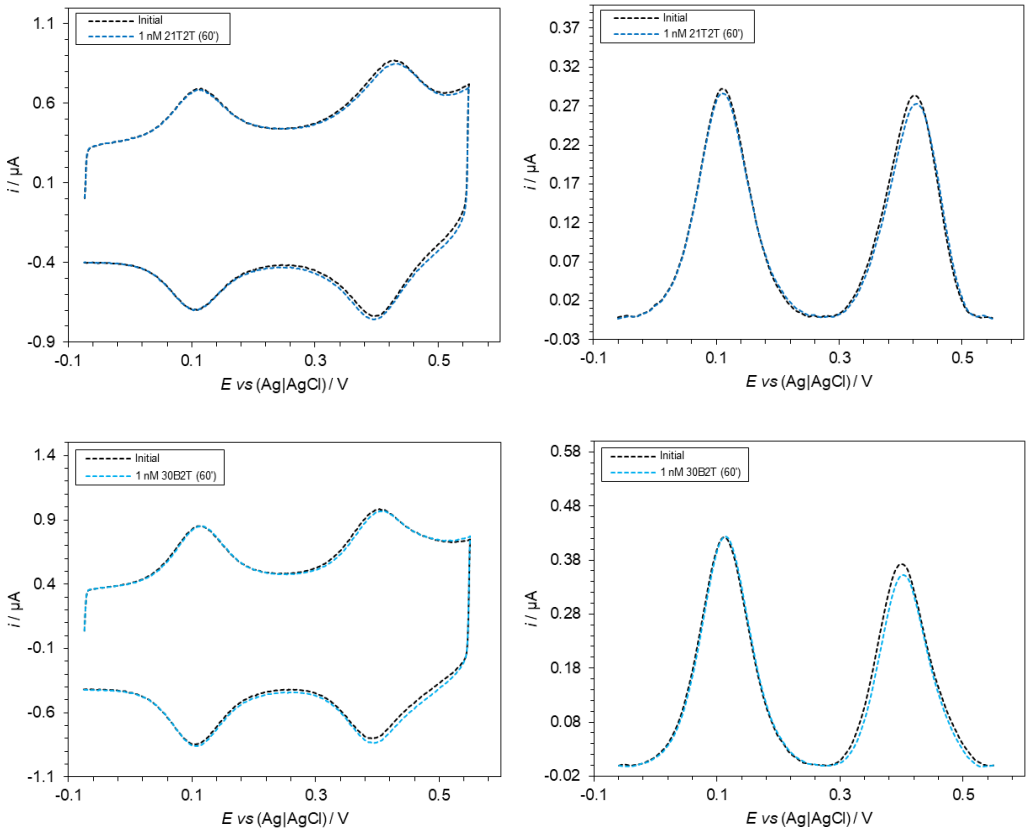

Figure 8.66: Left) CVs of **T1-21mer** (top) and **B1-30mer** (bottom) sensing 1 nM target; in 10 mM sodium phosphate buffer (pH 7) 1 M $NaClO_4$, scan rates = 1000 mV s^{-1}. Right) normalised and background-corrected anodic traces of the CVs shown on the left.

8.3.6. 1 nM Target Sensing with *(S)*-T1 and Mg^{2+}-Containing Solution

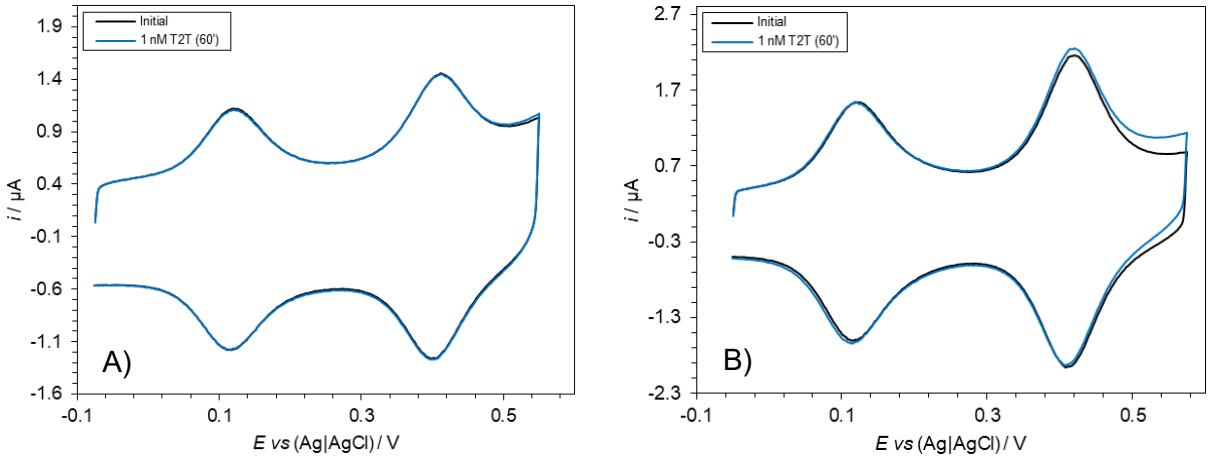

Figure 8.67: A) CVs of **(*S*)-T1** sensing 1 nM target; in 10 mM sodium phosphate buffer (pH 7.0) 1 M $NaClO_4$. B) CVs of **T1** sensing 1 nM target; in in 10 mM sodium phosphate buffer (pH 7.0) 1 M $Mg_2(ClO_4)_2$. Scan rates = 1000 mV s^{-1}

8.3.7. Shifted Modification Location Cyclic Voltammograms and Thermal Melting Data

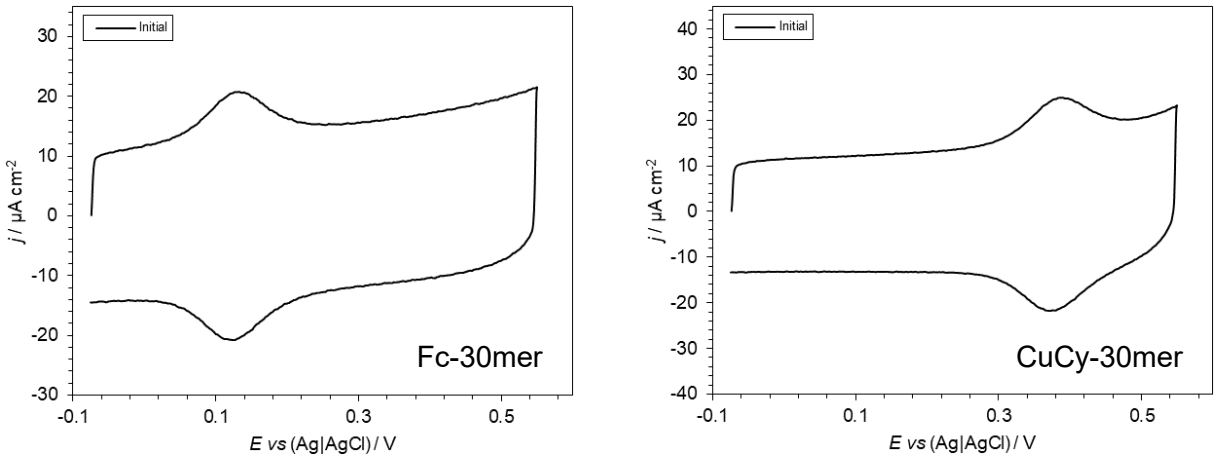

Figure 8.68: CVs of **Fc-30mer** (left) and **CuCy-30mer** (right); in 10 mM sodium phosphate buffer (pH 7.0) 1 M $NaClO_4$, scan rates = 1000 mV s^{-1}.

Table 8.3: Thermal melting temperatures for the CuCy-shifted probes when duplexed with equimolar equivalents of unmodified complementary targets with the base opposite the CuCy varied. [DNA] = 10 µM in 10 mM sodium phosphate buffer pH 7.0, 100 mM NaCl.

Base Opposite CuCy	CuCy5′ / ºC	CuCyMid / ºC	CuCy3′ / ºC
T	64.0 (± 0.5)	62.0 (± 0.5)	63.0 (± 0.5)
A	65.5 (± 1.5)	60.0 (± 0.5)	63.5 (± 0.5)

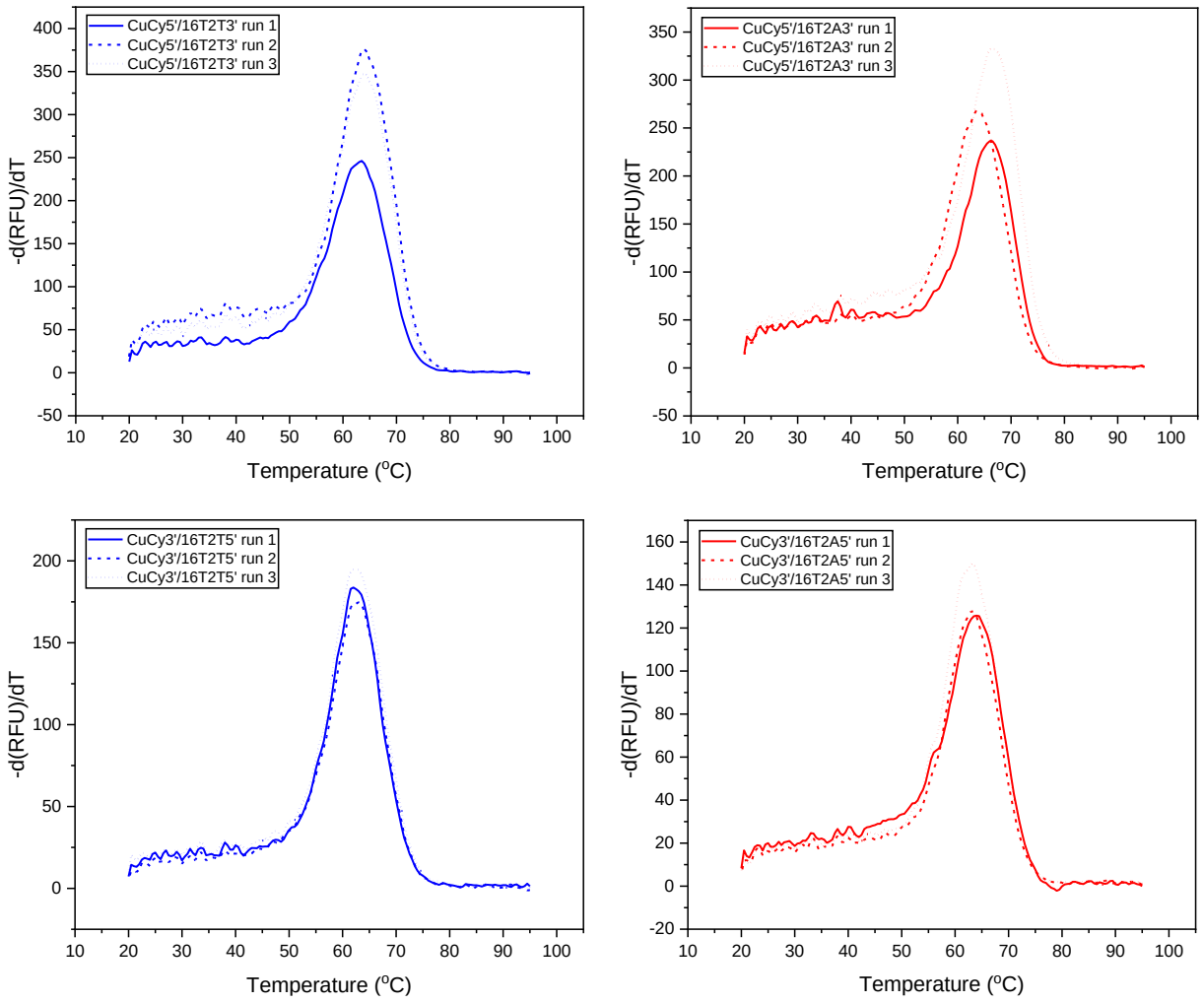

Figure 8.69: Thermal melting graphs for **CuCy5'** (top) and **CuCy3'** (bottom) varying the base opposite the CuCy, plotting temperature of the oligonucleotide sample versus the negative rate of change in the RFU of SYBR Green I.

8.3.8. Square Wave Voltammetry Studies

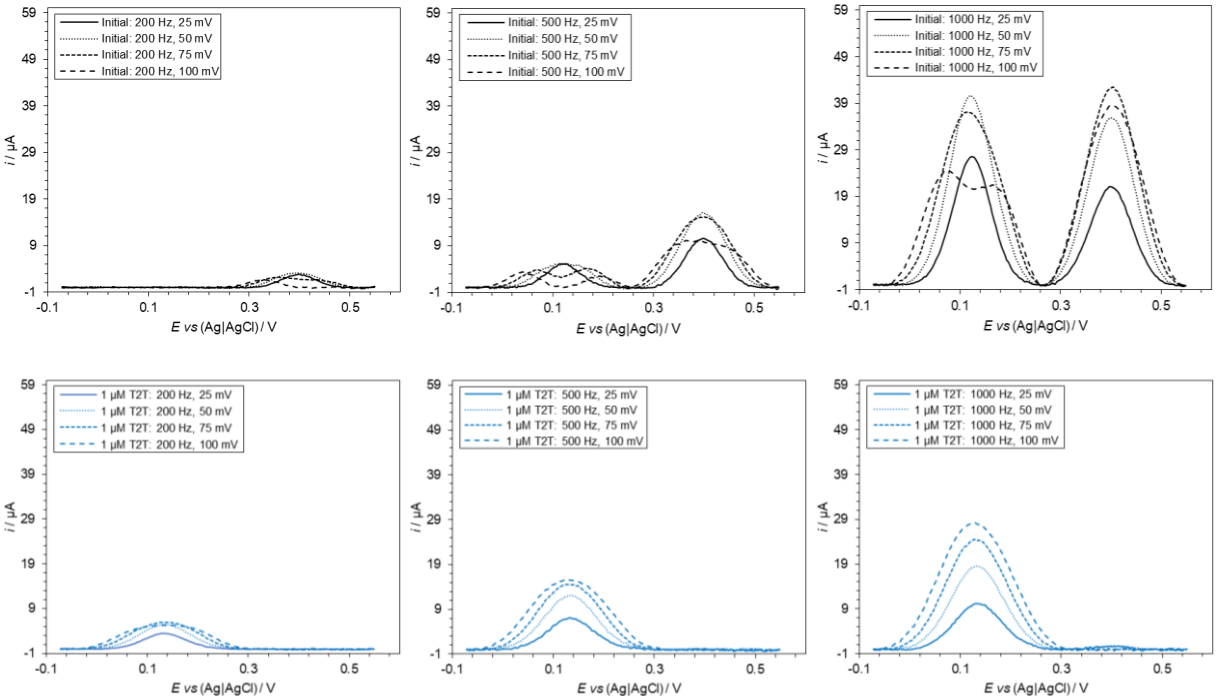

Figure 8.70: Initial SWVs (top) and target-added SWVs (1 µM, bottom) of **T1** measured at different frequency and amplitude combinations; in 10 mM sodium phosphate buffer (pH 7) 1 M $NaClO_4$.

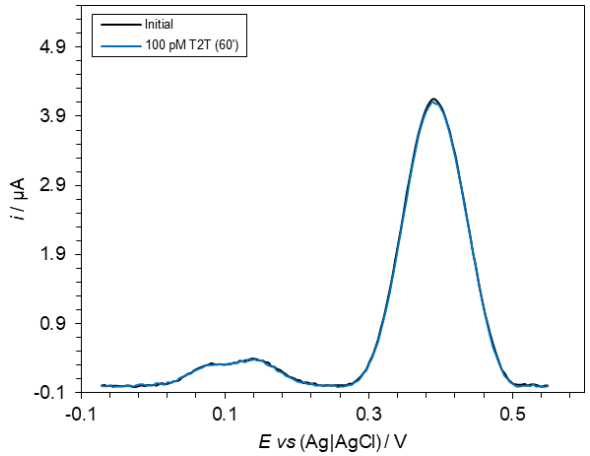

Figure 8.71: SWVs of **T1** sensing 100 pM T2T 60 minutes after target addition; in 10 mM TrisHCl buffer (pH 7.0) 100 mM NaCl, frequency = 200 Hz, amplitude = 50 mV, step = 1 mV.

8.3.9. T1 Sensing RNA Targets and Thermal Melting Data

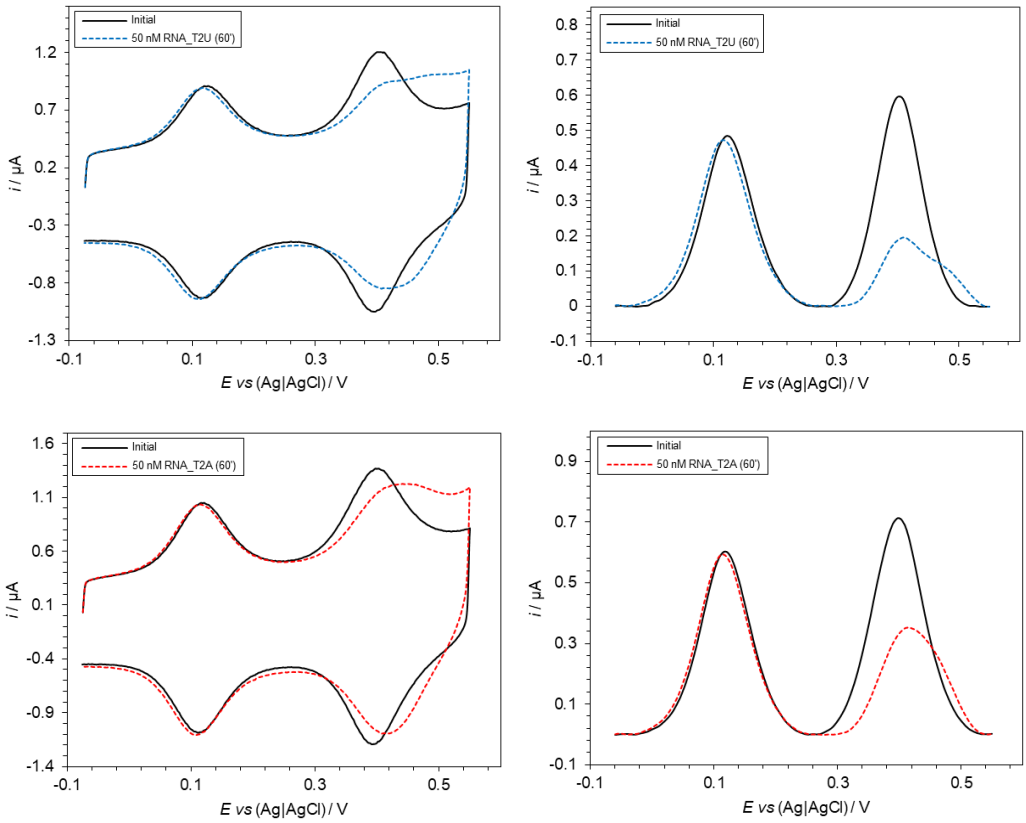

Figure 8.72: Left) CVs of **T1** sensing **RNA_T2U** (top) and **RNA_T2A** (bottom); in 10 mM sodium phosphate buffer (pH 7) 1 M $NaClO_4$, scan rates = 1000 mV s^{-1}. Right) normalised and background-corrected anodic traces of the CVs shown on the left.

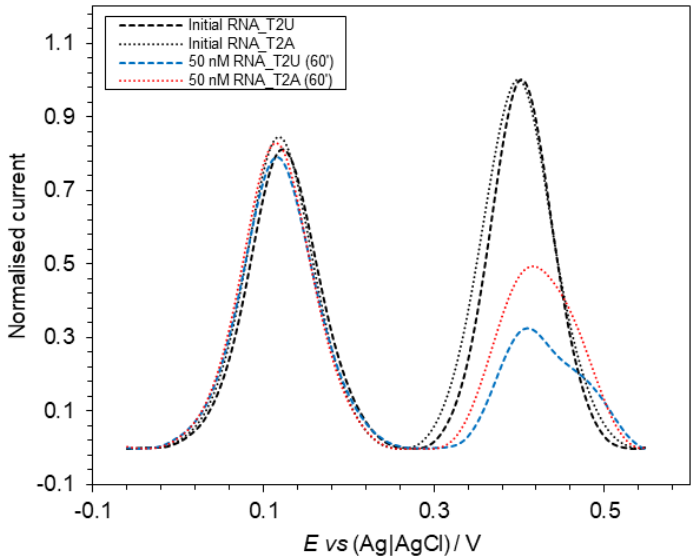

Figure 8.73: Overlaid normalised and background-corrected anodic traces of the CVs shown in Figure 8.72.

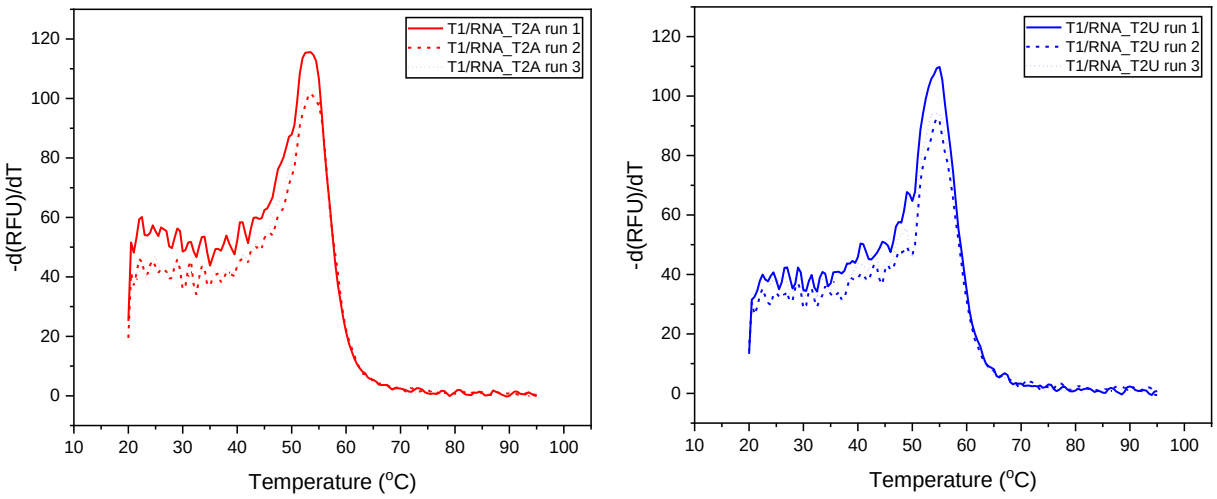

Figure 8.74: Thermal melting graphs for **T1–RNA_T2A** (left) and **T1–RNA_T2U** (right), plotting temperature of the oligonucleotide sample versus the negative rate of change in the RFU of SYBR Green I.

8.3.10. T1 Cyclic Voltammograms in Buffer/Serum Solutions

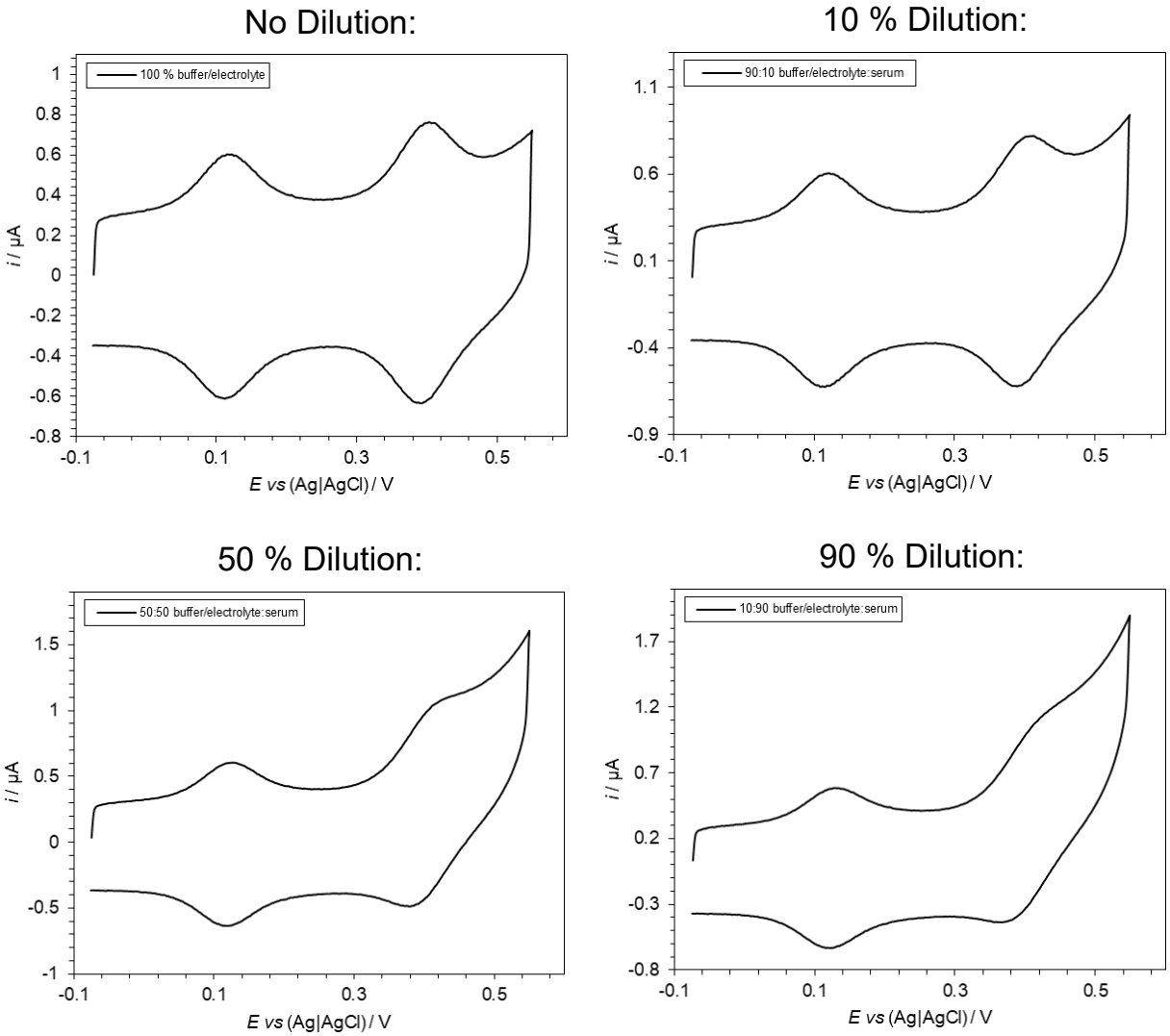

Figure 8.75: CVs of **T1** in solutions of buffer/electrolyte solutions (10 mM sodium phosphate buffer (pH 7.0) 1 M $NaClO_4$) diluted with human serum. Ratios shown are volume. Scan rates = 1000 mV s^{-1}.

8.3.11. miR135-1 Thermal Melting Data and 1 nM Target Sensing Cyclic Voltammograms

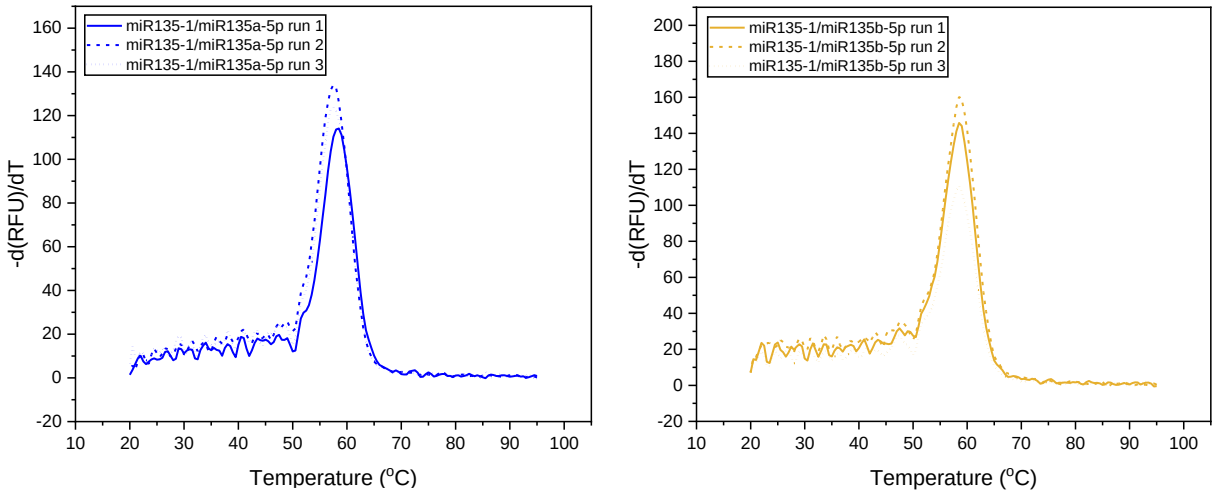

Figure 8.76: Thermal melting graphs for **miR135-1–miR135a-5p** (left) and **miR135-1–miR135b-5p** (right), plotting temperature of the oligonucleotide sample versus the negative rate of change in the RFU of SYBR Green I.

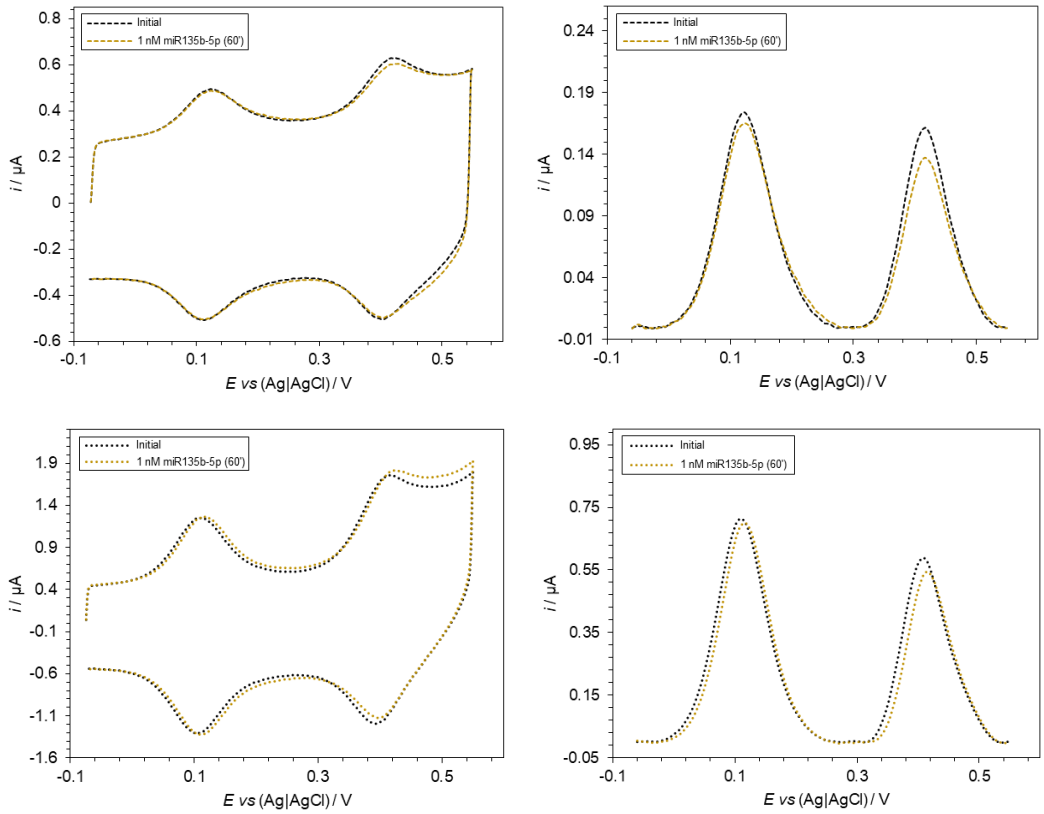

Figure 8.77: Left) CVs of **miR135-1** sensing 1 nM **miR135b-5p** in 90:10 buffer/electrolyte:saliva (top) and 90:10 buffer/electrolyte:serum (bottom); buffer/electrolyte = 10 mM sodium phosphate buffer (pH 7.0) 1 M $NaClO_4$, scan rates = 1000 mV s^{-1}. Right) normalised and background-corrected anodic traces of the CVs shown on the left.

8.4. Functionalisation of Metal-Organic Frameworks with Fluorescently-Modified DNA

8.4.1. Fluorescently-Modified Oligonucleotide Thermal Melting Data

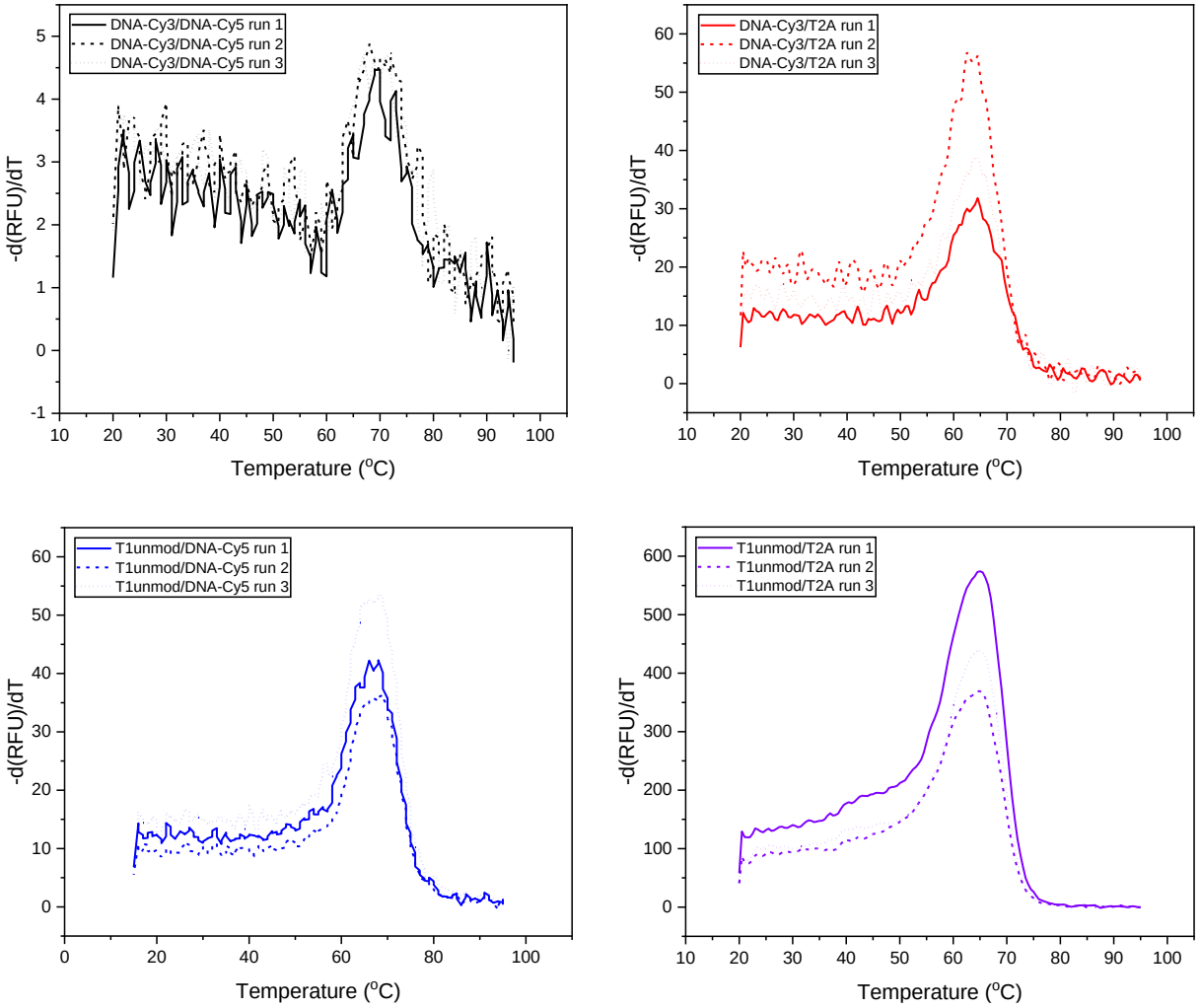

Figure 8.75: Thermal melting graphs for **DNA-Cy3**, **DNA-Cy5**, and **T1unmod** duplexes, plotting temperature of the oligonucleotide sample versus the negative rate of change in the RFU of SYBR Green I.

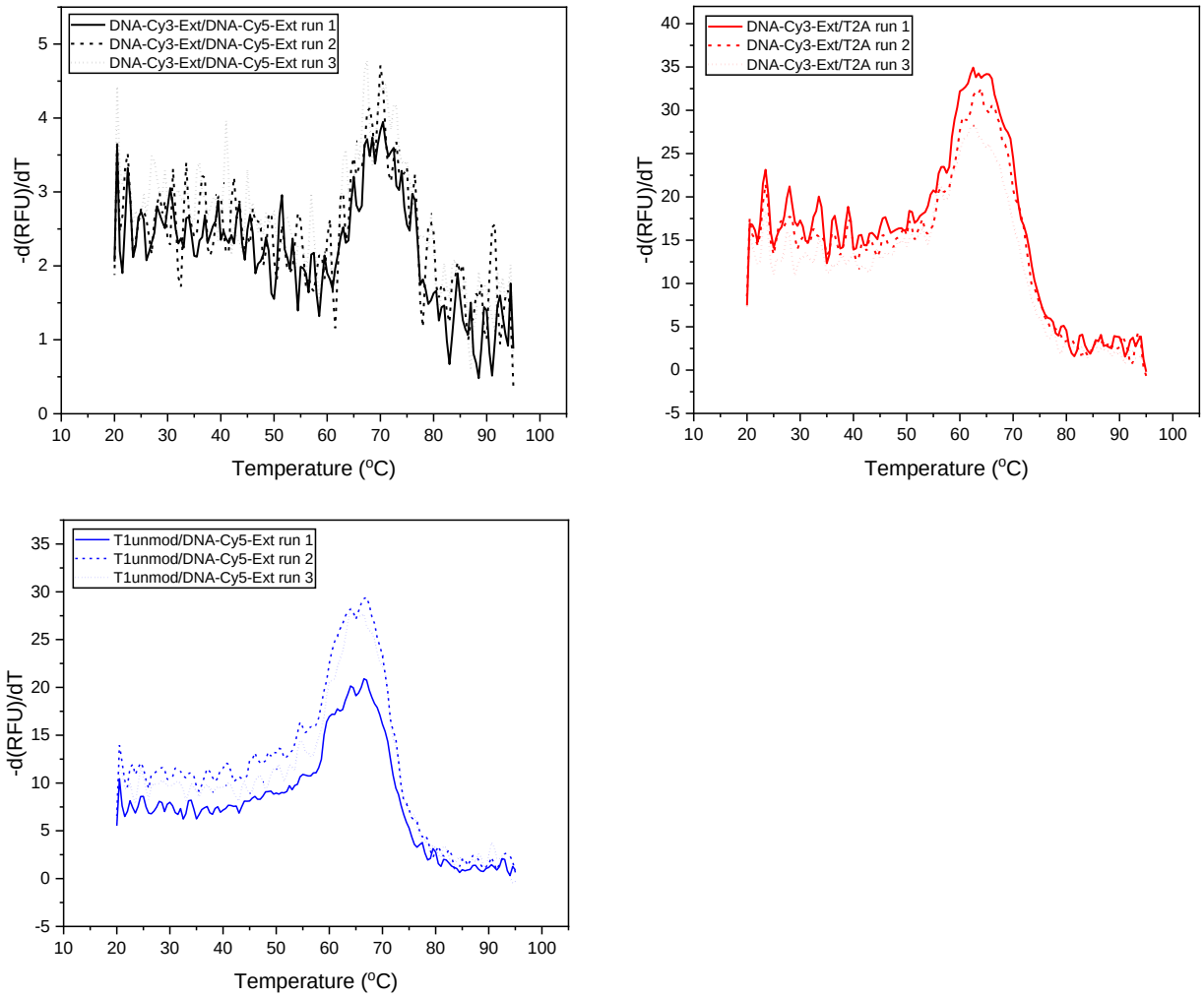

Figure 8.76: Thermal melting graphs for **DNA-Cy3-Ext** and **DNA-Cy5-Ext** duplexes, plotting temperature of the oligonucleotide sample versus the negative rate of change in the RFU of SYBR Green I.

8.4.2. Solution Fluorescence Spectroscopy

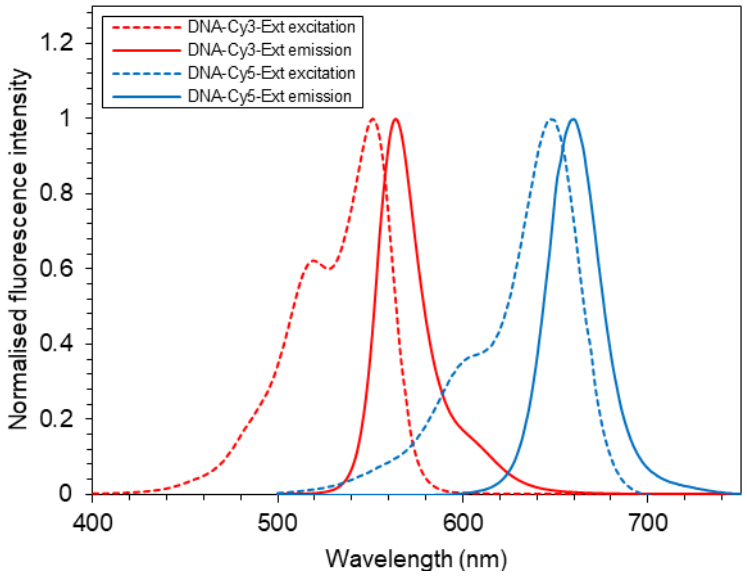

Figure 8.77: Normalised excitation and emission spectra of **DNA-Cy3-Ext** and **DNA-Cy5-Ext**. [DNA] = 1 μM. Measured in sodium phosphate buffer pH 7.0, 100 mM NaCl. DNA-Cy3 λ_{ex} = 554 nm, λ_{em} = 570 nm; DNA-Cy5 λ_{ex} = 650 nm, λ_{em} = 665 nm.

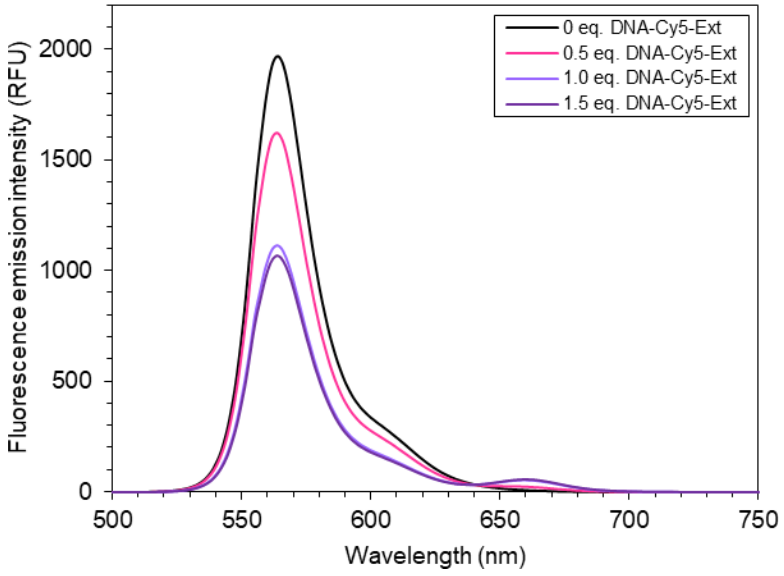

Figure 8.78: Emission spectra of **DNA-Cy5-Ext** titrated into a solution of **DNA-Cy3-Ext** (1 μM). The decrease in emission at 570 nm is indicative of the quenching of the Cy3 fluorescence by Cy5, and the small increase in emission at 660 nm is the result of FRET from the Cy3 to the Cy5. Measured in sodium phosphate buffer pH 7.0, 100 mM NaCl. λ_{ex} = 554 nm. Spectra have been background-subtracted using a spectrum of DNA-Cy5-Ext excited at 554 nm to account for the direct excitation of Cy5.

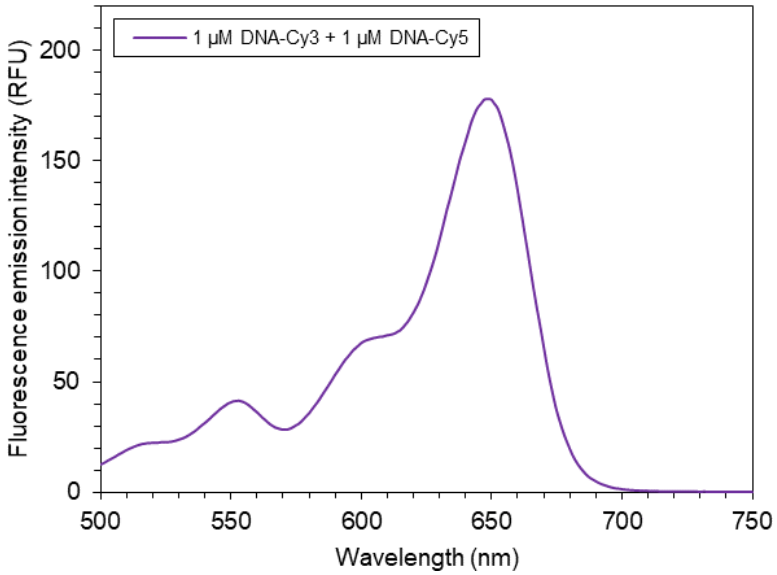

Figure 8.79: Excitation spectrum of equimolar amounts of **DNA-Cy3** and **DNA-Cy5** (1 µM), λ_{em} = 665 nm. Measured in sodium phosphate buffer pH 7.0, 100 mM NaCl.

8.4.3. MOF Characterisation

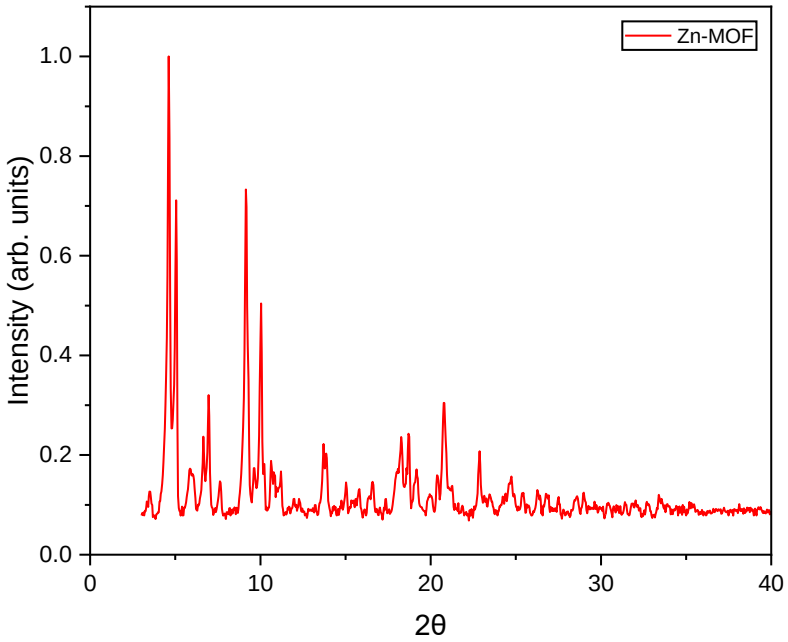

Figure 8.80: PXRD pattern of the Zn UiO-68 MOF.